Physics of Atomic Nuclei, Vol. 67, No. 2, 2004, pp. 211–216. Translated from Yadernaya Fizika, Vol. 67, No. 2, 2004, pp. 227–233.

NUCLEI
Theory

Neutron Yield upon the Irradiation of Thin TiD_2 Foils with a Superintense Laser Pulse

V. P. Krainov*

Moscow Institute for Physics and Technology,
Institutskiĭ proezd 9, Dolgoprudnyĭ, Moscow oblast, 141700 Russia

Received January 9, 2003; in final form, May 19, 2003

Abstract—The yield of neutrons from the thermonuclear-fusion reaction $D(d,n)^3He$ induced in a thin skin layer by the interaction of a high-intensity laser pulse of picosecond duration with thin TiD_2 foils is calculated. A multiple ionization of titanium atoms at the leading edge of the laser pulse is considered. The heating of free electrons proceeds via induced inverse bremsstrahlung in elastic electron scattering on multiply charged titanium ions. The electron temperature is calculated. It proves to be about 10 keV at the laser-pulse intensity of 5×10^{18} W/cm^2 at the peak. The neutron yield is estimated at 10^4 per laser pulse. These results are in qualitative agreement with experimental data. © *2004 MAIK "Nauka/Interperiodica".*

1. INTRODUCTION

Thermonuclear fusion caused by the irradiation of deuterated solid-state targets and clusters with the field of superintense laser pulses was intensively investigated both experimentally [1–5] and theoretically [6–9]. The number of neutrons emitted in the thermonuclear-fusion reaction $D(d,n)^3He$ induced by the interaction of superintense laser pulses with a dense subcritical deuterium plasma was measured in [10]. It was found that, in such interactions, neutrons arise as the result of a direct heating of deuterons. These neutrons provide information about the spectrum of accelerated deuterons and about the heating mechanism.

The Coulomb explosion of substance is a dominant mechanism in the case of femtosecond laser pulses. A considerable number of electrons are removed by the laser field from a plasma cloud, whereupon this cloud expands rapidly owing to the Coulomb repulsion of positively charged multiply ionized atomic ions. Accelerated deuterons collide with one another, generating the thermonuclear-fusion reaction. In the case of picosecond (or longer) laser pulses, however, the hydrodynamic pressure of the expanding electron gas is the basic mechanism of expansion, a quasineutral plasma expanding at a speed equal to the speed of sound.

The present theoretical investigation is devoted to considering the semiquantitative physics of the above processes for the example of the irradiation of thin (10 μm) TiD_2 foils with the field of a superintense laser pulse characterized by the peak intensity of 5×10^{18} W/cm^2, the laser frequency of $\omega = 1.18$ eV, and the pulse duration (FWHM) of 1.5 ps. These parameters are typical of experiments. Multiply charged atomic ions of titanium that emerge at the leading edge of the laser pulse are necessary for an intensive heating of electrons owing to induced inverse bremsstrahlung [11]. Indeed, the frequency of electron–ion collisions is proportional to the square of the atomic-ion charge. In the case of superintense light fields, ionization is an above-barrier process [12].

The Gaussian envelope of this pulse for the radiation-field strength has the form

$$F = F_0 \exp(-t^2/\tau^2), \tag{1}$$

where $F_0 = 11.9$ a.u. is the value of the strength at the peak and $\tau = 1.27$ ps.

Titanium deuteride TiD_2 is a gray dielectric powder of density $\rho = 4.0$ g/cm^3. Its molecular mass is 51.9 amu, so that the concentration of solid TiD_2 is $n_a = 4.64 \times 10^{22}$ cm^{-3}. The main objective of this study consists in approximately calculating the neutron yield during and after the irradiation of TiD_2 foils with a superintense laser pulse having the aforementioned parameters. The basic quantity determining the neutron yield is the kinetic energy of accelerated deuterons, since the probability of the thermonuclear-fusion reaction depends exponentially on this energy because of the tunnel character of deuteron fusion. A direct energy transfer from heated electrons to

*e-mail: krainov@online.ru

deuterons (and atomic ions of titanium) takes several tens or even hundreds of picoseconds. Therefore, there is no such transfer of energy in our case.

2. PENETRATION OF A LASER FIELD IN A DEUTERIUM PLASMA

At the leading edge of a laser pulse, the electromagnetic field penetrates through the entire dielectric plate and produces a single above-barrier ionization of titanium atoms (the first ionization potential of the titanium atom is equal to $E_1 = 6.8$ eV). According to the Bethe rule [13], the corresponding laser-field intensity F_1 can be expressed in terms of the first ionization potential E_1 as (hereafter, we employ the atomic system of units where the electron charge and mass and the Planck constant are equal to unity)

$$F_1 = E_1^2/4 = 0.0156 \text{ a.u.} \quad (2)$$

The instant of this above-barrier ionization is $t_1 = -3.27$ ps at the leading edge of a laser pulse (the peak of the pulse corresponds to the instant $t = 0$).

Thus, a dense plasma arises in the focal volume, the corresponding plasma frequency being

$$\omega_p = \sqrt{4\pi n_a} = 0.294 \text{ a.u.} \quad (3)$$

This frequency is much higher than the laser-pulse frequency of $\omega = 0.0434$ a.u. Immediately upon the first ionization, laser radiation therefore penetrates only into a thin skin layer at the plate surface. The small skin-layer depth is

$$l = c/\omega_p = 247 \text{ Å} = 466 \text{ a.u.} \quad (4)$$

This value is much smaller than the thickness of a TiD_2 plate (10 μm). Therefore, the laser field does not penetrate into the bulk of the plate until the critical density of the arising plasma is achieved owing to expansion. The critical plasma density is determined from the relation

$$\omega = \sqrt{4\pi n_c}. \quad (5)$$

The result is $n_c = 1.01 \times 10^{21}$ cm^{-3}. Thus, we have $n_a/n_c = 46$.

A considerable part of electromagnetic radiation is reflected from the arising plasma. Therefore, the electric-field strength within the skin layer is lower than that in the incident electromagnetic wave. The reflection coefficient depends on the degree of sharpness of the plasma–vacuum boundary. We assume that this boundary is not very sharp, so that it is qualitatively correct to equate the electric-field strength in the skin layer to that in the incident wave.

Let us first consider the model of an expanding plasma sphere in the focal volume, the initial radius being set to $R_0 = 5$ μm. For the free-electron density to decrease to the critical value, this radius must increase by the factor

$$R/R_0 = (n_a/n_c)^{1/3} = 3.6. \quad (6)$$

This increase in the radius is rather great. In view of this, neutron production in thermonuclear fusion will be taken into account below only in the skin layer.

The main mechanism of the expansion of the plasma cloud that is produced by a picosecond laser pulse is a hydrodynamic expansion occurring at the ion-sound speed [14]. This speed is rather low at initial stages of the multiple ionization of titanium atoms at the leading edge of the laser pulse, since the emitted electrons have not yet been heated. As a matter of fact, the plasma cloud does not expand until the fifth ionization of titanium atoms occurs.

Deuterons arising upon the sequential ionization of atoms in a TiD_2 film are light particles in relation to atomic ions of titanium. Therefore, deuterons move faster, so that the surface region of an expanding plasma includes an excess number of deuterons (together with the corresponding number of free electrons that are necessary for preserving plasma quasineutrality). The ion-sound speed is calculated for deuterons. One must also consider that the number of deuterons is twice as great as the number of atomic ions of titanium. The calculation is performed for the time intervals between successive events of titanium-atom ionization.

The main physical parameters characterizing the interaction of laser radiation with a solid body are quoted in Table 1. The first column gives the charge Z of atomic ions of titanium that are generated at the leading edge of the laser pulse. Deuterium atoms are ionized between the instants of time that correspond to $Z = 2$ and 3. The maximum charge of atomic ions of titanium is $Z = 12$ for the given value of the laser-pulse intensity at the peak.

The second column of Table 1 contains the ionization potentials of multiply charged atomic ions of titanium (in atomic units [15]). In the third column, we present the quantum states of emitted electrons within the atomic-shell model.

The fourth column displays the field-strength values at which, according to the Bethe model [12], multiply charged titanium ions of given degree of ionization undergo above-barrier ionization (we disregard tunnel ionization at the leading edge of the laser pulse because of a high value of the laser intensity at the peak and because of a short pulse duration):

$$F(Z) = (E_Z)^2/4Z. \quad (7)$$

In the fifth column, we present the instants of time at the leading edge of the laser pulse that were calculated according to (1); they correspond to ionization at a given charge Z of a titanium atomic ion.

Table 1. Main physical parameters characterizing the interaction of laser radiation with solid-state targets at the leading edge of a laser pulse

Z	E_Z, a.u.	State	F, a.u.	t, ps	γ	E_e, a.u.	ω_p, a.u.	l, a.u.
1	0.290	$4s^2$	0.0156	−3.27	1.967	0.004	0.294	466
2	0.496	$4s$	0.0308	−3.10	1.403	0.011	0.416	329
3	1.010	$3d^2$	0.0850	−2.82	0.726	0.085	0.657	208
4	1.591	$3d$	0.158	−2.64	0.490	0.277	0.720	190
5	3.649	$3p^6$	0.666	−2.16	0.176	5.920	0.778	176
6	4.392	$3p^5$	0.804	−2.08	0.160	7.960	0.354	387
7	5.175	$3p^4$	0.956	−2.02	0.146	10.47	0.213	643
8	6.262	$3p^3$	1.225	−1.91	0.125	16.69	0.121	1130
9	7.060	$3p^2$	1.385	−1.86	0.118	19.84	0.100	1370
10	7.935	$3p$	1.574	−1.81	0.110	24.49	0.086	1600
11	9.743	$3s^2$	2.157	−1.66	0.089	46.20	0.059	3480
12	10.71	$3s$	2.390	−1.61	0.084	55.00	0.056	3960

The sixth column contains the dimensionless Keldysh parameter [13]

$$\gamma = \frac{\omega\sqrt{2E_Z}}{F}, \tag{8}$$

which determines the character of ionization. Since $\gamma < 1$ for $Z > 2$, multiphoton ionization does not occur. The seventh column gives the mean kinetic energy of an electron emitted under conditions of above-barrier ionization induced by the linearly polarized field of laser radiation [16]:

$$E_e = 3\omega/4\gamma^3. \tag{9}$$

We can see that this kinetic energy is low in relation to the thermal energy acquired by each electron heated by a laser field.

In the eighth column, we display plasma-frequency values calculated for a given instant of time by the formula

$$\omega_p = \sqrt{4\pi(Z+2)n_a(t)}, \tag{10}$$

where the term "+2" takes into account two free electrons escaping from two deuterium atoms in each of the TiD_2 molecules for $Z > 2$. The quantity $n_a(t)$ is the current concentration of atomic ions of titanium; it decreases with time because of plasma-cloud expansion. It follows that, with increasing charge Z, the plasma frequency first increases and then decreases.

The last column in Table 1 gives the skin-layer depth determined by the relation

$$l = \frac{c}{\sqrt{\omega_p^2 - \omega^2}}. \tag{11}$$

First, this quantity decreases owing to an increase in the number of free electrons in the multiple ionization of titanium atoms, but, later on, it begins to increase because of plasma-cloud expansion.

3. HEATING OF ELECTRONS IN INDUCED INVERSE BREMSSTRAHLUNG IN THE MULTIPLE IONIZATION OF TITANIUM ATOMS

The laser frequency is higher than the frequency of electron–ion collisions because a fast heating by a superintense laser field leads to the emergence of hot electrons, which collide rarely with atomic ions. Therefore, the kinetic energy that each electron acquires upon one collision is equal to the doubled vibrational energy of the electron, $F^2/2\omega^2$.

The frequency of collisions between electrons and atomic ions of titanium that have a charge Z is given by the relation

$$\nu_{ei} = \frac{4\sqrt{2\pi}Z^2 n_a(Z)\Lambda}{3T^{3/2}}, \tag{12}$$

which is known in plasma theory. This relation is valid if the electron temperature is higher than the electron

Table 2. Heating of electrons at the leading edge of a laser pulse in the course of the multiple ionization of titanium atoms

Z	T, a.u.	V, a.u.	$n_a(Z)$
6	370	0.24	1.25×10^{-3}
7	390	0.33	4.01×10^{-4}
8	415	0.34	1.18×10^{-4}
9	390	0.34	7.28×10^{-5}
10	380	0.33	4.86×10^{-5}
11	420	0.34	2.10×10^{-5}
12	405	0.34	1.75×10^{-5}

vibrational energy. This inequality holds up to the instant $t = -1.6$ ps, which corresponds to the twelfth ionization of the titanium atom (see Table 1). Finally, the quantity

$$\Lambda = \ln \frac{T}{\hbar\omega} \tag{13}$$

is the quantum Coulomb logarithm.

Thus, the increase in the electron temperature within this time interval is determined by the differential equation

$$\frac{3}{2}\frac{dT}{dt} = \frac{F^2}{2\omega^2}\frac{4\sqrt{2\pi}Z^2 n_a(Z)\Lambda}{3T^{3/2}}, \tag{14}$$

where $n_a(Z)$ is the concentration of atomic ions of titanium at the instant corresponding to the charge Z. Integrating this equation with respect to time, we find the explicit time dependence of the growing electron temperature in the form

$$T^{5/2}(t) = T_0^{5/2} + \frac{10\sqrt{2\pi}}{9\omega^2} n_a(Z) F^2(t) Z^2(t)\Lambda, \tag{15}$$

where T_0 is the electron temperature prior to the ionization of a titanium atomic ion having the charge Z.

The values of T were calculated according to Eq. (15) at each step of the multiple ionization of a titanium atom. Table 2 presents the mean values of the ion-sound speed

$$V = \sqrt{\frac{\overline{T}}{M_d}}, \tag{16}$$

where M_d is the deuteron mass and $\overline{T}$ is the mean electron temperature within the time interval between the Zth and the $(Z+1)$th ionization. At the end of each step of ionization, we reduce the electron temperature as

$$\frac{Z}{Z+1} T \to T, \tag{17}$$

because new emitted electrons are produced with a kinetic energy (see Table 1) lower than the kinetic energy acquired by preceding electrons in electron–ion collisions. Table 2 gives the values of the temperature T. It also displays the results obtained for the concentration of atomic ions of titanium by using the relation

$$n_a(Z+1) = \frac{l}{l + V\Delta t} n_a(Z). \tag{18}$$

The values of the skin-layer depth l are given in Table 1.

As was mentioned above, deuterons move much faster than atomic ions of titanium. In view of this, the ion-sound speed is calculated under the assumption that the surface of the expanding plasma contains only deuterons and electrons. Table 2 quotes data beginning from the sixth ionization of titanium atoms, since, at previous instants of time, the laser field is rather weak and does not lead to the heating of electrons. The instants of time in Table 2 correspond to the instants of time in Table 1 for the ionization of titanium atoms having a charge Z.

The surface of the expanding plasma is assumed to be flat, since the expansion of the plasma in the direction orthogonal to the target surface is rather slow within the time interval being considered. The calculations are stopped when the dimensions of the plasma cloud become approximately identical in all directions—that is, when the distances along the normal to the target surface are about the focal diameter of a laser pulse (15 μm). In my opinion, this instant of time also corresponds to the completion of the thermonuclear-fusion reaction.

It can be seen that the ion-sound speed V is virtually constant. We assume that this speed does not change upon the completion of the multiple-ionization process either.

4. HEATING OF ELECTRONS AT THE PEAK AND THE TRAILING EDGE OF A LASER PULSE

Upon the completion of the multiple ionization of titanium atoms ($t = -1.6$ ps), the vibrational energy of electrons becomes higher than their thermal energy (see Tables 1, 2). In this case, relation (12) becomes inapplicable and the frequency of electron–ion collisions takes the form

$$\nu_{ei} = \frac{4\pi Z^2 n_a(t)\Lambda}{(F(t)/\omega)^3}. \tag{19}$$

The increase in the electron temperature is calculated from the equation

$$\frac{3}{2}\frac{dT}{dt} = \frac{F^2(t)}{2\omega^2}\frac{4\pi Z^2 n_a(t)\Lambda}{(F(t)/\omega)^3}. \tag{20}$$

We use this equation in the time interval from -1.6 to $+1.6$ ps (that is, in the vicinity of the laser-pulse peak), setting $Z = 12$. According to the data in Table 2, the initial electron temperature is $T_0 = 405$ a.u. By numerically integrating Eq. (20), we find that, within this time interval, the increase in the electron temperature is moderate: $\Delta T = 25$ a.u. The reason is that the frequency of electron–ion collisions is small because of a very high vibrational energy of electrons. Thus, the final electron temperature at the instant $+1.6$ ps is $T = 430$ a.u. The final density of atomic ions of titanium is $n_a = 1.4 \times 10^{-6}$ a.u. The final concentration of deuterons is twice as large as this value.

At $t > 1.6$ ps, the vibrational energy of electrons strongly decreases again at the trailing edge of the laser pulse, and we must calculate the heating of electrons according to formula (14), starting from $Z = 12$. The result is

$$T^{5/2}(t) = T^{5/2}(t_0 = 1.6\ \text{ps}) + \frac{10\sqrt{2\pi}}{9\omega^2} Z^2 \Lambda \int_{t_0}^{\infty} n_a(t) F^2(t) dt. \quad (21)$$

This contribution to the heating of electrons is also small because of a low concentration in a strongly expanded plasma. A numerical calculation yields the value of $\Delta T = 5$ a.u., so that the final electron temperature is $T = 435$ a.u. $= 11.8$ keV. Of course, the kinetic energy of deuterons differs from this value, since the deuterons have the same velocity V at the surface of the plasma cloud as electrons (see Table 2); therefore, this is the ion-sound speed. We assume that this velocity becomes the thermal velocity for deuterons because of their collisions upon the passage of the laser pulse. The kinetic energy of a deuteron can be estimated as

$$E_d = M_d V^2/2 = T/2 = 3T_d/2. \quad (22)$$

Thus, the final deuteron temperature is $T_d = 4$ keV.

5. THERMONUCLEAR-FUSION REACTION

In accordance with [17], the rate of the thermonuclear-fusion reaction $D(d, n)^3He$ is

$$\langle \sigma V \rangle = 10^{-19}\ \text{cm}^3/\text{s} \quad (23)$$

at the deuteron temperature of 4 keV. The neutron yield is calculated according to the equation

$$N_n = \frac{1}{4} N_d \langle \sigma V \rangle n_a t_f, \quad (24)$$

where N_d is the number of deuterons that participate in the thermonuclear-fusion reaction. A factor of $1/2$ takes into account the reduction of the atomic density with time owing to plasma expansion; the second factor of $1/2$ takes into account the fact that N_d deuterons collide with one another. The quantity t_f is the nuclear-reaction time. This time can be estimated as $t_f = S^{1/2}/V$ (later on, the plasma cloud transforms into a spheroidal formation). Further, we can recast N_d into the form

$$N_d = 2 n_a S l, \quad (25)$$

where $S = (15\ \mu\text{m})^2$ is the square of the focal radius of a laser pulse, the ion-sound speed is $V = 0.34$ a.u. according to the data in Table 2, $l = 176$ a.u. is the initial depth of the skin layer in the case of the fifth ionization of titanium atoms, and $n_a = 0.00687$ a.u. is the initial concentration of titanium atoms (the concentration of deuterons is twice as large as this value). Thus, we have $N_d = 2 \times 10^{11}$ deuterons in the initial skin layer.

Of course, only a small fraction of these deuterons participate in the thermonuclear-fusion reaction. It follows from relations (23) and (24) that $N_d \langle \sigma V \rangle = 3.2$ a.u.; therefore, the final result for the neutron yield is $N_n = 2 \times 10^4$.

Similar estimates follow from experiments with deuterium clusters irradiated with superintense laser pulses [2, 4]. It should be emphasized in conclusion that the estimates obtained in this study are approximate because of imperfect data on the focal diameter of a laser beam and on other parameters.

In addition, the following comment is in order: the fact that part of the energy of the generated laser plasma is expended in bremsstrahlung was disregarded in the present calculations.

6. CONCLUSION

The results of this study demonstrate (see also [18]) that the heating of electrons is relatively small. In [1], it was shown experimentally that some of the electrons acquire an energy of a few MeV. This occurs because of strong relativistic effects: the magnetic component of the Lorentz force acts on electrons oscillating along the direction of the electric-field vector at a speed close to the speed of light, this component being directed along the vector of laser-wave propagation—that is, orthogonally to the foil surface. In the ultrarelativistic case, this force is on the same order of magnitude as F_0. Over the skin-layer thickness l, it accelerates an electron to a kinetic energy of $F_0 l$. Using the values of $F_0 = 12$ a.u. and $l = 4000$ a.u., we find that such an electron acquires an energy of about 2 MeV. In contrast to the ponderomotive energy, this energy does not disappear when a laser pulse is switched off.

Of course, an electron having such a high energy cannot transfer it to a deuteron in a collision since

such collisions are very rare. The process of energy transfer looks as follows [19]. The flux of electrons moving along the direction of the laser beam in a plasma generates a strong ring magnetic field. In turn, this magnetic field acts on the flux of electrons in the radial direction, compressing it (pinch effect). Ions do not have time to be compressed because of inertia. As a result, the region of a noncompensated negative charge arises on the beam axis, and this leads to the propagation of the laser beam along this axis (relativistic self-focusing) because of the absence of screening. Therefore, the depth of the skin layer effectively increases [20]. This increase leads to a growth of the kinetic energy of some electrons in relation to the above estimate of 2 MeV. After the laser pulse is switched off, the Coulomb explosion of the noncompensated negative charge occurs, whereupon radially diverging electrons carry along deuterons by virtue of the plasma-electroneutrality condition. The deuteron energy becomes as high as a few hundred keV; of course, this increases the probability of the thermonuclear-fusion reaction with respect to the above estimates for deuteron energies of a few keV.

Another factor that causes the enhancement of the heating of electrons comes into play in the case of oblique incidence of a laser pulse onto a solid target. In this case, there exists an electric-field-strength component that is normal to the target surface (for a linearly polarized electromagnetic wave of so-called p polarization). Under the effect of this component, free electrons inside the plasma oscillate in the normal direction, periodically escaping from the plasma into a vacuum and returning to the plasma (with the laser-field frequency). While an electron resides in a vacuum, it can take, from the field, a kinetic energy on the same order of magnitude as its vibrational energy and return to the plasma with an energy that is much higher than that which it had before. This "vacuum-heating" mechanism was proposed by F. Brunel [21]. It enhances the heating of both the electron and the ion component. For thin foils, it is of importance that, because of the aforementioned fast motion of the electron flux, the charges are then separated in the direction normal to the foil surface. Owing to the emerging quasistatic electric field, ions escaping from the back surface of the foil are accelerated to energies of a few tens of MeV [22].

Thus, there exist a great number of physical factors that lead to the heating of both the electron and the ion component in a plasma irradiated with a superstrong laser pulse of femtosecond and picosecond duration.

ACKNOWLEDGMENTS

This work was supported in part by the Russian Foundation for Basic Research (project nos. 04-02-16499, 02-02-16678), by the International Center for Science and Technology (project no. 2155), and by CRDF (project no. MO-011-0).

REFERENCES

1. G. Pretzler *et al.,* Phys. Rev. E **58**, 1165 (1998).
2. T. Ditmire *et al.,* Nature **398**, 489 (1999).
3. J. W. G. Tisch *et al.,* Phys. Rev. A **60**, 3076 (1999).
4. J. Zweiback *et al.,* Phys. Rev. Lett. **85**, 3640 (2000).
5. M. Schnurer *et al.,* Eur. Phys. J. D **14**, 331 (2001).
6. V. P. Krainov and M. B. Smirnov, Zh. Éksp. Teor. Fiz. **119**, 719 (2001) [JETP **92**, 626 (2001)].
7. V. P. Krainov and M. B. Smirnov, Zh. Éksp. Teor. Fiz. **120,** 555 (2001) [JETP **93**, 485 (2001)].
8. P. B. Parks *et al.,* Phys. Rev. A **63**, 063203 (2001).
9. I. Last and J. Jortner, Phys. Rev. A **64**, 063201 (2001).
10. S. Fritzler *et al.*, Phys. Rev. Lett. **89**, 165004 (2002).
11. V. P. Krainov, Zh. Éksp. Teor. Fiz. **119**, 1109 (2001) [JETP **92,** 960 (2001)].
12. S. Augst *et al.,* J. Opt. Soc. Am. B **8**, 858 (1991).
13. N. B. Delone and V. P. Krainov, *Multiphoton Processes in Atoms,* 2nd ed. (Springer, Berlin, 2000).
14. V. P. Krainov and M. B. Smirnov, Phys. Rep. **380**, 237 (2002).
15. *Handbook of Chemistry and Physics*, Ed. by D. R. Lide, 79th ed. (CRC, Boca Raton, 1998–1999).
16. V. P. Krainov, J. Opt. Soc. Am. B **14**, 425 (1997).
17. E. Teller, *Fusion* (Academic, New York, 1981).
18. V. P. Krainov, Plasma Phys. Controlled Fusion **45**, L23 (2003).
19. A. Pukhov and J. Meyer-ter-Vehn, Phys. Rev. Lett. **76**, 3975 (1996).
20. R. Wagner *et al.,* Phys. Rev. Lett. **78**, 3125 (1997).
21. F. Brunel, Phys. Rev. Lett. **59**, 52 (1987).
22. A. J. Mackinnon *et al.*, Phys. Rev. Lett. **88**, 215006 (2002).

Translated by A. Isaakyan

Physics of Atomic Nuclei, Vol. 67, No. 2, 2004, pp. 217–225. Translated from Yadernaya Fizika, Vol. 67, No. 2, 2004, pp. 234–242.

NUCLEI
Theory

Internal Conversion in Hydrogen-like Ions

F. F. Karpeshin[1)], Yu. N. Novikov, and M. B. Trzhaskovskaya

Petersburg Nuclear Physics Institute, Russian Academy of Sciences, Gatchina, 188350 Russia

Received June 17, 2002; in final form, October 31, 2002

Abstract—The probability of internal gamma-ray conversion is theoretically investigated for hydrogen-like ions versus the corresponding neutral atoms. The relevant calculations are performed by the relativistic Dirac–Fock method. The results reveal that the effect of multiple ionization on the coefficients of internal conversion in the K shell is maximal near the ionization threshold and for transitions of high multipole order, where this effect can be as great as a few orders of magnitude. The distinction between the coefficient of internal conversion in the K shell of a neutral atom and that in the respective hydrogen-like ion decreases with increasing transition energy, but it remains sizable for transitions of practical importance. It is found that the ionization of an atom to a hydrogen-like ion with allowance for conversion in external atomic shells may change significantly (by up to eight orders of magnitude) the lifetime of the nucleus being considered. The predicted effects can be observed in experiments with beams of relativistic heavy ions.

Owing to the commissioning of facilities that are able to accumulate and identify relativistic reaction products [1], there appeared, in recent years, the possibility of studying special features of nuclear processes in highly ionized atoms [2–6]. A comparison of theoretical results obtained in this realm with relevant experimental data might serve as a modern test of quantum electrodynamics. Moreover, investigation of processes in multiply charged ions makes it possible to discover and explore new nuclear processes—for example, this led to the discovery of resonance subthreshold conversion for the 35.492-keV $M1$ transition in $^{125m}_{52}$Te [4–6].

The effect of atomic-shell screening on the probability of the internal-conversion process was discussed in many studies for ordinary atoms (see [7] and references therein) and for muonic atoms in [8, 9]. However, the majority of studies considered changes in the internal-conversion probability that were due either to the use of different atomic potentials in calculations or to a low-multiplicity ionization of an atom.

The objective of the present study is to analyze the behavior of the internal-conversion coefficients in hydrogen-like ions versus the behavior of the internal-conversion coefficients for the respective neutral atoms. The importance of such calculations became obvious as soon as the development of experimental techniques made it possible to study, at the GSI accelerator and at GANIL, nuclei deprived of electron shells. The effect of screening can be assessed on the basis of a comparison of the probabilities of the same conversion transition in a neutral atom and in the respective hydrogen-like ion. The distinctions between the probabilities of deexcitation by conversion must manifest themselves in the distinction between the lifetime of an excited level in a hydrogen-like ion and that in the respective neutral atom. Such distinctions between the lifetimes can explored experimentally.

We have performed comparative calculations of the coefficient of internal conversion in the K shells of the neutral atoms and hydrogen-like ions of $_{30}$Zn, $_{68}$Er and $_{81}$Tl. The choice of chemical elements was not dictated by the requirements of specific experiments, but it was motivated by the need for considering, for a theoretical analysis of the effect, representative elements from various regions of the periodic table. The calculations for the neutral atoms were performed by the Dirac–Fock method, exchange interaction being exactly taken into account [10–12]. For a neutral atom, the internal-conversion coefficient was calculated with allowance for a hole in the shell where conversion occurred; that is, the wave function for the conversion electron was determined in a self-consistent field of an ion having a vacancy in the K shell. For hydrogen-like ions, the electron wave functions in the initial and final states were calculated in the Coulomb field of a nucleus with allowance for its finite size. It is advisable to recall that the inclusion of both the static and the dynamical effect of finite nuclear sizes plays an important role in the theory of conversion [13]. These effects lead to considerable

[1)]Institute of Physics, St. Petersburg State University, St. Petersburg, 198504 Russia.

Table 1. Distinctions Δ in percent [see Eq. (1)] between the coefficients of internal conversion in the K shell of a neutral atom per electron and the internal-conversion coefficients for the corresponding hydrogen-like ion

Z	E_γ, keV	$E_k^{(\mathrm{H})}$, keV	$E1$	$M1$	$E2$	$M3$	$M4$	$E5$
30	12.695	0.3	−11	−9.8	−19	−16	−43	−91
	12.995	0.6	−6.5	−5.1	−14	−11	−36	−85
	13.395	1.0	−4.0	−2.6	−10	−7.8	−29	−78
	22.395	10	1.4	2.4	−0.1	2.3	−1.1	−17
	42.395	30	2.4	3.0	2.0	3.8	3.0	−2.9
	112.395	100	3.0	3.3	2.9	3.9	4.0	1.9
	512.395	500	3.3	3.4	3.3	3.6	3.7	3.3
	1012.395	1000	3.3	3.4	3.4	3.5	3.5	3.5
68	67.637	0.3	−32	−31	−37	−36	−53	−92
	67.937	0.6	−22	−21	−28	−27	−46	−89
	68.337	1.0	−16	−15	−23	−22	−41	−86
	77.337	10	−3.4	−2.3	−7.8	−6.3	−18	−52
	97.337	30	−0.9	0.0	−3.3	−1.8	−6.6	−24
	167.337	100	0.6	1.1	−0.3	0.9	−0.2	−5.8
	567.337	500	1.5	1.6	1.4	1.9	1.9	1.2
	1067.337	1000	1.6	1.7	1.6	1.9	2.0	1.8
81	99.063	0.3	−38	−37	−43	−42	−58	−92
	99.363	0.6	−27	−26	−33	−32	−50	−90
	99.763	1.0	−20	−19	−27	−26	−45	−88
	108.763	10	−4.8	−3.6	−10	−9.0	−22	−60
	128.763	30	−1.9	−0.7	−5.1	−3.7	−10	−31
	198.763	100	−0.1	0.7	−1.3	−0.1	−2.1	−8.8
	598.763	500	1.2	1.4	1.1	1.6	1.4	6.4
	1098.763	1000	1.3	1.6	1.4	1.7	1.8	1.6

Note: The internal-conversion coefficients for neutral atoms were calculated with allowance for a hole in the K shell (see main body of the text); $E_k^{(\mathrm{H})}$ is the conversion-electron energy in a hydrogen-like ion.

deviations of the internal-conversion coefficients from those values that could be obtained in the calculations with Coulomb wave functions, especially for transitions of low multipole order. By way of example, we indicate that, for $M1$ transitions in heavy nuclei, the inclusion of finite nuclear sizes may change the internal-conversion coefficient by a factor of 3.

In the case of a neutral atom, experimental data on the K-electron binding energy from [14] were employed in the calculations, while, for a hydrogen-like ion, use was made of the theoretical values obtained from the calculation by the Dirac–Fock method.

Table 1 presents the distinctions between the coefficients of internal conversion in the K shell of a neutral atom per electron, $\alpha_{\mathrm{at}}^{\tau L}$, and the internal-conversion coefficients $\alpha_{\mathrm{ion}}^{\tau L}$ for the hydrogen-like ion of the corresponding element; that is, the quantities

$$\Delta = \left(\frac{\alpha_{\mathrm{ion}}^{\tau L} - \alpha_{\mathrm{at}}^{\tau L}}{\alpha_{\mathrm{at}}^{\tau L}}\right) \cdot 100\%, \qquad (1)$$

where τ labels the electric ($\tau = E$) or the magnetic ($\tau = M$) type of nuclear transition and L is the multipolarity of the transition being considered. The internal-conversion coefficients are given for

eight values of the transition energy E_γ such that the kinetic energies of the conversion electron for hydrogen-like ions, $E_k^{(\mathrm{H})}$, take the same values in the range $0.3 \le E_k^{(\mathrm{H})} \le 1000$ keV for all of the elements being considered. The results reveal that, by and large, the effect of multiple ionization on the internal-conversion coefficient is maximal in the vicinity of the threshold and for transitions of high multipole order. In those cases, the changes in the coefficient of internal conversion in the K shell of a hydrogen-like ion in relation to the coefficient of internal conversion in the K shell of the respective neutral atom may be as large as one order of magnitude. With increasing transition energy, this difference in the internal-conversion coefficient decreases fast, but it may remain sizable for 100- to 200-keV transitions, which are of practical importance.

Against this background, it may seem surprising that Δ depends only slightly on the atomic number Z of an element. This quantity increases with increasing Z at low energies ($E_k^{(\mathrm{H})} \lesssim 10$ keV) and decreases slightly for heavier elements if $E_k^{(\mathrm{H})} > 100$ keV. This behavior may be understood if one considers that electron–electron interaction is characterized by the small parameter $1/Z$. In the behavior of the internal-conversion coefficient for high multipole orders, strong threshold effects that lead to the violation of electron–muon scaling were previously indicated in [9], where the values of these coefficients were compared with the conversion coefficients for muonic atoms. Physically, these effects may be explained by the fact that a conversion electron must overcome a strong attracting field (the higher the degree of ionization, the stronger this attracting field). At higher energies, an electron easily escapes from the atom being considered. It follows that, in the vicinity of the threshold, the internal-conversion coefficient is greater for an atom than for the respective ion, but that the inverse is true for these coefficients at high energies.

It should be noted that, in the values of the internal-conversion coefficients for a neutral atom, there is an uncertainty that is associated with the inability of the modern theory of conversion to resolve conclusively the question of whether it is necessary to take into account the hole in the shell upon conversion [12, 15]. Allowances made for the hole significantly affect the internal-conversion coefficients at low kinetic energies of the conversion electron ($E_k \lesssim 1$ keV). However, the nuclear transition energies E_γ listed in Table 1 are not very small in relation to the ionization threshold for the K shell in the neutral atoms since the K-electron binding energy is higher for a hydrogen-like ion than for the respective neutral atom. Since electron–electron interaction is characterized by the parameter $1/Z$, it becomes clear that the effect of the hole is the most significant at small Z. The distinctions Δ between the internal-conversion coefficients for the K shell in $_{30}$Zn are given in Table 2 for the case where the internal-conversion coefficients for the neutral atom were calculated without taking the hole into account. From a comparison of the data in Tables 1 and 2, it can be seen that, at the smallest values considered for the energies E_γ, the deviations Δ calculated with allowance for the hole differ somewhat from those in which the hole was disregarded, but that the order of magnitude of these distinctions and their character are similar in the two cases in question.

The distinctions Δ are determined by a number of factors, which partly compensate one another.

Table 2. Distinctions Δ in percent [see Eq. (1)] between the coefficients of internal conversion in the K shell of a neutral atom per electron and the internal-conversion coefficients for the respective hydrogen-like ion in the case of $_{30}$Zn (the internal-conversion coefficients for the neutral atom were calculated without allowance for a hole in the K shell)

E_γ, keV	$E_k^{(\mathrm{H})}$, keV	$E1$	$M1$	$E2$	$M3$	$M4$	$E5$
12.695	0.3	−9.2	−9.2	−12	−8.3	−37	−90
12.995	0.6	−4.5	−4.4	−7.2	−3.0	−29	−84
13.395	1.0	−2.0	−2.0	−4.1	−0.1	−22	−76
22.395	10	2.4	2.8	3.4	7.2	4.5	−13
42.395	30	2.7	3.4	3.8	6.7	6.6	0.3
112.395	100	3.1	3.4	3.5	5.2	5.8	3.7
512.395	500	3.2	3.3	3.4	3.9	4.2	3.9
1012.395	1000	3.1	3.2	3.3	3.6	3.8	3.7

Table 3. Binding energies ε_K of the K electron and its densities in the vicinity of a nucleus, $\rho_K(0)$, for neutral atoms and hydrogen-like ions

ε_K, keV			$\rho_K(0)$, a.u.		
$_{30}$Zn	$_{68}$Er	$_{81}$Tl	$_{30}$Zn	$_{68}$Er	$_{81}$Tl
Atom					
9.663	57.489	85.536	0.1413(6)	0.4642(7)	0.1294(8)
H-ion					
12.395	67.337	98.763	0.1462(6)	0.4733(7)	0.1317(8)

Note: Figures given parenthetically indicate the order of magnitude.

Table 4. Coefficients of internal conversion in the K and L shells along with the total internal-conversion coefficients $\alpha_{\rm tot}^{\tau L}$ for the $_{81}$Tl atom

E_γ, keV	E_k, keV	Shell	$E1$	$M1$	$E2$	$M3$	$E4$	$E5$
86.536	1.0	K	0.468(0)	0.103(2)	0.476(0)	0.103(3)	0.427(−2)	0.104(−3)
		L_1	0.522(−1)	0.165(1)	0.154(0)	0.253(3)	0.787(2)	0.109(4)
		L_2	0.232(−1)	0.172(0)	0.417(1)	0.363(2)	0.244(4)	0.340(5)
		L_3	0.243(−1)	0.151(−1)	0.355(1)	0.434(3)	0.174(4)	0.234(5)
		$\alpha_{\rm tot}$	0.599(0)	0.127(2)	0.110(2)	0.111(4)	0.625(4)	0.968(5)
185.536	100.0	K	0.744(−1)	0.121(1)	0.201(0)	0.171(2)	0.139(1)	0.397(1)
		L_1	0.882(−2)	0.186(0)	0.268(−1)	0.681(1)	0.143(1)	0.113(2)
		L_2	0.227(−2)	0.192(−1)	0.135(0)	0.131(1)	0.232(2)	0.192(3)
		L_3	0.202(−2)	0.155(−2)	0.851(−1)	0.436(1)	0.108(2)	0.836(2)
		$\alpha_{\rm tot}$	0.915(−1)	0.148(1)	0.531(0)	0.341(2)	0.505(2)	0.416(3)

Note: Figures given parenthetically indicate the order of magnitude.

Among these, we first indicate the K-electron binding energy ε_K, which increases with the degree of ionization. As a result, the conversion channel involving the K shell may be completely closed if the transition energy is close to the threshold. An excited nuclear level then decays either through a different channel or through subthreshold resonance conversion. This is the case for the $E_\gamma = 35.492$ keV $M1$ transition in $^{125m}_{52}$Te that was considered in detail in [4–6]. Table 3 displays the values of ε_K for the elements being considered. There, we present the experimental values of the binding energies from [14] for atoms and the calculated binding energies for the respective hydrogen-like ions. It can be seen that, in the absolute values, the increase in ε_K with the degree of ionization is much more pronounced for heavy elements. For example, ε_K increases by 13.2 keV in $_{81}$Tl and only by 2.7 keV in $_{30}$Zn. Therefore, it is more probable to observe experimental manifestations of this effect in heavy elements.

Second, the total internal-conversion coefficient $\alpha_{\rm tot}^{\tau L}$, which determines the lifetime of a nuclear level, receives, in the case of a neutral atom, a contribution from all atomic shells higher than the K shell. From Table 4, it can be seen that, for $_{81}$Tl, this contribution is about 20% for the case of $E1$ and $M1$ transitions. But even for $E2$ transitions at the conversion threshold ($E_k \sim 1$ keV), the contribution of the L_2 and L_3 shells alone is one order of magnitude greater than the contribution of the K shell. For higher multipole orders of $L = 4$ and 5, the contribution of all other shells may exceed the coefficient of internal conversion in the K shell by several orders of magnitude (up to eight!). Accordingly, the effect of ionization on the lifetime of a nucleus may be formidable, also reaching several orders of magnitude.

Third, a strong static effect arises upon the disappearance of screening in hydrogen-like ions. This effect consists in that, both in the initial and in the final state, the electron wave functions are pulled toward the nucleus being considered. The respective growth of the electron density in the vicinity of the nucleus leads to an increase in internal-conversion coefficient. In connection with the ionization of $^{235}_{92}$U by laser radiation, this effect was previously discussed in [16]. It was estimated on the basis of a comparison of the internal-conversion coefficients for an atom and the respective hydrogen-like ion for the case where both values were calculated by using the same binding energy. The conversion-electron energies then take the same value for the atom and for the ion, so that the distinction between the respective internal-conversion coefficients is entirely due to the pulling of the wave functions toward the nucleus. In our calculations, we used the experimental value of the binding energy ε_K for the neutral atom [14].

The effect of pulling is illustrated in Table 5, which displays the distinctions $\bar{\Delta}$ between the coefficient $\alpha_{\rm at}^{\tau L}$ for the $_{68}$Er atom and the coefficient $\bar{\alpha}_{\rm ion}^{\tau L}$ for the respective hydrogen-like ion,

$$\bar{\Delta} = \left(\frac{\bar{\alpha}_{\rm ion}^{\tau L} - \alpha_{\rm at}^{\tau L}}{\alpha_{\rm at}^{\tau L}}\right) \cdot 100\%, \qquad (2)$$

the coefficient $\bar{\alpha}_{\rm ion}^{\tau L}$ being calculated with the same value of ε_K as the internal-conversion coefficient for the neutral atom in question. For the neutral atom, the internal-conversion coefficients were rescaled to

Table 5. Static-effect-induced distinctions $\bar{\Delta}$ in percent [see Eq. (2)] between the internal-conversion coefficients for the neutral atom of $_{68}$Er and the respective hydrogen-like ion

E_γ, keV	E_k, keV	$E1$	$M1$	$E2$	$M3$	$M4$	$E5$
57.789	0.3	−19	−26	73	92	1255	1.6(7)
58.089	0.6	−10	−17	87	108	1131	1.0(6)
58.489	1.0	−5.0	−12	93	114	968	1.6(5)
67.489	10	5.0	−9.3	62	79	213	744
87.489	30	4.7	0.9	33	46	86	172
157.489	100	2.7	1.8	14	21	34	50
557.489	500	1.6	1.4	3.1	7.3	10	12
1057.489	1000	0.7	1.0	1.1	4.4	6.0	6.6

Note: Figures given parenthetically indicate the order of magnitude.

one electron. As might have been expected, $\bar{\Delta}$ is positive in the majority of cases; that is, $\bar{\alpha}^{\tau L}_{\rm ion}$ for a hydrogen-like ion is greater in magnitude than $\alpha^{\tau L}_{\rm at}$ for the respective atom. Only for transitions of low multipole order ($E1$ and $M1$ transitions) at low energies, $E_k \lesssim 10$ keV, are the internal-conversion coefficients for a hydrogen-like ion less than their counterparts for the respective atom, but the distinctions $\bar{\Delta}$ are modest in those cases. For other transitions, however, the effect may prove to be significant. By way of example, we indicate that, for the $E_k = 0.3$ keV $E5$ transition, the internal-conversion coefficients for the atom and the respective hydrogen-like ion differ by seven orders of magnitude. For the same $E5$ multipolarity, as well as for the $M5$ multipolarity (the results of the calculations for the $M5$ transition are not included in Table 5), the distinction near the maximum values of the internal-conversion coefficients at $E_k \approx 30$ keV is more than twofold. It should be emphasized that this effect is caused primarily by the change in the conversion-electron wave function, since the effect on the K-electron wave function does not exceed a few percent (see the values given in Table 3 for the density in the vicinity of the nucleus).

However, there exists a fourth effect. It is associated with the fact that the energy and the phase space of the conversion electron decrease upon taking into account an increase in the K-electron binding energy. This effect reduces internal-conversion coefficients. It should be noted that, while the static effect increases internal-conversion coefficients by an order of magnitude, the changes in them because of the effect of the phase-space reduction occur in the opposite direction and may be as great as two orders of magnitude, as in the case of $E_\gamma = 12.7$ keV $E5$ transitions in $_{30}$Zn. At low conversion-electron energies, the internal-conversion coefficients eventually prove to be an order of magnitude smaller in ions than in neutral atoms. In general, the actual distinctions Δ are much less than the static-effect-induced distinction $\bar{\Delta}$.

By using the renormalization method [7, 10], which is well known in the theory of internal conversion, it can be shown that, if the radius of the region where internal-conversion coefficients are formed [17] is small and if the kinetic energy of the conversion electron is not very low (a few tens of keV or higher), the internal conversion coefficients obey the renormalization relation

$$\frac{\alpha_i^{(1)}}{\alpha_i^{(2)}} \approx \frac{\rho_i^{(1)}(0)}{\rho_i^{(2)}(0)}, \qquad (3)$$

Table 6. Distinctions Δ_κ in percent [see Eq. (4)] between the conversion-electron density near the nucleus in the $_{81}$Tl atom and its hydrogen-like ion

$E_k^{(\rm H)}$, keV	κ					
	−1	−2	−3	−4	−5	−6
0.3	−37.8	−38.1	−43.1	−58.5	−78.4	−92.1
0.6	−26.9	−27.3	−33.1	−50.8	−73.8	−89.9
1.0	−20.6	−21.0	−27.2	−45.9	−70.3	−87.9
10	−5.2	−5.6	−10.5	−23.8	−42.1	−60.0
30	−2.4	−2.7	−5.3	−12.0	−21.4	−32.2
100	−1.0	−1.0	−1.7	−3.7	−6.5	−10.0
300	−0.3	−0.2	−0.3	−0.7	−1.4	−2.3
500	−0.2	−0.1	0.1	−0.2	−0.5	−0.9
1000	−0.1	−0.0	0.1	0.2	0.1	0.0

Table 7. Coefficients of internal conversion in the K shell of the hydrogen-like ion of $_{68}$Er

$E_k^{(\mathrm{H})}$, keV	$E1$	$E2$	$E3$	$E4$	$E5$
0.3	0.253(0)	0.637(0)	0.679(0)	0.439(0)	0.202(0)
0.6	0.285(0)	0.726(0)	0.800(0)	0.549(0)	0.277(0)
1.0	0.301(0)	0.776(0)	0.892(0)	0.659(0)	0.371(0)
10	0.254(0)	0.815(0)	0.161(1)	0.270(1)	0.434(1)
30	0.143(0)	0.551(0)	0.159(1)	0.433(1)	0.120(2)
100	0.350(−1)	0.135(0)	0.452(0)	0.150(1)	0.512(1)
300	0.486(−2)	0.146(−1)	0.409(−1)	0.113(0)	0.316(0)
500	0.183(−2)	0.489(−2)	0.120(−1)	0.286(−1)	0.677(−1)
1000	0.526(−3)	0.125(−2)	0.259(−2)	0.501(−2)	0.939(−2)
$E_k^{(\mathrm{H})}$, keV	$M1$	$M2$	$M3$	$M4$	$M5$
0.3	0.254(1)	0.280(2)	0.871(2)	0.130(3)	0.116(3)
0.6	0.287(1)	0.314(2)	0.987(2)	0.152(3)	0.144(3)
1.0	0.302(1)	0.329(2)	0.105(3)	0.168(3)	0.172(3)
10	0.244(1)	0.243(2)	0.945(2)	0.256(3)	0.584(3)
30	0.129(1)	0.108(2)	0.487(2)	0.186(3)	0.670(3)
100	0.280(0)	0.159(1)	0.675(1)	0.274(2)	0.110(3)
300	0.333(−1)	0.118(0)	0.352(0)	0.103(1)	0.299(1)
500	0.108(−1)	0.317(−1)	0.775(−1)	0.184(0)	0.433(0)
1000	0.227(−2)	0.553(−2)	0.108(−1)	0.199(−1)	0.359(−1)

Note: Figures given parenthetically indicate the order of magnitude.

where $\alpha_i^{(1)}$ and $\alpha_i^{(2)}$ are the internal-conversion coefficients in the ith atomic shell that are calculated in atomic fields by methods that take into account screening differently and $\rho_i^{(1)}(0)$ and $\rho_i^{(2)}(0)$ are the electron densities in these fields. In the case being considered, the index (1) refers to a hydrogen-like ion, while the index (2) refers to the respective neutral atom.

Our calculations revealed (see Table 3) that the change in the density $\rho_K(0)$ of K electrons in the vicinity of the nucleus upon going over from an atom to the respective hydrogen-like ion is 3.5% for $_{30}$Zn, 2.0% for $_{68}$Er, and 1.8% for $_{81}$Tl. A comparison of these changes with the data in Table 1 shows that, for energies in the region $E_k^{(\mathrm{H})} > 100$ keV, relation (3) is indeed valid to within a few percent. At lower values of $E_k^{(\mathrm{H})}$, however, the distinctions Δ are great and differ significantly from the above changes in the K-electron density—by way of example, we indicate that, at the energy value of $E_k^{(\mathrm{H})} = 0.3$ keV, $\alpha_{\mathrm{at}}^{E5}$ is greater than $\alpha_{\mathrm{ion}}^{E5}$ by a factor of about 10 for all of the elements considered here. Therefore, it is the conversion-electron wave function that is predominantly responsible for so drastic a change in the internal-conversion coefficients. For a few values of the energy $E_k^{(\mathrm{H})}$ and a few values of the relativistic quantum number $\kappa = (l - j)(2j + 1)$, where l and j are, respectively, the orbital angular and the total angular momentum of the electron, the changes in the electron density in the vicinity of the nucleus, $\rho_\kappa(0) = |\psi_\kappa(0)|^2$, where $\psi_\kappa(0)$ is the corresponding value of the continuous-spectrum wave function, upon going over from the $_{81}$Tl atom to its hydrogen-like ion are given in Table 6.

Table 8. Coefficients of internal conversion in the K shell of the hydrogen-like ion of $_{81}$Tl

$E_k^{(\mathrm{H})}$, keV	$E1$	$E2$	$E3$	$E4$	$E5$
0.3	0.109(0)	0.161(0)	0.115(0)	0.532(−1)	0.184(−1)
0.6	0.127(0)	0.189(0)	0.138(0)	0.669(−1)	0.248(−1)
1.0	0.136(0)	0.205(0)	0.155(0)	0.794(−1)	0.320(−1)
10	0.132(0)	0.241(0)	0.289(0)	0.304(0)	0.313(0)
30	0.900(−1)	0.203(0)	0.373(0)	0.679(0)	0.129(1)
100	0.314(−1)	0.844(−1)	0.218(0)	0.580(0)	0.162(1)
300	0.625(−2)	0.166(−1)	0.432(−1)	0.111(0)	0.288(0)
500	0.268(−2)	0.697(−2)	0.168(−1)	0.385(−1)	0.868(−1)
1000	0.860(−3)	0.216(−2)	0.455(−2)	0.873(−2)	0.160(−1)
$E_k^{(\mathrm{H})}$, keV	$M1$	$M2$	$M3$	$M4$	$M5$
0.3	0.228(1)	0.152(2)	0.296(2)	0.281(2)	0.160(2)
0.6	0.265(1)	0.176(2)	0.347(2)	0.337(2)	0.200(2)
1.0	0.285(1)	0.189(2)	0.375(2)	0.376(2)	0.235(2)
10	0.266(1)	0.167(2)	0.394(2)	0.616(2)	0.780(2)
30	0.169(1)	0.957(1)	0.270(2)	0.622(2)	0.132(3)
100	0.504(0)	0.219(1)	0.671(1)	0.194(2)	0.554(2)
300	0.755(−1)	0.232(0)	0.581(0)	0.143(1)	0.352(1)
500	0.258(−1)	0.687(−1)	0.149(0)	0.316(0)	0.666(0)
1000	0.542(−2)	0.128(−1)	0.235(−1)	0.407(−1)	0.693(−1)

Note: Figures given parenthetically indicate the order of magnitude.

It can be seen that, at small $E_k^{(\mathrm{H})}$, the distinction

$$\Delta_\kappa = \left[\frac{\rho_\kappa^{\mathrm{ion}}(0) - \rho_\kappa^{\mathrm{at}}(0)}{\rho_\kappa^{\mathrm{at}}(0)}\right] \cdot 100\% \qquad (4)$$

is about a few tens of percent. The values of Δ_κ are especially great for large values of κ. We note that, although Table 6 presents the distinctions in question only for $\kappa < 0$, the distinctions Δ_κ for corresponding $\kappa > 0$ take approximately the same values. Comparing the values of Δ_κ with the corresponding distinctions Δ between the internal-conversion coefficients from Table 1 for $_{81}$Tl, we can conclude that the distinction Δ between the coefficients of internal conversion in the K shell for an atom and the respective hydrogen-like ion is indeed due predominantly to the difference in the continuous-spectrum wave functions. Moreover, it turns out that, in the present case, the changes in the internal-conversion coefficients are proportional to the changes in the electron densities in the initial and the final state; that is,

$$\frac{\alpha_{\mathrm{ion}}^{\tau L}}{\alpha_{\mathrm{at}}^{\tau L}} \approx \frac{\rho_K^{\mathrm{ion}}(0)}{\rho_K^{\mathrm{at}}(0)} \frac{\rho_\kappa^{\mathrm{ion}}(0)}{\rho_\kappa^{\mathrm{at}}(0)}, \qquad (5)$$

where $\rho_\kappa(0)$ is the electron density in the final state at that value of κ which makes a dominant contribution to the conversion matrix element in summation over final states.

Relation (5) holds to a high precision, which is a fraction of a percent even for very low energies $E_k^{(\mathrm{H})}$. By way of example, we indicate that, for the $E5$ transition, the leading contribution to the coefficient of internal conversion in the K shell comes from the term corresponding to $\kappa = -6$. At $\kappa = -6$, the distinction Δ_κ is -92.1% for $_{81}$Tl in the case of the lowest energy considered here ($E_k^{(\mathrm{H})} = 0.3$ keV).

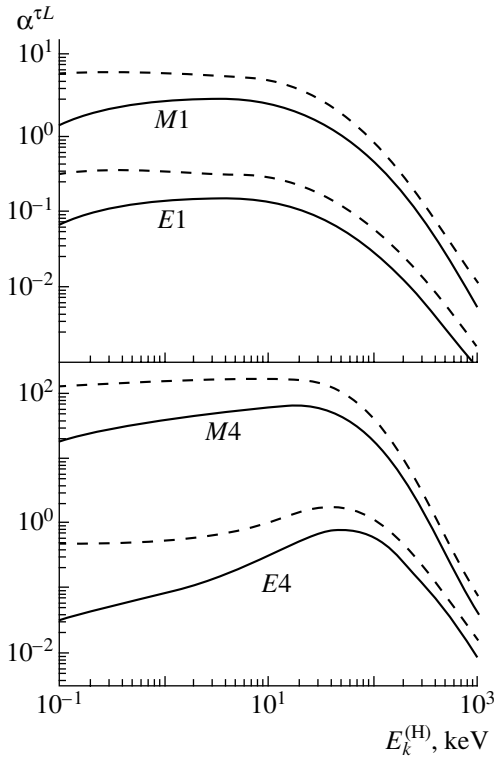

Coefficients $\alpha^{\tau L}$ of internal conversion in the K shell for (solid curves) the hydrogen-like ion of $_{81}$Tl tallium and (dashed curve) its neutral atom versus the energy $E_k^{(\mathrm{H})}$ of the conversion electron in the hydrogen-like ion. The values of the internal-conversion coefficients for the atom correspond to the actual number of electrons in the K shell.

It follows that the result obtained with the aid of formula (5) for the change in the internal-conversion coefficient upon going over from the $_{81}$Tl atom to the respective hydrogen-like ion is -92.0%. A direct calculation (see Table 1) also yields -92%. Let us consider yet another example—that of the $M4$ transition, in which the main contribution comes from the $\kappa = -4$ term. According to the calculation with the aid of Eq. (5), the change in the internal-conversion coefficient α^{M4} for $_{81}$Tl at $E_k^{(\mathrm{H})} = 0.3$ keV is -57.8%; a direct calculation yields $\Delta = -58\%$ in this case. So high a precision of fulfillment of the above proportionality relation, which takes into account changes in the density in the vicinity of the nucleus for the electron in the initial and in the final state is due to the fact that, even at very low conversion-electron energies and for transitions of high multipole order, the radius of the region where the coefficient of internal conversion in the K shell is formed is about the radius of the K shell itself.

It should also be noted that the internal-conversion coefficients for hydrogen-like ions may differ from the internal-conversion coefficients for atoms not only in magnitude but also in the character of their energy dependence. By way of example, we indicate that, in the case of a neutral atom, the internal-conversion coefficients for transitions of low multipole order ($E1$, $M1$) decrease with increasing $E_k^{(\mathrm{H})}$ at the lowest values of the energy $E_k^{(\mathrm{H})}$; at the same time, the internal-conversion coefficients for a hydrogen-like ion at the same values of $E_k^{(\mathrm{H})}$ first increase and begin decreasing only at energies of about a few keV. For transitions of high multipole order, the above increase in the internal-conversion coefficients persists up to $E_k^{(\mathrm{H})}$ values of a few tens of keV. This can be seen from the figure, where the internal-conversion coefficients α^{E1}, α^{M1}, α^{E4}, and α^{M4} for the $_{81}$Tl atom and for the respective hydrogen-like ion are displayed versus the energy $E_k^{(\mathrm{H})}$. The values of the internal-conversion coefficients for the atom were rescaled to the actual number of electrons in the K shell. The figure clearly demonstrates the distinctions between the magnitude and the behavior of the internal-conversion coefficients for a hydrogen-like ion and the magnitude and the behavior of the internal-conversion coefficients for the respective neutral atom. This effect provides a spectacular illustration of how the attraction field, which becomes more intense with increasing degree of ionization, affects internal-conversion coefficients near the threshold. The threshold distinctions between the electron and muon internal-conversion coefficients in the case of the $E3$ and $E4$ multipolarities [9] are similar to the above distinctions.

Since the distinctions between the magnitude and the behavior of the internal-conversion coefficients for a hydrogen-like ion and the magnitude and the behavior of the internal-conversion coefficients for the respective neutral atom may be quite significant, as was shown above, and since the first experimental investigations of nuclear transitions in hydrogen-like ions and nuclei completely deprived of their electron shells were performed at GSI and GANIL, we present the internal-conversion coefficients for the hydrogen-like ions of the $_{68}$Er and $_{81}$Tl elements in Tables 7 and 8. The present investigation of strong threshold effects arising upon ionization may be of use in interpreting relevant experimental data. For example, the results reported in [4, 6], where, for the case of multiple ionization, the coefficients of internal conversion in the K and L shells of the $^{125}_{52}$Te atom were found to be invariable up to the threshold of conversion in the K shell, initially seemed paradoxical. This circumstance stimulated the discovery of discrete conversion. From the above results, it follows, however, that, for a different multipole order, the behavior of the internal-conversion coefficients could be totally different.

The results of the calculations that were performed for three elements provide a qualitative pattern of the dependence of the coefficients of internal conversion in hydrogen-like ions on the number of the element and on the transition energy and multipolarity. These data make it possible assess the expected lifetimes with respect to radioactive decay for a nucleus in the hydrogen-like state and the state completely deprived of the electron shell. Knowledge of these lifetimes is of paramount importance for some applications, such as the investigation of astrophysical processes [18].

ACKNOWLEDGMENTS

This work was supported by the Russian Foundation for Basic Research (project nos. 99-02-17550, 01-P-0134) and DSWA (contract no. DTRA01-01-P-0134) (USA).

REFERENCES

1. T. Radon, H. Geissel, G. Münzerberg, *et al.*, Nucl. Phys. A **677**, 75 (2000).
2. W. R. Phillips, J. Copnell, D. W. Banes, *et al.*, Phys. Rev. A **47**, 3682 (1993).
3. F. F. Karpeshin, I. M. Band, M. B. Trzhaskovskaya, *et al.*, Phys. Rev. C **57**, 3085 (1998).
4. F. F. Karpeshin, M. R. Harston, F. Attallah, *et al.*, Phys. Rev. C **53**, 1640 (1996).
5. F. F. Karpeshin, I. M. Band, and M. B. Trzhaskovskaya, Zh. Éksp. Teor. Fiz. **116**, 1565 (1999) [JETP **89**, 845 (1999)].
6. M. R. Harston, T. Carreyre, J. F. Chemin, *et al.*, Nucl. Phys. A **676**, 143 (2000).
7. I. M. Band, M. A. Listengarten, and A. P. Feresin, *Anomalies in the Coefficients of Internal Gamma-Ray Conversion* (Nauka, Leningrad, 1976).
8. F. F. Karpeshin, I. M. Band, and M. A. Listengarten, Izv. Akad. Nauk SSSR, Ser. Fiz. **40**, 1164 (1976).
9. F. F. Karpeshin and V. E. Starodubskiĭ, Yad. Fiz. **35**, 1365 (1982) [Sov. J. Nucl. Phys. **35**, 795 (1982)].
10. I. M. Band, M. A. Listengarten, and M. B. Trzhaskovskaya, Izv. Akad. Nauk SSSR, Ser. Fiz. **53**, 910 (1989).
11. I. M. Band, M. A. Listengarten, and M. B. Trzhaskovskaya, Izv. Akad. Nauk SSSR, Ser. Fiz. **54**, 15 (1990).
12. I. M. Band and M. B. Trzhaskovskaya, At. Data Nucl. Data Tables **55**, 431 (1993).
13. L. A. Sliv, Zh. Éksp. Teor. Fiz. **21**, 770 (1951).
14. K. Siegbahn, C. Nordling, A. Fahlman, *et al.*, *ESCA: Atomic, Molecular, and Solid-State Structure Studied by Means of Electron Spectroscopy* (Almqvist and Wiksell, Uppsala, 1967).
15. I. M. Band and M. B. Trzhaskovskaya, Izv. Akad. Nauk SSSR, Ser. Fiz. **55**, 2141 (1991).
16. B. A. Zon and F. F. Karpeshin, Zh. Éksp. Teor. Fiz. **97**, 401 (1990) [Sov. Phys. JETP **70**, 224 (1990)].
17. I. M. Band, L. A. Sliv, and M. B. Trzhaskovskaya, Nucl. Phys. A **156**, 470 (1970).
18. Yu. N. Novikov, H. Schatz, P. Dendooven, *et al.*, Eur. Phys. J. A **11**, 257 (2001).

Translated by A. Isaakyan

Physics of Atomic Nuclei, Vol. 67, No. 2, 2004, pp. 226–240. From Yadernaya Fizika, Vol. 67, No. 2, 2004, pp. 243–257.

NUCLEI
Theory

Symmetric Elastic and Spin-Flip Low-Energy Collisions of the Hydrogen-Isotope Mesic Atoms in the Adiabatic Hyperspherical Approach*

D. I. Abramov[1)], V. V. Gusev[2)], and L. I. Ponomarev

Russian Research Centre Kurchatov Institute, pl. Kurchatova 1, Moscow, 123182 Russia

Received April 15, 2002; in final form, March 3, 2003

Abstract—The reduced adiabatic hyperspherical (RAHS) basis suggested previously is used to calculate elastic and spin-flip cross sections in the processes $(a\mu)_F + a \to (a\mu)_{F'} + a$, $a = (p, d, t)$, for collision energies $10^{-3} \le \varepsilon \le 10^2$ eV. The rapid convergence of the method is demonstrated: to achieve an accuracy of $\simeq 1\%$ in the calculated cross sections, it is sufficient to use $N \le 10$ of the basis RAHS functions. The comparison of the obtained results with the previous ones is presented. © *2004 MAIK "Nauka/Interperiodica".*

INTRODUCTION

The low-energy collisions in symmetric mesic atomic systems with two open channels

$$(a\mu)_F + a \to (a\mu)_{F'} + a$$
$$(F = F', \text{ elastic}; \quad F \ne F', \text{ spin-flip})$$

(F and F' are the total spins of mesic atom $a\mu$ in the initial and final ground states, respectively, and $a = p, d, t$) are important for the description of various mesic atomic processes, especially muon-catalyzed fusion [1].

In contrast to the asymmetric case [2], in symmetric low-energy collisions at $\varepsilon \lesssim 0.5$ eV, the spin–spin interaction of muon with nuclei should be taken into account [3]. This interaction results in the hyperfine splitting $\Delta E_a \sim 0.1$ eV of the ground-state energy E_a of mesic atom $a\mu$. In asymmetric systems, this splitting is negligible as compared with the isotopic one (~ 100 eV), but it certainly has to be taken into account in the symmetric case because it is comparable with the typical collision energies of mesic atoms ($\varepsilon = 0.04$ eV at $T = 300$ K).

The most extended and systematic calculations of cross sections of the symmetric collision processes were performed previously in the adiabatic approach [4], which is based on the decomposition of the three-body wave function over solutions of the Coulomb two-center (CTC) problem [5, 6]. However, this expansion converges slowly because the CTC basis does not properly represent the three-body wave function at large internuclear distances, and for its adequate description, it is necessary to keep too many CTC basis functions, including functions of the CTC continuous spectrum [7].

The disadvantages pointed out are absent in the adiabatic hyperspherical approach (AHSA) [8], which generalizes the traditional adiabatic approach and is widely used for the description of the Coulomb three-body systems in atomic and mesic atomic physics [9].

Several years ago [10], we suggested the reduced adiabatic hyperspherical approach (RAHSA) for the description of the aforementioned processes. In the framework of RAHSA, we developed the uniform numerical method [11, 12], which was successfully applied for the calculations of energies and local characteristics of bound states [13, 14] and resonances [15, 16] in the three-body mesic atomic systems as well as for the description of the scattering processes in the asymmetric systems $p\mu d$, $p\mu t$, and $d\mu t$ [2, 16, 17]. The main points of our algorithm are the following:

(i) To simplify the calculation of basis functions at nonzero angular momentum J, we use the reduced adiabatic hyperspherical (RAHS) basis [10, 11].

(ii) To overcome the numerical difficulties caused by the quasicrossings of the RAHS energy terms, we, first, use the variational principle for the simultaneous calculation of both basis functions and their derivatives with respect to hyperradius ρ and, second, reduce the scattering problem for the radial system to the boundary-value problem using the reference functions that satisfy boundary conditions at large ρ [18].

*This article was submitted by the authors in English.

[1)]St. Petersburg State University, St. Petersburg, Russia.

[2)]Institute for High Energy Physics, Protvino, Moscow oblast, 142284 Russia.

1063-7788/04/6702-0226$26.00

(iii) To overcome difficulties produced by the long-range matrix elements, we use in the numerical calculations the asymptotic formulas for RAHS matrix elements at large ρ.

In [19], the decomposition of the three-body wave function over eigenfunctions of the adiabatic hyperspherical (AHS) Hamiltonian, which includes the spin–spin interaction, has been used. On the contrary, we use the decomposition over RAHS basis and take into account the spin–spin interaction in the system of radial equations.

In what follows, we will present the calculations of the partial-wave σ_{ij}^J ($J \le 5$) and total σ_{ij} cross sections of the elastic and spin-flip collisions in all symmetric mesic hydrogen atom systems ($p\mu p$, $d\mu d$, $t\mu t$) at collision energies $10^{-3} \le \varepsilon \le 10^2$ eV by the method developed earlier [2, 10–15, 17].

1. SPATIAL RAHS BASIS

In the Jacobi coordinates $\{\mathbf{R}, \mathbf{r}\}$, the Hamiltonian of the three-particle system with charges $Z_a = Z_b = -Z_\mu = 1$ and masses m_a, m_b, m_μ ($m_a \ge m_b$) has the form

$$\hat{H} = -\frac{1}{2M}\Delta_R - \frac{1}{2\mu}\Delta_r + V + V_s, \qquad (1)$$
$$V = \frac{1}{R} - \frac{1}{r_a} - \frac{1}{r_b},$$

$$M^{-1} = m_a^{-1} + m_b^{-1}, \qquad \mu^{-1} = 1 + (m_a + m_b)^{-1},$$

$$\mathbf{R} = \mathbf{r}_a - \mathbf{r}_b, \qquad \mathbf{r} = \mathbf{r}_a\frac{m_a}{m_a + m_b} + \mathbf{r}_b\frac{m_b}{m_a + m_b},$$

where the mesic atomic units ($\hbar = e = m_\mu = 1$) are used, $\mathbf{r}_a$ and $\mathbf{r}_b$ are the vectors connecting nuclei a and b with the muon. Hamiltonian (1) includes the spin–spin interaction V_s of the muon with nuclei, which can be written in the form [3]

$$V_s = \Lambda[\delta(\mathbf{r}_a)\mathbf{s}_a \cdot \mathbf{s}_\mu + \delta(\mathbf{r}_b)\mathbf{s}_b \cdot \mathbf{s}_\mu] \qquad (2)$$
$$= \frac{\Lambda}{4\pi}\left[\frac{\delta(r_a)}{r_a^2}\mathbf{s}_a \cdot \mathbf{s}_\mu + \frac{\delta(r_b)}{r_b^2}\mathbf{s}_b \cdot \mathbf{s}_\mu\right],$$

where $\mathbf{s}_\mu$, $\mathbf{s}_a$, and $\mathbf{s}_b$ are spins of the muon and nuclei a and b. Constant Λ depends on the system considered and determines the hyperfine splitting ΔE_a of the ground state E_a of the atom $a\mu$ by the formula

$$\Delta E_a = \frac{\Lambda}{2}|\psi_{1s}(r_a = 0)|^2[F_2(F_2+1) - F_1(F_1+1)],$$

where $F_1 = 0$, $F_2 = 1$ for $p\mu$ and $t\mu$, and $F_1 = 1/2$, $F_2 = 3/2$ for $d\mu$, and ψ_{1s} is the ground state wave function of $a\mu$ atom. The values of ΔE_a are the following [20]:

$$\Delta E_p = 0.1820 \text{ eV}, \qquad \Delta E_d = 0.0485 \text{ eV},$$
$$\Delta E_t = 0.2373 \text{ eV}.$$

In the hyperspherical coordinates (ρ, χ, ϑ),

$$\rho = (2MR^2 + 2\mu r^2)^{1/2},$$
$$\tan(\chi/2) = (\mu/M)^{1/2} r/R,$$
$$\cos\vartheta = \mathbf{R}\cdot\mathbf{r}/Rr,$$

$\rho \in [0, \infty)$, $\chi \in [0, \pi]$, $\vartheta \in [0, \pi]$, the Hamiltonian $\hat{H}$ (1) takes the form [12]

$$\hat{H} = -\frac{1}{\rho^5}\frac{\partial}{\partial\rho}\rho^5\frac{\partial}{\partial\rho} + \frac{\hat{\mathbf{J}}^2 - 2(\hat{\mathbf{l}}\cdot\hat{\mathbf{J}})}{\rho^2\cos^2\chi/2} + h^R + V_s, \quad (3)$$

where $\hat{\mathbf{l}}$ and $\hat{\mathbf{J}}$ are the muon orbital angular momentum and the total one, respectively:

$$\hat{\mathbf{l}} = -i[\mathbf{r}\times\nabla_r], \qquad \hat{\mathbf{J}} = \hat{\mathbf{l}} - i[\mathbf{R}\times\nabla_R],$$
$$\hat{\mathbf{l}}^2 = -\frac{1}{\sin\vartheta}\frac{\partial}{\partial\vartheta}\sin\vartheta\frac{\partial}{\partial\vartheta} - \frac{1}{\sin^2\vartheta}\frac{\partial^2}{\partial\varphi^2}.$$

The RAHS Hamiltonian

$$h^R = -\frac{4}{\rho^2\sin^2\chi}\left(\frac{\partial}{\partial\chi}\sin^2\chi\frac{\partial}{\partial\chi} - \hat{\mathbf{l}}^2\right) + V(\rho,\chi) \qquad (4)$$

is used in our method instead of the traditional AHS Hamiltonian $h = h^R + [\hat{\mathbf{J}}^2 - 2(\hat{\mathbf{l}}\cdot\hat{\mathbf{J}})]/[\rho^2\cos^2(\chi/2)]$ containing the Coriolis term [8, 9].

The spatial RAHS basis [10] for symmetric systems ($m_a = m_b$) is defined as the set of eigenfunctions $\psi_{jmp}^{JK\lambda}(\rho|\chi,\vartheta,\Phi,\Theta,\varphi) = \psi_{jmp}^{JK\lambda}(\rho|\Omega)$ of six commuting operators: h^R (index j), $\hat{\mathbf{J}}^2$ (index J), $\hat{J}_3$ (index K), $\hat{J}_3'^2$ (index $m \ge 0$), $\hat{P}_{\text{tot}}$ (index $\lambda = \pm(-1)^J$), and $\hat{P}$ (index $p = \pm 1$). Here, $\hat{J}_3$ and $\hat{J}_3'$ are the projections of $\hat{\mathbf{J}}$ onto the third axes of space-fixed and rotating frames, respectively; $\hat{P}_{\text{tot}}$ is the inversion operator of all coordinates,

$$\hat{P}_{\text{tot}}: \qquad \mathbf{R} \to -\mathbf{R}, \quad \mathbf{r} \to -\mathbf{r} \qquad (5)$$
$$(\Phi \to \pi + \Phi, \Theta \to \pi - \Theta, \varphi \to \pi - \varphi),$$
$$\mathbf{R} = (R, \Theta, \Phi), \quad \mathbf{r} = (r, \vartheta, \varphi);$$

$\hat{P}$ is the inversion operator of muonic coordinates,

$$\hat{P}: \qquad \mathbf{r} \to -\mathbf{r} \quad (\varphi \to \varphi + \pi, \vartheta \to \pi - \vartheta), \quad (6)$$

its eigenvalues $p = 1$ and $p = -1$ corresponding to *gerade* (g) and *ungerade* (u) states of the system $a\mu a$.

The spatial RAHS basis function can be represented in the form of the product

$$\psi_{jmp}^{JK\lambda}(\rho|\chi,\vartheta,\Phi,\Theta,\varphi) \qquad (7)$$
$$= \varphi_{jmp}(\rho|\chi,\vartheta)D_{Km}^{J\lambda}(\Phi,\Theta,\varphi),$$

where $D^{J\lambda}_{Km}(\Phi,\Theta,\varphi)$ is the symmetrized Wigner D function, and function $\varphi_{jmp}(\rho|\chi,\vartheta)$ is the eigenfunction of Hamiltonian $h_m(\rho|\chi,\vartheta)$, which acts only on variables χ and ϑ [10, 13]:

$$h_m\varphi_{jmp}(\rho|\chi,\vartheta) = E_{jmp}(\rho)\varphi_{jmp}(\rho|\chi,\vartheta), \quad (8)$$

$$h_m = -\frac{4}{\rho^2\sin^2\chi}\left(\frac{\partial}{\partial\chi}\sin^2\chi\frac{\partial}{\partial\chi} + \frac{1}{\sin\vartheta}\frac{\partial}{\partial\vartheta}\sin\vartheta\frac{\partial}{\partial\vartheta} - \frac{m^2}{\sin^2\vartheta}\right) + V,$$

$E_{jmp}(\rho)$ being the corresponding eigenvalue (RAHS energy term).

For description of the scattering processes of atoms in the ground state, we need only RAHS basis functions with $K=0$ and normal parity $\lambda=(-1)^J$. In what follows, the indices K and λ will be omitted:

$$\psi^{JK\lambda}_{jmp}(\rho|\chi,\vartheta,\Phi,\Theta,\varphi) = \psi^J_{jmp}(\rho|\Omega), \quad (9)$$

$$d\Omega = \sin^2\chi\sin\Theta\sin\vartheta d\chi d\vartheta d\Phi d\Theta d\varphi.$$

The relation defining the symmetry of these functions with respect to permutation $\hat{P}_n$ of nuclei ($a\leftrightarrow b$) takes the form

$$\hat{P}_n\psi^J_{jmp}(\rho|\Omega) = p(-1)^J\psi^J_{jmp}(\rho|\Omega); \quad (10)$$

$$\hat{P}_n = \hat{P}_{\rm tot}\hat{P}$$

$$(\Phi\to\pi+\Phi, \Theta\to\pi-\Theta, \varphi\to-\varphi, \vartheta\to\pi-\vartheta).$$

2. SPIN-SPATIAL RAHS I AND F BASES

The basis elements in the space of the three-body spin functions are the common eigenfunctions of six commuting spin operators and they are specified by corresponding quantum numbers: spins of nuclei s_a and s_b (in our case $s_a=s_b\equiv s$), spin of the muon s_μ ($s_\mu=1/2$), the total spin S of three particles, its projection S_z, and, finally, the total spin of any two of three particles—the total spin I of nuclei (functions of I type) or the total spin F of the atom $a\mu$ (functions of F type). For the three-particle spin function of I type with total spin S, its projection S_z, and total spin of nuclei I, we use the notation

$$\chi^{SI}_{S_z} = \chi^S_{S_z}(a,b:I|\mu;\sigma), \quad (11)$$

where σ is the set of spin variables (we will omit it below), and the phase factor is chosen according to Condon and Shortley [21].[3)]

[3)]The connection of our notation with that in the monograph of Edwards [22] is given by the relations $\chi^J_M(a,b:j_{ab}|c) = w((j_a,j_b)j_{ab},j_c,J,M)$. In our case, $j_a=j_b=s$, $j_c=j_\mu=1/2$.

The symmetry of $\chi^S_{S_z}(a,b:I|\mu)$ with respect to the nuclei permutation is defined by the equation [23]

$$\chi^S_{S_z}(a,b:I|\mu) = (-1)^{2s-I}\chi^S_{S_z}(b,a:I|\mu). \quad (12)$$

As the spin of the muon is equal to $1/2$, the nuclear spin I in the subspace of three-body spin functions with fixed S and S_z can take only one, $I=S-1/2$ (if $S>2s-1/2$), or two, $I=S\pm1/2$ (if $S\le 2s-1/2$), values; i.e., the spin subspace has one or two dimensions. The case of one dimension is a trivial one. In the case of two dimensions, the spin functions (11) with $I=S\pm1/2$ form the I basis in this subspace.

We define the spin-spatial RAHS basis function of I type X^{JI}_{jm} as the product of the spatial RAHS basis function ψ^J_{jmp} (9) and spin function of I type $\chi^{SI}_{S_z}$ (11):

$$X^{JI}_{jm}(\rho|\Omega,\sigma) = \psi^J_{jmp}(\rho|\Omega)\chi^S_{S_z}(a,b:I|\mu;\sigma). \quad (13)$$

Properly symmetrized basis function $X^J_{jmp}(\rho|\Omega,\sigma)$ is defined by the relation

$$X^J_{jmp}(\rho|\Omega,\sigma) = X^{JI}_{jm}(\rho|\Omega,\sigma), \quad (14a)$$

where indices p and I are connected by the relation

$$p = (-1)^{J+I}. \quad (14b)$$

Relations (14) provide the correct symmetry of the spin-spatial RAHS basis functions (13) with respect to permutation of nuclei: they are symmetric ($p=+1=g$) for bosons ($dd\mu$ case, $s=1$) and antisymmetric ($p=-1=u$) for fermions ($pp\mu$ and $tt\mu$ cases, $s=1/2$), as follows from Eqs. (10), (12), and (14b).

The basis functions $X^J_{jmp}(\rho|\Omega,\sigma)$ tend at large ρ to the properly symmetrized atomic functions, which does not correspond, however, to definite atomic spin. This is not suitable for the statement of the scattering problem with adequate account of spin–spin interaction of muon with nuclei. The spin–spatial RAHS F-basis $Y^{JF}_{jm}(\rho|\Omega,\sigma)$ instead of I-basis $X^J_{jmp}(\rho|\Omega,\sigma)$ should be used for this purpose:

$$Y^{JF}_{jm}(\rho|\Omega,\sigma) = \sum_p U^J_{Fp}X^J_{jmp}(\rho|\Omega,\sigma), \quad (15)$$

$$F=\{F_\alpha\}, \qquad \alpha=1,2, \qquad F_2>F_1.$$

The matrices $U^J_{Fp}=U^J_{Fp}(s,S)$ at fixed (s,S) have the following explicit form. At even J, we have

$$\begin{pmatrix} p\mu p, & t\mu t \\ s=1/2, & S=1/2 \\ F_1=0, & F_2=1 \end{pmatrix} \quad (16)$$

$$\begin{pmatrix} Y_1 \\ Y_2 \end{pmatrix} = \frac{1}{2}\begin{pmatrix} 1 & \sqrt{3} \\ \sqrt{3} & -1 \end{pmatrix}\begin{pmatrix} X_g \\ X_u \end{pmatrix},$$

$$\begin{pmatrix} d\mu d \\ s=1,\ S=1/2 \\ F_1=1/2,\ F_2=3/2 \end{pmatrix}$$

$$\begin{pmatrix} Y_1 \\ Y_2 \end{pmatrix} = \frac{1}{\sqrt{3}}\begin{pmatrix} 1 & \sqrt{2} \\ \sqrt{2} & -1 \end{pmatrix}\begin{pmatrix} X_g \\ X_u \end{pmatrix},$$

$$\begin{pmatrix} d\mu d \\ s=1,\ S=3/2 \\ F_1=1/2,\ F_2=3/2 \end{pmatrix}$$

$$\begin{pmatrix} Y_1 \\ Y_2 \end{pmatrix} = \frac{1}{\sqrt{6}}\begin{pmatrix} \sqrt{5} & 1 \\ -1 & \sqrt{5} \end{pmatrix}\begin{pmatrix} X_g \\ X_u \end{pmatrix},$$

$$Y_\alpha = Y^{JF_\alpha}_{jm}(\rho|\Omega,\sigma), \qquad X_p = X^J_{jmp}(\rho|\Omega,\sigma), \quad p = g,u.$$

At odd J, the indices g and u have to be exchanged in (16).[4)]

The spin–spatial RAHS F-basis function $Y^{JF}_{jm}(\rho|\Omega,\sigma)$ tends, for $\rho\to\infty$, to the atomic wave function with spin F properly symmetrized with respect to nuclear permutation.

3. SYSTEM OF RADIAL EQUATIONS

The decomposition of the three-body wave function with fixed $s, S, S_z, J, K=0$, and $\lambda=(-1)^J$ over F-basis Y^{JF}_{jm} (15) has the form

$$\Psi^J(\mathbf{r},\mathbf{R},\sigma) = \rho^{-5/2}\sum_{j=1}^{\infty}\sum_{m=0}^{J}\sum_{F} f^{JF}_{jm}(\rho) \times Y^{JF}_{jm}(\rho|\Omega,\sigma). \quad (17)$$

The substitution of this expansion into the Schrödinger equation

$$(H-E)\,\Psi^J = 0 \quad (18)$$

leads to the system of coupled differential equations for hyperradial functions $f^F_{jm}(\rho)$ at fixed total angular momentum J (index J is omitted)

$$\left(-\frac{\partial^2}{\partial\rho^2} - E + \frac{15}{4\rho^2}\right) f^F_{im}(\rho) + \sum_{F'}\left\{E^{FF'}_{im}(\rho) + \sum_{j=1}^{\infty}\sum_{m'=0}^{J}\left[P^{FF'}_{im,jm'}(\rho) + \frac{\partial}{\partial\rho}Q^{FF'}_{im,jm'}(\rho) + Q^{FF'}_{im,jm'}(\rho)\frac{\partial}{\partial\rho} + \frac{1}{\rho^2}R^{FF'}_{im,jm'}(\rho) + V^{FF'}_{im,jm'}\right]\right\} f^{F'}_{jm'}(\rho) = 0. \quad (19)$$

At fixed J, i, m, j, m', matrix elements $B^{FF'} = \{E^{FF'}_{im}, P^{FF'}_{im,jm'}, Q^{FF'}_{im,jm'}, R^{FF'}_{im,jm'}\}$ are connected with matrix elements $B_{pp'}$ calculated earlier [2, 12] with RAHS basis functions $\psi^J_{jmp}(\rho|\Omega)$ by the orthogonal transformation

$$B^{FF'} = \sum_{p,p'} U_{Fp} B_{pp'} U^{-1}_{p'F'}. \quad (20)$$

At $m=m'$, $B_{pp'} = B_p\delta_{pp'}$ and explicit expressions for $B^{FF'}$ at even J have the form

$$\begin{pmatrix} p\mu p,\ t\mu t \\ s=1/2,\ S=1/2 \\ F_1=0,\ F_2=1 \end{pmatrix} \quad (21)$$

$$B^{FF'} = \frac{1}{4}\begin{pmatrix} B_g+3B_u & \sqrt{3}(B_g-B_u) \\ \sqrt{3}(B_g-B_u) & 3B_g+B_u \end{pmatrix},$$

$$\begin{pmatrix} d\mu d \\ s=1,\ S=1/2 \\ F_1=1/2,\ F_2=3/2 \end{pmatrix}$$

$$B^{FF'} = \frac{1}{3}\begin{pmatrix} B_g+2B_u & \sqrt{2}(B_g-B_u) \\ \sqrt{2}(B_g-B_u) & 2B_g+B_u \end{pmatrix},$$

$$\begin{pmatrix} d\mu d \\ s=1,\ S=3/2 \\ F_1=1/2,\ F_2=3/2 \end{pmatrix}$$

$$B^{FF'} = \frac{1}{6}\begin{pmatrix} 5B_g+B_u & -\sqrt{5}(B_g-B_u) \\ -\sqrt{5}(B_g-B_u) & B_g+5B_u \end{pmatrix}.$$

[4)] The analogous matrices used in [24] differ from (16) due to the different definition of spin function corresponding to $I=1$.

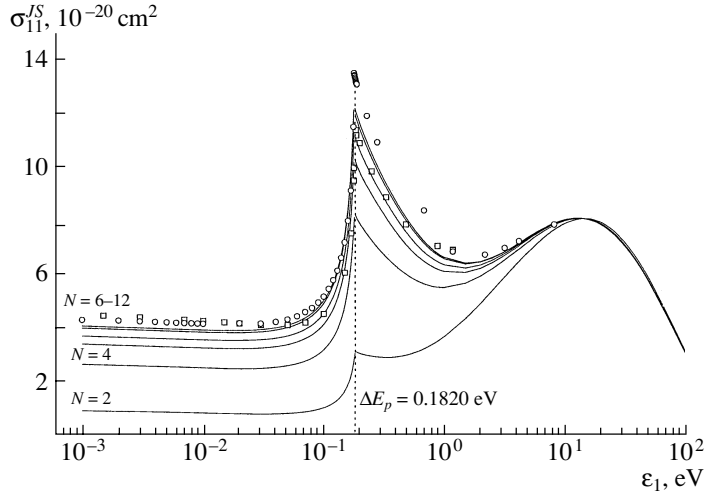

Fig. 1. Partial-wave cross section $\sigma_{11}^{JS}(\varepsilon_1)$ of elastic scattering $(p\mu)_{F=0} + p \to (p\mu)_{F=0} + p$, $J = 0$, $S = 1/2$, calculated with different number N of RAHS basis functions. Circles and squares are the results from [24] and [4], respectively.

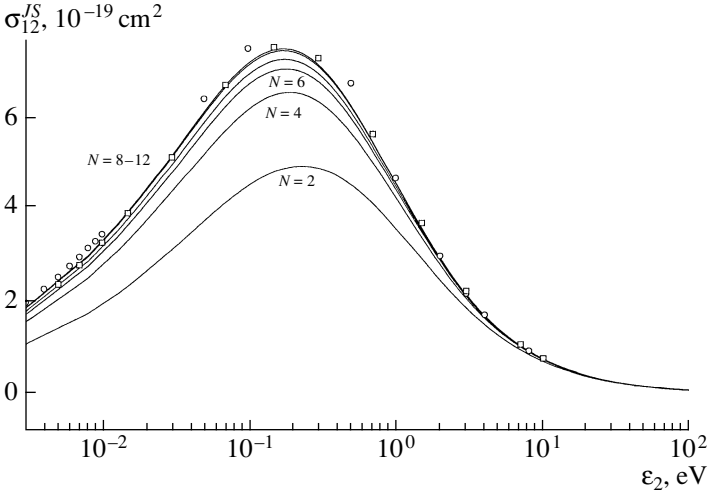

Fig. 2. Partial-wave cross section $\sigma_{12}^{JS}(\varepsilon_2)$ of spin-flip $(p\mu)_{F=0} + p \to (p\mu)_{F=1} + p$, $J = 0$, $S = 1/2$, calculated with different number N of RAHS basis functions. Circles and squares are the results from [24] and [4], respectively.

For odd J, these expressions differ from the displayed ones by the substitution $g \leftrightarrow u$.

In Eq. (19), the matrix $V_{im,jm'}^{FF'}$ of spin–spin interaction V_s (2) is diagonal with respect to F, F' at $\rho \to \infty$.

We restrict ourselves in this paper to the approximation in which matrix elements $V_{im,jm'}^{FF'}$ differ from zero for $i = j = 1$, $m = m' = 0$ only, and, in addition, we neglect the ρ dependence of this matrix:

$$V_{10,10}^{FF'}(\rho) = V_{10,10}^{FF'}(\infty) \equiv V_{FF'}, \qquad (22)$$

where diagonal matrix $V_{FF'}$ is given by the equations

$$\begin{pmatrix} p\mu p,\ t\mu t \\ s = 1/2 \\ F_1 = 0,\ F_2 = 1 \end{pmatrix} \quad V_{FF'} = \frac{\Delta E_{p,t}}{4} \begin{pmatrix} -3 & 0 \\ 0 & 1 \end{pmatrix}, \qquad (23)$$

$$\begin{pmatrix} d\mu d \\ s = 1 \\ F_1 = 1/2,\ F_2 = 3/2 \end{pmatrix} \quad V_{FF'} = \frac{\Delta E_d}{3} \begin{pmatrix} -2 & 0 \\ 0 & 1 \end{pmatrix}. \qquad (24)$$

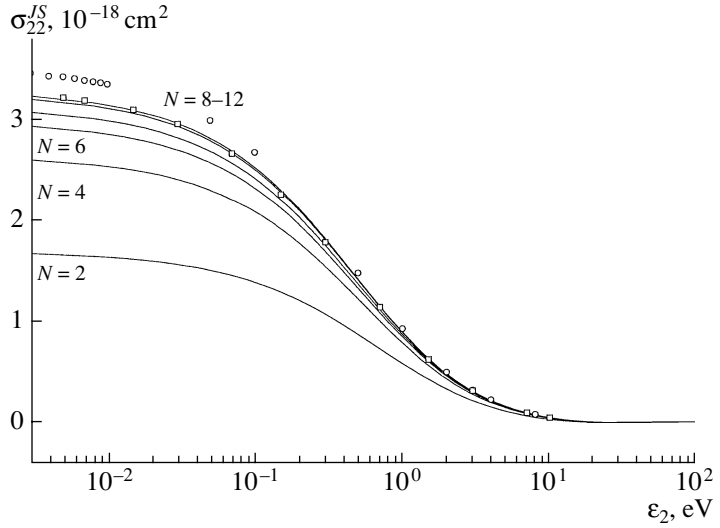

Fig. 3. Partial-wave cross section $\sigma_{22}^{JS}(\varepsilon_2)$ of elastic scattering $(p\mu)_{F=1} + p \to (p\mu)_{F=1} + p$, $J = 0$, $S = 1/2$, calculated with different number N of RAHS basis functions. Circles and squares are the results from [24] and [4], respectively.

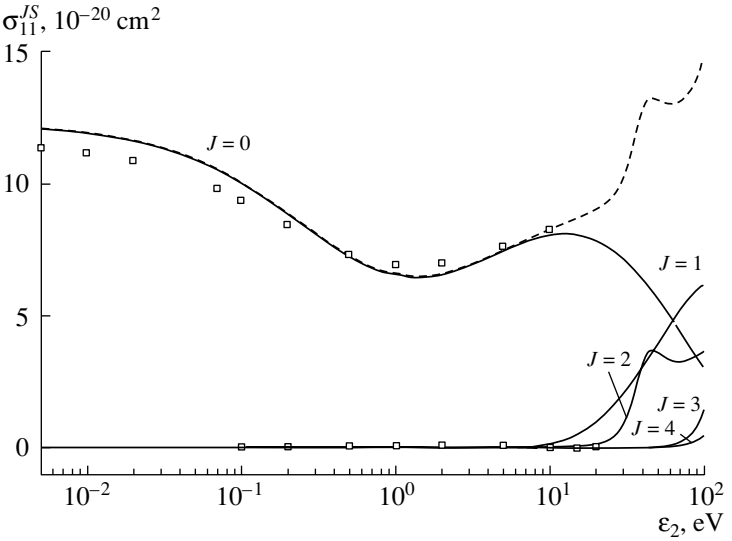

Fig. 4. Partial-wave cross sections $\sigma_{11}^{JS}(\varepsilon_2)$, $J = 0$–4, $S = 1/2$ (solid curves) and total cross section $\sigma_{FF}^{S}(\varepsilon_2)$ (dashed curve) of elastic scattering $(p\mu)_{F=0} + p \to (p\mu)_{F=0} + p$. Squares are the results from [4].

4. CROSS-SECTION CALCULATIONS

To calculate K matrix $K^{JS} = \{K_{FF'}^{JS}\} = \{K_{\alpha\beta}^{JS}\}$ in the case of two open channels $\alpha, \beta = 1, 2$, which corresponds to two spin values in the initial $F = F_\alpha$ and final $F' = F_\beta$ states, one has to find the regular at $\rho \to 0$ solutions $f_{jm}^{\beta}(\rho) = f_{jm}^{F_\beta}(\rho)$ of the truncated system (19) with $j \le \tilde{N}$. Two linearly independent solutions $f_{jm}^{\alpha\beta}(\rho)$ of that system enumerated by index $\alpha = (1, 2)$ correspond to the different initial spin states $F = F_\alpha$. The boundary conditions for these solutions have the form [2]

$$f_{im}^{\alpha\beta}(0) = 0, \quad i = 1{-}\tilde{N}, \quad m = 0{-}J, \quad \alpha, \beta = 1, 2; \tag{25}$$

$$f_{im}^{\alpha\beta}(\rho) \underset{\rho \to \infty}{=} 0, \quad i = 2{-}\tilde{N}, \quad m = 0{-}J, \quad \alpha, \beta = 1, 2;$$

$$f_{10}^{\alpha\beta}(\rho) \underset{\rho \to \infty}{=} \delta_{\alpha\beta} \sin(q_\beta \rho - \pi J_{\tilde{N}}/2) + (q_\alpha/q_\beta)^{1/2} K_{\alpha\beta}^{JS} \cos(q_\beta \rho - \pi J_{\tilde{N}}/2).$$

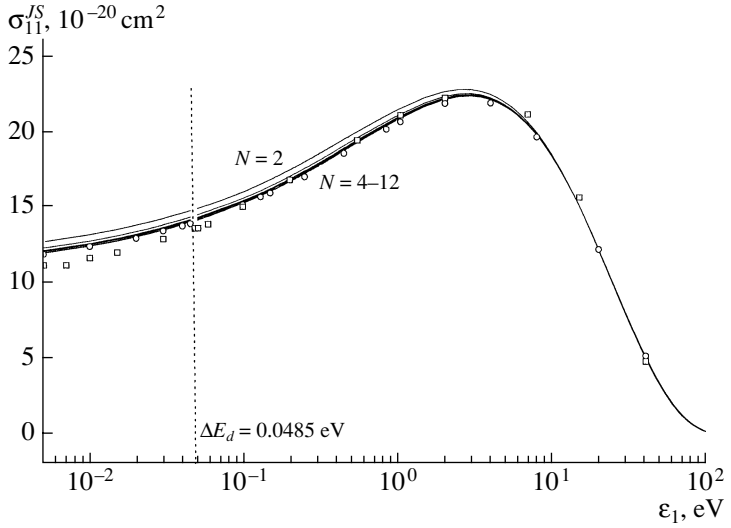

Fig. 5. Partial-wave cross section $\sigma_{11}^{JS}(\varepsilon_1)$ of elastic scattering $(d\mu)_{F=1/2} + d \to (d\mu)_{F=1/2} + d$, $J = 0, S = 1/2$, calculated with different numbers N of RAHS basis functions. Circles and squares are the results from [24] and [4], respectively.

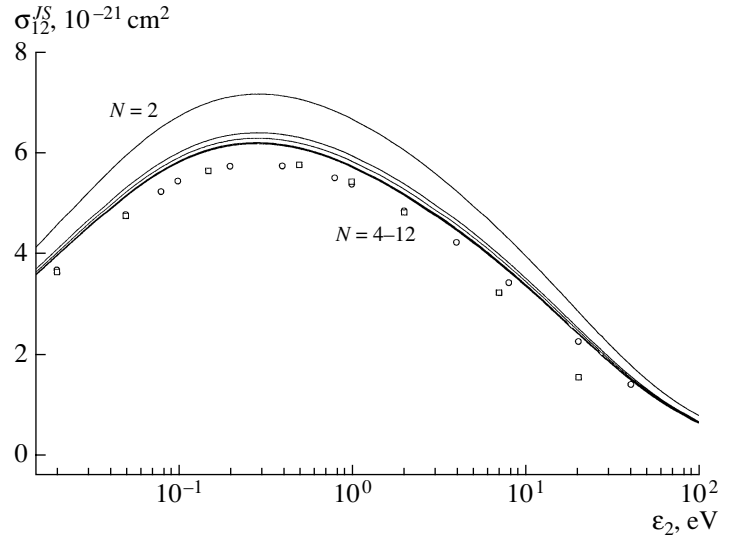

Fig. 6. Partial-wave cross section $\sigma_{12}^{JS}(\varepsilon_2)$ of spin-flip $(d\mu)_{F=1/2} + d \to (d\mu)_{F=3/2} + d$, $J = 0, S = 1/2$, calculated with different numbers N of RAHS basis functions. Circles and squares are the results from [24] and [4], respectively.

Here, $q_\alpha^2 = \varepsilon_\alpha$ is the relative kinetic energy of fragments in the channel F_α

$$\varepsilon_\alpha = E - E_\alpha, \tag{26}$$

where $E_\alpha = E_{10}(\infty) + V_\alpha$ is the energy of the ground state of $(a\mu)_F$ atom with atomic spin $F = F_\alpha$, $V_\alpha = V_{F_\alpha F_\alpha}$ is defined by Eq. (22), and $J_{\tilde{N}} = J + O(M^{-2})$ is defined in [2].

For given total angular momentum J and total spin S, the cross sections $\sigma_{\alpha\beta}^{JS}(\varepsilon)$ of the transition $F_\alpha \to F_\beta$ are expressed in terms of matrix elements $K_{\alpha\beta}^{JS}$ [24]:

$$\sigma_{\alpha\beta}^{JS}(\varepsilon) = \frac{4\pi}{k_\alpha^2}(2J+1)\frac{\delta_{\alpha\beta}(D^{JS})^2 + (K_{\alpha\beta}^{JS})^2}{(1 - D^{JS})^2 + (G^{JS})^2}, \tag{27}$$

where $\varepsilon = (\varepsilon_\alpha, \varepsilon_\beta)$ is scattering energy reckoned from E_α or E_β,

$$D^{JS} = K_{11}^{JS}K_{22}^{JS} - K_{12}^{JS}K_{21}^{JS},$$
$$G^{JS} = K_{11}^{JS} + K_{22}^{JS},$$
$$k_\alpha = (2\mu_a)^{1/2}q_\alpha = (2\mu_a\varepsilon_\alpha)^{1/2},$$
$$\mu_a^{-1} = (m_a + m_\mu)^{-1} + m_b^{-1}.$$

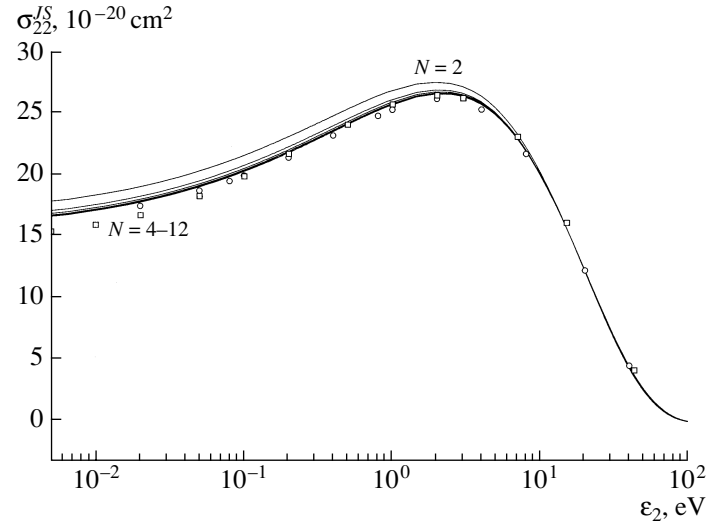

Fig. 7. Partial-wave cross section $\sigma_{22}^{JS}(\varepsilon_2)$ of elastic scattering $(d\mu)_{F=3/2} + d \to (d\mu)_{F'=3/2} + d$, $J = 0$, $S = 1/2$, calculated with different numbers N of RAHS basis functions. Circles and squares are the results from [24] and [4], respectively.

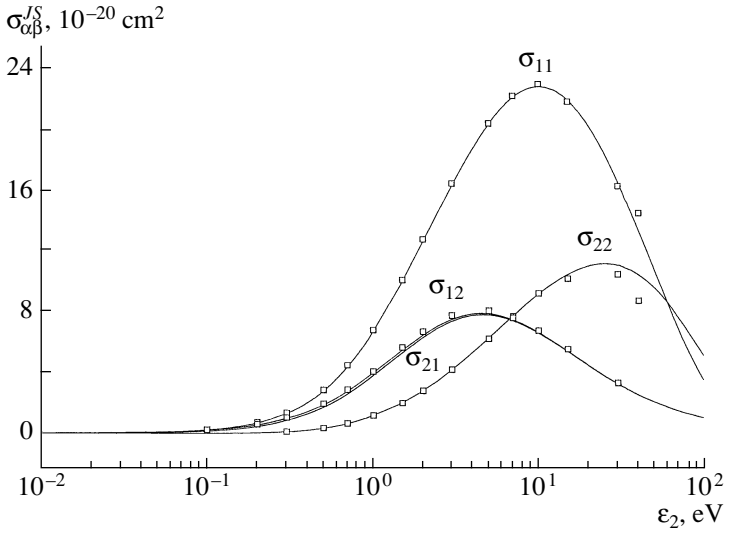

Fig. 8. Partial-wave cross sections $\sigma_{\alpha\beta}^{JS}(\varepsilon_2)$ of elastic scattering and spin-flip for the process $(d\mu)_{F_\alpha} + d \to (d\mu)_{F_\beta} + d$, $J = 1$, $S = 1/2$, $F_1 = 1/2$, $F_2 = 3/2$. Squares are the results from [4].

The partial-wave and total cross sections averaged over all possible S at given F_α and F_β have the form

$$\sigma_{\alpha\beta}^{J} = \sum_{S} W_{\alpha s}^{S} \sigma_{\alpha\beta}^{JS}, \quad \sigma_{\alpha\beta} = \sum_{J=0}^{\infty} \sigma_{\alpha\beta}^{J}, \tag{28}$$

where

$$W_{\alpha s}^{S} = \frac{2S+1}{(2F_\alpha + 1)(2s+1)} \tag{29}$$

is the statistical weight of the state with total spin S in the collision of atom $(a\mu)_{F_\alpha}$ and nucleus a with spin s. For the collisions $(p\mu)_F + p \to (p\mu)_{F'} + p$ and $(t\mu)_F + t \to (t\mu)_{F'} + t$ ($F_1 = 0, F_2 = 1$), the explicit expressions for cross sections $\sigma_{\alpha\beta}^{J}$ have the form

$$\sigma_{11}^{J} = \sigma_{11}^{JS=1/2}, \quad \sigma_{12}^{J} = \sigma_{12}^{JS=1/2}; \tag{30}$$
$$\sigma_{21}^{J} = \frac{1}{3}\sigma_{21}^{JS=1/2}, \quad \sigma_{22}^{J} = \frac{1}{3}\sigma_{22}^{JS=1/2} + \frac{2}{3}\sigma_{22}^{JS=3/2}.$$

For the collisions $(d\mu)_F + d \to (d\mu)_{F'} + d$ ($F_1 = 1/2, F_2 = 3/2$), we obtain

$$\sigma_{11}^{J} = \frac{1}{3}\sigma_{11}^{JS=1/2} + \frac{2}{3}\sigma_{11}^{JS=3/2}, \tag{31}$$
$$\sigma_{12}^{J} = \frac{1}{3}\sigma_{12}^{JS=1/2} + \frac{2}{3}\sigma_{12}^{JS=3/2};$$

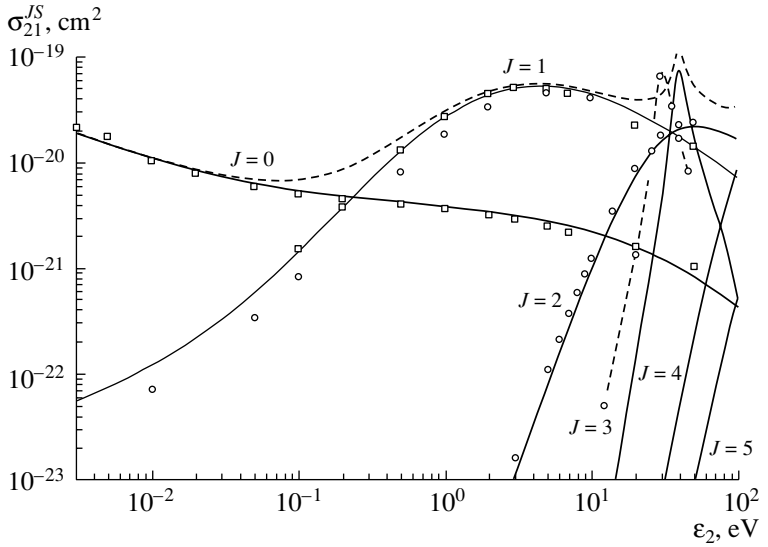

Fig. 9. Partial-wave cross sections $\sigma_{21}^{JS}(\varepsilon_2)$, $J = 0$–5 (solid curves) and total cross section $\sigma_{21}^{S}(\varepsilon_2)$ (dashed curve) of spin-flip $(d\mu)_{F=3/2} + d \to (d\mu)_{F=1/2} + d$, $S = 3/2$. Circles and squares are the results from [24] and [4], respectively. (Resonance shift for $J = 3$ is presented separately.)

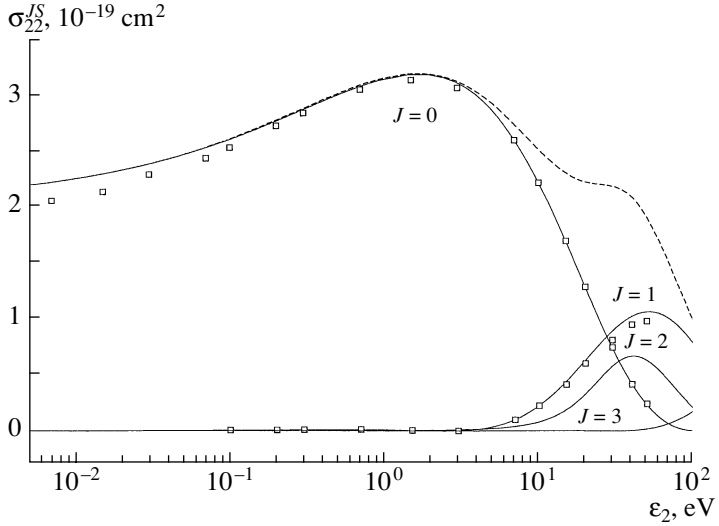

Fig. 10. Partial-wave cross sections $\sigma_{22}^{JS}(\varepsilon_2)$, $J = 0$–3 (solid curves) and total cross section $\sigma_{22}^{S}(\varepsilon_2)$ (dashed curve) of elastic scattering $(d\mu)_{F=3/2} + d \to (d\mu)_{F=3/2} + d$, $S = 5/2$. Squares are the results from [4].

$$\sigma_{21}^{J} = \frac{1}{6}\sigma_{21}^{JS=1/2} + \frac{1}{3}\sigma_{21}^{JS=3/2},$$

$$\sigma_{22}^{J} = \frac{1}{6}\sigma_{22}^{JS=1/2} + \frac{1}{3}\sigma_{22}^{JS=3/2} + \frac{1}{2}\sigma_{22}^{JS=5/2}.$$

5. NUMERICAL ALGORITHM

To calculate the RAHS basis functions, matrix elements, and the K matrix, a numerical code has been developed that can be used to calculate the characteristics of various three-body systems. The main features of the numerical algorithms were outlined in [11, 14].

RAHS basis functions $\varphi_{jmp}(\rho|\chi,\vartheta)$ (7) and matrix elements $P^{J}_{imp,jm'p'}(\rho)$, $Q^{J}_{imp,jm'p'}(\rho)$, $R^{J}_{imp,jm'p'}(\rho)$ were calculated on the orthogonal finite-element grid $[N_\chi \times N_\vartheta]$ using the second-order Lagrange elements. The calculations were performed on the interval of $\rho[0.01\sqrt{2M}, 30\sqrt{2M}]$. The grid step $\Delta\rho$ along the interval was adapted according to [14].

The number of nodes in χ and ϑ was taken equal to $N_\chi = 131$ and $N_\vartheta = 61$ for calculation of all mesic molecular systems. This provided an accuracy of calculation of $\sim 10^{-5}$ for all matrix elements. The ac-

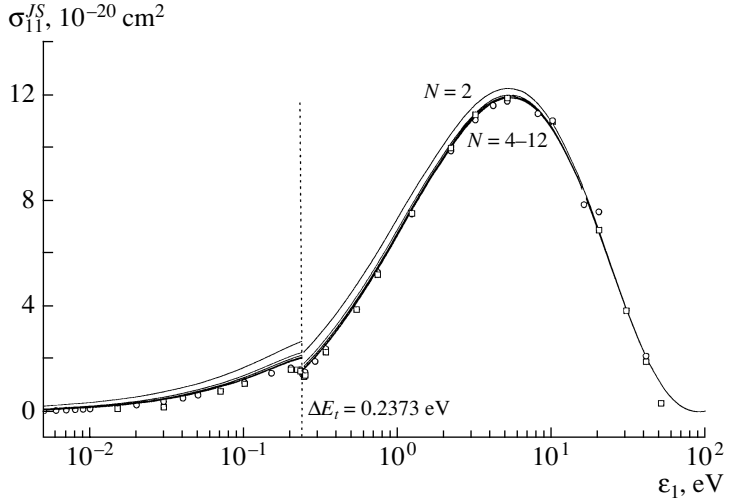

Fig. 11. Partial-wave cross section $\sigma_{11}^{JS}(\varepsilon_1)$ of elastic scattering $(t\mu)_{F=0} + t \to (t\mu)_{F'=0} + t$, $J = 0, S = 1/2$, calculated with different numbers N of RAHS basis functions. Circles and squares are the results from [24] and [4], respectively.

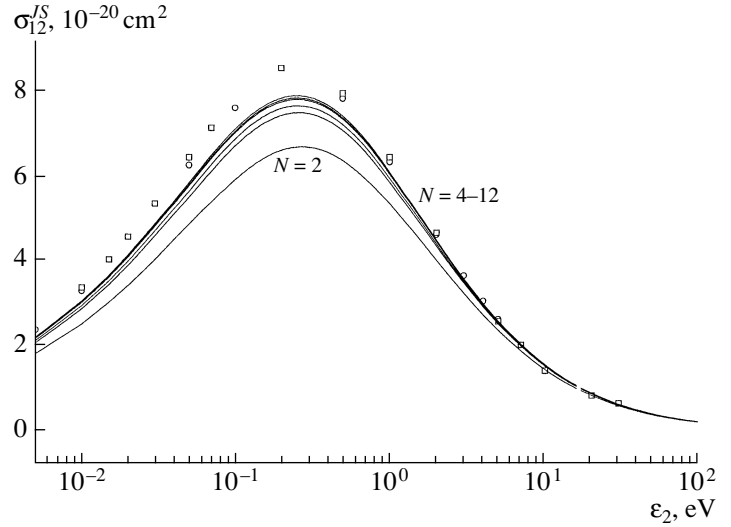

Fig. 12. Partial-wave cross section $\sigma_{12}^{JS}(\varepsilon_2)$ of elastic scattering $(t\mu)_{F=0} + t \to (t\mu)_{F=1} + t$, $J = 0, S = 1/2$, calculated with different numbers N of RAHS basis functions. Circles and squares are the results from [24] and [4], respectively.

curacy of calculation of potential curves $E_{jmp}(\rho)$ (8) is $\sim 10^{-6}$ for $0 \le \rho \le 10\sqrt{2M}$ and becomes worse ($\sim 10^{-5}$) with increasing ρ. Matrix elements were calculated with the set of basis functions $m = 0, i = 1$–6; $m = 1$, $i = 1$ for *gerade* ($p = g$) and *ungerade* ($p = u$) states, respectively, for the $p\mu p$, $d\mu d$, and $t\mu t$ systems.

The final results have been obtained with the number $N = 12$ of RAHS basis functions $\varphi_{jmp}(\rho|\chi, \vartheta)$ (7) with $m = 0$, $j \le \tilde{N} = 6$ for *gerade* and *ungerade* states. The test calculations for the systems $p\mu p$ and $d\mu d$ at $J = 1$ show that the contributions of basis functions with $m = 1$ or $j > 6$ are less than 2%, and they have not been taken into account in the final results.

To solve the system of radial equations (19), we use 300 finite elements on the interval $0 < \rho < \rho^* = 500$. This provides results with a relative accuracy of $\sim 10^{-4}$ in a wide region of collision energies excluding a narrow interval (≈ 0.01 eV) near threshold $\varepsilon = \Delta E_t$ of the collision $t\mu + t$.

The reliability of calculations is also confirmed by the symmetry of the K matrix: in our calculations $K_{\alpha\beta}^{JS} = K_{\beta\alpha}^{JS}$ with a relative accuracy of $\sim 10^{-5}$.

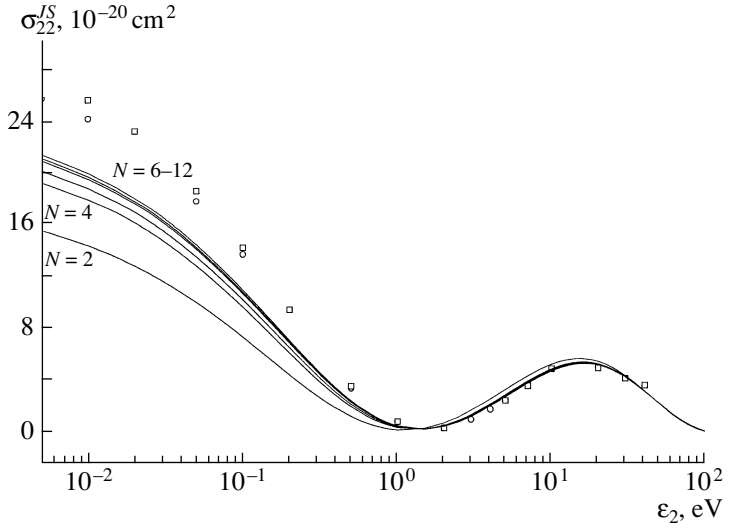

Fig. 13. Partial-wave cross section $\sigma_{22}^{JS}(\varepsilon_2)$ of elastic scattering $(t\mu)_{F=1} + t \to (t\mu)_{F=1} + t$, $J = 0$, $S = 1/2$, calculated with different numbers N of RAHS basis functions. Circles and squares are the results from [24] and [4], respectively.

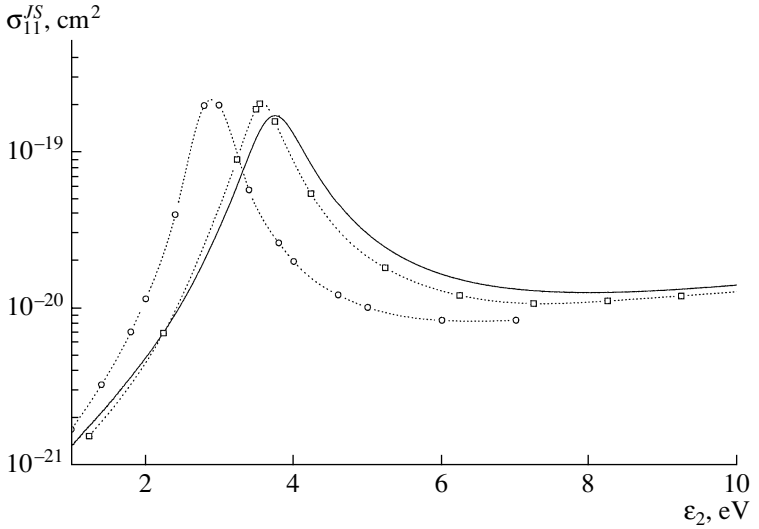

Fig. 14. Partial-wave cross section $\sigma_{11}^{JS}(\varepsilon_2)$ of the scattering process $(t\mu)_{F=1} + t \to (t\mu)_{F=0} + t$, $S = 1/2$ in the vicinity of resonance in the partial-wave $J = 2$ at $\varepsilon_1 \approx 4$ eV. Circles and squares are the results from [24] and [4], respectively.

6. RESULTS AND DISCUSSION

The calculated elastic and spin-flip cross sections $\sigma_{\alpha\beta}^{JS}(\varepsilon_\alpha)$ are presented in Figs. 1–13. The first channel corresponds to the spin state $F_1 = 0$ for $p\mu$ and $t\mu$ atoms and $F_1 = 1/2$ for $d\mu$ atom. For the second channel, $F_2 = 1$ for $p\mu$ and $t\mu$ atoms and $F_2 = 3/2$ for $d\mu$ atom. The results obtained demonstrate the rapid convergence upon increasing the number N of RAHS basis functions used and fairly good agreement with the results obtained in the improved two-level approximation [24] (circles), in the adiabatic-expansion method [4] (squares), and in the hyperspherical close-coupling method [19] (in Fig. 1, results of [19] for $p\mu + p$ collision coincide in the scale of the figure with those of [4]). The significant discrepancies take place for the $t\mu t$ system (see Figs. 12 and 13) and for the $d\mu d$ system with $J = 3$ (Fig. 9). Threshold phenomena at $\varepsilon = \Delta E_a$ (see Figs. 1, 5, and 11) need special treatment, especially more accurate asymptotic expressions for the effective potentials. On the average, the results of the calculations in the improved two-level approximation [24] agree with our results with a precision of 10–15%, and results obtained in the adiabatic approach [4] agree with a precision of 1–5%. However, in the vicinity of

Table 1. Spin-flip rates λ_p^J and λ_p for the reaction $(p\mu)_{F=1} + p \to (p\mu)_{F'=0} + p$

ε_2, eV	$J=0$	$J=1$	$J=2$	$J=3$	$J=4$	λ_p
0.005	0.171×10^{11}	0.202×10^{3}				0.171×10^{11}
0.010	0.171×10^{11}	0.431×10^{3}				0.171×10^{11}
0.100	0.172×10^{11}	0.840×10^{4}	0.138×10^{0}			0.172×10^{11}
0.500	0.162×10^{11}	0.169×10^{6}	0.367×10^{2}			0.162×10^{11}
1.000	0.144×10^{11}	0.773×10^{6}	0.624×10^{3}	0.892×10^{3}		0.144×10^{11}
5.000	0.878×10^{10}	0.293×10^{8}	0.779×10^{6}	0.359×10^{2}	0.885×10^{2}	0.881×10^{10}
10.000	0.660×10^{10}	0.117×10^{9}	0.189×10^{8}	0.383×10^{4}	0.163×10^{0}	0.674×10^{10}
50.000	0.317×10^{10}	0.949×10^{9}	0.163×10^{11}	0.560×10^{8}	0.578×10^{6}	0.204×10^{10}
100.000	0.227×10^{10}	0.135×10^{10}	0.528×10^{10}	0.144×10^{10}	0.422×10^{8}	0.104×10^{11}

Table 2. Spin-flip rates λ_d^J and λ_d for reaction $(d\mu)_{F=3/2} + d \to (d\mu)_{F'=1/2} + d^*$

ε_2, eV	$J=0$	$J=1$	$J=2$	$J=3$	$J=4$	λ_d
0.005	0.371×10^{8}	0.181×10^{6}				0.373×10^{8}
0.010	0.387×10^{8}	0.416×10^{6}				0.391×10^{8}
0.100	0.591×10^{8}	0.151×10^{8}	0.379×10^{0}			0.741×10^{8}
0.500	0.102×10^{9}	0.299×10^{9}	0.269×10^{3}	0.366×10^{2}		0.401×10^{9}
1.000	0.130×10^{9}	0.875×10^{9}	0.555×10^{4}	0.314×10^{0}		0.100×10^{10}
5.000	0.205×10^{9}	0.383×10^{10}	0.620×10^{7}	0.128×10^{5}	0.258×10^{1}	0.404×10^{10}
10.000	0.229×10^{9}	0.456×10^{10}	0.100×10^{9}	0.115×10^{7}	0.511×10^{3}	0.489×10^{10}
50.000	0.190×10^{9}	0.323×10^{10}	0.493×10^{10}	0.266×10^{10}	0.887×10^{8}	0.111×10^{11}
100.000	0.137×10^{9}	0.227×10^{10}	0.526×10^{10}	0.922×10^{8}	0.341×10^{10}	0.114×10^{11}

* The contribution $\lambda^J = 0.181 \times 10^9$ at $J=5$ at $\varepsilon_2 = 100$ eV is much less than at $J=4$. It is included in λ_d.

resonance (see Fig. 14), these discrepancies became substantial.

The partial-wave λ_a^J and total λ_a spin-flip rates are defined by the relations

$$\lambda_a^J = \sigma_{21}^J v_a n_0, \qquad \lambda_a = \sum_J \lambda_a^J, \qquad (32)$$

where σ_{21}^J is the averaged spin-flip cross section (28), (30), (31); v_a is the relative velocity of the $(a\mu)_{F_2} + a$ system; and $n_0 = 4.25 \times 10^{22}$ cm^{-3} is the density of liquid hydrogen.

The rates λ_a are presented in Fig. 15 and in Tables 1–3: at collision energy $\varepsilon_2 \le 1$ eV, $\lambda_p \approx$ const and $\lambda_t \approx$ const; $\lambda_d \approx$ const only at $\varepsilon_2 \le 0.01$ eV and it changes drastically: ~30 times in the energy range 0.01–1.0 eV and ~500 times in the energy range 0.01–100 eV; the quite specific resonance structure takes place at $\varepsilon_2 > 1$ eV. The rates λ_a are in good agreement with results of [4, 24, 25, 19]. At the same time, the theoretical value of λ_d for the reaction $(d\mu)_{F=3/2} + d \to (d\mu)_{F=1/2} + d$ still differs substantially (~40%) from the experimental one [26]. The reason for such a large difference is not yet clear.

Table 3. Spin-flip rates λ_t^J andλ_t for reaction $(t\mu)_{F=1} + t \to (t\mu)_{F'=0} + t$

ε_2, eV	$J = 0$	$J = 1$	$J = 2$	$J = 3$	$J = 4$	λ_t
0.005	0.119×10^{10}					0.119×10^{10}
0.010	0.119×10^{10}	0.552×10^{4}				0.119×10^{10}
0.100	0.120×10^{10}	0.890×10^{5}				0.120×10^{10}
0.500	0.122×10^{10}	0.131×10^{7}	0.108×10^{6}			0.122×10^{10}
1.000	0.119×10^{10}	0.487×10^{7}	0.204×10^{7}			0.119×10^{10}
5.000	0.942×10^{9}	0.667×10^{8}	0.377×10^{10}	0.124×10^{2}		0.478×10^{10}
10.000	0.785×10^{9}	0.133×10^{9}	0.164×10^{10}	0.997×10^{2}		0.255×10^{10}
50.000	0.420×10^{9}	0.236×10^{9}	0.972×10^{9}	0.125×10^{5}	0.270×10^{1}	0.163×10^{10}
100.000	0.307×10^{9}	0.231×10^{9}	0.495×10^{9}	0.100×10^{6}	0.216×10^{0}	0.103×10^{10}

Table 4. Elastic cross sections σ_{11} of the reaction $(p\mu)_{F=0} + p \to (p\mu)_{F=0} + p$ at room temperature (collision energy $\varepsilon = 0.04$ eV)

References	σ_{11}, 10^{-21} cm^2	Remarks
Zeldovich and Gershtein, 1960 [27]	1.2	Scattering length approximation
Cohen *et al.*, 1960 [28]	8.2	Adiabatic expantion
Dzhelepov *et al.*, 1965 [29]	167 ± 30	Experiment
Alberigi *et al.*, 1967 [30]	7.6 ± 0.7	Experiment
Matveenko and Ponomarev, 1970 [31]	2.5	Two-level adiabatic approximation
Matveenko *et al.*, 1975 [32]	0.23	Two-level adiabatic approach
Ponomarev *et al.*, 1979 [33]	35	"Simple approach" in two-level adiabatic approximation
Bertin *et al.*, 1978 [34]	14 ± 2	Experiment
Melezhik *et al.*, 1983 [35]	19	Adiabatic approach
Bracci *et al.*, 1989 [4]	41	Adiabatic approach ($\approx$500 basis functions)
This work	40.2	AHSA (12 basis functions)

Elastic scattering process $(p\mu)_{F=0} + p \to (p\mu)_{F=0} + p$ for many years was a subject of experimental and theoretical investigations, whose controversial results are presented in Table 4. We hope that our calculations will help to close a long discussion of this problem.

One of the main results of this paper is the confirmation of the elaborate and tedious calculations that were performed in the adiabatic representation [7]. These calculations were used as a basis for the preparation of the atlas of mesic-atom scattering cross sections [36], which was used for the description of muon-catalyzed fusion kinetics. This paper gives an

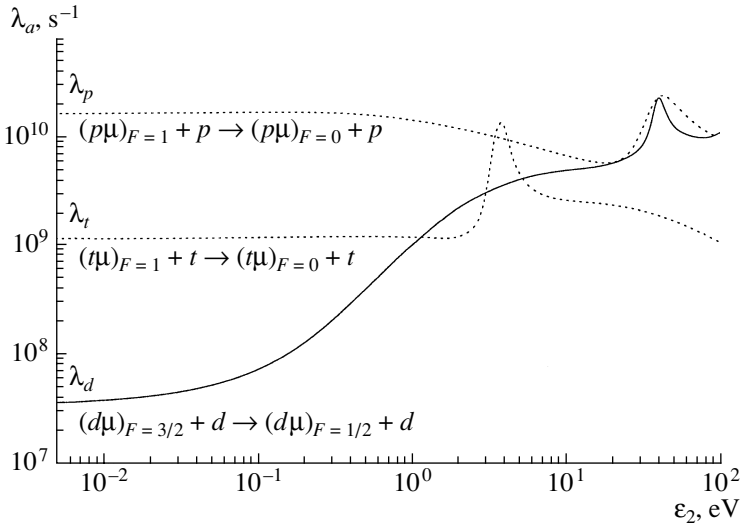

Fig. 15. Spin-flip rates $\lambda_a(\varepsilon_2)$ (32) for the processes $(a\mu)_{F_2} + a \to (a\mu)_{F_1} + a$.

independent cross-check of all these calculations and confirms almost all results obtained previously.

ACKNOWLEDGMENTS

We are deeply grateful to Prof. S.S. Gershtein and Prof. M.P. Faifman for stimulating discussions. One of us (D.I.A.) is grateful to Prof. C.D. Lin for the hospitality at KSU. We are grateful to Prof. I. Shimamura and participants of his seminar for comments and discussions.

This work was supported by INTAS (grant no. 97-11032).

REFERENCES

1. L. I. Ponomarev, Contemp. Phys. **31**, 219 (1990).
2. D. I. Abramov, V. V. Gusev, and L. I. Ponomarev, Yad. Fiz. **64**, 1442 (2001) [Phys. At. Nucl. **64**, 1364 (2001)].
3. S. S. Gershteĭn, Zh. Éksp. Teor. Fiz. **34**, 463 (1958); **40**, 698 (1961).
4. L. Bracci, C. Chiccoli, G. Fiorentini, *et al.*, Muon Catal. Fusion **4**, 247 (1989).
5. M. Born, Nachr. Akad. Wiss. Göttingen **1**, 1 (1951); M. Born and Huang Kun, *Dynamical Theory of Crystal Lattices* (Clarendon Press, Oxford, 1954).
6. I. V. Komarov, L. I. Ponomarev, and S. Yu. Slavyanov, *Spheroidal and Coulomb Spheroidal Function* (Nauka, Moscow, 1976) [in Russian].
7. S. I. Vinitsky and L. I. Ponomarev, Fiz. Élem. Chastits At. Yadra **13**, 1336 (1982) [Sov. J. Part. Nucl. **13**, 557 (1982)].
8. J. Macek, J. Phys. B **1**, 831 (1968).
9. C. D. Lin, Phys. Rep. **257**, 1 (1995).
10. D. I. Abramov, V. V. Gusev, and L. I. Ponomarev, in *Contributed Papers, 14th International Conference on Few Body Problems in Physics, Williamsburg, 1994*, pp. 745, 749.
11. V. V. Gusev, V. I. Puzynin, V. V. Kostrykin, *et al.*, Few-Body Syst. **9**, 137 (1990).
12. D. I. Abramov, V. V. Gusev, and L. I. Ponomarev, Yad. Fiz. **60**, 1259 (1997) [Phys. At. Nucl. **60**, 1133 (1997)].
13. D. I. Abramov, V. V. Gusev, and L. I. Ponomarev, Hyperfine Interact. **101–102**, 375 (1996).
14. D. I. Abramov, L. N. Bogdanova, V. V. Gusev, and L. I. Ponomarev, Hyperfine Interact. **101–102**, 301 (1996); Yad. Fiz. **61**, 520 (1998) [Phys. At. Nucl. **61**, 457 (1998)].
15. D. I. Abramov and V. V. Gusev, J. Phys. B **33**, 891 (2000).
16. D. I. Abramov, V. V. Gusev, and L. I. Ponomarev, Hyperfine Interact. **119**, 127 (1999).
17. V. V. Gusev, L. I. Ponomarev, and E. A. Solov'ev, Hyperfine Interact. **82**, 53 (1993).
18. D. I. Abramov, V. V. Gusev, and L. I. Ponomarev, Preprint of Kurchatov Institute No. IAE-6121/1, RRC (Moscow, 1999).
19. A. Igarashi, I. Shimamura, and N. Toshima, Phys. Rev. A **58**, 1166 (1998).
20. D. Bakalov, Muon Catal. Fusion **3**, 321 (1988).
21. E. U. Condon and G. H. Shortley, *The Theory of Atomic Spectra* (Macmillan, New York, 1935).
22. A. R. Edmonds, *Angular Momentum in Quantum Mechanics* (Princeton Univ. Press, Princeton, 1974).
23. L. D. Landau and E. M. Lifshitz, *Quantum Mechanics* (Addison-Wesley, New York, 1977).
24. M. Bubak and M. P. Faifman, Preprint No. E4-87-464 (Joint Inst. Nucl. Res., Dubna, 1987).
25. L. Bracci, C. Chiccoli, G. Fiorentini, *et al.*, Phys. Lett. A **134**, 435 (1989).
26. N. I. Voropaev *et al.*, Hyperfine Interact. **118**, 135 (1999).

27. Ya. B. Zeldovich and S. S. Gershtein, Usp. Fiz. Nauk **71**, 581 (1960).
28. S. Cohen, D. J. Judd, and R. J. Riddel, Phys. Rev. **119**, 384 (1960).
29. V. P. Dzelepov, P. F. Ermolov, and V. V. Filchenkov, Zh. Éksp. Teor. Fiz. **49**, 393 (1965).
30. A. Alberigi *et al.*, Nuovo Cimento B **47**, 72 (1967).
31. A. V. Matveenko and L. I. Ponomarev, Zh. Éksp. Teor. Fiz. **59**, 1953 (1970).
32. A. V. Matveenko, L. I. Ponomarev, and M. P. Faifman, Zh. Éksp. Teor. Fiz. **68**, 437 (1975) [Sov. Phys. JETP **41**, 212 (1975)].
33. L. I. Ponomarev, L. N. Somov, and M. P. Faifman, Yad. Fiz. **29**, 133 (1979) [Sov. J. Nucl. Phys. **29**, 67 (1979)].
34. A. Bertin, I. Massa, and M. Piccinini, Phys. Lett. B **78B**, 355 (1978).
35. V. S. Melezhik, L. I. Ponomarev, and M. P. Faifman, Zh. Éksp. Teor. Fiz. **85**, 434 (1983) [Sov. Phys. JETP **58**, 254 (1983)].
36. A. Adamczak, M. P. Faifman, L. I. Ponomarev, *et al.*, At. Data Nucl. Data Tables **62**, 255 (1996).

Physics of Atomic Nuclei, Vol. 67, No. 2, 2004, pp. 241–249. Translated from Yadernaya Fizika, Vol. 67, No. 2, 2004, pp. 258–266.

NUCLEI
Theory

P-Even Correlations in Binary and Ternary Nuclear Fission Induced by Polarized Neutrons

S. G. Kadmensky

Voronezh State University, Universitetskaya pl. 1, Voronezh, 394693 Russia

Received October 8, 2002; in final form, January 13, 2003

Abstract—The evolution of a fissile nucleus from transition fission states specified at the saddle point of the deformation potential to fission states associated with prescission configurations of this nucleus and characterized by a pearlike shape of the nucleus is studied within the quantum-mechanical theory of fission processes that is based on the time-independent formalism. The coefficients of P-even asymmetries in the angular distributions of a light fragment and a third particle are calculated on the basis of the idea of the one-step mechanism of the production of a third particle and two fragments from the ternary fission of nuclei that is induced by polarized thermal neutrons. In order to confirm the developed concepts, it is proposed to repeat, at a higher level of statistical accuracy, experiments devoted to observing left–right asymmetries in the angular distributions of alpha particles from the ternary fission of nuclei. © *2004 MAIK "Nauka/Interperiodica".*

1. INTRODUCTION

Correlations of the P-even type in the binary fission of nuclei that is induced by polarized thermal neutrons were discovered by the authors of [1–3], who studied the coefficients $(\alpha_{\rm LF}^{\rm LR})^b$ associated with the emergence of left–right asymmetry of the form $\mathbf{n}_{\rm LF}\cdot[\mathbf{n}_k\times\boldsymbol{\sigma}]$ in the angular distributions of fission fragments, where $\mathbf{n}_{\rm LF}=\mathbf{k}_{\rm LF}/k_{\rm LF}$, $\mathbf{n}_k=\mathbf{k}_n/k_n$, and $|\boldsymbol{\sigma}|=1$; here, $\mathbf{k}_n$ and $\boldsymbol{\sigma}$ are the neutron wave vector and spin, respectively, while $\mathbf{k}_{\rm LF}$ is the light-fission-fragment wave vector. For ^{233}U target nuclei, the coefficient $(\alpha_{\rm LF}^{\rm LR})^b$ proved to be

$$(\alpha_{\rm LF}^{\rm LR})^b=-(0.233\pm0.025)\times10^{-3}. \qquad (1)$$

In [4, 5], an experimental investigation of the analogous coefficient $(\alpha_{\rm LF}^{\rm LR})^t$ for the ternary fission of ^{233}U nuclei resulted in estimating it at

$$(\alpha_{\rm LF}^{\rm LR})^t\approx-(0.57\pm0.13)\times10^{-3}, \qquad (2)$$

whence one can see that the sign of this coefficient is identical to that of the coefficient in (1) and that its magnitude is commensurate with that in (1) and is independent of the energy of a third particle.

In the angular distribution of a third particle from the ternary fission of ^{233}U nuclei that is induced by polarized thermal neutrons, there appears the coefficient $(\alpha_{\rm TP}^{\rm LR})^t$ of left–right anisotropy, which is associated with correlations of the form $\mathbf{n}_{\rm TP}\cdot[\mathbf{n}_k\times\boldsymbol{\sigma}]$ (where $\mathbf{n}_{\rm TP}$ is the unit vector aligned with the wave vector $\mathbf{k}_{\rm TP}$ of the third particle), the value of this coefficient being [4]

$$(\alpha_{\rm TP}^{\rm LR})^t=-(0.08\pm0.08)\times10^{-3}. \qquad (3)$$

This estimate was obtained for the case where an alpha particle was taken to be the third particle. The value in (3) is much less in magnitude than the analogous coefficient $(\alpha_{\rm LF}^{\rm LR})^t$ in (2) for a light fragment originating from the ternary fission of a ^{233}U nucleus and is uncertain at the statistical-accuracy level currently achieved in experiments.

A theoretical investigation of P-even correlations for binary nuclear fission was performed in [6], where it was shown that the scale of the experimental coefficients $(\alpha_{\rm LF}^{\rm LR})^b$ can be qualitatively explained.

On the basis of the ideas developed in [7–9], it was concluded in [5] that the coefficient $(\alpha_{\rm LF}^{\rm LR})^b$ of left–right asymmetry for a light fragment from binary nuclear fission is close in magnitude to the analogous coefficient $(\alpha_{\rm LF}^{\rm LR})^t$ for ternary fission. At the same time, two situations proved to be possible in [5] for the values of the coefficients $(\alpha_{\rm TP}^{\rm LR})^t$ for a third particle, depending on the mechanism of ternary nuclear fission. For the one-step mechanism, in which case two fragments and a third particle emerge simultaneously upon a double rupture of the neck of a fissile nucleus, the asymmetry coefficients $(\alpha_{\rm LF}^{\rm LR})^t$ and $(\alpha_{\rm TP}^{\rm LR})^t$ are close in magnitude. But for the two-step (sequential) mechanism of ternary fission, in which case a single rupture of the neck of a fissile nucleus

1063-7788/04/6702-0241$26.00

leads to the formation of two fission fragments at the first stage, whereupon one of these fragments emits a third particle, the coefficient $(\alpha_{\mathrm{TP}}^{\mathrm{LR}})^t$ must be close to zero because of the presence of a large number of statistically independent channels of third-particle emission.

In [5], it was assumed that the experimental value of the coefficient $(\alpha_{\mathrm{TP}}^{\mathrm{LR}})^t$ in (3) is indicative of its proximity to zero; on this basis, it was concluded there that ternary nuclear fission proceeds via the two-step mechanism.

On the basis of the ideas of the theory of open Fermi systems [10], methods developed in analyzing the angular distributions of protons emitted by polarized deformed nuclei [11, 12], and A. Bohr's concept of transition fission states [7], a quantum-mechanical approach to describing binary nuclear fission was proposed in [13, 14]. This approach, supplemented with the use of the adiabatic approximation for the asymptotic region of the fissile system, made it possible to obtain an explicit dependence of partial-width amplitudes and potential fission phase shifts on the spins, relative orbital angular momenta, and orientation of the axes of fission fragments. In [15], this approach was generalized to the case of ternary nuclear fission.

On the basis of the ideas developed in [13–16], the coefficients of P-odd asymmetries in the angular distributions of fragments originating from binary and ternary nuclear fission were explored in [17], and arguments in favor of the one-step mechanism of ternary nuclear fission were adduced there.

The present study is aimed at analyzing the coefficients of left–right asymmetry in binary and ternary nuclear fission with the aid of the concepts formulated in [13–15, 17] and at investigating, on this basis, the mechanisms of binary and ternary nuclear fission.

2. STRUCTURE OF THE WAVE FUNCTIONS FOR NEUTRON RESONANCES AND THEIR FISSION WIDTHS

As was shown in [6], P-even asymmetries for the binary fission of unpolarized target nuclei characterized by a spin I, its projection M_I onto the z axis of the laboratory frame, and a parity π and exposed to polarized thermal neutrons inducing this fission process arise because of interference effects in the angular distributions of light fission fragments emitted from s- and p-wave neutron resonances that are populated upon neutron capture by a target nucleus. We describe a neutron-resonance state in terms of a wave function $\Psi_\sigma^{J_\sigma M_\sigma \pi_\sigma}$ and a complex energy $\bar{E}_\sigma^{J_\sigma \pi_\sigma} = (E_\sigma^{J_\sigma \pi_\sigma} - i\bar{\Gamma}_\sigma^{J_\sigma \pi_\sigma}/2)$, where $E_\sigma^{J_\sigma \pi_\sigma}$ is the real part of the resonance energy; $\bar{\Gamma}_\sigma^{J_\sigma \pi_\sigma}$ is the total decay width of the resonance; the index σ takes the values s and p for s- and p-wave neutron resonances, respectively; and the indices J_σ, M_σ, π_σ, and σ specify, respectively, the spin, its projection onto the z axis of the laboratory frame, parity, and other quantum numbers of the neutron resonance in question with $\pi_s = \pi$ and $\pi_p = \bar{\pi}_s = -\pi$. Because of the dynamic enhancement of the Coriolis interaction effect on the structure of neutron-resonance states, there occurs, in a deformed axisymmetric compound nucleus, a complete mixing of neutron-resonance states described by the wave functions $\Psi_{\sigma K_\sigma}^{J_\sigma M_\sigma \pi_\sigma}$ and characterized by a fixed value of the spin projection K_σ onto the symmetry axis of a compound nucleus [18], this axis being aligned with the z' axis of the intrinsic coordinate frame associated with this nucleus. Therefore, the neutron-resonance wave function $\Psi_\sigma^{J_\sigma M_\sigma \pi_\sigma}$ has the form

$$\Psi_\sigma^{J_\sigma M_\sigma \pi_\sigma} = \sum_{K_\sigma} a_{K_\sigma}^{J_\sigma} \Psi_{\sigma K_\sigma}^{J_\sigma M_\sigma \pi_\sigma}, \qquad (4)$$

where the signs of the coefficients $a_{K_\sigma}^{J_\sigma}$ are distributed at random, while the mean values of their moduli are equal to $(2J_\sigma + 1)^{-1/2}$. The total fission width of the neutron resonance specified by the wave function in the form (4) can then be represented as [18, 19]

$$\Gamma_\sigma^{J_\sigma \pi_\sigma} = \sum_{K_\sigma} (a_{K_\sigma}^{J_\sigma})^2 \Gamma_{\sigma K_\sigma}^{J_\sigma \pi_\sigma}. \qquad (5)$$

Using Bohr's concept of transition fission states [7], one can isolate, in the wave function $\Psi_{\sigma K_\sigma}^{J_\sigma M_\sigma \pi_\sigma}$, the component that is related to the wave functions $\Psi_{rK_\sigma}^{J_\sigma M_\sigma \pi_\sigma}$ for the above transition states r as [6]

$$\Psi_{\sigma K_\sigma}^{J_\sigma M_\sigma \pi_\sigma} = \sum_\nu b_{\nu\sigma}^{J_\sigma \pi_\sigma} \varphi_{\nu K_\sigma}^{J_\sigma M_\sigma \pi_\sigma} + \sum_r b_{r\sigma K_\sigma}^{J_\sigma \pi_\sigma} \Psi_{rK_\sigma}^{J_\sigma M_\sigma \pi_\sigma}, \qquad (6)$$

where N wave functions $\varphi_{\nu K_\sigma}^{J_\sigma M_\sigma \pi_\sigma}$ that are associated with nucleonic particle–hole excitations of the nucleus form a multinucleon basis of random Wigner matrices [7]. The coefficients $b_{\nu\sigma K_\sigma}^{J_\sigma \pi_\sigma}$ and $b_{r\sigma K_\sigma}^{J_\sigma \pi_\sigma}$ in (6) have a random character, the mean values of their squares being equal to $1/N$. The transition fission states are specified at those values of the deformation parameters β_λ ($\lambda = 2, 3, 4, \ldots$) of the compound nucleus that correspond to the saddle point of the deformation potential, $\beta_\lambda = \beta_\lambda^{\mathrm{sad}}$; as a matter of fact, these are doorway states for physical nuclear-fission channels, and this explains the large fluctuations of the fission widths of the neutron resonances involved [7]. The evolution of a fissile nucleus from transition fission states to asymptotic states, where there appear

fission fragments, occurs in accordance with the dynamical quantum-mechanical scenario.

In order to explain P-even and P-odd asymmetries in binary nuclear fission induced by polarized neutrons, Sushkov and Flambaum [6] assumed that the nucleus undergoing fission has a pearlike axisymmetric shape in transition fission states. Their assumption, which was crucial there for this explanation, was criticized by Bunakov and Gudkov [8, 9] in view of the fact that, as a rule, the nucleus undergoing fission does not have static octupole deformations at the saddle point of the deformation potential, where one defines [7] transition fission states, such deformations appearing only in prescission nuclear configurations.

In developing the quantum-mechanical theory of the fission process, it was shown [13–15] that partial fission widths are controlled by the structure of the wave function for a fissile nucleus in the vicinity of the point of its scission into fission fragments ($R \approx R_{\rm sc}$), where $\mathbf{R} = \mathbf{R}_1 - \mathbf{R}_2$, $\mathbf{R}_i$ being the c.m. coordinate of the ith fission fragment ($i = 1, 2,\ A_1 < A_2$). Obviously, this coordinate is that of the relative motion of the fragments, while the solid angle $\Omega \equiv \theta, \varphi$ specifies the direction of the radius vector $\mathbf{R}$ in the laboratory frame and, simultaneously, the direction $\mathbf{n}_{\rm LF}$ of light-fission-fragment emission. The trajectories along which the nucleus undergoing fission travels from the saddle point to the scission point $R = R_{\rm sc}$ may lie in different valleys of its deformation potential. If one introduces a set of wave functions $\Psi^{JM\pi}_{qK}$ corresponding to states of a fissile nucleus in the above valleys near the point $R = R_{\rm sc}$ at deformation-parameter values associated with the multipolarity μ, $\beta_\mu = \beta^{\rm sc}_{\mu q}$, and with various fission modes q, then, in the vicinity of this point, the wave function for the nucleus undergoing fission and arising upon its evolution from a transition fission state at the saddle point with the wave function $\Psi^{JM\pi}_{qK}$ to various fission modes q admits the representation [19]

$$\sum_q c^{J\pi}_{qrK}\Psi^{JM\pi}_{qK}, \tag{7}$$

where the coefficients $c^{J\pi}_{qrK}$ are of a dynamical character. For fragment-mass- and fragment-charge-asymmetric fission processes, the wave function $\Psi^{JM\pi}_{qK}$ describes a fissile-nucleus state where the nucleus has a pearlike axisymmetric shape and where static octupole ($\mu = 3$) deformations differ from zero, $\beta^{\rm sc}_{3q} \neq 0$. The total fission width $\Gamma^{J_\sigma\pi_\sigma b}_\sigma$ with respect to the binary fission of a $\sigma J_\sigma M_\sigma \pi_\sigma$ neutron resonance can then be represented in the form

$$\Gamma^{J_\sigma\pi_\sigma b}_\sigma = \sum_{K_\sigma rq}(a^{J_\sigma}_{K_\sigma})^2(b^{J_\sigma\pi_\sigma}_{r\sigma K_\sigma})^2(c^{J_\sigma\pi_\sigma}_{qrK_\sigma})^2\Gamma^{J_\sigma\pi_\sigma b}_{qK_\sigma}, \tag{8}$$

where $\Gamma^{J_\sigma\pi_\sigma b}_{qK_\sigma}$ is the total fission width with respect to the mode where the nucleus undergoing fission has the wave function $\Psi^{J_\sigma M_\sigma\pi_\sigma}_{qK_\sigma}$. In turn, the quantity $\Gamma^{J_\sigma\pi_\sigma b}_{qK_\sigma}$ is determined by the sum of partial fission widths [13, 14]; that is,

$$\Gamma^{J_\sigma\pi_\sigma b}_{qK_\sigma} = \sum_c \Gamma^{J_\sigma\pi_\sigma b}_{qK_\sigma c} = \sum_{cJ_1J_2jL}\Gamma^{J_\sigma\pi_\sigma b}_{qK_\sigma cJ_1J_2jL}, \tag{9}$$

where J_i is the spin of the ith fission fragment; L is the relative orbital angular momentum of fission fragments; j is an intermediate spin that is determined by the vector composition of the spin J_2 and the orbital angular momentum L; and the index c combines the spin projections K_i, the parities π_i, and other quantum numbers σ_i, including the atomic weights A_i, the charges Z_i, the energies E_i, and the deformations $\beta_{\mu i}$ of fission fragments. In (9), primary fragments are taken to mean fission fragments, the term "primary fragments" being associated with the fact that the rupture of the nucleus undergoing fission leads to the production of these fragments in states that are strongly nonequilibrium in the values of their deformation parameters $\beta_{\mu i}$. As the result of their subsequent evolution, the fragments go over to highly excited states that are equilibrium in the values of their deformation parameters, whereupon they undergo deexcitation, emitting neutrons and gamma rays and transforming into final fission fragments that occur in the ground or long-lived isomeric states usually recorded by detectors.

If use is made of the concept of a pearlike axisymmetric shape of the fissile nucleus in the prescission state, the wave function for this state can be represented in the form [7]

$$\begin{aligned}\Psi^{JM\pi}_{qK}(\omega,\xi) &= \sqrt{\frac{2J+1}{16\pi^2}} \\ &\times [(1-\delta_{K,0})\{D^J_{MK}(\omega)\chi^\pi_{qK}(\xi) \\ &+ (-1)^{J+K}D^J_{M-K}(\omega)\chi^\pi_{\overline{qK}}(\xi)\} \\ &+ \delta_{K,0}\sqrt{2}D^J_{M0}(\omega)\chi^\pi_{qn}(\xi)],\end{aligned} \tag{10}$$

where $D^J_{MK}(\omega)$ is a generalized spherical harmonic that is dependent on the Euler angles $(\alpha, \beta, \gamma) \equiv \omega$ characterizing the orientation of the axes of the fissile nucleus with respect to the axes of the laboratory frame. The intrinsic wave functions for the fissile nucleus, $\chi^\pi_{qn}(\xi)$ for $K = 0$ and $\chi^\pi_{qK}(\xi)$ for $K \neq 0$, which are dependent on the intrinsic coordinates ξ of the nucleus, have the form

$$\chi^\pi_{qn}(\xi) = \frac{1}{\sqrt{2}}(\psi_{qn}(\xi) + \pi\hat{p}\psi_{qn}(\xi))i^{\frac{(1-\pi)}{2}}; \tag{11}$$

$$\chi^\pi_{qK}(\xi) = \frac{1}{\sqrt{2}}(\psi_{qK}(\xi) + \pi\hat{p}\psi_{qK}(\xi))i^{\frac{(1-\pi)}{2}},$$

where $\hat{p}$ is the operator of the reflection of spatial coordinates and the functions $\psi_{qn}(\xi)$ and $\psi_{qK}(\xi)$ are not parity eigenstates and correspond to a pearlike shape of the fissile nucleus. We also have $\chi^{\pi}_{\overline{qK}}(\xi) = \tau\chi^{\pi}_{qK}(\xi)$, where τ is the time-inversion operator and $\chi^{\pi}_{qn}(\xi)$ is an eigenfunction of the operator τ for the eigenvalue $n = (-1)^J$ [7].

In turn, the wave function $\Psi^{J_i M_i \pi_i}_{\sigma_i K_i}(\omega_i, \xi_i)$ for the ith axisymmetric fragment that does not involve static odd deformations, including octupole deformations, can be represented in the form (10), where the indices $Jq\pi K\omega\xi$ are replaced by the indices $J_i\sigma_i\pi_i K_i\omega_i\xi_i$ and where the intrinsic wave functions χ^{π}_{qK}, $\chi^{\pi}_{\overline{qK}}$, and χ^{π}_{qn} are replaced by the respective intrinsic wave functions $\chi^{\pi_i}_{\sigma_i K_i}$, $\chi^{\pi_i}_{\overline{\sigma_i K_i}}$, and $\chi^{\pi_i}_{\sigma_i n_i}$ for fission fragments.

With the aid of the methods developed in [13, 14], it can be shown that the fission width $\Gamma^{J\pi}_{qKc}$ (9) is independent of the spin J and the parity π of the nuclear state in question, but that it is determined exclusively by the structure of the wave functions for this state and for the fission fragments in the channel c [see Eqs. (10) and (11), respectively]. Therefore, the neutron-resonance fission width $\Gamma^{J_\sigma\pi_\sigma b}_{\sigma}$ (8) can be represented in the form

$$\Gamma^{J_\sigma\pi_\sigma b}_{\sigma} = \sum_{K_\sigma r q c} (a^{J_\sigma}_{K_\sigma})^2 (b^{J_\sigma\pi_\sigma}_{r\sigma K_\sigma})^2 (c^{J_\sigma\pi_\sigma}_{qrK_\sigma})^2 \Gamma^{b}_{qK_\sigma c}. \quad (12)$$

3. ANGULAR DISTRIBUTIONS OF FRAGMENTS ORIGINATING FROM BINARY NUCLEAR FISSION INDUCED BY POLARIZED THERMAL NEUTRONS

Following [6], we choose the z axis of the laboratory frame to be aligned with the direction of the polarized-neutron spin $\boldsymbol{\sigma}$ and represent the incident-neutron wave function in the form

$$e^{-i\mathbf{k}_n\cdot\mathbf{r}_n}\chi_{1/2\,1/2}(\sigma) = 4\pi \sum_{jj_z l_n m_n} i^{l_n} j_{l_n}(k_n r_n) \quad (13)$$
$$\times\, Y^{*}_{l_m m_n}(\Omega_{\mathbf{k}_n}) C^{jj_z}_{l_n 1/2\, m_n\, 1/2} \Phi_{jl_n j_z}(\mathbf{r}_n, \boldsymbol{\sigma}),$$

where $\Phi_{jl_n j_z}(\mathbf{r}_n, \boldsymbol{\sigma})$ is the spin–orbit wave function for a neutron having an orbital angular momentum l_n, its projection being denoted by m_n, while the solid angle $\Omega_{\mathbf{k}_n}$ specifies the direction of the vector $\mathbf{k}_n$ in the laboratory frame.

Relying on the theory of resonance nuclear reactions in the formulation that was given in [16] and which takes correctly into account the symmetry properties of wave functions under time inversion and using the formalism that was developed in [6, 13, 14], we find that, in the c.m. frame, the differential cross section for (n, f) reactions of polarized-neutron-induced binary fission of unpolarized target nuclei having a spin I and a spin projection M_I onto the z axis of the laboratory frame can be represented in the form

$$\frac{d\sigma^{b}_{nf}(\theta,\varphi)}{d\Omega} = \frac{2\pi^2}{k_n^2}\frac{1}{(2I+1)}\sum_{M_I}|A_{M_I}(\theta,\varphi,\xi_1,\xi_2)|^2, \quad (14)$$

where the amplitude $A_{M_I}(\theta,\varphi,\xi_1,\xi_2)$ is given by

$$A_{M_I}(\theta,\varphi,\xi_1,\xi_2) = \sum_{sJ_sK_sqc} C^{J_sM_s}_{I1/2M_I1/2} Y_{00}(\Omega_{\mathbf{k}}) a^{J_s}_{K_s} \quad (15)$$
$$\times \sum_r b^{J_s\pi}_{rsK_s} c^{J_s\pi}_{qrK_s} \sqrt{\Gamma^{b}_{qK_sc}}$$
$$\times\, u^{J_s\pi}_{s} e^{i\delta^b_c} \Psi^{J_sM_s\pi}_{K_sc}(\theta,\varphi,\xi_1,\xi_2)$$
$$+ \sum_{pJ_pK_pjj_zm_nqc} C^{J_pM_p}_{IjM_Ij_z} C^{jj_z}_{11/2m_n1/2} Y_{1m_n}(\Omega_{\mathbf{k}}) a^{J_p}_{K_p}$$
$$\times \sum_r b^{J_p\bar{\pi}}_{rpK_p} c^{J_p\bar{\pi}}_{qrK_p} \sqrt{\Gamma^{b}_{qK_p}}\, u^{J_p\bar{\pi}}_{pj} e^{i\delta^b_c} \Psi^{J_pM_p\bar{\pi}}_{K_pc}(\theta,\varphi,\xi_1,\xi_2).$$

In Eq. (15), we have used the notation

$$u^{J_s\pi}_{s} = \frac{\sqrt{\Gamma^{J_s\pi}_{sn}}e^{i\delta_{sn}}}{E - E^{J_s\pi}_{s} + \dfrac{i\bar{\Gamma}^{J_s\pi}_{s}}{2}}, \quad (16)$$

$$u^{J_p\bar{\pi}}_{pj} = \frac{\sqrt{\Gamma^{J_p\bar{\pi}}_{pjn}}e^{i\delta_{pjn}}}{E - E^{J_p\bar{\pi}}_{p} + \dfrac{i\bar{\Gamma}^{J_p\bar{\pi}}_{p}}{2}},$$

$$\Psi^{JM\pi}_{Kc}(\theta,\varphi,\xi_1,\xi_2) \quad (17)$$
$$= \sqrt{\frac{2J+1}{8\pi}}\{D^{J}_{MK}(\varphi,\theta,0) f_c(\xi_1,\xi_2)$$
$$+ (-1)^{J+K}\pi D^{J}_{M-k}(\varphi,\theta,0) f_{\bar{c}}(\xi_1,\xi_2)\},$$

where E is the total c.m. energy of the nucleus undergoing fission; $\sqrt{\Gamma^{J_s\pi}_{sn}}$ and $\sqrt{\Gamma^{J_p\bar{\pi}}_{pjn}}$ are the amplitudes of the width of, respectively, s- and p-wave neutron resonances; δ_{sn} and δ_{pjn} are the potential neutron phase shifts; δ^b_c is the potential fission phase shift in the channel c; and the functions f_c and $f_{\bar{c}}$ are defined in terms of the fission-fragment wave function (11) and those that are time-conjugate to them as

$$f_c(\xi_1,\xi_2) = \chi^{\pi}_{\sigma_1K_1}(\xi_1)\chi^{\pi}_{\sigma_2K_2}(\xi_2) \quad (18)$$
$$+ (-1)^{J_1+K_1}\chi^{\pi}_{\overline{\sigma_1K_1}}(\xi_1)\chi^{\pi}_{\sigma_2K_2}(\xi_2)$$
$$+ (-1)^{J_2+K_2}\chi^{\pi}_{\sigma_1K_1}(\xi_1)\chi^{\pi}_{\overline{\sigma_2K_2}}(\xi_2)$$

$$+ (-1)^{J_1+J_2+K_1+K_2}\chi^{\pi}_{\sigma_1 K_1}(\xi_1)\chi^{\pi}_{\sigma_2 K_2}(\xi_2),$$

these functions being different from zero under the condition that the indices $K_i = \pm|K_i|$ of the functions $\chi^{\pi}_{\sigma_i K_i}$ and $\chi^{\pi}_{\overline{\sigma_i K_i}}$ satisfy the constraint $\sum_i K_i = K$. In constructing expression (15), it was considered that the potential fission phase shifts δ^b_c are independent not only of the spin and parity of the fissile nucleus but also of the spins, parities, and orbital angular momenta of fission fragments [13, 14]; also, use was made of rather accurate [20] A. Bohr's approximation [7] for the angular distributions of fission fragments. Substituting the amplitude given by (15) into (14) and performing integration with respect to the intrinsic variables ξ_1 and ξ_2 of fission fragments with allowance for the orthonormality of the functions $\chi^{\pi}_{\sigma_i K_i}(\xi_i)$ and $\chi^{\pi}_{\overline{\sigma_i K_i}}(\xi_i)$, we reduce the differential cross section (14) to the form

$$\frac{d\sigma^b_{nf}(\theta,\varphi)}{d\Omega} = \frac{\pi}{k_n^2}\frac{1}{2(2I+1)}\{A_0 + A_1(\theta,\varphi)\}, \quad (19)$$

where $\left(\frac{\pi}{k_n^2}\frac{4\pi}{2(2I+1)}A_0\right)$ is the total cross section for (n,f) reactions of binary nuclear fission induced by polarized thermal neutrons with allowance for only s-wave neutron resonances, the quantity A_0 being

$$A_0 = \frac{1}{4\pi}\sum_{ss' J_s K_s rq}(2J_s+1)(a^{J_s}_{K_s})^2 b^{J_s\pi}_{rsK_s} b^{J_s\pi}_{rs'K_s} \quad (20)$$
$$\times (c^{J_s\pi}_{qrK_s})^2 \Gamma^b_{qK_s}\mathrm{Re}\left(u^{J_s\pi}_s (u^{J'_s\pi}_{s'})^*\right).$$

The term $A_1(\theta,\varphi)$ appearing in (19) and determining the character of P-even asymmetries has the form

$$A_1(\theta,\varphi) = \sum_{spJ_sJ_pjK_sm_nq} Q(J_s,J_p,j,K_s,I)\Gamma^b_{qK_s} \quad (21)$$
$$\times \mathrm{Re}\Bigg\{u^{J_s\pi}_s (u^{J_p\bar{\pi}}_{pj})^* a^{J_s}_{K_s} a^{J_p}_{K_s}$$
$$\times \sum_r \left(b^{J_s\pi}_{rsK_s} c^{J_s\pi}_{qrK_s} b^{J_p\bar{\pi}}_{\tilde{r}pK_s} c^{J_p\bar{\pi}}_{q\tilde{r}K_s}\right) Y_{1m_n}(\Omega_{\mathbf{k}}) Y_{1-m_n}(\Omega)$$
$$\times \left(C^{1-m_n}_{1/2j1/2(1/2-m_n)}\right)^2 (-1)^{m_n}\frac{4\pi}{3}\Bigg\},$$

where

$$Q(J_s,J_p,j,K_s,I) = 2(2J_s+1)(2J_p+1)\sqrt{2j+1} \quad (22)$$
$$\times (-1)^{1+j-I-K_s+J_s-J_p}\begin{Bmatrix} 1/2 & 1 & j \\ J_p & I & J_s \end{Bmatrix} C^{10}_{J_sJ_pK_s-K_s}.$$

In (21), the index $\tilde{r}$ labels that transition fission state of the p-wave neutron resonance involved which, in the vicinity of the nuclear scission point, transforms into the same intrinsic state q of the nucleus undergoing fission as the transition fission state r of the respective s-wave neutron resonance.

Upon expressing the Cartesian projections of the unit vector $\mathbf{n}_k$ in terms of spherical harmonics depending on angles that specify the direction of this vector in the laboratory frame [21],

$$(\mathbf{n}_k)_x = \sqrt{\frac{2\pi}{3}}\{Y_{1-1}(\theta,\varphi) - Y_{11}(\theta,\varphi)\}; \quad (23)$$
$$(\mathbf{n}_k)_y = \sqrt{\frac{2\pi}{3}}i\{Y_{11}(\theta,\varphi) + Y_{1-1}(\theta,\varphi)\};$$
$$(\mathbf{n}_k)_z = \sqrt{\frac{4\pi}{3}}Y_{10}(\theta,\varphi),$$

and employing similar formulas for the unit vector $\mathbf{n}_{\mathrm{LF}}$ determining the direction of light-fission-fragment emission, this direction being coincident with the direction of the vector $\mathbf{R}$ by definition of this vector, we can recast the quantity $A_1(\theta,\varphi)$ into a form where P-even asymmetries are isolated explicitly. Specifically, we have

$$A_1(\theta,\varphi) = \sum_{spJ_sJ_pK_sjrq} Q(J_s,J_p,j,K_s,I)\Gamma^b_{qK_s} \quad (24)$$
$$\times \sqrt{\Gamma^{J_s\pi}_{sn}}\sqrt{\Gamma^{J_p\bar{\pi}}_{pjn}} a^{J_s}_{K_s} a^{J_p}_{K_s} b^{J_s\pi}_{rsK_s} b^{J_p\bar{\pi}}_{\tilde{r}pK_s} c^{J_s\pi}_{qrK_s} c^{J_p\bar{\pi}}_{q\tilde{r}K_s}$$
$$\times \left|E - E^{J_s\pi}_s + \frac{i\bar{\Gamma}^{J_s\pi}_s}{2}\right|^{-1}\left|E - E^{J_p\bar{\pi}}_p + \frac{i\bar{\Gamma}^{J_p\bar{\pi}}_p}{2}\right|^{-1}$$
$$\times \{(\mathbf{n}_k\cdot\mathbf{n}_{\mathrm{LF}})\cos\varepsilon - \beta_j \mathbf{n}_{\mathrm{LF}}\cdot[\mathbf{n}_k\times\boldsymbol{\sigma}]\sin\varepsilon\},$$

where

$$\beta_j = \begin{cases} 1, & j = 1/2, \\ -1/2, & j = 3/2; \end{cases} \quad (25)$$
$$\varepsilon = \arg\left(\frac{E - E^{J_s\pi}_s + \frac{i\bar{\Gamma}^{J_s\pi}_s}{2}}{E - E^{J_p\bar{\pi}}_p + \frac{i\bar{\Gamma}^{J_p\bar{\pi}}_p}{2}}\right).$$

In deriving Eq. (24), use was made of the fact that, for thermal neutrons, the potential neutron phase shifts δ_{sn} and δ_{pjn} are much smaller than unity.

Defining the coefficient of P-even left–right asymmetry as

$$(\alpha^{\mathrm{LR}}_{\mathrm{LF}})^b = \frac{\sigma^b_+ - \sigma^b_-}{\sigma^b_+ + \sigma^b_-}, \quad (26)$$

where σ^b_+ and σ^b_- are the differential cross sections (19) for the cases where a light fission fragment

is emitted, respectively, along and against the direction of the neutron vector $[\mathbf{k}_n \times \boldsymbol{\sigma}]$, and employing Eqs. (19) and (24), we can obtain

$$(\alpha_{\mathrm{LF}}^{\mathrm{LR}})^b = -\frac{1}{A_0}\sum_{spJ_sJ_pK_sjrq} Q(J_s, J_p, j, K_s, I)\Gamma^b_{qK_s} \tag{27}$$
$$\times \sqrt{\Gamma^{J_s\pi}_{sn}}\sqrt{\Gamma^{J_p\bar{\pi}}_{pjn}}a^{J_s}_{K_s}a^{J_p}_{K_s}b^{J_s\pi}_{rsK_s}b^{J_p\bar{\pi}}_{\tilde{r}pK_s}c^{J_s\pi}_{qrK_s}c^{J_p\bar{\pi}}_{q\tilde{r}K_s}$$
$$\times \left|E - E_s^{J_s\pi} + \frac{i\bar{\Gamma}_s^{J_s\pi}}{2}\right|^{-1}\left|E - E_p^{J_p\bar{\pi}} + \frac{i\bar{\Gamma}_p^{J_p\bar{\pi}}}{2}\right|^{-1}$$
$$\times \beta_j \sin\varepsilon.$$

In the simplest case where, in the vicinity of the thermal point, only one s- and only one p-wave neutron resonance are significant, their spins being denoted by J_s and J_p, respectively, formula (19) can be significantly simplified with allowance for (24). The result is

$$\frac{d\sigma^b_{nf}(\theta,\varphi)}{d\Omega} = \frac{\sigma_0^b}{4\pi}\left\{1 + \sum_j d^b_{sJ_spJ_p}(j)\right. \tag{28}$$
$$\left.\times\,(\mathbf{n}_k\cdot\mathbf{n}_{\mathrm{LF}}\cos\varepsilon - \beta_j\mathbf{n}_{\mathrm{LF}}[\mathbf{n}_k\times\boldsymbol{\sigma}]\sin\varepsilon)\right\},$$

where σ_0^b is the total cross section for (n,f) reactions involving the excitation of one s-wave neutron resonance [17],

$$\sigma_0^b = \frac{\pi}{k_n^2}\frac{(2J_s+1)}{2(2I+1)}\frac{\Gamma_s^{J_s\pi b}\Gamma_{sn}^{J_s\pi}}{(E-E_s^{J_s\pi})^2 + \left(\frac{\bar{\Gamma}_s^{J_s\pi}}{2}\right)^2}, \tag{29}$$

and where $d^b_{sJ_spJ_p}(j)$ has the form

$$d^b_{sJ_spJ_p}(j) = \sum_{K_srq} Q(J_s, J_p, j, K_s, I)\frac{\Gamma^b_{qK_s}}{\Gamma_s^{J_s\pi b}} \tag{30}$$
$$\times\sqrt{\frac{\Gamma^{J_p\bar{\pi}}_{pjn}}{\Gamma^{J_s\pi}_{sn}}}\left|\frac{E - E_s^{J_s\pi} + \frac{i\bar{\Gamma}_s^{J_s\pi}}{2}}{E - E_p^{J_p\bar{\pi}} + \frac{i\bar{\Gamma}_p^{J_p\bar{\pi}}}{2}}\right|$$
$$\times a^{J_s}_{K_s}a^{J_p}_{K_s}b^{J_s\pi}_{rsK_s}b^{J_p\bar{\pi}}_{\tilde{r}pK_s}c^{J_s\pi}_{qrK_s}c^{J_p\bar{\pi}}_{q\tilde{r}K_s},$$

the total width $\Gamma_{sn}^{J_s\pi b}$ with respect to the binary fission of the s-wave resonance being given by (8). In this case, the coefficient $(\alpha_{\mathrm{LF}}^{\mathrm{LR}})^b$ of left–right asymmetry [see Eq. (27)] takes the form

$$(\alpha_{\mathrm{LF}}^{\mathrm{LR}})^b = -\sum_j d^b_{sJ_spJ_p}(j)\beta_j\sin\varepsilon\frac{1}{A_0}. \tag{31}$$

If we assume that the fission widths of s- and p-wave neutron resonances are determined by the only values of the parameters K_s, r, and q, formula (31) reduces to a formula similar to its counterpart in [6], the distinction between these two being associated with the difference in the definition of the phase ε in (25), where the symmetry of neutronic widths under time inversion and the properties of the potential neutron and fission phase shifts are taken consistently into account.

In general, formula (27) for the asymmetry coefficient differs from its counterpart in [6], first, by the inclusion of the Coriolis mixing of the spin projections K_s in neutron resonances; second, by a clear definition of the potential fission phase shifts; and, finally, by the inclusion of the evolution of a fissile nucleus from transition fission states r to asymptotic states q, in which the nucleus has already assumed pearlike shapes.

The experimental values of the coefficients $(\alpha_{\mathrm{LF}}^{\mathrm{LR}})^b$ of P-even left–right asymmetries in binary nuclear fission induced by polarized thermal neutrons are about 10^{-4} [1–4], which is close to the ratio of the neutronic widths of s- and p-wave neutron resonances in the vicinity of the thermal point [6], this ratio being $\sqrt{\Gamma^{J_s\pi}_{sn}/\Gamma^{J_p\bar{\pi}}_{pjn}} \approx (k_nR_A) \approx 3\times10^{-4}$, where R_A is the radius that the nucleus undergoing fission has in the region of the first minimum of the deformation potential. Since the coefficients $a^{J_s}_{K_s}$ and $b^{J_s\pi}_{rsK_s}$ for s-wave neutron resonances are close to, respectively, the coefficients $a^{J_p}_{K_s}$ and $b^{J_p\bar{\pi}}_{\tilde{r}pK_s}$s for p-wave neutron resonances and since the phase ε is not small, so that $|\cos\varepsilon| \approx |\sin\varepsilon|$ [6], it follows from (27) that the values of the coefficient $(\alpha_{\mathrm{LF}}^{\mathrm{LR}})^b$ have a correct scale if the coefficients $c^{J_s\pi}_{qrK_s}$ and $c^{J_p\bar{\pi}}_{q\tilde{r}K_s}$ are quite close in magnitude. From Eq. (8), it follows that, in this case, the total fission widths of s- and p-wave neutron resonances are also close. This implies that, at the saddle point of the deformation potential, the energies $E^{J_s\pi rK_s}$ and $E^{J_p\bar{\pi}\tilde{r}K_s}$ of the $J_s\pi rK_s$ and $J_p\bar{\pi}\tilde{r}K_s$ transition fission states, which have opposite parities and which determine the fission widths of s- and p-wave neutron resonances, must be higher than the fission-barrier energy and that their differences must be quite small for the coefficients $c^{J_s\pi}_{qrK_s}$ and $c^{J_p\bar{\pi}}_{q\tilde{r}K_s}$ to be close in magnitude. A detailed analysis of this situation will be given in a subsequent publication.

4. COEFFICIENTS OF P-EVEN ASYMMETRIES IN TERNARY NUCLEAR FISSION

Here, use will be made of the results presented in [15], where, in contrast to time-dependent approaches traditionally applied in these realms [22], the quantum-mechanical theory of ternary nuclear fission is developed on the basis of the theory of open Fermi systems [10] with the aid of the time-independent formalism and the adiabatic approximation for a light and the complementary heavy fragment in the asymptotic region of the nucleus undergoing fission into two fragments and a third (lightest) particle. Under the assumption that two fragments and a third particle, which is taken to be an alpha particle, are produced simultaneously through the one-step mechanism, the double-differential cross section for the process in which unpolarized nuclei bombarded with polarized thermal neutrons undergo ternary fission can be represented in the form [16]

$$\frac{d^2\sigma^t_{nf}(\theta,\varphi,\theta_3)}{d\Omega d\Omega_3} = \frac{d\sigma^t_{nf}(\theta,\varphi)}{d\Omega}|M(\tilde{\theta}_3)|^2. \qquad (32)$$

Here, the differential cross section $\frac{d\sigma^t_{nf}(\theta,\varphi)}{d\Omega}$ is given by the formulas that are obtained from (19)–(25) by replacing the binary-fission-channel index $c\beta L$, where $c \equiv \sigma_1 K_1 \sigma_2 K_2$ and $\beta \equiv J_1 J_2 j$, by the ternary-fission-channel index $c\beta Ll\lambda$, where l is the orbital angular momentum of the third particle with respect to the center of mass of two ternary-fission fragments and the index λ specifies the dependence of the fission-width amplitudes on the asymptotic energy E_α of the alpha particle involved. Of course, this entails the replacement of the fission width Γ^b_{qKc} of the prescission state q with respect to binary fission by the fission width Γ^t_{qKc} of the analogous state with respect to ternary fission and the replacement of the potential fission phase shift δ^b_c for binary fission by the analogous phase shift $\delta^t_{cl\lambda}$ for ternary fission. The amplitude $M(\tilde{\theta}_3)$, which depends on the angle $\tilde{\theta}_3$ between the directions of alpha-particle emission and the emission of a light ternary-fission fragment, is given by [15]

$$M(\tilde{\theta}_3) = \sum_l g_l Y_{l0}(\tilde{\theta}_3), \qquad (33)$$

where the coefficients g_l are such that the distribution $|M(\tilde{\theta}_3)|^2$ satisfies the normalization condition

$$\int |M(\tilde{\theta}_3)|^2 d\Omega_3 = \sum_l |g_l|^2 = 1, \qquad (34)$$

with Ω_3 being the solid angle that specifies the direction of alpha-particle emission in the laboratory frame. Using the expansion

$$Y_{l0}(\tilde{\theta}_3) = \sum_m \sqrt{\frac{4\pi}{2l+1}} Y^*_{lm}(\Omega_3) Y_{lm}(\Omega) \qquad (35)$$

and the theorem of multiplication of generalized spherical harmonics [7], we can represent the distribution $|M(\tilde{\theta}_3)|^2$ in the form

$$|M(\tilde{\theta}_3)|^2 = \sum_{\mathcal{L}} B_{\mathcal{L}} Y_{\mathcal{L}0}(\tilde{\theta}_3) \qquad (36)$$

$$= \sum_{\mathcal{L}M} B_{\mathcal{L}} \sqrt{\frac{4\pi}{2\mathcal{L}+1}} Y_{\mathcal{L}M}(\Omega_3) Y^*_{\mathcal{L}M}(\Omega),$$

where

$$B_{\mathcal{L}} = \sum_{ll'} g_l g^*_{l'} (C^{\mathcal{L}0}_{ll'00})^2 \sqrt{\frac{(2l+1)(2l'+1)}{4\pi(2\mathcal{L}+1)}}. \qquad (37)$$

In order to describe a P-even left–right asymmetry of the form $\mathbf{k}_{\mathrm{LF}} \cdot [\mathbf{k}_n \times \boldsymbol{\sigma}]$ that correlations between the direction of light-fragment emission and the neutron vector $[\mathbf{k}_n \times \boldsymbol{\sigma}]$ induce in the angular distribution of fragments originating from the ternary fission of nuclei bombarded with polarized resonance neutrons, it is convenient to fix the direction of third-particle emission at an angle of $\tilde{\theta}_3 = 90^\circ$ with respect to the direction of light-fragment emission. In this case, all harmonics corresponding to odd values of $\mathcal{L}$ do not contribute to $|M(\tilde{\theta}_3)|^2$; as a result, the distribution $|M(\tilde{\theta}_3)|^2$ is identical for the directions of light-fragment emission along and against the vector $[\mathbf{k}_n \times \boldsymbol{\sigma}]$. For a light ternary-fission fragment, the coefficient $(\alpha^{\mathrm{LR}}_{\mathrm{LF}})^t$ of left–right asymmetry will then be given by expression (27), where it is necessary to make the substitutions corresponding to the transition from $\frac{d\sigma^b_{nf}(\theta,\varphi)}{d\Omega}$ to $\frac{d\sigma^t_{nf}(\theta,\varphi)}{d\Omega}$ in Eq. (32). If the relative probabilities $W_{\alpha q}$ of alpha-particle emission in ternary fission, which are given by $W_{\alpha q} = \Gamma^t_{qK_s}/\Gamma^b_{qK_s}$, have approximately the same value for all fission modes q, the asymmetry coefficient $(\alpha^{\mathrm{LR}}_{\mathrm{LF}})^t$ will be close to the corresponding coefficient in (27) for binary nuclear fission. For ^{233}U fission induced by thermal neutrons, it is of importance to refine the value of the coefficient $(\alpha^{\mathrm{LR}}_{\mathrm{LF}})^t$ in (2) experimentally, since a comparison of this coefficient with the analogous coefficient $(\alpha^{\mathrm{LR}}_{\mathrm{LF}})^b$ in (1) would make it possible to assess the dependence of the probabilities $W_\alpha q$ on the types of prescission configurations q of the nucleus undergoing fission. It is also of interest to study the coefficients $(\alpha^{\mathrm{LR}}_{\mathrm{LF}})^t$ in the ternary fission of nuclei like ^{235}U and ^{239}Pu, since the coefficients $(\alpha^{\mathrm{LR}}_{\mathrm{LF}})^b$ are

already known for the binary fission of these nuclei that is induced by polarized thermal neutrons.

Let us now consider, for a third particle emitted in ternary nuclear fission, theoretical values of the coefficient $(\alpha_{\rm TP}^{\rm LR})^t$ of P-even left–right asymmetry corresponding to a correlation of the form $\mathbf{k}_3 \cdot [\mathbf{k}_n \times \boldsymbol{\sigma}]$. Experimentally, this coefficient was measured in [4] without fixing the direction of light-fission-fragment emission, in which case it is implied that the double-differential cross section (32) is integrated over the solid angle Ω. If one considers that the spherical harmonic $Y_{1-m_n}(\Omega)$ appears in expression (21) for the quantity A_1 determining P-even asymmetries and integrates, over the solid angle Ω, this harmonic multiplied by the function $Y^*_{\mathcal{L}M}(\Omega)$ appearing in the distribution $|M(\tilde{\theta}_3)|^2$ [see Eq. (36)], it is straightforward to derive, for the differential cross section $\dfrac{d\sigma^t_{nf}(\theta_3,\varphi_3)}{d\Omega_3}$ associated with the third particle, the formula that is obtained from formula (19) [with allowance for (21)] for the differential cross section $\dfrac{d\sigma^b_{nf}(\theta,\varphi)}{d\Omega}$ upon replacing the index b by the index t and the function $Y_{1-m_n}(\Omega)$ by the function $\eta_3 Y_{1-m_n}(\Omega_3)$, where η_3 is independent of m_n and is given by $\eta_3 = B_1\sqrt{4\pi/3}$. The coefficient $(\alpha_{\rm TP}^{\rm LR})^t$ of P-even left–right asymmetry in the angular distribution of a third particle is then expressed in terms of the analogous coefficient for a light fragment as

$$(\alpha_{\rm TP}^{\rm LR})^t = \eta_3(\alpha_{\rm LF}^{\rm LR})^t. \qquad (38)$$

It should be noted that that the factor η_3 in (38) coincides with the factor η_3 that was found in [17] and which relates the coefficient of P-odd asymmetry for a third particle to that for a light fragment in ternary nuclear fission induced by polarized thermal neutrons. For ^{233}U fission, the value of the factor η_3 was calculated in [15, 17] for the case where an alpha particle was taken to play the role of a third particle, information about the experimental angular distributions of alpha particles being employed in those calculations. The result was $\eta_3 = 0.116$. Using formula (38) and the value of the coefficient $(\alpha_{\rm LF}^{\rm LR})^b$ in (1) for ^{233}U target nuclei in order to estimate $(\alpha_{\rm LF}^{\rm LR})^t$, we obtain

$$(\alpha_{\rm TP}^{\rm LR})^t = -(0.26 \pm 0.03) \times 10^{-4}. \qquad (39)$$

A comparison of the value of the coefficient $(\alpha_{\rm TP}^{\rm LR})^t$ in (39) for ^{233}U with the corresponding experimental value in (3) leads to the conclusion that the nonzero value of the $(\alpha_{\rm TP}^{\rm LR})^t$ in (39) could be observed as soon as the statistical accuracy of relevant experiments is improved by at least a factor of 4. An experimental corroboration of the results obtained by theoretically calculating, for an alpha particle from ternary nuclear fission induced by polarized thermal neutrons, the coefficient $(\alpha_{\rm TP}^{\rm LR})^t$ of P-even left–right asymmetry and the coefficient $(\alpha_{\rm TP}^{\rm PNC})^t$ of P-odd asymmetry [16] would confirm the one-step mechanism of ternary nuclear fission.

5. CONCLUSION

The above analysis of the evolution of a fissile nucleus from neutron resonance states through transition fission states to prescission nuclear states having a pearlike axisymmetric shape has confirmed the potential of the developed quantum-mechanical theory for describing binary and ternary nuclear fission.

It is highly desirable that experimentalists investigate P-even and P-odd asymmetries for a third particle from ternary fission at a statistical-accuracy level that is sufficient for testing the predictions of the present study.

ACKNOWLEDGMENTS

I am grateful to V.E. Bunakov, W.I. Furman, and A.A. Barabanov for stimulating discussions and L.V. Rodionova for assistance in performing numerical calculations.

This work was supported by INTAS (grant no. 99-00229) and the program Universities of Russia (project no. UR-02.01.011).

REFERENCES

1. A. K. Petukhov, G. A. Petrov, S. I. Stepanov, *et al.*, Pis'ma Zh. Éksp. Teor. Fiz. **30**, 324 (1979) [JETP Lett. **30**, 439 (1979)].
2. V. A. Vesna, V. V. Lobashev, *et al.*, Pis'ma Zh. Éksp. Teor. Fiz. **31**, 704 (1980) [JETP Lett. **31**, 663 (1980)].
3. A. P. Aleksandrovich, A. I. Gagarsky, G. A. Petrov, *et al.,* Nucl. Phys. A **567**, 541 (1994).
4. P. Jesinger, A. Köetzle, F. Gönnenwein, *et al.,* Yad. Fiz. **65**, 662 (2002) [Phys. At. Nucl. **65**, 630 (2002)].
5. V. E. Bunakov, Yad. Fiz. **65**, 648 (2002) [Phys. At. Nucl. **65**, 616 (2002)]; V. E. Bunakov and F. Goennenwein, Yad. Fiz. **65**, 2096 (2002) [Phys. At. Nucl. **65**, 2036 (2002)].
6. O. P. Sushkov and V. V. Flambaum, Usp. Fiz. Nauk **136**, 3 (1982).
7. A. Bohr and B. R. Mottelson, *Nuclear Structure* (Benjamin, New York, 1969, 1975; Mir, Moscow, 1971, 1977), Vols. 1, 2.
8. V. E. Bunakov and V. P. Gudkov, Nucl. Phys. A **401**, 23 (1983).
9. V. E. Bunakov and V. P. Gudkov, Z. Phys. A **321**, 271 (1985).

10. S. G. Kadmensky, Yad. Fiz. **64**, 478 (2001) [Phys. At. Nucl. **64**, 423 (2001)].
11. S. G. Kadmensky and A. A. Sanzogni, Phys. Rev. C **62**, 054601 (2000).
12. S. G. Kadmensky, Yad. Fiz. **65**, 863 (2002) [Phys. At. Nucl. **65**, 831 (2002)].
13. S. G. Kadmensky, in *Proceedings of the IX International Symposium ISINN, Dubna, 2001,* p. 128.
14. S. G. Kadmensky, Yad. Fiz. **65**, 1424 (2002) [Phys. At. Nucl. **65**, 1390 (2002)].
15. S. G. Kadmensky, Yad. Fiz. **65**, 1833 (2002) [Phys. At. Nucl. **65**, 1785 (2002)].
16. A. M. Lane and R. G. Thomas, *R-Matrix Theory of Nuclear Reactions* (Los-Alamos, 1958; Inostr. Lit., Moscow, 1969).
17. S. G. Kadmensky, Yad. Fiz. **66**, 615 (2003) [Phys. At. Nucl. **66**, 589 (2003)].
18. S. G. Kadmenskiĭ, V. P. Markushev, and V. I. Furman, Yad. Fiz. **35**, 300 (1982) [Sov. J. Nucl. Phys. **35**, 166 (1982)].
19. W. I. Furman and J. Kliman, in *Proceedings of the International Symposium on Nuclear Physics, Gaussig, 1987*, p. 86.
20. S. G. Kadmensky and L. V. Rodionova, Yad. Fiz. **66**, 814 (2003) [Phys. At. Nucl. **66**, 1219 (2003)].
21. D. A. Varshalovich, A. N. Moskalev, and V. K. Khersonskii, *Quantum Theory of Angular Momentum* (Nauka, Leningrad, 1975; World Sci., Singapore 1988).
22. O. Tanimura and T. Fliessbach, Z. Phys. A **328**, 475 (1987).

Translated by A. Isaakyan

Physics of Atomic Nuclei, Vol. 67, No. 2, 2004, pp. 250–255. Translated from Yadernaya Fizika, Vol. 67, No. 2, 2004, pp. 267–272.

NUCLEI
Theory

Unitary Approach to Quasielastic Scattering Reactions

J. V. Mebonia and P. J. Saralidze

Tbilisi State University, pr. Chavchavadze 1, GE-380077 Tbilisi, Republic of Georgia

Received November 26, 2002; in final form, April 1, 2003

Abstract—The possibility of deriving an approximate unitary solution to integral Faddeev equations within the K-matrix formalism is considered. Explicit expressions for the amplitudes of elastic, inelastic, and quasielastic three-body scattering are obtained under the assumption of a mechanism of a truly single collision. Specific calculations are performed for quasielastic-scattering reactions of the $d(N, 2N)N$ type. Good agreement between the results of these calculations and experimental data indicates that, in developing approximate methods, it is highly desirable to respect fundamental physical principles.

Investigation of quasielastic scattering reactions belonging to the $(N, 2N)$ and $(N, N\alpha)$ types and to some similar types provides important information about nuclear-physics problems. Although quasielastic-scattering reactions are multiparticle processes in the majority of cases, some model assumptions are usually made in order to reduce their description to solving relevant three-body problems. For this reason, the approach proposed by Faddeev [1] had a crucial effect on the development of theoretical methods for studying quasielastic-scattering reactions. Since severe technical difficulties impede attempts at directly solving Faddeev equations, one has to invoke various approximate methods. However, approximate amplitudes that such methods produce often do not obey three-body unitarity. There exist, however, unitary schemes [2–4], but they are rather cumbersome and inconvenient in practical calculations.

One of the unitary schemes was proposed in [5]. Its basic idea consists in approximately solving Faddeev equations within the K-matrix formalism, which makes it possible to preserve the unitarity of the T matrix.

Let us consider the scattering of three nonrelativistic particles in the approximation of pair interaction,

$$V = \sum_{\alpha=1}^{3} V_\alpha, \tag{1}$$

where V_α is the potential simulating the interaction of particles β and γ ($\alpha\beta\gamma = 123, 231, 312$).

The three-body Green's function for free particles, $G_0(Z)$, can be broken down into non-Hermitian and Hermitian parts, $G_1(Z)$ and $G_2(Z)$, respectively,

$$G_1(Z) = \frac{1}{2}G_0(Z) - \frac{1}{2}G_0(Z^*), \tag{2}$$

$$G_2(Z) = \frac{1}{2}G_0(Z) + \frac{1}{2}G_0(Z^*), \tag{3}$$

where Z is a complex parameter, $\mathrm{Re}(Z) = E$ being the total energy of the system.

We introduce the Hermitian operator $K(Z)$ as that which satisfies the equation

$$K(Z) = V - VG_2(Z)K(Z). \tag{4}$$

The T matrix for three-body scattering can then be expressed in terms of the operator $K(Z)$ as

$$T(Z) = \{1 + K(Z)G_1(Z)\}^{-1}K(Z). \tag{5}$$

Thus, we can avoid explicitly solving the Lippmann–Schwinger equation for the T matrix with the Green's function $G_0(Z)$. Instead, we solve Eq. (4) for the Hermitian $K(Z)$ matrix, whereupon we express the T matrix in terms of the operator $K(Z)$. An advantage of this method for finding $T(Z)$ is that any approximate solution to Eq. (4) ensures the unitarity of the T matrix. However, there are well-known difficulties associated with Eq. (4), which are characteristic of the three-body character of the problem and which give no way to solve it unambiguously. Following Faddeev's idea, we introduce auxiliary operators $K^\alpha(Z)$,

$$K(Z) = \sum_{\alpha=1}^{3} K^\alpha(Z), \tag{6}$$

for which one can write the set of Faddeev integral equations

$$K^\alpha(Z) = K_\alpha(Z)\{1 - G_2(Z)[K^\beta(Z) + K^\gamma(Z)]\}, \tag{7}$$

where the operator $K_\alpha(Z)$ is a two-body Hermitian operator characterizing the three-body problem and satisfying the integral equation

$$K_\alpha(Z) = V_\alpha\{1 - G_2(Z)K_\alpha(Z)\}. \quad (8)$$

From the definition, it can be seen that the operator $K_\alpha(Z)$ is an analog of the full two-body $T_\alpha(Z)$ matrix in the three-body problem:

$$T_\alpha(Z) = V_\alpha[1 - G_0(Z)T_\alpha(Z)]. \quad (9)$$

These operators are related by the Heitler equation

$$T_\alpha(Z) = K_\alpha(Z)[1 - G_1(Z)T_\alpha(Z)]. \quad (10)$$

We will further consider only the leading-order solution to Eqs. (7) and suppress the argument Z (we assume that all operators depend on it):

$$K^\alpha \approx K_\alpha. \quad (11)$$

The analogous approximation in the Faddeev equations for the T matrix is referred to as the three-body impulse approximation (TBIA) [6]. For this reason, the approximation specified by Eq. (11) is called the unitarized three-body impulse approximation (UTBIA). We deem that it is this approximation that corresponds to a truly single collision because it provides a unitary solution to the problem in the lowest order such that the total probability is conserved. From formulas (5), (6), (10), and (11), we then obtain

$$T = \sum_{\alpha\beta\gamma}(1 - T_\beta G_1)(1 - T_\alpha G_1) \quad (12)$$
$$\times \{(1 - T_\gamma G_1)(1 - T_\alpha G_1)^{-1}(1 - T_\alpha G_1 T_\beta G_1)$$
$$\times (1 - T_\alpha G_1) + T_\gamma G_1(1 - T_\beta G_1)$$
$$\times (1 - T_\alpha G_1\}^{-1}T_\gamma,$$

where $\alpha\beta\gamma = 123, 231, 312$.

Of course, expression (12) is very complicated and is therefore inappropriate for applications in practice, but it can be simplified if the operator norm $||T_\gamma G_1 T_\alpha G_1||$ is much smaller than unity,

$$||T_\gamma G_1 T_\alpha G_1|| \ll 1. \quad (13)$$

It can be expected that the higher the energy of collisions, the higher the accuracy to which the condition in (13) is satisfied. The simplified form of expression (12) is

$$T = \sum_{\alpha\beta\gamma}\{1 - (T_\alpha + T_\beta)G_1\}T_\gamma. \quad (14)$$

In contrast to (12), expression (14) satisfies three-body unitarity only with the precision specified by the condition in (13).

From expression (14), it follows that, in the Faddeev iteration series, the first-order terms and the second-order terms involving the non-Hermitian part of the Green's function must be retained in order to ensure the unitarity of the approximate T matrix.

The operator in (14) describes the scattering of three free particles. Given the expressions for the asymptotic wave functions, one can apply this operator to any specific three-body problem. We consider two such problems.

(i) Elastic (or inelastic) scattering of particle 1 on the (2, 3) bound system:

$$1 + (2,3) \to 1 + (2,3). \quad (15)$$

The respective matrix element has the form

$$M = \langle \mathbf{k}\nu, \Psi_f|T_3 + T_2 - T_3 G_1 T_2 \quad (16)$$
$$- T_2 G_1 T_3|\Psi_i, \mathbf{k}_0\nu_0\rangle,$$

where Ψ_i and Ψ_f are the wave functions for the (2, 3) bound system in the initial and the final state, respectively, and the symbol $\mathbf{k}_0\nu_0$ ($\mathbf{k}\nu$) stands for the momentum of the projectile and the projection of its spin before (after) the collision.

In the case of elastic scattering, formula (16) reduces to the Osborn formula [7] in the approximation of fixed scatterers or the Glauber–Sitenko formula [8, 9] with allowance for the eikonal approximation. It should be noted that, under relevant conditions, the Glauber–Sitenko formula is an exact formula for elastic scattering in the sense that it involves all terms of the iteration series associated with multiple scattering.

(ii) Particle 1 breaks the (2, 3) bound system into its constituents,

$$1 + (2,3) \to 1 + 2 + 3, \quad (17)$$

so that, in the final state, there appear three free particles having momenta $\mathbf{k}_1$, $\mathbf{k}_2$, and $\mathbf{k}_3$ and spin projections ν_1, ν_2, and ν_3.

Usually, this process is referred to as a disintegration process. Its matrix element has the form

$$M = \langle \mathbf{k}_1\nu_1, \mathbf{k}_2\nu_2, \mathbf{k}_3\nu_3|T_3 + T_2 \quad (18)$$
$$- (T_1 + T_2)G_1 T_3 - (T_1 + T_3)G_1 T_2|\Psi_i, \mathbf{k}_0\nu_0\rangle.$$

Let us consider the particular case where two final-state particles are recorded in coincidence, their energies E_1 and E_2 being much greater than the energy of the third particle:

$$E_1, E_2 \gg E_3. \quad (19)$$

This is precisely the condition under which the quasielastic reaction mechanism is realized. In this case, it is natural to assume that the breakup of the (2, 3) system is caused by the interaction of the recorded particles. This means that only the terms involving the operator T_3 must be retained in (18).

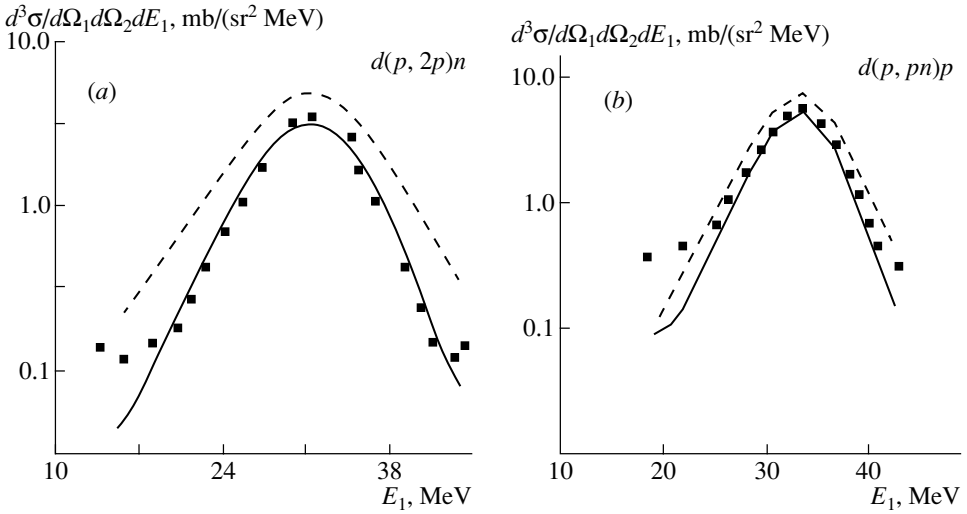

Fig. 1. Differential cross section for the reactions (*a*) $d(p, 2p)n$ and (*b*) $d(p, pn)p$ versus E_1 for $E = 65.0$ MeV and $\theta_1 = -\theta_2 = 43.57°$: (solid curve) results of the UTBIA calculations and (dashed curve) results of the TBIA calculations. The displayed experimental data were borrowed from [14].

Thus, the UTBIA expression for the matrix element describing the quasielastic-scattering reaction in question has the form

$$M(\mathrm{UTBIA}) = \langle \mathbf{k}_1\nu_1, \mathbf{k}_2\nu_2, \mathbf{k}_3\nu_3|T_3 - (T_1 + T_2)G_1T_3 - T_3G_1T_2|\Psi_i, \mathbf{k}_0\nu_0\rangle. \quad (20)$$

For the sake of comparison, we also present the TBIA expression for this matrix element:

$$M(\mathrm{TBIA}) = \langle \mathbf{k}_1\nu_1, \mathbf{k}_2\nu_2, \mathbf{k}_3\nu_3|T_3|\Psi_i, \mathbf{k}_0\nu_0\rangle. \quad (21)$$

A nucleon–deuteron (Nd) collision is one of the most familiar three-body reactions. The problem of elastic (or quasielastic) Nd scattering can be solved in a closed form for any realistic NN potential. Two different NN potentials leading to the same two-nucleon on-shell amplitudes may yield, in the three-nucleon problem, two different two-nucleon off-shell amplitudes. For this reason, an analysis of Nd scattering by a reliable theoretical method can help to select more appropriate NN potentials. On the other hand, various approximate methods for solving three-body problems can be tested by applying them to Nd scattering with an eye to extending the ones that passed this test most successfully to more complicated cases. It should be noted that the reaction $d(N, 2N)N$ is the simplest quasielastic-scattering process, the majority of other processes belonging to this type involving composite fragments. In view of this, we perform here a systematic analysis of the reactions $d(p, 2p)n$, $d(p, pn)p$, and $d(n, 2n)p$ for various sets of kinematical parameters and assess the potential of the UTBIA.

As a rule, experiments studying quasielastic-scattering reactions are carried out in coplanar geometry in the laboratory frame and are based on detecting two final-state particles in coincidence, their solid angles (Ω_1, Ω_2) and the energy of one of them (say, E_1) being measured at a given projectile energy. The remaining kinematical parameters can be determined from the energy- and momentum-conservation law.

The general form of the differential cross section for the reaction $d(N, 2N)N$ is

$$\frac{d^3\sigma}{d\Omega_1 d\Omega_2 dE_1} = \frac{3}{8}\pi^4 m^3 \frac{k_1 k_2^2}{k_0} \sum_{\text{spins}} |\hat{A}M|^2 \times \frac{1}{|2k_2 - k_0\cos(\theta_2) + k_1\cos(\theta_1 + \theta_2)|}, \quad (22)$$

where m is the nucleon mass, θ_1 and θ_2 are the scattering angles of the detected particles, and $\hat{A}$ is the operator of antisymmetrization with respect to identical particles. Summation is performed over the projections of the spins of the initial-state and final-state particles; these spin projections appear explicitly upon going over to the partial-wave expansions of the deuteron wave function Ψ_i and of the matrix elements of the operators T_α. We use the system of units in which $\hbar = c = 1$.

Further, the differential cross section is plotted as a function of only one of the parameters θ_1, θ_2, and E_1 (most often E_1) by projecting the fivefold differential cross section onto the respective axis. The E_1 dependence is sometimes replaced by the dependence on the so-called arc length S [10, 11] related to the

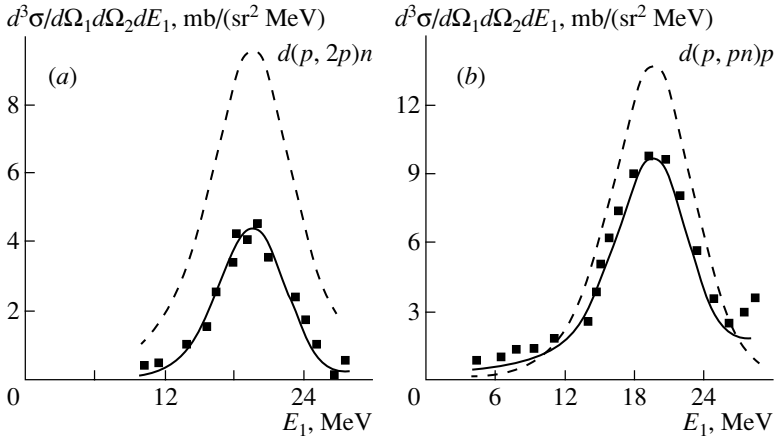

Fig. 2. As in Fig. 1, but for $E = 41.5$ MeV and $\theta_1 = -\theta_2 = 43°$. The displayed experimental data were borrowed from [15].

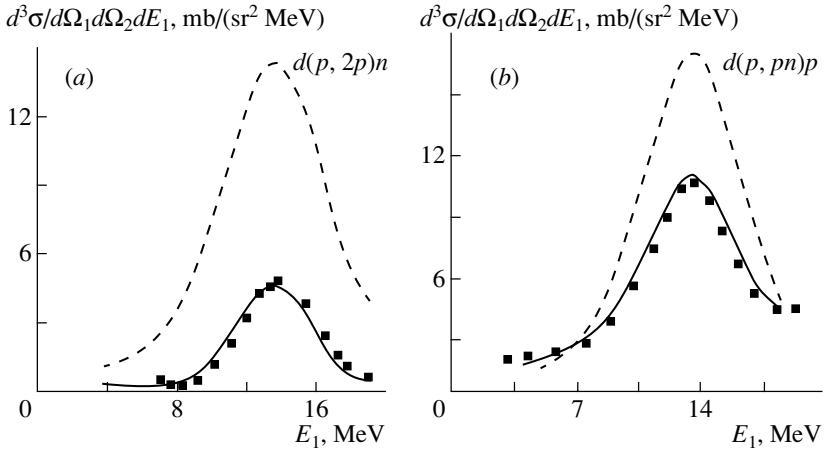

Fig. 3. As in Fig. 1, but for $E = 30.0$ MeV and $\theta_1 = -\theta_2 = 42.5°$ in the reaction $d(p, 2, p)n$ and $\theta_1 = -\theta_2 = 43°$ in the reaction $d(p, pn)p$. The displayed experimental data were borrowed from [15].

energies of the final-state particles by the equation

$$dS = \sqrt{dE_1^2 + dE_2^2}, \qquad (23)$$

where $S = 0$ for $E_2 = 0$ and $E_1 \neq 0$.

The differential cross section $d\sigma/(d\Omega_1 d\Omega_2 dS)$ can readily be determined with the aid of formulas (22) and (23).

Preliminary calculations of the differential cross section for the reaction $d(N, 2N)N$ that were based on the UTBIA were performed in [5, 12] by using only S-wave two-nucleon amplitudes ($L = 0$). Here, we pursue further a systematic analysis of this reaction, taking into account other partial waves ($^1S_1$, $^1P_1$, $^1D_2$, $^3S_1 + {}^3D_1$, $^3P_1$, $^3P_2 + {}^3F_2$, and $^3D_2$) and considering various sets of kinematical parameters. In our calculations, we use the off-shell two-nucleon T_α matrices and the radial part of the deuteron wave function for the Mongan potential [13], which is nonlocal and separable. Some typical results of our calculations are shown in Figs. 1–5. The solid curves correspond to the UTBIA calculations with the matrix element (20). For the sake of comparison, we also present (dashed curves) the results of the TBIA calculations with the matrix element (21). The respective experimental data were borrowed from [10, 14–16]. It can be seen that, in all cases, the UTBIA results faithfully reproduce special features of the measured differential cross sections. We deliberately pay particular attention to the low-energy domain ($E < 100$ MeV), where the reaction mechanism is unclear and where the reaction amplitude is more sensitive to off-shell effects, so that it is easier to reveal advantages of various theoretical methods and their drawbacks. With increasing energy (at $E > 100$ MeV), the aforementioned problems gradually become nonexistent, whereupon all methods appear to provide equivalent results.

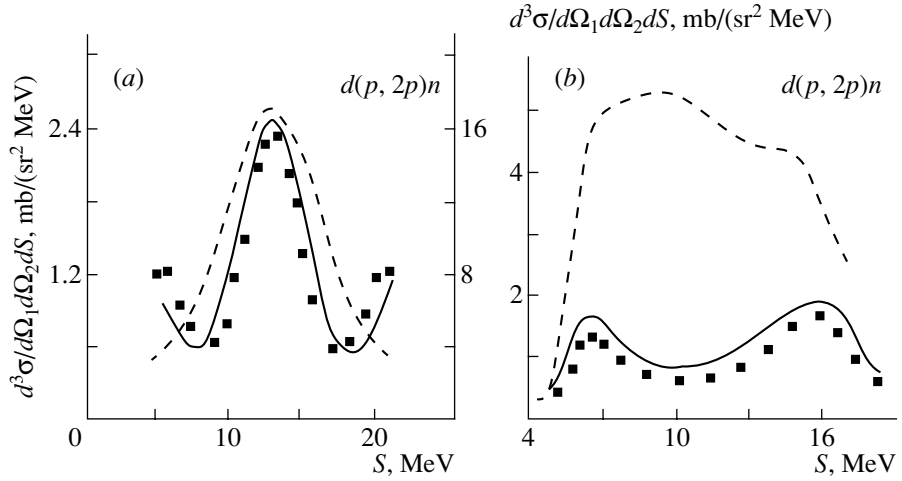

Fig. 4. As in Fig. 1a, but for the dependence of the differential cross section on S at $E = 19.0$ MeV for (a) $\theta_1 = -\theta_2 = 41^\circ$ and (b) $\theta_1 = 52^\circ$ and $\theta_2 = -63^\circ$. The displayed experimental data were borrowed from [10] (the dashed curve in Fig. 4a corresponds to the right-hand scale).

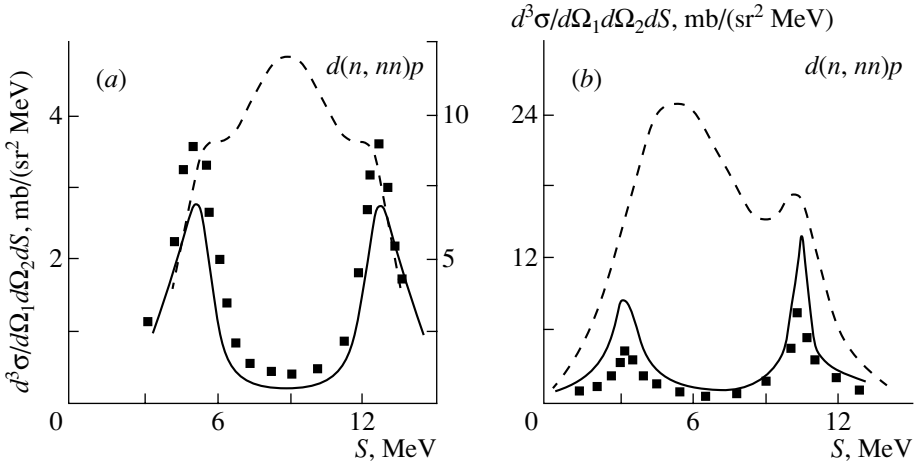

Fig. 5. As in Fig. 1, but for the reaction $d(n, 2n)p$ at $E = 13.0$ MeV for (a) $\theta_1 = -\theta_2 = 50.5^\circ$ and (b) $\theta_1 = 39^\circ$ and $\theta_2 = -62.5^\circ$. The displayed experimental data were borrowed from [16] (the dashed curve in Fig. 5a corresponds to the right-hand scale).

It is interesting to note that, with decreasing energy, the differential cross sections for the quasielastic-scattering reactions $d(p, 2p)n$ and $d(p, pn)p$ in the same kinematical domains differ substantially. This is a consequence of the Pauli exclusion principle. Indeed, it follows from this principle that, at low energies, a proton–neutron pair can be either in the $^1S_0$ or in the $^3S_1$ state, whereas a pair of protons can occupy only the former state. As a result, the maximum of the differential cross section for the quasielastic-scattering reaction $d(p, pn)p$ is 2 to 3 times larger than that for $d(p, 2p)n$. The theoretical results show such a difference only upon the unitarization of the respective amplitudes—that is, upon taking into account the single-scattering mechanism in accordance with our procedure, which we believe to be consistent. With increasing energy, the contribution of other states increases, with the result that the difference between the pp and np amplitudes gradually disappears. Therefore, the differential cross sections for pp and np collisions become nearly identical (see Figs. 1a and 1b).

From a general analysis, it follows that the role of unitarization becomes less significant with increasing energy. However, both the magnitude and the shape of the differential cross section depend strongly on the scattering angles θ_1 and θ_2 of detected particles.

The proposed unitary method is simpler than other unitary methods. However, it proved to be quite efficient and, what is of importance, involves no free

parameter. It is remarkable that UTBIA calculations are able to reproduce adequately the differential-cross-section shape, which is rather complicated. This agreement is observed even at the energy of $E = 13$ MeV (Fig. 5), although there is no reason to believe that the condition in (13) is satisfied at this energy value.

The results of the present study demonstrate that approximate theoretical methods that respect fundamental physical principles are consistent and are able to provide an adequate description of observed processes.

REFERENCES

1. L. D. Faddeev, Zh. Éksp. Teor. Fiz. **39**, 1459 (1960) [Sov. Phys. JETP **12**, 1014 (1960)].
2. R. T. Cahill, Nucl. Phys. A **194**, 599 (1972).
3. K. L. Kowalski, Phys. Rev. D **5**, 395 (1972).
4. T. Sasakawa, Nucl. Phys. A **203**, 496 (1973).
5. J. V. Mebonia and T. I. Kvaratskhelia, Phys. Lett. B **90B**, 17 (1980).
6. J. V. Mebonia, Phys. Lett. B **30B**, 153 (1969).
7. T. A. Osborn, Ann. Phys. (N.Y.) **58**, 417 (1970).
8. R. J. Glauber, Lect. Theor. Phys. (N.Y.) **1**, 315 (1959).
9. A. G. Sitenko, Ukr. Fiz. Zh. (Russ. Ed.) **4**, 152 (1959).
10. H. Patberg *et al.*, Phys. Rev. C **53**, 1497 (1996).
11. J. Zejma *et al.*, Phys. Rev. C **55**, 42 (1997).
12. J. V. Mebonia and T. I. Kvaratskhelia, Preprint No. 84-67P (Inst. Theor. Phys., Kiev, 1984).
13. Th. Mongan, Phys. Rev. **178**, 1597 (1969).
14. V. K. Cheng and P. G. Roos, Nucl. Phys. A **225**, 397 (1974).
15. J. L. Durand *et al.*, Phys. Rev. C **6**, 393 (1972).
16. J. Strate *et al.*, Nucl. Phys. A **501**, 51 (1989).

Translated by R. Rogalyov

Physics of Atomic Nuclei, Vol. 67, No. 2, 2004, pp. 256–272. Translated from Yadernaya Fizika, Vol. 67, No. 2, 2004, pp. 273–289.

ELEMENTARY PARTICLES AND FIELDS
Experiment

Features of pC Interactions at a Momentum of 4.2 GeV/c versus the Degree of Centrality of a Collision between a Proton and a Carbon Nucleus: Kinematical Features of Secondaries

A. S. Galoyan[1)], E. N. Kladnitskaya[*], O. V. Rogachevsky[2)], R. Togoo[3)], and V. V. Uzhinskii

Joint Institute for Nuclear Research, Dubna, Moscow oblast, 141980 Russia

Received October 18, 2002; in final form, March 3, 2003

Abstract—The mean values of the momenta and emission angles of charged pions and protons in the laboratory frame are presented both for the total ensemble of interactions between 4.2-GeV/c protons and a carbon nucleus and for six groups of events characterized by different degrees of collision centrality. The distributions with respect to the total and the transverse momentum are presented for the particles being studied, along with the longitudinal-rapidity distributions. Our experimental data are compared with the predictions of the cascade–evaporation model and of two versions of the refined FRITIOF model. It is shown that, as the degree of collision centrality becomes higher, the mean momenta and rapidities of secondaries decrease, the transverse momenta remain virtually unchanged, and the mean angles of particle emission increase. This is consistent with the pattern of particle cascading in nuclei. However, the mean transverse momentum $\langle p_t \rangle$ of participant protons that was obtained on the basis of the cascade–evaporation model decreases with increasing degree of collision centrality, in contrast to what is observed in our experiment. A satisfactory description of experimental data is obtained on the basis of the refined FRITIOF model taking into account Δ^+ and Δ^0 isobars. The stopping power of carbon nuclei for 4.2-GeV/c protons is also determined. © *2004 MAIK "Nauka/Interperiodica".*

INTRODUCTION

The interactions of protons with a carbon nucleus (pC interactions) at a momentum of 4.2 GeV/c under the conditions of 4π geometry were explored in a number of studies [1–9]. A detailed analysis of the multiplicities of charged secondaries from collisions between protons and carbon nuclei at various values of the impact parameter was given in [9]. The present study is a continuation of that which was reported there. Here, we present the kinematical features of secondaries, including the momentum, angular, and rapidity distributions of charged pions and protons for six groups of pC interactions from peripheral to central ones. In just the same way as in [9], the experimental results are compared with the predictions of the cascade–evaporation model [10] and two versions of the modified FRITIOF model. The stopping power of a carbon nucleus for 4.2-GeV/c protons is considered individually. Investigation of these features is of importance for reconstructing the space-time pattern of pC interactions at various values of the impact parameter—in particular, for clarifying the role of particle rescatterings in a carbon nucleus and for obtaining deeper insight into the mechanism of hadron–nucleus interactions.

It is well known that the spectrum of fast leading protons in pA interactions can be described quite successfully on the basis of the Glauber approach—that is, within the pattern of successive collisions between an incident particle and the nucleons of the target nucleus [11, 12]. In the central rapidity region and in the region of target-nucleus fragmentation, where, at energies of a few GeV, the contribution of target-nucleus nucleons is large, one can expect a violation of this pattern. Therefore, it is interesting to investigate the features of leading and nonleading hadrons.

It is assumed that the intranuclear-cascade model [13] describes particle yields from hadron–nucleus interactions well at the energy value being considered. It was shown in [9] that this model reproduces the multiplicity distributions of particles produced in pC interactions. At the same time, the model considerably overestimates the multiplicity of negatively charged pions in multinucleon collisions. It can be

[1)]Joint Institute for Nuclear Research, Dubna, Moscow oblast, 141980 Russia; Yerevan Physics Institute, ul. Brat'ev Alikhanian 2, Yerevan, 375036 Armenia.

[2)]Joint Institute for Nuclear Research, Dubna, Moscow oblast, 141980 Russia; Petersburg Nuclear Physics Institute, Russian Academy of Sciences, Gatchina, 188350 Russia.

[3)]Institute of Physics and Technology, Ulan Bator, Mongolia.

[*]e-mail: klad@sunhe.jinr.ru

expected that the drawbacks of the cascade model will manifest themselves most clearly in the momentum distributions of negatively charged pions, especially in multiple collisions.

In the Glauber approach, as well as in the cascade model, it is assumed that hadron–nucleus and nucleus–nucleus interactions can be represented as a set of elementary-particle interactions.

As to the FRITIOF model [14, 15], it assumes a two-body kinematics of inelastic nucleon–nucleon interactions; that is, $a + b \to a' + b'$, where a' and b' are excited states of primary nucleons. The excited states are characterized by a mass. The projectile mass increases as the result of successive collisions in the target nucleus, and this leads to an increase in the multiplicity of particles produced in its decay. In the present version of the FRITIOF model, it is assumed that excited nucleons of a target nucleus leave the nucleus without undergoing additional collisions and decay beyond it. In order to simulate cascade processes in a target nucleus within the modified FRITIOF model, use is made of the Reggeon cascade model [16]. A more detailed description of the model can be found in [17, 18].

The possibility of describing, on the basis of the FRITIOF model and the intranuclear-cascade model, the multiplicities of particles produced in pC interactions at $p_p = 4.2$ GeV/c was investigated in [9]. It was shown there that the cascade–evaporation model [10] overestimates the multiplicity of negatively charged pions in multinucleon interactions, but that the FRITIOF model underestimates the multiplicity of product pions. Since it was noticed in the experiment that the multiplicity of positively charged pions is proportional to the multiplicity of participant protons, there arose the idea to take into account, within the FRITIOF model, $p \to n + \pi^+$ and $n \to p + \pi^-$ transitions caused by the existence of virtual Δ^+ and Δ^0 isobars in nuclei or their appearance in the Reggeon cascade. This made it possible to obtain a satisfactory description of the multiplicities of product particles versus the degree of centrality of collisions between protons and carbon nuclei.

Below, we present the kinematical features of particles in events differing by the degree of collision centrality. These data make it possible to reveal those phase-space regions where attempts at describing experimental results on the basis of the existing models run into the most serious difficulties. First of all, an analysis of peripheral interactions enables us to test the correctness of simulating elementary interactions. In multinucleon interactions, one can expect manifestations of collective effects. If they exist (for example, a fireball involving all colliding nucleons arises in central collisions), the kinematical features of particles must be weakly dependent on the degree of collision centrality. It will be shown below whether this is indeed so.

The ensuing exposition is organized as follows.

In Section 1, we give a brief description of special features of the experimental data used here. Further, we present the kinematical features of charged pions in Section 2 and the properties of participant protons in Section 3.

In Section 4, we determine the stopping power of carbon nuclei. In the physics of fast-particle propagation through matter, the stopping power is defined as the mean kinetic energy lost by a particle per unit path. It is assumed that these losses are low and that the particle moves nearly along a straight line. In the physics of nuclear collisions, energy losses are high, and it is difficult to discriminate between the projectile that survived and particles knocked out of the target. Therefore, the change in the rapidities of interacting nucleons is more often considered in high-energy physics [19, 20]. A systematics of the stopping power of nuclei that was found in this way is given in [21]. For a determination close to the classical one, use is usually made of model calculations. We rely on the FRITIOF model version that takes into account delta isobars. As was shown in [9], the momentum region $p > 1.4$ GeV/c is dominated by surviving protons, the momenta of nucleons knocked out of the target nucleus being less than 1.4 GeV/c. In Section 4, the features of leading ($p > 1.4$ GeV/c) and nonleading ($p \leq 1.4$ GeV/c) protons are considered separately; also, data on the distribution of energy between different types of secondaries are given there.

In the Conclusions, we summarize the main results of our study.

1. EXPERIMENTAL DATA

The experimental data used here were obtained on the basis of processing stereophotographs from the 2-m propane bubble chamber constructed at the High Energy Laboratory of the Joint Institute for Nuclear Research (JINR, Dubna), placed in a magnetic field of strength 1.5 T, and irradiated with a beam of protons accelerated to a momentum of 4.2 GeV/c at the JINR synchrophasotron.

Methodological issues associated with selecting events of inelastic pC interactions from the entire ensemble of proton interactions with propane (C_3H_8) by introducing corrections for the number of secondaries and their angular and momentum features, as well as weights taking into account positively charged particles of momenta in excess of 0.5 GeV/c, were

Table 1. Mean multiplicities of particles from pC interactions at 4.2 GeV/c versus the degree of collision centrality Q according to (expt) our experimental data and (FRITIOF) the predictions of the FRITIOF model with allowance for Δ isobars

Q		N_{ev}, %	$\langle n_{\pi^-}\rangle$	$\langle n_{\pi^+}\rangle$	$\langle n_{\text{part-p}}\rangle$	$\langle n_{\text{part-p}}\rangle$, $0.3 < p \leq 1.4$ (GeV/c)	$\langle n_{\text{part-p}}\rangle$, $p > 1.4$ (GeV/c)
1	Expt.	2289 (27.3)	0.522 ± 0.013	0.416 ± 0.010	1.054 ± 0.015	0.466 ± 0.011	0.588 ± 0.020
	FRITIOF	28457 (28.4)	0.479 ± 0.004	0.379 ± 0.003	1.088 ± 0.005	0.303 ± 0.003	0.785 ± 0.006
2	Expt.	3814 (45.6)	0.321 ± 0.007	0.660 ± 0.008	1.743 ± 0.010	1.003 ± 0.010	0.740 ± 0.018
	FRITIOF	37635 (37.6)	0.321 ± 0.003	0.662 ± 0.004	1.658 ± 0.004	0.864 ± 0.004	0.794 ± 0.005
3	Expt.	1477 (17.6)	0.423 ± 0.016	0.965 ± 0.020	2.526 ± 0.024	1.863 ± 0.025	0.664 ± 0.027
	FRITIOF	16675 (16.7)	0.424 ± 0.005	0.787 ± 0.006	2.624 ± 0.007	1.912 ± 0.007	0.712 ± 0.007
4	Expt.	575 (6.9)	0.476 ± 0.027	1.22 ± 0.04	3.22 ± 0.04	2.65 ± 0.05	0.57 ± 0.04
	FRITIOF	9551 (9.6)	0.448 ± 0.006	0.857 ± 0.008	3.54 ± 0.01	2.927 ± 0.010	0.62 ± 0.01
5	Expt.	164 (2.0)	0.43 ± 0.05	1.40 ± 0.08	4.02 ± 0.09	3.55 ± 0.10	0.47 ± 0.06
	FRITIOF	5166 (5.2)	0.45 ± 0.01	0.89 ± 0.01	4.46 ± 0.02	3.923 ± 0.016	0.54 ± 0.01
≥ 6	Expt.	52 (0.6)	0.36 ± 0.07	1.58 ± 0.16	5.10 ± 0.18	4.54 ± 0.21	0.56 ± 0.11
	FRITIOF	2516 (2.5)	0.46 ± 0.01	0.93 ± 0.02	5.75 ± 0.03	5.316 ± 0.024	0.44 ± 0.01
All	Expt.	8371 (100)	0.407 ± 0.006	0.706 ± 0.007	1.860 ± 0.010	1.192 ± 0.011	0.668 ± 0.012
events	FRITIOF	100 000 (100)	0.406 ± 0.002	0.640 ± 0.002	2.085 ± 0.004	1.346 ± 0.004	0.739 ± 0.003

Note: In parenthesis, we present the fraction (in %) of events corresponding to given Q.

considered in [1, 2, 22]. In the ensemble of pC interactions that was subjected to the analysis, we selected, among secondary particles, positively and negatively charged pions, participant protons of momentum in the region $p > 0.3$ GeV/c, and evaporated protons of momentum in the range $0.15 < p \leq 0.3$ GeV/c. [4)]

The degree of centrality of a pC interaction was characterized by the quantity Q defined as $Q = n_+ - n_- - n_{p_{\text{evap}}}$, where n_+ and n_- are the multiplicities of, respectively, positively and negatively charged particles in an event and $n_{p_{\text{evap}}}$ is the multiplicity of evaporated protons. The quantity Q correlates with the impact parameter of a hadron–nucleus collision [9]. The degree of collision centrality grows with increasing Q.

The number of pC events analyzed here and the mean multiplicities of secondaries for all pC interactions and for six event groups characterized by different degrees of collision centrality are given in Table 1. The results obtained by analyzing the multiplicity distributions of secondaries are presented in [9], along with the Q dependences of the multiplicities. Table 1 also displays the mean multiplicities of secondaries according to the predictions of the modified FRITIOF model taking into account a 20% admixture of Δ^+ and Δ^0 isobars among the nucleons of the carbon nucleus. In [9], the experimental data on the multiplicities of secondaries were compared with the predictions of the modified FRITIOF model. In the present study, we consider the kinematical features of secondaries in six event groups characterized by different values of Q.

2. KINEMATICAL FEATURES OF CHARGED PIONS

The mean values of the total ($\langle p_\pi \rangle$) and the transverse ($\langle p_t^\pi \rangle$) momentum of negatively charged pions and the mean values of their emission angles in experimental events are given in Table 2, along with respective predictions of the FRITIOF model taking into account delta isobars. The same experimental data are also shown in Fig. 1, together with the results of the calculations within the cascade-evaporation model and within the FRITIOF model taking into account delta isobars. As might have been expected, the mean momenta of particles decrease with increasing

[4)] Protons of momenta below 150 MeV/c are not recorded in the propane bubble chamber because of a short range ($l < 2$ mm).

Table 2. Mean momenta and emission angles of pions in pC interactions at 4.2 GeV/c versus the degree of collision centrality Q [according to (expt) our experimental data and (FRITIOF) the predictions of the FRITIOF model taking into account Δ isobars]

Q		$\langle p_{\pi^-}\rangle$, GeV/c	$\langle p_t^{\pi^-}\rangle$, GeV/$c$	$\langle\theta_{\pi^-}\rangle$, deg	$\langle p_{\pi^+}\rangle$, GeV/c	$\langle p_t^{\pi^+}\rangle$, GeV/$c$	$\langle\theta_{\pi^+}\rangle$, deg
1	Expt.	0.567 ± 0.014	0.246 ± 0.005	45.2 ± 1.0	0.564 ± 0.007	0.239 ± 0.002	39.1 ± 0.4
	FRITIOF	0.496 ± 0.003	0.241 ± 0.001	47.4 ± 0.3	0.592 ± 0.004	0.238 ± 0.001	38.2 ± 0.3
2	Expt.	0.518 ± 0.010	0.255 ± 0.004	49.5 ± 1.0	0.554 ± 0.004	0.269 ± 0.002	47.7 ± 0.3
	FRITIOF	0.449 ± 0.003	0.222 ± 0.001	49.6 ± 0.3	0.533 ± 0.002	0.242 ± 0.001	44.0 ± 0.2
3	Expt.	0.424 ± 0.014	0.248 ± 0.007	57.3 ± 1.5	0.505 ± 0.006	0.275 ± 0.003	55.3 ± 0.5
	FRITIOF	0.378 ± 0.003	0.214 ± 0.001	56.4 ± 0.4	0.428 ± 0.003	0.229 ± 0.001	51.4 ± 0.3
4	Expt.	0.375 ± 0.018	0.236 ± 0.011	62.1 ± 2.3	0.475 ± 0.007	0.265 ± 0.004	57.4 ± 0.7
	FRITIOF	0.333 ± 0.003	0.207 ± 0.002	60.9 ± 0.6	0.373 ± 0.003	0.217 ± 0.001	55.2 ± 0.4
5	Expt.	0.38 ± 0.04	0.215 ± 0.025	62.3 ± 4.9	0.430 ± 0.8012	0.267 ± 0.007	64.9 ± 1.2
	FRITIOF	0.314 ± 0.004	0.208 ± 0.002	63.1 ± 0.8	0.337 ± 0.002	0.209 ± 0.002	58.6 ± 0.5
≥ 6	Expt.	0.45 ± 0.07	0.27 ± 0.06	62.3 ± 11.0	0.446 ± 0.020	0.30 ± 0.012	68.7 ± 2.0
	FRITIOF	0.295 ± 0.005	0.199 ± 0.003	66.8 ± 1.1	0.311 ± 0.004	0.203 ± 0.002	61.5 ± 0.7
All	Expt.	0.503 ± 0.007	0.248 ± 0.003	50.8 ± 0.6	0.528 ± 0.003	0.265 ± 0.001	50.3 ± 0.2
events	FRITIOF	0.429 ± 0.002	0.224 ± 0.001	52.4 ± 0.2	0.480 ± 0.001	0.232 ± 0.001	47.6 ± 0.1

degree of collision centrality. The mean momenta of positively charged pions exceed the mean momenta of negatively charged pions both in the $Q = 2$–4 groups and in the entire ensemble of pC interactions (see Table 2). In $Q = 1$ events, which are predominantly proton–neutron interactions, the mean momenta of positively and negatively charged pions agree with each other.

Within the errors, the mean transverse momentum of negatively charged pions is independent of Q. The mean transverse momentum of positively charged pions, $\langle p_t\rangle$, increases in going over from $Q = 1$ to $Q = 2$ events and then remains at the same level up to $Q = 5$ events. In the group involving the most central ($Q \geq 6$) events, one can observe an approximately 10% increase in $\langle p_t^{\pi^+}\rangle$ with respect to the momentum at smaller values of Q.

The mean pion emission angles quoted in Table 2 grow with increasing Q. This is characteristic of the pion-production process—as the impact parameter decreases, the probability of pion rescattering becomes higher, which leads to a decrease in the mean momentum of pions and to an increase in the mean value of their emission angle; this is eventually responsible for a weak dependence of the mean value of p_t on the degree of centrality of pC interactions.

Figures 2–7 display the distributions of charged pions with respect to the kinematical variables. As can be seen, the total-momentum distributions of positively and negatively charged pions become softer upon going over from peripheral ($Q \leq 2$) to central ($Q \geq 4$) interactions; therefore, the mean momenta of pions decrease (see Table 2 and Fig. 1). The spectra of positively charged pions are on average somewhat harder than the spectra of negatively charged pions. In the most central ($Q \geq 6$) interactions, the spectra of negatively and positively charged pions differ in shape (Figs. 2, 3) but the respective mean momenta are identical.

The transverse-momentum distributions of pions depend on Q more weakly than the total-momentum distributions (see Table 2 and Figs. 4, 5). The overwhelming majority of pions have transverse-momentum values not higher than 0.5 GeV/c; nevertheless, hard collisions resulting in the production of high-p_t pions occur in the interactions of protons with a carbon nucleus (see Figs. 4, 5).

The rapidity distributions of negatively and positively charged pions are shown in, respectively, Figs. 6 and 7 for six groups of events characterized by various degrees of centrality of pC collisions. One can see that, as the quantity Q increases, the maximum of the pion distributions shifts to the region

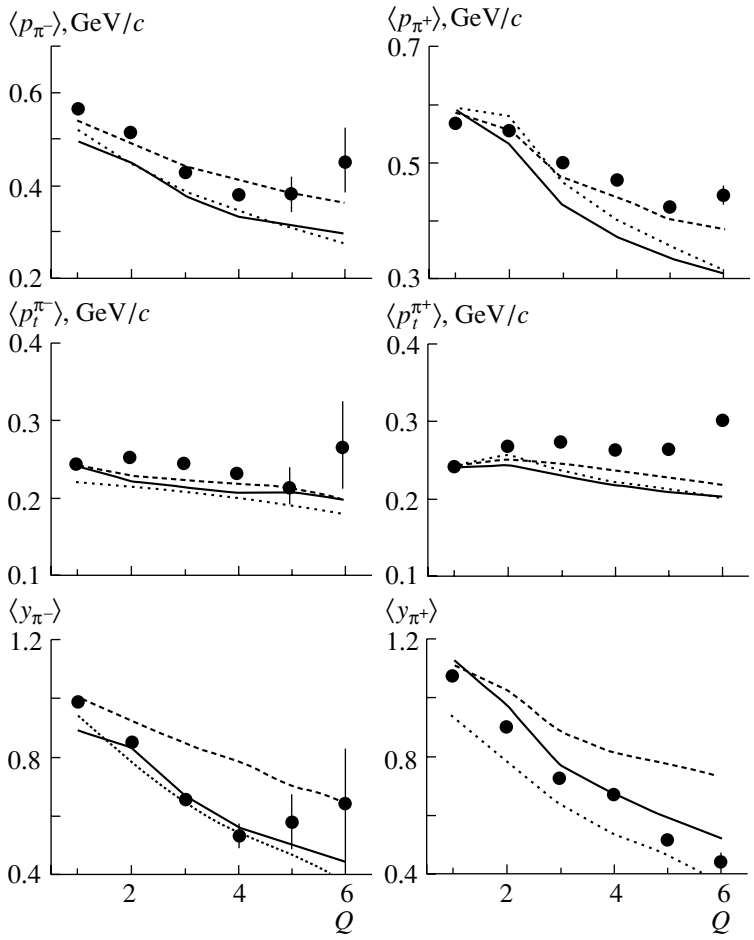

Fig. 1. Mean features of charged pions versus Q: (closed circles) experimental data; (solid and dashed curves) results of the calculations performed on the basis of the FRITIOF model, respectively, with and without allowance for Δ^+ and Δ^0 isobars; and (dotted curves) results of the calculations on the basis of the cascade–evaporation model.

of carbon-nucleus fragmentation. Figure 1 illustrates the change in the mean rapidities of charged pions as we go over from peripheral to central interactions. The mean rapidities of charged pions change from values corresponding to proton–nucleon interactions at 4.2 GeV/c ($\langle y\rangle_{pN} = 1.1$) to smaller values that characterize proton–nucleon interactions at lower energies. The mean rapidities of positively charged pions exceed somewhat the mean rapidities of negatively charged pions, and this is natural in the case of incident protons. It should be emphasized that, in $Q = 1$ events, the distribution of negatively charged pions has two maxima, that at $y \sim 0.5$ and that at $y \sim 1.5$ (see Fig. 6). In all other distributions, there is no two-peak structure.

The theoretical models qualitatively reproduce the Q dependence of the mean momentum of pions. The predictions of the FRITIOF model disregarding delta isobars are in the best agreement with the experimental data (see Fig. 1). However, this version of the model considerably underestimates the multiplicities of product pions [9]. The cascade–evaporation model overestimates the multiplicities of pions [9]. The multiplicity of negatively charged pions is well described by the FRITIOF model taking into account the production of delta isobars (see Table 1). All models underestimate the mean transverse momenta of pions. The differential distributions with respect to p and p_t enable us to draw more specific conclusions about the drawbacks of the models.

The predictions of the theoretical models and the experimental data differ most strongly at low and high momenta of pions (see Figs. 2, 3). According to the data in Figs. 2 and 3, the cascade–evaporation model overestimates the yield of soft pions ($p <$ 300 MeV/c). The FRITIOF model disregarding delta isobars strongly underestimates the yield of soft pions; for this reason, this model gives high values of the mean momenta. In the FRITIOF model version taking into account delta isobars, the mean momenta of negatively charged pions are below the

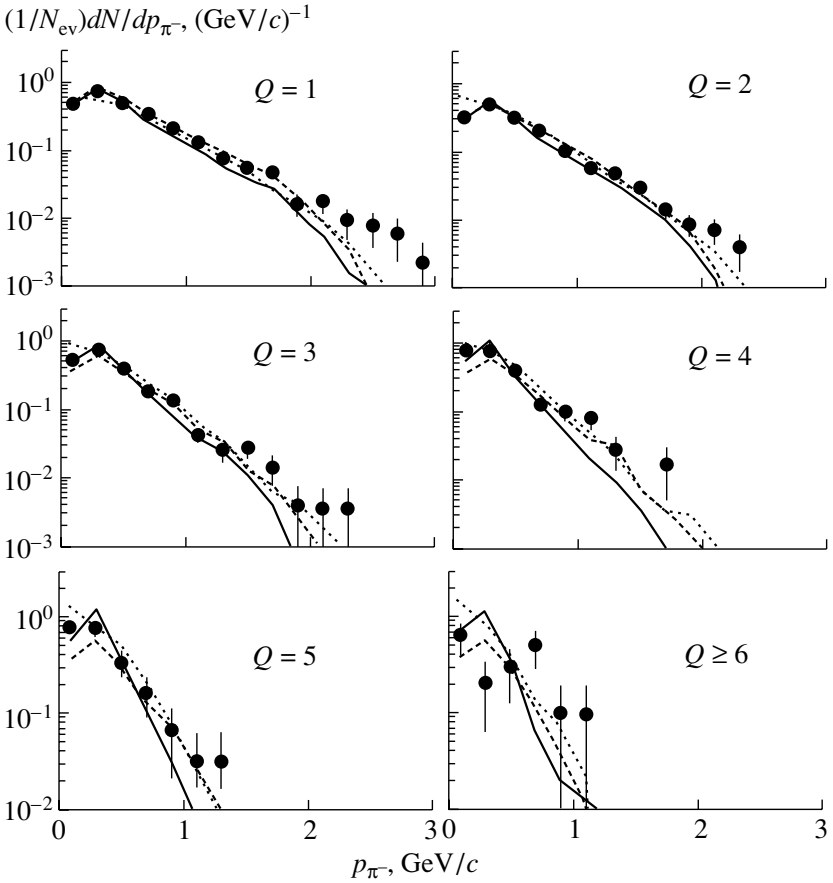

Fig. 2. Distributions of negatively charged pions with respect to the total momentum at various values of Q. The notation is identical to that in Fig. 1.

corresponding experimental data, and this is due to a small yield of energetic pions. The situation around the spectra of positively charged pions is more complicated. In $Q = 3$–4 events, the shape of the calculated spectra strongly differs from the experimental distributions—the model underestimates the yield of fast pions (see Fig. 3). Events of this group involve essentially multiparticle interactions. Investigation of such interactions may give impetus to a further development of the models.

An analysis of the differential distributions with respect to p_t and of the model predictions leads to results that are similar to those presented above. The cascade-evaporation model overestimates the yield of pions having low transverse momenta ($p_t <$ 200 MeV/c) (see Figs. 4, 5). All models underestimate the probability of the production of pions having high transverse momenta and describe poorly the spectra of positively charged pions in multiparticle interactions (see Fig. 5).

The strongest discrepancies between the theoretical predictions and the experimental data are observed for the rapidity distributions of charged pions. As can be seen from Figs. 6 and 7, the cascade–evaporation model assumes an excess production of pions in the target-fragmentation region. The FRITIOF model disregarding delta isobars leads to overly hard spectra; moreover, it strongly underestimates the multiplicity of pions produced in multinucleon interactions (see Figs. 6, 7). The FRITIOF model version taking into account delta isobars gives intermediate results that are the most acceptable, but there remain problems in it that are associated with the description of multinucleon collisions.

3. KINEMATICAL FEATURES OF PARTICIPANT PROTONS

As was shown in [9], the predictions of all models for the multiplicities of participant protons in the groups of interactions under consideration are in agreement with the experimental data. Therefore, an analysis of the distributions of protons with respect to kinematical variables becomes of paramount importance. The mean kinematical features of participant protons are quoted in Tables 3 and 4. Figure 8 supplements the data in Tables 3 and 4, giving a

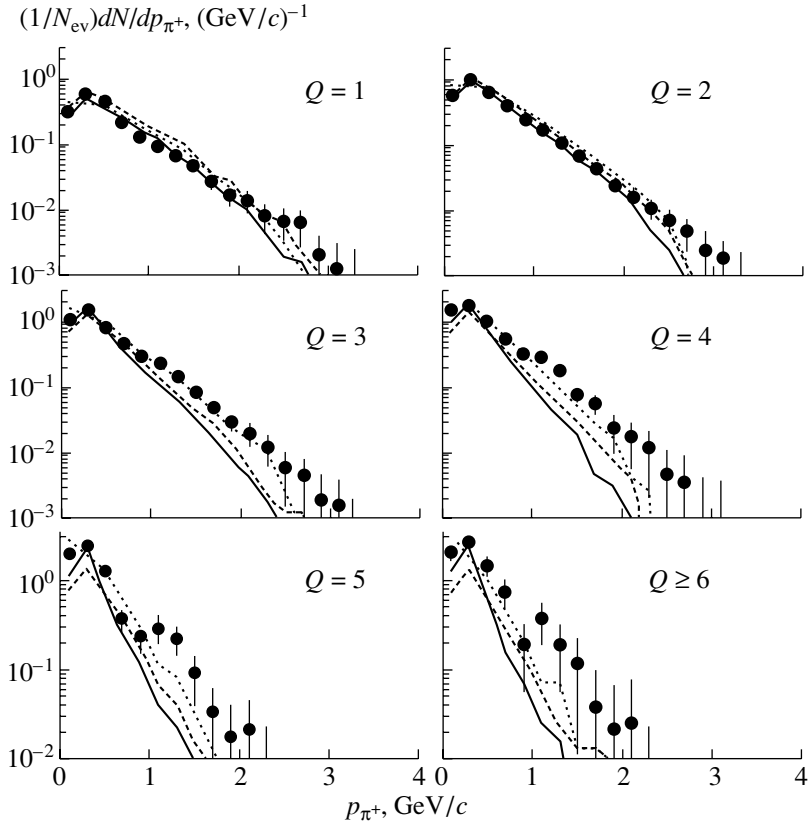

Fig. 3. Total-momentum distributions of positively charged pions at various values of Q. The notation is identical to that in Fig. 1.

general idea of the model predictions. Figures 9–11 display the differential distributions of participant protons.

According to the experimental data, the momentum spectrum of participant protons becomes considerably softer as we go over from peripheral to central interactions (see Figs. 8, 9[5)]). The mean momentum of protons decreases by a factor greater than two (see Table 3 and Fig. 9) as Q changes from one to six. To a considerable extent, these changes are due to an increase in the fraction of target protons (whose momentum is on average less than 1 GeV/c) among the total number of participant protons. In $Q = 1$ events, the mean multiplicities of leading protons ($p > 1.4$ GeV/c) and protons arising as target-nucleus fragments ($p \leq 1.4$ GeV/c) are commensurate, but, with increasing Q, this relationship changes sharply. Figure 9 clearly illustrates the enrichment of the spectrum of participant protons in target protons with increasing Q.

Among target protons, we singled out two groups: the first included protons of momenta from 0.3 to 0.75 GeV/c, while the second consisted of protons having momenta from 0.75 to 1.4 GeV/c. A greater fraction of target protons belonged to the first group. Protons of this group are characterized by a weak Q dependence of the mean momentum (see Table 3 and Fig. 8). Most likely, this is because the probability that protons from this group undergo inelastic interactions in the nucleus is low. The mean momentum of target protons, which are faster ($p > 0.75$ GeV/c), decreases with increasing Q. This conclusion can be drawn from a comparison of the Q dependence of the mean momenta of all target protons ($0.3 \leq p < 1.4$ GeV/c) and the proton momenta from the interval 0.3–0.75 GeV/c (see Tables 3, 4). This result indicates that fast target protons participate in inelastic interactions in the nucleus.

The mean transverse momentum of participant protons is independent of the degree of collision centrality from $Q = 2$ (see Table 3 and Fig. 8). This is due to strong correlation between the decrease (with increasing Q) in the mean momentum of participant

[5)]The presence of protons with momenta $p > 4$ GeV/c in the momentum distributions is associated with errors in determining the momentum of energetic particles. The maximum admissible error in determining the momentum of a particle was 30%.

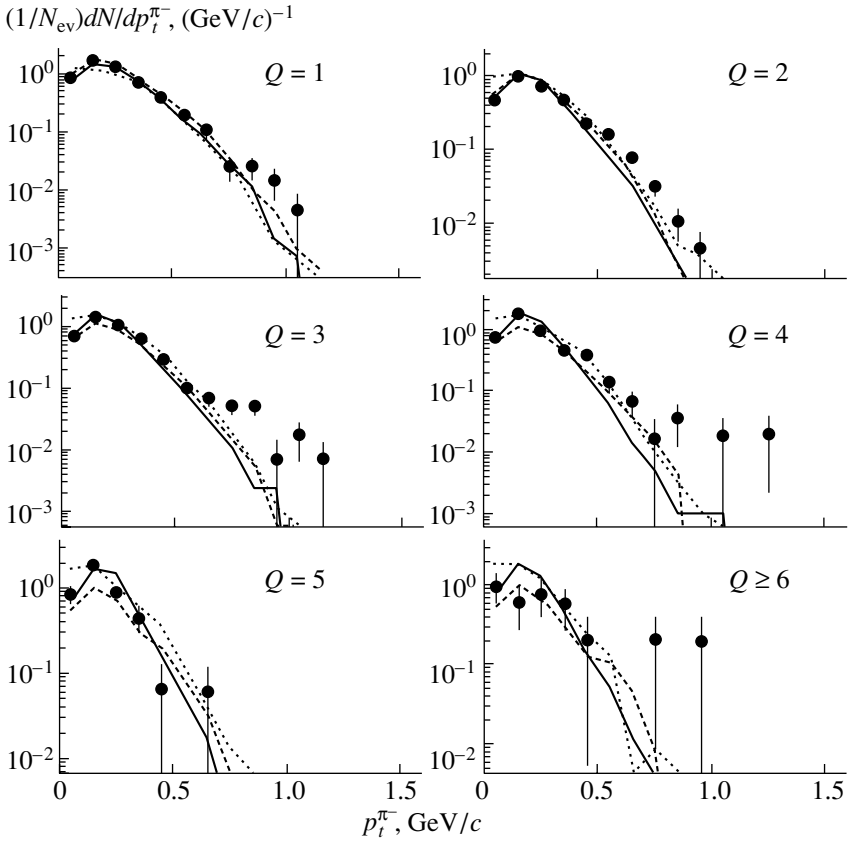

Fig. 4. Transverse-momentum distributions of negatively charged pions at various values of Q. The notation is identical to that in Fig. 1.

protons and the increase in their mean emission angle (see Table 3). This feature is peculiar to target protons (see Table 4) constituting the majority of participant protons. Leading protons ($p > 1.4$ GeV/c) show a totally different dependence of the mean transverse momentum on Q: the values of $\langle p_t \rangle$ are 1.5 to 2 times higher in central than in peripheral interactions (see Table 4). This circumstance has virtually no effect on $\langle p_t \rangle$ of all participant protons because leading protons constitute but a small fraction of them. Central interactions are characterized by a relatively small (about 25%) reduction of the leading-proton momentum in relation to peripheral interactions, but the respective increase in the mean emission angle is rather large (by a factor of 2 to 2.5) (see Table 4).

In Fig. 10, the transverse-momentum distributions of participant protons are shown for events characterized by different values of Q. One can see that the experimental data agree well with the distributions calculated within two versions of the modified FRITIOF model; there is also agreement with the predictions of the cascade–evaporation model up to $p_t \leq 1.4$ GeV/c.

As one goes over from peripheral to central interactions, the mean rapidities of participant protons are shifted, in just the same way as those of pions, from the value of $y = 1.1$, which corresponds to pN interactions, to smaller values (see Fig. 8). Figure 11 displays the rapidity distributions of participant protons for events characterized by different degrees of centrality of pC interactions. For $Q = 1$ events, the rapidity distribution of participant protons has a two-peak structure. A broad peak at $y \sim 1.7$ is associated with leading protons and is analogous to that in pn interactions. It seems that the peak at $y \sim 0.5$ is related to the peak appearing in the distributions of negatively charged pions (see Fig. 6) and is caused by processes like $n \to p + \pi^-$. With increasing Q, the rapidity distributions are shifted to the region of target-nucleus fragmentation.

All models describe rather well the momentum spectra of protons for $Q \geq 3$. For $Q = 1$ and 2 events, one can observe that the results of the calculations deviate strongly from experimental data (see Fig. 9). In the spectrum of protons that is predicted by the cascade–evaporation model for $Q = 1$, there is a peak at $p \sim 4$ GeV/c due to elastic rescatterings of incident protons on nucleons of the target nucleus and

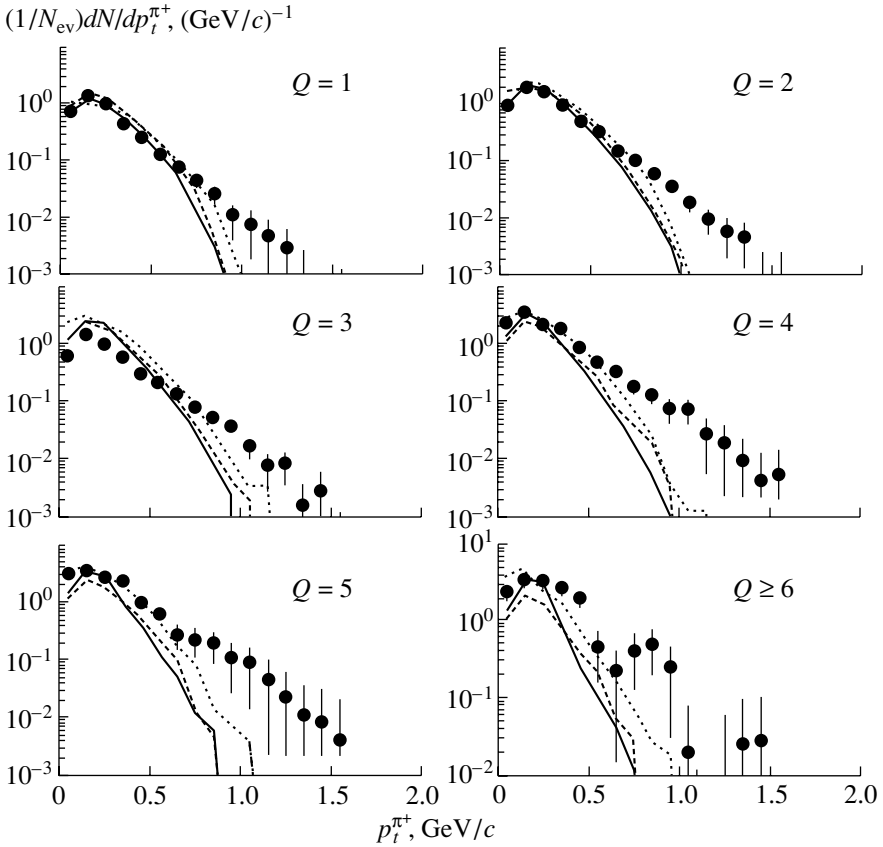

Fig. 5. Transverse-momentum distributions of positively charged pions at various values of Q. The notation is identical to that in Fig. 1.

a minimum at $p \sim 3$ GeV/c due to an unsatisfactory simulation of NN interactions. In the FRITIOF model disregarding delta isobars and elastic rescatterings, there is no peak. However, this model predicts an overestimated yield of protons having momenta of about 2 GeV/c and underestimates the yield of soft protons. The predictions of the FRITIOF model version taking into account delta isobars are close to the experimental data everywhere, with the exception of the region around $p \sim 4$ GeV/c. Thus, the existing methods for taking into account elastic rescatterings within a nucleus cannot be considered to be satisfactory.

The agreement between the momentum spectra calculated within the FRITIOF model and the experimental data is improved for $Q \geq 2$. As previously, the cascade–evaporation model predicts a peak at $p \sim 4$ GeV/c in $Q = 2$ events and dips at $p \sim 3$ GeV/c in $Q \geq 2$ events.

The models describe well the transverse-momentum distributions of protons everywhere, with the exception of the region of high p_t ($p_t > 1.5$ GeV/c). It should be noted that, in peripheral interactions ($Q \leq 3$), the yield of protons having low p_t ($p_t < 0.4$ GeV/c) is underestimated (see Fig. 10).

The drawbacks of the models manifest themselves most clearly in describing the rapidity distributions of protons (see Fig. 11). Considering $Q = 1$ events, one can see that, in disagreement with the experimental data, the cascade–evaporation model leads to a minimum in the region of the first maximum at $y \sim 1.7$. Since events of this group are enriched in proton–neutron interactions, the minimum is unambiguously associated with an unsatisfactory simulation of the proton spectra in NN collisions within the model. The peak at $y \sim 2$ in the results of the calculations is due to elastic rescatterings. The FRITIOF model disregarding delta isobars predicts an overestimated proton yield in the central region. The predictions of the FRITIOF model version taking into account delta isobars are closer to the experimental data. All models fail to describe the peak at $y \sim 0.5$.

For $Q = 2$ events, the models make similar predictions, but the cascade–evaporation model and the FRITIOF model version taking into account delta isobars describe the peak at $y \sim 0.4$ somewhat better. Thus, there exist problems in theoretically describing peripheral interactions.

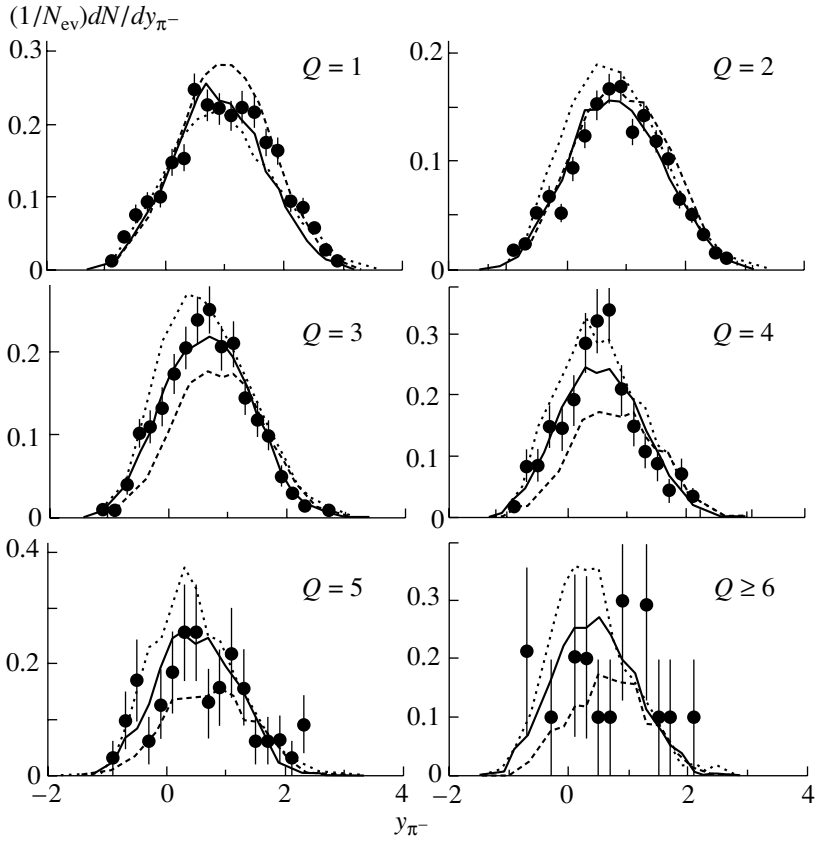

Fig. 6. Rapidity distributions of negatively charged pions at various values of Q. The notation is identical to that in Fig. 1.

The modified FRITIOF model taking into account delta isobars and the cascade–evaporation model qualitatively reproduce the rapidity distributions of participant protons for $Q \geq 3$ events. Here, the most serious difficulties arise at $y \sim 0$.

4. STOPPING POWER OF A CARBON NUCLEUS

It is of interest to determine the stopping power of a nucleus as light as the carbon nucleus for protons having the momentum of 4.2 GeV/c and its dependence on the degree of centrality of pC interactions. The stopping power of a target nucleus is characterized by the energy lost by a projectile in its interaction with the target. In order to determine the stopping power of a target nucleus, it is therefore necessary to single out, among all secondaries, the primary particle that survived upon the interaction and to measure its energy. This is not always possible.

For a leading proton, Agakishiev *et al.* [3] took a positively charged particle having the highest momentum in an event. In experiments with electrons, a greater part of leading protons [19, 20] could be identified. We applied a different approach to separating leading protons, that which is based on the use of the FRITIOF model. Since the FRITIOF model describes satisfactorily the momentum spectra of all participant protons, it would be natural to assume that it also describes satisfactorily the spectra of leading protons and participant protons from a target nucleus. This assumption formed a basis of our method for separating leading protons. Within the FRITIOF model version taking into account delta isobars, one can obtain the spectra of leading protons and participant protons from a carbon nucleus (see Fig. 2 in [9]). The boundary between the two spectra, p^{b}, was chosen with allowance for the condition

$$\langle n_{p\text{-lead}}\rangle(p_{p\text{-lead}} < p^{\mathrm{b}}) \simeq \langle n_{p_{\mathrm{tar}}}\rangle(p_{p_{\mathrm{tar}}} > p^{\mathrm{b}}).$$

From this condition, it follows that $p^{\mathrm{b}} = 1.4$ GeV/c: the mean multiplicity of leading protons having momenta in the region $p \leq 1.4$ GeV/c appears to be 0.1, while the mean multiplicity of target protons with momenta of $p > 1.4$ GeV/c is 0.09. Further, all protons having momenta in excess of 1.4 GeV/c are considered to be leading, while participant protons of momentum in the range $0.3 < p \leq 1.4$ GeV/c are taken to be target protons (see Table 1 and Fig. 2 in [9]).

From the point of view of the modified FRITIOF

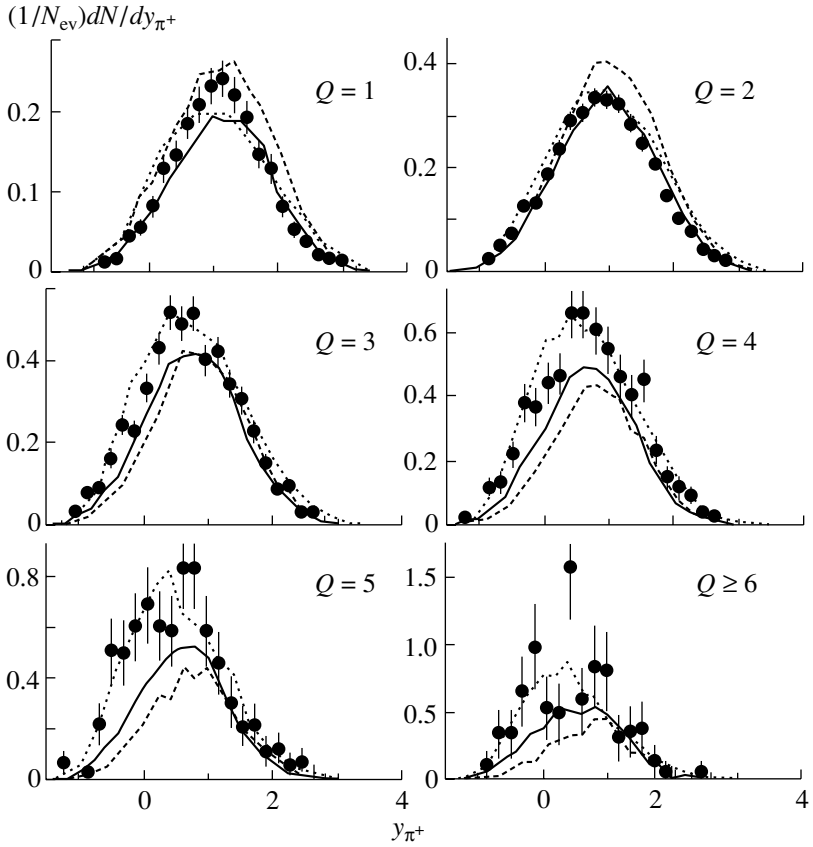

Fig. 7. Rapidity distributions of positively charged pions at various values of Q. The notation is identical to that in Fig. 1.

model taking into account delta isobars, the chosen boundary is the most appropriate for selecting leading protons from peripheral ($Q \leq 2$) interactions—that is, for the majority of pC interactions. In these events, the fraction of leading protons having momenta in the region $p \leq 1.4$ GeV/c is less than 10%.

In central interactions, a primary proton loses a considerable part of its energy (see Table 4), and the fraction of leading protons having momenta in the region $p \leq 1.4$ GeV/c increases to 40%. As follows from the data in Table 1, the number of such events does not exceed 8%.

As to the fraction of target protons having momenta in the region $p > 1.4$ GeV/c, it is maximal in $Q = 1$ events and decreases fast to 1% in $Q \geq 5$ events. This result reflects the softening of the spectra of fast target protons with increasing Q, which was discussed above (see Table 4). According to the modified FRITIOF model taking into account Δ isobars, the admixture of target protons among protons of momentum in the region $p \geq 1.4$ GeV/c varies from 15 to 8%, depending on Q, while the admixture of leading protons among protons of momentum in the range 0.3–1.4 GeV/c is 7 to 8%.

A comparison of the experimental mean multiplicities of leading and target protons with their counterparts calculated within the modified FRITIOF model involving delta isobars shows (see Table 1) that, for the majority of the groups, the distinction does not exceed 10%. The mean angular and momentum features of leading protons and protons originating from fragmentation are presented in Table 4. It can be seen that, in the interaction with a carbon nucleus, the primary proton loses a considerable part of its momentum. In central collisions, this part is equal, on average, to half of the primary momentum.

A feature that is peculiar to leading protons from experimental events, but which is not reproduced by the model predictions, is that their mean transverse momentum increases sharply as we go over from peripheral to central interactions (see Table 4).

The mean momentum of target protons decreases with increasing Q, but to a lesser extent and owing primarily to protons of momentum in the region $p > 0.75$ GeV/c because the mean momentum of protons with momenta of $0.3 \leq p < 0.75$ GeV/c is virtually independent of Q (see Table 3). The mean transverse momentum of target protons is independent of Q for all $Q > 1$ events, remaining at a level of 400 MeV/c.

Table 3. Mean momenta and emission angles of participant protons in pC interactions at 4.2 GeV/c versus the degree of collision centrality Q according to (expt) our experimental data and (FRITIOF) the predictions of the FRITIOF model taking into account delta isobars

Q		$\langle p_{\text{part-p}}\rangle$, GeV/$c$	$\langle p_t^{\text{part-p}}\rangle$, GeV/$c$	$\langle\theta_{\text{part-p}}\rangle$, deg	$\langle p_{\text{part-p}}\rangle$, GeV/$c$	$\langle p_t^{\text{part-p}}\rangle$, GeV/$c$	$\langle\theta_{\text{part-p}}\rangle$, deg
					$0.3 \le p < 0.75$ GeV/c		
1	Expt.	1.878 ± 0.024	0.394 ± 0.006	21.2 ± 0.4	0.500 ± 0.004	0.305 ± 0.004	44.9 ± 0.8
	FRITIOF	2.331 ± 0.007	0.444 ± 0.001	16.9 ± 0.1	0.549 ± 0.002	0.332 ± 0.003	42.6 ± 0.4
2	Expt.	1.542 ± 0.011	0.444 ± 0.003	30.5 ± 0.3	0.488 ± 0.002	0.328 ± 0.002	53.4 ± 0.5
	FRITIOF	1.666 ± 0.005	0.474 ± 0.001	30.3 ± 0.1	0.520 ± 0.001	0.376 ± 0.001	57.9 ± 0.2
3	Expt.	1.108 ± 0.013	0.451 ± 0.004	41.6 ± 0.5	0.473 ± 0.003	0.335 ± 0.003	59.2 ± 0.7
	FRITIOF	1.121 ± 0.004	0.463 ± 0.001	42.7 ± 0.2	0.502 ± 0.001	0.379 ± 0.001	63.0 ± 0.2
4	Expt.	0.902 ± 0.015	0.440 ± 0.001	48.0 ± 0.7	0.467 ± 0.003	0.336 ± 0.004	62.1 ± 1.0
	FRITIOF	0.905 ± 0.004	0.441 ± 0.001	48.7 ± 0.2	0.492 ± 0.001	0.379 ± 0.001	64.5 ± 0.2
5	Expt.	0.778 ± 0.020	0.429 ± 0.009	49.0 ± 1.1	0.468 ± 0.006	0.336 ± 0.006	58.3 ± 1.4
	FRITIOF	0.790 ± 0.004	0.428 ± 0.001	52.7 ± 0.2	0.487 ± 0.001	0.377 ± 0.001	65.6 ± 0.3
≥ 6	Expt.	0.751 ± 0.032	0.454 ± 0.015	56.2 ± 2.0	0.457 ± 0.009	0.344 ± 0.010	65.4 ± 2.4
	FRITIOF	0.686 ± 0.004	0.409 ± 0.002	56.7 ± 0.3	0.474 ± 0.001	0.374 ± 0.001	66.7 ± 0.3
All	Expt.	1.368 ± 0.007	0.437 ± 0.002	35.0 ± 0.2	0.479 ± 0.001	0.330 ± 0.001	56.5 ± 0.3
events	FRITIOF	1.362 ± 0.002	0.452 ± 0.001	38.22 ± 0.07	0.499	0.376	62.42 ± 0.1

Table 4. Mean momenta and emission angles of leading and target protons in pC interactions at 4.2 GeV/c versus the degree of collision centrality Q according to (expt) our experimental data and (FRITIOF) the predictions of the FRITIOF model taking into account delta isobars

Q		$\langle p_{\text{part-p}}\rangle$, GeV/$c$	$\langle p_t^{\text{part-p}}\rangle$, GeV/$c$	$\langle\theta_{\text{part-p}}\rangle$, deg	$\langle p_{\text{part-p}}\rangle$, GeV/$c$	$\langle p_t^{\text{part-p}}\rangle$, GeV/$c$	$\langle\theta_{\text{part-p}}\rangle$, deg
		$p \ge 1.4$ GeV/c			$0.3 \le p < 1.4$ GeV/c		
1	Expt.	2.76 ± 0.03	0.424 ± 0.011	10.0 ± 0.2	0.764 ± 0.008	0.357 ± 0.005	35.4 ± 0.6
	FRITIOF	2.894 ± 0.006	0.453 ± 0.002	10.67 ± 0.06	0.874 ± 0.003	0.418 ± 0.002	33.2 ± 0.2
2	Expt.	2.66 ± 0.02	0.519 ± 0.006	12.8 ± 0.2	0.717 ± 0.004	0.388 ± 0.002	45.3 ± 0.3
	FRITIOF	2.643 ± 0.05	0.498 ± 0.002	12.84 ± 0.06	0.768 ± 0.002	0.451 ± 0.001	46.4 ± 0.2
3	Expt.	2.35 ± 0.03	0.594 ± 0.013	16.5 ± 0.4	0.665 ± 0.005	0.400 ± 0.004	50.5 ± 0.5
	FRITIOF	2.277 ± 0.006	0.533 ± 0.003	15.4 ± 0.1	0.690 ± 0.002	0.437 ± 0.001	52.9 ± 0.2
4	Expt.	2.12 ± 0.03	0.625 ± 0.022	18.6 ± 0.7	0.638 ± 0.007	0.400 ± 0.005	54.4 ± 0.8
	FRITIOF	2.113 ± 0.007	0.509 ± 0.004	15.6 ± 0.2	0.650 ± 0.002	0.427 ± 0.001	55.7 ± 0.2
5	Expt.	2.02 ± 0.06	0.682 ± 0.049	21.2 ± 1.7	0.613 ± 0.011	0.396 ± 0.008	52.7 ± 1.2
	FRITIOF	2.012 ± 0.009	0.496 ± 0.006	15.7 ± 0.2	0.621 ± 0.002	0.418 ± 0.001	57.8 ± 0.2
≥ 6	Expt.	2.02 ± 0.10	0.816 ± 0.076	26.9 ± 3.4	0.594 ± 0.017	0.410 ± 0.012	59.8 ± 2.1
	FRITIOF	1.889 ± 0.012	0.442 ± 0.009	14.5 ± 0.3	0.586 ± 0.002	0.407 ± 0.001	60.1 ± 0.3
All	Expt.	2.58 ± 0.01	0.519 ± 0.005	13.3 ± 0.1	0.687 ± 0.003	0.391 ± 0.002	47.1 ± 0.2
events	FRITIOF	2.589 ± 0.003	0.490 ± 0.001	12.94 ± 0.04	0.692 ± 0.001	0.431 ± 0.001	52.1 ± 0.1

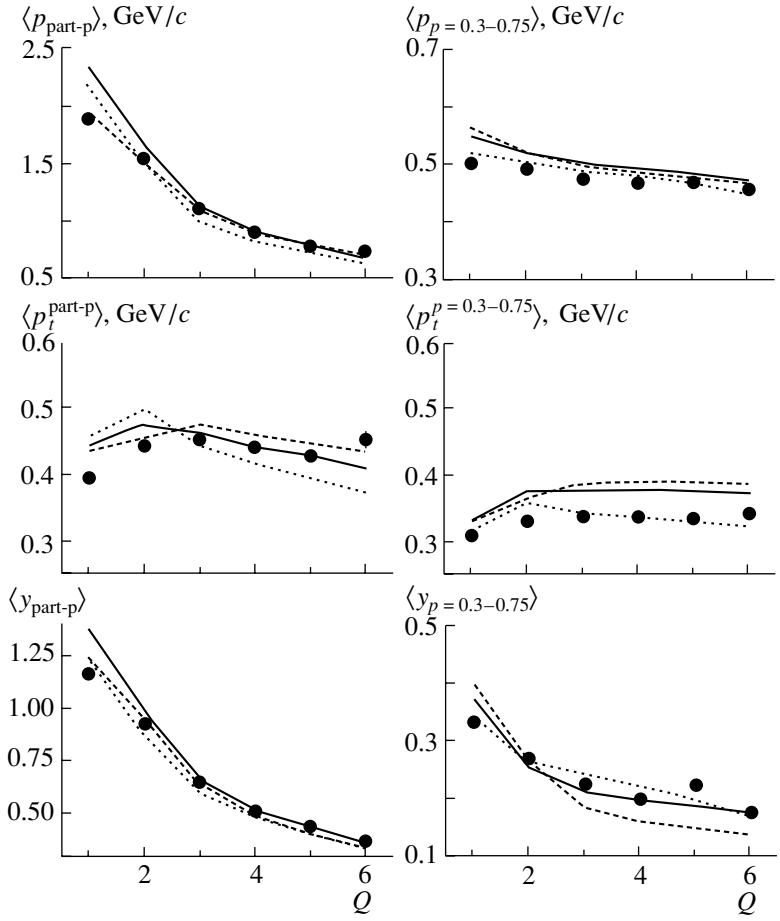

Fig. 8. Mean features of participant protons versus Q: (left-hand graphs) features of all participant protons and (right-hand graphs) features of protons having momenta in the range $0.3 \le p < 0.75$ GeV/c. The notation is identical to that in Fig. 1.

Target protons are characterized by large emission angles. In the $Q > 1$ groups, the FRITIOF model satisfactorily reproduces the features of protons having momenta in the region $0.3 \le p < 1.4$ GeV/c (deviation does not exceed 10%).

Knowing the energy carried away by leading protons whose momenta take values in the region $p > 1.4$ GeV/c, one can find the kinetic energy $\Delta T = T_0 - \langle n_{\text{lead-}p}\rangle\langle T_{\text{lead-}p}\rangle$ expended by a projectile proton in the course of interaction with a carbon nucleus. At the momentum of 4.2 GeV/c, the kinetic energy of a proton before the interaction is $T_0 = 3.36$ GeV. Table 5 lists the values of ΔT that were obtained for all groups of pC events in the experiment and from the calculation within the FRITIOF model involving delta isobars. It can be seen that, in the course of interaction with a carbon nucleus, a proton loses a considerable part of its energy even in a peripheral collision. As we go over from $Q = 1$, 2 to $Q = 5$, 6 events, this fraction increases from 60 to 80%. The calculations within the FRITIOF model lead to a similar result (see Table 4). Therefore, even such a light nucleus as that of carbon has a high stopping power for protons of momentum 4.2 GeV/c.

The conditions of our experiment make it possible to obtain the distribution of the energy ΔT among secondary particles—that is, to determine the total energies of positively and negatively charged pions, participant protons from the target nucleus ($0.3 \le p < 1.4$ GeV/c), and evaporated protons ($p < 0.3$ GeV/c). The values of these energies are given in Table 5. It can be concluded from the data in this table that, in $Q = 1$, 2 events, charged particles carry less than half of the energy ΔT. With increasing Q, the energy fraction carried away by positively charged pions increases owing to the growth of their multiplicity. In contrast to this, the total energy of negatively charged pions remains virtually unchanged within the interval $Q = 2$–6. With increasing Q, the energy fraction carried by target protons grows owing to an increase in their multiplicity (see Tables 1, 5). The general pattern is as follows: with increasing Q, the energy losses of a primary proton in a collision with a carbon nucleus grow, the energy carried away by positively charged pions and protons increases, and

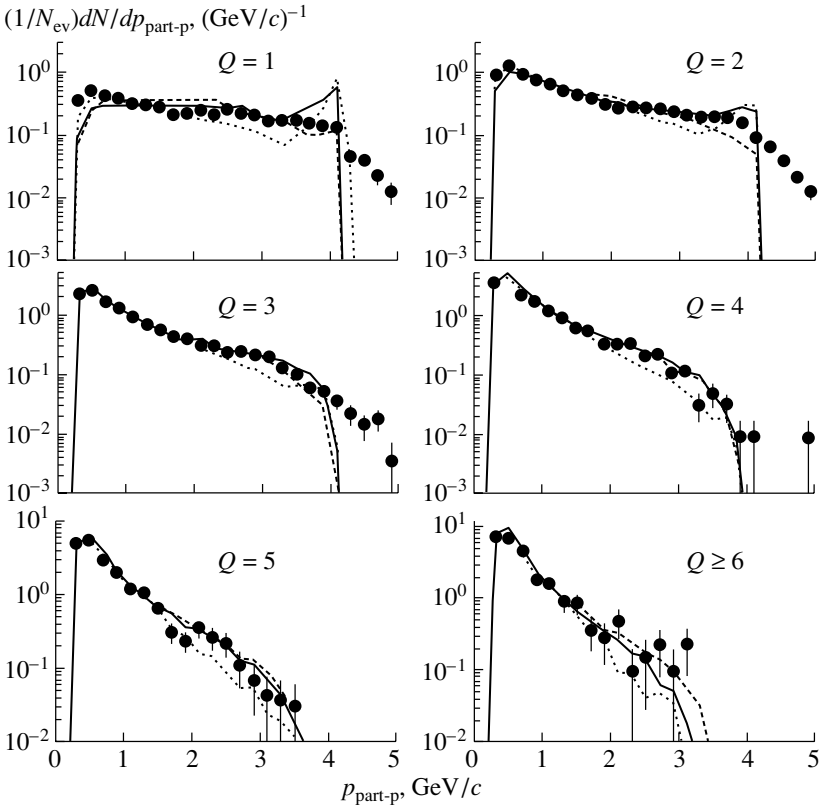

Fig. 9. Total-momentum distributions of participant protons at various values of Q. The notation is identical to that in Fig. 1.

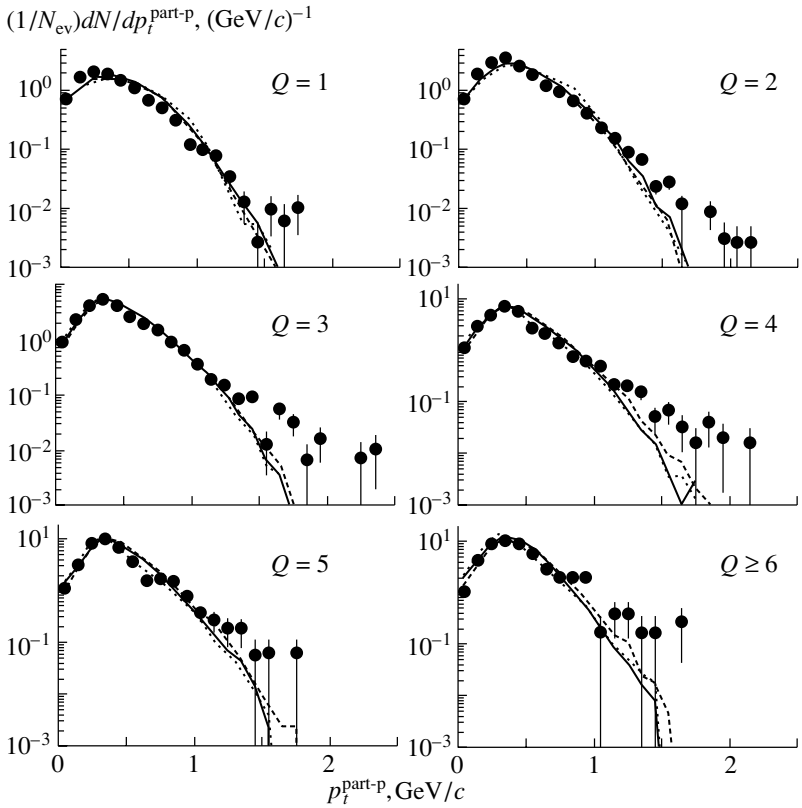

Fig. 10. Transverse-momentum distributions of participant protons at various values of Q. The notation is identical to that in Fig. 1.

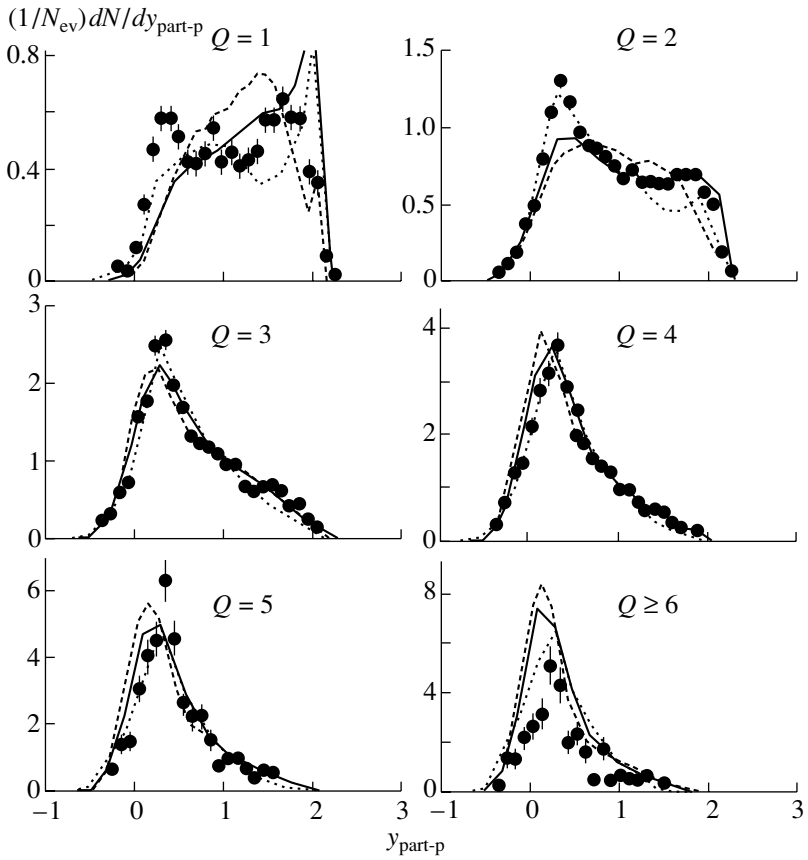

Fig. 11. Rapidity distributions of participant protons at various values of Q. The notation is identical to that in Fig. 1.

the energy of negatively charged and neutral particles is virtually independent of Q (this is not so only for $Q = 1$ events).

The FRITIOF model systematically underestimates the energy carried away by positively and negatively charged pions.

CONCLUSIONS

(i) New experimental data on the kinematical features of secondaries from pC interactions at a momentum of 4.2 GeV/c have been presented versus the degree of collision centrality.

(ii) It has been shown that, with increasing degree of collision centrality, the mean momenta and mean rapidities of secondaries decrease, the transverse momenta remain virtually unchanged, and the mean emission angles increase.

(iii) With the aid of the FRITIOF model taking into account delta isobars, the boundary between leading and nonleading protons has been found to be 1.4 GeV/c. It has been established that a weak dependence of the mean momentum on Q is typical of nonleading protons. The mean transverse momentum of leading protons in central interactions ($p \geq$ 1.4 GeV/c) is 1.5 to 2 times higher than that in peripheral collisions characterized by $Q \sim 1, 2$.

(iv) The stopping power of a carbon nucleus has been determined. It has been shown that, in interactions, protons lose a significant fraction of their energy. Upon going over from peripheral events characterized by $Q = 1, 2$ to central events characterized by $Q = 5, 6$, this fraction increases from 60 to 80%.

(v) It has been found that, in $Q = 1$ and $Q = 2$ events, charged particles carry less than half of the energy lost by leading protons. With increasing Q, the energy fraction carried away by positively charged pions increases owing to the growth of their multiplicity. The total energy of negatively charged pions undergoes virtually no changes in the interval $Q =$ 2–6. With increasing Q, the energy fraction of target protons grows owing to an increase in their multiplicity.

(vi) It has been established that the models used underestimate the mean transverse momenta of pions. The cascade–evaporation model overestimates the yield of soft pions ($p < 300$ MeV/c). In the FRITIOF model version taking into account delta isobars, small values of the mean momenta of pions

Table 5. Energies (in GeV) carried away by secondary particles in pC interactions at 4.2 GeV/c versus the degree of collision centrality Q according to (expt) our experimental data and (FRITIOF) the predictions of the FRITIOF model taking into account delta isobars

Q		$\Delta T_{\text{lead-}p}$	$\sum E_{\pi^-}$	$\sum E_{\pi^+}$	$\sum T_{\text{part-p}}$, $0.3 \le p < 1.4$ GeV/c	$\sum T_{\text{ev-}p}$	$\sum E_{n_{\text{ch}}}$	$\sum E_{n_{\text{neut}}}$
1	Expt.	2.193 ± 0.032	0.311 ± 0.012	0.245 ± 0.007	0.138 ± 0.004	0.018	0.712 ± 0.015	1.481 ± 0.035
	FRITIOF	1.703 ± 0.005	0.250 ± 0.003	0.234 ± 0.003	0.110 ± 0.001	0.005	0.599 ± 0.004	1.104 ± 0.006
2	Expt.	1.962 ± 0.018	0.175 ± 0.005	0.383 ± 0.006	0.267 ± 0.004	0.012	0.837 ± 0.009	1.125 ± 0.020
	FRITIOF	1.871 ± 0.007	0.154 ± 0.002	0.371 ± 0.003	0.257 ± 0.002	0.007	0.789 ± 0.004	1.081 ± 0.008
3	Expt.	2.299 ± 0.031	0.193 ± 0.009	0.515 ± 0.012	0.440 ± 0.008	0.019	1.167 ± 0.017	1.132 ± 0.035
	FRITIOF	2.270 ± 0.008	0.175 ± 0.002	0.362 ± 0.004	0.474 ± 0.003	0.019	1.030 ± 0.006	1.240 ± 0.010
4	Expt.	2.565 ± 0.035	0.195 ± 0.014	0.615 ± 0.022	0.582 ± 0.015	0.020	1.412 ± 0.030	1.153 ± 0.046
	FRITIOF	2.507 ± 0.010	0.165 ± 0.003	0.348 ± 0.004	0.654 ± 0.006	0.029	1.196 ± 0.008	1.311 ± 0.013
5	Expt.	2.755 ± 0.062	0.179 ± 0.026	0.650 ± 0.040	0.727 ± 0.032	0.021	1.577 ± 0.057	1.178 ± 0.084
	FRITIOF	2.668 ± 0.012	0.158 ± 0.004	0.333 ± 0.006	0.812 ± 0.008	0.031	1.333 ± 0.010	1.337 ± 0.016
≥ 6	Expt.	2.642 ± 0.130	0.174 ± 0.041	0.757 ± 0.082	0.881 ± 0.061	0.014	1.826 ± 0.110	0.816 ± 0.170
	FRITIOF	2.846 ± 0.015	0.154 ± 0.004	0.321 ± 0.008	0.994 ± 0.010	0.016	1.486 ± 0.014	1.361 ± 0.021
All	Expt.	2.145 ± 0.013	0.217 ± 0.004	0.393 ± 0.004	0.297 ± 0.004	0.015	0.922 ± 0.007	1.223 ± 0.022
events	FRITIOF	2.028 ± 0.006	0.187 ± 0.012	0.326 ± 0.012	0.337 ± 0.002	0.012	0.862 ± 0.003	1.166 ± 0.007

are associated with the small yield of energetic pions. All models underestimate the probability of the production of pions having high transverse momenta. The models describe poorly the spectra of positively charged pions from multiparticle interactions.

(vii) All models describe rather well the momentum spectra of protons in $Q \ge 3$ events. For peripheral events characterized by $Q = 1$ and 2, the results of the calculations differ considerably from the experimental data. The inability of the cascade–evaporation model to describe the proton spectrum at $Q = 1$ is due to an unsatisfactorily simulation of NN interactions.

(viii) The FRITIOF model describes qualitatively the distribution of energy between product particles. The model systematically underestimates the energy carried by positively and negatively charged pions.

ACKNOWLEDGMENTS

We are grateful to the technical staff for viewing relevant films and for measuring events and to the members of a collaboration involved in investigations at the 2-m propane bubble chamber for placing the required experimental data at our disposal.

This work was supported in part by the Russian Foundation for Basic Research (project nos. 00-01-00307, 01-02-16407, 01-02-16431) and INTAS (grant no. 00-00366).

REFERENCES

1. G. N. Agakishiev *et al.,* Yad. Fiz. **40**, 1209 (1984) [Sov. J. Nucl. Phys. **39**, 344 (1984)]; G. N. Agakishiev *et al.*, Z. Phys. C **27**, 177 (1985).
2. G. N. Agakishiev *et al.,* Yad. Fiz. **45**, 1047 (1987) [Sov. J. Nucl. Phys. **45**, 1037 (1987)]; D. Armutliisky *et al.*, Z. Phys. A **328**, 455 (1987).
3. G. N. Agakishiev *et al.,* Yad. Fiz. **49**, 481 (1989) [Sov. J. Nucl. Phys. **49**, 300 (1989)].
4. A. I. Bondarenko, R. A. Bondarenko, and E. N. Kladnitskaya, Yad. Fiz. **60**, 2004 (1997) [Phys. At. Nucl. **60**, 1833 (1997)].
5. A. I. Bondarenko *et al.*, Yad. Fiz. **62**, 1612 (1999) [Phys. At. Nucl. **62**, 1513 (1999)].
6. S. Batskovich *et al.,* Yad. Fiz. **56** (4), 211 (1993) [Phys. At. Nucl. **56**, 540 (1993)].
7. G. N. Agakishiev *et al.,* Yad. Fiz. **56** (10), 170 (1993) [Phys. At. Nucl. **56**, 1397 (1993)].
8. G. N. Agakishiev *et al.,* Yad. Fiz. **51**, 1591 (1990) [Sov. J. Nucl. Phys. **51**, 1004 (1990)].
9. A. S. Galoyan *et al.*, Preprint No. R1-2002-54 (Joint Inst. Nucl. Res., Dubna, 2002); Yad. Fiz. **66**, 868 (2003) [Phys. At. Nucl. **66**, 836 (2003)].

10. V. S. Barashenkov, F. Zh. Zheregi, and Zh. Zh. Musul'manbekov, Preprint No. R2-83-117 (Joint Inst. Nucl. Res., Dubna, 1983).
11. O. Kofoed-Hansen, Nucl. Phys. B **54**, 42 (1973); A. Kloving *et al.*, Nucl. Phys. B **54**, 29 (1973).
12. G. B. Alaverdyan *et al.,* Yad. Fiz. **31**, 776 (1980) [Sov. J. Nucl. Phys. **31**, 692 (1980)].
13. V. S. Barashenkov and V. D. Toneev, *Interaction of High-Energy Particles and Nuclei with Nuclei* (Atomizdat, Moscow, 1972); V. D. Toneev and K. K. Gudima, Nucl. Phys. A **400**, 173 (1983).
14. B. Andersson *et al.*, Nucl. Phys. B **281**, 289 (1987).
15. B. Nilsson-Almquist and E. Stenlund, Comput. Phys. Commun. **43**, 387 (1987).
16. Kh. El-Waged and V. V. Uzhinskii, Yad. Fiz. **60**, 925 (1997) [Phys. At. Nucl. **60**, 828 (1997)].
17. EMU-01 Collab. (M. I. Adamovich *et al.*), Z. Phys. A **358**, 337 (1997).
18. A. I. Bondarenko *et al.,* Yad. Fiz. **65**, 95 (2002) [Phys. At. Nucl. **65**, 90 (2002)].
19. S. Toothacher *et al.*, Phys. Lett. B **197**, 295 (1987).
20. D. S. Barton *et al.*, Phys. Rev. D **27**, 2580 (1983).
21. F. Videback and O. Hansen, Phys. Rev. C **52**, 2684 (1995).
22. A. I. Bondarenko *et al.,* Soobshch. OIYaI No. R1-98-292 (Dubna, 1998).

Translated by A. Isaakyan

Physics of Atomic Nuclei, Vol. 67, No. 2, 2004, pp. 273–280. From Yadernaya Fizika, Vol. 67, No. 2, 2004, pp. 290–297.

ELEMENTARY PARTICLES AND FIELDS
Experiment

Flow Effects in High-Energy Nucleus Collisions with Ag(Br) in Emulsion*

M. I. Adamovich†[1], N. P. Andreeva[2], E. S. Basova[3], V. Bradnová[4], V. I. Bubnov[2], M. M. Chernyavsky[1], A. S. Gaitinov[2], K. G. Gulamov[5], M. Haiduc[6], D. Hasegan[6], L. Just[7], E. K. Kanygina[2], S. P. Kharlamov[1], A. D. Kovalenko[4], S. A. Krasnov[4], A. Kravčáková[8], V. G. Larionova[1], I. A. Lebedev[2], O. V. Levitskaya[9], N. S. Lukicheva[5], A. K. Musaeva[2], S. Z. Nasyrov[3], V. S. Navotny[5], G. I. Orlova[1], N. G. Peresadko[1], L. N. Philippova[2], V. A. Plyushchev[10], V. V. Rusakova[4], N. Saidkhanov[5], N. A. Salmanova[1], A. M. Seitimbetov[2], M. I. Tretyakova†[1], T. P. Trofimova[3], S. Vokál[8], J. Vrláková[8], P. I. Zarubin[4], and S. I. Zhokhova[5]

Received April 10, 2002; in final form, January 16, 2003

Abstract—Various flow phenomena observed by a unique emulsion method are reviewed. The experimental data of the emission of projectile and target fragments and relativistic particles in collisions of 1–160 A GeV/c ^{16}O, ^{22}Ne, ^{28}Si, ^{32}S, ^{84}Kr, ^{197}Au, and ^{208}Pb nuclei with ^{108}Ag (^{80}Br) targets are investigated. The transverse-momentum approach, the flow-angle analysis using principal vectors, the azimuthal correlation functions, the method of azimuthal correlations between charged secondaries, and the method of Fourier expansion of the azimuthal angle distributions are applied. Evidence of the directed flow of spectators has been obtained in the medium-impact nuclear interactions. In azimuthal distributions, with respect to the reaction plane, the signal of the elliptic flow of participants has been observed. © *2004 MAIK "Nauka/Interperiodica".*

1. INTRODUCTION

Reactions between heavy nuclei at high energies have been investigated for a number of years at the Dubna, Brookhaven, and CERN accelerators. A characteristic feature of nucleus–nucleus collisions is that the direction of the outgoing particles projected onto the transverse plane is correlated with the orientation of the impact parameter. These azimuthal correlations are usually referred to as "collective flow" [1].

The directed fluid-like emission of nuclear matter in energetic collisions of two nuclei was first predicted by [2]. Then many experiments were devoted to the study of hydrodynamical behavior of nuclear matter in nucleus–nucleus collisions [3].

The first conclusive evidence of collective sideward flow was provided by heavy-ion experiments around 1 A GeV/c [4]. Their 4π detectors were able to measure event by event the four-momenta of all particles.

This phenomenon was also observed at ultrarelativistic energies by the E877 Collaboration in Au + Au collisions at a beam momentum of about 11 A GeV/c [5] and, only recently, in Pb + Pb collisions at 158 A GeV/c by the NA49 and WA98 Collaborations [6]. One of the main motivations of such a study is that the experimental observation of asymmetries in azimuthal distributions for noncentral collisions at ultrarelativistic energies could be sensitive to the formation of quark–gluon plasma [7]. At intermediate energies, they yield information on

*This article was submitted by the authors in English.

†Deceased.

[1]Lebedev Institute of Physics, Russian Academy of Sciences, Leninskiĭ pr. 53, Moscow, 117924 Russia.
[2]Energy Physics Institute, Almaty, Kazakhstan.
[3]Institute of Nuclear Physics, Tashkent, Uzbekistan.
[4]Joint Institute for Nuclear Research, Dubna, Moscow oblast, 141980 Russia.
[5]Physical-Technical Institute, Tashkent, Uzbekistan.
[6]Institution of Gravitation and Space Research, Bucharest, Romania.
[7]Institute of Experimental Physics, Slovak Academy of Sciences, Košice, Slovakia.
[8]Department of Nuclear Physics, Šafárik University, Košice, Slovakia.
[9]Petersburg Nuclear Physics Institute, Russian Academy of Sciences, Gatchina, 188350 Russia.
[10]Khlopin Radium Institute, St. Petersburg, Russia.

the nuclear compressibility [8] and on the in-medium nucleon–nucleon cross section [9].

The quantification of the collective flow in nucleus–nucleus collisions usually starts by determining an event plane that is strongly correlated with the reaction plane, which in turn is given by the directions of the impact parameter b and the beam.

Different aspects of flow phenomena have been observed: the bounce-off of the spectator fragments and the side splash of participant matter which occurs in the reaction plane and the squeeze-out of nucleons perpendicular to the reaction plane [10].

The goal of the present paper is to review the various flow phenomena observed by a unique emulsion method at momenta between 1 and 160 A GeV/c.

2. EXPERIMENT

Stacks of NIKFI BR-2 nuclear emulsions were irradiated by a 1.55 A GeV/c ^{84}Kr beam at SIS in Darmstadt; by ^{16}O, ^{22}Ne, ^{28}Si, and ^{32}S at the Dubna synchrophasotron (4.1–4.5 A GeV/c); by ^{28}Si and ^{197}Au beams at BNL AGS (14.6 and 11.6 A GeV/c); and by ^{208}Pb beams at CERN SPS (158 A GeV/c). The details of the experiments can be found in previous papers of the Dubna [11], Krypton [12], and EMU01 [13] Collaborations and in the references therein. In some cases, the experimental data were compared with cascade calculations [14].

Secondary charged particles were classified into the following groups:

1. Projectile spectator fragments (PF)—with charges $Z_{\mathrm{PF}} \geq 1$ and $\beta \approx 0.98$, emitted inside the fragmentation cone [15].

2. Target fragments (TF)—so-called h particles—consisting of fast g particles, mainly recoil protons with velocity $0.23 \leq \beta < 0.7$, and slow b particles, target fragments with velocity $\beta < 0.23$.

3. Relativistic s particles—fast singly charged particles with $\beta \geq 0.7$.

For all particles, the polar (Θ) and azimuthal (Ψ) emission angles have been measured and charges of multiply charged projectile fragments have been determined.

For the present analysis, we selected events of inelastic interactions of the projectile nucleus with Ag(Br) target nuclei at medium impact parameters. Selected events, if not saying anything else, are characterized by the number of TFs $N_{\mathrm{TF}} \geq 8$ (representing interactions with Ag or Br targets) and $N_{\mathrm{PF}} \geq 4$, where N_{PF} is the number of PFs (or $N_\alpha \geq 3$ in the case of ^{197}Au-induced interactions, N_α being the number of projectile alpha fragments). In the last case, these two criteria correspond approximately to an impact parameter cut at about $0.8(R_{\mathrm{Au}} + R_{\mathrm{Ag(Br)}})$ [13].

3. RESULTS

There are many methods that are ideally suited to study emission patterns and event shapes in relativistic nuclear reactions. For our analysis, we adopted the transverse-momentum approach [16], the flow-angle analysis using principal vectors [17], the azimuthal correlation functions [18], the method of azimuthal correlations between charged secondaries [19], and the method of Fourier expansion of the azimuthal angle distribution [7].

In the transverse-momentum analysis, the reaction plane is defined by the direction of the incident nucleus and the plane vector $\mathbf{R}_i$, which is constructed individually for each PF from the transverse momenta $\mathbf{P}_{T,j}$ of all remaining PFs in the same event as $\mathbf{R}_i = \sum A_j \mathbf{P}_{T,j}$, where $j \neq i$ $(i, j = 1, 2, \ldots, N_{\mathrm{PF}})$ and A_j is the mass of the fragment. The definition of $\mathbf{R}$ ensures that the autocorrelations are removed by calculating $\mathbf{R}$ for each fragment separately from the transverse momenta of all remaining fragments, without including the fragment itself [16]. Assuming that each jth PF has the same longitudinal momentum per nucleon P_L as the projectile nucleus, the transverse momentum per nucleon of the jth fragment is given by $P_{T,j} = P_L \tan\Theta_j$, where Θ_j is the emission angle of the jth fragment. Then we find the projection of $\mathbf{P}_{T,i}$ onto the corresponding $\mathbf{R}_i$ by $P_{R,i} = \mathbf{P}_{T,i} \cdot \mathbf{R}_i / |\mathbf{R}_i|$. The average values $\langle P_R \rangle$ for nuclear interactions on Ag(Br) targets ($N_{\mathrm{TF}} \geq 8$) are shown in Table 1 as a function of beam mass and momentum. Given in Table 1, λ characterizes effect of flow (see below). The mean value of P_R is zero if $P_{T,i}$ is randomly distributed in the azimuthal plane and is nonzero if the energy flow of fragments deviates from the zero-angle direction, i.e., if bounce-off of PFs occurs. One observes that our data significantly differ from zero and display the bounce-off of the PFs.

To investigate whether the obtained value represents a significant flow of transverse momenta, the same procedure has been applied to mixed events (ME) which lack a dynamic effect in the reaction plane. The ME have been generated from the original total sample of fragments randomly distributed in the new events. The results are shown in Table 1. The randomized events do not exhibit this bounce-off effect.

Also, the plane vector $\mathbf{R}$ of the TFs has been constructed for each event according to the previously used formula. The coefficient $A_j = 1$ and, instead of $\mathbf{P}_{T,j}$, a unit vector of the azimuthal direction of Ψ_j has been considered. The sum runs over all TFs in the given event. The distribution of the relative azimuthal angle ($\Delta\Psi_{\mathrm{PF-TF}}$) between "projectile" and "target" plane vectors (Fig. 1*a*) shows a strong correlation between them. The average azimuthal angles between

Table 1. The values of $\langle P_R \rangle_{\rm exp}$, $\langle P_R \rangle_{\rm ME}$, and λ for different projectile masses and momenta

Momentum, A GeV/c	Beam	$\langle P_R \rangle_{\rm exp}$, A MeV/c	$\langle P_R \rangle_{\rm ME}$, A MeV/c	λ
1.55	^{84}Kr	23.6 ± 2.3*	0.6*	0.47 ± 0.04
4.1	^{22}Ne	16.1 ± 2.6	0.8	0.53 ± 0.06
4.5	^{16}O	12.8 ± 2.8	−0.7	0.62 ± 0.09
4.5	^{28}Si	6.1 ± 2.3	0.1	0.39 ± 0.10
4.5	^{32}S	18.4 ± 2.1	1.3	0.54 ± 0.06
11.6	^{197}Au	32.0 ± 1.8*	−0.2*	0.41 ± 0.02
14.6	^{28}Si	7.2 ± 2.5	0.5	0.43 ± 0.10

* Singly charged PFs are not included in $N_{\rm PF}$.

them are $112° \pm 4°$ and $107° \pm 3°$ for ^{84}Kr and ^{197}Au primaries [12, 13]. The E877 Collaboration has previously reported [20] a corresponding pronounced event anisotropy.

In order to test the reaction plane determination, the method proposed in [16] has been used. Each event was randomly divided into two parts and the reaction planes have been estimated separately for these subevents. The distribution of the differences between the azimuthal angles of the two constructed reaction planes obtained in ^{197}Au-induced collisions in emulsion [13] is shown in Fig. 1*b*. This distribution is peaked at 0° with a width $\sigma \approx 50°$. The fact that the distribution is not flat and peaks at zero indicates that the obtained reaction planes are not accidental, but reflects physical correlations among the emitted fragments.

To verify this, we have performed the same test using mixed events. The resulting distribution, shown as a dashed histogram in Fig. 1*b* is constant and does not show any correlations.

The width σ of the experimental distribution was found to be related to the width σ_0 of the distribution of found event planes around the true reaction plane by $\sigma_0 = \sigma/2$ [21]. This value serves as a measure for the resolution of the plane vector $\mathbf{R}$. The obtained value of $\sigma_0 \approx 25°$ is comparable to the values reported in [22] and with the value $\sigma_0 \approx 23°$ obtained in ^{84}Kr-induced collisions with Ag(Br) targets [12].

We obtained similar results using the flow-angle analysis proposed by Heckmann [17]. In this method, the unit vectors in the directions of the emission of PFs and TFs are summed to give their principal vectors $\mathbf{V}_{\rm PF}$ and $\mathbf{V}_{\rm TF}$, respectively. These vectors are assumed to be in the direction of their sources with respect to the beam direction.

The values of the flow angle Θ_F for PFs (the polar angle of the vector $\mathbf{V}_{\rm PF}$) are given in Table 2 for different centrality groups. One can see that the flow angles of PFs are small for all cases of centrality, but they strongly increase at lower energies. On the other hand, the increase in the mean value $\langle \Theta_F \rangle$ with decreasing impact parameter (increasing N_s, N_g, or N_h) is clearly seen at all beam and energy combinations.

The experimental values are greater than the cascade calculations (values in brackets) and ME sample. This fact can be considered as an indication of the sideward flow, i.e., the bounce-off of the PFs. It

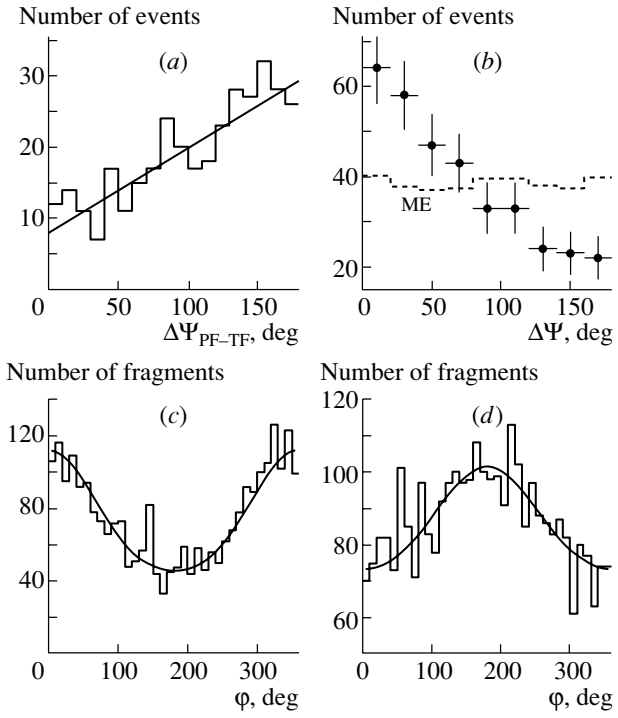

Fig. 1. (*a*) The relative azimuthal angle between two reaction planes made from PFs and TFs, (*b*) test of the reaction plane determination, (*c*) the azimuthal angle distribution of projectile, and (*d*) target fragments relative to the reaction plane in ^{197}Au + Ag(Br) collisions at 11.6 A GeV/c.

Table 2. The values of Θ_F for different projectile masses, momenta, and centrality groups

Momentum, A GeV/c	Beam	Θ_F, deg	Centrality criteria
1.55	^{84}Kr	$1.4 \pm 0.1^*$	$N_g = 1$–6
		$2.0 \pm 0.1^*$	$N_g \geq 7$
4.1	^{22}Ne	0.54 ± 0.03 (0.41)	$N_h = 7$–13
		0.80 ± 0.08 (0.41)	$N_h = 14$–27
		1.26 ± 0.40 (0.40)	$N_h \geq 28$
4.5	^{28}Si	0.51 ± 0.04 (0.33)	$N_h = 7$–13
		0.61 ± 0.04 (0.42)	$N_h = 14$–27
		0.82 ± 0.15 (0.42)	$N_h \geq 28$
11.6	^{197}Au	0.26 ± 0.02 (0.23**)*	$N_s < 100$
		0.32 ± 0.02 (0.23**)*	$N_s = 100$–200
		0.47 ± 0.06 (0.30**)*	$N_s > 200$
14.6	^{28}Si	0.15 ± 0.02 (0.14)	$N_h = 8$–13
		0.15 ± 0.01 (0.15)	$N_h = 14$–19
		0.23 ± 0.05 (0.17)	$N_h \geq 28$

* Singly charged PFs are not included in N_{PF}.

** ME calculations.

was also shown (but not illustrated here) that the tendency toward emission of PFs and TFs in opposite directions in the azimuthal plane is reinforced with increasing centrality.

To avoid an event-by-event estimate of the event plane, we also tried an azimuthal correlation function analysis. Then the collective flow can be parametrized in terms of azimuthal angle distributions of projectile fragment pairs. Following [18], let us assume that the probability distribution $P(\Psi)$ of the angle Ψ between the transverse momenta of two correlated fragments is $P(\Psi) = A^2(1 + 0.5\lambda^2\cos(\Psi))$, where A is a normalization constant. The azimuthal correlation function $C(\Psi)$ is defined by $C(\Psi) = P_{\mathrm{corr}}(\Psi)/P_{\mathrm{uncorr}}(\Psi)$, where $P_{\mathrm{corr}}(\Psi)$ represents the distribution of the angle Ψ for correlated fragment pairs occurring in the same event and $P_{\mathrm{uncorr}}(\Psi)$ is obtained from the distribution of the uncorrelated fragment pairs generated by event mixing. If $C(\Psi) > 1$ at small values of Ψ and $C(\Psi) < 1$ at large Ψ, then it is an indication of collective flow. The magnitude of the observed flow can be characterized by the value of λ obtained from a fit of $A^2(1 + 0.5\lambda^2\cos(\Psi))$ to $C(\Psi)$ with $A = 1$.

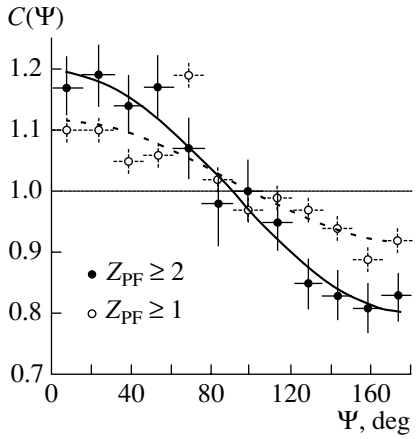

Fig. 2. The variation of $C(\Psi)$ as a function of Ψ for PFs measured in ^{197}Au + Ag(Br) collisions at 11.6 A GeV/c.

The dependence of $C(\Psi)$ on Ψ in the case of Au-induced collisions is shown in Fig. 2. The fitted values of λ given in Table 1 indicate the presence of the collective flow of nuclear matter. Within the errors, the values of λ seem to be independent of the projectile mass and momentum. The exclusion of the singly charged PFs makes the value of λ higher ($\lambda_{\mathrm{Kr+Ag(Br)}} = 0.706 \pm 0.055$ and $\lambda_{\mathrm{Au+Ag(Br)}} = 0.612 \pm 0.020$).

A complementary analysis of the azimuthal intra- and intergroup correlations has been made in part of the data sample. Interactions of ^{12}C, ^{22}Ne, ^{24}Mg, and ^{28}Si with Ag(Br) and Pb nuclei have been investigated (see [11, 23] and references therein). The angle

Table 3. The values of the fitted parameters v_1 and v_2 for spectator fragments, relativistic particles with projectile-like pseudorapidities, and fast target fragments

	v_1	v_2	χ^2
^{84}Kr + Ag(Br) at 1.55 A GeV/c			
Projectile spectator fragments	0.227 ± 0.022	-0.006 ± 0.023	1.01
Target spectator fragments	-0.213 ± 0.018	0.016 ± 0.018	1.82
s particles ($0.6 \leq \eta_{\text{rel}} < 2.13$)	0.148 ± 0.017	0.005 ± 0.017	1.39
g particles	-0.169 ± 0.014	-0.025 ± 0.014	0.83
^{197}Au + Ag(Br) at 11.6 A GeV/c			
Projectile spectator fragments	0.222 ± 0.013	0.027 ± 0.013	1.38
Target spectator fragments	-0.082 ± 0.013	0.006 ± 0.013	0.76
s particles ($0.6 \leq \eta_{\text{rel}} < 1.56$)	0.060 ± 0.006	0.008 ± 0.006	0.91
g particles	-0.069 ± 0.011	-0.009 ± 0.011	0.54

between the ith and jth particles, ε_{ij}, in the azimuthal plane was measured. Then the coefficient β_1 of asymmetry in the azimuthal plane was calculated by $\beta_1 = \sum \cos(\varepsilon_{ij})/(n(n-1))^{1/2}$, $i = 1, \ldots, n, i \neq j$, where $n > 2$ is the number of particles of a given type. The azimuthal asymmetry for s particles and TFs was observed in nonperipheral collisions with Ag(Br) nuclei, and it increases with increasing centrality of nuclear collisions (measured by the total charge of noninteracting PFs).

It is now customary to extract information on flow by determination of the Fourier coefficients v_i [7] of the azimuthal distributions $F(\varphi) = F_0[1 + 2v_1\cos(\varphi) + 2v_2\cos(2\varphi)]$. In the transverse plane, one evaluates event by event the angle of the reaction plane. The azimuthal angle distribution of secondary particles relative to the reaction plane is constructed. There is a flow if this distribution is not isotropic. The $\cos(\varphi)$ term is sensitive to the yield within the reaction plane. The parameter v_1 is denoted as "directed flow" and is a measure of the strength of the flow. The parameter v_2, so called "elliptic flow," reflects the particle emission perpendicular to the direction of the reaction plane.

To exhibit agreement of the results of this analysis and those performed earlier, the azimuthal distributions of PFs and TFs relative to the reaction plane were constructed and fitted by the above-mentioned Fourier function (Figs. 1c, 1d). The autocorrelations were removed in the case of projectile fragments. The values of the fitted parameters v_1 and v_2 for different charged fragments emitted in ^{84}Kr- and ^{197}Au-induced collisions in emulsion [12, 13] are shown in Table 3. We observe the directed flow of spectator matter—the preferential emission of PFs (with $Z_{\text{PF}} \geq 2$) in the direction of the reaction plane ($v_1 > 0$) and TFs (b particles, slow target fragments with $\beta < 0.23$) opposite to this direction ($v_1 < 0$).

Thus far, we have discussed the flow of spectator fragments. Now we turn our attention to the participating nuclear matter. As participants, we can consider s and g particles. As the elliptic flow is caused by hot matter which has been stopped, it should be centered around midrapidity. For our analysis, we define the relative pseudorapidity η_{rel} by $\eta_{\text{rel}} = (\eta - \eta_{\text{c.m.}})/\eta_{\text{c.m.}}$, where $\eta_{\text{c.m.}}$ and η are the pseudorapidities of the center-of-mass and of the detected particle in the laboratory frame, respectively. The azimuthal distributions of s particles around the central pseudorapidity, satisfying $-0.6 < \eta_{\text{rel}} < 0.6$, relative to the reaction plane, were examined. Calculations made within the framework of the cascade code [14] showed that the ratio of shower pions to protons in this group is about 2 : 1 in the Kr experiment, but increases with primary energy and reaches about 120 : 1 in the Pb experiment at 158 A GeV/c (the η window is $-0.1 < \eta_{\text{rel}} < 0.1$ now).

A clearly visible double-humped structure indicating the preferred emission perpendicular to the reaction plane ($v_2 < 0$) was obtained in 1.55 A GeV/c

Table 4. The values of the fitted parameters v_1 and v_2 for relativistic particles near central pseudorapidity

	v_1	v_2	χ^2
	s particles ($-0.6 < \eta_{\rm rel} < 0.6$)		
^{84}Kr + Ag(Br) at 1.55 A GeV/c	-0.022 ± 0.024	-0.094 ± 0.025	0.97
^{22}Ne + Ag(Br) at 4.1 A GeV/c	0.025 ± 0.014	0.016 ± 0.014	0.97
^{16}O + Ag(Br) at 4.5 A GeV/c	0.026 ± 0.025	0.013 ± 0.025	1.37
^{32}S + Ag(Br) at 4.5 A GeV/c	-0.038 ± 0.015	0.007 ± 0.015	1.27
^{197}Au + Ag(Br) at 11.6 A GeV/c	-0.001 ± 0.005	0.006 ± 0.005	1.14
	s particles ($-0.1 < \eta_{\rm rel} < 0.1$)		
^{208}Pb + Ag(Br) at 158 A GeV/c	0.037 ± 0.016	0.046 ± 0.015	0.73

^{84}Kr + Ag(Br) collisions (Fig. 3*a*). The result of a fit according to the formula for $F(\varphi)$ is shown in Table 4. Hence, the relativistic s particles near central pseudorapidity exhibit the effect of squeeze-out or so-called "out-of-plane elliptic flow." This effect is possibly associated with final-state interaction of relativistic particles produced in the hot zone with spectator matter located in the reaction plane [24]. Thus, only the direction perpendicular to the reaction plane is not blocked by the spectator nuclear matter. In ^{16}O-, ^{22}Ne-, and ^{32}S-induced collisions with ^{108}Ag(^{80}Br) at Dubna energies as well as in the EMU01 ^{197}Au + Ag(Br) experiment at AGS energy, no signal for the elliptic flow was detected and the value of v_2 is about zero. In the ultrarelativistic EMU12 experiment performed at SPS energy 158 A GeV/c, ^{208}Pb interactions with Ag(Br) targets in emulsion were selected.

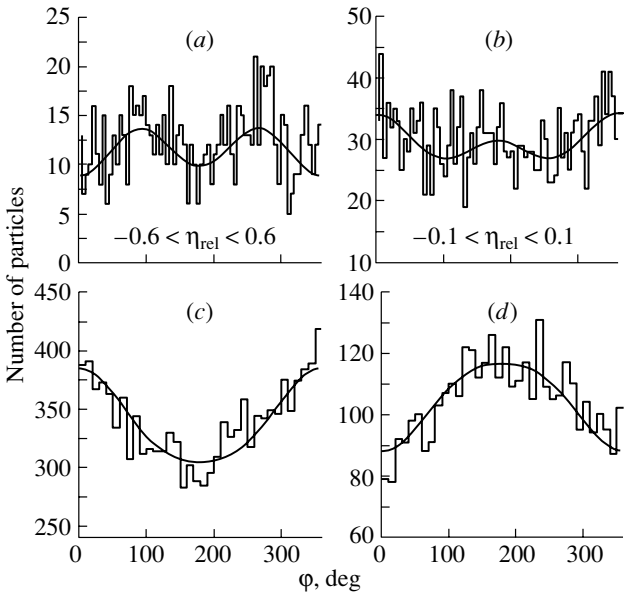

Fig. 3. The azimuthal angle distribution of s particles in (*a*) 1.55 A GeV/c Kr and (*b*) 158 A GeV/c Pb experiments relative to the reaction plane; azimuthal distribution of (*c*) s particles ($0.6 \le \eta_{\rm rel} < 1.56$) and (*d*) g particles relative to the reaction plane in ^{197}Au + Ag(Br) collisions at 11.6 A GeV/c.

In this case, the reaction plane was constructed from the target fragments and the analysis of the azimuthal angle distributions of the relativistic s particles relative to this reaction plane was performed (Fig. 3*b*). The signal of the "in-plane elliptic flow" was obtained for relativistic s particles (mainly pions) with the values of η near $\eta_{\rm c.m.}$.

The dependence of the v_2 parameter as a function of beam energy is shown in Fig. 4. The values of v_2 measured by the unique emulsion method are compared with the values from other experiments with different beams at different energies [25–28]. The change of the sign of the elliptic flow measured at midrapidity is detected at Dubna energies (3–4 A GeV) by the unique emulsion data.

The relativistic s particles with projectile-like pseudorapidities in 1.55 A GeV/c ^{84}Kr ($0.6 \le \eta_{\rm rel} < 2.13$)- and in 11.6 A GeV/c ^{197}Au ($0.6 \le \eta_{rel} < 1.56$)-induced collisions on Ag(Br) targets in emulsion (Fig. 3*c* and Table 3) are preferentially emitted into the reaction plane ($v_1 > 0$). This positive "directed flow" is weaker at higher primary energy. Here, $\eta_{\rm rel} = 2.13$ and 1.56 are relative pseudorapidities corresponding to the fragmentation cone (see [15]). Projectile spectator protons were excluded from this analysis. On the other hand, a clear emission of fast TFs (g particles), mainly protons (possible deposit of pions is less than 20%), measured in the same experiments (Fig. 3*d*), opposite to the direction of the reaction plane ($v_1 < 0$, negative "directed flow") was

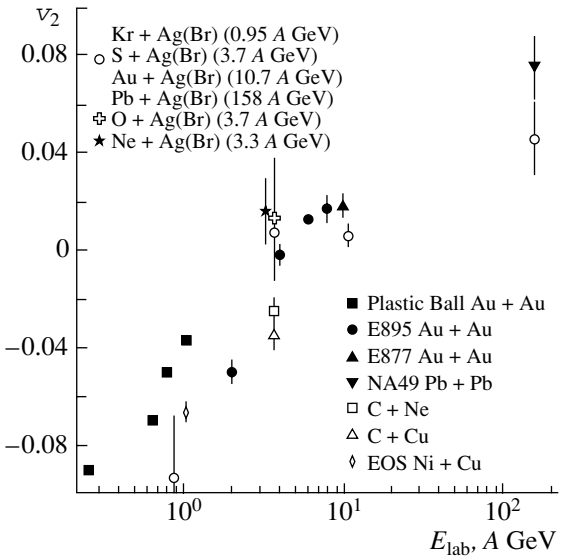

Fig. 4. The systematics of v_2 as a function of beam energy.

registered. These two results demonstrate the side splash of the participating protons at the projectile-like pseudorapidity region ($\eta_{rel} \geq 0.6$) and of the target knocked-out protons (g particles). This directed flow of the projectile and target participants is significantly weaker at higher primary energy, which is consistent with the sideward flow measurements of the E895 Collaboration in Au + Au collisions at beam energies from 2 to 8 A GeV [29]. Experimental data on directed flow presented in Table 3 support the observation of the E877 Collaboration [30] that the directed flow signal increases with particle mass. The values of parameter v_1 for projectile spectator fragments got significantly smaller when singly charged PFs were included ($v_1 = 0.139 \pm 0.013$ in ^{84}Kr + Ag(Br) collisions and $v_1 = 0.130 \pm 0.009$ in ^{197}Au + Ag(Br) collisions).

4. CONCLUSIONS

Investigations of ^{16}O-, ^{22}Ne-, ^{28}Si-, ^{32}S-, ^{84}Kr-, ^{197}Au-, and ^{208}Pb-induced nuclear interactions at 1–160 A GeV/c have been made using a unique emulsion track detector.

The methods of transverse momenta, principal vectors, azimuthal correlation functions, azimuthal correlations between charged secondaries, and the Fourier expansion of the azimuthal angle distributions have been applied. Evidence of the directed flow of spectator fragments is observed in the medium-impact nuclear interactions accompanied by strong azimuthal correlations in the emission of fragments. In azimuthal distributions, with respect to the direction of the reaction plane, the elliptic flow of the participants is seen. The change of the sign of the elliptic flow of relativistic s particles measured at midrapidity is observed at primary energies of about 3–4 A GeV.

ACKNOWLEDGMENTS

This work was supported by the Agency for Science at the Ministry of Education of the Slovak Republic (grant no. 1/9036/02) and by the Russian Foundation for Basic Research (project no. 03-02-17079).

REFERENCES

1. J.-Y. Ollitrault, Nucl. Phys. A **638**, 195c (1998).
2. W. Scheid, H. Muller, and W. Greiner, Phys. Rev. Lett. **32**, 741 (1974).
3. K. H. Kampert, J. Phys. G **15**, 691 (1989).
4. H. H. Gutbrod, A. M. Poskanzer, and H. G. Ritter, Rep. Prog. Phys. **52**, 1267 (1989).
5. E877 Collab. (J. Barrette *et al.*), Phys. Rev. C **56**, 3254 (1997).
6. A. M. Poskanzer *et al.*, Nucl. Phys. A **638**, 463c (1998); S. Nishimura *et al.*, Nucl. Phys. A **638**, 459c (1998).
7. J.-Y. Ollitrault, Phys. Rev. D **46**, 229 (1992).
8. G. Welke *et al.*, Phys. Rev. C **38**, 2101 (1988).
9. G. D. Westfall *et al.*, Phys. Rev. Lett. **71**, 1986 (1993).
10. W. Reisdorf and H. G. Ritter, Annu. Rev. Nucl. Part. Sci. **47**, 663 (1997).
11. A. El-Naghy *et al.*, Preprint No. E1-87-472 (Joint Inst. Nucl. Res., Dubna, 1987); B. P. Bannik *et al.*, Z. Phys. A **329**, 341 (1988); J. Phys. G **14**, 949 (1988); N. P. Andreeva *et al.*, Acta Phys. Slov. **38**, 65 (1988); B. U. Ameeva *et al.*, Yad. Fiz. **51**, 1047 (1990).
12. M. I. Adamovich *et al.*, Yad. Fiz. **60**, 1580 (1997) [Phys. At. Nucl. **60**, 1435 (1997)]; M. I. Adamovich *et al.*, Eur. Phys. J. A **6**, 427 (1999).
13. M. I. Adamovich *et al.* (EMU01 Collab.), Eur. Phys. J. A **2**, 61 (1998).
14. G. J. Musulmanbekov, in *Proc. of the 11th EMU01-Collaboration Meeting, Dubna, 1992,* p. 288.
15. S. A. Krasnov *et al.*, Czech. J. Phys. **46**, 531 (1996).
16. P. Danielewicz and G. Odyniec, Phys. Lett. B **157B**, 146 (1985).
17. H. H. Heckman, Y. J. Karant, and E. M. Friedlander, Phys. Rev. C **34**, 1333 (1986).
18. S. Wang *et al.*, Phys. Rev. C **44**, 1091 (1991).
19. B. U. Ameeva *et al.*, Yad. Fiz. **47**, 1309 (1988).
20. E877 Collab. (J. Barrette *et al.*), Phys. Rev. Lett. **73**, 2532 (1994).
21. W. K. Wilson *et al.*, Phys. Rev. C **45**, 738 (1992).
22. P. L. Jain, G. Singh, and A. Mukhopadhyay, Phys. Rev. Lett. **74**, 1534 (1995).

23. S. Vokál, in *Proc. of the X Int. Seminar on High-Energy Physics Problems, Relativistic Nuclear Physics & Quantum Chromodynamics, Dubna, 1990* (World Sci., Singapore, 1991), p. 420; *Proc. of the XXI Int. Symposium on Multiparticle Dynamics, Wuhan, 1991* (World Sci., Singapore, 1992), p. 611.
24. A. Kugler, Czech. J. Phys. **45**, 545 (1995).
25. N. N. Ajitanand *et al.*, Nucl. Phys. A **638**, 451c (1998).
26. E895 Collab. (C. Pinkenburg *et al.*), Phys. Rev. Lett. **83**, 1295 (1999).
27. EOS Collab. (J. Chance *et al.*), Phys. Rev. Lett. **78**, 2535 (1997).
28. L. Chkhaidze, T. Djobava, and L. Kharkhelauri, hep-ex/9912035 (1999).
29. E895 Collab. (H. Liu *et al.*), Phys. Rev. Lett. **84**, 5488 (2000).
30. E877 Collab. (J. Barrette *et al.*), Phys. Rev. C **59**, 884 (1999).

Physics of Atomic Nuclei, Vol. 67, No. 2, 2004, pp. 281–286. Translated from Yadernaya Fizika, Vol. 67, No. 2, 2004, pp. 298–303.

ELEMENTARY PARTICLES AND FIELDS
Theory

Employing Higgs Boson Production at Photon Colliders to Discriminate between the Two Higgs Doublet Model and the Standard Model in the Process $e\gamma \to eh$

I. F. Ginzburg* **and M. V. Vychugin****

Institute of Mathematics, Siberian Division, Russian Academy of Sciences, Universitetskiĭ pr. 4, Novosibirsk, 630090 Russia
Novosibirsk State University, ul. Pirogova 2, Novosibirsk, 630090 Russia
Received October 24, 2002; in final form, February 25, 2003

Abstract—The possibility of employing experiments at photon colliders to discriminate between various models of electroweak-symmetry breaking is discussed for the case where experiments at LHC and at future linear electron–positron colliders reveal no disagreement with the predictions of the Standard Model (SM)—that is, the case of an SM-like scenario. The two Higgs boson doublet model (2HDM) is considered as an alternative to the SM. A comparison of the cross sections obtained for the process $e\gamma \to eh$ within the SM and the natural 2HDM shows that investigation of this cross section would make it possible to discriminate between these models of electroweak-symmetry breaking reliably and to confirm or disprove the results obtained by studying the reaction $\gamma\gamma \to h$. © *2004 MAIK "Nauka/Interperiodica".*

1. INTRODUCTION

At present, the Standard Model of electroweak interaction (SM) has been confirmed to a high precision. However, experimental data have not yet revealed a specific mechanism responsible for the breakdown of $SU(2) \times U(1)$ electroweak symmetry and, in particular, the nature of the Higgs sector of the theory.

Usually, physics programs for new high-energy colliders imply that new particles and interactions will be observed there. Yet, it may appear that experiments at the Tevatron, LHC, and linear e^+e^- colliders will result in detecting only a Higgs boson, but that no other new particles will be found. The quite probable situation where the measured widths of the discovered Higgs boson with respect to its decays to other particles (or the squares of its coupling constants) will prove to be in agreement with the predictions of the minimal Standard Model within the experimental errors (SM-like scenario) [1] will be the most difficult for interpretation. This picture could arise both in the SM and in other (alternative) models. In this case, the main tasks for experiments at high-energy colliders will reduce to seeking deviations of the measured cross sections for the interactions of known particles from their SM counterparts and these deviations will become signals of new physics. The SM admits various versions of new interactions at short distances, and the respective types of observable deviations from SM predictions may differ pronouncedly. It follows that, in studying deviations from SM predictions, one has to examine popular alternative models.

In the present article, we consider, as an alternative to the SM, the two Higgs boson doublet model (2HDM), which is of importance and which is widely discussed in the literature, and analyze the problem of discriminating between the models for the case where the SM-like scenario is realized.

2. 2HDM

Natural parameter set. The 2HDM Lagrangian has the form

$$\mathcal{L} = \mathcal{L}^{\mathrm{SM}}_{g+f} + \mathcal{L}_{\mathrm{H}} + \mathcal{L}_{\mathrm{Y}}, \qquad (1)$$

where $\mathcal{L}^{\mathrm{SM}}_{g+f}$ describes $SU(2) \times U(1)$-symmetric interaction of gauge bosons with fermions that is identical to that within the SM, $\mathcal{L}_{\mathrm{H}}$ is the Lagrangian for scalar fields ϕ_i, and $\mathcal{L}_{\mathrm{Y}}$ represents the (Yukawa-type) interaction between fermions and scalars. After going over to physical fields (upon electroweak-symmetry breaking), the CP invariance of the theory can be violated. It is naturally conserved in the absence of (ϕ_1, ϕ_2) mixing (Z_2 symmetry). The violation of CP invariance is usually described by supplementing the potential with a term that leads to a soft breakdown of Z_2 symmetry (only in the mass term). The minimization of the potential then leads to vacuum expectation values of Higgs fields with different phases.

*e-mail: ginzburg@math.nsc.ru
**e-mail: vychugin@math.nsc.ru

This phase difference can be removed by appropriately rotating the fields and varying some parameters in the potential (gauge of the potential form) [2]. In this gauge, the Lagrangian for scalar fields is given by

$$\mathcal{L}_{\rm H} = \sum_i (D_\mu \phi_i)^\dagger (D_\mu \phi_i) + V, \qquad (2)$$

$$V = \frac{\lambda_1}{2}(\phi_1^\dagger \phi_1)^2 + \frac{\lambda_2}{2}(\phi_2^\dagger \phi_2)^2 \qquad (3)$$
$$+ \lambda_3 (\phi_1^\dagger \phi_1)(\phi_2^\dagger \phi_2) + \lambda_4 (\phi_1^\dagger \phi_2)(\phi_2^\dagger \phi_1)$$
$$+ \frac{1}{2}\left[\lambda_5 (\phi_1^\dagger \phi_2)^2 + \text{h.c.}\right] + \mathcal{M}(\phi) + \text{const}.$$

It is convenient to express the mass term $\mathcal{M}(\phi)$ in terms of the coefficients λ_i; the only free parameter μ (responsible for a soft breakdown of Z_2 symmetry); and the vacuum expectation values of the Higgs fields, $\langle \phi_i \rangle = \frac{1}{\sqrt{2}} \begin{pmatrix} 0 \\ v_i \end{pmatrix}$ (both of these expectation values are real in the chosen gauge of the potential form, $\sqrt{v_1^2 + v_2^2} = v = (\sqrt{2} G_{\rm F})^{-1/2} = 246\ \text{GeV}$). We then have

$$\mathcal{M}(\phi) = -\frac{1}{2}[\hat{m}_{11}^2 (\phi_1^\dagger \phi_1) + \hat{m}_{22}^2 (\phi_2^\dagger \phi_2)] \qquad (4)$$
$$+ \frac{\mu^2}{2v^2}\left(v_2 \phi_1^\dagger - v_1 \phi_2^\dagger\right)(v_2 \phi_1 - v_1 \phi_2)$$
$$+ i v_1 v_2 \text{Im}\lambda_5 [\phi_1^\dagger \phi_2 - \text{h.c.}];$$
$$\hat{m}_{11}^2 = \lambda_1 v_1^2 + \lambda_{345} v_2^2, \quad \hat{m}_{22}^2 = \lambda_2 v_2^2 + \lambda_{345} v_1^2$$
$$(\lambda_{345} = \lambda_3 + \lambda_4 + \text{Re}\lambda_5).$$

In [2], it was shown that the observed weak violation of CP invariance and the smallness of flavor-changing neutral currents (FCNC) naturally constrains, for the parameters of the theory, the region of possible values ($\text{Im}\lambda_5$ and μ/v must simultaneously take relatively small values). Within the 2HDM, there are five observable Higgs bosons, the charged bosons $\text{H}^\pm$ and three neutral ones. In the absence of CP violation, these neutral states are two scalars, h and H ($M_h < M_{\rm H}$), and one CP pseudoscalar A. In the case of CP violation, the neutral physical states are mixtures of h, H, and A, so that they are not parity eigenstates. If CP violation is weak—and this is the case considered here—these physical states can be treated as h or H states involving a small admixture of A (and H or h, respectively) or as an A state involving a small admixture of H and h.

It should be noted that, at small μ, the masses of all Higgs bosons are controlled by the ordinary Higgs mechanism, $M_i^2 \sim \lambda_i v^2$. At large μ, however, the mass origin is not directly connected with the Higgs mechanism, $M_{H^\pm}^2, M_A^2, M_H^2 + M_h^2 \approx \mu^2$.

We assume that Yukawa interaction is described by the II model (arising, for example, within the minimal supersymmetric standard model, MSSM), where, prior to electroweak-symmetry breaking, the first Higgs doublet interacts only with d quarks and charged leptons ℓ, while the second one interacts with u quarks and heavy neutrinos, if any—see, for example, [3]. Supplemented with this Yukawa interaction, the 2HDM is referred to as the 2HDM(II).

In our analysis, we employ the ratios χ_i of the couplings of the observed Higgs boson to either quarks $i = u, d$ or gauge bosons $i = V = Z, W$ to the respective SM coupling constants,

$$\chi_i = \frac{g_i}{g_i^{\rm SM}} \qquad (i = V, u, d). \qquad (5)$$

The distinctions between the 2HDM and the minimal Standard Model that are significant for our purposes consist in the presence of charged Higgs bosons and in the possibility that the sign of some Higgs boson couplings to matter are opposite to those in the SM.

SM-like scenario within 2HDM. This possibility can be realized for various values of the coupling constants. In particular, this scenario involves the so-called decoupling limit of the theory as well, where the origin of particle masses has actually nothing to do with the Higgs mechanism (large μ). This decoupling limit is inconsistent with the requirement of the natural smallness of CP-violation and FCNC effects.

For the Lagrangian parameters, the possible ranges that are compatible with the expected measurement errors are listed in the table (which is borrowed from [1]) for the case where there is no CP violation. Although the table contains the required notation, some explanations are in order.

There exist two types of realization that are denoted there as $A_{\phi\pm}$ and $B_{\phi\pm q}$. The first index specifies the type of the Higgs boson to be observed, $\phi = h$ or H, while the second indicates the sign of the coupling constant g_V^ϕ.

For the $A_{\phi\pm}$ realization, the main coupling constants of the Higgs boson to be observed are approximately identical, $\chi_V \approx \chi_u \approx \chi_d \approx \pm 1$. For example, A_{H-} is the realization where the heavy Higgs boson H is to be observed and where $\chi_V^H \approx -1$.

In the case of the $B_{\phi\pm q}$ realization, $\chi_i \approx 1$ for some coupling constants, while $\chi_j \approx -1$ for the others. For these realizations, the third index $q = d, u$ denotes the type of the quark whose coupling to the Higgs boson to be observed has the sign opposite to that of the coupling constant g_V.

Table

Type	Notation	Boson to be observed	χ_V	μ	$\tan\beta = \frac{v_2}{v_1}$		Coupling
$A_{\phi\pm}$: $\chi_V \approx \chi_u \approx \chi_d$	A_{h+}	h	$\approx +1$		$\sqrt{\left\|\frac{\epsilon_d}{\epsilon_u}\right\|}$	$\lesssim 1$	$\epsilon_V = -\frac{\epsilon_u\epsilon_d}{2}$
	A_{H+}	H	$\approx +1$	$\mu \approx 0$		$\lesssim 1$	
	A_{h-}	h	≈ -1			$\ll 1$	
	A_{H-}	H	≈ -1	$\mu \approx 0$		$\gg 1$	
$B_{\phi\pm d}$: $\chi_V \approx \chi_u \approx -\chi_d$	B_{h+d}	h	$\approx +1$	$\mu \approx 0$	$\sqrt{\frac{2}{\epsilon_V}} \gtrsim 10$		$\epsilon_u = -\frac{\epsilon_V\epsilon_d}{2}$
	$B_{H\pm d}$	H	$\approx \pm 1$				
$B_{\phi\pm u}$: $\chi_V \approx \chi_d \approx -\chi_u$	$B_{h\pm u}$	h	$\approx \pm 1$	$\mu \approx 0$	$\sqrt{\frac{\epsilon_V}{2}} \lesssim 0.1$		$\epsilon_d = -\frac{\epsilon_V\epsilon_u}{2}$
	B_{H+u}	H	$\approx +1$				

$$\chi_i = \frac{g_i}{g_i^{\mathrm{SM}}} = \pm(1-\epsilon_i),$$

$$i = V(\equiv Z, W), \quad \text{or} \quad i = u(\equiv t, c), \quad \text{or} \quad i = d, \ell(\equiv b, \tau); \quad \epsilon_V > 0, \quad \epsilon_u\epsilon_d < 0$$

3. POSSIBILITY OF DISCRIMINATING BETWEEN THE MODELS IN QUESTION AT PHOTON COLLIDERS

The most important contribution to solving the problem of discriminating between the models in question is expected from measurements at photon colliders [4], which are an important part of projects for linear colliders [5]. Investigation of Higgs boson production in photon interactions is of particular importance here and is associated with exploring the effective $h\gamma\gamma$ and $hZ\gamma$ vertices, which are of special interest for the following reasons:

(i) In the SM, these vertices appear only at the loop level (they are absent there at the tree level); therefore, the background for the possible anomalous $h\gamma\gamma$ and $hZ\gamma$ interactions is much less than that for the majority of other processes within the SM.

(ii) Higgs boson interaction with photons proceeds via loops involving all charged particles. Within the SM, where the masses of particles are controlled by their interaction with the Higgs boson, each charged particle heavier than the Higgs boson makes a contribution to the $h\gamma\gamma$ and $hZ\gamma$ vertices that depends on the particle spin but not on its mass (there is no "decoupling" of heavy charged particles). In view of this, investigation of the corresponding reactions $\gamma\gamma \to h$, $e\gamma \to eh$, and $e^+e^- \to h\gamma$ may provide information about the existence of new charged particles that are too heavy to be observed directly.

(iii) A recent analysis revealed that the cross section for the production of a Higgs boson in the interaction of two photons can be measured at a photon collider to a rather high precision (higher than 2% if $M_h < 150$ GeV [6]).

***hγγ* and *hZγ* vertices.** In [1], the possibility of discriminating between the SM and the 2HDM involving a natural set of parameters was studied, within the SM-like scenario, for the production of a Higgs boson in the process $\gamma\gamma \to h$ at a photon collider and its decay $h \to Z\gamma$. It turned out that, for the 2HDM(II), the deviation of the observed cross sections for the process $\gamma\gamma \to h$ from the SM predictions will be five times as great as the expected experimental errors [6] for the $A_{\phi\pm}$ and $B_{\phi\pm d}$ realizations (Fig. 1*a*) and about two times as great as those for one of the $B_{\phi\pm u}$ realizations. These considerable deviations from the SM predictions for the $A_{\phi\pm}$ and $B_{\phi\pm d}$ realizations are due to the presence of an additional (heavy) charged particle in the 2HDM (charged Higgs boson); for the $B_{\phi\pm u}$ realization, the reason for this is that the sign of t-quark coupling to the Higgs boson is opposite to that in the SM.

The on-shell effective $hZ\gamma$ vertex (that is, the decay $h \to Z\gamma$) was also studied in [1]. It was shown that, for this vertex, the distinction between the cross sections predicted within the SM and the 2HDM is less than that for the process $\gamma\gamma \to h$ (Fig. 1*b*).

The decay $h \to Z\gamma$ cannot be observed directly, the respective vertex manifesting itself only in the processes $e^+e^- \to h\gamma$ (s channel) and $e\gamma \to eh$ (t channel). The first process has a very small cross section, and we will not discuss it below. In the process $e\gamma \to eh$, the $hZ\gamma$ vertex appears far off the mass shell, so that the distinction between the predictions of the SM and the 2HDM for this process can be noticeably different from that for the decay processes. This was the motivation of the present study.

We now consider in detail the process $e\gamma \to eh$ for the SM-like scenario, assuming that the 2HDM

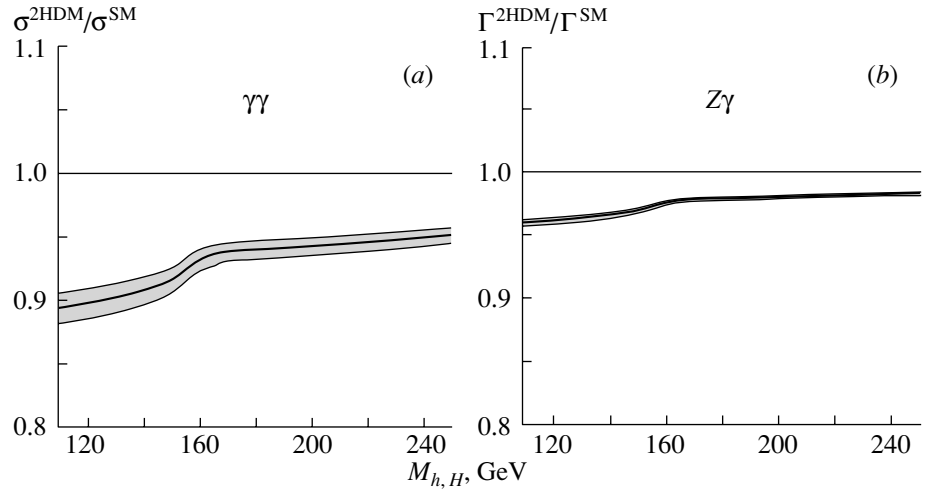

Fig. 1. Results from [1] for the $A_{\phi\pm}$ or the $B_{\phi\pm d}$ realizations: (a) ratio $\sigma_{\gamma\gamma}^{\rm 2HDM}/\sigma_{\gamma\gamma}^{\rm SM}$ and (b) ratio $\Gamma^{\rm 2HDM}(h \to Z\gamma)/\Gamma^{\rm SM}(h \to Z\gamma)$. The central curves represent the case of $|\chi_i| = 1$, while the shaded regions correspond to the scatter of the parameters that is compatible with the expected errors in the e^+e^- mode of the TESLA experiment.

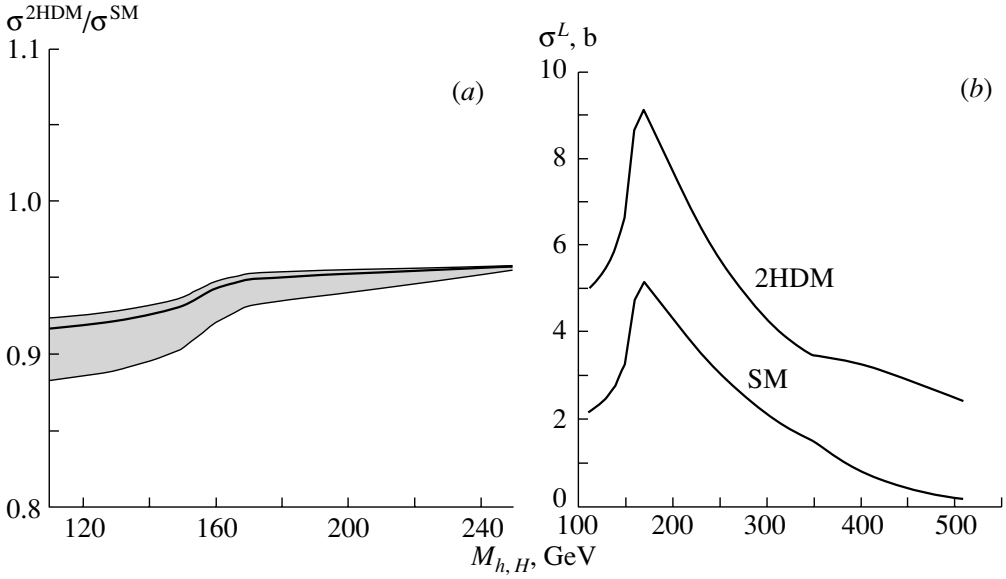

Fig. 2. Cross section for the process $e\gamma \to eh$ induced by electrons of right-hand circular polarization according to the SM and 2HDM predictions at $\sqrt{s} = 1.5$ TeV and $Q^2 \geq 1000$ GeV^2: (a) ratio $\sigma^{\rm 2HDM}/\sigma^{\rm SM}$ for the $A_{\phi\pm}$ or $B_{\phi\pm d}$ realizations and (b) cross section calculated for the process $e\gamma \to eh$ within the SM and the 2HDM for the $B_{\phi\pm u}$ realization.

has a natural parameter set (small μ) and that the charged Higgs boson is too heavy to be observed at LHC or at a linear electron–positron collider ($M_{H^\pm} > 500$ GeV)—this is one of the conditions necessary for the realization of the SM-like scenario.

In [7, 8], this process was studied in detail within the SM and within models deviating from it only slightly. Here, we list some features of the process $e\gamma \to eh$ [8] that are of importance for our purposes.

The amplitude of this process is controlled by three groups of diagrams:

(i) those that involve photon exchange between the initial and final electrons (including the $h\gamma\gamma$ triangle);

(ii) those that involve Z-boson exchange between the initial and final electrons (including the $hZ\gamma$ triangle);

(iii) box diagrams involving four-leg loops.

For physical amplitudes, this partition is approximately gauge-invariant to a rather high precision (about m_e/M_Z). Hence, we can consider the contributions of these groups of diagrams without specifying the choice of gauge.

For the process $e\gamma \to eh$, the contributions of box diagrams are numerically small over a wide region of the electron-momentum transfer.

If the transverse momentum of the scattered electron is above 30 GeV, the contributions from photon and Z-boson exchanges are close to each other, with the photon and Z-boson virtualities being $Q^2 > 900$ GeV^2 and $M_Z^2 + Q^2 > 8000$ GeV^2, respectively. This is the reason why the cross sections for the process $e\gamma \to eh$ induced by electrons having left- and right-hand circular polarizations differ very strongly (the cross section for the latter case is about one-third as large as that for the former case).

The photon polarization affects the cross section only slightly.

For the process $e\gamma \to eh$, the cross section integrated over the region $Q^2 \equiv -(p_e - p'_e)^2 \geq 1000$ GeV^2 was calculated here at an energy value of $\sqrt{s_{e\gamma}} = 1500$ GeV for the left-hand circular polarization of electrons and unpolarized photons.

An effective inclusion of radiative corrections to the diagrams involving γ and Z exchanges reduces to replacing the universal fine-structure constant (only for these vertices) by the quantity $\alpha(Q^2)$ [8]. Within the region $Q^2 \geq 1000$ GeV^2, which is considered here, we set $\alpha(Q^2) \approx \alpha(M_Z^2) = 1/128$. For the constants appearing in the results, we took the values from [9].

In our calculations, we used the known expressions for triangle loop integrals that describe Higgs boson interaction with photons (see, for example, [3]); we also used the expressions for the box diagrams from [8]. The numerical results were obtained by means of the FF package of Fortran subroutines [10].

The main results are displayed in Fig. 2. They depend only on type of chosen realization ($A_{\varphi\pm}$, $B_{\phi\pm d}$, or $B_{\phi\pm u}$) but not on a specific choice of realization (see table). In particular, the results are independent of whether a light Higgs boson, $\phi = h$, or a heavy one, $\phi = H$, would be observed. In the figures, the central curve represents the solutions corresponding to $|\chi_u| = |\chi_d| = |\chi_V| = 1$. Here, the Higgs boson mass is plotted along the abscissa, with either the light (h) or the heavy (H) boson being observed.

For the $A_{\phi\pm}$ and $B_{\phi\pm d}$ realizations, the deviation from the SM predictions is due to the appearance of the loop involving a charged Higgs boson (Fig. 2*a*). For the $A_{\phi\pm}$ realization, the expected experimental errors in measuring the couplings of the Higgs boson to quarks and gauge bosons in the e^+e^- mode of the linear collider TESLA admit deviations from the case of $|\chi_i| = 1$ in both directions (shaded region around the central curve). Only if the quantities $|\chi_i|$ differ from unity can the $B_{\phi\pm d}$ realization occur. In this case, the solid curve is inaccessible (that is, the equalities $|\chi_u| = |\chi_d| = |\chi_V| = 1$ cannot hold simultaneously), and all possible values of the cross section differ from the predictions more strongly than the central curve indicates (shaded region below that curve). The results presented here were obtained for the natural parameter set corresponding to $\mu \approx 0$. For a different set ($\mu \neq 0$), the deviation of the calculated cross sections from that obtained within the SM depends on μ according to the $(1 - \mu^2/M_{H^\pm}^2)$ law.

In the case of the $B_{\phi\pm u}$ realization, our results differ substantially from those predicted by the SM (Fig. 2*b*). Here, the contribution of the t-quark loop has an opposite sign, its magnitude being greater than 20% of the W-boson contribution. As a result, the ratio of the cross sections calculated within the 2HDM and the SM exceeds two. In the figures, we therefore plotted the cross sections themselves rather than their ratio.

Thus, our expectations came true. The effect has appeared to be commensurate with that for photon collisions, so that investigation of the reaction $e\gamma \to eh$ will enable us to confirm or to disprove with confidence the conclusions drawn from the results for the reaction $\gamma\gamma \to h$.

ACKNOWLEDGMENTS

We are grateful to M. Krawczyk, P. Olsen, I. Ivanov, and V. Serbo for stimulating discussions.

This work was supported by the Russian Foundation for Basic Research (project nos. 02-02-17884, 00-15-96691), INTAS (grant no. 00-00679), and the program Universities of Russia (project no. UR.02.01.005).

REFERENCES

1. I. F. Ginzburg, M. Krawczyk, and P. Osland, hep-ph/0101208; hep-ph/0101229; hep-ph/0101331.
2. I. F. Ginzburg, M. Krawczyk, and P. Osland, hep-ph/0211371; I. F. Ginzburg and M. V. Vychugin, hep-ph/0201117.
3. J. F. Gunion, H. E. Haber, G. Kane, and S. Dawson, *The Higgs Hunter's Guide* (Addison-Wesley, Reading, 1990).
4. I. F. Ginzburg, G. L. Kotkin, V. G. Serbo, and V. I. Telnov, Pis'ma Zh. Éksp. Teor. Fiz. **34**, 514 (1981) [JETP Lett. **34**, 491 (1981)]; Nucl. Instrum. Methods Phys. Res. **205**, 47 (1983); I. F. Ginzburg, G. L. Kotkin, S. L. Panfil, *et al.*, Nucl. Instrum. Methods Phys. Res. **219**, 5 (1984).
5. R. D. Heuer *et al.*, TESLA Technical Design Report, DESY 2001-011, Part III, TESLA Report 2001-23, TESLA FEL 2001-05 (2001).

6. G. Jikia and S. Söldner-Rembold, Nucl. Phys. B (Proc. Suppl.) **82**, 373 (2000); M. Melles, W. J. Stirling, and V. A. Khoze, Phys. Rev. D **61**, 054015 (2000).
7. E. Gabrielli, V. A. Ilyin, and B. Mele, Phys. Rev. D **56**, 5945 (1997); **60**, 113005 (1999).
8. A. T. Banin, I. F. Ginzburg, and I. P. Ivanov, Phys. Rev. D **59**, 115001 (1999); I. F. Ginzburg and I. P. Ivanov, Eur. Phys. J. C **22**, 411 (2001).
9. Particle Data Group, Eur. Phys. J. C **15**, 249 (2000).
10. G. J. Van Oldenborgh, NIKHEF-H/90-15 (Sept. 1990); G. J. Van Oldenborgh and J. A. M. Vermaseren, Z. Phys. C **46**, 425 (1990).

Translated by O. Chernavskaya

Physics of Atomic Nuclei, Vol. 67, No. 2, 2004, pp. 287–295. Translated from Yadernaya Fizika, Vol. 67, No. 2, 2004, pp. 304–313.

ELEMENTARY PARTICLES AND FIELDS
Theory

Effects of Four-Fermion Contact Interactions in the Bhabha Process at Linear Electron–Positron Colliders

A. A. Pankov*

Gomel State Technical University, pr. Oktyabrya 48, Gomel, 246768 Belarus

Received April 23, 2002; in final form, January 30, 2003

Abstract—For the case of longitudinally polarized primary beams, effects are investigated that are induced by four-fermion contact interactions in the process $e^+e^- \to e^+e^-$ occurring at linear electron–positron colliders of energy in the range $\sqrt{s} = 0.5$–1 TeV. Model-independent constraints on the parameters of four-fermion contact interactions are obtained. It is shown that the sensitivity of the Bhabha process to the parameter Λ_{LR} is considerably higher than the sensitivity of the leptonic process $e^+e^- \to \mu^+\mu^-$; at the same time, the sensitivities of these processes to the parameters Λ_{RR} and Λ_{LL} are commensurate.

1. INTRODUCTION

Should it be found that experimental data obtained at linear electron–positron colliders for fermion-pair production in annihilation processes like

$$e^+ + e^- \to \bar{f} + f, \qquad (1)$$

where $f = \mu, \tau, q$ ($q = u, d, c, s, b$), deviate from the predictions of the Standard Model, this would be indicative of the existence of new physics beyond the Standard Model. At low energies, such deviations can be systematically described and investigated in terms of the formalism of effective Lagrangians. Within this approach, an effective Lagrangian is constructed from matter fields that are present in the Standard Model. Moreover, the low-energy effective Lagrangian possesses the same symmetry properties as the Standard Model. The resulting interaction involves, in addition to the interaction occurring in the Standard Model and appearing as the leading term of a series, a number of higher order terms in the scale parameter $1/\Lambda^n$ that are formed by local operators of higher dimension. Thus, effects of nonstandard physics may manifest themselves at energies much less than the parameter Λ as deviations of observables (such as cross sections, asymmetries, and angular distributions) from the relevant predictions of the Standard Model and may correspond to some effective contact interactions.

The effective Lagrangian for $eeff$ interaction is diagonal in the fermion flavor and preserves helicity, its specific form being [1]

$$\mathcal{L}_{\mathrm{CI}} = \frac{1}{1+\delta_{ef}} \sum_{i,j} g^2_{\mathrm{eff}} \epsilon_{ij} \left(\bar{e}_i \gamma_\mu e_i\right) \left(\bar{f}_j \gamma^\mu f_j\right). \qquad (2)$$

The following notation has been used in this expression: the indices $i, j = L, R$ correspond to fermions of left- and right-handed helicity, respectively, and the index f denotes the fermion type, so that $\delta_{ef} = 1$ at $f = e$. For the four-fermion coupling constants, use is made of the parametrization $\epsilon_{ij} = \eta_{ij}/\Lambda^2_{ij}$. Here, it is assumed that the strength of interaction is determined by the constant $g^2_{\mathrm{eff}} = 4\pi$. The choice of the constant g_{eff} in this form is motivated by considerations according to which contact interactions become strong for $\sqrt{s} \to \Lambda_{ij}$. The quantity η_{ij} takes the values of $\eta_{ij} = \pm 1$ or the value of $\eta_{ij} = 0$, the scale parameter Λ_{ij} remaining a free independent variable. The positive and the negative sign here correspond to, respectively, a constructive and a destructive character of the interference between the contact interactions and the Standard Model amplitudes describing photon and Z-boson exchanges.

Various nonstandard-physics types where fermion interactions are characterized by particle exchanges in the s, t, and u channels can be described by an effective four-fermion contact interaction, provided that the square of the exchanged-particle mass is much greater than the corresponding Mandelstam variables. This concerns, for example, effects caused by the exchanges of a heavy Z' boson [2], leptoquarks [3], and supersymmetric leptons and quarks in supersymmetric theories characterized by R-parity violation [4]. Thus, contact interactions can be considered as a convenient parametrization of nonstandard-physics-induced deviations from predictions of the Standard Model.

In the present study, we consider effects of contact

*e-mail: pankov@gstu.gomel.by

Table 1. Models of four-fermion contact interactions and their parametrization in the process $e^+e^- \to \bar{f}f$

Model	η_{LL}	η_{RR}	η_{LR}	η_{RL}
LL	± 1	0	0	0
RR	0	± 1	0	0
LR	0	0	± 1	0
RL	0	0	0	± 1
VV	± 1	± 1	± 1	± 1
AA	± 1	± 1	∓ 1	∓ 1
$LL + RR$	± 1	± 1	0	0
$LR + RL$	0	0	± 1	± 1

interactions in the Bhabha scattering process

$$e^+ + e^- \to e^+ + e^-. \qquad (3)$$

From expression (2) for the Lagrangian of contact interactions, it follows that, for a given fermion f in process (1), there are in all four possible types of interaction that correspond to the total number of independent models. It is determined by the total number of helicity combinations $ij = LL$, LR, RL, and RR. In the Bhabha scattering process, which involves only electrons and positrons, the number of independent effective coupling constants is less by one—that is, there are three of them in all. Any one of these possibilities, which is often referred to in the literature as a model, or any of their combinations may be realized in nature. The list of the models, along with their parametrizations, that are most extensively discussed in the literature in analyzing experimental data in terms of four-fermion contact interactions is given in Table 1 [5].

A global analysis of experimental data on neutral currents was recently performed in [6, 7], and the corresponding constraints on the individual parameters of four-fermion contact interactions were given there. These data included those from processes leading to fermion-pair production in electron–positron annihilation at the LEP collider and occurring at energies in the range $\sqrt{s} = 130$–207 GeV—in particular, from elastic Bhabha scattering. The absence of signals from nonstandard physics in experiments featuring leptons and quarks made it possible to set constraints on the corresponding parameters Λ_{ij}, the most stringent of them being at a level of $\Lambda_{ij} > 10$–20 TeV at a 95% C.L. Owing to a high sensitivity of such processes at high energies, future linear electron–positron colliders of energy in the range $\sqrt{s} = 0.5$–1 TeV will provide the best possibilities for seeking and studying effects induced by $eeff$ contact interactions in process (1), especially for polarized primary beams [8–10].

That four-fermion contact interactions involve a large number of parameters [1] presents a serious problem, which considerably complicates a model-independent analysis. Indeed, the contact-interaction-induced deviations of observables from the predictions of the Standard Model may simultaneously depend, in the most general case, on a few effective coupling constants. For example, there may be up to four of them for processes of the type in (1) and up to three of them for the Bhabha scattering process. In view of this wide variety of parameters, the problem of separating and empirically determining them is quite involved both from the theoretical and from the experimental point of view. Obviously, all possible versions of four-fermion contact interactions must generally be taken into account in processing (fitting) experimental data. At the same time, the articles available in the literature that are devoted to exploring four-fermion contact interactions present, for these coupling constants, constraints that were obtained by varying one or, at best, two independent parameters at zero values of the remaining ones. Upon simultaneously taking into account a few chiral coupling constants, the contributions induced by them may cancel one another, with the result that observables will become less sensitive to the parameters Λ_{ij}. Previously, this problem was comprehensively studied in [8–10] for processes of the type in (1), and a relevant solution was given there in a general form. In particular, an approach was developed that makes it possible to perform a model-independent analysis of four-fermion contact interactions in such a way as to take simultaneously into account the entire set of interaction parameters. This approach is based on the use of new integrated observables and on the possibility of obtaining longitudinally polarized primary beams at future linear electron–positron colliders. It is the longitudinal polarization of electron–positron beams that enables one to isolate helicity cross sections for processes of the type in (1), whereby one can solve the problem of separating and extracting the parameters of four-fermion contact interactions. A solution to this problem for processes of the type in (1) was given in a general form with allowance for the entire set of four-fermion coupling constants. In the present study, an attempt is made to solve this problem for the Bhabha scattering process (3) and to obtain model-independent constraints on the parameters of contact interactions.

The ensuing exposition is organized as follows. In Section 2, we define polarization observables for the scattering process (3) that make it possible to perform a model-independent analysis of contact interactions. In this section, we also give a detailed analysis of the

sensitivity of observables to contact interactions, examine the dependence of observables on the scattering angle, and consider some other similar issues. In Section 3, we derive model-independent constraints on the scale parameter Λ_{ij} from a χ^2 analysis of polarized cross sections and present a comparative analysis of constraints that follow from the leptonic quasielastic process $e^+e^- \to \mu^+\mu^-$ and the Bhabha scattering process.

2. POLARIZATION OBSERVABLES

In the Born approximation taking into account the exchange of a photon and a Z boson in the s and t channels, as well as the contribution from the four-fermion contact interactions (2), the differential cross section for the scattering process (3) induced by longitudinally polarized electron–positron beams can be represented in the form

$$\frac{d\sigma(P^-,P^+)}{d\cos\theta} = (1-P^-P^+)\frac{d\sigma_1}{d\cos\theta} \qquad (4)$$
$$+ (1+P^-P^+)\frac{d\sigma_2}{d\cos\theta} + (P^+-P^-)\frac{d\sigma_P}{d\cos\theta},$$

where P^- and P^+ are the longitudinal polarizations of, respectively, the electron and the positron beam and θ is the final-electron emission angle with respect to the direction of the primary electron beam in the c.m. frame of the electron–positron pair. The differential cross sections appearing in (4) are given by

$$\frac{d\sigma_1}{d\cos\theta} = \frac{\pi\alpha^2}{4s}\left[A_+(1+\cos\theta)^2 + A_-(1-\cos\theta)^2\right], \qquad (5)$$

$$\frac{d\sigma_2}{d\cos\theta} = \frac{\pi\alpha^2}{4s}4A_0,$$
$$\frac{d\sigma_P}{d\cos\theta} = \frac{\pi\alpha^2}{4s}A_+^P(1+\cos\theta)^2.$$

The functions $A_0(s,t)$, $A_\pm(s,t)$, and $A_+^P(s,t)$ can be represented in the form

$$A_0(s,t) = \left(\frac{s}{t}\right)^2\left|1+g_Rg_L\chi_Z(t)+\frac{t}{\alpha}\epsilon_{LR}\right|^2, \qquad (6)$$

$$A_+(s,t) = \frac{1}{2}$$
$$\times\left|1+\frac{s}{t}+g_L^2\left(\chi_Z(s)+\frac{s}{t}\chi_Z(t)\right)+2\frac{s}{\alpha}\epsilon_{LL}\right|^2$$
$$+\frac{1}{2}\left|1+\frac{s}{t}+g_R^2\left(\chi_Z(s)+\frac{s}{t}\chi_Z(t)\right)+2\frac{s}{\alpha}\epsilon_{RR}\right|^2,$$

$$A_-(s) = \left|1+g_Rg_L\chi_Z(s)+\frac{s}{\alpha}\epsilon_{LR}\right|^2,$$

$$A_+^P(s,t) = \frac{1}{2}$$
$$\times\left|1+\frac{s}{t}+g_L^2\left(\chi_Z(s)+\frac{s}{t}\chi_Z(t)\right)+2\frac{s}{\alpha}\epsilon_{LL}\right|^2$$
$$-\frac{1}{2}\left|1+\frac{s}{t}+g_R^2\left(\chi_Z(s)+\frac{s}{t}\chi_Z(t)\right)+2\frac{s}{\alpha}\epsilon_{RR}\right|^2,$$

where α is the fine-structure constant; $t=-s(1-\cos\theta)/2$; $\chi_Z(s)=s/(s-M_Z^2+iM_Z\Gamma_Z)$ and $\chi_Z(t)=t/(t-M_Z^2)$ are the propagators of the neutral gauge Z boson in the s and t channels, respectively; and Γ_Z and M_Z are its total decay width and mass, respectively. It is assumed here that the chiral coupling constants for electrons of right- and left-handed helicity (g_R and g_L, respectively) are normalized in the following way within the Standard Model: $g_R=\tan\theta_W$ and $g_L=-\cot 2\theta_W$, where θ_W is the Weinberg angle.

We note that the polarized differential cross section given by (4)–(6) coincides with the corresponding expression obtained for the cross section in [11] on the basis of the Standard Model under the condition $\epsilon_{ij}=0$. In particular, the functions B appearing in the expression for the cross section in [11] are related to the functions A in (6) by the equations

$$B_1 = A_0(\epsilon_{LR}=0), \qquad (7)$$
$$B_2 = A_-(\epsilon_{LR}=0),$$
$$B_3 = A_+(\epsilon_{LL}=\epsilon_{RR}=0),$$
$$B_6 = A_+^P(\epsilon_{LL}=\epsilon_{RR}=0).$$

If the beams involved are both polarized, there arises the possibility of measuring the polarized cross sections for beam polarizations of four configurations $++$, $--$, $+-$, and $-+$ corresponding to the combinations $(P^-,P^+)=(P_1,P_2)$, $(-P_1,-P_2)$, $(P_1,-P_2)$, and $(-P_1,P_2)$, where $P_{1,2}>0$. Upon introducing the simplified notation $d\sigma\equiv d\sigma/d\cos\theta$ for differential cross sections, the polarized cross sections can be represented in the form

$$d\sigma_{++}\equiv d\sigma(P_1,P_2) = (1-P_1P_2)d\sigma_1 \qquad (8)$$
$$+(1+P_1P_2)d\sigma_2+(P_2-P_1)d\sigma_P,$$
$$d\sigma_{--}\equiv d\sigma(-P_1,-P_2) = (1-P_1P_2)d\sigma_1$$
$$+(1+P_1P_2)d\sigma_2-(P_2-P_1)d\sigma_P,$$
$$d\sigma_{+-}\equiv d\sigma(P_1,-P_2) = (1+P_1P_2)d\sigma_1$$
$$+(1-P_1P_2)d\sigma_2-(P_2+P_1)d\sigma_P,$$
$$d\sigma_{-+}\equiv d\sigma(-P_1,P_2) = (1+P_1P_2)d\sigma_1$$
$$+(1-P_1P_2)d\sigma_2+(P_2+P_1)d\sigma_P.$$

In order to extract, from the measured polarized cross sections $d\sigma_{\alpha\beta}$ ($\alpha\beta=++,+-,-+,++$), the quantities $d\sigma_1$, $d\sigma_2$, and $d\sigma_P$ carrying information about the parameters of four-fermion interactions, it is necessary to invert the set of Eqs. (8). We represent the

corresponding solution in the form

$$d\sigma_1 = \frac{1}{8}\Bigg[\left(1-\frac{1}{P_1P_2}\right)(d\sigma_{++}+d\sigma_{--}) + \left(1+\frac{1}{P_1P_2}\right)(d\sigma_{+-}+d\sigma_{-+})\Bigg], \quad (9)$$

$$d\sigma_2 = \frac{1}{8}\Bigg[\left(1+\frac{1}{P_1P_2}\right)(d\sigma_{++}+d\sigma_{--}) + \left(1-\frac{1}{P_1P_2}\right)(d\sigma_{+-}+d\sigma_{-+})\Bigg],$$

$$d\sigma_P = -\frac{1}{2(P_1+P_2)}(d\sigma_{+-}-d\sigma_{-+}) = \frac{1}{2(P_2-P_1)}(d\sigma_{++}-d\sigma_{--}).$$

We note that the equations contained in (8) are not linearly independent; in view of this, it is necessary for deriving the solution in (9) that not only the requirements $P_1 \neq 0$ and $P_2 \neq 0$ but also the requirement $P_1 \neq \pm P_2$ be satisfied. From Eqs. (5) and (6), it can easily be seen that $d\sigma_2$ depends on only one parameter (ϵ_{LR}) and that $d\sigma_P$ depends on two parameters (ϵ_{RR}, ϵ_{LL}); finally, $d\sigma_1$ depends on all three parameters. In order to obtain model-independent constraints on the parameters of electron contact interactions, it is therefore necessary to have information about all polarization observables in (9). In this connection, the role of a longitudinal polarization in a model-independent analysis of contact interactions becomes more transparent. In particular, it can be seen from Eqs. (4)–(6) that, in the absence of polarization ($P_1 = P_2 = 0$), the differential cross section is expressed in terms of $d\sigma_1$ and $d\sigma_2$, where the interference terms of contact interactions—they are proportional to ϵ_{LR} and are contained in the expressions for $A_0(s,t)$ and $A_-(s)$—have opposite signs. This structure of the unpolarized cross section leads to a partial cancellation of contact-interaction-induced effects for $(-t) \to s$. Experimental information about the parameter ϵ_{LR} will be more precise if it is extracted from $d\sigma_2$ by measuring the polarized cross sections (9). The dependence of the unpolarized cross section on the contact-interaction parameters ϵ_{LL} and ϵ_{RR} is realized through the dependence of the cross section on the function $A_+(s,t)$. In the linear approximation in these parameters, their contribution to the cross section can be represented in the form $d\sigma(\mathrm{SM}+\mathrm{CI}) - d\sigma(\mathrm{SM}) \propto \epsilon_{LL} + \epsilon_{RR}$, the approximate equality $g_L^2 \approx g_R^2$ being taken into account in deriving this expression. Therefore, the unpolarized cross section may produce only a correlation of the form $|\epsilon_{LL} + \epsilon_{RR}| < \mathrm{const}$ rather than constraints on contact interactions.

In performing a quantitative analysis aimed at assessing constraints on Λ_{ij}, we set the degrees of initial-beam polarizations to $P_1 = 0.8$ and $P_2 = 0.6$. As to the detection of final electron–positron pairs, its efficiency was set to $\epsilon = 90\%$, which is a value close to that achieved at LEP2. For the sake of completeness, we note that the planned features of the collider and detector to be used correspond to the following energy values and the full scattering-angle interval: $\sqrt{s} =$ 0.5 and 1 TeV and $|\cos\theta| \leq 0.9$. In calculating the angular distributions, we break down the full interval over which the scattering angle is measured into nine equidistant bins of width $\Delta z = 0.2$ ($z \equiv \cos\theta$).

Further, we determine the number of events in each bin for four possible combinations of polarizations:

$$N_{++}, \quad N_{--}, \quad N_{+-}, \quad N_{-+}. \quad (10)$$

These are quantities that are directly measured in experiments,

$$N_{\alpha\beta}^{\mathrm{bin}} = \frac{1}{4}\mathcal{L}_{\mathrm{int}}\epsilon\int_{\mathrm{bin}}(d\sigma_{\alpha\beta}/dz)dz, \quad (11)$$

where $\alpha\beta = ++, +-, -+, ++$ and $\mathcal{L}_{\mathrm{int}}$ stands for the integrated luminosity $\mathcal{L}_{\mathrm{int}} = \int \mathcal{L}dt$ accumulated over a year. In performing the ensuing quantitative analysis, we additionally assume that the luminosity integrated over a year is distributed in equal shares between all four combinations of electron- and positron-beam polarizations in (8).

For an energy of $\sqrt{s} = 500$ GeV and an integrated luminosity of $\mathcal{L}_{\mathrm{int}} = 50$ fb^{-1}, Fig. 1 displays, in the form of histograms, the Standard Model predictions for the angular distributions of the numbers of events in bins, N_{++}^{bin} and N_{+-}^{bin}, these distributions being calculated in the effective Born approximation [12, 13]. In this figure, one can see that the cross section has a characteristic peak for forward scattering because of the photon pole in the t channel. The presence of this peak makes it possible to obtain vast statistics in the kinematical region where $t \to 0$. The angular distributions of the number of events for other polarization configurations in (8) are not presented in Fig. 1 since they are similar to those given there.

The relative contact-interaction-induced deviations of the cross sections $d\sigma_1$, $d\sigma_2$, and $d\sigma_P$ from their behavior predicted by the Standard Model can be represented in the form

$$\Delta_{\mathcal{O}} = \frac{\mathcal{O}(\mathrm{SM}+\mathrm{CI}) - \mathcal{O}(\mathrm{SM})}{\mathcal{O}(\mathrm{SM})}, \quad (12)$$

where $\mathcal{O} = d\sigma_1$, $d\sigma_2$, $d\sigma_P$. For the above luminosity value, the angular distributions of these relative deviations for the observables in (9) are given in Figs. 2*a*

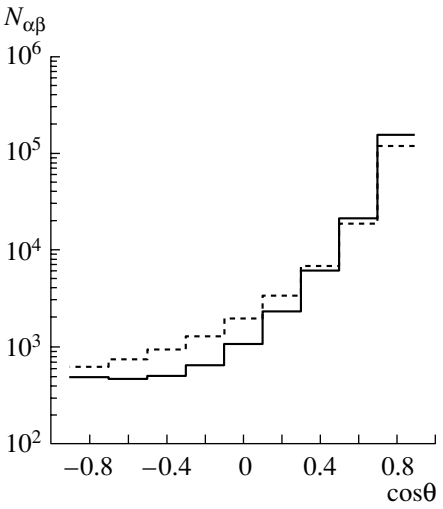

Fig. 1. Angular distributions of the number of events in bins, (solid-line histogram) N_{+-}^{bin} and (dashed-line histogram) N_{++}^{bin}, for the process $e^+e^- \to e^+e^-$ according to Standard Model predictions at an energy of $\sqrt{s} =$ 0.5 TeV and an integrated luminosity of $\mathcal{L}_{\text{int}} = 50$ fb^{-1}.

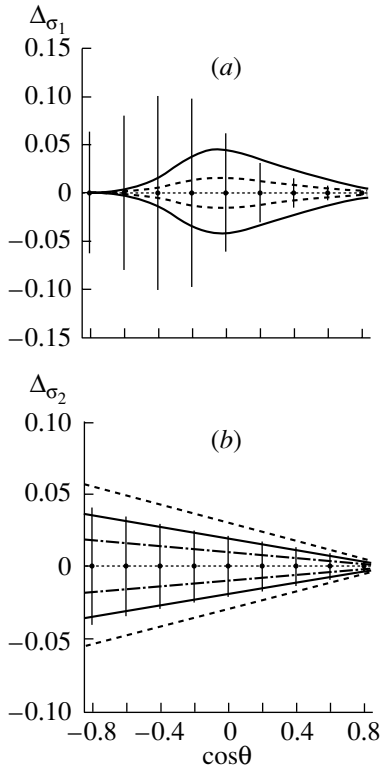

Fig. 2. Angular distributions of the relative deviations (*a*) Δ_{σ_1} at $\Lambda_{RR} =$ (solid curves) 30 and (dashed curves) 50 TeV and (*b*) Δ_{σ_2} at $\Lambda_{LR} =$ (dashed curves) 40, (solid curves) 50, and (dash-dotted curves) 70 TeV from Standard Model predictions for $P_1 = 0.8$ and $P_2 = 0.6$. The curves above (below) the abscissa correspond to the destructive (constructive) interference between the contact interactions and the Standard Model amplitudes. The vertical lines represent the expected statistical uncertainty at $\mathcal{L}_{\text{int}} = 50$ fb^{-1}.

and 2*b* for the parameter Λ_{ij} set to the values indicated in the caption under the figure. By analogy with what was done in assessing the numbers of events in individual bins in Fig. 1, the relative deviations in (12) are normalized to the scattering cross sections calculated within the Standard Model. In order to estimate the sensitivity of the observables in question, it is necessary to compare the relative deviations with the expected relative statistical errors, the latter being represented by vertical lines in Figs. 2*a* and 2*b*. More detailed information about the sensitivity of the observables is provided by the statistical significance defined as the statistical deviation $\Delta_{\mathcal{O}}$ expressed in units of the relative statistical uncertainty in each bin; that is,

$$\mathcal{S}(\mathcal{O})^{\text{bin}} = \frac{\Delta_{\mathcal{O}}^{\text{bin}}}{\delta\mathcal{O}^{\text{bin}}}, \qquad (13)$$

where $\mathcal{O}^{\text{bin}} = \sigma_1^{\text{bin}}$, σ_2^{bin}, σ_P^{bin}, and $\sigma^{\text{bin}} \equiv \int_{\text{bin}}(d\sigma/dz)dz$. In (13), $\Delta_{\mathcal{O}}$ stands for the relative deviation of an observable from its behavior within the Standard Model [see Eq. (12)], while $\delta\mathcal{O}$ is the relative statistical uncertainty of measurements.

For the observables $d\sigma_1$ and $d\sigma_2$, the angular dependences of the statistical significance are displayed in Figs. 3*a* and 3*b*, respectively, for the same values of the parameters Λ_{ij} as in Figs. 2*a* and 2*b*. From Fig. 3*a*, it can be seen that the sensitivity of the cross section $d\sigma_1$ to the contact interactions is the highest in the kinematical region of final-electron scattering into the forward hemisphere. In addition, Fig. 3*a* shows that, at preset values of the energy $\sqrt{s}$ and the luminosity $\mathcal{L}_{\text{int}}$, the sensitivity of the observable $d\sigma_1$ to the parameter Λ_{RR} (and to Λ_{LL} as well) is higher than 30 TeV. In contrast to what we have for the observable $d\sigma_1$, the statistical significance $\mathcal{S}(d\sigma_2)$ is virtually independent of the choice of the kinematical region, which is specified by the function $\cos\theta$, since this sensitivity is a slowly varying function of $\cos\theta$ (see Fig. 3*b*). It is owing to this property of the observable $d\sigma_2$ that it is more sensitive to the contact interactions than the observable $d\sigma_1$. Moreover, it can easily be seen from Fig. 3*b* that the sensitivity of $d\sigma_2$ to the parameter Λ_{LR} is higher than 50 TeV.

3. CONSTRAINTS ON *eeee* CONTACT INTERACTIONS

In assessing the potential of linear electron–positron colliders for seeking nonstandard-physics effects, such as contact interactions, much attention is given to developing procedures for processing and analyzing experimental data. The choice of procedure

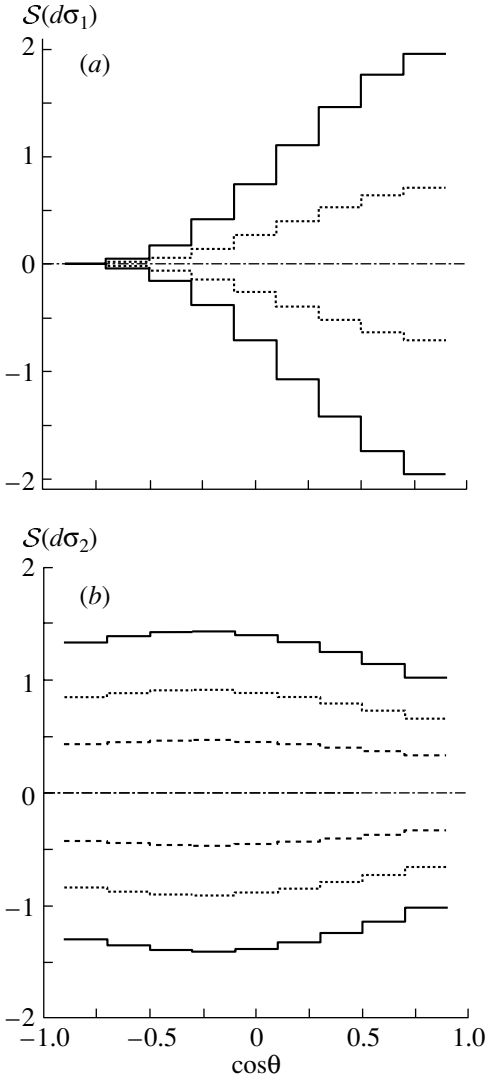

Fig. 3. Angular distributions of the statistical significances (*a*) $\mathcal{S}(d\sigma_1)$ at $\Lambda_{RR} =$ (solid curve) 30 and (dotted curve) 50 TeV and (*b*) $\mathcal{S}(d\sigma_2)$ at $\Lambda_{LR} =$ (solid curve) 40, (dotted curve) 50, and (dashed curve) 70 TeV. The polarization and luminosity values were taken to be identical to those chosen for Fig. 2.

depends greatly on specific conditions and factors associated with experimental details, as well as on the physical and technical features of the accelerator facilities and detectors used. Even without this experimental information, however, one can derive a preliminary estimate for the sensitivity of observables of the process in (3) to the parameters of *eeee* contact interactions. One of the popular procedures underlying calculations of this type is based on analyzing a χ^2 functional that characterizes manifestations of interactions belonging to a new (nonstandard) type [14]. For differential cross sections, the functional χ^2 has the form

$$\chi^2(\mathcal{O}) = \sum_{\text{bins}} \left(\frac{\Delta_{\mathcal{O}}^{\text{bin}}}{\delta \mathcal{O}^{\text{bin}}} \right)^2, \qquad (14)$$

where $\delta\mathcal{O}^{\text{bin}}$ stands for the relative experimental uncertainty that, in contrast to the uncertainty appearing in (13), involves both a statistical and a systematic contribution.

In performing a quantitative analysis—in particular, in calculating differential cross sections for scattering with allowance for radiative corrections—we make use of the formalism of QED structure functions [15–18]. Following the notation adopted in [18], we represent the scattering cross section with allowance for radiative corrections in the form

$$d\sigma^{\text{rad}}(q^2) = \int dx_1 dx_2 D(x_1, q^2) \qquad (15)$$
$$\times\, D(x_2, q^2) d\sigma((1 - x_1 x_2)q^2)(1 + \delta_{fe})\Theta(\text{cuts}),$$

where $D(x, q^2)$ is the electron (positron) structure function. The factor δ_{fe} takes into account the emission of photons from final states, while the function Θ(cuts) ensures the inclusion of experimental cuts on the kinematics of the process. The cross section $d\sigma$ appearing in the respective integrand is taken in the effective Born approximation involving electroweak corrections [12, 13]. In this approximation, the quantities $\alpha(s)$, M_Z, G_{F}, and Γ_Z play the role of input parameters [15–18].

In assessing uncertainties, we varied the integrated luminosity over the interval between 50 and 500 fb^{-1} in order to determine the relative contribution of the statistical component to $\delta\mathcal{O}$. The systematic error arises from the uncertainties in measuring the luminosity, $\delta\mathcal{L}_{\text{int}}/\mathcal{L}_{\text{int}} = 0.5\%$; the efficiency of detection of the final electron–positron pair, $\delta\epsilon/\epsilon = 0.5\%$; and, finally, the degrees of the longitudinal electron and positron polarizations, $\delta P_1/P_1 = \delta P_2/P_2 = 0.5\%$.

In the simplest case, which is realized for the observable σ_2 because of its one-parameter dependence on ϵ_{LR}, the corresponding absolute deviation from the predictions of the Standard Model for $\sqrt{s} \ll \Lambda_{LR}$ is determined primarily by the interference term and can be represented in the form

$$\Delta\sigma_2^{\text{bin}} \equiv \sigma_2^{\text{bin}}(\text{SM} + \text{CI}) - \sigma_2^{\text{bin}}(\text{SM}) \qquad (16)$$
$$\simeq 2\pi\alpha s \epsilon_{LR} \int_{\text{bin}} \frac{d\cos\theta}{t} \left(1 + g_R g_L \chi_Z(t)\right).$$

The absolute error in the cross section σ_2 is determined in accordance with expression (9) in terms of

the directly measured quantities σ_{++}, σ_{--}, σ_{+-}, and σ_{-+} as

$$(\delta\sigma_2)^2 = \frac{1}{8^2} \times \left[\left(1+\frac{1}{P_1P_2}\right)^2\left((\delta\sigma_{++})^2+(\delta\sigma_{--})^2\right) + \left(1-\frac{1}{P_1P_2}\right)^2\left((\delta\sigma_{+-})^2+(\delta\sigma_{-+})^2\right)\right] + \left(\frac{\sigma_{++}+\sigma_{--}-\sigma_{+-}-\sigma_{-+}}{8P_1P_2}\right)^2 \times \left[\left(\frac{\delta P_1}{P_1}\right)^2+\left(\frac{\delta P_2}{P_2}\right)^2\right], \quad (17)$$

where

$$\left(\frac{\delta\sigma_{\alpha\beta}}{\sigma_{\alpha\beta}}\right)^2 = \frac{1}{N_{\alpha\beta}} + \left(\frac{\delta\mathcal{L}_{\rm int}}{\mathcal{L}_{\rm int}}\right)^2 + \left(\frac{\delta\epsilon}{\epsilon}\right)^2. \quad (18)$$

Similar expressions for uncertainties hold for the cross sections σ_1 and σ_P as well.

In deriving constraints on the parameters of four-fermion contact interactions, we rely on the assumption that the results of future experiments devoted to measuring the cross section for process (3) will agree with the predictions of the Standard Model within the expected accuracy of the measurements. In this case, the requirement imposed on the functional in (14) and expressed in the form of the inequality

$$\chi^2 < \chi^2_{\rm C.L.} \quad (19)$$

makes it possible to determine the region allowed for the parameters of four-fermion contact interactions. Here, $\chi^2_{\rm C.L.}$ is the number specified by a preassigned confidence level (C.L.). We choose it to be $\chi^2_{\rm C.L.} = 3.84$ and 5.99 at a preset 95% confidence level for, respectively, a one- and a two-parameter fit [14].

We begin our quantitative analysis by considering the simplest case of a one-parameter dependence. This is so for the cross section σ_2, because, in accordance with (16), we have $\Delta\sigma_2 = \Delta\sigma_2(\epsilon_{LR})$ for this observable. Therefore, constraints on the parameter ϵ_{LR} are obtained from a one-parameter fit. From the practical point of view, it is necessary to solve inequality (19) in order to obtain model-independent constraints on the parameter ϵ_{LR}. Figure 4 displays the corresponding constraints on the scale parameter Λ_{LR} that were obtained at an energy of $\sqrt{s} = 0.5$ TeV for input values of the integrated luminosity $\mathcal{L}_{\rm int}$ between 50 and 500 fb^{-1}. As might have been expected, the most stringent constraints on the parameter Λ_{LR} are obtained at the maximum possible values of the luminosity. The lower limit in this constraint on Λ_{LR} exceeds the linear-collider energy by a factor of 110 to 170. We emphasize once again that so high a sensitivity of the observable σ_2 is due primarily to the equality of the contributions to the functional χ^2 from all bins realizing an equidistant partition of the entire kinematical region of $\cos\theta$ (see Fig. 3*b*). An increase in the energy of the electron–positron beams used leads to a further growth of the sensitivity of observables and to the corresponding increase in the lower limits on the admissible values of the scale parameters Λ_{ij} (see Fig. 5).

We further proceed to consider the polarized cross section σ_P, which depends on two parameters, ϵ_{RR} and ϵ_{LL}, simultaneously. From expressions (4) and (5) for the relevant cross sections, it can be seen that, in the linear approximation in the parameters ϵ_{RR} and

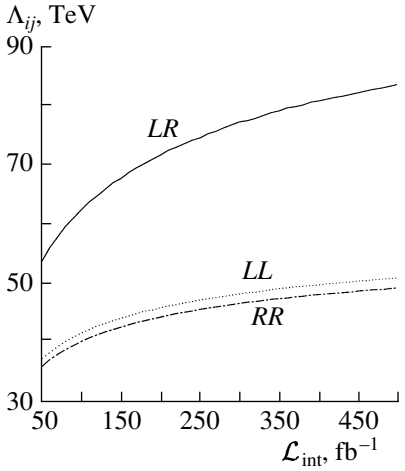

Fig. 4. Model-independent constraints (at a 95% C.L.) on the scale parameters Λ_{ij} from an analysis of the process in (3) at $\sqrt{s} = 0.5$ TeV, $|P^-| = 0.8$, and $|P^+| = 0.6$: (solid curve) Λ_{LR}, (dotted curve) Λ_{LL}, and (dash-dotted curve) Λ_{RR}.

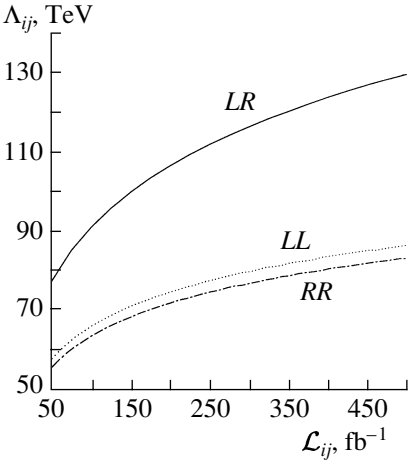

Fig. 5. As in Fig. 4, but at $\sqrt{s} = 1$ TeV.

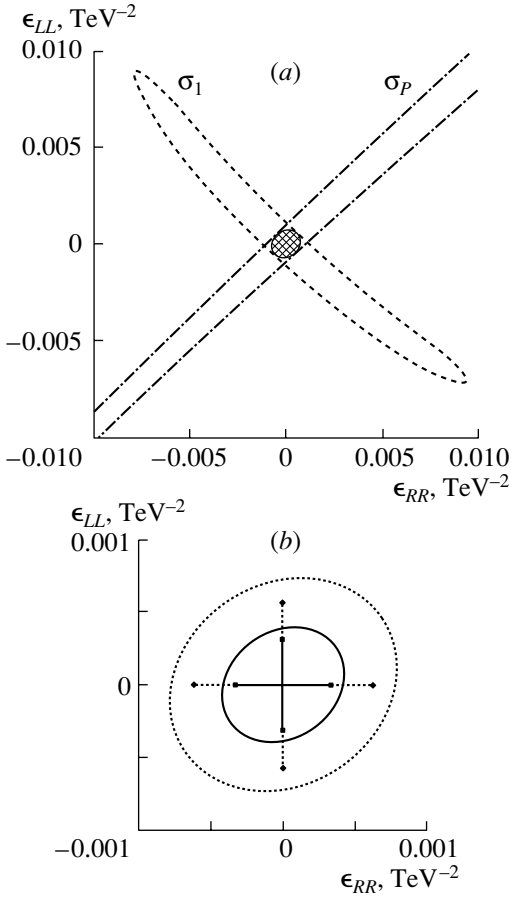

Fig. 6. (*a*) Allowed regions (at a 95% C.L.) in the $(\epsilon_{RR}, \epsilon_{LL})$ parameter plane that were obtained from σ_1 and σ_P at $\sqrt{s} = 0.5$ TeV and $\mathcal{L}_{\text{int}} = 50$ fb^{-1}; (*b*) combined allowed regions as obtained from σ_1 and σ_P at $\sqrt{s} = 0.5$ TeV for $\mathcal{L}_{\text{int}} =$ (external ellipse) 50 and (internal ellipse) 500 fb^{-1}.

ϵ_{LL} and with allowance for the relation $|g_L| \approx |g_R|$ in the Standard Model, the deviation of the cross section σ_P from the behavior predicted by the Standard Model can be represented in the form

$$\Delta\sigma_P \propto (\epsilon_{LL} - \epsilon_{RR}). \tag{20}$$

This linear approximation describes the dependence of the observable in question on the parameters of the contact interactions quite adequately. In the (ϵ_{RR}, ϵ_{LL}) plane, Fig. 6*a* shows the allowed region that was obtained for a general case from a two-parameter fit to data on the cross section σ_P with allowance for the linear and quadratic terms in the parameters of the contact interactions. Owing to the fact that the main contribution to $\Delta\sigma_P$ is linear in $(\epsilon_{LL} - \epsilon_{RR})$, the allowed region in the parameter plane has the form of a straight band traversing the first and the third quadrant. As a matter of fact, only a correlation between the parameters ϵ_{LL} and ϵ_{RR} rather than a closed allowed region lying in the vicinity of the point $\epsilon_{LL} = \epsilon_{RR} = 0$ can be obtained with the aid of σ_P. In order to obtain a closed region, it is necessary to include the observable σ_1 in the analysis. As can be seen from (4) and (5), this observable depends on three parameters, ϵ_{RR}, ϵ_{LL}, and ϵ_{LR}. By analogy with (20), its dependence on the first two parameters in the linear approximation in these parameters can be represented in the form

$$\Delta\sigma_1 \propto (\epsilon_{LL} + \epsilon_{RR}). \tag{21}$$

It follows that, from the observable σ_1, one obtains a correlation between the parameters in (21); together with the dependence in (20), this correlation will make it possible to constrain the allowed region in the $(\epsilon_{RR}, \epsilon_{LL})$ plane quite severely and to localize it in the vicinity of the point $\epsilon_{LL} = \epsilon_{RR} = 0$. From the practical point of view, a simultaneous two-parameter fit to the observables σ_1 and σ_P must be performed in order to obtain such a region. The corresponding functional χ^2 has the form

$$\chi^2 = \chi^2(\sigma_1) + \chi^2(\sigma_P). \tag{22}$$

As to the dependence of σ_1 on the third parameter ϵ_{LR}, it was considered, in implementing the fitting procedure, that the region of this parameter is subjected to the constraint that follows from the two-parameter fit to σ_2 and which is rather stringent. The result obtained from a global fit to the observables σ_1 and σ_P is presented in Fig. 6*a* in the form of a shaded ellipse including the point $\epsilon_{ii} = 0$ ($i = L, R$). Figure 6*b* displays the same ellipse representing the model-independent constraints on the parameters ϵ_{LL} and ϵ_{RR} for two values of the integrated luminosity of an electron–positron collider, $\mathcal{L}_{\text{int}} = 50$ and 500 fb^{-1}. Constraints on the parameters ϵ_{LL} and ϵ_{RR} can easily be transformed into the corresponding limiting values for the scale parameters Λ_{LL} and Λ_{RR} (see Figs. 4, 5). As might have been expected, the sensitivity of the observables σ_1 and σ_P to Λ_{RR} and Λ_{LL} is much lower than the sensitivity of σ_2 to Λ_{LR}.

For the sake of comparison, the model-dependent constraints on the parameters ϵ_{LL} and ϵ_{RR} for models of the LL and RR types (see Table 1) are also given in Fig. 6*b*. They are represented by vertical and horizontal straight-line segments whose beginnings and ends correspond to, respectively, the minimum and the maximum limiting values of relevant parameters. These constraints were derived by varying only one variable (parameter) at zero values of the remaining ones. In other words, these model-dependent constraints were obtained from one-parameter fits. As can be seen from Fig. 6*b*, the model-dependent constraints in question are more stringent than their model-independent counterparts. This is due primarily to choosing $\chi^2_{\text{C.L.}} = 3.84$ (at a 95% C.L.) for one-parameter fits. In addition, there is no correlation

Table 2. Model-independent constraints on Λ_{ij} (at a 95% C.L.) from an analysis of the processes $e^+e^- \to e^+e^-$ and $e^+e^- \to \mu^+\mu^-$ at an energy of polarized electron–positron beams that is equal to 0.5 TeV (the degrees of beam polarization are $|P^-| = 0.8$ and $|P^+| = 0.6$; the integrated luminosity is set to the values indicated in the table; the values of Λ_{ij} are given in TeV)

Process	$\mathcal{L}_{\text{int}}$, fb^{-1}	Λ_{LL}	Λ_{RR}	Λ_{LR}	Λ_{RL}
$e^+e^- \to \mu^+\mu^-$	50	35	35	31	31
	500	47	49	51	52
$e^+e^- \to e^+e^-$	50	38	36	54	
	500	51	49	84	

between ϵ_{ij} values in a one-parameter case, but such a correlation does in fact affect the quantitative result.

It is worthwhile to highlight once again the role of polarization in performing a model-independent analysis of contact interactions in the process in (3). The unpolarized cross section depends on all three parameters of the contact interactions, ϵ_{LL}, ϵ_{RR}, and ϵ_{LR}. It is clear that, at a fixed energy value and in the absence of polarization, it is impossible to separate completely signals induced by different contact interactions. At best, correlation regions can be obtained in the parameter plane. From Eqs. (4)–(6), it can indeed be seen that, for unpolarized electron–positron beams, $P^- = P^+ = 0$, the cross section has the form $d\sigma^{\text{unp}} = d\sigma_1 + d\sigma_2$. Thus, the dependence of the cross section $d\sigma^{\text{unp}}$ on the parameters ϵ_{LL} and ϵ_{RR} is determined by the corresponding dependence of the cross section $d\sigma_1$. In view of this, the unpolarized cross section provides only a correlation between the parameters ϵ_{LL} and ϵ_{RR} that is similar to that which was obtained for the observable $d\sigma_1$ in the presence of polarization (see Fig. 6*a*). As to the parameter ϵ_{LR}, it can be extracted by isolating the cross section $d\sigma_2$, which depends only on this parameter. At the same time, it can be seen from (8) that, without resorting to polarized electron and positron beams, it is impossible to separate $d\sigma_2$ from the cross sections $d\sigma_{\alpha\beta}$, which are measured directly in experiments. Thus, only with the aid of experiments with polarized beams can one perform a model-independent analysis of contact interactions in the process in (3) and obtain relevant constraints on their parameters.

It is instructive to compare the potential for revealing effects of contact interactions in the Bhabha scattering process $e^+e^- \to e^+e^-$ with that in another leptonic process, $e^+e^- \to \mu^+\mu^-$. For the latter, a model-independent analysis of contact interactions was recently performed in [8–10]. The corresponding constraints on the parameters Λ_{ij} from an analysis of elastic- and quasielastic-annihilation processes are given in Table 2. It should be noted that the sensitivities of the processes in question to the parameters Λ_{RR} and Λ_{LL} are commensurate, but that the Bhabha process is much more sensitive to the scale parameter Λ_{LR}, which is nondiagonal in the helicity indices.

ACKNOWLEDGMENTS

I am grateful to A.A. Babich and N. Paver for stimulating discussions and enlightening comments.

REFERENCES

1. E. J. Eichten, K. D. Lane, and M. E. Peskin, Phys. Rev. Lett. **50**, 811 (1983).
2. A. A. Babich, A. A. Pankov, and N. Paver, Phys. Lett. B **452**, 355 (1999).
3. J. Kalinowski, R. Rückl, H. Spiesberger, and P. Zerwas, Phys. Lett. B **406**, 314 (1997).
4. T. G. Rizzo, Phys. Rev. D **59**, 113004 (1999).
5. H. Kroha, Phys. Rev. D **46**, 58 (1992).
6. A. F. Zarnecki, Eur. Phys. J. C **11**, 539 (1999).
7. A. F. Zarnecki, Nucl. Phys. B (Proc. Suppl.) **79**, 158 (1999).
8. A. A. Pankov and N. Paver, Phys. Lett. B **432**, 159 (1998).
9. A. A. Babich, P. Osland, A. A. Pankov, and N. Paver, Phys. Lett. B **476**, 95 (2000); **481**, 263 (2000); **518**, 128 (2001).
10. A. A. Pankov, Yad. Fiz. **65**, 547 (2002) [Phys. At. Nucl. **65**, 521 (2002)].
11. R. Budny, Phys. Lett. B **55B**, 227 (1975).
12. M. Consoli, W. Hollik, and F. Jegerlehner, Preprint CERN-TH-5527-89.
13. F. Berends, G. Burges, W. Hollik, and W. L. van Neerven, Phys. Lett. B **203**, 177 (1988).
14. D. E. Groom *et al.*, Eur. Phys. J. C **15**, 191 (2000).
15. O. Beenaker, F. Berends, and L. Trentadue, in *Radiative Corrections for e^+e^- Collisions*, Ed. by J. H. Kühn (Springer, Berlin, 1989), p. 3.
16. O. Nicrosini and L. Trentadue, in *Radiative Corrections for e^+e^- Collisions*, Ed. by J. H. Kühn (Springer, Berlin, 1989), p. 25.
17. É. A. Kuraev and V. S. Fadin, Yad. Fiz. **41**, 733 (1985) [Sov. J. Nucl. Phys. **41**, 466 (1985)].
18. P. Chiappetta *et al.*, *Physics at LEP2*, Ed. by G. Altarelli, T. Sjöstrand, and F. Zwirner (Geneva, 1996), CERN 96-01, Vol. 1, p. 577.

Translated by A. Isaakyan

Physics of Atomic Nuclei, Vol. 67, No. 2, 2004, pp. 296–305. Translated from Yadernaya Fizika, Vol. 67, No. 2, 2004, pp. 314–323.

ELEMENTARY PARTICLES AND FIELDS
Theory

Investigation of the $H\tau\tau$ and Hbb Coupling Constants for a Scalar (Pseudoscalar) Higgs Boson at a Future Linear Electron–Positron Collider

V. V. Braguta[1], A. A. Likhoded[1),2)*], A. E. Chalov[1)], and R. Rosenfeld[2)]**

Received September 13, 2002; in final form, February 21, 2003

Abstract—The possibility of setting constraints on the couplings of a scalar (pseudoscalar) Higgs boson to the tau lepton and the b quark in the reactions $e^+e^- \to \nu\bar{\nu}\tau^+\tau^-$ and $e^+e^- \to \nu\bar{\nu}b\bar{b}$ at a future linear electron–positron collider of total energy $\sqrt{s} = 500$ GeV is studied. The admixture of a new hypothetical pseudoscalar state of the Higgs boson in the $Hf\bar{f}$ vertex is parametrized in the form $(m_f/v)(a + i\gamma_5 b)$. On the basis of an analysis of differential distributions for the processes under study, it is shown that data from the future linear collider TESLA will make it possible to constrain the parameters a and b as $-0.32 \le \Delta a \le 0.24$ and $-0.73 \le b \le 0.73$ in the case of the reaction $e^+e^- \to \nu\bar{\nu}\tau^+\tau^-$ and as $-0.026 \le \Delta a \le 0.027$ and $-0.23 \le b \le 0.23$ in the case of the reaction $e^+e^- \to \nu\bar{\nu}b\bar{b}$. It is emphasized that the contribution of the fusion subprocess $WW \to H$ in the channel involving an electron neutrino is of particular importance, since this contribution enhances the sensitivity of data to the parameters being analyzed. © *2004 MAIK "Nauka/Interperiodica"*.

1. INTRODUCTION

The origin of fermion masses and of mixing is one of the important problems in particle physics. At present, the relevant quantities play the role of input parameters for the Standard Model, which has been tested quite thoroughly. Measurement of these quantities to the highest possible experimental precision will make it possible to constrain the class of extended models that are able to predict their values theoretically.

In all probability, the fermion masses are directly related to the presently known mechanism of electroweak-symmetry breaking. Within the simplest model, the electroweak scalar doublet characterized by an ad hoc potential ϕ^4 is responsible for symmetry breaking, predicting an observable Higgs boson ($J^{PC} = 0^{++}$). The most popular extensions of the Standard Model—for example, the supersymmetric standard model—predict, in addition to a light scalar state, the existence of a $J^{PC} = 0^{-+}$ pseudoscalar Higgs boson as well. The possibility of electroweak-symmetry breaking because of new strong interactions is an alternative version, and there can exist a pseudoscalar Higgs boson in this case as well [1]. In this connection, it seems especially important to distinguish between these scenarios. This can be accomplished by thoroughly studying the CP properties of the expected scalar (pseudoscalar) particle.

A method for analyzing the CP nature of the Higgs boson on the basis of its decay into fermions or gauge bosons was developed in [2] and was applied in [3] to studying the production of a Higgs boson in the reaction $e^+e^- \to ZH$. It is worth noting that investigations at a photon–photon collider, where different polarizations of initial photons will make it possible to single out different CP states [4], are likely to provide the most direct means for determining the CP properties of the Higgs boson.

Data on the ZHH coupling constant can also be obtained from an analysis of the threshold behavior and angular distributions in the process $e^+e^- \to ZH$. In particular, the CP and spin properties of the Higgs boson can be determined in this way to a fairly high degree of precision [5].

At future hadron colliders, such as LHC, an analysis of the azimuthal angular distribution of detected final jets in the subprocess of gauge-boson fusion will provide an efficient possibility for studying the CP properties of HWW coupling [6].

Data that will be obtained by measuring, in the process $pp \to t\bar{t}H$ at LHC [7] and the process $e^+e^- \to t\bar{t}H$ at a future linear electron–positron collider [8], the coupling of the Higgs boson to the

[1)]Institute for High Energy Physics, Protvino, Moscow oblast, 142284 Russia.
[2)]Instituto de Física Teórica, Univ. Estadual Paulista (UNESP), Rua Pamplona 145, Br-01405-900 São Paulo, Brazil.
[*]e-mail: andre@ift.unesp.br
[**]e-mail: rosenfel@ift.unesp.br

t quark will also be of use in determining the CP properties of the Higgs boson.

The possibilities of studying the CP properties of the Higgs boson were also analyzed for the case of a $\mu^+\mu^-$ collider [9].

In the present study, the possibility of determining the relative contributions of scalar and pseudoscalar Higgs bosons to the $H\tau^+\tau^-$ and $Hb\bar{b}$ interaction vertices are explored for the reactions $e^+e^- \to \nu\bar{\nu}\tau^+\tau^-$ and $e^+e^- \to \nu\bar{\nu}b\bar{b}$ at the future linear electron–positron collider TESLA of total energy $\sqrt{s} = 500$ GeV and integrated luminosity 1 ab^{-1} [10]. It is assumed that, earlier, a Higgs boson will have been discovered at LHC, but a detailed determination of its CP nature will become the most immediate task of experiments at this linear collider.

In contrast to the studies reported in [11, 12], where the authors considered only the subprocesses of radiative Higgs boson production—for example, $e^+e^- \to Z^* \to ZH$—we analyze here all possible contributions to the processes $e^+e^- \to \nu\bar{\nu}\tau^+\tau^-$ and $e^+e^- \to \nu\bar{\nu}b\bar{b}$, where ν is an electron, a muon, or a tau-lepton neutrino. In particular, a special role of the channel featuring an electron neutrino, where the subprocess of gauge-boson fusion is dominant in Higgs boson production for $M_H < 180$ GeV at $\sqrt{s} \geq 500$ GeV, is emphasized.

The ensuing exposition is organized as follows. In Section 2, we present a general form of the interaction of a scalar (pseudoscalar) Higgs boson with fermions. In Sections 3 and 4, we quote the results obtained from an analysis of the processes $e^+e^- \to \nu\bar{\nu}b\bar{b}$ and $e^+e^- \to \nu\bar{\nu}\tau^+\tau^-$. The last section contains general conclusions and an outlook.

2. STRUCTURE OF $Hf\bar{f}$ INTERACTION

In extensions of the Standard Model that involve extra scalar and pseudoscalar bosons, the lightest spinless particle may be a combination of states that are not parity eigenstates [12]. In addition, it is reasonable to assume that the coupling constants characterizing the interaction of this scalar (pseudoscalar) Higgs boson with gauge bosons and fermions are independent parameters. In this case, the strength of $Hf\bar{f}$ interaction can be parametrized as

$$\frac{m_f}{v}(a + i\gamma_5 b), \qquad (1)$$

where $v = 246$ GeV and where, in the Standard Model, $a = 1$ and $b = 0$. Considering the processes $e^+e^- \to \nu\bar{\nu}\tau^+\tau^-$ and $e^+e^- \to \nu\bar{\nu}b\bar{b}$, we will investigate the case where a and b are independent free parameters and the cases where only one of these parameters deviates from the respective values in the Standard Model. It will be shown below that, in the case where a and b are independent, the resulting constraints on the model parameters appear to be insensitivity regions around the circle $\sqrt{a^2 + b^2} = 1$ in the ab plane.

It should be emphasized that data on the two processes in question (without allowance for the subsequent decays of tau leptons and b quarks) include not only a linear dependence on the parameter a, this dependence being specified by the contribution of the interference of diagrams involving Higgs boson exchange and background diagrams, but also a^2 and b^2 dependences, which are determined by the direct contribution of diagrams involving Higgs boson exchange. In view of this, searches for deviations from the predictions of the Standard Model—such as those that may arise in supersymmetric models—are possible even at the level of processes without the subsequent decays of τ and b.

An analysis of the processes involving the subsequent decays of tau leptons and b quarks will provide the possibility of studying P-odd correlations, which will make it possible to separate the contributions of the scalar and the pseudoscalar component of Higgs boson coupling to fermions and to determine the sign of the pseudoscalar component. Such an analysis will become the subject of subsequent publications.

In simulating the aforementioned processes by the Monte Carlo method, the differential distributions subjected to analysis were represented in the form of expansions in powers of the parameters a and b with coefficients equal to kinematical factors; that is,

$$\frac{d\sigma}{d\mathcal{O}} = A_0 + a \cdot A_1 + a^2 \cdot A_2 + ab \cdot A_3 + b \cdot A_4 + b^2 \cdot A_5 \ldots,$$

where $\mathcal{O}$ is a quantity observed experimentally and A_i are purely kinematical factors that arise upon squaring the amplitudes of the processes and performing integration over the phase space, which involve no dependence on the parameters a and b, and which are the subject of a direct Monte Carlo simulation. It will be shown below that $A_3 = A_4 = 0$ for the processes being considered.

The data were simulated with allowance for the special features of the TESLA project; the response of the detector was simulated by using the 3.01 version of the SIMDET version [13]. For both processes under study, the Higgs boson mass was set to the value of $M_H = 120$ GeV.

3. PROCESS $e^+e^- \to \nu\bar{\nu}b\bar{b}$

Within the Standard Model, the cross section for the reaction $e^+e^- \to \nu\bar{\nu}b\bar{b}$ is determined by the contributions of three main subprocesses involving an electron, a muon, and a tau-lepton neutrino in the final state:

(i) the subprocess $e^+e^- \to \nu_e\bar{\nu}_e b\bar{b}$ described by 23 Feynman diagrams (one diagram involving the radiative production of a Higgs boson, $Z^* \to ZH$; one diagram involving the production of a Higgs boson via fusion, $WW \to H$; and 21 background diagrams of the Standard Model);

(ii) the subprocess $e^+e^- \to \nu_\mu\bar{\nu}_\mu b\bar{b}$ described by 11 Feynman diagrams (one diagram involving the radiative production of a Higgs boson, $Z^* \to ZH$, and 10 background diagrams of the Standard Model);

(iii) the subprocess $e^+e^- \to \nu_\tau\bar{\nu}_\tau b\bar{b}$ described by 11 Feynman diagrams (one diagram involving the radiative production of a Higgs boson, $Z^* \to ZH$, and 10 background diagrams of the Standard Model).

At $M_H = 120$ GeV and $\sqrt{s} = 500$ GeV, the total cross section for the reaction $e^+e^- \to \nu\bar{\nu}b\bar{b}$ is determined by a dominant contribution of the subprocess involving an electron neutrino, the cross section for this subprocess being about 0.16 pb; the contribution of the remaining two subprocesses to the total cross section is at a level of 0.01 pb. The main reason for this is that, in the channel featuring an electron neutrino, there is a diagram that involves the fusion process $WW \to H$ in the central region and which makes a significant contribution to Higgs boson production, this contribution being a nondecreasing function of energy; at the same time, the remaining two channels of Higgs boson production are determined by the radiative-production process $e^+e^- \to Z^* \to HZ$.

In studying the process $e^+e^- \to \nu\bar{\nu}b\bar{b}$, we analyze a standard set of experimentally observable distributions—namely, the momentum and scattering-angle distributions of a b jet; the invariant-mass distribution of a pair of b jets; and, in addition, the distribution with respect to the quantity

$$T_{\rm cor} = \frac{1}{(\sqrt{s}/2)^3}\mathbf{p}_e \cdot [\mathbf{p}_b \times \mathbf{p}_{\bar{b}}],$$

which is highly sensitive to various possible CP-odd effects in the Higgs sector [14]. The above differential distributions of the cross section for the process $e^+e^- \to \nu\bar{\nu}b\bar{b}$ within the Standard Model are displayed in Figs. 1a–1d with allowance for the contributions from all three subprocesses (closed circles) and the contribution from only the subprocess involving the muon neutrino (crosses enclosed by circles). From these distributions, it can easily be seen that, as might have been expected, the cross section in question is dominated by the subprocess involving an electron neutrino, its cross section being an order of magnitude larger that the cross sections for the respective subprocesses involving a muon and a tau-lepton neutrino (where Higgs boson production is determined by the radiative-production mechanism, $e^+e^- \to Z^* \to ZH$). This circumstance gives every reason to hope that investigation of the electron channel of the reaction will make it possible to strengthen the constraints on the Hbb coupling constants considerably and to disperse the pessimism displayed in [11].

In determining the sensitivity of the process to the coupling constants of the Higgs boson, it is of importance to assess the relative contributions of signal and background diagrams (in the present case, these are diagrams involving a Higgs boson and those that do not involve it, respectively). By way of illustration, the differential distributions of the cross section for the process in question with respect to the b-jet scattering angle are displayed in Fig. 2 for (closed circles) the contribution of all Standard Model diagrams (both signal and background ones) and (crosses circumvented by circles) the contribution of diagrams featuring a Higgs boson, which include interference diagrams, these results being given for only the channel involving a muon neutrino (Fig. 2a) and for the sum of all three channels (Fig. 2b). From a comparison of Figs. 2a and 2b, one can see that not only is the cross section itself for the subprocess involving a muon neutrino small, but also the relative contribution of diagrams involving a Higgs boson are much less for this subrocess than for the subprocess involving an electron neutrino, where such a contribution is commensurate with the contribution of the background diagrams within the Standard Model.

In exploring the question of whether it is possible in principle to set constraints on the model parameters, it is interesting above all to analyze the sensitivity of the process under analysis to these parameters. Figure 3 shows the total cross section for the reaction $e^+e^- \to \nu\bar{\nu}b\bar{b}$ versus Δa and b, where $\Delta a = a - 1$. It can be seen from this figure that the dependence on the parameter b has the shape of a parabola that attains a minimum at $b = 0$, this confirming that the expansion of the total cross section features no term linear in b. A different situation is observed for the dependence on the parameter a (Δa). Here, the minimum of the parabola is shifted to the region of negative values of Δa, this indicating the presence of a term linear in a. In addition, the sensitivity of the cross section for the process in question is higher in the region of positive values of Δa; hence, it is natural to expect that the resulting constraints on the parameter a will be more stringent in this region [15]. The presence of terms linear in a is explained by the

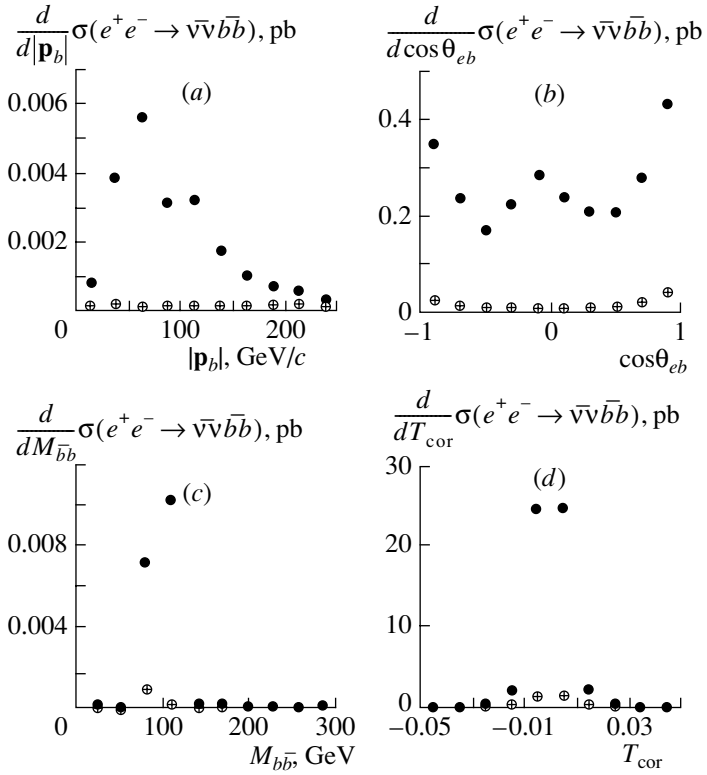

Fig. 1. Differential distributions of the cross section for the process $e^+e^- \to \nu\bar{\nu}b\bar{b}$ with respect to (*a*) the *b*-quark momentum, (*b*) *b*-quark scattering angle with respect to the direction of initial beams, (*c*) the $b\bar{b}$ invariant mass, and (*d*) the correlation $T_{\rm cor}$ for the Standard Model at $\sqrt{s} = 500$ GeV and $M_H = 120$ GeV: (•) contributions of three subprocesses involving ν_e, ν_μ, and ν_τ and ($\oplus$) contributions of the subprocess involving a muon neutrino.

interference between the diagrams involving a Higgs boson and the background diagrams in the Standard Model. No similar effect occurs for the parameter b since, in the respective vertex, this parameter is multiplied by an imaginary unit, with the result that the first powers of b are canceled in the interference terms

$$M_i M_j^\dagger + M_j M_i^\dagger.$$

Terms that are linear in the parameter b could arise owing to the emergence of the antisymmetric tensor $i\epsilon^{ijkl}$ upon evaluating the trace $\mathrm{tr}[\gamma_5\gamma_i\gamma_j\gamma_k\gamma_l]$, because this would lead to the cancellation of pure imaginary factors. In the process being considered, the number of independent momenta is insufficient, however; in all probability, this effect may emerge only upon taking into account the subsequent decays of b jets.

The sensitivity of the process in question to variations in the parameters Δa and b can be illustrated by considering the example of differential distributions. The distribution of the relevant cross section with respect to the b-jet scattering angle is displayed in Fig. 4 for (*a*) the channel involving a muon neutrino and (*b*) the sum of all channels, these results being given for the case of the Higgs boson in the Standard Model ($a = 1$, $b = 0$) and for the case of a pseudoscalar-boson admixture ($a = 0.5$, $b = 0.5$). It can easily be seen that the absolute value of the deviation associated with the variations in the parameters is about 0.001 for the muon-neutrino channel and is about 0.1 for the total distribution nearly over the entire kinematical region. This confirms once again the importance of the contribution from the subprocess featuring an electron neutrino.

In setting constraints on the coupling constants a and b, it is also of importance to find experimental observables that are the most sensitive to these parameters. For this, it is reasonable to analyze the so-called sensitivity function

$$S = \frac{\sigma_i^{\rm SM} - \sigma_i^{\rm NEW}}{\Delta\sigma_i^{\rm expt}}, \qquad (2)$$

which is constructed for each bin of the distribution under study. In the definition of the sensitivity function in (2), $\sigma_i^{\rm SM}$ is the value of this distribution within the Standard Model ($a = 1$, $b = 0$) in the ith bin, $\sigma_i^{\rm NEW}$ is the value of the distribution in the ith bin when one parameter or both of them deviate from their

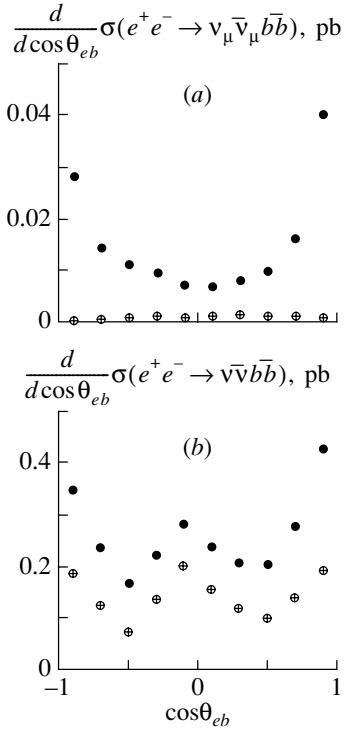

Fig. 2. Differential distributions of the cross section for the process $e^+e^- \to \nu\bar{\nu}b\bar{b}$ with respect to the b-jet scattering angle for (a) the channel involving a muon neutrino and (b) the sum of all three channels: (•) contribution of all diagrams in the Standard Model (both signal and background ones) and (⊕) contribution of diagrams involving Higgs boson exchange, including the interference diagrams.

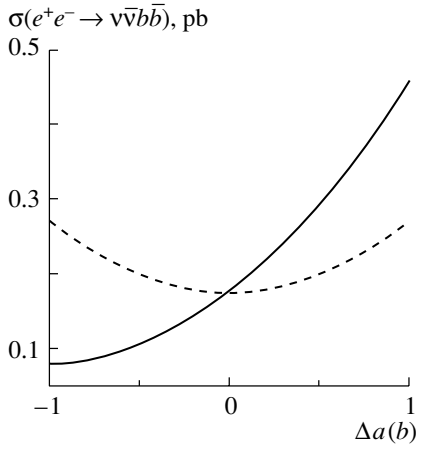

Fig. 3. Total cross section for the reaction $e^+e^- \to \nu\bar{\nu}b\bar{b}$ versus the parameters (solid curve) Δa and (dashed curve) b.

Standard Model values, and $\Delta\sigma_i^{\text{expt}}$ is the expected value of the experimental error in the ith bin (an algorithm for calculating this error is given below). For

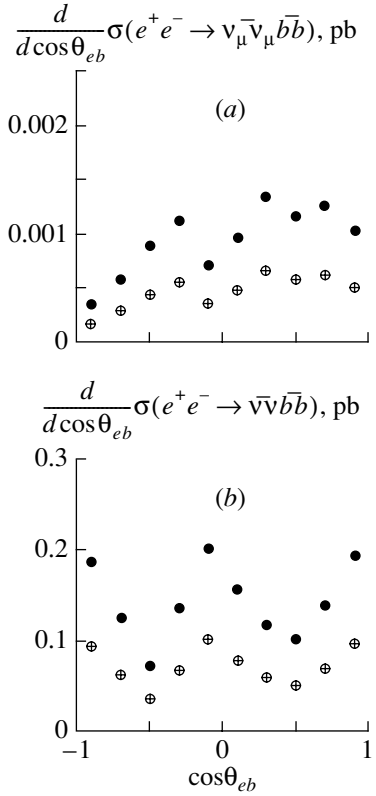

Fig. 4. Differential distribution of the cross section for the process $e^+e^- \to \nu\bar{\nu}b\bar{b}$ with respect to the b-jet scattering angle with allowance for (a) only the channel involving a muon neutrino and (b) all three channels: (•) contribution of the Higgs boson within the Standard Model ($a = 1$, $b = 0$) and (⊕) results including the contribution from a pseudoscalar-boson admixture ($a = 0.5$, $b = 0.5$).

each of the distributions subjected to analysis, Fig. 5 shows the sensitivity function constructed in the way outlined above. For the purposes of illustration, the case of $a = 1$ and $b = 0.5$ is chosen to exemplify new physics. In calculating the experimental error in a bin, use was made of the integrated-luminosity value of $\int \mathcal{L}dt = 1\ \text{ab}^{-1}$. Closed circles represent the values of the function S for the total distribution, while crosses enclosed by circles correspond to the muon-neutrino channel. It can be seen that the highest sensitivity is achieved for the distribution with respect to the b-jet scattering angle, in which case S varies around a virtually constant high level over the entire kinematical region; for the other observables, either the function S is small, or its maximum is localized in an extremely narrow region of the phase space. The example of the behavior of the function S highlights once again the importance of the electron-neutrino channel (involving WW fusion), which significantly enhances the effect from the variations in the parameters being considered. This behavior of the function

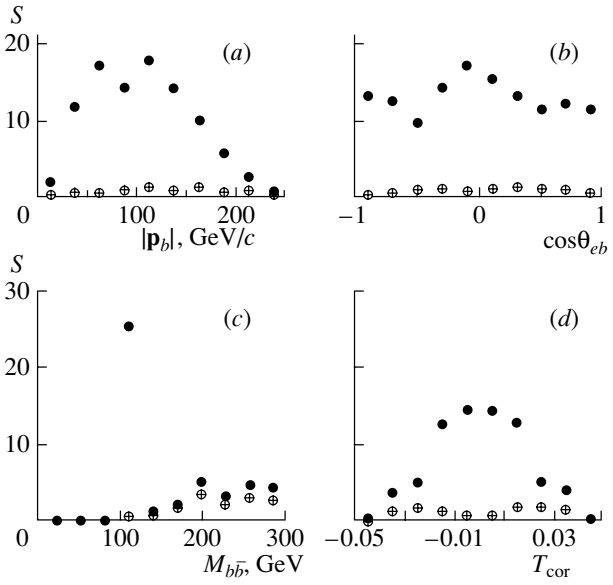

Fig. 5. Sensitivity function at $a = 1$ and $b = 0.5$ for the distributions with respect to (a) the momentum of the b quark, (b) its scattering angle, (c) the invariant mass of the $b\bar{b}$ pair, and (d) the correlation T_{cor}: ($\bullet$) values of this function for the total distribution with allowance for all three subprocesses and ($\oplus$) analogous results for the subprocess involving a muon neutrino.

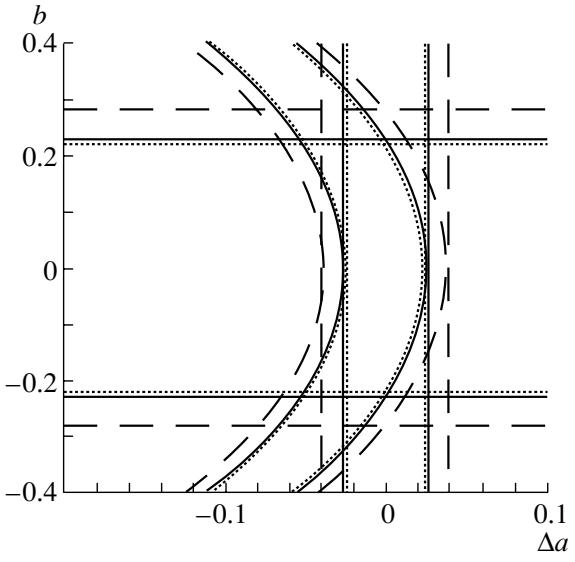

Fig. 6. Allowed regions of the parameters a and b at $\sqrt{s} =$ 500 GeV for the Higgs boson mass of $M_H = 120$ GeV. In the case where the parameters Δa and b are considered to be independent, the allowed region at a confidence level of 95% is bounded by concentric curves. The region between the horizontal straight lines is the region that is allowed for the parameter b at $\Delta a = 0$. The region between the vertical straight lines is that which is allowed for the parameter a at $b = 0$. The cases of the integrated luminosity equal to 100 fb^{-1}, 1 ab^{-1}, and 10 ab^{-1} are represented by the dashed, solid, and dotted lines, respectively.

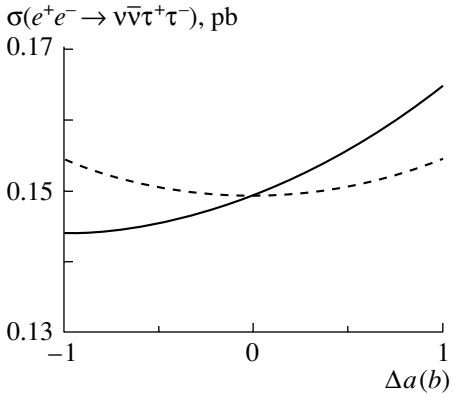

Fig. 7. Total cross section for the reaction $e^+e^- \to \nu\bar{\nu}\tau^+\tau^-$ versus the parameters (solid curve) Δa and (dashed curve) b.

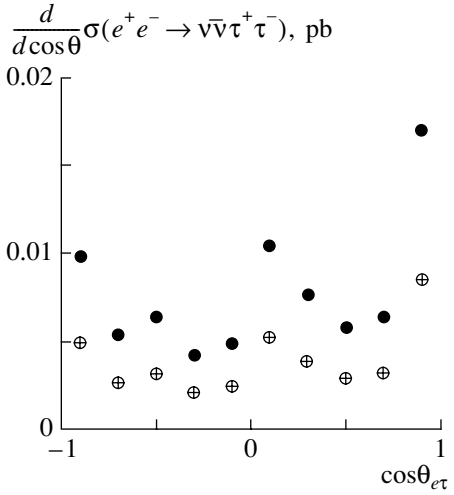

Fig. 8. Differential cross section for the reaction $e^+e^- \to \nu\bar{\nu}\tau^+\tau^-$ with respect to the tau-lepton scattering angle for ($\bullet$) the case of the Higgs boson contribution within the Standard Model ($a = 1, b = 0$) and ($\oplus$) for the case of $a = 0.5$ and $b = 0.5$.

S also gives reason to hope for results that are not as pessimistic as in [11].

The problem of suppressing the contributions from background processes is an important point in such investigations. For the reaction $e^+e^- \to \nu\bar{\nu}b\bar{b}$, background processes include $e^+e^- \to e^+e^-ZZ \to e^+e^-b\bar{b}\nu\bar{\nu}$ (where the final-state electron–positron pair is undetected), $e^+e^- \to \nu\bar{\nu}W^+W^- \to \nu\bar{\nu}b\bar{b}\nu\bar{\nu}$, and $e^+e^- \to ZZZ \to b\bar{b}\nu\bar{\nu}\nu\bar{\nu}$. As was shown in [16], however, either the cross sections for these processes are extremely small, or their contribution can be suppressed to a level of 0.2 fb.

In order to determine, for the parameters a and b, the regions that can be excluded on the basis of

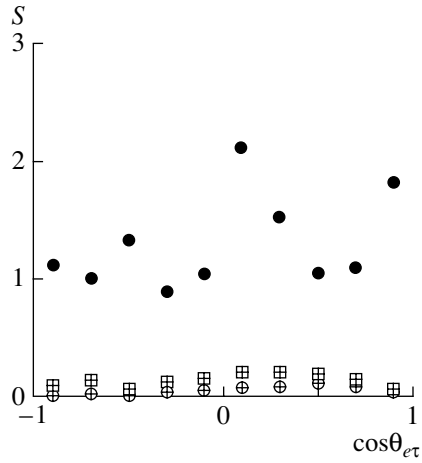

Fig. 9. Sensitivity function for $a = 1$ and $b = 0.5$ at $\sqrt{s} = 500$ GeV and the integrated luminosity of $\int \mathcal{L}dt = 1$ ab^{-1}. Points represent the values of the function for the contribution of (•) all three subprocesses, (⊞) the channel involving the tau-lepton neutrino, and (⊕) the muon-neutrino channel.

data from experiments at a future linear collider, we use a conventional χ^2 method, where the expected experimental error $\Delta\sigma_i^{\text{expt}}$ is defined as

$$\Delta\sigma_i^{\text{expt}} = \sigma_i^{\text{SM}}\sqrt{\delta_{\text{syst}}^2 + \delta_{\text{stat}}^2}, \qquad (3)$$

where the statistical error in a bin of the distribution being considered is given by

$$\delta_{\text{stat}} = \frac{1}{\sqrt{\sigma_i^{\text{SM}}\varepsilon_{b\bar{b}}\int \mathcal{L}dt}}, \qquad (4)$$

with $\varepsilon_{b\bar{b}}$ being the efficiency of reconstruction of a pair of b jets. The analysis performed in [16] revealed that the use of the b-trigger algorithm in reconstructing b jets will make it possible to reach the efficiency of $\varepsilon_{b\bar{b}} = 56\%$. The systematic error receives contributions from the detector resolution, the uncertainty in measuring the luminosity (about 0.5%), the errors in separating background processes, and some other effects.

From an analysis of various kinematical distributions for the process being studied, it was found that the most stringent constraints on the model parameters can be obtained from data on the differential distribution with respect to the scattering angle of b jets in the case where the kinematical region is broken down into ten bins, this confirming the conclusions drawn from the above analysis of the sensitivity function.

For the parameters a and b, the regions that can excluded on the basis of data from experiments at the TESLA collider [10] are shown in Fig. 6 for the total energy of $\sqrt{s}$ =500 GeV and the Higgs boson mass of $M_H = 120$ GeV. For the case where the parameters Δa and b are taken to be independent, the allowed region at a confidence level of 95% is bounded by the concentric curves. The region between the horizontal straight lines is the region allowed for the parameter b at $\Delta a = 0$. The region between the vertical straight lines is that which is allowed for the parameter a at $b = 0$. The cases of the integrated luminosity equal to 100 fb^{-1}, 1 ab^{-1}, and 10 ab^{-1} are represented by the dashed, solid, and dotted lines, respectively.

The resulting constraints on the parameters a and b can be written as

$$-0.041 \le \Delta a \le 0.039 \text{ for } \int \mathcal{L}dt = 100 \text{ fb}^{-1}, \quad (5)$$
$$-0.026 \le \Delta a \le 0.027 \text{ for } \int \mathcal{L}dt = 1 \text{ ab}^{-1},$$
$$-0.024 \le \Delta a \le 0.024 \text{ for } \int \mathcal{L}dt = 10 \text{ ab}^{-1}$$

in the case of $b = 0$ and free Δa and as

$$-0.28 \le b \le 0.28 \text{ for } \int \mathcal{L}dt = 100 \text{ fb}^{-1}, \qquad (6)$$
$$-0.23 \le b \le 0.23 \text{ for } \int \mathcal{L}dt = 1 \text{ ab}^{-1},$$
$$-0.22 \le b \le 0.22 \text{ for } \int \mathcal{L}dt = 10 \text{ ab}^{-1}$$

in the case of $\Delta a = 0$ and free b. For the case of Higgs boson masses around $M_H = 120$ GeV, these results can be approximated to a high precision by means of the multiplication of these constraints by the factor $(M_H/120 \text{ GeV})^2$.

4. PROCESS $e^+e^- \to \nu\bar{\nu}\tau^+\tau^-$

The process $e^+e^- \to \nu\bar{\nu}\tau^+\tau^-$, where $\nu = \nu_e, \nu_\mu, \nu_\tau$, receives contributions from

(i) the subprocess $e^+e^- \to \nu_e\bar{\nu}_e\tau^+\tau^-$, which is described by 21 Feynman diagrams (one diagram involving the radiative production of the Higgs boson, $Z^* \to ZH$; one diagram involving Higgs boson production via the fusion process $WW \to H$; and 19 background diagrams of the Standard Model);

(ii) the subprocess $e^+e^- \to \nu_\mu\bar{\nu}_\mu\tau^+\tau^-$, which is described by 11 Feynman diagrams (one diagram involving the radiative production of a Higgs boson, $Z^* \to ZH$, and ten background diagrams of the Standard Model);

(iii) the subprocess $e^+e^- \to \nu_\tau\bar{\nu}_\tau\tau^+\tau^-$, which is described by 20 Feynman diagrams (one diagram involving the radiative production of a Higgs boson, $Z^* \to ZH$, and 19 background diagrams of the Standard Model).

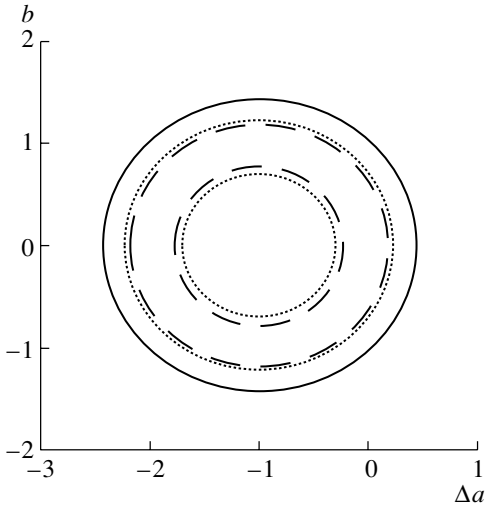

Fig. 10. Regions allowed for the parameters a and b for $\int \mathcal{L}dt =$ (region bounded by the solid curve) 100 fb^{-1}, (region bounded the dotted curves) 1 ab^{-1}, and (region bounded by the dashed curves) 10 ab^{-1}.

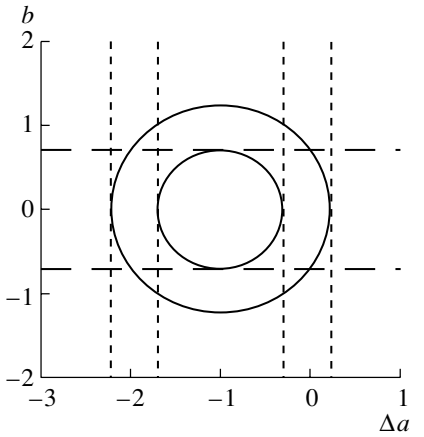

Fig. 11. Region allowed for the parameters a and b ($\sqrt{s} =$ 500 GeV, $\int \mathcal{L}dt = 1$ ab^{-1}, $M_H = 120$ GeV) at a confidence level of 95% for the cases of (region bounded by the solid curves) independent parameters a and b, (region between the vertical straight lines) a fixed parameter b ($b = 0$), and (region between the horizontal straight lines) a fixed parameter Δa ($\Delta a = 0$).

At $\sqrt{s} = 500$ GeV and $M_H = 120$ GeV, the total cross section summed over all three of the above subprocesses is $\sigma \simeq 0.17$ pb; in just the same way as in the case of b-quark production, the channel featuring an electron neutrino in the final state is dominant.

Figure 7 shows the total cross section for the reaction $e^+e^- \to \nu\bar{\nu}\tau^+\tau^-$ (sum over all three channels) versus the parameters Δa and b, where $\Delta a = a - 1$. In just the same way as in the case of b-quark production, the dependence on the parameter b has the shape of a parabola attaining a minimum at $b = 0$; the dependence on the parameter a also has a quadratic character, but the minimum of the respective parabola is shifted to the region of negative values of Δa, this again indicating the presence of a term linear in a. Comparing Figs. 3 and 7, we can see that the sensitivity of the process $e^+e^- \to \nu\bar{\nu}b\bar{b}$ to variations in the parameters a and b is lower, which is due largely to the distinction between the b-quark and the tau-lepton mass.

In many respects, the behavior of the differential distributions of the cross section for the process $e^+e^- \to \nu\bar{\nu}\tau^+\tau^-$ is similar to that in the case of the process $e^+e^- \to \nu\bar{\nu}b\bar{b}$. As before, the Higgs boson contribution to the total distribution reproduces the shape of the distribution within the Standard Model, but the magnitude of the distribution is much smaller. A lower sensitivity of the process $e^+e^- \to \nu\bar{\nu}\tau^+\tau^-$ to the contribution of diagrams involving Higgs boson exchange also affects the relative sensitivity of the distributions to variations in the parameters a and b. The differential distribution of the cross section for the reaction $e^+e^- \to \nu\bar{\nu}\tau^+\tau^-$ with respect to the tau-lepton scattering angle is displayed in Fig. 8 for (closed circles) the case of the Higgs boson contribution within the Standard Model ($a = 1$, $b = 0$) and (crosses enclosed by circles) the case of $a = 0.5$ and $b = 0.5$.

In just the same way as in the case of the process $e^+e^- \to \nu\bar{\nu}b\bar{b}$, the differential distribution of the cross section with respect to the tau-lepton scattering angle shows the highest sensitivity to variations in the parameters a and b. For the case of $a = 1$ and $b = 0.5$, the behavior of the sensitivity function defined in (2) is illustrated in Fig. 9 for $\sqrt{s} = 500$ GeV and the integrated luminosity of $\int \mathcal{L}dt = 1$ ab^{-1}. Closed circles represent the values of this function for the case where all three subprocesses are taken into account, while crosses enclosed by boxes and circles correspond to the channels involving a tau-lepton and a muon neutrino, respectively. It can easily be seen that, as before, the electron-neutrino channel is dominant and that it has the strongest effect on the sensitivity of the total process.

A particular role of the differential distribution with respect to the tau-lepton scattering angle is also due to the fact that, in relation to the case of b jets in the final state, the reconstruction of tau leptons in the final state is more difficult, but, in contrast to what must be done for other distributions, only the reconstruction of the direction of the tau-lepton momentum is required for the distribution with respect to $\cos\theta_{e\tau}$.

In the ensuing analysis, we assume that a tau-lepton pair in the final state can be reconstructed in an experiment studying tau-lepton decay into π and ρ mesons. The channels $\tau \to \pi\nu$ and $\tau \to \rho\nu$

are the most important decay modes; taken together, they contribute 13% to the branching fraction of the decay of a τ pair. As was shown in investigations at LEP/SLC, the inclusion of other channels—such as $\tau^\pm \to \pi^-\pi^+\pi^\pm\nu$ and $\tau^\pm \to \pi^0\pi^0\pi^\pm\nu$—along with the leptonic modes of tau-lepton decay, may increase the statistics of tau-lepton decays to 82%.

There are several basic methods that can be used to reconstruct tau-lepton pairs in the final state [4b, 17]. A new method that makes it possible to achieve a high reconstruction efficiency was recently proposed in [18]. This method is based on an analysis of the decay chain $\tau^\pm \to \rho^\pm\bar{\nu}_\tau(\nu_\tau)$, $\rho^\pm \to \pi^\pm\pi^0$. The method was used in [19] to study the CP nature of the Higgs boson in the channel $\tau \to \rho\nu$.

The results obtained by analyzing experimental data from LEP (see, for example, [20]) indicate that the efficiency of reconstruction of tau leptons varies between 51 and 80%. For the ensuing analysis of the process $e^+e^- \to \nu\bar{\nu}\tau^+\tau^-$, we will take a conservative estimate of the efficiency of reconstruction of a τ pair, $\varepsilon_{\tau\tau} = 50\%$.

Investigation of contributions from possible background processes—such as $e^+e^- \to e^+e^-ZZ \to e^+e^-\tau^+\tau^-\nu\bar{\nu}$ (where the final-state electron–positron pair escaped detection), $e^+e^- \to \nu\bar{\nu}W^+W^- \to \nu\bar{\nu}\tau^+\tau^-\nu\bar{\nu}$, and $e^+e^- \to ZZZ \to \tau^+\tau^-\nu\bar{\nu}\nu\bar{\nu}$—is yet another important facet of the present analysis. However, the behavior and the magnitude of the cross sections for these processes are similar to the behavior and the magnitude of the cross sections for the analogous background processes associated with the reaction $e^+e^- \to \nu\bar{\nu}b\bar{b}$, so that the inclusion of the contributions from the background reactions in question does not involve particular technical difficulties [16].

In studying, for the parameters a and b, the regions that can be excluded on the basis of data from experiments at a future electron–positron collider of total energy $\sqrt{s} = 500$ GeV, the following comment concerning the dependence of the resulting constraints on the integrated luminosity of the collider is in order. The regions allowed for the parameters a and b are shown in Fig. 10 for (region bounded by the solid curve) $\int \mathcal{L}dt = 100\ \text{fb}^{-1}$, (region bounded by the dotted curves) 1 ab^{-1}, and (region bounded by the dashed lines) 10 ab^{-1}. In contrast to what occurs in the case of the process $e^+e^- \to \nu\bar{\nu}b\bar{b}$, an inner contour does not arise here at the integrated luminosity of 100 fb^{-1}, so that the allowed region has the shape of a circle [21]. This distinction is a direct corollary of a lower sensitivity of the process $e^+e^- \to \nu\bar{\nu}\tau^+\tau^-$ to variations in the parameters being considered.

For $\sqrt{s} = 500$ GeV, $\int \mathcal{L}dt = 1\ \text{ab}^{-1}$, and $M_H = 120$ GeV, the region allowed for the parameters a and b at a confidence level of 95% is displayed in Fig. 11 for (region bounded by the solid curves) the case where the parameters a and b are independent, (region between the vertical straight lines) the case of the parameter b fixed at $b = 0$, and (region between the horizontal straight lines) the case of the parameter a fixed in such a way that $\Delta a = 0$. On the basis of the assumption that the Standard Model is valid in principle, so that effects of new physics can manifest themselves only in the form of small deviations from the predictions of the Standard Model (within the experimental error), the left region in the case of $b = 0$ can be excluded as an unphysical one.

For the case of $\int \mathcal{L}dt = 1\ \text{ab}^{-1}$, the corresponding constraints can then be written as follows:

(i) in the case of two independent parameters,

$$(0.70)^2 \le (\Delta a + 1)^2 + b^2 \le (1.23)^2;$$

(ii) in the case of $b = 0$ and free Δa,

$$-0.32 \le \Delta a \le 0.24; \qquad (7)$$

(iii) in the case of $\Delta a = 0$ and free b,

$$-0.73 \le b \le 0.73. \qquad (8)$$

For the case of Higgs boson masses around $M_H = 120$ GeV, these results can also be approximated by means of the multiplication of the respective constraints by the factor $(M_H/120\ \text{GeV})^2$.

It can be seen that the constraints in (7) and (8) are one order of magnitude more lenient than those that are given in (5) and (6) and which were derived from the analysis of the process $e^+e^- \to \nu\bar{\nu}b\bar{b}$, this being explained by a smaller Yukawa coupling constant of the Higgs boson.

5. CONCLUSION

The possibility of discovering a scalar Higgs boson in studying the processes $e^+e^- \to \nu\bar{\nu}b\bar{b}$ and $e^+e^- \to \nu\bar{\nu}\tau^+\tau^-$ in experiments at a future linear collider has been explored in the present study. It has been shown that the sensitivity of these processes to variations in the $Hb\bar{b}$ and $H\tau^+\tau^-$ coupling constants is determined by the contribution of the fusion subprocess $WW \to H$.

It has also been found that experiments at future colliders will provide the possibility of either discovering the presence of a pseudoscalar state of the Higgs boson or imposing stringent constraints on the region allowed for the coupling constants.

In particular, data on the process $e^+e^- \to \nu\bar{\nu}b\bar{b}$ from the future linear collider TESLA of integrated

luminosity $\int \mathcal{L}dt = 1$ ab^{-1} and total energy $\sqrt{s} =$ 500 GeV would make it possible to constrain the region of the parameters a and b at a level of a few percent (at free a and fixed b) and at a level of ten percent (for free b and fixed a):

$$-0.026 \leq \Delta a \leq 0.027,$$
$$-0.23 \leq b \leq 0.23.$$

These results are commensurate with the results of the analysis performed in [10], where a global fit at $\int \mathcal{L}dt = 500$ fb^{-1} and $\sqrt{s} = 500$ GeV predicted the relative precision in determining the Yukawa coupling constant g_{Hbb} at a level of 2.2%.

In conclusion, we would like to make a few comments concerning future experiments. Let us assume that data from a future collider will reveal the presence of a deviation from the predictions of the Standard Model in processes involving a Higgs boson. In addition, we assume that data from independent measurements of the partial Higgs boson widths $\Gamma_{H\to b\bar{b}}$ and $\Gamma_{H\to\tau^+\tau^-}$ are available, for example, from data on the resonance production of a Higgs boson at a muon collider. It can easily be seen that, if use is made of the parametrization in (1), as is done here, the partial widths of the Higgs boson are $\Gamma_{H\to f\bar{f}} \sim (a^2 + b^2)$; at the same time, the observables explored here exhibit a different dependence:

$$\frac{d\sigma}{d\mathcal{O}} = A_0 + a \cdot A_1 + a^2 \cdot A_2 + b^2 \cdot A_3.$$

By combining the results obtained by studying the processes $e^+e^- \to \nu\bar{\nu}b\bar{b}(\nu\bar{\nu}\tau^+\tau^-)$ with data from a measurement of the partial widths $\Gamma_{H\to b\bar{b}(H\to\tau^+\tau^-)}$, it is then possible to separate the contributions of the scalar and pseudoscalar coupling constants a and b, whereby one obtains direct information about the CP origin of the Higgs sector.

ACKNOWLEDGMENTS

We are grateful to Claudio Dib for stimulating discussions and enlightening comments.

This work was supported by FAPESP (grant no. 2001/06391-4), the Russian Foundation for Basic Research (project nos. 99-02-16558, 00-15-96645), the Ministry for Higher Education of the Russian Federation (project no. E00-3.3-62), and CRDF (grant no. MO-011-0). The work of R. Rosenfeld was supported in part by FAPESP and CNPq.

REFERENCES

1. C. T. Hill and E. H. Simmons, hep-ph/0203079, and references therein.
2. J. R. Dell'Aquila and C. A. Nelson, Nucl. Phys. B **320**, 61, 86 (1989).
3. B. K. Bullock, K. Hagiwara, and Alan D. Martin, Phys. Lett. B **273**, 501 (1991); Nucl. Phys. B **395**, 499 (1993).
4. (a) B. Grzadkowski and J. F. Gunion, Phys. Lett. B **294**, 361 (1992); (b) M. Krämer, J. Kühn, M. L. Stong, and P. M. Zerwas, Z. Phys. C **64**, 21 (1994); J. F. Gunion and J. G. Kelly, Phys. Lett. B **333**, 110 (1994).
5. K. Hagiwara and M. L. Stong, Z. Phys. C **62**, 99 (1994); D. J. Miller, S. Y. Choi, B. Eberle, *et al.*, Phys. Lett. B **505**, 149 (2001); V. Barger, K. Cheung, A. Djouadi, *et al.*, Phys. Rev. D **49**, 79 (1994); K. Hagiwara, S. Ishihara, J. Kamoshita, and B. A. Kniehl, Eur. Phys. J. C **14**, 457 (2000); T. Han and J. Jiang, Phys. Rev. D **63**, 096007 (2001).
6. T. Plehn, D. Rainwater, and D. Zeppenfeld, Phys. Rev. Lett. **88**, 051801 (2002).
7. J. F. Gunion and J. Pliszka, Phys. Lett. B **444**, 136 (1998).
8. J. F. Gunion, B. Grzadkowski, and X.-G. He, Phys. Rev. Lett. **77**, 5172 (1996).
9. D. Atwood and A. Soni, Phys. Rev. Rev. D **52**, 6271 (1995); V. D. Barger, M. S. Berger, J. F. Gunion, and T. Han, Phys. Rep. **286**, 1 (1997); V. D. Barger, T. Han, and C.-G. Zhou, Phys. Lett. B **480**, 140 (2000); B. Grzadkowski, J. F. Gunion, and J. Pliszka, Nucl. Phys. B **583**, 49 (2000).
10. R.-D. Heuer *et al.*, hep-ph/0106315.
11. G. Bower, *Talk Presented at the Linear Collider Workshop, Chicago, January 7–9, 2002.*
12. B. Grzadkowski and J. F. Gunion, Phys. Lett. B **350**, 218 (1995); B. Grzadkowski, J. F. Gunion, and J. Kalinowski, Phys. Rev. D **60**, 075011 (1999).
13. M. Pohl and H. J. Schreiber, Report DESY 99-030.
14. V. Braguta, A. Chalov, and A. Likhoded, Phys. Rev. D **65**, 054038 (2002).
15. V. Braguta, A. Chalov, A. Likhoded, and R. Rosenfeld, hep-ph/0208133.
16. K. Desch and N. Meyer, LC Notes, LC-PHSM-2001-025 (http://www.desy.de/lcnotes/2001/025/ww-fus.ps.gz).
17. T. Pierzchala, E. Richter-Was, Z. Was, and M. Worek, Acta Phys. Polon. B **32**, 1277 (2001).
18. Z. Was and M. Worek, hep-ph/0202007.
19. G. R. Bower *et al.*, hep-ph/0204292.
20. DELPHI Collab., Nucl. Phys. B (Proc. Suppl.) **98**, 191 (2001).
21. A. Chalov, A. Likhoded, and R. Rosenfeld, hep-ph/0205146.

Translated by A. Isaakyan

Physics of Atomic Nuclei, Vol. 67, No. 2, 2004, pp. 306–313. Translated from Yadernaya Fizika, Vol. 67, No. 2, 2004, pp. 324–331.

ELEMENTARY PARTICLES AND FIELDS
Theory

Generalized Amplitude of an n-Vertex One-Loop Process in a Strong Magnetic Field

A. V. Kuznetsov*, N. V. Mikheev, and D. A. Rumyantsev*****

Yaroslavl State University, Sovetskaya ul. 14, Yaroslavl, 150000 Russia

Received July 24, 2002; in final form, February 3, 2003

Abstract—A general analysis of the amplitude for an n-vertex one-loop process in a strong magnetic field is performed by using the asymptotic form of the electron propagator in a field. With an eye to applications of the results obtained in the present study, the analysis is performed for photon–neutrino processes, where one of the vertices is taken in a general form [a scalar (S), a pseudoscalar (P), a vector (V), or an axial (A) one], while the other vertices have a vector form. It is shown that, for an odd number of vertices, only an amplitude of the $SV_1 \dots V_{n-1}$ form grows linearly with increasing magnetic-field strength, but that only $PV_1 \dots V_{n-1}$, $VV_1 \dots V_{n-1}$, and $AV_1 \dots V_{n-1}$ amplitudes show a linear growth for an even number of vertices. For the processes $\gamma\gamma \to \nu\bar{\nu}$ (within models featuring an effective scalar $\nu\nu ee$ coupling) and $\gamma\gamma \to \nu\bar{\nu}\gamma$ (within the Standard Model), general expressions are obtained for the amplitudes at arbitrary values of particle energies. The cross section for the process $\gamma\gamma \to \nu\bar{\nu}\gamma$ is obtained in the limiting case of high photon energies. © *2004 MAIK "Nauka/Interperiodica".*

1. INTRODUCTION

At the present time, interest in astrophysical objects where a magnetic field of strength in excess of the critical value of $B_e = m^2/e \simeq 4.41 \times 10^{13}$ G[1)] can arise is still rather keen. Such objects include so-called magnetars, which are neutron stars featuring a magnetic field of strength about 4×10^{14} G [1, 2]. The possible mechanisms of generation of astrophysical magnetic fields of strength $B \gg B_e$ (up to 10^{17}–10^{18} G [3–6]) are also discussed in the literature. There are reasons to believe that fields of strength on the order of 10^{24} G could exist in the early Universe (see [7] and references therein).

The understanding of a decisive role of quantum processes in the dynamics of some astrophysical objects (such as supernovas) has given a strong impetus to advances in elementary-particle astrophysics, which is one of the vigorously developing branches of the physical sciences. Of particular interest is investigation of the effect that a strong external field exerts on quantum processes, since not only is a strong field sometimes able to catalyze various processes, changing their kinematics substantially, but it can also induce new interactions. It is especially important to take into account the effect of an external field on loop quantum processes where initial and final states involve only electrically neutral particles—for example, photons and neutrinos, as well as hypothetical axions and familons. The effect of an external field on such processes is associated with the following two factors: (i) Virtual charged fermions are sensitive to the effect of a field. (ii) A strong magnetic field changes significantly the dispersion properties of photons and, hence, their kinematics.

Investigation of photon–neutrino loop processes has a rather long history. Two-vertex loop processes, including the transition $\gamma \to \gamma$ (photon polarization operator in an external field), the decay $\gamma \to \nu\bar{\nu}$, and the transition $\nu \to \nu\gamma$ (which is also referred to as the neutrino Cherenkov process), were studied by various authors (see, for example, [8–15] and references therein). The most general expression for a two-vertex loop amplitude of the form $j \to f\bar{f} \to j'$ in a constant uniform magnetic field and in a crossed field was obtained in [16], where all possible combinations of scalar, pseudoscalar, vector, and pseudovector interactions of the generalized currents j and j' with fermions were considered.

The splitting of a photon into two photons in a magnetic field ($\gamma \to \gamma\gamma$)—it is forbidden in a vacuum—is a three-vertex loop process that has attracted the attention of theorists for many years. The review article of Papanyan and Ritus [17] on this process contains an extensive list of references to earlier studies devoted to the subject in question;

*e-mail: avkuzn@uniyar.ac.ru
**e-mail: mikheev@uniyar.ac.ru
***e-mail: rda@uniyar.ac.ru

1)Here, we use the natural system of units where $c = \hbar = 1$; m is the electron mass. Throughout this article, $e > 0$ stands for an elementary charge.

among more recent studies, we would like to mention those that are reported in [18–22]. The conversion of a photon pair into a neutrino pair, $\gamma\gamma \to \nu\bar{\nu}$, is yet another three-vertex loop processes, which is of interest as a possible channel of the cooling of stars. A detailed review of studies devoted to this process can be found, for example, in our recent article [23].

Since, in accordance with the Gell-Mann theorem [24], the process $\gamma\gamma \to \nu\bar{\nu}$ is strongly suppressed in a vacuum, the four-vertex loop process $\gamma\gamma \to \nu\bar{\nu}\gamma$, which involves an additional photon, was considered in a number of studies. Despite an extra factor α, the latter process has a higher probability than the respective two-photon process. The process $\gamma\gamma \to \nu\bar{\nu}\gamma$ was investigated both in a vacuum [25–30] and in a strong magnetic field at low photon energies [31–33], which has a stimulating effect.

Thus, the problem of calculating the amplitude of an n-vertex one-loop quantum process in a strong external magnetic field is of importance since the results of such calculations can be used to analyze the processes $\gamma\gamma \to \nu\bar{\nu}$ and $\gamma\gamma \to \nu\bar{\nu}\gamma$, which are of interest for astrophysics, and axion and familon processes like $\gamma\gamma \to \gamma a$ and $\gamma\gamma \to \gamma\Phi$.

The ensuing exposition is organized as follows. In Section 2, we perform a general analysis of the amplitude for an n-vertex one-loop process in a strong magnetic field. In Section 3, we calculate the amplitude where one of the vertices is taken in a general form [a scalar (S), a pseudoscalar (P), a vector (V), or an axial (A) amplitude], while the remaining vertices are taken in a vector form and are associated with photons. This amplitude is the main result of this study. In Sections 4 and 5, we present explicit analytic expressions for the amplitudes of the processes $\gamma\gamma \to \nu\bar{\nu}$ and $\gamma\gamma \to \nu\bar{\nu}\gamma$, respectively, these expressions reducing, in the limit of low energies, to the formulas available in the literature. The cross section for the process $\gamma\gamma \to \nu\bar{\nu}\gamma$ in the limiting case of high photon energies is obtained for the first time. In the Conclusion, we summarize the main results of this study.

2. GENERAL ANALYSIS OF AN n-VERTEX ONE-LOOP PROCESS IN A STRONG MAGNETIC FIELD

We start from an effective Lagrangian for the interaction of the generalized currents j and electrons in the form

$$\mathcal{L}(x) = \sum_i g_i[\bar{\psi}_e(x)\Gamma_i\psi_e(x)]j_i(x), \qquad (1)$$

where the generalized index $i = S, P, V, A$ labels the matrices Γ_i in such a way that $\Gamma_S = 1$, $\Gamma_P = \gamma_5$, $\Gamma_V = \gamma_\alpha$, and $\Gamma_A = \gamma_\alpha\gamma_5$; j is the corresponding quantum object, a current (j_S, j_P, $j_{V\alpha}$, or $j_{A\alpha}$) or the photon-field vector; g_i are coupling constants; and $\psi_e(x)$ is an exact solution to the Dirac equation for electrons in a constant external magnetic field. In particular, we have $g_V = e$ and $\Gamma_V = \gamma_\alpha$ for electron–photon interaction, $j_{V\alpha}(x)$ having the meaning of the vector potential of the photon electromagnetic field.

The fermion propagator in a magnetic field can be represented in the form [34]

$$S(x_1, x_2) = e^{i\Phi(x_1,x_2)}\hat{S}(x_1 - x_2), \qquad (2)$$

$$\Phi(x_1, x_2) = -e\int_{x_1}^{x_2} d\xi_\mu \left[A_\mu(\xi) + \frac{1}{2}F_{\mu\nu}(\xi - x_2)_\nu\right], \qquad (3)$$

where A_μ is the 4-potential and $F_{\mu\nu}$ is the strength tensor of the constant uniform external magnetic field. The translation-invariant part of the propagator, $\hat{S}(x_1 - x_2)$, admits various representations. For our purposes, it is convenient to use its asymptotic expression in the limit $eB/|m^2 - p_\parallel^2| \gg 1$ [35, 36]; that is,

$$\hat{S}(X) \simeq \frac{ieB}{2\pi}\exp\left(-\frac{eBX_\perp^2}{4}\right) \times \int \frac{d^2p}{(2\pi)^2}\frac{(p\gamma)_\parallel + m}{p_\parallel^2 - m^2 + i0}\Pi_- e^{-i(pX)_\parallel}, \qquad (4)$$

where

$$d^2p = dp_0dp_3, \quad \Pi_\pm = \frac{1}{2}(1 \pm i\gamma_1\gamma_2),$$
$$\Pi_\pm^2 = \Pi_\pm, \quad [\Pi_\pm, (a\gamma)_\parallel] = 0.$$

Here, γ_α are the Dirac matrices in the standard representation and the 4-vectors equipped with the subscripts $\perp$ and $\parallel$ refer to, respectively, Euclidean {1, 2} and Minkowski {0, 3} subspaces, provided that the field **B** is directed along the third axis. For arbitrary vectors a_μ and b_μ, we have

$$a_\perp = (0, a_1, a_2, 0), \quad a_\parallel = (a_0, 0, 0, a_3), \qquad (5)$$
$$(ab)_\perp = (a\Lambda b) = a_1b_1 + a_2b_2,$$
$$(ab)_\parallel = (a\tilde{\Lambda}b) = a_0b_0 - a_3b_3,$$

where we have introduced the matrices $\Lambda_{\alpha\beta} = (\varphi\varphi)_{\alpha\beta}$ and $\tilde{\Lambda}_{\alpha\beta} = (\tilde{\varphi}\tilde{\varphi})_{\alpha\beta}$, with $\varphi_{\alpha\beta} = F_{\alpha\beta}/B$ and $\tilde{\varphi}_{\alpha\beta} = \frac{1}{2}\varepsilon_{\alpha\beta\mu\nu}\varphi_{\mu\nu}$ being, respectively, the strength tensor of the external magnetic field in the dimensionless form and its dual counterpart. These matrices are related by the equation $\tilde{\Lambda}_{\alpha\beta} - \Lambda_{\alpha\beta} = g_{\alpha\beta} = \mathrm{diag}(1, -1, -1, -1)$, and the tensor indices of the

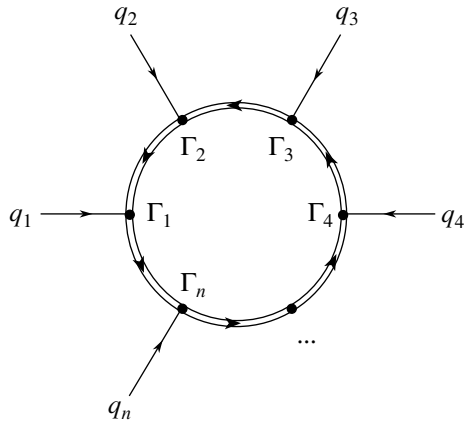

Fig. 1. Feynman diagram for an n-vertex one-loop process in a strong magnetic field. Double lines represent the electron propagators constructed on the basis of exact solutions to the Dirac equation in an external field.

4-vectors and tensors enclosed by parentheses are assumed to be consecutively contracted [for example, $(a\Lambda b) = a_\alpha \Lambda_{\alpha\beta} b_\beta$].

Although the propagator in (2) involves the phase $\Phi(x_1, x_2)$, which is not invariant under translations or gauge transformations, the total phase Φ_{tot} of n propagators in the loop is invariant under translations and gauge transformations:[2)]

$$\Phi_{\text{tot}} = -\frac{eB}{2}\sum_{i=1}^{n}(x_i\varphi x_{i+1})\Big|_{x_{n+1}=x_1} \tag{6}$$
$$= -\frac{eB}{2}\sum_{l=2}^{n-1}\sum_{k=1}^{l-1}(Z_k\varphi Z_l),$$

$$Z_i = x_i - x_{i+1}, \quad Z_n = x_n - x_1, \quad \sum_{i=1}^{n} Z_i = 0.$$

The invariant amplitude constructed for an n-vertex one-loop process with the aid of the effective Lagrangian (1) is described by the Feynman diagram in Fig. 1. With allowance for relations (2), (3), and (6), the amplitude can be recast into the form

$$\mathcal{M}_n = i^{n+1}\int\prod_{k=1}^{n-1} d^4 Z_k \tag{7}$$
$$\times \operatorname{tr}\left\{\prod_{l=1}^{n}[g_l\Gamma_l j_l \hat{S}(Z_l)]\right\} e^{i\Phi_{\text{tot}}} \exp\left(-i\sum_{j=1}^{n-1} Q_j Z_j\right),$$

$$Q_k = \sum_{i=1}^{k} q_i, \qquad Q_n = 0,$$

where j_l is the Fourier transform of the generalized current $j_l(x)$.

Substituting the propagator in (4) and the total phase in (6) into the amplitude in (7) and performing four-dimensional integration with respect to Z_i, we obtain

$$\mathcal{M}_n \simeq \frac{i(-1)^n eB}{(2\pi)^3}\exp\left(-\frac{R_{\perp n}}{2eB}\right) \tag{8}$$
$$\times \int d^2p \operatorname{tr}\left\{\prod_{k=1}^{n}[g_k\Gamma_k j_k S_\parallel(p - Q_k)]\right\},$$

where $S_\parallel(p) = \Pi_-((p\gamma)_\parallel + m)/(p_\parallel^2 - m^2 + i0)$ and $R_{\perp n}$ is a bilinear combination of the longitudinal components of the external momenta that, at $n = 2, 3$, for example, has the form

$$R_{\perp 2} = q_{\perp 1}^2,$$
$$R_{\perp 3} = q_{\perp 1}^2 + q_{\perp 2}^2 + (q_1\Lambda q_2) - i(q_1\varphi q_2),$$

its general form for $n \geq 3$ being

$$R_{\perp n} = \sum_{k=1}^{n-1} Q_{\perp k}^2 - \sum_{k=2}^{n-1}\sum_{j=1}^{k-1}[(Q_k\Lambda Q_j) - i(Q_k\varphi Q_j)].$$

It can be seen from (8) that, in the approximation where the magnetic-field strength is a maximum physical parameter, $eB \gg q_\perp^2, q_\parallel^2$, the amplitude will depend only on the longitudinal components of the momenta.

3. PROCESSES INVOLVING PHOTONS

Suppose that the vertices $\Gamma_1, \ldots, \Gamma_{n-1}$ are of a vector character and are associated with photons, while the vertex Γ_n is arbitrary. The total amplitude is described by $(n-1)!$ diagrams corresponding to $(n-1)!$ permutations of photons. In the approximation $q_\perp^2 \ll eB$, the amplitude in (8) can be recast into the form

$$\mathcal{M}_n \simeq i(-1)^n e^{n-1} g_n j_n \frac{eB}{2\pi}\left\{\prod_{i=1}^{n-1}\varepsilon_{\alpha_i}^{(i)}\right\} T_{\alpha_1,\ldots,\alpha_{n-1}} \tag{9}$$
$$+ \text{ all permutations of photons,}$$

where $\varepsilon_\alpha^{(i)}$ is the polarization vector of the ith photon having a momentum q_i and

$$T_{\alpha_1,\ldots,\alpha_{n-1}} \tag{10}$$
$$= \int \frac{d^2p}{(2\pi)^2}\operatorname{tr}\left\{\Gamma_n S_\parallel(p)\prod_{i=1}^{n-1}[\gamma_\parallel\alpha_i S_\parallel(p - Q_i)]\right\}.$$

[2)] In Eq. (B.3) presented in [37], the expression for the total phase in terms of Z_i is valid only for $n = 2, 3$.

It should be noted that, in the amplitude in (9), the projection operator Π_- singles out, of two possible photons polarizations (longitudinal and transverse one in the notation introduced by Adler [38]),

$$\varepsilon_\alpha^{\parallel} = \frac{\varphi_{\alpha\beta}q_\beta}{\sqrt{(q\varphi\varphi q)}}, \qquad \varepsilon_\alpha^{(\perp)} = \frac{\tilde{\varphi}_{\alpha\beta}q_\beta}{\sqrt{(q\tilde{\varphi}\tilde{\varphi}q)}}, \qquad (11)$$

photons of one polarization ($\perp$).

We will show that an amplitude of the $SV_1\ldots V_{n-1}$ form grows linearly with increasing magnetic-field strength only for an odd number of vertices, but that $PV_1\ldots V_{n-1}$, $VV_1\ldots V_{n-1}$, and $AV_1\ldots V_{n-1}$ amplitudes show a linear growth only in the case where the number of vertices is even.

With the aid of the Dirac charge-conjugation matrix

$$\hat{C} = \gamma_2\gamma_0, \qquad \hat{C} = -\hat{C}^T, \qquad \hat{C}^2 = 1,$$

we rewrite $T_{\alpha_1,\ldots,\alpha_{n-1}}$ in the form

$$T_{\alpha_1,\ldots,\alpha_{n-1}} = \int \frac{d^2p}{(2\pi)^2} \qquad (12)$$

$$\times\,\mathrm{tr}\Big\{\hat{C}\Gamma_n\hat{C}\hat{C}\frac{(\hat{p}_\parallel + m)}{p_\parallel^2 - m^2 + i0}\hat{C}\prod_{i=1}^{n-1}\hat{C}\gamma_{\parallel\alpha_i}\hat{C}\hat{C}$$

$$\times\frac{[(\hat{p}-\hat{Q}_i)_\parallel + m]}{(p-Q_i)_\parallel^2 - m^2 + i0}\hat{C}\hat{C}\Pi_-\hat{C}\Big\}.$$

Taking into account the relations

$$\hat{C}\gamma_{\parallel\alpha_i}\hat{C} = -\gamma_{\parallel\alpha_i}^T, \quad \hat{C}\Pi_\pm\hat{C} = \Pi_\mp, \quad \Pi_\pm^T = \Pi_\pm$$

and making the change of variable $p \to -p + Q_{n-1}$, we find, instead of (12), that

$$T_{\alpha_1,\ldots,\alpha_{n-1}} = (-1)^{n-1}\int \frac{d^2p}{(2\pi)^2} \qquad (13)$$

$$\times\,\mathrm{tr}\Big\{\frac{[(\hat{p}-\hat{Q}_{n-1})_\parallel + m]}{(p-Q_{n-1})_\parallel^2 - m^2 + i0}\hat{C}\Gamma_n^T\hat{C}$$

$$\times\prod_{i=n-1}^{1}\frac{[(\hat{p}+\hat{Q}_i-\hat{Q}_{n-1})_\parallel + m]}{(p+Q_i-Q_{n-1})_\parallel^2 - m^2 + i0}\gamma_{\parallel\alpha_i}\Pi_+\Big\}.$$

We note that, in this expression, the factors under the product sign are arranged in the order of decreasing index i. Thus, we arrive at the following conclusions:

(i) In the case where the vertex Γ_n is of a scalar character, Eq. (13) yields

$$T_{\alpha_1,\ldots,\alpha_{n-1}} = (-1)^{n-1}T_{\alpha_{n-1},\ldots,\alpha_1},$$

whence it follows that, at $n = 2k$, such terms in the amplitude $\mathcal{M}_n$ that are taken in pairs cancel each other, but that, at $n = 2k+1$, the analogous terms in $\mathcal{M}_n$ are doubled when taken in pairs.

(ii) In the case where the vertex Γ_n is of a pseudoscalar, a vector, or a pseudovector character, we find from Eq. (13), with allowance for the relation

$$\gamma_5\Pi_\pm = \pm\frac{1}{2}(\gamma\tilde{\varphi}\gamma)\Pi_\pm,$$

that

$$T_{\alpha_1,\ldots,\alpha_{n-1}} = (-1)^n T_{\alpha_{n-1},\ldots,\alpha_1}.$$

From this relation, it analogously follows that we have a pairwise cancellation of such terms in $\mathcal{M}_n$ at $n = 2k+1$ and their pairwise doubling at $n = 2k$.

The ensuing calculations can be significantly simplified upon expanding the polarization vectors $\varepsilon_\alpha^{(i)}$, the generalized current $(j_n)_\alpha$, and the tensor $T_{\alpha_1,\ldots,\alpha_{n-1}}$ in an orthonormalized basis of 4-vectors. With the aid of the magnetic-field tensor and the 4-momentum, it is convenient, in the general case, to construct the basis in the form

$$b_\mu^{(1)} = \frac{(\varphi q)_\mu}{\sqrt{q_\perp^2}}, \qquad b_\mu^{(2)} = \frac{(\tilde{\varphi}q)_\mu}{\sqrt{q_\parallel^2}},$$

$$b_\mu^{(3)} = \frac{q_\parallel^2(\Lambda q)_\mu - q_\perp^2(\tilde{\Lambda}q)_\mu}{\sqrt{q^2q_\parallel^2q_\perp^2}}, \quad b_\mu^{(4)} = \frac{q_\mu}{\sqrt{q^2}}.$$

We note that the vectors $b_\mu^{(i)}$ are eigenvectors of the photon polarization operator in a magnetic field. As was indicated above, the structure of amplitudes in a strong magnetic field is such that only the vector $b_\mu^{(2)}$ survives in the basis. We then have

$$\varepsilon_{\alpha_i}^{(i)} = \frac{(q_i\tilde{\varphi}\varepsilon^{(i)})(\tilde{\varphi}q_i)_{\alpha_i}}{q_{\parallel i}^2}, \qquad (14)$$

$$(j_n)_{\alpha_n} = \frac{(q_n\tilde{\varphi}j_n)(\tilde{\varphi}q_n)_{\alpha_n}}{q_{\parallel n}^2},$$

$$T_{\alpha_1,\ldots,\alpha_m} = \frac{\prod_{i=1}^{m}(\tilde{\varphi}q_i)_{\alpha_i}}{\sum_{\{2\}}\prod_{i=1}^{m}(\tilde{\varphi}q_i)_{\alpha_i}}I_m, \qquad (15)$$

where

$$I_m = \sum_{\{2\}} T_{\alpha_1,\ldots,\alpha_m}.$$

The symbol $\sum_{\{2\}}$ implies that the sum is taken over all possible contractions of an arbitrary tensor $A_{\alpha_1,\ldots,\alpha_m}$ with the tensor $\tilde{\Lambda}_{\alpha_1\alpha_2}\ldots\tilde{\Lambda}_{\alpha_{m-1}\alpha_m}$ if $m = 2k$, the symmetry properties of $\tilde{\Lambda}_{\alpha\beta}$ being taken here into account, or with the tensor

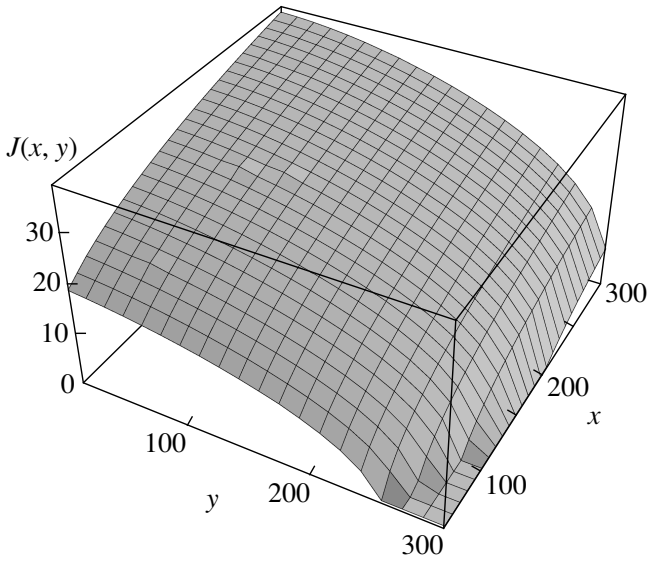

Fig. 2. Results obtained by numerically calculating the function $J(x,y)$ (36), which appears in the cross section (35) for the process $\gamma\gamma \to \nu\bar{\nu}\gamma$.

$q_{j\alpha}\tilde{\Lambda}_{\alpha_1\alpha_2}\ldots\tilde{\Lambda}_{\alpha\alpha_i}\ldots\tilde{\Lambda}_{\alpha_{m-1}\alpha_m}$ if $m = 2k-1$. By way of example, we indicate that, at $m = 4$,

$$\sum_{\{2\}} A_{\alpha_1\alpha_2\alpha_3\alpha_4} = A_{\alpha_1\alpha_2\alpha_3\alpha_4}\tilde{\Lambda}_{\alpha_1\alpha_2}\tilde{\Lambda}_{\alpha_3\alpha_4} \quad (16)$$

$$+ A_{\alpha_1\alpha_2\alpha_3\alpha_4}\tilde{\Lambda}_{\alpha_1\alpha_3}\tilde{\Lambda}_{\alpha_2\alpha_4} + A_{\alpha_1\alpha_2\alpha_3\alpha_4}\tilde{\Lambda}_{\alpha_1\alpha_4}\tilde{\Lambda}_{\alpha_2\alpha_3}$$

in the first case and that, at $m = 3$,

$$\sum_{\{2\}} A_{\alpha_1\alpha_2\alpha_3} = \sum_{j=1}^{3}\Big\{A_{\alpha_1\alpha_2\alpha_3}q_{j\|\alpha_3}\tilde{\Lambda}_{\alpha_1\alpha_2} \quad (17)$$

$$+ A_{\alpha_1\alpha_2\alpha_3}q_{j\|\alpha_2}\tilde{\Lambda}_{\alpha_1\alpha_3} + A_{\alpha_1\alpha_2\alpha_3}q_{j\|\alpha_1}\tilde{\Lambda}_{\alpha_2\alpha_3}\Big\}$$

in the second case.

Substituting the expansions in (14) and (15) into the amplitude in (9), we obtain

$$\mathcal{M}^S_{2k+1} = -\frac{ie^{2k+1}B}{\pi}g_S j_S \frac{\prod_{i=1}^{2k}(q_i\tilde{\varphi}\varepsilon^{(i)})}{\sum_{\{2\}}\prod_{i=1}^{2k}(\tilde{\varphi}q_i)_{\alpha_i}}\{I_{2k} \quad (18)$$

$$+ ((2k)!/2 - 1 \text{ permutations of photons})\}$$

for an odd number of vertices and a scalar coupling ($g_{2k+1} = g_S$);

$$\mathcal{M}^V_{2k} = \frac{ie^{2k}B}{\pi}g_V \frac{(q_{2k}\tilde{\varphi}j_V)\prod_{i=1}^{2k-1}(q_i\tilde{\varphi}\varepsilon^{(i)})}{\sum_{\{2\}}\prod_{i=1}^{2k}(\tilde{\varphi}q_i)_{\alpha_i}}\{I_{2k} \quad (19)$$

$$+((2k-1)!/2 - 1 \text{ permutations of photons})\}$$

for an even number of vertices and a vector coupling ($g_{2k} = g_V$);

$$\mathcal{M}^A_{2k} = -\mathcal{M}^V_{2k}[j_{V\alpha} \to (\tilde{\varphi}j_A)_\alpha, g_V \to g_A] \quad (20)$$

for an even number of vertices and a pseudovector coupling ($g_{2k} = g_A$); and

$$\mathcal{M}^P_{2k} = \frac{ie^{2k}B}{\pi}g_P j_P \frac{\prod_{i=1}^{2k-1}(q_i\tilde{\varphi}\varepsilon^{(i)})}{\sum_{\{2\}}\prod_{i=1}^{2k-1}(\tilde{\varphi}q_i)_{\alpha_i}}\{I_{2k-1} \quad (21)$$

$$+ ((2k-1)!/2 - 1 \text{ permutations of photons})\}$$

for an even number of vertices and a pseudoscalar coupling ($g_{2k} = g_P$).

An analysis reveals that the calculation of an amplitude of any type can be reduced to the calculation of a scalar integral of the form

$$S_n(Q_1,\ldots,Q_n) \quad (22)$$
$$= \int \frac{d^2p}{(2\pi)^2}\prod_{i=1}^{n}\frac{1}{(p-Q_i)^2 - m^2 + i0}.$$

It should be noted that, in evaluating expression (22), the use of the standard Feynman parametrization may prove to be inappropriate because the multiplicity of the integral increases. For example, we can see that, at $n = 3$, the double integral in (22) transforms into an integral with respect to two Feynman variables, while, at $n = 4$, there will be three such variables, and so on.

We propose a different way—a direct calculation of the double integral with respect to the variables p_0 and p_3 without introducing Feynman variables. We integrate (22) with respect to p_0 by using residue theory and make the change of variable $p_3 - Q_{i3} \to p_3$. The result is

$$S_n(Q_1,\ldots,Q_n) = -\frac{i}{4\pi}\sum_{i=1}^{n}\int_0^{+\infty}\frac{dp_3}{E} \quad (23)$$

$$\times\prod_{\substack{l=1\\ l\neq i}}^{n}\frac{1}{(E-d_{il0})^2 - (p_3 - d_{il3})^2 - m^2}$$

$$+ (p_3 \leftrightarrow -p_3),$$

where $E = \sqrt{p_3^2 + m^2}$ and $d_{il\alpha} = Q_{i\alpha} - Q_{l\alpha}$.

Making the change of variable $E + p_3 = k$, we can recast expression (23) into the form

$$S_n(Q_1,\ldots,Q_n) = (-1)^n \frac{i}{4\pi}\sum_{i=1}^{n}\int_m^{+\infty}\frac{dk}{k}\prod_{\substack{l=1\\ l\neq i}}^{n}\frac{k}{k^2(d_{il0}+d_{il3}) - k(d_{il})_\parallel^2 + m^2(d_{il0}-d_{il3})} + (d_{il3}\leftrightarrow -d_{il3}). \quad (24)$$

We recall that $a_\parallel^2 = a_0^2 - a_3^2$ and $(ab)_\parallel = a_0b_0 - a_3b_3$. Upon performing integration in (24), we finally obtain

$$S_n(Q_1,\ldots,Q_n) = \frac{i}{8m^2\pi}\sum_{i=1}^{n}\sum_{\substack{l=1\\ l\neq i}}^{n}\left[H\left(\frac{(d_{il})_\parallel^2}{4m^2}\right)+1\right]\mathrm{Re}\left\{\prod_{\substack{k=1\\ k\neq i,l}}^{n}\frac{1}{Y_{ilk}}\right\}, \quad (25)$$

where

$$Y_{ilk} = (d_{lk}d_{ik})_\parallel + i(d_{lk}\tilde{\varphi}d_{ik})\sqrt{\frac{4m^2}{(d_{il})_\parallel^2}-1}.$$

The function $H(z)$ is defined as follows:

$$H(z) = \frac{1}{2\sqrt{-z(1-z)}}\ln\frac{\sqrt{1-z}+\sqrt{-z}}{\sqrt{1-z}-\sqrt{-z}} - 1, \quad z<0;$$

$$H(z) = \frac{1}{\sqrt{z(1-z)}}\arctan\sqrt{\frac{z}{1-z}} - 1, \quad 0<z<1;$$

$$H(z) = -\frac{1}{2\sqrt{z(z-1)}}\ln\frac{\sqrt{z}+\sqrt{z-1}}{\sqrt{z}-\sqrt{z-1}} - 1 + \frac{i\pi}{2\sqrt{z(z-1)}}, \quad z>1.$$

Its asymptotic behavior is given by

$$H(z) \simeq \frac{2}{3}z + \frac{8}{15}z^2 + \frac{16}{35}z^3, \quad |z|\ll 1; \quad (26)$$

$$H(z) \simeq -1 - \frac{1}{2z}\ln 4|z|, \quad |z|\gg 1. \quad (27)$$

4. PROCESS $\gamma\gamma\to\nu\bar{\nu}$

Let us use the above results to calculate the amplitudes of specific quantum processes. In describing the process $\gamma\gamma\to\nu\bar{\nu}$ enhanced by a magnetic field, we rely on the model featuring an effective scalar $\nu\nu ee$ coupling [23]. At arbitrary values of the photon energy, we find from (18) and (25) that

$$\mathcal{M}_3^S = \frac{2\alpha}{\pi}\frac{B}{B_e}g_S j_s m \times \frac{(q_1\tilde{\varphi}\varepsilon^{(1)})(q_2\tilde{\varphi}\varepsilon^{(2)})}{4m^2[(q_1q_3)_\parallel^2 - q_{1\parallel}^2q_{3\parallel}^2] + q_{1\parallel}^2q_{2\parallel}^2q_{3\parallel}^2} \times\left\{[q_{1\parallel}^2q_{3\parallel}^2 - 2m^2(q_{3\parallel}^2+q_{1\parallel}^2-q_{2\parallel}^2)]H\left(\frac{q_{1\parallel}^2}{4m^2}\right) + [q_{2\parallel}^2q_{3\parallel}^2 - 2m^2(q_{3\parallel}^2+q_{2\parallel}^2-q_{1\parallel}^2)]H\left(\frac{q_{2\parallel}^2}{4m^2}\right) + q_{3\parallel}^2(4m^2-q_{3\parallel}^2)H\left(\frac{q_{3\parallel}^2}{4m^2}\right) - 2q_{3\parallel}^2(q_1q_2)_\parallel\right\}, \quad (28)$$

where $\alpha = e^2/4\pi$ is the fine-structure constant; g_S is the scalar-coupling constant, which, for example, in the left–right-symmetric extension of the Standard Model [39] has the form $g_S = -4\zeta G_\mathrm{F}/\sqrt{2}$ (ζ is the small angle of mixing of light and heavy charged vector W bosons forming states related to left- and right-hand currents, and G_F is the Fermi constant for weak interaction); $j_s = [\bar{\nu}_e(p_1)\nu_e(-p_2)]$ is the Fourier transform of the scalar neutrino current; and $q_3 = p_1 + p_2$ is the total momentum of the neutrino pair.

Upon the substitution of the photon polarizations from (11) into (28) and the use of the asymptotic expressions in (26) and (27), we obtain the following asymptotic results for the relevant amplitude:

(i) at low photon energies ($\omega_{1,2}\lesssim m$),

$$\mathcal{M}_3^S \simeq \frac{8\alpha}{3\pi}\frac{G_\mathrm{F}}{\sqrt{2}}\frac{\zeta}{m}\frac{B}{B_e}[\bar{\nu}_e(p_1)\nu_e(-p_2)]\sqrt{q_{1\parallel}^2q_{2\parallel}^2}; \quad (29)$$

(ii) at high photon energies ($\omega_{1,2}\gg m$), the result in the leading-logarithm approximation is

$$\mathcal{M}_3^S \simeq \frac{16\alpha}{\pi}\frac{G_\mathrm{F}}{\sqrt{2}}\zeta\frac{B}{B_e}m^3 \times[\bar{\nu}_e(p_1)\nu_e(-p_2)]\frac{1}{\sqrt{q_{1\parallel}^2q_{2\parallel}^2}}\ln\frac{\sqrt{q_{1\parallel}^2q_{2\parallel}^2}}{m^2}. \quad (30)$$

These formulas reproduce the results obtained in [23].

5. PROCESS $\gamma\gamma\to\nu\bar{\nu}\gamma$

In [31], the effect of a magnetic field on the amplitude of the process $\gamma\gamma\to\nu\bar{\nu}\gamma$ was investigated within the Standard Model in the low-energy limit. At arbitrary photon energies, the amplitude for the

process $\gamma\gamma \to \nu\bar{\nu}\gamma$ can be obtained from (19), (20), and (25) in the form

$$\mathcal{M}_4^V + \mathcal{M}_4^A = -\frac{8ie^3}{\pi^2}\frac{B}{B_e}\frac{G_\mathrm{F}}{\sqrt{2}}m^2 \times (q_1\tilde{\varphi}\varepsilon^{(1)})(q_2\tilde{\varphi}\varepsilon^{(2)})(q_3\tilde{\varphi}\varepsilon^{(3)}) \times [C_V(j\tilde{\varphi}q_4) + C_A(j\tilde{\varphi}\tilde{\varphi}q_4)] \times \frac{1}{D}\{I_4(q_{1\parallel}, q_{2\parallel}, q_{3\parallel}) + I_4(q_{2\parallel}, q_{1\parallel}, q_{3\parallel}) + I_4(q_{1\parallel}, q_{3\parallel}, q_{2\parallel})\}, \quad (31)$$

where C_V and C_A are the vector and the axial coupling constant in the effective $\nu\nu ee$ Lagrangian of the Standard Model [$C_V = \pm 1/2 + 2\sin^2\theta_\mathrm{W}$ and $C_A = \pm 1/2$, with θ_W being the Weinberg angle; here, the upper (lower) sign corresponds to the electron neutrino (muon and tau neutrinos)]; $j_\alpha = [\bar{\nu}_e(p_1)\gamma_\alpha(1+\gamma_5)\nu_e(-p_2)]$ is the Fourier transform of the neutrino current; $q_4 = p_1 + p_2$ is the total momentum of the neutrino pair; and

$$D = (q_1q_2)_\parallel(q_3q_4)_\parallel + (q_1q_3)_\parallel(q_2q_4)_\parallel + (q_1q_4)_\parallel(q_2q_3)_\parallel.$$

The form factor $I_4(q_{1\parallel}, q_{2\parallel}, q_{3\parallel})$ is given by

$$I_4(q_{1\parallel}, q_{2\parallel}, q_{3\parallel}) = S_3(q_{1\parallel} + q_{2\parallel}, q_{4\parallel}, 0) + S_3(q_{1\parallel}, q_{4\parallel}, 0) + S_3(q_{1\parallel} + q_{2\parallel}, q_{1\parallel}, 0) + S_3(q_{2\parallel} - q_{3\parallel}, q_{2\parallel}, 0) + [6m^2 - (q_1+q_2)_\parallel^2 - (q_2-q_3)_\parallel^2] \times S_4(q_{1\parallel}, q_{1\parallel} + q_{2\parallel}, q_{4\parallel}, 0). \quad (32)$$

Using the asymptotic expressions for $H(z)$, we obtain the following results:

(i) In the case of low photon energies ($\omega_{1,2,3} \ll m$),

$$\mathcal{M}_4^V + \mathcal{M}_4^A \simeq -\frac{2e^3}{15\pi^2}\frac{B}{B_e}\frac{G_\mathrm{F}}{\sqrt{2}}\frac{1}{m^4} \times (q_1\tilde{\varphi}\varepsilon^{(1)})(q_2\tilde{\varphi}\varepsilon^{(2)})(q_3\tilde{\varphi}\varepsilon^{(3)}) \times [C_V(j\tilde{\varphi}q_4) + C_A(j\tilde{\varphi}\tilde{\varphi}q_4)], \quad (33)$$

which is in perfect agreement with the results presented in [33, 40]. In our opinion, the amplitude obtained in [31] for the process $\gamma\gamma \to \nu\bar{\nu}\gamma$ in the same approximation is overestimated by a factor of 2.

(ii) At high photon energies ($\omega_{1,2,3} \gg m$), the result in the leading-logarithm approximation is

$$\mathcal{M}_4^V + \mathcal{M}_4^A \simeq -\frac{8e^3}{3\pi^2}\frac{G_\mathrm{F}}{\sqrt{2}}\frac{B}{B_e}m^4 \times (q_1\tilde{\varphi}\varepsilon^{(1)})(q_2\tilde{\varphi}\varepsilon^{(2)})(q_3\tilde{\varphi}\varepsilon^{(3)}) \times [C_V(j\tilde{\varphi}q_4) + C_A(j\tilde{\varphi}\tilde{\varphi}q_4)] \times \frac{1}{q_{1\parallel}^2q_{2\parallel}^2q_{3\parallel}^2q_{4\parallel}^2}\ln\frac{\sqrt{q_{1\parallel}^2q_{2\parallel}^2q_{3\parallel}^2}}{m^3}.$$

To the best of our knowledge, this result was obtained for the first time.

Substituting the photon polarizations from (11) into (33) and (34) and calculating the cross section for the process $\gamma\gamma \to \nu\bar{\nu}\gamma$ by a standard method, we find that, in the limit $\omega_{1,2,3} \ll m$, it is one-fourth as large as the corresponding result in [31]. In the opposite case of $\omega_{1,2,3} \gg m$, the cross section can be represented in the form

$$\sigma(\omega_{1,2,3} \gg m) \simeq \frac{32\alpha^3G_\mathrm{F}^2}{3\pi^4}\left(\frac{B}{B_e}\right)^2 \times \frac{m^8}{q_{1\parallel}^2q_{2\parallel}^2q^2}\ln^2\frac{\sqrt{q_{1\parallel}^2q_{2\parallel}^2}}{m^4}J\left(\frac{q_\parallel}{2m}, \frac{q_\perp}{2m}\right), \quad (35)$$

where $q = q_1 + q_2$ is the total momentum of primary photons.

The dependence of the cross section (35) on the momenta $q_\parallel$ and $q_\perp$ is determined by the integral

$$J(x,y) = \int \frac{d^3s}{2\pi s_0(s_0^2 - s_3^2)} \times \left\{\overline{C_A^2} + 4(\overline{C_V^2} - \overline{C_A^2})\frac{x(x-s_0) - y(y-s_1)}{4x(x-s_0) + s_0^2 - s_3^2}\right\} \times \Theta[x(x-s_0) - y(y-s_1)], \quad (36)$$

where $d^3s = ds_1ds_2ds_3$ and $s_0 = \sqrt{1 + s_1^2 + s_2^2 + s_3^2}$.

The constants $\overline{C_V^2} = 0.93$ and $\overline{C_A^2} = 0.75$ appearing under the integral sign in (36) result from summation over all channels of the production of electron, muon, and tau-lepton neutrinos.

The results of a numerical calculation of the integral in (36) are shown in Fig. 2.

6. CONCLUSION

We have performed a general analysis of the amplitude for an n-vertex one-loop process in a strong magnetic field and have considered the photon–neutrino processes $\gamma\gamma \to \nu\bar{\nu}$ and $\gamma\gamma \to \nu\bar{\nu}\gamma$. We have shown that different types of effective neutrino–electron interaction lead to different field-strength dependences of the amplitude. By way of example, we indicate that, in the case of an odd number of vertices and of an effective scalar $\nu\nu ee$ coupling, which exists in the extension of the Standard Model with broken left–right symmetry, the amplitude is enhanced by an external magnetic field, while, for an even number of vertices, such an enhancement is observed only in the case of effective pseudoscalar,

vector, or axial coupling. It has been proven that all types of amplitudes can be expressed in terms of elementary functions. We note that, in deriving the amplitudes in (18)–(21), we have not assumed that photons are real. This makes it possible to use these amplitudes to describe processes in which the number of real photons is smaller by one and which occur in the presence of an additional relatively weak external electromagnetic field—for example, the Coulomb field of a nucleus [32, 33]. The general expressions (28) and (31) have been obtained for the amplitudes of the processes $\gamma\gamma \to \nu\bar{\nu}$ and $\gamma\gamma \to \nu\bar{\nu}\gamma$ at arbitrary photon energies. The cross section for the process $\gamma\gamma \to \nu\bar{\nu}\gamma$ has been calculated in the limiting case of high photon energies.

ACKNOWLEDGMENTS

This work was supported in part by the Russian Foundation for Basic Research (project no. 01-02-17334), by the Ministry for Higher Education of the Russian Federation (grant no. E02-11.0-48), and by the Ministry for Industry and Science of the Russian Federation (presidential grant for support of leading scientific schools, no. 1916.2003.2).

REFERENCES

1. C. Kouveliotou *et al.*, Astrophys. J. **510**, L115 (1999).
2. K. Hurley *et al.*, Nature **397**, 41 (1999).
3. G. S. Bisnovatyĭ-Kogan, Astron. Zh. **47**, 813 (1970) [Sov. Astron. **14**, 652 (1970)].
4. R. C. Duncan and C. Thompson, Astrophys. J. **392**, L9 (1992).
5. P. Bocquet *et al.*, Astron. Astrophys. **301**, 757 (1995).
6. C. Y. Cardall, M. Prakash, and J. M. Lattimer, Astrophys. J. **554**, 322 (2001).
7. D. Grasso and H. R. Rubinstein, Phys. Rep. **348**, 163 (2001).
8. W.-Y. Tsai, Phys. Rev. D **10**, 2699 (1974).
9. A. E. Shabad, Tr. Fiz. Inst. Akad. Nauk SSSR **192**, 5 (1988).
10. D. V. Gal'tsov and N. S. Nikitina, Zh. Éksp. Teor. Fiz. **62**, 2008 (1972) [Sov. Phys. JETP **35**, 1047 (1972)].
11. V. V. Skobelev, Zh. Éksp. Teor. Fiz. **71**, 1263 (1976) [Sov. Phys. JETP **44**, 660 (1976)].
12. L. L. DeRaad, Jr., K. A. Milton, and N. D. Hari Dass, Phys. Rev. D **14**, 3326 (1976).
13. V. V. Skobelev, Zh. Éksp. Teor. Fiz. **108**, 3 (1995) [JETP **81**, 1 (1995)].
14. A. A. Gvozdev, N. V. Mikheev, and L. A. Vassilevskaya, Phys. Rev. D **54**, 5674 (1996).
15. A. N. Ioannisian and G. G. Raffelt, Phys. Rev. D **55**, 7038 (1997).
16. M. Yu. Borovkov, A. V. Kuznetsov, and N. V. Mikheev, Yad. Fiz. **62**, 1714 (1999) [Phys. At. Nucl. **62**, 1601 (1999)].
17. V. O. Papanyan and V. I. Ritus, Tr. Fiz. Inst. Akad. Nauk SSSR **168**, 120 (1986).
18. S. L. Adler and C. Schubert, Phys. Rev. Lett. **77**, 1695 (1996).
19. V. N. Baier, A. I. Milstein, and R. Zh. Shaisultanov, Phys. Rev. Lett. **77**, 1691 (1996).
20. V. N. Baĭer, A. I. Mil'steĭn, and R. Zh. Shaisultanov, Zh. Éksp. Teor. Fiz. **111**, 52 (1997) [JETP **84**, 29 (1997)].
21. M. V. Chistyakov, A. V. Kuznetsov, and N. V. Mikheev, Phys. Lett. B **434**, 67 (1998).
22. A. V. Kuznetsov, N. V. Mikheev, and M. V. Chistyakov, Yad. Fiz. **62**, 1638 (1999) [Phys. At. Nucl. **62**, 1535 (1999)].
23. A. V. Kuznetsov, N. V. Mikheev, and D. A. Rumyantsev, Yad. Fiz. **66**, 319 (2003) [Phys. At. Nucl. **66**, 294 (2003)].
24. M. Gell-Mann, Phys. Rev. Lett. **6**, 70 (1961).
25. Nguen Van Hieu and E. P. Shabalin, Zh. Éksp. Teor. Fiz. **44**, 1003 (1963) [Sov. Phys. JETP **17**, 464 (1963)].
26. D. A. Dicus and W. W. Repko, Phys. Rev. Lett. **79**, 569 (1997).
27. D. A. Dicus, C. Kao, and W. W. Repko, Phys. Rev. D **59**, 013005 (1999).
28. A. Abada, J. Matias, and R. Pittau, Phys. Rev. D **59**, 013008 (1999).
29. A. Abada, J. Matias, and R. Pittau, Nucl. Phys. B **543**, 255 (1999).
30. A. Abada, J. Matias, and R. Pittau, Phys. Lett. B **450**, 173 (1999).
31. Yu. M. Loskutov and V. V. Skobelev, Teor. Mat. Fiz. **70**, 303 (1987).
32. V. V. Skobelev, Zh. Éksp. Teor. Fiz. **120**, 786 (2001) [JETP **93**, 685 (2001)].
33. A. V. Kuznetsov and N. V. Mikheev, Pis'ma Zh. Éksp. Teor. Fiz. **75**, 531 (2002) [JETP Lett. **75**, 441 (2002)].
34. J. Schwinger, Phys. Rev. **82**, 664 (1951).
35. V. V. Skobelev, Izv. Vyssh. Uchebn. Zaved., Ser. Fiz., No. 10, 142 (1975).
36. Yu. M. Loskutov and V. V. Skobelev, Phys. Lett. A **56A**, 151 (1976).
37. N. V. Mikheev, A. Ya. Parkhomenko, and L. A. Vassilevskaya, Phys. Rev. D **60**, 035001 (1999).
38. S. L. Adler, Ann. Phys. (N.Y.) **67**, 599 (1971).
39. M. A. B. Bég, R. Budny, R. N. Mohapatra, and A. Sirlin, Phys. Rev. Lett. **38**, 1252 (1977).
40. H. Gies and R. Zh. Shaisultanov, Phys. Rev. D **62**, 073003 (2000).

Translated by A. Isaakyan

Physics of Atomic Nuclei, Vol. 67, No. 2, 2004, pp. 314–327. From Yadernaya Fizika, Vol. 67, No. 2, 2004, pp. 332–345.

ELEMENTARY PARTICLES AND FIELDS
Theory

CP Violation in $K_{S,\,L} \to \pi^+\pi^-\gamma$ and $K_{S,\,L} \to \pi^+\pi^-e^+e^-$ Decays*

S. S. Bulanov**

Institute of Theoretical and Experimental Physics,
Bol'shaya Cheremushkinskaya ul. 25, Moscow, 117259 Russia

Received July 29, 2002; in final form, December 30, 2002

Abstract—The dependence of $K_{S,\,L} \to \pi^+\pi^-\gamma$ decay probabilities on photon polarization is calculated. The phases of the terms of the amplitude that arise from the pion–pion interaction are obtained by using a simple realistic model of pion–pion interaction via virtual ρ meson, instead of chiral perturbation theory (ChPT). The results are compared with those of other authors and the origin of the discrepancies is explained. It is shown that the standard ChPT approach for $K_{S,\,L} \to \pi^+\pi^-\gamma$ decays cannot reproduce the contribution of the ρ meson to the P-wave $\pi\pi$ interaction. The departure of the photon spectrum from pure bremsstrahlung due to the pion-loop contribution to the electric direct emission amplitude is calculated. It is shown that the interference between the terms of amplitude with different CP parity appears only when the photon is polarized (linearly or circularly). Instead of measuring the linear polarization, the angular correlation between the $\pi^+\pi^-$ and e^+e^- planes in $K_{S,\,L} \to \pi^+\pi^-e^+e^-$ decay can be studied.

1. INTRODUCTION

The theoretical and experimental study of the CP violation in the radiative decays of the K_L and K_S has a long history. In view of future precise measurements of these decays, we have recalculated the above effects. Generally, our results are in agreement with the previous ones. A few discrepancies (see Conclusion) are caused by more realistic evaluation of pion loops in the present paper.

The pattern of the CP violation in the $K_{L,\,S} \to \pi^+\pi^-\gamma$ decays was theoretically predicted in the 1960s. Chew [1] determined the amplitude structure of $K^0_{1,2} \to \pi^+\pi^-\gamma$ decays. He calculated the pion-loop contribution to the direct emission amplitude and stated the possibility of the CP violation in the case where the amplitude is a sum of terms with different CP parity. Costa and Kabir [2], as well as Sehgal and Wolfenstein [3], studied the interference of the K^0_1 and K^0_2 in the decays into $\pi^+\pi^-\gamma$, identifying this effect with the CP violation. They also qualitatively discussed the dependence of the decay probability on the photon polarization. Dolgov and Ponomarev [4] paid special attention to the K_L decay. They realized that the CP-violation effects in the K_L decay should be larger than in the K_S decay. They also found that the measurement of the photon polarization could enhance the signals of the CP violation. They qualitatively discussed the measurement of the angular correlation between the $\pi^+\pi^-$ and e^+e^- planes in $K_L \to \pi^+\pi^-e^+e^-$ decay instead of measuring the linear polarization.

In the 1990s, $K_{L,\,S} \to \pi^+\pi^-\gamma$ decays were thoroughly studied using chiral perturbation theory (ChPT) with special emphasis on the K_L-meson decay. The K_L decay attracted special attention because, as is known experimentally, the contributions of the K_L decay amplitude terms with different CP parity are of comparable magnitude and this makes the CP violation distinctively seen. Contrary to this, in the case of the K_S decay, the CP violation is difficult to detect due to the fact that the internal bremsstrahlung contribution shades the contribution of the direct emission.

D'Ambrosio and Isidori [5] and D'Ambrosio *et al.* [6] presented a complete calculation of the direct emission contribution to the $K_{S,\,L} \to \pi^+\pi^-\gamma$ decay amplitude up to the sixth order of momenta in the framework of the ChPT. In view of future precise measurements and the new data on direct CP violation obtained by the KTeV Collaboration (Alavi-Harati *et al.*) [7], several authors addressed the problem of short-distance contributions to the direct CP-violating observables in the radiative K-meson decays. He and Valencia [8] studied the $s \to d\gamma$ transition. They described the long-distance contribution in the framework of the ChPT and subtracted it from the physical amplitudes of the $K \to \pi\pi\gamma$ decays in order to constrain the new, short-distance, interactions.

*This article was submitted by the author in English.

** e-mail: bulanov@heron.itep.ru

They also illustrated two types of models in which the short-distance interactions could be significantly enhanced with respect to the Standard Model, namely, the left–right symmetric model and supersymmetry.

Colangelo *et al.* [9] analyzed the supersymmetric contributions to the direct CP-violating observables in $K \to \pi\pi\gamma$ decays induced by gluino-mediated magnetic-penguin operators. They found that the direct CP violation could be substantially enhanced with respect to its Standard Model value, especially in the scenario where the direct CP violation is dominated by supersymmetric contributions.

Tandean and Valencia [10] also revisited the $K_L \to \pi^+\pi^-\gamma$ decay in order to study the possible contributions of $s \to d\gamma$ as well as gluonic, $s \to dg$, transitions to the direct CP-violating observables in the framework of two models: left–right symmetric model and supersymmetry.

The experimental studies of the K_L decay were reported in [11–13]. In 1980, Carrol *et al.* [11] first observed both the internal bremsstrahlung and the direct emission contributions in the K_L decay. Ramberg *et al.* [12] in 1993 presented more precise measurements of the pattern of the CP violation in the K_L decay. Kettell [13] summarized the recent more precise results.

In the case of the K_S decay only, the internal bremsstrahlung contribution was found by Ramberg *et al.* [12] and by Taureg *et al.* [14]. The latter established the upper bounds for the branching ratio of the interference of internal bremsstrahlung and electric direct emission. The theoretical study of the K_S decay was performed by D'Ambrosio *et al.* [15], where the electric direct emission amplitude was calculated in the framework of the ChPT. They also studied the photon spectrum departure from the pure internal bremsstrahlung expectation due to the interference of the internal bremsstrahlung and the electric direct emission. In [15], it was also noted that the measurement of this interference would provide a test of the proposed models.

In regard to the future higher precision experiments on the CP violation, it is important to study in more detail the properties of the phases caused by the $\pi\pi$ interaction in the $K_{L,\,S} \to \pi^+\pi^-\gamma$ decays. More precise calculation of these phases is a prerequisite for extracting the precise values of the CP-violating parameters in the K-meson decays.

In the present paper, we calculate the probability of the $K_{S,\,L} \to \pi^+\pi^-\gamma$ decays, using, instead of the ChPT, a simple realistic model of $\pi\pi$ interaction via virtual ρ meson, proposed by Lee and Vaughn [16] for the purposes of studying the P-wave resonance in the $\pi\pi$ scattering. This model was elaborated in [1] for the purposes of describing the electric direct emission in the $K \to 2\pi\gamma$ decays. In the framework of this model, we shall derive the phases of the amplitude terms connected with the $\pi\pi$ interaction. According to the approach used in [1], we shall show that the phase of the electric direct emission amplitude is not equal to the phase of the $\pi\pi$ scattering in the P wave, which could be expected according to the final-state interaction theorem formulated by Watson [17], Fermi [18], and Fubini *et al.* [19]. This happens due to the fact that the interaction of pions occurs not in the final state, but in the intermediate state.

We shall calculate the departure of the photon spectrum from bremsstrahlung due to the pion-loop contribution to the direct emission amplitude in the K_S decay. Then we shall compare our results on the photon energy dependence of the interference between the internal bremsstrahlung and the electric direct emission in the K_S decay with the results of [5, 15] obtained in the framework of ChPT. It will be proved that the "interference branching ratio" differs from the one obtained in [15] (see table) and that the standard ChPT approach even with higher order counterterms taken into account cannot reproduce the contribution of the ρ meson. If the counterterm contributions are set to zero ($k_f = 0$), the result of the present paper and the one obtained in [15] for the interference branching ratio are in agreement for the photon energy cut $\omega > 20$ MeV. However, for the photon energy cuts $\omega > 50$ MeV and $\omega > 100$ MeV, a discrepancy appears. It is due to the fact that the photon spectra of the interference contributions differ. This can be clearly seen from Fig. 1, where the result of the present paper (solid curve) along with the results of [15] (dashed curves, $k_f = -0.5,\ 0,\ +0.5$) for the photon spectra of the interference contributions are shown.

If the counterterm contributions are switched on, then we shall see that the arising discrepancy is rather large for values of the counterterm contributions given in [15] (e.g., in the case of $\omega > 20$ MeV for $k_f = 0.5$, the result of the present paper is 1.7 times smaller than that of [15], while for $k_f = -0.5$ it is 3.3 times larger—see table). It should be stressed that the counterterm contributions do not depend on the photon energy and they exhibit behavior different from the results of the present paper (see Fig. 1). We shall show that the discrepancy between these results appears due to the difference in models used to calculate the amplitude of $\pi\pi$ scattering in the P wave. We shall notice that this difference appears due to the fact that, in [5, 15], the ρ-meson contribution shows up only in low-energy constants, while resonance behavior was not reproduced. Such an approach did not take into account the photon energy dependence of the δ_1^1 phase, i.e., the behavior of the ρ propagator. Instead, we shall take into account the additional phase shift

Internal bremsstrahlung (B) and interference contributions (Interf) to the branching ratios of the $K_S \to \pi^+\pi^-\gamma$ decay for different ω cuts along with the results of [15]

Cut in ω, MeV	$B \times 10^3$		Interf $\times 10^6$					
	present paper	[15]	present paper	k_f [15]				
				0	0.5	1.0	−0.5	−1.0
> 20	4.81	4.80	−6.3	−6.2	−10.5	−14.8	−1.9	2.4
> 50	1.78	1.73	−4.8	−5.0	−8.3	−11.7	−1.6	1.8
> 100	0.44	0.31	−1.7	−2.0	−3.3	−4.7	−0.6	0.7

produced by pion loops and the energy dependence of the P-wave $\pi\pi$-scattering phase. We shall use the approach of [1, 16] in order to describe the phase energy dependence, which appears in the amplitude through the pion-loop contributions to the ρ-meson propagator.

In order to show that the inclusion of the ρ meson in the analysis of the electric direct emission in the $K \to \pi\pi\gamma$ decays is important, we shall address the problem of $\pi\pi$ scattering in the P wave. We shall compare the experimental data with the results obtained in the framework of different models: (a) the ChPT, (b) the ChPT with ρ-meson contribution taken into account, and (c) a simple realistic model. We shall see that the results calculated within the framework of the ChPT coincide with the experimental data only for low energies, because the ChPT does not take into account the resonance contribution of the ρ meson. Then we shall see that the model of $\pi\pi$ interaction via ρ meson and the ChPT with ρ-meson contribution show the same behavior of the P-wave $\pi\pi$-scattering phase.

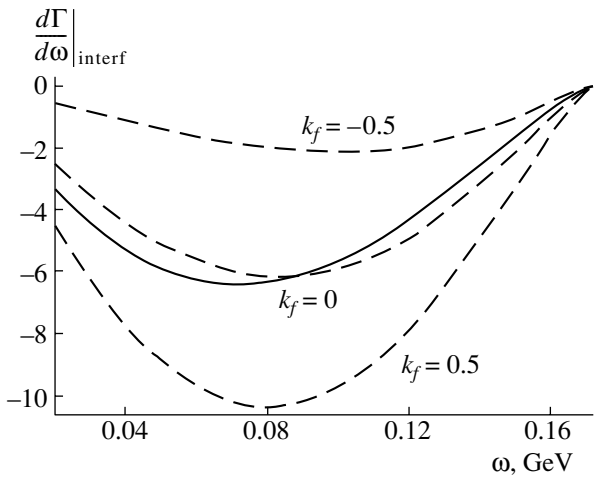

Fig. 1. The photon energy dependence of the interference contribution. The result of the present paper is represented by solid curve; the results of ChPT, by dashed curves.

In regard to the effects of CP violation in the $K_{S,L} \to \pi^+\pi^-\gamma$ decays, we shall note that, in the case of the K_S decay, the contribution of the CP-violating magnetic direct emission to the decay probability is negligibly small, in contrast to the case of the K_L decay, where the contributions of the CP-conserving magnetic direct emission and CP-violating internal bremsstrahlung to the decay probability are of comparable magnitude, as was theoretically predicted in [5, 6] and experimentally confirmed in [11–13]. Therefore, in the case of the K_S decay, we shall consider the interference between the amplitude terms with different CP parity, due to the fact that the interference is the largest term in which the CP-violating effects reside. As we shall see, one has to measure the polarization of photons to analyze the interference, because it is nonzero only when the polarization of the photon is observed. We note that this phenomenon was discussed qualitatively by Costa and Kabir [2], Sehgal and Wolfenstein [3], Dolgov and Ponomarev [4], and McGuigan and Sanda [20] for both K_S and K_L decays. The quantitative analysis of the K_L-decay amplitude dependence on the photon polarization was performed by Sehgal and van Leusen [21–23].

According to the approach proposed in [21] for K_L decay, we shall examine the $K_S \to \pi^+\pi^-\gamma$ decay probability with the polarized photon, taking into account various cases of the photon polarization, and we shall show that the measurement of the linear polarization in principle allows extraction of terms with opposite CP parity. In the present paper, we address the problem of studying the effects of different cases of the photon polarization in the K_S decay. As an alternative to measuring the linear photon polarization, the angular correlation of the $\pi^+\pi^-$ and e^+e^- planes in $K_{S,L} \to \pi^+\pi^-e^+e^-$ decay can be studied, as was first suggested in [4]. The structure of the $K_L \to \pi^+\pi^-e^+e^-$ decay amplitude was studied by Sehgal and Wanninger [24], Heiliger and Sehgal [25], and Elwood and Wise [26], where the CP-violating asymmetry, arising from the angular correlation of the

$\pi^+\pi^-$ and e^+e^- planes, was also obtained. The predictions of [24–26] on the $K_L \to \pi^+\pi^-e^+e^-$ decay branching ratio and CP-violating asymmetry were confirmed by the KTeV Collaboration [27].

The problem of pion-loop contribution in the $K_L \to \pi^+\pi^-e^+e^-$ decay was studied by Elwood *et al.* [28] in the framework of the ChPT. Their approach included both $\pi\pi \to \pi\pi$ and $\pi\pi \to \pi\pi\gamma^*$ rescattering. Previous estimates of the effect of pion-loop contribution in [24, 25] used the measured pion phase shifts and neglected $\pi\pi \to \pi\pi\gamma^*$. They found that the contribution of the $\pi\pi \to \pi\pi\gamma^*$ rescattering could enhance the CP-violating asymmetry by about 45% over the estimates given in [26], resulting in a value of the asymmetry which is in good agreement with the experimental data [27]. These results were summarized by Savage [29]. A more precise calculation of the $K_L \to \pi^+\pi^-e^+e^-$ decay branching ratio up to next-to-leading order in the framework of the ChPT was presented by Pichl [30]. Ecker and Pichl [31] updated the theoretical analysis of the CP-violating asymmetry in the $K_L \to \pi^+\pi^-e^+e^-$ decay using the ChPT and the most recent phenomenological information.

In the present paper, we shall calculate the CP-violating asymmetry in the case of the $K_L \to \pi^+\pi^-e^+e^-$ decay in order to compare our results with those of [28, 29]. The result of [28, 29] for the CP-violating asymmetry is 14%, and we shall find that the asymmetry is $(13.4 \pm 0.9)\%$. The central values coincide within the accuracy of the calculation. We shall also calculate the CP-violating asymmetry in the case of the $K_S \to \pi^+\pi^-e^+e^-$ decay and we shall find it to be substantially smaller: $(5.1 \pm 0.4) \times 10^{-5}$. This could be qualitatively expected from the analysis of the $K_S \to \pi^+\pi^-\gamma$ decay, because the CP-violating asymmetry depends on the interference of the amplitude terms with opposite CP parity. The CP-violating magnetic direct emission amplitude is very small in the K_S decay, in contrast to that of the K_L, where the CP-conserving magnetic emission and CP-violating internal bremsstrahlung are of comparable magnitude. In order to detect the asymmetry experimentally, one will need more than 10^{10} $K_S \to \pi^+\pi^-e^+e^-$ decays, because one should have a statistical error smaller than the magnitude of the effect.

The paper is organized as follows. In Section 2, we discuss the structure of the $K_{S,\,L} \to \pi^+\pi^-\gamma$ decay amplitude. In Section 3, we present a simple realistic model of $\pi\pi$ scattering in the P wave and derive an expression for pion-loop contribution to the direct emission amplitude in the framework of this model. We discuss the spectrum departure from pure internal bremsstrahlung due to pion-loop contribution in K_S decay in Section 4. We compare our results on the spectrum departure with the results obtained in the framework of ChPT in Section 5. In Section 6, we discuss the different models of the $\pi\pi$ scattering in the P wave and compare them with experimental data. In Section 7, we carry out an analysis of the dependence of the $K_{S,L}$ decay amplitude on the photon polarization in terms of Stokes vectors. We also discuss the angular correlation in $K_{S,\,L} \to \pi^+\pi^-e^+e^-$ decays and calculate the CP-violating asymmetry in $K_S \to \pi^+\pi^-e^+e^-$ decay in this section. Section 8 is devoted to the discussion of the main results and conclusions.

2. THE AMPLITUDE STRUCTURE

We start by labeling the momenta of the particles involved in the decay

$$K_{S,\,L}(r) \to \pi^+(p)\pi^-(q)\gamma(k,e), \tag{1}$$

where e is a 4-vector of the photon wave function.

It is convenient to define three expressions:

$$T_B = \frac{pe}{pk} - \frac{qe}{qk}, \tag{2}$$

$$T_E = (pe)(qk) - (qe)(pk), \tag{3}$$

$$T_M = \varepsilon_{\mu\nu\rho\sigma}p_\mu q_\nu k_\rho e_\sigma, \tag{4}$$

where $\varepsilon_{\mu\nu\rho\sigma}$ is the totally antisymmetric tensor.

The amplitudes of $K_{S,\,L} \to \pi^+\pi^-\gamma$ decays are made up of two components: the internal bremsstrahlung (B), proportional to T_B, and direct emission (D) [2, 3, 6]. In turn, direct emission is a sum of an electric term (E_D), proportional to T_E, and a magnetic term (M_D), proportional to T_M. We note that $T_E = T_B(pk)(qk)$; however, due to the different origin of the internal bremsstrahlung and electric direct emission, it is convenient to treat them separately.

In accordance with the above, the amplitudes of the $K_{S,\,L} \to \pi^+\pi^-\gamma$ decays can be written as follows:

$$A(K_S \to \pi^+\pi^-\gamma) = \hat{e}Ae^{i\delta_0^0}T_B + \hat{e}(a+b)T_E + i\hat{e}\eta_{+-}cT_M, \tag{5}$$

$$A(K_L \to \pi^+\pi^-\gamma) = \eta_{+-}\hat{e}Ae^{i\delta_0^0}T_B + \hat{e}\eta_{+-}(a+b)T_E + i\hat{e}cT_M, \tag{6}$$

where δ_0^0 is the S-wave pion scattering phase. Here, the upper index is isospin, the lower index is angular momentum, η_{+-} is the well-known CP-violation parameter in the $K_L \to \pi^+\pi^-$ decay, and $\hat{e}$ is the unit electrical charge. The imaginary unit in front of the factor c stems from the hermiticity of the Hamiltonian describing direct emission, neglecting final state

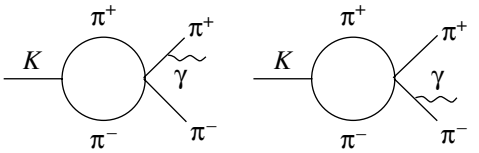

Fig. 2. The interaction of pions in the case of the internal bremsstrahlung.

interaction. The factor $A \equiv A(K \to \pi^+\pi^-)$ is determined by the Low theorem for bremsstrahlung [32]. The term $(a+b)$ is the electric direct emission coupling, while c is the magnetic direct emission coupling.

As follows from Eqs. (5), (6), the electric direct emission coupling is divided into two terms. The first term (a) describes the loops of heavy particles. The second term (b) describes the loops of pions. Such subdivision is convenient because the pion-loop contribution has an absorptive part and hence a phase, contrary to the contribution of heavy-particle loops.

The phases of direct emission couplings a and c are dictated by the final state interaction theorem [17–19, 33]. According to the law of conservation of angular momentum, we have $J_\gamma = J_{\pi\pi} = 1$. Here, J_γ is the total angular momentum of the photon, and $J_{\pi\pi}$ is the total angular momentum of two pions. Since $J_{\pi\pi} = l_{\pi\pi}$, where $l_{\pi\pi}$ is the orbital momentum of the two pions, the spatial part of the two-pion wave function should be antisymmetric, and the isospin part of the wave function should also be antisymmetric, according to the Bose generalized principles; i.e., $J_{\pi\pi} = 1\,(P$ wave), $T = 1$, where T is the isospin of two pions. As a result, we have for the phases

$$a = |a|e^{i\delta_1^1}, \qquad c = |c|e^{i\delta_1^1},$$

where δ_1^1 is the pion P-wave scattering phase.

3. CONTRIBUTION FROM PION LOOPS

The phases of the pion loops and bremsstrahlung contributions in Eqs. (5), (6) are defined by the strong interaction of pions. Let us describe the simple realistic model of the $\pi\pi$ interaction mentioned above, which we shall use while considering the $\pi\pi$ scattering in the P wave. The Lagrangian of this model [16] has the following form:

$$L = -\frac{g}{\sqrt{2}}\varepsilon_{ijk}(\phi^i\partial_\mu\phi^j - \partial_\mu\phi^i\phi^j)B_\mu^k, \qquad (7)$$

where i, j, k are isotopic indices, ϕ is the pion field, B_μ^k is the ρ-meson field, and g is the interaction constant of $\rho\pi\pi$. The P-wave resonance in $\pi\pi$ scattering is due

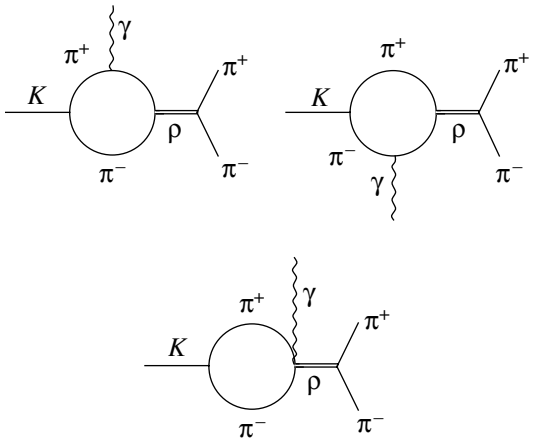

Fig. 3. The emission of the photon from the loops of virtual particles (D).

to the resonant structure of the ρ-meson propagator, the relevant part of which is

$$D^{\mu\nu}(k) = -D(k^2)g^{\mu\nu}, \qquad (8)$$
$$D(k^2) = [k^2 - m_\rho^2 - \Sigma(k^2)]^{-1},$$

where $\Sigma(k^2)$ is the ρ self-energy operator; in the "resonance approximation" in which we consider only the sum of the iterated bubble diagrams with pions running in the loop, $\Sigma(k^2)$ is given by the following expression:

$$\Sigma(s) = J(s) - J(m_\rho^2) + i\mathrm{Im}(\Sigma(s)), \qquad (9)$$

with

$$\mathrm{Im}(\Sigma(s)) = -\frac{g^2}{48\pi}\frac{(s-4m_\pi^2)^{3/2}}{s^{1/2}}\theta(s-4m_\pi^2), \quad (10)$$

$$J(s) = \frac{g^2}{48\pi}\left\{\frac{(s-4m_\pi^2)^{3/2}}{s^{1/2}}\right. \qquad (11)$$
$$\left.\times \ln\left[\frac{s^{1/2}+(s-4m_\pi^2)^{1/2}}{s^{1/2}-(s-4m_\pi^2)^{1/2}}\right] - \xi s\right\},$$

$$\xi = \frac{m_\rho^2 - 4m_\pi^2}{m_\rho^2} + \frac{m_\rho + 2m_\pi}{m_\rho} \qquad (12)$$
$$\times \frac{(m_\rho^2 - 4m_\pi^2)^{1/2}}{m_\rho}\ln\left[\frac{m_\rho + (m_\rho^2 - 4m_\pi^2)^{1/2}}{m_\rho - (m_\rho^2 - 4m_\pi^2)^{1/2}}\right].$$

Here, $\theta(x)$ is a step function: $\theta(x) = 0$ for $x < 0$ and $\theta(x) = 1$ for $x \geq 0$.

In the case of internal bremsstrahlung contribution to the $K_{S,\,L}$-decay probability, the interaction of pions can be described by the diagrams shown in Fig. 2. Though pions are in the P wave in the final state, as was shown in the previous section,

this group of diagrams results in the δ_0^0 phase of the amplitude, as was assumed in [5, 6, 10, 15, 20, 21, 24]. It is due to the fact that the interaction of pions occurs not in the final state, but in the intermediate one. The diagrams of Fig. 2 contribute to the $K\pi\pi$ vertex; these corrections are taken into account by using the amplitude of the $K_S \to \pi^+\pi^-$ decay as the interaction constant and assuming it equal to its experimental value.

The emission of the photon from the loops of pions is governed by another group of diagrams shown in Fig. 3. Each of these diagrams is divergent, but their sum is finite. A similar result holds in the ChPT. A straightforward calculation of this finite expression gives a result that is not gauge invariant. This effect arises from the cancellation of two four-dimensional integrals proportional to l^2 and $l_\mu l_\nu$. The evaluation of these two integrals in the framework of the dimensional regularization scheme leads to a constant term that restores the gauge invariance [34].

Further, we shall neglect the energy dependence of the $K\pi\pi$ vertex. We shall take the amplitude of the $K_S \to \pi^+\pi^-$ decay as the interaction constant and use the experimental result for it.

We find for the matrix element arising from the diagrams, shown in Fig. 3,

$$E_D^{\text{loop}} = \frac{\hat{e}g^2AD(s)}{(2\pi)^4}\left[\int \frac{4((r+l)e)(l(q-p))d^4l}{(l^2-m_\pi^2)((r+l)^2-m_\pi^2)((r+l-k)^2-m_\pi^2)}\right. \tag{13}$$
$$\left. + \int \frac{4(le)(l(q-p))d^4l}{(l^2-m_\pi^2)((l+k)^2-m_\pi^2)((r+l)^2-m_\pi^2)} - 2\int \frac{((q-p)e)d^4l}{(l^2-m_\pi^2)((r+l)^2-m_\pi^2)}\right]$$
$$= \frac{\hat{e}g^2A}{\pi^2}F(s)D(s)\frac{T_E}{rk} = \hat{e}bT_E,$$

with

$$F(s) = \frac{1}{2} + \frac{s}{2rk} \tag{14}$$
$$\times\left[\beta\,\text{arctanh}\left(\frac{1}{\beta}\right) - \beta_0\,\text{arctanh}\left(\frac{1}{\beta_0}\right)\right]$$
$$-\frac{m_\pi^2}{rk}\left(\text{arctanh}^2\left(\frac{1}{\beta}\right) - \text{arctanh}^2\left(\frac{1}{\beta_0}\right)\right)$$
$$+\frac{i\pi}{2rk}\left(\frac{s}{2}(\beta-\beta_0) - 2m_\pi^2\right.$$
$$\left.\times\left(\text{arctanh}\left(\frac{1}{\beta}\right) - \text{arctanh}\left(\frac{1}{\beta_0}\right)\right)\right),$$

where $s = (r-k)^2$, $\beta = \sqrt{1-4m_\pi^2/s}$, and $\beta_0 = \sqrt{1-4m_\pi^2/m_K^2}$. We take the amplitude of the $\rho \to \pi\pi$ decay as the interaction constant g and use the experimental result for it.

We note that, since $F(s)$ is complex, the phase of the loop contribution is not equal to the pion P-wave scattering phase. The photon energy dependence of the b phase ($\arg(b) = \delta_b$) is shown in Fig. 4.

Heavy particles in the loop can also contribute to the electric direct emission amplitude, though they do not produce any additional phase. The possible intermediate states are πK, $K\eta$, and KK. However, the KK loop vanishes in the limit $m_{K^0} = m_{K^+}$. The contribution of these loops can be calculated under the assumption that the interaction constants are the same as in the pion-loop case ($g_{K\pi\pi} = g_{K\pi K} = g_{KK\eta} = g_{KKK}$ and the same for the interaction with ρ).

4. THE SPECTRUM DEPARTURE FROM PURE BREMSSTRAHLUNG

Now we can use the results on the $K_S \to \pi^+\pi^-\gamma$ decay probability, obtained in the previous section, to estimate the departure of the photon spectrum from the pure bremsstrahlung. We neglect the CP-violating magnetic direct emission amplitude. The calculations are carried out in the K_S rest frame ($r = (m_K, 0, 0, 0)$, $k = (\omega, \omega, 0, 0)$), where

$$s = m_K^2 - 2m_K\omega, \quad \beta = \sqrt{1 - \frac{4m_\pi^2}{m_K^2 - 2m_K\omega}},$$
$$rk = m_K\omega.$$

Thus, for the double differential decay width with an unpolarized photon, we obtain

$$\frac{d\Gamma(K_S \to \pi^+\pi^-\gamma)}{d\omega d\cos\theta} = \frac{2\alpha}{\pi}\frac{\beta^3}{\beta_0}\left(1 - \frac{2\omega}{m_K}\right) \tag{15}$$
$$\times \sin^2\theta\Gamma(K_S \to \pi^+\pi^-)\left[\frac{1}{\omega(1-\beta^2\cos^2\theta)^2}\right.$$
$$\left. + \frac{m_K^4|a+b|^2\omega^3}{16|A|^2} + \frac{\text{Re}(be^{-i\delta_0^0})\omega m_K^2}{2|A|(1-\beta^2\cos^2\theta)}\right].$$

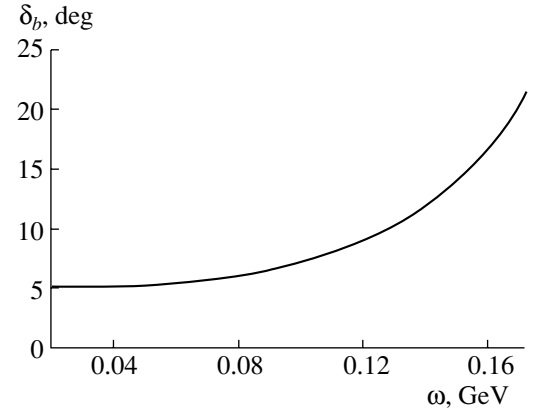

Fig. 4. The photon energy dependence of the pion-loop phase δ_b ($b = |b|e^{i\delta_b}$).

Here, θ is an angle between the photon and π^+ in the dipion rest frame and $\alpha = \hat{e}^2/4\pi$. Integrating Eq. (15) over $\cos\theta$ between the limits $-1 \le \cos\theta \le 1$, we obtain the following result for the differential decay width:

$$\frac{d\Gamma(K_S \to \pi^+\pi^-\gamma)}{d\omega} = \frac{2\alpha}{\pi}\frac{\beta^3}{\beta_0}\left(1 - \frac{2\omega}{m_K}\right) \quad (16)$$
$$\times \Gamma(K_S \to \pi^+\pi^-)\left\{\frac{1}{\omega}\left[\frac{1+\beta^2}{2\beta^3}\ln\frac{1+\beta}{1-\beta} - \frac{1}{\beta^2}\right]\right.$$
$$+ \frac{m_K^4\omega^3}{12}\frac{|b|^2}{|A|^2} + \frac{\mathrm{Re}((a+b)e^{-i\delta_0^0})\omega m_K^2}{2|A|}$$
$$\left.\times\left[\frac{2}{\beta^2} - \frac{1-\beta^2}{\beta^3}\ln\frac{1+\beta}{1-\beta}\right]\right\}.$$

The second and the third terms in the curly brackets govern the departure of photon spectrum from the pure bremsstrahlung. We characterize the departure of the spectrum by the ratio

$$R = \frac{\left.\frac{d\Gamma}{d\omega}\right|_{\text{interf}}}{\left.\frac{d\Gamma}{d\omega}\right|_{B}}, \quad (17)$$

where $\left.\frac{d\Gamma}{d\omega}\right|_B$ governs the pure bremsstrahlung spectrum and $\left.\frac{d\Gamma}{d\omega}\right|_{\text{interf}}$ governs the departure of the photon spectrum due to the interference of the internal bremsstrahlung and the electric direct emission.

The ratio increases with increasing ω and varies from 0.1% at $\omega = 50$ MeV to 1% at $\omega = 160$ MeV (see Fig. 5).

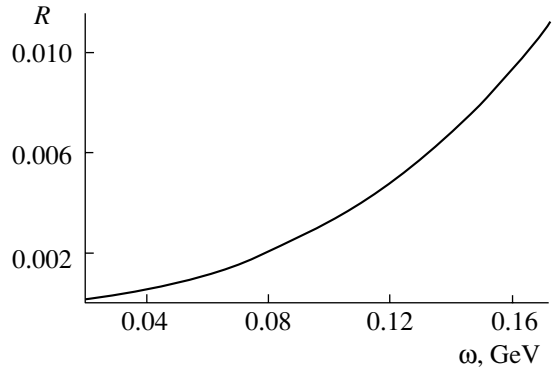

Fig. 5. The photon energy dependence of the ratio R defined in Eq. (17).

5. COMPARISON WITH ChPT

Let us compare the results on the interference branching ratio in the K_S decay obtained in [5, 15] with the results presented above. In the framework of the ChPT, the electric direct emission amplitude is a sum of the loop contribution and the counterterm contributions. The counterterms are needed in the ChPT to reabsorb divergences arising from loops at each order in momenta, because the ChPT is a nonrenormalizable theory.

In general, the loop contribution and the counterterm contributions are separately scale-dependent. However, in this case, the counterterm contributions are scale-independent and the loop contribution is finite, as was shown in [5, 15]. A similar result for the loop contribution is obtained in the present paper [see Eq. (13)].

Counterterm contributions do not depend on the photon energy, in contrast to the loop contribution, as is shown in [5, 15],

$$E_{\text{ct}} = \frac{\hat{e}G_8 m_K^3}{4\pi^2 F_\pi} N_{E_1}, \quad (18)$$

where G_8 is the interaction constant of the $|\Delta S| = 1$ nonleptonic weak Lagrangian in the framework of the ChPT. The index 8 is due to the fact that the Lagrangian transforms under $SU(3)_L \times SU(3)_R$ as an $(8_L, 1_R)$ or $(27_L, 1_R)$. Only the octet part of the Lagrangian was taken into account in [15]. The value of G_8 was determined from the experimental data on the $K_S \to \pi^+\pi^-$ decay probability: $A(K_S \to \pi^+\pi^-) = 2G_8F_\pi(m_K^2 - m_\pi^2)$, $|G_8| = 9 \times 10^{-6}\,\text{GeV}^{-2}$. F_π is the constant of the pion leptonic decay: $F_\pi = 93.3$ MeV; N_{E_1} is a sum of the counterterm constants and should be fixed from the experimental data.

The loop contribution according to [5, 15] is equal to

$$E_{\text{loop}} = -\frac{\hat{e}G_8 m_K(m_K^2 - m_\pi^2)}{8\pi^2 F_\pi} \times (4h_{\pi\pi} + h_{\pi K} + h_{K\eta}), \quad (19)$$

where $h_{\pi\pi}$, $h_{\pi K}$, and $h_{K\eta}$ denote the contributions of corresponding loops. Regarding the $\pi\pi$ loop, it was found in [5, 15] that it dominates the loop contribution to the electric direct emission amplitude and is equal to

$$E_{\text{loop}}^{\pi\pi} = -\frac{\hat{e}G_8 m_K(m_K^2 - m_\pi^2)}{8\pi^2 F_\pi \omega^2} \times \left\{ s\left[\beta \ln\left(\frac{1+\beta}{\beta-1}\right) - \beta_0 \ln\left(\frac{1+\beta_0}{\beta_0-1}\right)\right] + m_K\omega + m_\pi^2\left[\ln^2\left(\frac{1+\beta_0}{\beta_0-1}\right) - \ln^2\left(\frac{1+\beta}{\beta-1}\right)\right]\right\}. \quad (20)$$

We notice that expression (20) is proportional to $(m_K^2 - m_\pi^2)$, i.e., to the weak vertex $K\pi\pi$ with pions on-shell in the framework of the ChPT. Thus, the results obtained in the ChPT confirm the assumption we made while considering the diagrams of Fig. 3. We took $A(K_S \to \pi^+\pi^-)$ as the interaction constant and considered pions on-shell.

In [5, 15], the "interference branching ratio" was calculated for different values of $N_{E_1} = 1.15k_f$, where $k_f = 0, \pm 0.5, \pm 1$, because the ChPT cannot fix the values of the counterterm contributions; they can only be fixed experimentally.

In order to compare the results of the present paper on the interference branching ratio with the results obtained in the framework of the ChPT, we present the internal bremsstrahlung and interference contributions to the branching ratio of the $K_S \to \pi^+\pi^-\gamma$ decay, for different values of the ω cut, along with the results of [15] in the table. As can be seen from the table, in the case of $k_f = 0$, the interference branching ratio obtained in the present paper and the one obtained in the framework of the ChPT are in agreement for the photon energy cut $\omega > 20$ MeV. However, for the photon energy cuts $\omega > 50$ MeV and $\omega > 100$ MeV, a discrepancy appears. It is due to the fact that the photon spectra of these results differ. It can be clearly seen from Fig. 1, where the result of the present paper (solid curve) along with the results of [15] (dashed curves, $k_f = -0.5, 0, +0.5$) for the photon spectra of the interference contribution are shown.

If the counterterm contributions are switched on, then the arising discrepancy is rather large for values of the counterterm contributions given in [15] (e.g., in the case of $\omega > 20$ MeV for $k_f = 0.5$, the interference branching ratio obtained in the present paper is 1.7 times smaller than the one obtained in [15]; for $k_f = -0.5$, it is 3.3 times larger—see table). It should be stressed that the counterterm contributions do not depend on the photon energy (18) and they exhibit behavior different from the results of the present paper (see Fig. 1). The obtained discrepancy is due to the fact that, in [5, 15], the ρ-meson contribution shows up only in low-energy constants, while the resonance contribution was not considered. The phase of the electric direct emission amplitude was taken to be $\delta_1^1(m_K)$, and the phase of $\pi\pi$ scattering in the P wave at energy $\sqrt{s} = m_K$. Instead, we used a simple realistic model of $\pi\pi$ scattering via ρ meson, taking into account the energy dependence of the $\delta_1^1(s)$ phase.

Indeed, in the case of the $\pi\pi$ scattering in the framework of the ChPT, the ρ meson shows up in low-energy constants and as a direct resonance [35]. However, in papers on $K \to \pi\pi\gamma$ decays based on the ChPT approach, only low-energy constants were accounted for. Such an approach did not take into account the energy dependence of the $\delta_1^1(s)$ phase, in other words, the behavior of the ρ-meson propagator, because the contributions of low-energy constants do not depend on the energy. Thus, some dynamical features are missing in the ChPT approach for the $K \to \pi\pi\gamma$ decays. As can be seen from Fig. 1, the standard ChPT approach even with higher order counterterms taken into account cannot reproduce the contribution of the ρ meson.

In order to show that the inclusion of the ρ meson in the analysis of the electric direct emission in the $K \to \pi\pi\gamma$ decays is important, we address the problem of $\pi\pi$ scattering in the P wave in the following section.

6. PION–PION SCATTERING

In order to confirm our assumption that a simple realistic model for describing the $\pi\pi$ interaction in the P wave is more appropriate than the standard ChPT approach, let us compare the results of different models for $\pi\pi$ scattering with experimental data. In the framework of the ChPT, the amplitude of $\pi\pi$ scattering to one loop takes the form [35]

$$A(s,t,u) = \frac{s - M^2}{F_\pi^2} + B(s,t,u) + C(s,t,u) + O(p^6). \quad (21)$$

Here,

$$s = (p_1 + p_2)^2, \quad t = (p_1 - p_1'), \quad u = (p_1 - p_2'), \quad s + t + u = 4m_\pi^2,$$

where p_1, p_2 and p_1', p_2' are momenta of pions before and after scattering, respectively;

$$B(s,t,u) = (6F_\pi^4)^{-1}\left\{3(s^2 - M^4)K(s) \right. \quad (22)$$

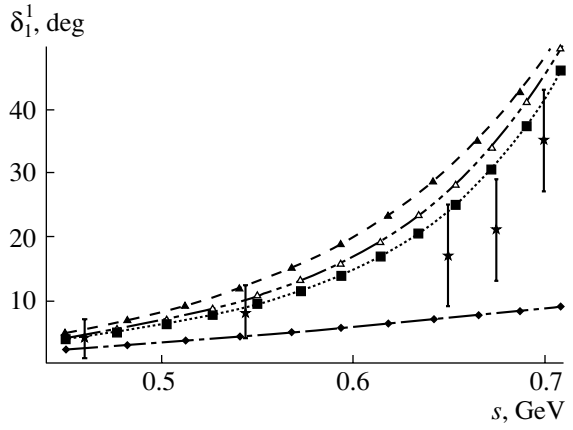

Fig. 6. The energy dependence of the $\pi\pi$-scattering phase $\delta_1^1(s)$ in the P wave. Dots represent calculations in the framework of the ChPT: without ρ-meson contribution (diamonds); with the ρ-meson contribution taken into account, according to Eqs. (3.11)–(3.14) of [40] (closed triangles); and with ρ in the two-loop approximation, according to the result [39] (open triangles). The results of the present paper are represented by squares, and the experimental data are represented by stars.

$$+[t(t-u)-2M^2t+4M^2u-2M^4]K(t)$$
$$+[u(u-t)-2M^2u+4M^2t-2M^4]K(u)\big\},$$
$$C(s,t,u)=(96\pi^2F_\pi^4)^{-1} \qquad (23)$$
$$\times\big\{2\,(l_1-4/3)\,(s-2M^2)^2+(l_2-5/6)$$
$$\times[s^2+(t-u)^2]-12M^2s+15M^4\big\},$$

and

$$K(q^2)=\frac{1}{16\pi^2}\left(\sigma\ln\frac{\sigma-1}{\sigma+1}+2\right),$$
$$\sigma=\left(1-\frac{4M^2}{q^2}\right)^{1/2}.$$

This representation involves four constants: F_π defined above, M related to the physical pion mass as $M=(1.01\pm0.1)m_\pi$ [35], and $l_1=0.4\pm0.3$ and $l_2=1.2\pm0.4$, which are extracted from $\pi\pi$ data [36] and K_{e4} decay [37].

The two-loop representation of the scattering amplitude yields the first three terms in the chiral expansion of the partial wave amplitudes [38]:

$$t_l^I(s)=t_l^I(s)_2+t_l^I(s)_4+t_l^I(s)_6+O(p^8). \qquad (24)$$

This representation involves 12 constants. The leading order contains F_π and M; the next-to-leading order, l_1, l_2, l_3, l_4. The contribution of the last two constants was not included in the scattering amplitude of [35], though they appear in the next-to-leading order. This fact is due to the smallness of the contributions proportional to these constants. The next-to-next-to-leading order generates six coupling constants $r_1,\ldots,r_6$.

Two different categories of these constants should be distinguished. First are the terms that survive in the chiral limit (l_1, l_2, r_5, r_6). They can be determined from the experimental data, as was mentioned above for l_1 and l_2. The constants $r_5(m_\rho)=3.8\pm1.0$ and $r_6(m_\rho)=1.0\pm0.1$ were calculated using the experimental data on $\pi\pi$ scattering and Roy equations in [39]. Second are symmetry breaking terms. The corresponding vertices are proportional to a power of the quark mass and involve the constants l_3, l_4, r_1, r_2, r_3, r_4, which may be determined by using other than $\pi\pi$ scattering experimental information. The constant $l_4=4.4\pm0.2$ can be fixed by using experimental data on the pion scalar form factor. The contributions of l_3 to the scattering amplitude are very small and can be neglected, as was shown in [39]. For $r_1,\ldots,r_4$, the theoretical estimates were used in [39].

The ρ-meson contribution is taken into account in the framework of the ChPT by considering the pole diagrams of $\pi\pi$ scattering via virtual ρ meson. This procedure gives rise to an additional term in the expression for the amplitude of $\pi\pi$ scattering, as was shown in [35, 40].

In order to compare the amplitude with the experimental data on P-wave $\pi\pi$ scattering [41], we should expand the combination with definite isospin in the s channel

$$T^1(s,t)=A(t,u,s)-A(u,s,t) \qquad (25)$$

into partial waves with different angular momenta:

$$T^1(s,t)=32\pi\sum_{l=0}^{\infty}(2l+1)P_l(\cos\theta)t_l^1(s),$$
$$s=4(m_\pi^2+q^2),\quad t=-2q^2(1-\cos\theta),$$

where θ is the scattering angle in the c.m. system of the initial pions. The partial amplitude of P-wave scattering is

$$t_1^1(s)=\frac{1}{64\pi}\int_{-1}^{1}T^1P_1(\cos\theta)d\cos\theta. \qquad (26)$$

In Fig. 6, we present the behavior of the phase δ_1^1 calculated in the framework of the ChPT in the one-loop approximation (with and without ρ) and the simple realistic model along with experimental data [41]. We also present the behavior of the phase δ_1^1 calculated in the framework of the ChPT with ρ in the two-loop approximation in [39]. According to the standard approach used when considering phases of $\pi\pi$ scattering, we utilize the elastic unitarity to

determine δ_1^1 in the framework of the ChPT with and without ρ. Namely,

$$\mathrm{Im}(t_1^1) = \frac{2q}{\sqrt{s}}\left(\mathrm{Re}(t_1^1)\right)^2.$$

Then the phase takes the form

$$\delta_1^1 = \arctan\left(\frac{2q}{\sqrt{s}}\mathrm{Re}(t_1^1)\right). \qquad (27)$$

As is seen from Fig. 6, the result obtained in the framework of the ChPT without ρ is in strict disagreement with the experimental data. It is due to the fact that the ρ contribution was not taken into account. In fact, the use of Eq. (27) is equivalent to taking into account the imaginary part of bubble diagrams, which we considered above when calculating the pion-loop contributions to the ρ propagator. Due to this fact, the behavior of the phases calculated in the framework of the ChPT with ρ and in the framework of the simple realistic model should be similar, as is shown in Fig. 6. However, the use of unitarity to determine δ_1^1 in the framework of the ChPT with ρ in the one-loop as well as in the two-loop approximation is equivalent to taking into account the imaginary parts of the one-loop diagrams, which describe the "resonance" structure of the ρ-meson propagator. Instead, we considered the sum of the iterated bubble diagrams to calculate the pion-loop contributions to the ρ propagator, as is shown in Section 3. This fact leads to the difference between the result for the phase obtained in the framework of the ChPT with ρ contribution taken into account and the result of the present paper, as can be seen in Fig. 7, which presents a magnified part of Fig. 6. The two-loop approximation gives a result for δ_1^1 that is in better agreement with the result of the present paper than the one-loop approximation. Thus, the inclusion of the ρ meson into the analysis of the electric direct emission in the $K \to \pi\pi\gamma$ decays is important.

The theoretical curves shown in Figs. 6 and 7 are determined with some uncertainty due to the fact that we use the values obtained from the experimental data for the interaction constants and the masses. However, the experimental errors of the interaction constants are very small, i.e., $F_\pi = 93.3 \pm 0.3$ MeV, $g = 6.08 \pm 0.03$, resulting in an uncertainty near 0.5%. The experimental results for the amplitude and the phase of the $\pi\pi$ scattering have an uncertainty near 15%; therefore, we do not show the errors of the theoretical values in Figs. 6 and 7.

7. ANALYSIS IN TERMS OF STOKES VECTORS

For further calculations, we will need the magnetic direct emission coupling c. It can be estimated

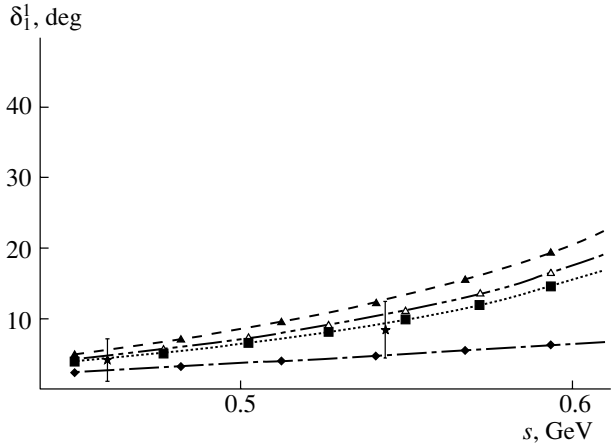

Fig. 7. The energy dependence of the $\pi\pi$-scattering phase $\delta_1^1(s)$ in the P wave at low energies. Note that this figure is a magnified part of the previous figure. The notation is the same as in Fig. 6.

using the experimental data on the direct emission contribution to the $K_L \to \pi^+\pi^-\gamma$ decay [12, 13]. The corresponding double differential decay width for an unpolarized photon is

$$\frac{d\Gamma(K_L \to \pi^+\pi^-\gamma)}{d\omega\, d\cos\theta} = \frac{2\alpha}{\pi}\frac{\beta^3}{\beta_0}\left(1 - \frac{2\omega}{m_K}\right) \qquad (28)$$
$$\times \frac{\Gamma(K_L \to \pi^+\pi^-)c^2m_K^4}{16|A|^2|\eta_{+-}|^2}\sin^2\theta.$$

Identifying this expression with the direct emission rate given in [12, 13], we obtain $|c| = 0.76|A|$.

It is worth mentioning that there is no interference between the amplitude terms with opposite CP parity if photon polarization is not observed. However, the interference is nonzero when the polarization is measured, as was repeatedly emphasized in [2–4, 20]. Therefore, any CP violation involving interference of electric and magnetic amplitudes is encoded in the polarization state of the photon.

To determine the nature of this interference, we write the $K_{S,\,L} \to \pi^+\pi^-\gamma$ decay amplitude more generally as

$$A(K_{S,L} \to \pi^+\pi^-\gamma) = ET_E + MT_M, \qquad (29)$$

where for the K_S decay E and M have the form

$$E = \frac{\hat{e}Ae^{i\delta_0^0}}{(pk)(qk)} + \hat{e}(a+b) \text{ and } M = i\hat{e}\eta_{+-}c, \quad (30)$$

and in the case of the K_L decay we have

$$E = \eta_{+-}\left[\frac{\hat{e}Ae^{i\delta_0^0}}{(pk)(qk)} + \hat{e}a + b)\right] \text{ and } M = i\hat{e}c. \qquad (31)$$

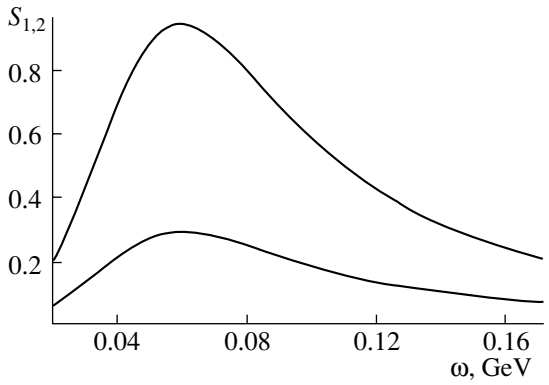

Fig. 8. Stokes parameters S_1 (upper curve) and S_2 (lower curve) for the $K_L \to \pi^+\pi^-\gamma$ decay.

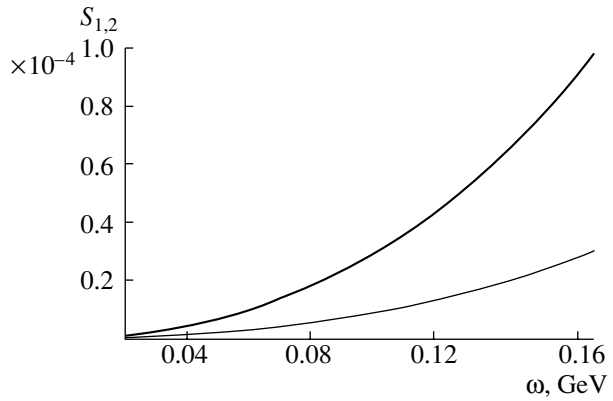

Fig. 9. Stokes parameters S_1 (upper curve) and S_2 (lower curve) for the $K_S \to \pi^+\pi^-\gamma$ decay.

The photon polarization can be defined in the terms of the density matrix [42]

$$\rho = \begin{pmatrix} |E|^2 & E^*M \\ EM^* & |M|^2 \end{pmatrix} = \frac{1}{2}(|E|^2 + |M|^2)\,[1 + \mathbf{S}\cdot\boldsymbol{\tau}]\,, \tag{32}$$

where $\boldsymbol{\tau} = (\tau_1, \tau_2, \tau_3)$ denotes Pauli matrices and $\mathbf{S}$ is the Stokes vector of the photon with components

$$S_1 = 2\mathrm{Re}(E^*M)/(|E|^2 + |M^2|), \tag{33}$$

$$S_2 = 2\mathrm{Im}(E^*M)/(|E|^2 + |M^2|), \tag{34}$$

$$S_3 = (|E|^2 - |M|^2)/(|E|^2 + |M^2|). \tag{35}$$

The effects of CP violation reside in components S_1 and S_2, while the component S_3 measures the relative strength of the amplitude terms with opposite CP parity. The component S_2 is the net circular polarization of the photon; it is proportional to the difference of $|E - iM|^2$ and $|E + iM|^2$, which are the probabilities for left-handed and right-handed polarization. The S_1 component appears as a coefficient of an interference term in the case of linear polarization. If one chooses the polarization angle ϕ as the angle between $\mathbf{e}$, the polarization vector, and the unit vector $\mathbf{n}_\pi$ normal to the decay plane ($\mathbf{k} = (0, 0, \omega)$, $\mathbf{n}_\pi = (1, 0, 0)$, $\mathbf{p} = (0, p\sin\theta, p\cos\theta)$), then the decay amplitude will be proportional to the following expression:

$$|A(K_{S,\,L} \to \pi^+\pi^-\gamma)|^2 \sim 1 - (S_3\cos 2\phi + S_1 \sin 2\phi). \tag{36}$$

It is obvious from (36) that the measurement of linear polarization in principle allows one to extract the terms with opposite CP parity (E and M):

$$|A(K_{S,\,L} \to \pi^+\pi^-\gamma)|^2 \sim |E|^2, \quad \phi = \pi/2 + \pi n,$$

$$|A(K_{S,\,L} \to \pi^+\pi^-\gamma)|^2 \sim |M|^2, \quad \phi = \pi n,$$

where n is integer.

In order to obtain a quantitative estimate of the CP-violation effects, we study the photon energy dependence of the Stokes vector components. We show the photon energy dependence of the S_1 and S_2 components in the K_L decay in Fig. 8 and in the K_S decay in Fig. 9. In Fig. 10, we demonstrate the S_3-component photon energy dependence in $K_{L,S} \to \pi^+\pi^-\gamma$ decays to obtain the estimate of the relative strength of the CP-violation effects in the decays under consideration. We see that the obtained results on the $K_L \to \pi^+\pi^-\gamma$ decay coincide with the results of [21–23]. Taking into account the physical meaning of the S_3, we conclude that the CP-violation effects in $K_S \to \pi^+\pi^-\gamma$ decay are rather small. The reason is that the bremsstrahlung contribution shades the magnetic-direct emission contribution even for high photon energies.

It was suggested in [24–26] to use in place of $\mathbf{e}$ the vector $\mathbf{n}_l$ normal to the e^+e^- plane in the decay $K_L \to \pi^+\pi^-e^+e^-$. This can be achieved by replacing e_μ in the radiative amplitudes (5) and (6) by $(\hat{e}/k^2)\overline{u}(k_-)\gamma_\mu v(k_+)$, where k_+ and k_- are momenta of e^+ and e^-, respectively, and $v(k_+)$ and $\overline{u}(k_-)$ are wave functions of e^+ and e^-, respectively. This motivates the study of the distribution $d\Gamma/d\phi$ in the decays $K_{S,\,L} \to \pi^+\pi^-e^+e^-$, where ϕ is an angle between $\pi^+\pi^-$ and e^+e^- planes.

The distribution $d\Gamma/d\phi$ can be written in the general form

$$\frac{d\Gamma}{d\phi} = \Gamma_1\cos^2\phi + \Gamma_2\sin^2\phi + \Gamma_3\sin\phi\cos\phi. \tag{37}$$

The last term changes sign under the transformation $\phi \to \pi - \phi$ and produces an asymmetry $A^{L,S}_{\pi\pi,ee}$ in the distribution of the angle ϕ between the vectors normal to the $\pi^+\pi^-$ and e^+e^- planes. The asymmetry is

defined by the following expression:

$$A^{L,S}_{\pi\pi,ee} = \frac{\left(\int_0^{\pi/2} - \int_{\pi/2}^{\pi} + \int_{\pi}^{3\pi/2} - \int_{3\pi/2}^{2\pi}\right)(d\Gamma/d\phi)d\phi}{\left(\int_0^{\pi/2} + \int_{\pi/2}^{\pi} + \int_{\pi}^{3\pi/2} + \int_{3\pi/2}^{2\pi}\right)(d\Gamma/d\phi)d\phi}. \quad (38)$$

In the case of the K_L decay, the contributions of the amplitude terms with different CP parity to the decay probability are of comparable magnitude. This fact should result in a significant value of the asymmetry. This was demonstrated in [21–26, 28, 29]. The $K_L \to \pi^+\pi^-e^+e^-$ decay probability and the CP-violating asymmetry from the correlation of the $\pi^+\pi^-$ and e^+e^- planes calculated in [21–26, 28, 29],

$$\mathrm{Br}(K_L \to \pi^+\pi^-e^+e^-) = 3.1 \times 10^{-7}, \quad (39)$$
$$|A^L_{\pi\pi,ee}| = 14\%,$$

are in accordance with the recent experimental data published by KTeV [27] [$\mathrm{Br}^{\mathrm{exp}}(K_L \to \pi^+\pi^-e^+e^-) = (3.32 \pm 0.14 \pm 0.28) \times 10^{-7}$, $|A^L_{\pi\pi,ee}|^{\mathrm{exp}} = (13.6 \pm 2.5 \pm 1.2)\%$].

The CP-violating asymmetry $A^{L,S}_{\pi\pi,ee}$ arises from the interference of the amplitude terms with different CP parity. $A^{L,S}_{\pi\pi,ee}$ is proportional to the expression

$$\int d\cos\theta_\pi ds dk^2 \sin^2\theta_\pi \beta^3 X^2 \mathrm{Re}[ME^*]\left(\frac{s}{k^2}\right), \quad (40)$$

where

$$X = \left[\left(\frac{m_K^2 - s - k^2}{2}\right)^2 - sk^2\right]^{1/2},$$

θ_π is the angle between π^+ 3-momentum and the K_L 3-momentum in the $\pi^+\pi^-$ rest frame, $s = (p+q)^2$, and $k^2 = (k_+ + k_-)^2$. The resulting CP-violating asymmetry in the $K_L \to \pi^+\pi^-e^+e^-$ decay is

$$|A^L_{\pi\pi,ee}| = (13.4 \pm 0.9)\%. \quad (41)$$

The value of the asymmetry is determined with some uncertainty due to the fact that we use the values obtained from the experimental data for interaction constants, masses, and phase δ_0^0. The central values of the asymmetry obtained in the present paper and in [21–26, 28, 29] coincide within the accuracy of the calculation.

According to the results of the present paper, the CP-violating asymmetry in the $K_S \to \pi^+\pi^-e^+e^-$ decay is

$$|A^S_{\pi\pi,ee}| = (5.1 \pm 0.4) \times 10^{-5}. \quad (42)$$

This value of the asymmetry could be expected qualitatively from the analysis of the $K_S \to \pi^+\pi^-\gamma$ decay amplitude, where the CP-violating magnetic direct emission contribution is rather small compared to the CP-conserving part of the amplitude.

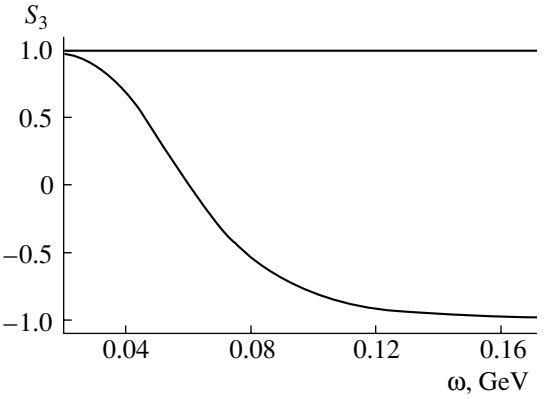

Fig. 10. Stokes parameter S_3 for the $K_S \to \pi^+\pi^-\gamma$ decay (straight line $S_3 = 1$) and for the $K_L \to \pi^+\pi^-\gamma$ decay (lower curve).

8. CONCLUSION

In the case of the radiative K-meson decays, we calculated the phases of amplitude terms using a simple realistic model of pion–pion interaction [16]. Also, we calculated the pion-loop contribution (E_D^{loop}) to the electric direct emission amplitude. The interference of the E_D^{loop} with the bremsstrahlung contribution is the main source of the departure of the photon spectrum from pure bremsstrahlung. To detect this effect, the photon spectrum should be measured with an accuracy better than 1% for photon energies near 160 MeV and better than 0.1% for photon energies near 50 MeV.

We compared our results on the interference contribution to the $K_S \to \pi^+\pi^-\gamma$ decay probability with those of [5, 15] and found that the interference branching ratio differs from the one obtained in [5, 15] (see table). If the counterterm contributions are set to zero ($k_f = 0$), the result of the present paper and the result obtained in the framework of the ChPT are in agreement for the photon energy cut $\omega > 20$ MeV. However, for the photon energy cuts $\omega > 50$ MeV and $\omega > 100$ MeV, a discrepancy appears. It is due to the fact that the photon spectra of these results differ. It can be clearly seen from Fig. 1, where the result of the present paper (solid curve) and the results of [15] (dashed curves, $k_f = -0.5,\ 0,\ +0.5$) for the photon spectra of the interference contribution are shown.

If the counterterm contributions are switched on, then the arising discrepancy is rather large for values of the counterterm contributions given in [15] (e.g., in the case of $\omega > 20$ MeV for $k_f = 0.5$, the result of the

present paper is 1.7 times smaller that the one of [15]; for $k_f = -0.5$, it is 3.3 times larger—see table). It should be stressed that the counterterm contributions do not depend on the photon energy and they exhibit behavior different from the results of the present paper (see Fig. 1). This discrepancy arises from different models of $\pi\pi$ interaction and the fact that we took into account the energy dependence of the phases, while in the ChPT approach the phases were taken at the energy $\sqrt{s} = m_K$. Thus, it is clear that the standard ChPT approach for the $K \to \pi\pi\gamma$ decays even with higher order counterterms taken into account cannot reproduce the contribution of the ρ meson.

Actually, in the case of $\pi\pi$ scattering in the framework of the ChPT, the ρ meson shows up in two ways: as low-energy constants and as a direct resonance. However, in papers on $K \to \pi\pi\gamma$ decays, only low-energy constants are accounted for. Such an approach does not take into account the energy dependence of the $\delta_1^1(s)$ phase, i.e., the behavior of the ρ propagator, because the contribution of low-energy constants does not depend on the photon energy. Thus, some dynamical features are missing in the ChPT approach for the $K \to \pi\pi\gamma$ decays.

In order to show that the inclusion of the ρ meson in the analysis of the electric direct emission in the $K \to \pi\pi\gamma$ decays is important, we addressed the problem of the $\pi\pi$ scattering in the P wave. We compared with the experimental data the predictions for the phase of the $\pi\pi$ scattering in the P wave obtained in the framework of different models. As seen from Fig. 6, the simple realistic model and the ChPT with ρ are in accordance with the experimental data. The ChPT without ρ shows strong disagreement with the data. In Fig. 7, we present the behavior of the phase at low energies. The ChPT with ρ and our simple realistic model predictions differ due to the fact that actually the one-loop approximation was used to describe the ρ-meson contribution to the phase obtained in the framework of the ChPT with ρ, while we summed the iterated bubble diagrams to obtain the phase. Thus, we can conclude from the analysis of the $\pi\pi$ scattering in the P wave that the inclusion of the ρ meson, which is done in the present paper, in the $K \to \pi\pi\gamma$ decays is important.

Regarding the dependence of the K_S decay probability on photon polarization, we found that the measurement of the linear polarization allowed in principle extraction of terms with opposite CP parity.

We also studied the $K_{S,\,L} \to \pi^+\pi^- e^+ e^-$ decays. The CP-violating asymmetry in the case of the K_L decay was found to be $(13.4 \pm 0.9)\%$. The central values of the asymmetry obtained in the present paper and in [21–26, 28, 29] coincide within the accuracy of the calculation. We found that the CP-violating asymmetry in the case of the K_S decay is substantially smaller than in the K_L case, being equal to $(5.1 \pm 0.4) \times 10^{-5}$, as could be expected from the analysis of the $K_S \to \pi^+\pi^-\gamma$ decay.

ACKNOWLEDGMENTS

I appreciate L.B. Okun's scientific supervision and formulation of this problem. I would also like to thank R.B. Nevzorov for fruitful discussions and G. D'Ambrosio, M.I. Vysotsky, and E.P. Shabalin for valuable remarks.

This work was supported by the Russian Foundation for Basic Research (project no. 96-02-18010).

REFERENCES

1. H. Chew, Nuovo Cimento **26**, 1109 (1962).
2. G. Costa and P. K. Kabir, Nuovo Cimento A **51**, 564 (1967).
3. L. M. Sehgal and L. Wolfenstein, Phys. Rev. **162**, 1362 (1967).
4. A. D. Dolgov and L. A. Ponomarev, Yad. Fiz. **4**, 367 (1967) [Sov. J. Nucl. Phys. **4**, 262 (1967)].
5. G. D'Ambrosio and G. Isidori, Z. Phys. C **65**, 649 (1995).
6. G. D'Ambrosio, M. Miragliuolo, and P. Santorelli, *Radiative Non-Leptonic Decays: The DAΦNE Physics Handbook* (Frascati, 1992), p. 265.
7. A. Alavi-Harati *et al.*, Phys. Rev. Lett. **83**, 22 (1999).
8. X.-G. He and G. Valencia, Phys. Rev. D **61**, 075003 (2000); hep-ph/9908298.
9. G. Colangelo, G. Isidori, and J. Portoles, Phys. Lett. B **470**, 134 (1999).
10. J. Tandean and G. Valencia, Phys. Rev. D **62**, 116007 (2000); hep-ph/0008238.
11. A. S. Carrol *et al.*, Phys. Rev. Lett. **44**, 529 (1980).
12. E. J. Ramberg *et al.*, Phys. Rev. Lett. **70**, 2525 (1993).
13. S. Kettell, in *Proc. of the 3rd Workshop on Physics and Detectors for DAΦNE (DAΦNE 99), Frascati, Italy, 1999,* p. 449; hep-ex/0002009.
14. H. Taureg *et al.*, Phys. Lett. B **65B**, 92 (1976).
15. G. D'Ambrosio, M. Miragliuolo, and F. Sannino, Z. Phys. C **59**, 451 (1993).
16. B. W. Lee and M. T. Vaughn, Phys. Rev. Lett. **4**, 578 (1960).
17. K. Watson, Phys. Rev. **95**, 228 (1954).
18. E. Fermi, Nuovo Cimento Suppl. **2**, 58 (1955).
19. S. Fubini, Y. Nambu, and V. Wataghin, Phys. Rev. **111**, 329 (1958).
20. M. McGuigan and A. I. Sanda, Phys. Rev. D **36**, 1413 (1987).
21. L. M. Sehgal and J. van Leusen, Phys. Rev. Lett. **83**, 4933 (1999).
22. L. M. Sehgal, in *Chicago Conference on Kaon Physics (K 99), Chicago, IL, 1999*; hep-ph/9908338.
23. L. M. Sehgal and J. van Leusen, hep-ph/0006336.

24. L. M. Sehgal and M. Wanninger, Phys. Rev. D **46**, 1035 (1992).
25. P. Heiliger and L. M. Sehgal, Phys. Rev. D **48**, 4146 (1993).
26. J. K. Elwood and M. B. Wise, Phys. Rev. D **52**, 5095 (1995).
27. A. Alavi-Harati *et al.*, Phys. Rev. Lett. **84**, 408 (2000); hep-ex/9908020.
28. J. K. Elwood, M. B. Wise, M. J. Savage, and J. W. Walden, Phys. Rev. D **53**, 4078 (1996).
29. M. J. Savage, in *Chicago Conference on Kaon Physics (K 99), Chicago, IL, 1999*.
30. H. Pichl, Eur. Phys. J. C **20**, 371 (2001).
31. G. Ecker and H. Pichl, Phys. Lett. B **507**, 193 (2001).
32. F. E. Low, Phys. Rev. **110**, 974 (1958).
33. L. B. Okun, *Leptons and Quarks* (North-Holland, Amsterdam, 1982).
34. R. B. Nevzorov, private communication.
35. J. Gasser and H. Leutwyler, Ann. Phys. (N.Y.) **158**, 142 (1984).
36. C. Riggenbach, J. Gasser, J. F. Donoghue, and B. R. Holstein, Phys. Rev. D **43**, 127 (1991).
37. J. Bijnens, Nucl. Phys. B **337**, 635 (1990).
38. J. Bijnens, G. Colangelo, G. Ecker, *et al.*, Phys. Lett. B **374**, 210 (1996).
39. G. Colangelo, J. Gasser, and H. Leutwyler, Nucl. Phys. B **603**, 125 (2001).
40. V. Bernard, N. Kaiser, and U.-G. Meissner, Nucl. Phys. B **364**, 283 (1991).
41. E. A. Alekseeva *et al.*, Zh. Éksp. Teor. Fiz. **82**, 1007 (1982) [Sov. Phys. JETP **55**, 591 (1982)].
42. A. I. Akhieser and V. B. Berestetskii, *Quantum Electrodynamics* (Interscience, New York, 1981).

Physics of Atomic Nuclei, Vol. 67, No. 2, 2004, pp. 328–336. Translated from Yadernaya Fizika, Vol. 67, No. 2, 2004, pp. 346–354.

ELEMENTARY PARTICLES AND FIELDS
Theory

Production of Charged Higgs Bosons at LHC in Light-Quark Annihilation

S. R. Slabospitsky*

Institute for High Energy Physics, Protvino, Moscow oblast, 142284 Russia

Received May 28, 2002; in final form, December 24, 2002

Abstract—The CMS potential (at LHC) for seeking the production of a charged Higgs boson is investigated for large values of $\tan\beta$ (between 20 and 50) and a relatively light charged Higgs boson ($M_H = 200$–400 GeV). A simple parametrization is proposed for the $M_\perp(j, \not{E}_\perp)$ distributions of signal and background events. The possibility of measuring the mass of the charged Higgs boson and $\tan\beta$ is investigated. © *2004 MAIK "Nauka/Interperiodica".*

1. INTRODUCTION

A charged Higgs boson ($H^\pm$) appears in many well-motivated extensions of the Standard Model (for example, in the minimal supersymmetric standard model [1]). Two free parameters, M_H (mass) and $\tan\beta$ (ratio of the respective vacuum expectation values) determine all properties and couplings of the $H^\pm$ boson. Searches for these objects have been performed in many experiments. For any value of $\tan\beta$, four collaborations at LEP set lower limits on the $H^\pm$-boson mass in a model-independent way, $M(H^\pm) > 78.5$ GeV [2]. Two experiments at the Tevatron, CDF and D0, performed a few searches for $H^\pm$ [3]. They ruled out the small-$\tan\beta$ (below unity) and the large-$\tan\beta$ (above 40) region up to 120 and 160 GeV, respectively. An additional indirect limit on the parameters of the charged Higgs bosons can be obtained from low-energy physics—for example, from an analysis of the branching ratios for the decays $D_s \to \tau\nu$ and $B \to \tau\nu$ [4].

The potential of LHC for discovering $H^\pm$ was investigated both by the ATLAS [5] and by the CMS [6, 7] Collaboration. It was established that, for a heavy charged Higgs boson with $M(H^\pm) > m_t$ (where m_t is the t-quark mass), the associated production of a top quark and a Higgs boson in the subprocesses

$$gb \to tH^\pm, \quad gg \to tH^\pm\bar{b}$$

is the most promising channel [8–11].

In the present article, we consider the additional subprocess of $H^\pm$-boson production through the annihilation of a light $q\bar{q}'$ pair from the initial hadrons (protons):

$$q\bar{q}' \to H^\pm, \quad q = d, u, s, c, b. \tag{1}$$

The production of $H^\pm$ bosons in this s-channel with subsequent $H^\pm$ decay to a $t\bar{b}$ pair was investigated earlier (see [12–14]).

Here, we investigate the CMS potential for studying s-channel $H^\pm$-boson production via light-quark annihilation with subsequent $H^\pm$ decay to a $\tau^\pm\nu_\tau$ lepton pair (see also [14]):

$$q\bar{q}' \to H^\pm \to \tau^\pm\nu_\tau.$$

We perform our calculation for the case of pp collisions at $\sqrt{s} = 14$ TeV,

$$pp \to H^\pm X \tag{2}$$

for large values of $\tan\beta$ and four values of the mass of the charged Higgs boson:

$$\tan\beta = 50; \quad M_H = 200, 250, 300, 400 \text{ GeV}. \tag{3}$$

We use the CTEQ5L parametrization [15] of parton distributions. All estimates of the expected number of events were obtained for a three-year low-luminosity run of LHC:

$$L_{\text{int}} \equiv \int \mathcal{L}dt = 30 \text{ fb}^{-1}. \tag{4}$$

We employed the TopReX 3.25 event generator [16] to calculate the signal and background processes and then applied the well-known PYTHIA 6.157 package [17] to describe the hadronization of quarks and gluons. A proper simulation of the detector response was performed by passing all generated events through the fast Monte Carlo package CMSJET 4.703 [18].

Upon the application of all appropriate cuts, the expected number of signal events proves to be relatively large (about 10^2–10^3) for $M_H = 200$–400 GeV and $\tan\beta \sim 40$–50. Therefore, not only does this s-channel $H^\pm$-boson-production process allow one to

*e-mail: Sergey.Slabospitsky@mx.ihep.ru

1063-7788/04/6702-0328$26.00

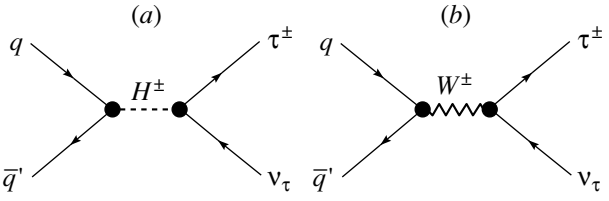

Fig. 1. Diagrams describing the annihilation of light quarks ($q = d, u, s, c, b$) into a $\tau^{\pm}\nu_{\tau}$ pair via (a) $H^{\pm}$- and (b) $W^{\pm}$-boson exchange.

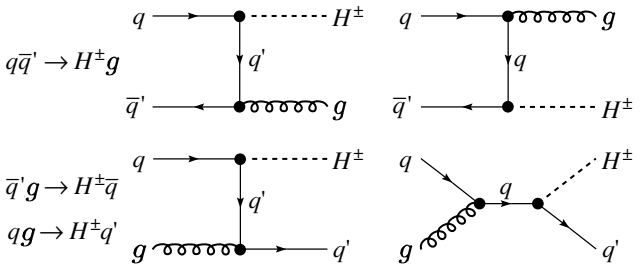

Fig. 2. Diagrams describing next-to-leading-order corrections to the $2 \to 1$ process of $H^{\pm}$-boson production ($q = d, u, s, c, b$).

establish the presence of a signal from $H^{\pm}$ bosons, but it also makes it possible to measure the parameters (the mass and $\tan\beta$) of the charged Higgs boson.

2. SIGNAL-EVENT GENERATION

Figure 1a presents the diagram describing the process under consideration, that in (1). Note that Higgs boson couplings to fermions are proportional to the masses of these fermions [1]. Therefore, the corresponding production cross section has a strong dependence on the light-quark masses. In our calculations, we use the so-called "current" values of m_q (in GeV) [19],

$$m_d = 0.009, \quad m_u = 0.005, \quad m_s = 0.150,$$
$$m_c = 1.250, \quad m_b = 4.800,$$

which are less (especially for light d, u, and s quarks) than the quark-mass values in PYTHIA ($m_d = m_u = 300$ MeV; see [17]).

We also took into account radiative QCD corrections to the $2 \to 1$ process (1). In doing this, we calculated the next-to-leading-order processes ($2 \to 2$) (see the diagrams in Fig. 2)

$$q\bar{q}' \to H^{\pm}g, \qquad qg \to H^{\pm}q', \qquad (5)$$
$$\bar{q}'g \to H^{\pm}\bar{q}.$$

It is well known that the inclusion of such processes at low $\hat{k}_{\perp}$ (where $\hat{k}_{\perp}$ is the transverse momentum of the final particle, $H^{\pm}$, q, or g, in the c.m. frame of colliding partons) leads to the double-counting problem. To demonstrate this, we note that, in this region ($\hat{k}_{\perp} \to 0$), the virtual quark entering into the $q\bar{q}'H^{\pm}$ vertex has a very low virtuality and can therefore be considered as an on-shell parton. As a result, any $2 \to 2$ process in (5) can be factorized into two subprocesses. The first is the splitting of an primary parton (q or g) into two partons:

$$q \to qg, \quad \bar{q}' \to \bar{q}'g, \quad g \to q\bar{q}.$$

The second is quark–antiquark annihilation into $H^{\pm}$, where one quark (antiquark) comes from the primary hadron, while the second quark appears owing to parton splitting. However, this process (annihilation) has already been taken into account as the process in (1). This problem was considered in detail by Balazs *et al.* [20], who calculated the total $\mathcal{O}(\alpha_s)$ QCD corrections [reactions (5)] to the s-channel production process (1), including a QCD resummation over multiple soft-gluon emission. In our numerical calculations, we rely on an approximation that ensures desirable accuracy (see [21] for details). This approximate method is based on considering the distribution of the charged Higgs boson with respect to the transverse momentum $p_{\perp}(H)$ defined in the c.m. frame of colliding protons. In the region of low $p_{\perp}(H)$, the main contribution to Higgs boson production comes from the $2 \to 1$ process (1), while, at high $p_{\perp}(H)$, Higgs boson production is due primarily to the $2 \to 2$ process (5).

Thus, the method of event generation is as follows. First, we generate events involving $H^{\pm}$-boson production via the $2 \to 1$ process (1). Any event from this sample will be accepted if the transverse momentum of the charged Higgs boson is less than some value p_0. After that, we generate a second sample of events due to the $2 \to 2$ process (5) at the transverse momentum of final partons that satisfies the condition $\hat{k}_{\perp} > \hat{k}_0$. Any event from this second sample will be accepted if $p_{\perp}(H) > p_0$. Thus, the resulting (total) sample of $H^{\pm}$-boson-production events is the sum of two contributions:

$$N(pp \to H^{\pm}X)$$
$$= N^{(2\to1)}(pp \to H^{\pm}; p_{\perp}(H) < p_0)$$
$$+ N^{(2\to2)}(pp \to H^{\pm}\text{jet}; \hat{k}_{\perp} \geq \hat{k}_0, p_{\perp}(H) \geq p_0).$$

Our numerical calculations revealed that the smoothest behavior of the resulting $p_{\perp}(H)$ distribution is achieved for the following values of the above parameters:

$$\hat{k}_0 \approx 20 \text{ GeV}, \quad p_0 = 29.5 \text{ GeV} \quad \text{for}$$
$$M_H = 200\text{–}400 \text{ GeV}.$$

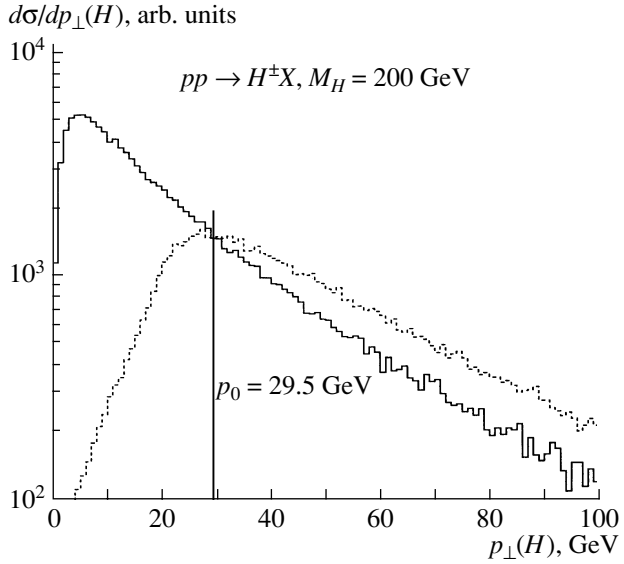

Fig. 3. Distribution $d\sigma/dp_\perp(H)$ for $H^\pm$-boson production in (solid histogram) the leading-order subprocess (1) and (dashed histogram) the next-to-leading-order subprocesses (5). The vertical line corresponds to the parameter value of $p_0 = 29.5$ GeV (see main body of the text).

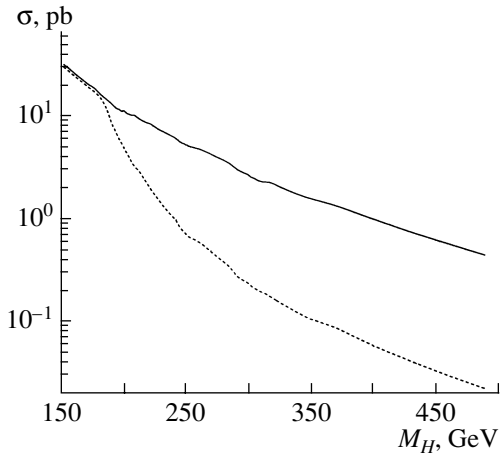

Fig. 4. Total cross section for $H^\pm$-boson production in pp collisions [reaction (2)] at $\sqrt{s} = 14$ TeV and $\tan\beta = 50$ versus the mass M_H of the charged Higgs boson (solid curve). The dashed curve represents the same cross section multiplied by the branching fraction for the decays $H^\pm \to \tau^\pm\nu_\tau$.

The corresponding distribution with respect to $p_\perp(H)$ is shown in Fig. 3.

The behavior of the total production cross section for $\tan\beta = 50$ versus M_H is displayed in Fig. 4. For $\tan\beta \geq 10$, the branching ratio for the $H^\pm \to \tau^\pm\nu_\tau$ decay is virtually independent of $\tan\beta$ (see Fig. 5*a*). Therefore, the $\tan\beta$ dependence of the cross section for $H^\pm$ production has a very simple quadratic form,

$$\sigma(pp \to H^\pm X) \propto \tan^2\beta. \qquad (6)$$

At the same time, the branching fraction $\mathrm{Br}(H^\pm \to \tau^\pm\nu_\tau)$ has a strong dependence on the mass of the charged Higgs boson in the range $M_H = 200$–400 GeV (see Fig. 5*b*) owing to the opening of the decay channel $H^\pm \to t\bar{b}$. Therefore, a simultaneous measurement of the cross section for the production of a charged Higgs boson and of its mass provides the possibility of indirectly determining the value of the parameter $\tan\beta$.

3. SIGNAL–BACKGROUND SEPARATION

The most important and irremovable background comes from $\tau^\pm\nu_\tau$ production via virtual (Drell–Yan) $W^\pm$-boson exchange (see Fig. 1*b*). All other possible sources of background make relatively small contributions; therefore, we will not consider them here.

Because of $H^\pm f\bar{f}'$ and $W^\pm f\bar{f}'$ interactions, final τ leptons produced via H- or W-boson exchanges have opposite polarizations (see [8]). This feature provides an effective way to suppress the background.

In order to identify and reconstruct the hadronic decays of the τ lepton, we use an algorithm that allows one to identify τ jets in the one-prong decay mode (where the final state involves one charged particle, the others being neutral). A detailed description of the respective procedure is given in [6]. The algorithm used is based on the fact that the hadronic decays of the τ leptons from $H^\pm \to \tau^\pm\nu_\tau$ decays are seen as a narrow low-multiplicity hadron jet, with a large fraction of the calorimetric energy being due to a single charged hadron. Recall that τ leptons produced in the decays of $H^\pm$ and $W^\pm$ bosons have opposite polarizations. It follows that, in the total energy of the τ jet, the fraction that is carried away by the charged hadron from $W^\pm$-boson decay is much less than that in the case of $H^\pm$-boson decay. This can clearly be seen from Fig. 6, which shows the distribution of signal ($H^\pm$) and background (W^*) events with respect to the variable R_h,

$$R_h \equiv E(h^\pm)/E(\mathrm{jet}),$$

where $E(h^\pm)$ and $E(\mathrm{jet})$ are the energies of the charged hadron and the τ jet, respectively. Note that the best signal–background separation in terms of this variable is achieved for $R_0 \geq 0.8$.

To suppress a large W + jet background involving the decays $W \to \tau\nu$ ($\tau \to h\nu$), we also require a strong central-jet veto; that is, no other jet with $E_\perp \geq 20$ GeV must appear in the region $|\eta| \leq 4.5$ (where $E_\perp$ is the transverse energy, $E_\perp = E\sin\theta$, θ being the azimuthal angle, and η is the pseudorapidity).

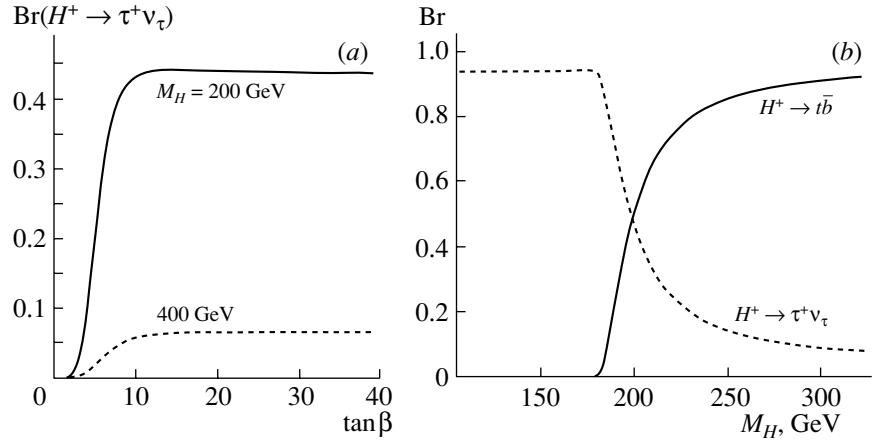

Fig. 5. Branching fractions of $H^\pm$-boson decays to $\tau^\pm\nu_\tau$ and $t\bar{b}$ pairs versus (*a*) $\tan\beta$ and (*b*) M_H.

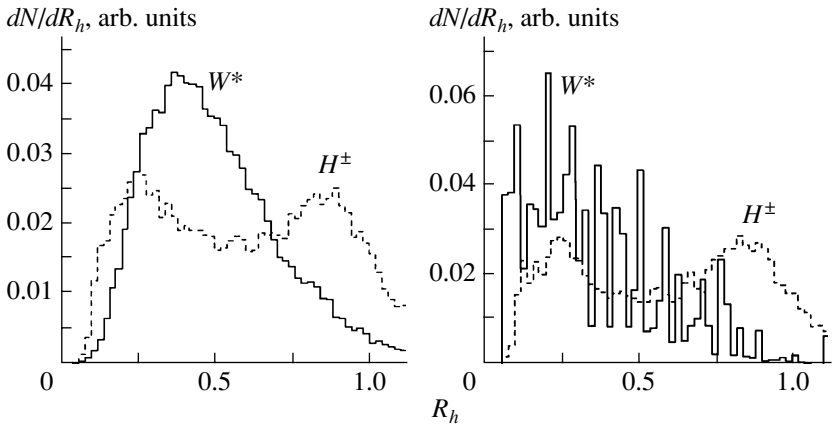

Fig. 6. Distribution dN/dR_h of events versus the variable R_h. The solid-line (dashed-line) histograms correspond to background (signal) events. The left histograms were obtained before any cuts, while the right ones correspond to the requirements of jet veto and $E_\perp(\tau\,\text{jet}), \not{E}_\perp \geq 50$ GeV.

Thus, the following kinematic cuts are applied to separate a $H^\pm \to \tau^\pm\nu_\tau$ (with $\tau^\pm \to \pi^\pm + X^0 + \nu$) signal. There must be (i) one identified τ jet with $E_\perp \geq 50$ GeV and $|\eta| < 2.0$; (ii) a missing transverse energy, $\not{E}_\perp \geq 50$ GeV; (iii) no other hadronic jets with $E_\perp(j) \geq 20$ GeV in the region $|\eta| \leq 4.5$ (jet veto); (iv) no other identified objects (leptons, photons) with $E_\perp \geq 10$ GeV in the region $|\eta| \leq 2.4$; and (v) $R_h \geq R_0 = 0.8$ (to suppress the W^*-boson contribution).

The expected numbers of events for an integrated luminosity of 30 fb^{-1} and the corresponding signal significances ($N_S/\sqrt{N_S + N_B}$, where N_S and N_B are the numbers of, respectively, signal and background events) after the application of all cuts are given in Table 1.

4. PARAMETRIZATION OF THE $M_\perp$ DISTRIBUTION

Since the expected numbers of signal and background events are relatively large, $N_S \sim (10^2{-}10^3)$ and $N_B \sim 10^3$ (see Table 1), we can try to determine the parameters of the $H^\pm$ bosons—namely, the mass of the charged Higgs boson (M_H) and $\tan\beta$. This can be done by fitting the distribution in the transverse mass $M_\perp(j,\, \not{E}_\perp)$ for the τ jet and in the missing energy:[1)]

$$M_\perp^2 = (E_\perp(j) + \not{E}_\perp)^2 - (\mathbf{p}_\perp(j) + \not{\mathbf{E}}_\perp)^2. \quad (7)$$

Here, $E_\perp(j)$ and $\mathbf{p}_\perp(j)$ are, respectively, the transverse energy and the transverse momentum of the τ jet, while $\not{E}_\perp$ and $\not{\mathbf{E}}_\perp$ are the missing transverse energy and the missing transverse momentum in an event.

[1)] In what follows, the symbol "j" labels τ jets.

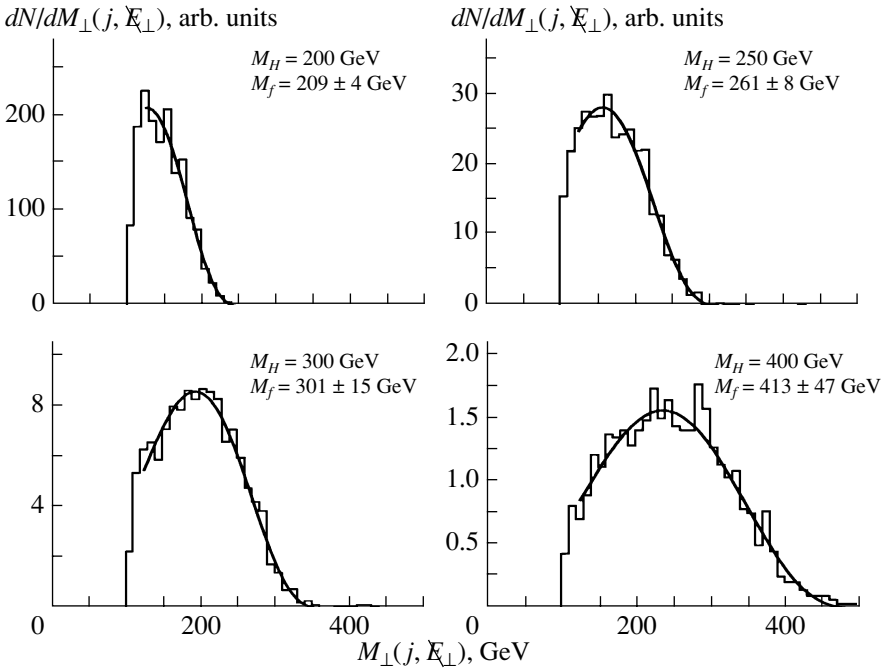

Fig. 7. Distribution $dN/dM_\perp(j,\not{E}_\perp)$ for signal events at four input values of the $H^\pm$-boson mass. The curves represent the results obtained by fitting the distribution to the function $F_S(M_\perp, M_f)$ in (10).

The procedure for identifying and reconstructing τ jets cannot reconstruct the full τ-lepton momentum because of the undetected neutrino from the decays $\tau^\pm \to h^\pm(h^0)\nu_\tau$. As a result, the well-known sharp two-body decay Jacobian peak in the $m_\perp(\tau,\nu)$ distribution transforms into a wide bump in the observable $M_\perp(j, \not{E}_\perp)$ distribution (see [6, 8] and Fig. 7).

The form of the distribution with respect to $M_\perp(j, \not{E}_\perp)$ results from the convolution of the theoretical $m_\perp(\tau,\nu)$ distribution [where τ and ν originate from the processes in (1) and (5)] and the "fragmentation" (or "decay") of the product τ lepton into the observable hadronic τ jet. This fragmentation process depends on the experimental device (detector acceptance, resolution, efficiency, etc.), as well as on the τ-jet-reconstruction algorithm, and cannot be calculated theoretically. At the same time, any appropriate functional form describing this fragmentation will provide a suitable parametrization in our case.

Table 1. Total number of signal (N_S) events and significance criterion ($N_S/\sqrt{N_S+N_B}$) after the application of all cuts (the number of events was generated for $\tan\beta = 50$ and four values of the $H^\pm$-boson mass; the integrated luminosity was $L_{int} = 30$ fb^{-1}; the total number of background events after the application of all cuts was $N_B = 1756$)

M_H, GeV	N_S	$\frac{N_S}{\sqrt{N_S+N_B}}$
200	1627	28
250	344	7.5
300	129	3.0
400	35	0.83

For the respective fragmentation function $D_{\tau\to j}(z)$, we use the simple parametrization [22]

$$D_{\tau\to j}(z) \propto z^\alpha (z_0 - z)^\lambda, \qquad (8)$$

where the scaling variable $z = p_\perp(j)/p_\perp(\tau)$ is the ratio of the transverse momentum of the τ jet $[p_\perp(j)]$ to the transverse momentum of the parent τ lepton $[p_\perp(\tau)]$. In contrast to what occurs in the case of quark fragmentation, the reconstructed momentum of the τ jet may be higher than the momentum of the parent τ lepton because of the detector resolution and the τ-jet-reconstruction algorithm.

We use the parametrization of $D_{\tau\to j}(z)$ in the form (8) to fit the corresponding z distributions for all values of the mass of the charged Higgs boson that are considered here—namely, for $m_H = 200$, 250, 300, and 400 GeV (see Table 2). Here, we do not need a good fit over the entire region of z. We are interested in the values of z that are close to unity, because this region corresponds to the maximum values of $M_\perp(j,\not{E}_\perp)$ that are close to M_H. Therefore, we use below the following set of parameters for $D_{\tau\to j}(z)$

Table 2. Fitted parameters of the fragmentation function $D_{\tau\to j}(z)$ from (8) (a fit was constructed at the fixed value of $z_0 = 1.22$ and four values of the $H^\pm$-boson mass over the range $0.65 < z < 1.2$)

M_H, GeV	α	λ	χ^2/N
200	6.9 ± 0.4	3.35 ± 0.17	42/23
250	6.5 ± 1.0	3.09 ± 0.32	3.2/23
300	6.6 ± 1.8	3.49 ± 0.61	1.8/23
400	6.1 ± 4.2	3.26 ± 1.44	0.23/23

from (8):

$$\alpha = 6.5, \quad \lambda = 3.5, \quad z_0 = 1.22. \tag{9}$$

Further, the form of the $M_\perp(j, \not{E}_\perp)$ distribution can be determined by taking the convolution of the $m_\perp(\tau,\nu)$ distribution of the τ lepton and neutrino [$\propto 1/\sqrt{M_H^2 - m_\perp(\tau,\nu)}$] with the fragmentation function $D_{\tau\to j}(z)$ (8); that is,

$$\frac{dN}{dM_\perp(j,\not{E}_\perp)} = F_S(M_\perp, M_f) \tag{10}$$
$$\equiv F_0 \int\limits_{M_\perp/M_f}^{z_0} \frac{M_\perp}{M_f} \frac{z^{\alpha-1}(z_0 - z)^\lambda}{\sqrt{z^2 - M_\perp^2/M_f^2}} dz,$$

where F_0 is a normalization factor and M_f is the mass of the charged Higgs boson to be determined from a fit.

The results of the fitting procedure by means of the parametrization $F_S(M_\perp, M_f)$ are shown in Fig. 7. One can see that not only does the proposed parametrization (10) provide a rather good description of the shape of the $M_\perp(j, \not{E}_\perp)$ distribution, but it also makes it possible to determine the fitted parameter M_f, which appears to be very close to the input mass of the charged Higgs boson.

In order to describe the $M_\perp(j, \not{E}_\perp)$ distribution of background events, we employed the traditional simple parametrization

$$F_B(M_\perp) = a_0 \exp(a_1 M_\perp + a_2 M_\perp^\delta). \tag{11}$$

From a fit to the background events, we obtained the following values of these parameters (a_0 is a normalization factor):

$$a_1 = -0.042 \pm 0.0007, \tag{12}$$
$$a_2 = 0.00019 \pm 0.000026,$$
$$\delta = 1.769 \pm 0.0288.$$

Table 3. Results of constructing a fit to the distribution in $M_\perp(j, \not{E}_\perp)$ for a sample of signal and background events for $M_\perp \geq 100$ GeV

M_H, GeV	M_f, GeV	N_B^f	N_S^f	$\dfrac{N_S^f}{\sqrt{N_B^f + N_S^f}}$
200	201.6 ± 2.1	1694	1444	25.8
250	255.6 ± 9.2	1694	250	5.9
300	305.0 ± 19.0	1694	115	2.7
400	392.0 ± 42.0	1694	41	1.0

5. SEPARATION OF THE SIGNAL AND DETERMINATION OF THE PARAMETERS OF THE CHARGED HIGGS BOSON

In fitting the $M_\perp(j, \not{E}_\perp)$ distribution for a joint sample of signal and background events, we can determine the normalization factors [F_0 in $F_S(M_\perp, M_f)$ and a_0 in $F_B(M_\perp)$] and the adjusted mass of the $H^\pm$ boson [M_f in $F_S(M_\perp, M_f)$].

This fitting procedure yielded results shown in Fig. 8 and in Table 3. One can see that the fitted mass (M_f) of the charged Higgs boson agrees with the input values (M_H) within the errors. Therefore, the proposed parametrization of the $M_\perp(j, \not{E}_\perp)$ distributions for signal events provides a reasonable way to determine the mass of the charged Higgs boson.

Using the normalization parameters F_0 and a_0 for signal and background events, we can then evaluate the corresponding numbers of events:

$$N_S^f = \int\limits_{M_{\perp,\min}} F_S(M_\perp, M_f) dM_\perp,$$
$$N_B^f = \int\limits_{M_{\perp,\min}} F_B(M_\perp) dM_\perp.$$

These evaluated values are given in Table 3. One can see that the values found for N_B^f and N_S^f from our fit are in good agreement with the expected (generated) numbers N_B and N_S (see Table 1).

As a criterion for detecting a signal, we use the following significance criterion (it corresponds to a 99% confidence level):

$$\frac{N_S^f}{\sqrt{N_S^f + N_B^f}} \geq 3. \tag{13}$$

It can be seen from Table 3 that, at a chosen value of the parameter $\tan\beta$ ($\tan\beta = 50$), the proposed procedure enables us to separate the signal of a charged

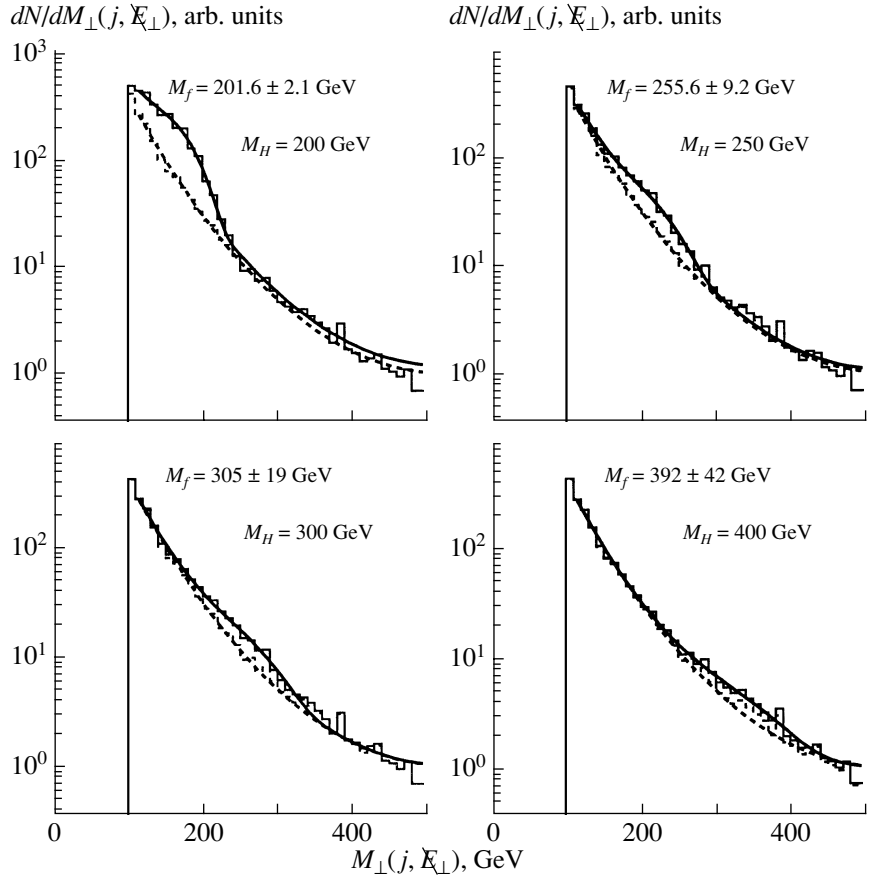

Fig. 8. Results obtained by fitting the distribution $dN/dM_\perp(j, \not{E}_\perp)$ to the sum of the parametrizations used for F_S and F_B: (solid curve) fit for signal and background events and (dashed curve) fit for only background events.

Higgs boson over a rather wide mass region, $M_H \leq 300$ GeV.

It was indicated above that, for $M_H \geq 200$ GeV, the cross section for $H^\pm$ production has a nearly quadratic dependence on $\tan\beta$ [see (6)]. Having determined the boson mass M_f from the fit, we can therefore compare the number of signal events that is extracted from the fit (N_S^f) with that expected (N_S) within the minimal supersymmetric standard model (N_S calculated on the basis of this model at $M_H = M_f$). As a result, we could determine the parameter $\tan\beta$ from the simple equation

$$\tan\beta_f = 50\sqrt{\frac{N_S^f}{N_S(M_f, \tan\beta = 50)}}, \qquad (14)$$

where $N_S(M_f, \tan\beta = 50)$ is the expected number of $H^\pm$-boson events according to the simulation at $M_H = M_f$ and $\tan\beta = 50$ [our default parameters, see (3)].

The corresponding uncertainty is evaluated as follows:

$$\delta(\tan\beta_f) = \frac{\tan\beta_f}{2}\sqrt{\delta_N^2 + \delta_M^2}, \qquad (15)$$

where δ_N is the relative error due to the parametrization of F_S. The second relative error (δ_M) is associated with the variation of the cross section in response

Table 4. Values of the parameters M_f and $\tan\beta_f$ from a fit to the $M_\perp(j, \not{E}_\perp)$ distribution for a joint sample of signal and background events (signal events were generated for the charged Higgs boson whose mass is set to the input value of $M_H = 200$ GeV and for several input values of $\tan\beta$)

$\tan\beta$	M_f, GeV	$\tan\beta_f$
50	201 ± 2	48.3 ± 2.6
40	203 ± 3	39.3 ± 4.1
30	205 ± 5	31.3 ± 5.2
20	212 ± 13	19.8 ± 7.6
15	222 ± 28	16.2 ± 10.6

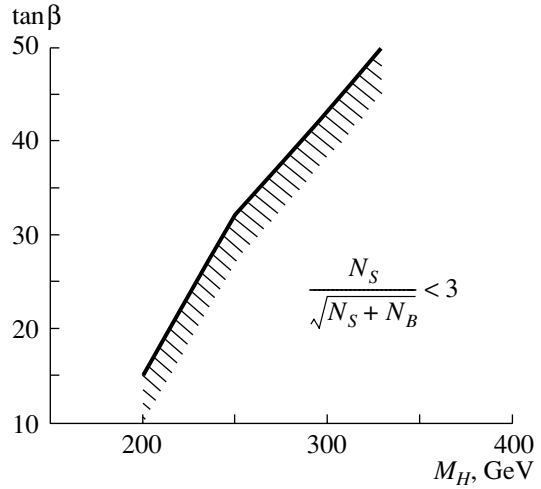

Fig. 9. Allowed region of the $H^{\pm}$-boson parameters (in the $M_H \times \tan\beta$ plane) that is accessible to investigation in s-channel $H^{\pm}$-boson production (left upper corner).

to a variation in M_H within its own errors:

$$\delta_M = \frac{1}{2\sigma}|\sigma(M_f - \Delta M) - \sigma(M_f + \Delta M)|.$$

The fitted values of M_f for several input values of $\tan\beta$ are given in Table 4. Obviously, a decrease in $\tan\beta$ leads to a decrease in the number of signal events. As a result, the error in M_f becomes greater. The corresponding extracted values of $\tan\beta$ (for the input value of $M_H = 200$ GeV) are given in Table 4.

Using the criterion in (13), we can evaluate the area (in the $M_H \times \tan\beta$ plot) that can be explored by using this process of s-channel $H^{\pm}$-boson production followed by a decay to $\tau^{\pm}\nu_{\tau}$ and hadronic τ decays. This region is shown in Fig. 9 (upper left corner).

6. CONCLUSION

We have investigated the CMS potential for studying $H^{\pm}$-boson production via the s-channel annihilation of light quarks. This has been done for a large value of $\tan\beta$ ($= 20$–50) and a relatively light charge Higgs boson ($M_H = 200$–400 GeV). Simple kinematical cuts have been proposed for signal–background separation. After the application of these cuts, a relatively large number of signal events ($N_S \sim 10^2$–10^3) may be expected. It follows that, for this region of the $H^{\pm}$-boson parameter space, $H^{\pm}$-boson production can be investigated with a good significance.

For the $M_{\perp}(j, \not{E}_{\perp})$ distributions of signal and background events, we have found simple parametrizations that make it possible to determine the mass of the charged Higgs boson, and this fitted mass value has proven to be very close to the input values of M_H. Comparing the number of signal events that was found from the fit with that which is expected within the minimal supersymmetric standard model, we can determine $\tan\beta$ with a reasonably high accuracy. Using a standard significance criterion, we have determined, in the $M_H \times \tan\beta$ plane, the region where this method can be applied.

ACKNOWLEDGMENTS

I am grateful to D. Denegri for proposing to study this topic. Many thanks are also due to S. Abdullin, H.-J. He, R. Kinnunen, A. Miagkov, A. Nikitenko, V. Obraztsov, and N. Stepanov for stimulating discussions.

REFERENCES

1. H. P. Nilles, Phys. Rep. **110**, 1 (1984); H. E. Haber and G. L. Kane, Phys. Rep. **117**, 75 (1985); J. F. Gunion, H. E. Haber, G. L. Kane, and S. Dawson, *The Higgs Hunters' Guide* (Addison-Wesley, Reading, 1990).
2. A. G. Holzner, Searches for Charged Higgs Bosons at LEP, in *XXXVI Rencontres de Moriond, "Electroweak Interactions and Unified Theories," Les Arcs, France, March 2001*; hep-ex/0105045.
3. CDF Collab. (F. Abe *et al.*), Phys. Rev. Lett. **79**, 357 (1997); hep-ex/9704003; CDF Collab. (T. Affolder *et al.*), Phys. Rev. D **62**, 012004 (2000); hep-ex/9912013; D0 Collab. (B. Abbott *et al.*), Phys. Rev. Lett. **82**, 4975 (1999); hep-ex/9902028; D0 Collab. (V. M. Abazov *et al.*), Phys. Rev. Lett. **88**, 151803 (2002); hep-ex/0102039.
4. M. L. Mangano and S. R. Slabospitsky, Phys. Lett. B **410**, 299 (1997); hep-ph/9707248.
5. K. A. Assamagan, ATLAS Internal Notes, ATL-PHYS-99-013 (1999); ATL-PHYS-99-025 (1999); ATL-PHYS-2000-031 (2000); K. A. Assamagan, Y. Coadou, and A. Deandrea, hep-ph/0203121.
6. R. Kinnunen, CMS Internal Note, CMS NOTE 2000/045 (2000).
7. D. Denegri *et al.*, CMS Internal Note, CMS NOTE 2001-032 (2001); hep-ph/0112045.
8. D. P. Roy, Phys. Lett. B **459**, 607 (1999); hep-ph/9905542; M. Drees, M. Guchait, and D. P. Roy, Phys. Lett. B **471**, 39 (1999); hep-ph/9909266; D. P. Roy, hep-ph/0102091.
9. A. Djouadi *et al.*, hep-ph/0002258.
10. M. Beneke *et al.*, hep-ph/0003033.
11. A. C. Bawa, C. S. Kim, and A. D. Martin, Z. Phys. C **47**, 75 (1990); V. Barger, R. J. N. Phillips, and D. P. Roy, Phys. Lett. B **324**, 236 (1994); S. Moretti and K. Odagiri, Phys. Rev. D **55**, 5627 (1997); J. F. Gunion, Phys. Lett. B **322**, 125 (1994); F. Borzumati, J.-L. Kneur, and N. Polonsky, Phys. Rev. D **60**,

115011 (1999); D. J. Miller, S. Moretti, D. P. Roy, and W. J. Stirling, Phys. Rev. D **61**, 055011 (2000); hep-ph/9906230; A. Belyaev, D. Garcia, J. Guasch, and J. Sola, hep-ph/0203031.
12. H.-J. He and C.-P. Yuan, Phys. Rev. Lett. **83**, 28 (1999); hep-ph/9810367; T. M. Tait, hep-ph/9907462; T. M. Tait and C.-P. Yuan, Phys. Rev. D **63**, 014018 (2001); hep-ph/0007298.
13. M. V. Foursa, D. A. Murashov, and S. R. Slabospitsky, hep-ph/0008198.
14. J. L. Diaz-Cruz, H.-J. He, and C.-P. Yuan, hep-ph/0103178.
15. CTEQ Collab. (H. L. Lai *et al.*), hep-ph/9903282.
16. S. R. Slabospitsky and L. Sonnenschein, Comput. Phys. Commun. **148**, 87 (2002); hep-ph/0201292.
17. T. Sjöstrand, P. Eden, C. Friberg, *et al.*, Comput. Phys. Commun. **135**, 238 (2001); hep-ph/0010017.
18. S. Abdullin, A. Khanov, and N. Stepanov, Technical Note, CMS TN/94-180 (1999).
19. D. E. Groom *et al.* (Review of Particle Physics), Eur. Phys. J. C **15**, 1 (2000).
20. C. Balazs, H.-J. He, and C.-P. Yuan, Phys. Rev. D **60**, 114001 (1999); hep-ph/9812263.
21. E. E. Boos, L. V. Dudko, and V. I. Savrin, CMS Internal Note, CMS NOTE 2000/065 (2000).
22. V. G. Kartvelishvili, A. K. Likhoded, and V. A. Petrov, Phys. Lett. B **78B**, 615 (1978).

Translated by S. Slabospitsky

Physics of Atomic Nuclei, Vol. 67, No. 2, 2004, pp. 337–349. Translated from Yadernaya Fizika, Vol. 67, No. 2, 2004, pp. 355–367.

ELEMENTARY PARTICLES AND FIELDS
Theory

Scaling of Semi-inclusive Events in *pp* Interactions

A. I. Golokhvastov*

Joint Institute for Nuclear Research, Dubna, Moscow oblast, 141980 Russia

Received June 20, 2002; in final form, January 31, 2003

Abstract—The normalized single-particle semi-inclusive double-differential spectrum of π^- mesons from *pp* interactions at 6.6–400 GeV/c and the relative concentration of π^0 and K^0_S mesons in such events of fixed multiplicity of π^- mesons are completely determined by specifying any feature of this spectrum—for example, $\langle y^2\rangle_n$ or $\langle E\rangle_n$. Therefore, a two-parameter sample of semi-inclusive events that depends on the energy and the multiplicity reduces to a one-parameter sample. © *2004 MAIK "Nauka/Interperiodica"*.

1. INVARIANCE OF RAPIDITY SPECTRA

The term "semi-inclusive" was introduced by Koba, Nielsen, and Olesen [1], who studied the scaling of semi-inclusive spectra (this is so-called KNO-II scaling, which was not confirmed, however, in experiments [2, 3]). A semi-inclusive spectrum is a kinematical spectrum of particles of some sort in events where the number of these particles is fixed.

Let us consider the semi-inclusive rapidity distributions of π^- mesons in *pp* interactions. In order to determine the rapidity of a particle, $y = \frac{1}{2}\ln[(E + p_{||})/(E - p_{||})]$ (where E is the particle energy and $p_{||}$ is its longitudinal momentum), it is usually necessary to identify it—more precisely, to know its mass. However, almost all negative particles from *pp* interactions are π^- mesons, and this is the reason why the amount of data on this reaction is quite vast. The reaction is also rather convenient for a theoretical description owing to its symmetry in the c.m. frame and owing to the absence of π^- mesons from the fragmentation process.

Some of the studies [2–10] whose results are used here report the spectra of negative particles for a fixed number of negative particles, while others present the spectra of π^- mesons (the admixture of K^- mesons being statistically subtracted) at a fixed number of negative particles; finally, the remaining ones give the spectra of π^- at a fixed number of π^-. However, these spectra agree within the errors after normalization: the admixture of K^- mesons is small, and their rapidity spectra are similar to the spectra of π^- mesons. Therefore, negative particles and π^- mesons will not be distinguished below.

Several normalized (to unity) single-particle semi-inclusive rapidity distributions of negative particles in *pp* interactions are displayed in Fig. 1 for three initial energies and four multiplicities of π^- mesons (n) [3, 6, 9]:

$$\tilde\rho_n(y) = \frac{1}{n\sigma_n}\frac{d\sigma_n}{dy}, \qquad \int \tilde\rho_n(y)dy = 1 \qquad (1)$$

(the tilde symbol is used here to indicate that ρ is normalized to unity [4, 11]). Thus, the quantity $\tilde\rho_n(y)$ is the density of the probability that an arbitrarily chosen π^- meson in any event featuring n π^- mesons has a rapidity y.

The density of the probability that a π^- meson arbitrarily taken in an event chosen at random has the rapidity y is $\sum P_n\tilde\rho_n(y)$, where P_n is the probability of an event characterized by the multiplicity n. The normalized inclusive spectrum $\tilde\rho(y) = \langle n\rangle^{-1}\sum nP_n\tilde\rho_n(y)$ does not have a probabilistic meaning as clear as that. It would coincide with the semi-inclusive spectrum if the latter were independent of n, but, as one can see from Fig. 1, this is not so in actual distributions.

The distributions in Fig. 1 become broader with increasing initial energy $\sqrt{s}$ (the mean particle energy increases) and narrower with increasing multiplicity (the energy per particle decreases). It is possible to obtain several distributions of the same width if each successive distribution corresponds to a higher multiplicity and, accordingly, a higher energy. In general, the shapes of the distributions of the same width can differ from one another.

However, the existing experimental data are indicative of the coincidence of the shapes of the rapidity distributions in this case. Figure 2 displays the central statistical moments of 53 rapidity spectra obtained for various multiplicities of π^- mesons and 11 values of

*e-mail: golokhv@sunhe.jinr.ru

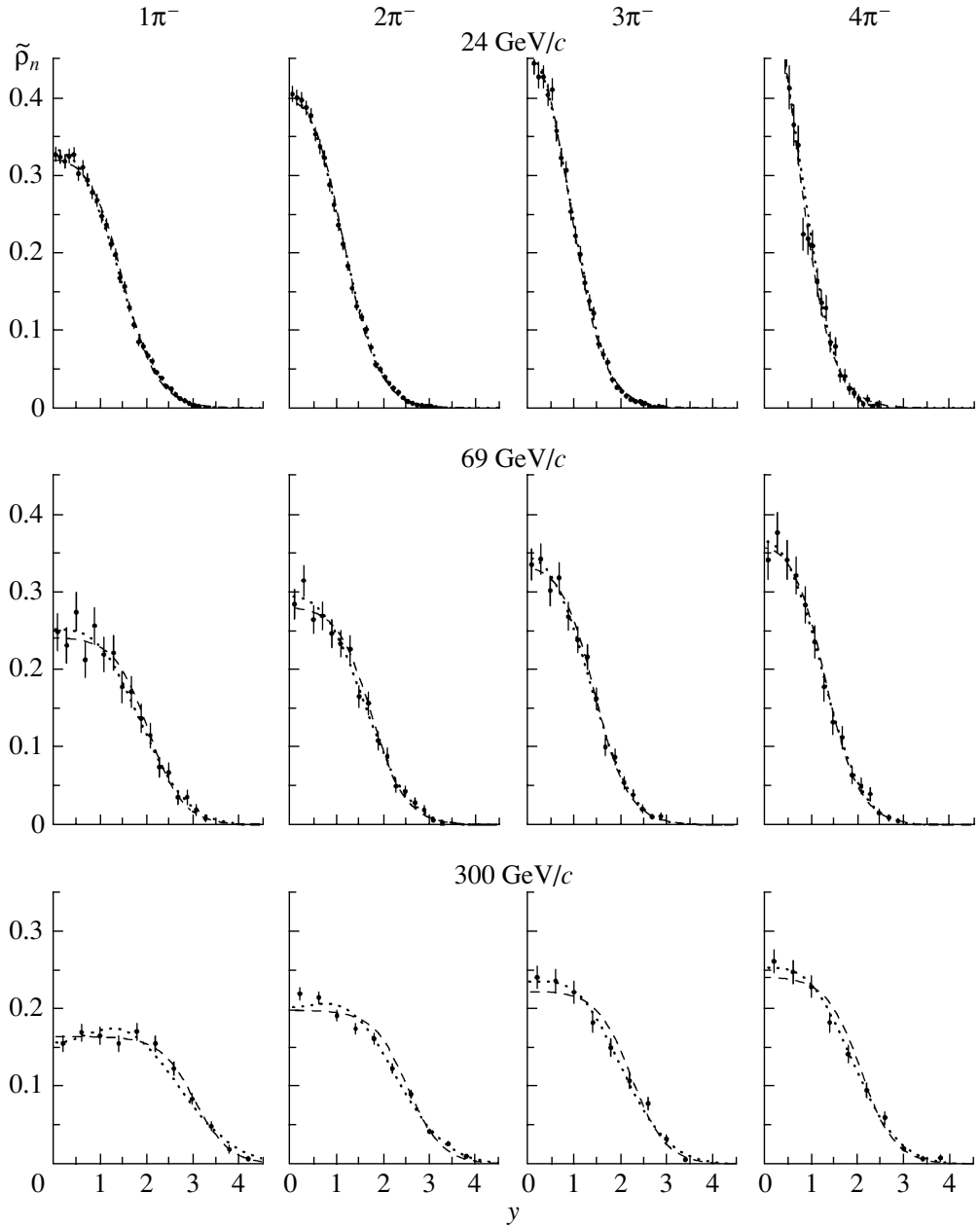

Fig. 1. Normalized (to unity) single-particle semi-inclusive rapidity spectra of π^- mesons in pp interactions, $\tilde{\rho}_n(y) = (1/n\sigma_n)(d\sigma_n/dy)$, at 24, 69, and 300 GeV/c and the multiplicities of π^- mesons from one to four. The spectra become broader with increasing energy and narrower with increasing multiplicity. The dotted and dashed curves correspond to the approximations in the form (4) and in the form (5), respectively.

the primary-proton momentum in the interval 6.6–400 GeV/c [2–10]:

$$\langle y^q \rangle_n \equiv \int y^q \tilde{\rho}_n(y) dy. \qquad (2)$$

These 53 points include only those data whose errors in the variance $\langle y^2 \rangle_n$ do not exceed 10%, this corresponding to about 30% for $\langle y^8 \rangle_n$.

It is clear from the figure that the groups of points associated with different energy values agree with one another within the experimental errors; that is, distributions that are characterized by the same values of the variance $\langle y^2 \rangle_n$ have the same higher moments and, therefore, coincide. It should be noted that this type of agreement is also observed for groups of points corresponding to primary momenta that differ by an order of magnitude (with increasing experimental statistics, the number of points for which the

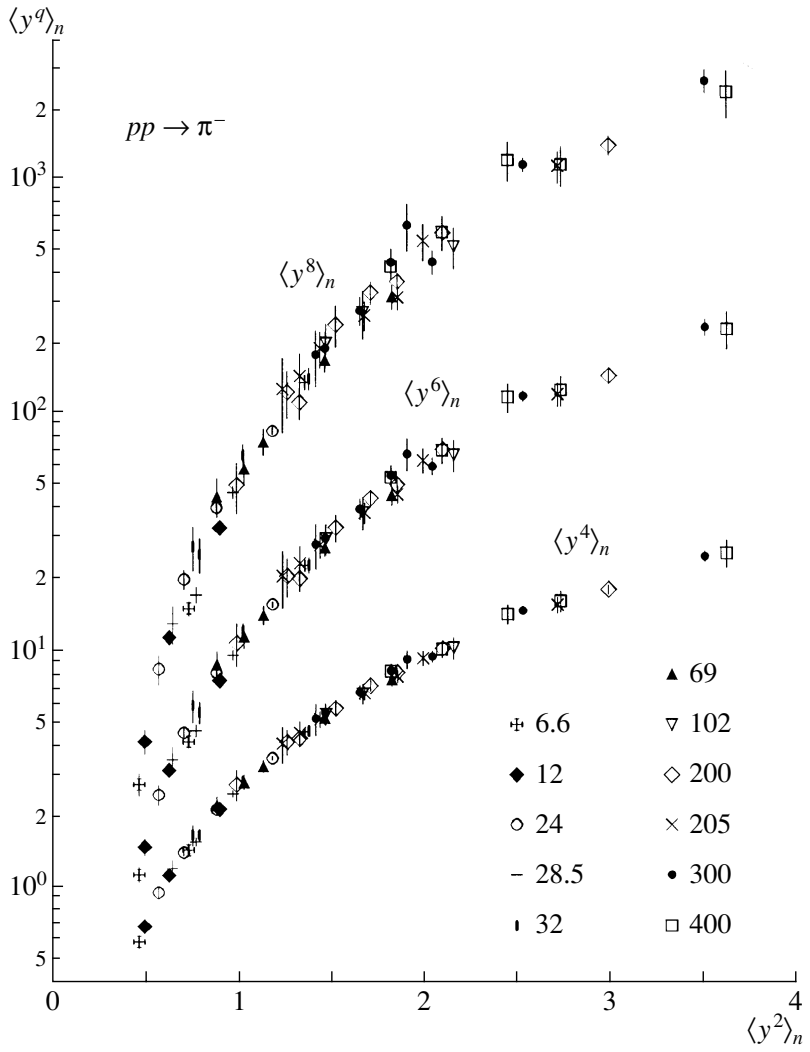

Fig. 2. Central statistical moments of 53 rapidity spectra $\langle y^q \rangle_n = \int y^q \tilde{\rho}_n(y) dy$ for various multiplicities of π^- mesons and 11 values of the primary-proton momentum from 6.6 to 400 GeV/c. Points characterized by the same variance $\langle y^2 \rangle_n$ also have the same values of the other moments; that is, the distributions coincide. The values of the primary-proton momenta (in GeV/c) are shown in the figure (as well as in Figs. 3–7 and 9 below).

agreement is observed becomes greater because there appear events with higher n).

Thus, the two-parameter set of rapidity distributions for different values of $\sqrt{s}$ and n in Fig. 1 can be described in terms of a function whose shape depends on a single parameter—for example, on $\langle y^2 \rangle$ [12].

It is worth noting that the height of the normalized (to unity) spectrum $\tilde{\rho}_n(0)$ decreases, of course, with increasing $\sqrt{s}$ owing to the broadening of the spectrum and increases with increasing n owing to the shrinkage of the spectrum. For the unnormalized spectrum $n\tilde{\rho}_n(y)$, these rather weak dependences are additionally multiplied by n; as a result, the frequently studied dependence of $n\tilde{\rho}_n(0)$ on n (see, for example, [2, 3, 13]) reflects predominantly the dependence of n on n.

2. INVARIANCE OF THE TOTAL SPECTRA

Figure 3 shows the mean transverse momenta of π^- mesons in events of fixed topology versus the variance $\langle y^2 \rangle_n$ of their rapidity distribution [2, 4, 6, 10, 14]. The points $\langle p_T \rangle_n$ at 12.9, 24, and 28.5 GeV/c were obtained by approximating the data from [14]; the rapidities for 12.9 GeV/c were taken from the data for 12 GeV/c in [9].

It is clear from the figure that the mean transverse momenta of π^- mesons are identical in semi-inclusive events characterized by identical rapidity spectra. We give sufficient grounds to assume that, for these events, the total double-differential distribu-

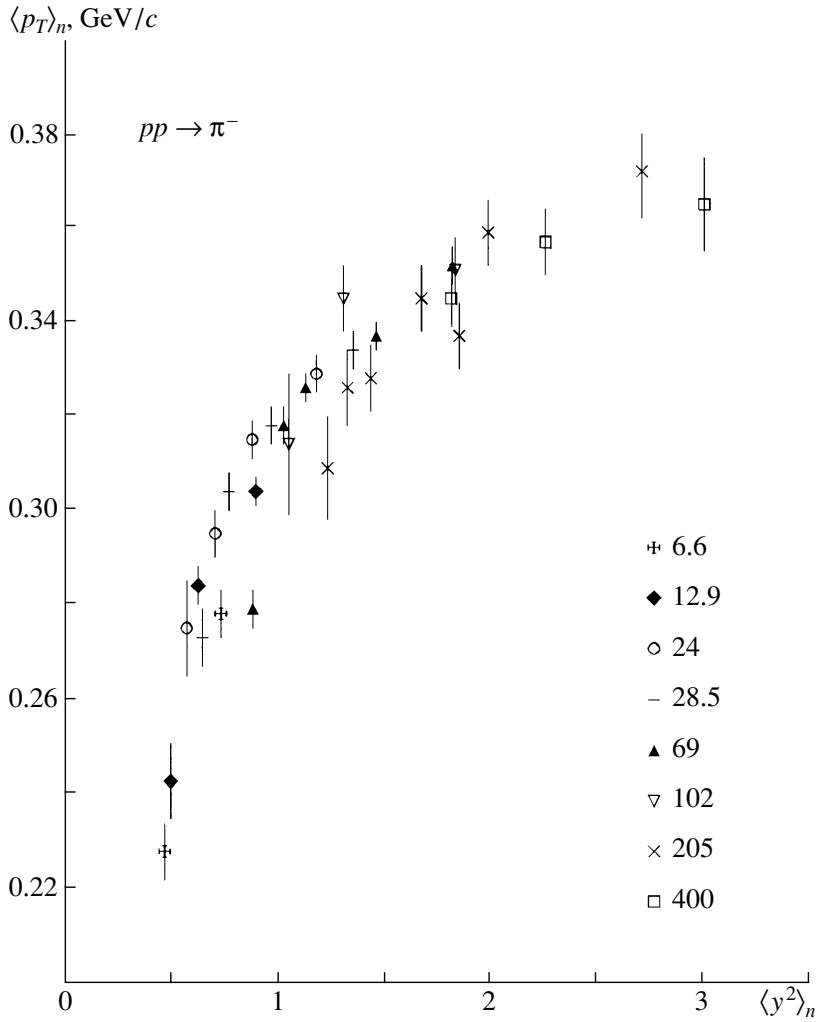

Fig. 3. Mean transverse momenta of π^- mesons in events of fixed topology, $\langle p_T\rangle_n$, versus the variance of their rapidity distribution $\langle y^2\rangle_n$. We can see that, in semi-inclusive events having the same rapidity spectra of π^- mesons, the mean transverse momenta are identical.

tions are identical:

$$\frac{1}{n\sigma_n}\frac{d^2\sigma_n}{dydp_T}(\sqrt{s},n) = \frac{1}{n\sigma_n}\frac{d^2\sigma_n}{dydp_T}[f(\sqrt{s},n)]. \quad (3)$$

In other words, the shape of the single-particle spectrum $f(\sqrt{s},n)$ at various $\sqrt{s}$ and n depends on only one parameter—for example, on $\langle y^2\rangle$ or $\langle p_T\rangle$. In Section 4, we will give one more illustration of this assumption, the equality of the mean energies of π^- mesons in the events being considered.

In Fig. 3, the mean transverse momentum of negative particles decreases with increasing multiplicity, this being similar to the shrinkage of the rapidity spectrum in Fig. 1: the energy per particle decreases. At the same time, an increase in $\langle p_T\rangle$ at the multiplicity in the central rapidity region was found at the ISR and S$\bar{p}p$S energies [15, 16]. We emphasize that these trends do not contradict each other because they simply cannot be compared with each other. The data given in [15, 16] were obtained through a complicated selection of events and particles in these events.

We also note that, if we select events where all secondaries occur in a narrow central rapidity gap, the primary energy in these events will entirely go over to the transverse momenta. If, on the contrary, we select events where emission angles are small, the mean transverse momentum will also be low. An intermediate trigger will lead to an intermediate result.

In addition, experiments with colliding beams do not detect $p_T < 150$ MeV/c particles. Aivazyan *et al.* [17] showed that, even at $p_{\text{lab}} = 250$ GeV/c, a descending dependence of $\langle p_T\rangle$ transforms into an ascending dependence as one increases the detection threshold with respect to p_T. Unfortunately, collider experiments are usually unable to provide, for a

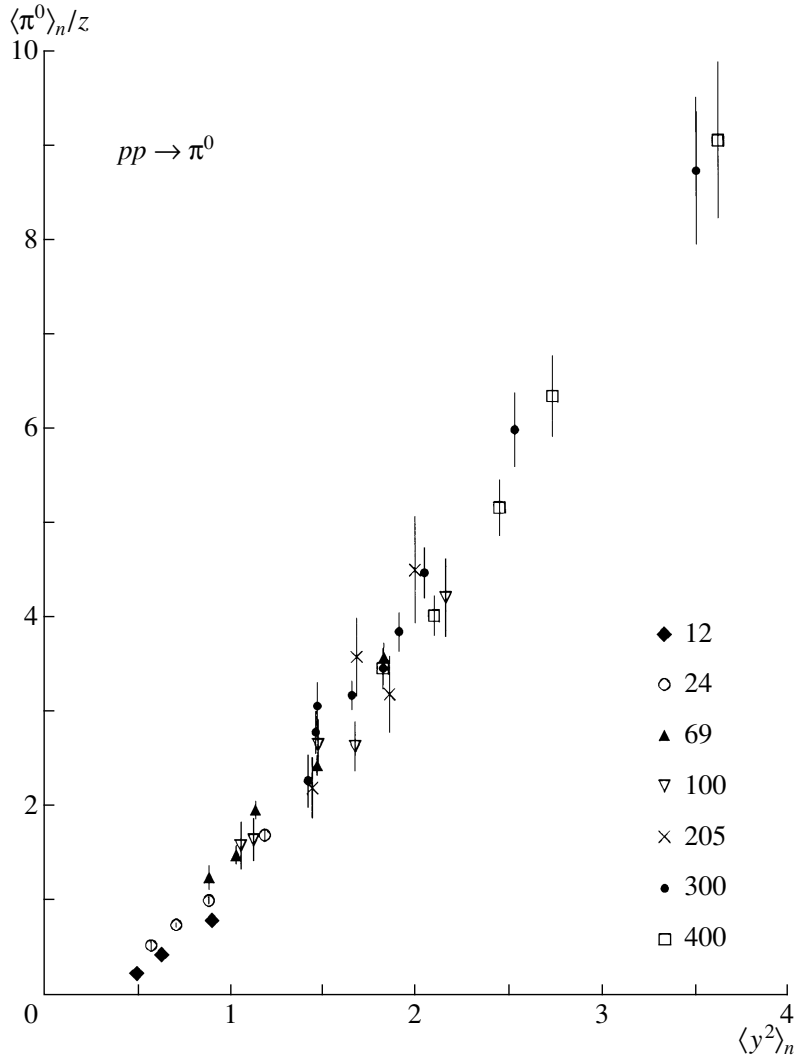

Fig. 4. Ratio of the mean multiplicity of π^0 mesons, $\langle\pi^0\rangle_n$, in events where the multiplicity of π^- mesons is fixed to the normalized multiplicity of π^- mesons, $z = n/\langle n\rangle$. We can see that the relative concentration of π^0 mesons is identical for semi-inclusive events characterized by identical rapidity spectra.

minimum-bias trigger, comprehensive data over the entire phase space (either with respect to y or with respect to p_T) that are necessary for investigating soft processes.

Breakstone *et al.* [18] (ISR) also obtained a growth of $\langle p_T\rangle_n$ in the central rapidity gap (for negative particles inclusive), but as a function of the multiplicity in the full rapidity interval. However, $\langle p_T\rangle_n$ in [18] decreases at high rapidities (in the c.m. frame). The authors of [18] did not report the behavior of $\langle p_T\rangle_n$ for all negative particles.

3. INVARIANCE OF THE NEUTRAL MESON CONCENTRATION

It would be natural to expect that events in which the spectra of π^- mesons are identical have some coincident feature of the relative yield of some other particles that are not directly related to π^- mesons. However, we do not know which one is precisely this feature. By way of example, we indicate that, in thermodynamic models, where the coincidence of spectra implies the equality of temperatures, we would observe an invariable value for the ratio of the mean multiplicity of these particles to their generation volume. In multiperipheral models, the ratio of the multiplicities of heavy and light particles at coinciding chain lengths (width of the rapidity spectrum) is expected to depend on the momentum transfer between the links of the chain (that is, on the ratio of the chain length to the number of links).

Experimental data on the yields of π^0 and K^0_S mesons in semi-inclusive events are indicative of their similar invariant behavior versus the variance of the

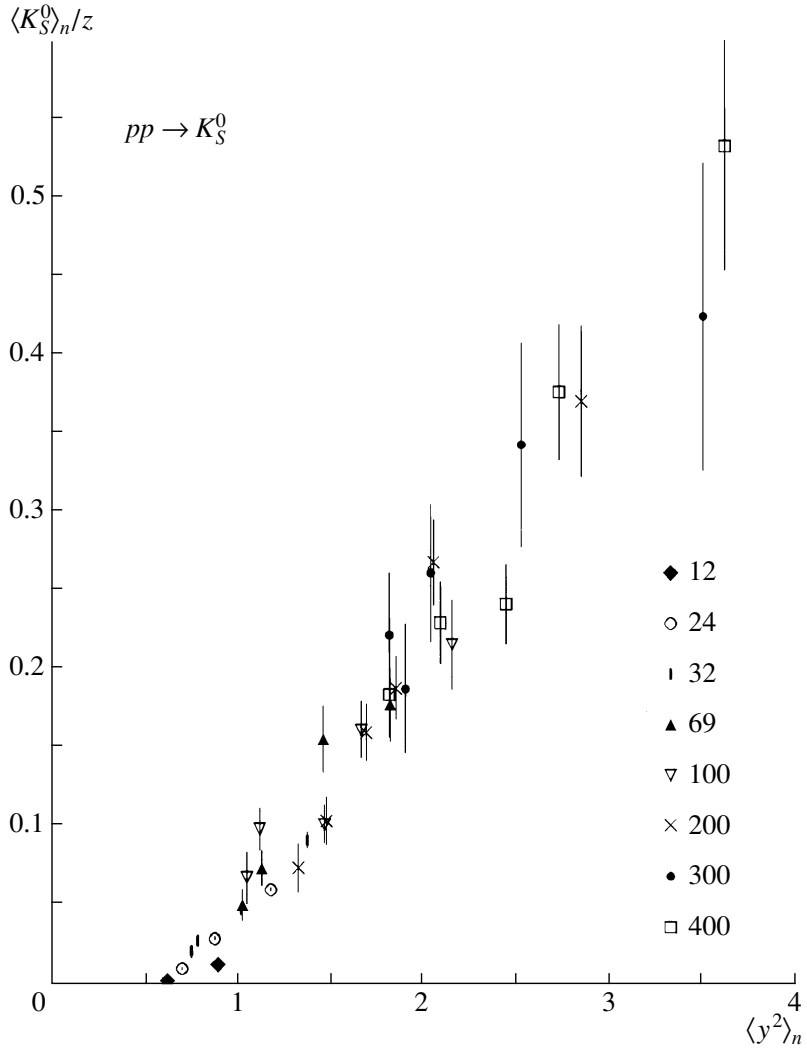

Fig. 5. Ratio of the mean multiplicity of K_S^0 mesons, $\langle K_S^0\rangle_n$, at a fixed number of π^- mesons to the normalized multiplicity of π^- mesons, $z = n/\langle n\rangle$. We can see that the relative concentration of K_S^0 mesons is also identical in semi-inclusive events characterized by identical rapidity spectra of π^- mesons.

rapidity spectrum of π^- mesons (the variable that was already used in Figs. 2, 3). Figure 4 displays the ratio of the mean multiplicity of π^0 mesons, $\langle\pi^0\rangle_n$, at a fixed multiplicity of π^- mesons [19–27] to the normalized multiplicity of π^- mesons, $z = n/\langle n\rangle$. Data obtained in various experiments at the same energies (12 GeV/c [19, 22], 100 GeV/c [23, 24], and 300 GeV/c [21, 26]) were averaged with allowance for the experimental errors. The points for which the errors exceed 15% were discarded.

Figure 5 shows similar data for $\langle K_S^0\rangle_n$, the mean multiplicity of K_S^0 mesons at a fixed multiplicity of π^- mesons [22–32]. As before, data obtained at the same energies (100 GeV/c [23, 24], 200 GeV/c [25, 31], and 400 GeV/c [27, 32]) are averaged. Points for which the errors exceed 25% are omitted.

At moderate energies, the spectrum of π^- mesons in semi-inclusive events involving K mesons is most likely softer than in other events. This can probably explain the fact that the point associated with one π^- meson for 12 GeV/c in Fig. 5 (the extreme right point) is shifted to the right with respect to the general dependence. The same is true for Fig. 4, but to a lesser extent.

The concentration of π^0 and K_S^0 mesons decreases with increasing multiplicity of π^- mesons, and this is similar to the decrease in $\langle y^2\rangle$ and $\langle p_T\rangle$ with increasing n (see also [33]).

We conclude that, irrespective of the primary energy and of the multiplicity of π^- mesons, the normalized single-particle double-differential spectrum of π^- mesons and the concentration of π^0 and K_S^0

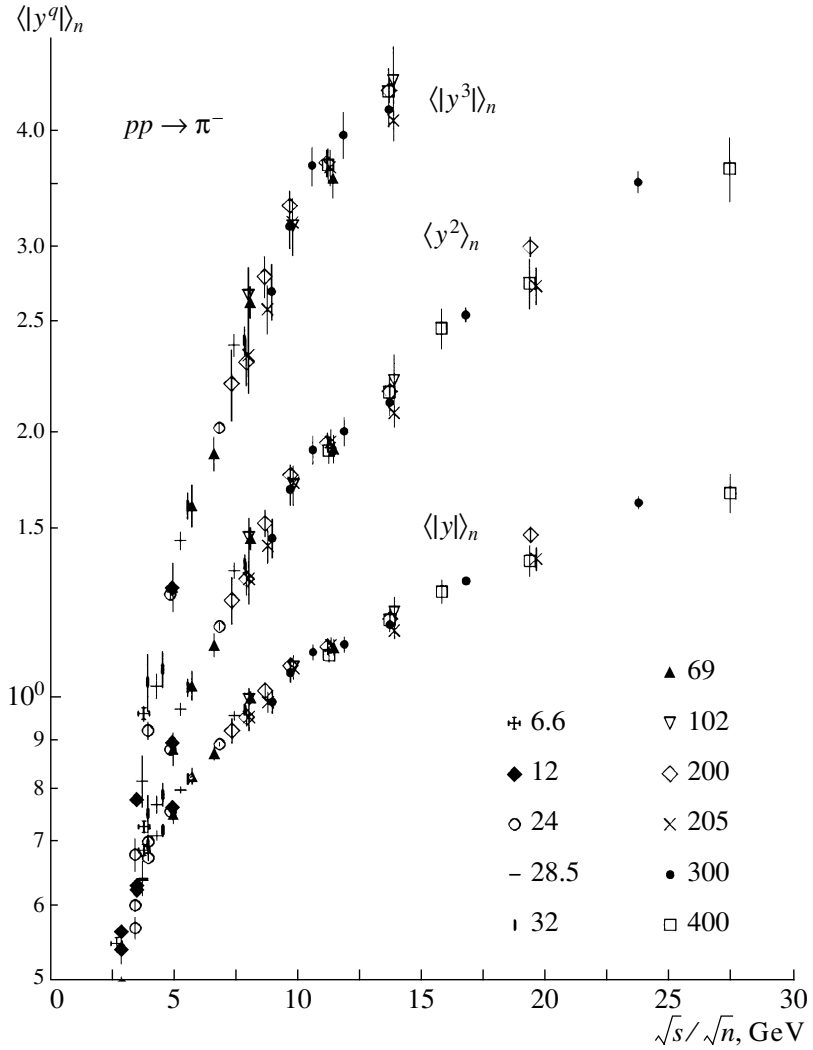

Fig. 6. Statistical moments of the semi-inclusive rapidity spectra, $\langle|y^q|\rangle_n = \int |y^q|\tilde{\rho}_n(y)dy$, versus the scaling parameter $\sqrt{s}/\sqrt{n}$. We can see that the groups of points corresponding to different energies agree; that is, the shape of the rapidity spectrum depends only on $\sqrt{s}/\sqrt{n}$.

mesons in semi-inclusive events are completely determined by one feature of this spectrum—for example, $\langle y^2\rangle_n$ or $\langle p_T\rangle_n$. Thus, the two-parameter sample of semi-inclusive events that depends on the energy and multiplicity reduces to a one-parameter sample, this parameter depending on $\sqrt{s}$ and n.

4. APPROXIMATION OF A SCALING PARAMETER

It should be noted from the outset that the universality of the spectra and concentrations of mesons, which is illustrated in Figs. 2–5, does not depend on any approximation. Also, the term "scaling" for the parameter $f(\sqrt{s}, n)$ in (3), as well as the word "scaling" in the title of the present article, is chosen rather by convention: the invariance of the spectra here has nothing to do with a scale invariance, because the spectra being considered are simply coincident without scaling, in contrast to what occurs in the case of KNO-II scaling [1].

For this parameter, a satisfactory approximation that brings together the data at different values of the energy $\sqrt{s}$ and the multiplicity n is rather simple: $\sqrt{s}/\sqrt{n}$, s/n (which is the same), or any function of s/n [12]. Figure 6 shows the dependence of various moments of the rapidity spectra on $\sqrt{s}/\sqrt{n}$. We can see that the groups of points corresponding to different energies superimpose; that is, the shape of the rapidity spectrum depends only on the ratio $\sqrt{s}/\sqrt{n}$. This result is an intermediate between two extreme possibilities:

(a) The multiplicity of π^- mesons is proportional

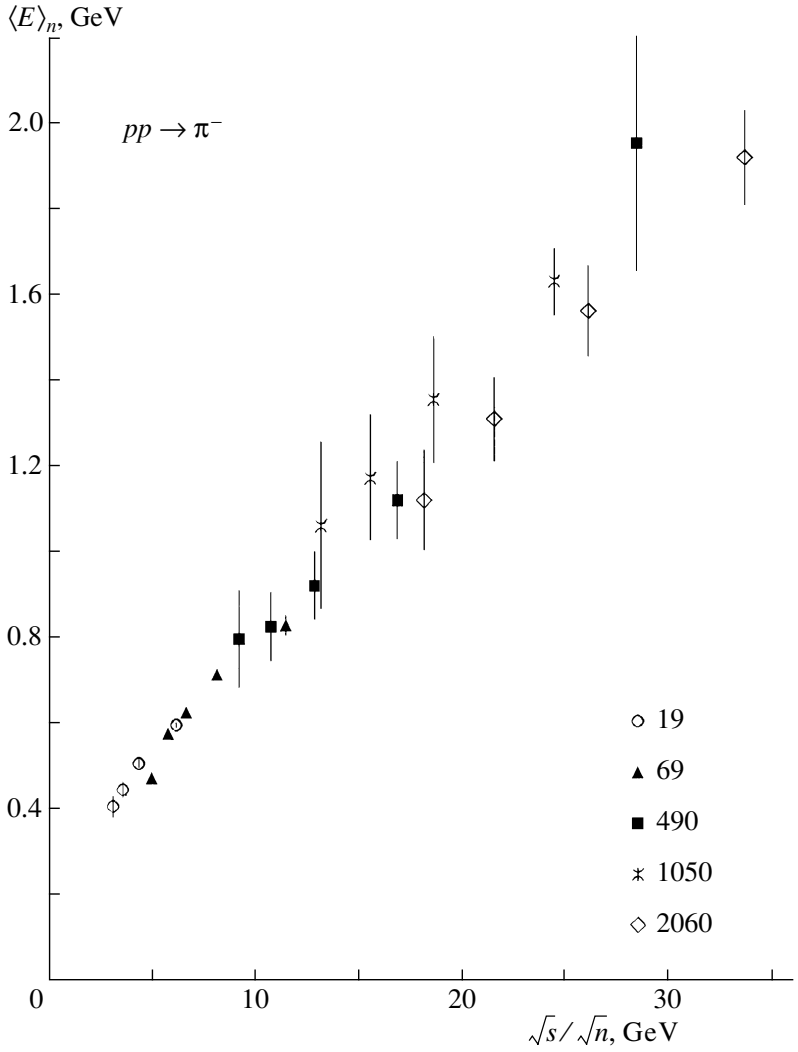

Fig. 7. Mean energies of π^- mesons in events of fixed topology versus the scaling parameter $\sqrt{s}/\sqrt{n}$. We can see that, in semi-inclusive events characterized by identical rapidity spectra of π^- mesons, the mean energies are identical.

to the inelasticity factor for π^- mesons in an event ($\sum E_{\pi^-}/\sqrt{s}$), in which case the spectrum depends only on $\sqrt{s}$; that is, it does not depend on the multiplicity, as occurs, for example, in the case of nucleus–nucleus collisions at different impact parameters.

(b) The multiplicity does not depend on the inelasticity factor, in which case the spectrum depends only on $\sqrt{s}/n$, as may occur in annihilation reactions, where the inelasticity factor (for all product particles) is always equal to unity. By the way, the scale parameter from [1] ($\langle n\rangle/n$) even goes beyond this boundary ($\langle n\rangle$ grows more slowly than $\sqrt{s}$).

Within the errors the parameter $\sqrt{s}/\sqrt{n}$ is unambiguously related to the variance $\langle y^2\rangle_n$ of the rapidity spectrum, and the former may be used instead of the latter in Figs. 2–5. In addition, Figs. 3–5 could also be supplemented with points corresponding to energies at which there are no data on the semi-inclusive rapidity spectra of π^- mesons [34–39]. The dependence on $\langle y^2\rangle_n$ is used in Figs. 2–5 in order to avoid relating the statement of invariance to a specific choice of the scaling parameter.

Figure 7 displays the $\sqrt{s}/\sqrt{n}$ dependence of the mean energy of π^- mesons, $\langle E\rangle_n$, in semi-inclusive events for the experiments reported in [6, 35, 40], where, in most cases, there are no data on the rapidity spectra. The groups of points corresponding to different primary energies agree, which is yet another point in support of the assumption that the double-differential spectra (3) are invariant.

5. APPROXIMATIONS OF THE RAPIDITY SPECTRA

The dotted curves in Fig. 1 represent the approximations of the experimental data in terms of the

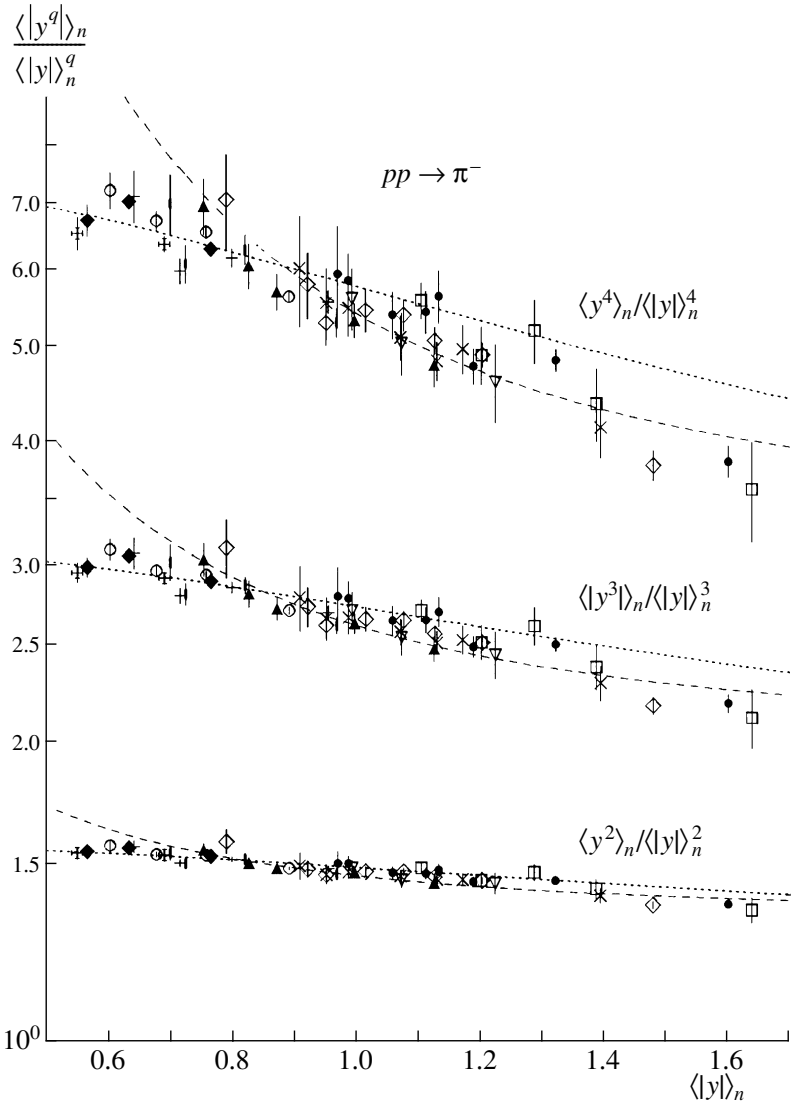

Fig. 8. Ratios of the central statistical moments $\langle|y^q|\rangle_n = \int |y^q|\tilde{\rho}_n(y)dy$ for the same experimental rapidity spectra as in Fig. 2 (the notation being identical to that in Fig. 2). The dotted and dashed curves correspond to the approximations in terms of (4) and (5), respectively.

function [41]

$$\tilde{\rho}_n(y) = \frac{1}{2\sqrt{2\pi Y_\mathrm{G}}} \times \left[\exp\frac{-(y-Y_\mathrm{G})^2}{2Y_\mathrm{G}} + \exp\frac{-(y+Y_\mathrm{G})^2}{2Y_\mathrm{G}}\right], \quad (4)$$

which involves two identical Gaussian distributions characterized by the variances $\sigma^2 = Y_\mathrm{G}$ and shifted by $\pm Y_\mathrm{G}$ from the c.m. frame. With increasing Y_G—that is, with increasing energy and decreasing multiplicity—the Gaussian distributions move apart, so that the resulting distribution becomes two-humped. At large Y_G, the half-width of this function increases approximately in proportion to $Y_\mathrm{G} + Y_\mathrm{G}^{1/2}$. This two-fireball picture is typical of fragmentational models (see [42, 43] and references therein).

The dashed curves in Fig. 1 correspond to the approximation by a symmetrized Fermi distribution with a diffuseness parameter of 0.37 [44]:

$$\tilde{\rho}_n(y) = \frac{1}{2Y_\mathrm{F}} \times \left[\left(\exp\frac{y-Y_\mathrm{F}}{0.37}+1\right)^{-1} - \left(\exp\frac{y+Y_\mathrm{F}}{0.37}+1\right)^{-1}\right]. \quad (5)$$

With increasing Y_F, this function transforms into a flat distribution of half-width Y_F, its edge degradation being smeared over about 1.6 (from 0.9 to 0.1 of the plateau height). A flat rapidity distribution of secondaries is predicted by the hypothesis of scale

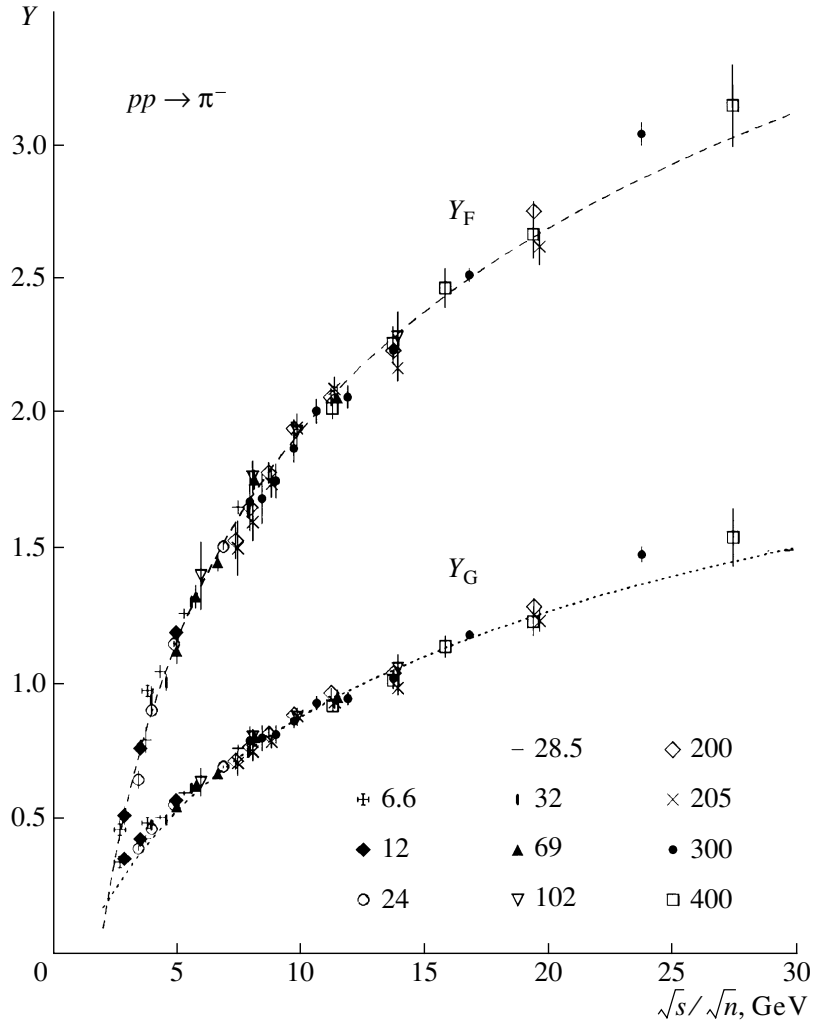

Fig. 9. Fitted values of the parameters Y_G and Y_F in the approximations (4) and (5) of the rapidity spectra of π^- mesons versus $\sqrt{s}/\sqrt{n}$. The curves correspond to approximations in the form (6).

invariance [45] and by the multiperipheral and parton models (see [46]).

We note, however, that by no means is a flat distribution in semi-inclusive events related to other specific features of multiperipheral-type models. In our case, the growth of the mean multiplicity with energy and the multiplicity distribution can be specified irrespective of the rapidity spectrum. On the other hand, the multiplicity in the multiperipheral or the string model is fixed only upon (and as the result of) the formation of the rapidity distribution. In this respect, our case is closer to that of the thermodynamic or the hydrodynamic model, where the multiplicity is determined at the first instant of a collision event. By the way, the Fermi model at a fixed impact parameter also leads to a pseudorapidity distribution close to a flat one (in [47], Fermi presented the angular distribution).

Among modern models, the Lund Fritiof model is conceptually closer to the approximation in (4), while the dual parton model is closer to that in (5) (see, for example, [48]).

The ratios of the central moments for the same experimental spectra as in Fig. 2 are shown in Fig. 8, along with the curves corresponding to the approximations in (4) and (5). The approximation in (4) provides a better description of the statistical moments at low energies, while the approximation in (5) is better in this sense at high energies. However, the spectra in Fig. 1 are virtually insensitive to this difference. The reason is that the values of the higher moments in Fig. 8 are determined primarily by the last points of the spectrum $\tilde{\rho}_n(y)$ at the maximum values of y. By the way, the position of the last point on the y axis depends on experimental statistics. In the case of vaster statistics, the values of the moment may be shifted somewhat upward.

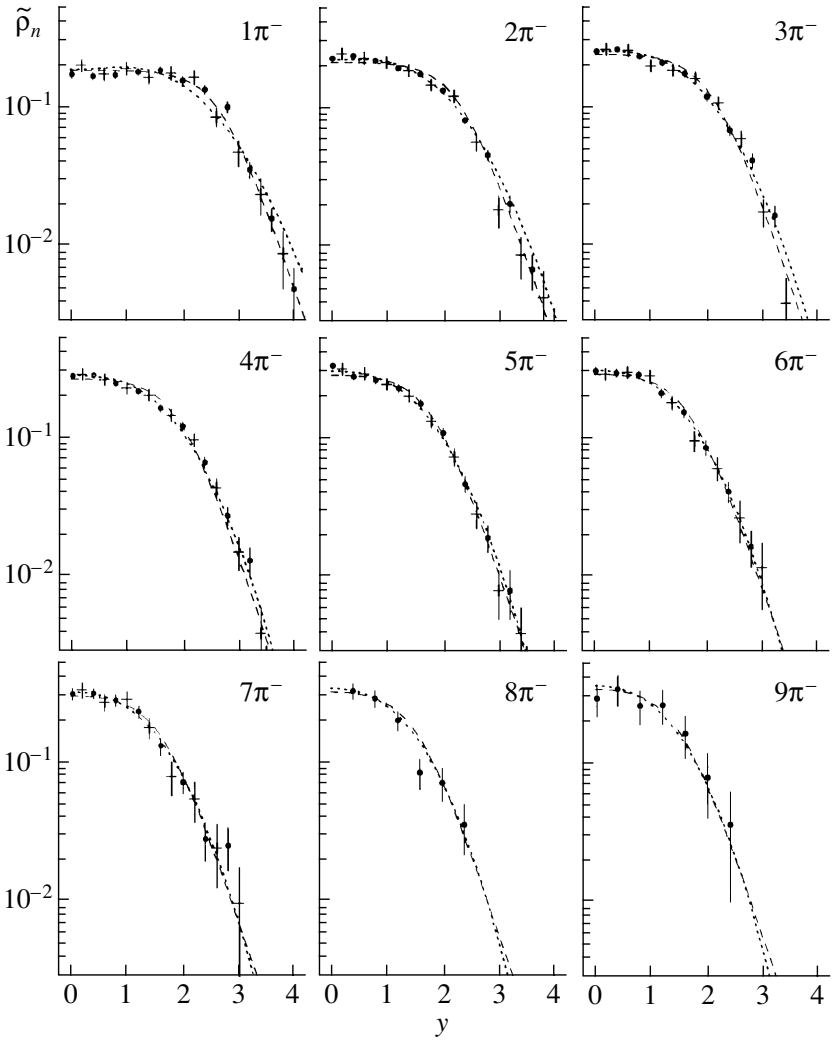

Fig. 10. Normalized (to unity) single-particle semi-inclusive rapidity spectra of π^- mesons in pp interactions, $\tilde{\rho}_n(y) = (1/n\sigma_n)(d\sigma_n/dy)$, at (•) 200 and (+) 205 GeV/c for the π^--meson multiplicities of one to nine. The dotted curves correspond to the approximations in (4) and (6), while the dashed curves correspond to (5) and (6).

The fitted values of the parameters Y_{G} and Y_{F} in the approximations (4) and (5) of the experimental rapidity spectra [2–10] are displayed in Fig. 9 versus $\sqrt{s}/\sqrt{n}$. The curves in the figure represent the functions

$$Y_{\mathrm{G}} = l - l^{0.64} + 0.26, \quad Y_{\mathrm{F}} = l + l^{0.19} - 1.60, \quad (6)$$

where

$$l = \ln\left(\frac{\sqrt{s}}{\sqrt{n}}\Big/ M_p c^2\right),$$

with M_p being the proton mass.

Figure 10 shows the rapidity spectra of π^- mesons in pp interactions at 200 GeV/c [3] and 205 GeV/c [4]. In addition to a logarithmic scale and the presence of high multiplicities, this figure differs from Fig. 1 in that, here, the parameters Y_{G} and Y_{F} for the approximations in (4) and (5) were obtained from expressions (6) rather than from a fit.

The distinction between the approximations in (4) and (5) becomes significant only at the energy of the S$\bar{p}p$S collider. Figure 11 displays the inclusive pseudorapidity spectra of negatively charged particles (the density of the mean multiplicity) according to the calculation employing the spectra of all charged particles from the UA5 experiment [13] for nondiffractive (NSD) $\bar{p}p$ interactions, $d\langle n\rangle/d\eta = (1/\sigma)(d\sigma/d\eta)$, where $\eta = -\ln[\tan(\theta/2)]$.

The same figure shows the curves representing the inclusive rapidity spectra of negatively charged particles in pp interactions. They were obtained by using the approximation specified by Eqs. (4) and (6), the approximation specified by Eqs. (5) and (6), and the experimental multiplicity distributions of nega-

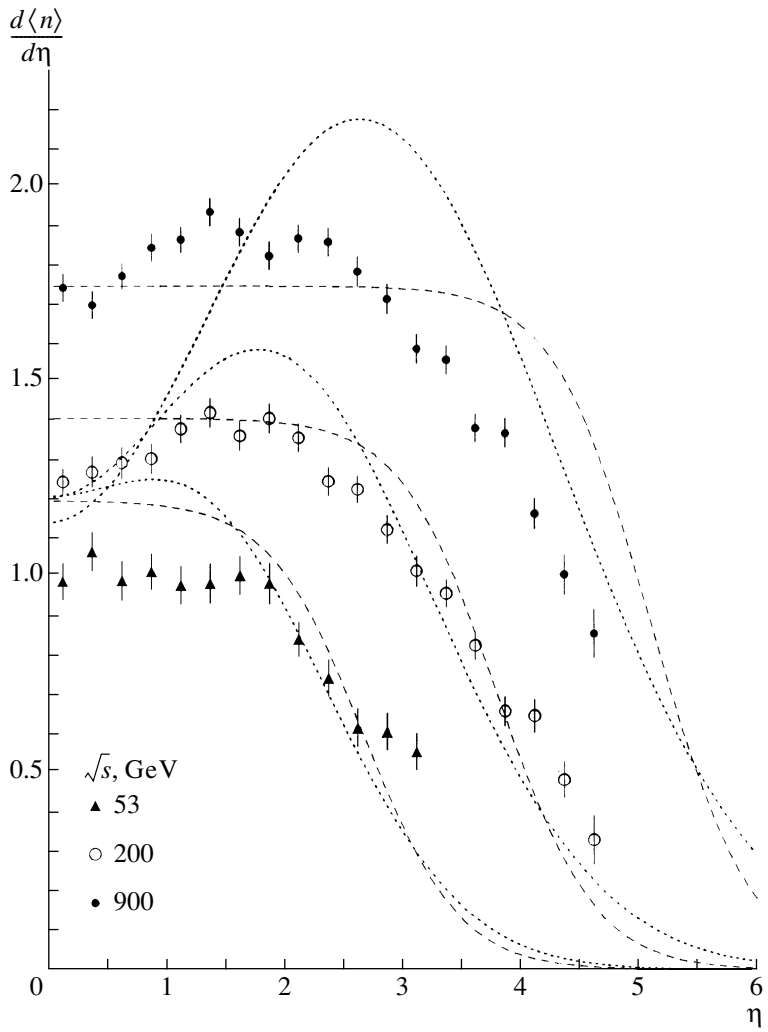

Fig. 11. Inclusive pseudorapidity spectra of negatively charged particles in $\bar{p}p$ interactions, $d\langle n\rangle/d\eta = (1/\sigma_{\mathrm{NSD}})(d\sigma/d\eta)$, according to the calculations employing the spectra of all charged particles from the UA5 experiment. The curves represent the inclusive rapidity spectra obtained for negatively charged particles in pp interactions by using the approximations in (dotted curve) (4) and (dashed curve) (5) and (6), as well as the experimental multiplicity distributions. The spectra are not normalized to unity, the areas under the curves being equal to the mean multiplicity.

tively charged particles [49, 50]. The areas under the curves are equal to the mean multiplicities of these particles. The spectra averaged over the multiplicity differ only slightly from the spectra calculated for a fixed multiplicity equal to the mean one (not shown in the figure), but the spectra for different values of n can deviate rather strongly.

Of course, it is not quite correct to compare the spectra of negatively charged particles in $\bar{p}p$ and pp interactions—in the latter case, the spectra of positively charged particles are significantly broader than those of negatively charged particles (see, for example, [51]). The use of the pseudorapidity variable instead of the rapidity is not correct either, to say nothing about the extrapolation of our approximations to S$\bar{p}p$S energies. Figure 11 merely demonstrates the distinction between the behavior of the approximation in (4) and the behavior of approximation in (5).

REFERENCES

1. Z. Koba, H. B. Nielsen, and P. Olesen, Phys. Lett. B **38B**, 25 (1972).
2. C. Bromberg *et al.*, Nucl. Phys. B **107**, 82 (1976).
3. B. Y. Oh *et al.*, Nucl. Phys. B **116**, 13 (1976).
4. T. Kafka *et al.*, Phys. Rev. D **16**, 1261 (1977).
5. C. M. Bromberg *et al.*, Phys. Rev. D **9**, 1864 (1974).
6. V. V. Ammosov *et al.*, Nuovo Cimento A **40**, 237 (1977).
7. E. E. Zabrodin *et al.*, Phys. Rev. D **52**, 1316 (1995).
8. J. Hanlon *et al.*, Nucl. Phys. B **52**, 96 (1973).
9. V. Blobel *et al.*, Nucl. Phys. B **69**, 454 (1974).
10. E. Gellert, Preprint LBL-749 (Berkeley, 1972).
11. J. Whitmore, Phys. Rep. **27**, 187 (1976).

12. A. I. Golokhvastov, Z. Phys. C **26**, 469 (1984).
13. G. J. Alner *et al.*, Z. Phys. C **33**, 1 (1986).
14. D. B. Smith, Preprint UCRL-20632 (Berkeley, 1971).
15. G. Arnison *et al.*, Phys. Lett. B **118B**, 167 (1982).
16. A. Breakstone *et al.*, Phys. Lett. B **132B**, 463 (1983).
17. V. V. Aivazyan *et al.*, Phys. Lett. B **209B**, 103 (1988).
18. A. Breakstone *et al.*, Europhys. Lett. **7**, 131 (1988).
19. K. Holt *et al.*, Nucl. Phys. B **103**, 221 (1976).
20. M. Boratav *et al.*, Nucl. Phys. B **111**, 529 (1976).
21. T. Kafka *et al.*, Phys. Rev. D **19**, 76 (1979).
22. K. Jaeger *et al.*, Phys. Rev. D **11**, 1756 (1975).
23. M. Alston-Garnjost *et al.*, Phys. Rev. Lett. **35**, 142 (1975).
24. J. W. Chapman *et al.*, Phys. Lett. B **47B**, 465 (1973).
25. K. Jaeger *et al.*, Phys. Rev. D **11**, 2405 (1975).
26. A. Sheng *et al.*, Phys. Rev. D **11**, 1733 (1975).
27. R. D. Kass *et al.*, Phys. Rev. D **20**, 605 (1979).
28. H. Fesefeldt *et al.*, Nucl. Phys. B **147**, 317 (1979).
29. M. Yu. Bogolyubskiĭ *et al.,* Yad. Fiz. **50**, 683 (1989) [Sov. J. Nucl. Phys. **50**, 424 (1989)].
30. V. V. Ammosov *et al.*, Nucl. Phys. B **115**, 269 (1976).
31. J. Allday *et al.*, Z. Phys. C **40**, 29 (1988).
32. H. Kichimi *et al.*, Phys. Rev. D **20**, 37 (1979).
33. M. Gaździcki, Eur. Phys. J. C **8**, 131 (1999).
34. C. N. Booth *et al.*, Phys. Rev. D **27**, 2018 (1983).
35. H. Bøggild *et al.*, Nucl. Phys. B **27**, 285 (1971).
36. J. L. Bailly *et al.*, Z. Phys. C **22**, 119 (1984).
37. K. Alpgård *et al.*, Nucl. Phys. B **103**, 234 (1976).
38. D. Brick *et al.*, Nucl. Phys. B **164**, 1 (1980).
39. M. Asai *et al.*, Z. Phys. C **27**, 11 (1985).
40. W. Bell *et al.*, Z. Phys. A **325**, 7 (1986).
41. A. I. Golokhvastov, Z. Phys. C **64**, 301 (1994).
42. J. Benecke *et al.*, Phys. Rev. **188**, 2159 (1969).
43. T. T. Chou and C. N. Yang, Phys. Rev. Lett. **25**, 1072 (1970).
44. M. E. Grypeos *et al.*, Fiz. Élem. Chastits At. Yadra **32**, 1494 (2001).
45. R. P. Feynman, Phys. Rev. Lett. **23**, 1415 (1969).
46. Yu. P. Nikitin and I. L. Rozental, *The Theory of Multiparticle Processes* (Atomizdat, Moscow, 1976).
47. E. Fermi, Phys. Rev. **81**, 683 (1951).
48. G. Giacomelli, Int. J. Mod. Phys. A **5**, 223 (1990).
49. R. E. Ansorge *et al.*, Z. Phys. C **43**, 357 (1989).
50. A. Breakstone *et al.*, Phys. Rev. D **30**, 528 (1984).
51. A. Breakstone *et al.*, Phys. Lett. B **132B**, 458 (1983).

Translated by M. Kobrinsky

Physics of Atomic Nuclei, Vol. 67, No. 2, 2004, pp. 350–358. Translated from Yadernaya Fizika, Vol. 67, No. 2, 2004, pp. 368–376.

ELEMENTARY PARTICLES AND FIELDS
Theory

Contribution of the Charged Higgs Boson to the Production of a $t\bar{b}$ Pair in Hadron Collisions

D. A. Murashev[1)]*, S. R. Slabospitsky[1)], and M. V. Foursa[2)]*****

Received May 28, 2002; in final form, January 14, 2003

Abstract—The contribution of the charged Higgs boson to the production of a $t\bar{b}$ pair in pp collisions at LHC is investigated. It is shown that, due to $H^{\pm}$-boson exchange, the total yield of $t\bar{b}$ pairs is modified significantly for small and large values of $\tan\beta$. At small values of $\tan\beta$, the production of right-handed t quarks is also expected, however, in contrast to what occurs in the case of only $W^{\pm}$-boson exchange, generating left-handed t quarks exclusively. This fact provides the possibility of separating the $H^{\pm}$ and $W^{\pm}$ contributions by investigating the angular distributions of products originating from top-quark decay. A detailed simulation of signal and relevant background processes is performed. © *2004 MAIK "Nauka/Interperiodica".*

1. INTRODUCTION

The existence of the charged Higgs boson $H^{\pm}$ is predicted by many extensions of the Standard Model (see, for example, [1]). Searches for a charged Higgs boson were carried out in e^+e^- annihilation at LEP-2 (CERN) [2] and at the Tevatron in top-quark decays [3]. Such searches will be one of the main experimental tasks at the future LHC machine [4–6]. The reactions $gb \to tH^{\pm}$ and $gg \to t\bar{b}H^{\pm}$ are the main channels for $H^{\pm}$-boson searches [5–7].

In the present study, we explore the additional possibility of investigating a signal from a charged Higgs boson in the subprocesses of quark–antiquark annihilation in pp collisions at hadronic colliders:

$$pp \to t\bar{b}X. \qquad (1)$$

Note that $t\bar{b}$ production through W-boson exchange in the s-channel was considered earlier (see [8, 9]). In particular, it was shown that this process is of paramount importance for investigating the electroweak vertex of tWb interactions [4, 10].

New physics beyond the Standard Model can modify the nature of t-quark interactions (see [4] and references therein). In particular, the contribution of charged Higgs bosons to the process in (1) can be considered as a manifestation of new physics. Not only does the existence of the $H^{\pm}$ boson lead to a modification of the total cross section for $t\bar{b}$ production, but this also changes the angular distributions of top-quark-decay products.

Here, we study the production of charged Higgs bosons in pp collisions at the future LHC machine (CERN) at the energy of $\sqrt{s} = 14$ TeV. The strategy of searches for $H^{\pm}$-boson production is determined, in particular, by the Higgs boson mass (see [5]). For relatively light $H^{\pm}$, say, $m_{H^{\pm}} < m_t$, the most promising possibility is to investigate t-quark decay to $H^{\pm}$ and a b quark. Here, we assume that the charged Higgs boson is heavier than the top quark. As a result, we consider top-quark decays to a $W^{\pm}b$ pair that are followed only by the leptonic decays of $W^{\pm}$ bosons, because, for hadronic $W^{\pm}$ decays, it is very difficult to separate a signal against a huge QCD background.

Note that typical differential distributions (with respect to the transverse momentum $p_{\perp}$ and the pseudorapidity η) of the t quark and its decay products are virtually coincident with those for the production of a $t\bar{b}$ pair within the Standard Model (that is, via only $W^{\pm}$-boson exchange). In order to separate the $H^{\pm}$ contribution, we therefore explore the polarization properties of the t quark, which are different for the $W^{\pm} \to t\bar{b}$ and the $H^{\pm} \to t\bar{b}$ contribution at small values of $\tan\beta$. We found specific kinematical cuts that make it possible to separate the $H^{\pm}$ and $W^{\pm}$ contributions in reaction (1).

The ensuing exposition is organized as follows. In Section 2, we calculate the matrix elements squared for the process being considered. The behavior of the total cross section for the production of a $t\bar{b}$ pair as

[1)]Institute for High Energy Physics, Protvino, Moscow oblast, 142284 Russia.
[2)]Moscow Institute for Physics and Technology, Institutskiĭ proezd 9, Dolgoprudnyĭ, Moscow oblast, 141700 Russia.
*e-mail: murashev@mx.ihep.su
**e-mail: Sergey.Slabospitsky@ihep.ru
***e-mail: zyx@go.ru

a function of m_H and $\tan\beta$ is analyzed in Section 3. The differential distributions with respect to $p_\perp$ and η and the angular distributions of top-quark-decay products are also discussed in this section. A detailed simulation of the signal and relevant background processes is given in Section 4. The main results are summarized in the Conclusion.

2. CALCULATIONS OF THE MATRIX ELEMENTS

In the model involving two doublets of Higgs bosons, the Lagrangian describing the $\bar{t}H^\pm b$ vertex has the form [1, 4, 5]

$$\mathcal{L} = \sqrt{\frac{G_\mathrm{F}}{\sqrt{2}}}H^\pm\{\tan\beta\bar{U}_L V_{ij} M_D D_R + \cot\beta\bar{U}_R M_U V_{ij} D_L + \tan\beta\bar{\nu}_L M_l l_R\}, \quad (2)$$

where the symbols U and D refer to, respectively, up- and down-type quarks; ν and l correspond to neutrinos and charged leptons, respectively; the symbols L and R correspond to, respectively, left- and right-handed fermions; V_{ij} is the Cabbibo–Kobayashi–Maskawa matrix element; M_D and M_U are the quark masses; M_L is the charged-lepton mass; $\tan\beta$ is the ratio of the vacuum expectation values for two Higgs doublets; and G_F is the Fermi constant.

The subprocess of $t\bar{b}$ production through $H^\pm$- and $W^\pm$-boson exchanges in the annihilation of two light quarks q_1 and $\bar{q}_2$,

$$q_1\bar{q}_2 \to (H^\pm + W^\pm) \to t\bar{b}, \quad (3)$$

is described by two diagrams in Fig. 1.

It is convenient to represent the corresponding matrix element squared as the sum of three terms corresponding to $H^\pm$-boson (T_H) and $W^\pm$-boson (T_W) exchanges and their interference (T_I); that is,

$$|T_{2\to2}|^2 = |T_H|^2 + |T_W|^2 + |T_I|^2, \quad (4)$$

where

$$|T_H|^2 = \frac{16G_\mathrm{F}^2|V_{12}|^2|V_{tb}|^2}{\left(\hat{s}-m_H^2\right)^2+\Gamma_H^2 m_H^2} \times \left[\left(m_t^2\cot^2\beta + m_b^2\tan^2\beta\right)(p_t p_b) - 2m_b^2 m_t^2\right] \times \left[\left(m_1^2\cot^2\beta + m_2^2\tan^2\beta\right)(p_1 p_2) - 2m_1^2 m_2^2\right],$$

$$|T_W|^2 = \frac{128m_W^4 G_\mathrm{F}^2|V_{12}|^2|V_{tb}|^2}{\left(\hat{s}-m_W^2\right)^2+\Gamma_W^2 m_W^2}(p_t p_2)(p_b p_1),$$

$$|T_I|^2 = \frac{32G_\mathrm{F}^2|V_{12}|^2|V_{tb}|^2 m_t m_b A}{A^2+B^2} \times \left[-m_1^2\cot^2\beta(p_t p_2) + m_2^2(p_t p_1) + m_1^2(p_b p_2) - m_2^2\tan^2\beta(p_b p_1)\right].$$

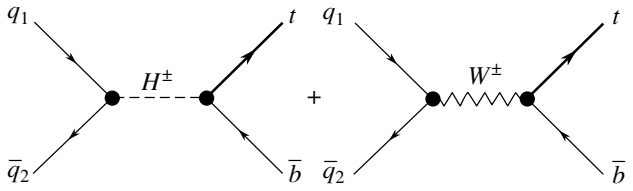

Fig. 1. Feynman diagrams for the subprocess $q_1\bar{q}_2 \to (H^\pm + W^\pm) \to t\bar{b}$.

Here, $\hat{s}$ is the square of the total energy of colliding partons; m_H and Γ_H are, respectively, the mass and the decay width of the $H^\pm$ boson; m_W and Γ_W are the analogous quantities for the $W^\pm$ boson; m_i and p_i are the quark masses and 4-momenta, respectively; $A = (\hat{s}-m_W^2)(\hat{s}-m_H^2) + \Gamma_W m_W \Gamma_H m_H$; and $B = (\hat{s}-m_W^2)\Gamma_H m_H - (\hat{s}-m_H^2)\Gamma_W m_W$.

With an eye to studying the polarization properties of the t quark in reaction (1), we also calculate the square of the matrix element for the subprocesses in (3), taking into account subsequent top-quark decay,

$$q_1\bar{q}_2 \to (H^\pm + W^\pm) \to \bar{b}t(\to bW^\pm) \longrightarrow b\bar{b}l^\pm\nu_l. \quad (5)$$

In just the same way as for the subprocesses in (3), we represent $|T_{2\to4}|^2$ as the sum of three terms corresponding to $H^\pm$ and $W^\pm$ exchanges and their interference; that is,

$$|T_{2\to4}|^2 = |T_H|^2 + |T_W|^2 + |T_I|^2, \quad (6)$$

where

$$|T_H|^2 = \frac{2048m_W^4 G_\mathrm{F}^4|V_{tb}|^4|V_{12}|^2(p_b k_1)}{((\hat{s}-m_H^2)^2+\Gamma_H^2 m_H^2)C_W C_t} \times \left\{(q_1 q_2)[m_1^2\cot^2\beta + m_2^2\tan^2\beta] - 2m_1^2 m_2^2\right\} \times \left\{m_b^2\tan^2\beta[2(k_2 p_t)(p_{\bar{b}} p_t) - (k_2 p_{\bar{b}})p_t^2] + m_t^4\cot^2\beta(k_2 p_{\bar{b}}) - 2m_b^2 m_t^2(k_2 p_t)\right\},$$

$$|T_W|^2 = \frac{8192m_W^8 G_\mathrm{F}^4|V_{tb}|^4|V_{12}|^2(p_b k_1)(p_{\bar{b}} q_1)}{((\hat{s}-m_W^2)^2+\Gamma_W^2 m_W^2)C_W C_t} \times \left[2(q_2 p_t)(k_2 p_t) - (q_2 k_2)p_t^2\right],$$

$$|T_I|^2 = \frac{4096m_W^6 G_\mathrm{F}^4|V_{tb}|^4|V_{12}|^2 A m_1 m_2}{(A^2+B^2)C_W C_t} \times \left\{m_t^2\cot^2\beta[(q_1 p_{\bar{b}})(p_t k_2) + (q_1 p_t)(p_{\bar{b}} k_2) - (q_1 k_2)(p_{\bar{b}} p_t)] + m_t^2[(q_2 k_2)(p_{\bar{b}} p_t) - (q_2 p_{\bar{b}})(p_t k_2) - (q_2, p_t)(p_{\bar{b}}, k_2)] + m_b^2\tan^2\beta[2(q_2 p_t)(p_t k_2) - (q_2 k_2)p_t^2] + m_b^2[(q_1 k_1)p_t^2 - 2(q_1 p_t)(p_t k_2)]\right\}.$$

Here, A and B were defined in (4); $C_W = (p_W^2 - m_W^2)^2 + \Gamma_W^2 m_W^2$ and $C_t = (p_t^2 - m_t^2)^2 + \Gamma_t^2 m_t^2$; p_t and p_W are the momenta of the top quark and the W

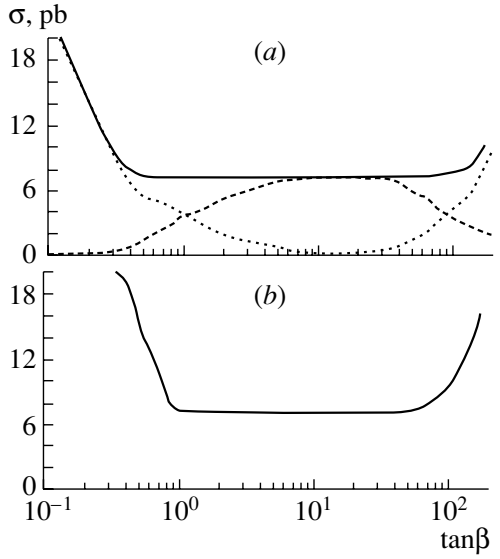

Fig. 2. Cross section for $(t\bar{b} + \bar{t}b)$ production as a function of $\tan\beta$ for two values of $m_{H^\pm} = (a)$ 90 and (b) 200 GeV (solid curves). The dashed and the dotted curve represent the relevant production cross section multiplied by the branching ratios for t-quark decays to $bW^\pm$ and $bH^\pm$, respectively.

boson, respectively; and k_1 and k_2 are the momenta of the neutrino and the charged lepton, respectively.

Note that the matrix element squared (6) corresponding to the subprocess in (5) is calculated for the first time.

3. TOTAL CROSS SECTIONS AND DIFFERENTIAL DISTRIBUTIONS

In our numerical calculations, we used the parton distributions from [11]. The evolution parameter Q^2 was chosen to be $Q^2 = \hat{s}$. The b- and t-quark masses were set to the following values [12]:

$$m_b = 4.5\ \text{GeV}, \qquad m_t = 173.8\ \text{GeV}. \qquad (7)$$

For a fixed value of the mass of the charged Higgs boson, the largest cross section is expected at large and small values of $\tan\beta$ (see Fig. 2).

The $H^\pm$-boson contribution to reaction (1) leads to an increase in the cross section for $t\bar{b}$ production. However, the modification of the "observable" number of events, $N_{\text{ev}}(Wb\bar{b}) \sim \sigma(t\bar{b})B(t \to bW^\pm)$, depends on $m_{H^\pm}$. For an $H^\pm$ boson lighter than the top quark ($m_{H^\pm} < m_t$), the branching fraction of $t \to bW$ decay [$\text{B}(t \to bW)$] may be significantly smaller than that in the Standard Model [4, 5]. As a result, we should expect a decrease in N_{ev} in relation to the case of the Standard Model. For a heavy $H^\pm$ boson ($m_{H^\pm} > m_t$), there is no decay channel $t \to bH^\pm$. Therefore, one has $B(t \to bW^\pm) \approx 1$, and we should expect an increase in the $W^\pm b\bar{b}$ yield.

The cross sections "experimentally seen" for t-quark production in reaction (1),

$$\sigma(pp \to \bar{b}t(\to bW)X) = \sigma(pp \to t\bar{b}X)B(t \to bW), \qquad (8)$$

are presented in Fig. 2 for two values of $m_{H^\pm}$ (90, 200 GeV). Note that, for small and large values of $\tan\beta$, the $H^\pm$-boson contribution leads to a noticeable modification of $t\bar{b}$ production, while, for an intermediate range of $\tan\beta$ (0.8–15), the $H^\pm$ contribution becomes negligible.

The differential distributions of final-state particles (t, W, b, l) with respect to the transverse momentum and the pseudorapidity are shown in Figs. 3 and 4, respectively, according to calculations at the parton level. As can be seen from these figures, the differential distributions for the cases of $H^\pm$ and $W^\pm$ exchanges have nearly the same shape. Therefore, the contribution of new physics may lead only to the deviation of the expected number of events. It follows that, in order to clarify the nature of possible deviations from the predictions of the Standard Model, it is necessary to examine additional quantities that exhibit different types of behavior within and beyond the Standard Model.

For this purpose, we explored the polarization properties of the t quark produced in reaction (1). It is well known that subprocess (3) proceeding through $W^\pm$ exchange leads to the production of almost left-handed t quarks [4]. At the same time, the contribution of the charged Higgs boson leads to the production of right-handed (left-handed) t quarks for small (large) values of $\tan\beta$ (see [5]). Note that, for a left-handed t quark, the b quark (charged lepton) travels predominantly along (against) the direction of the top-quark momentum (see [4]). Naturally, the situation is inverse for right-handed quarks.

In order to separate the $W^\pm$ and $H^\pm$ contributions, we examine below the angular distributions of the t-quark-decay products ($t \to bl\nu$),

$$dN/d\cos\theta^*, \qquad (9)$$

where θ^* is the angle between the direction of the t-quark momentum and the momentum of the final b quark or charged lepton in the top-quark rest frame.

The corresponding angular distributions of the b quark and charged lepton from t-quark decay according to the calculations with the matrix element (6) are displayed in Fig. 5 separately for only $W^\pm$ or $H^\pm$ exchange (see the histograms in Figs. 5*a*, 5*b*, 5*e*, 5*f*). In evaluating these distributions, we set $m_{H^\pm} =$ 200 GeV and $\tan\beta = 0.1$.

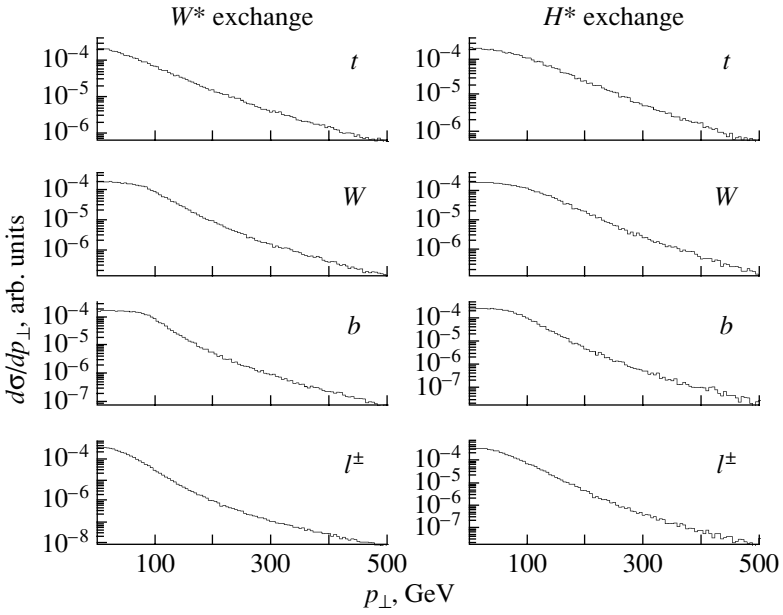

Fig. 3. Transverse-momentum distribution of the top quark and the products of its decay $t \to bW(\to bl\nu)$ in reaction (1). The left (right) figures correspond to $t\bar{b}$ production through $W^{\pm}$ ($H^{\pm}$) exchange.

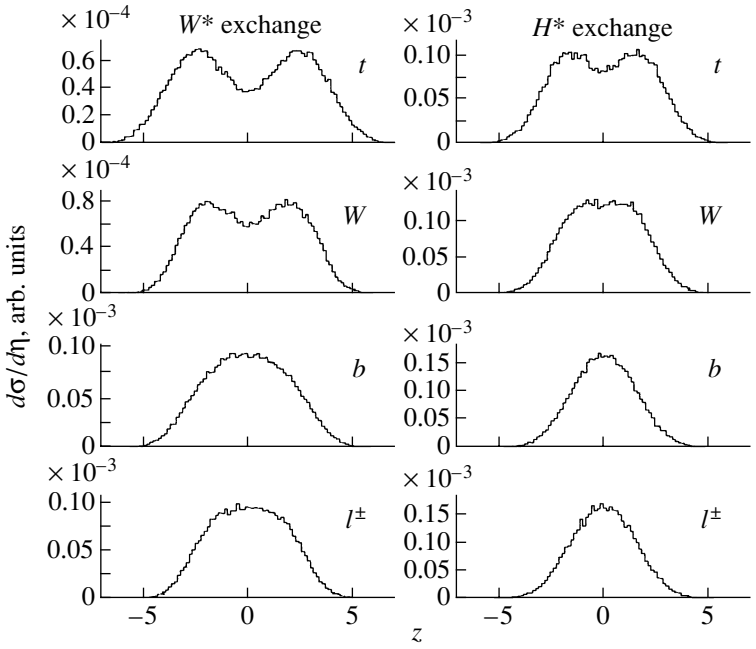

Fig. 4. Distributions $d\sigma/d\eta$ with respect to the pseudorapidity η for the t quark and its decay products.

4. CALCULATIONS OF THE SIGNAL AND BACKGROUND PROCESSES

We have performed a detailed simulation of process (1) followed by t-quark decays to an electron and a muon ($t \to be\nu_e$, $t \to b\mu\nu_\mu$) and the relevant background reactions for a three-year low-luminosity run of LHC:

$$\sqrt{s} = 14 \text{ TeV} \quad \text{and} \quad \int \mathcal{L}dt = 30 \text{ fb}^{-1}. \qquad (10)$$

The simulation was performed for the following values of the parameters of the charged Higgs boson:

$$m_{H^{\pm}} = 200 \text{ GeV}, \quad \tan\beta = 0.1. \qquad (11)$$

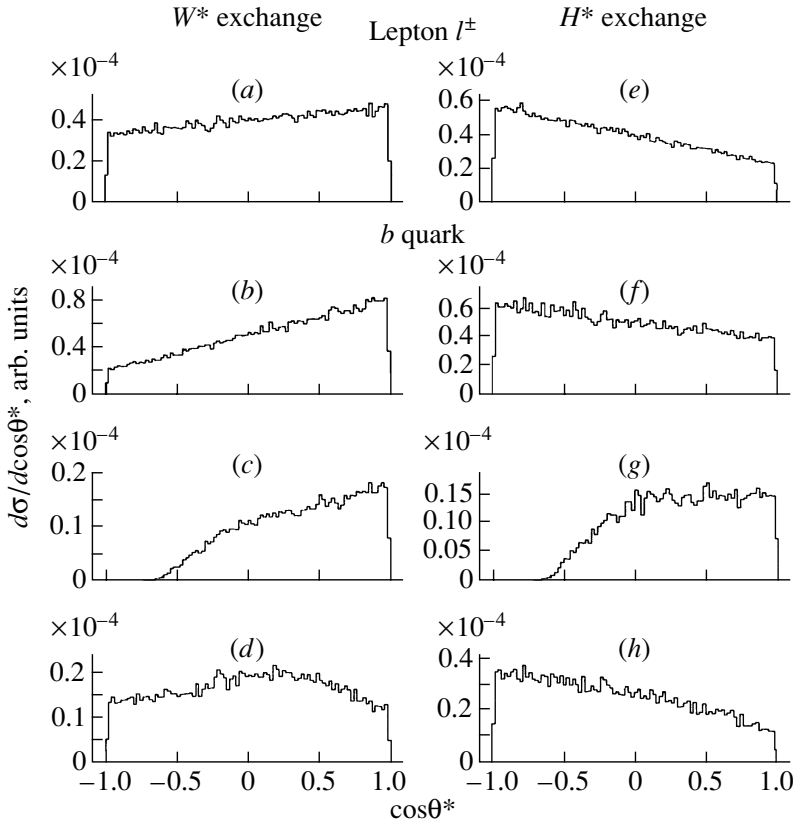

Fig. 5. Distributions $d\sigma/d\cos\theta^*$ of the charged lepton and b quark originating from t-quark decay. All of the distributions are obtained from the calculation for reaction (1) at the parton level for $W^{\pm}$-boson exchange (W^*) and the $H^{\pm}$-boson contribution (H^*). The histograms in Figs. 5*a*, 5*b*, 5*e*, and 5*f* were calculated without any cuts, while the histograms in Figs. 5*c*, 5*g*, 5*d*, and 5*h* were constructed by using the H cut (13) and the SH cut (14), respectively.

Note that our result is not very sensitive to variations in m_H, but the chosen small value of $\tan\beta$ ($\tan\beta < 0.2$) is of importance for the ensuing analysis.

In simulating the signal and background processes, we relied on the TopReX 3.25 event generator [13]. We used PYTHIA 6.134 [14] to simulate the hadronization of quarks and gluons. We performed the simulation, taking into account the ability of the CMS detector at LHC [15]. For a "fast" detector simulation, all events were passed through the CMSJET 4.703 package [16].

As a result, each final event contains information about the momenta of "detected" photons and charged leptons (e, μ) and about hadronic jets and missing energy $E_{\perp\text{mis}}$ (see [16] for details). For any hadronic jet, the CMSJET package estimates the probability that this jet originates from a b-quark fragmentation. The efficiencies of the b tagging of jets originating from the b quark, c quark, and light partons (u, d, s quarks and gluon) are about 60%, 10%, and 1 to 2%, respectively [16]. In what follows, we refer to a b-tagged jet as a B jet.

For our choice of the $H^{\pm}$-boson parameters [see (11)], the cross section for $(t\bar{b} + \bar{t}b)$ production in reaction (1) due to the $H^{\pm}$-boson contribution at $\sqrt{s} = 14$ TeV is

$$\sigma(H^{\pm}) = 9.7 \text{ pb}. \qquad (12)$$

There are several sources of background to the process in (1) (all of the cross-section values imply summation over particles and antiparticles). These are

$t\bar{t}$ production:

$$gg(q\bar{q}) \to t\bar{t}, \quad \sigma(t\bar{t}) = 600 \text{ pb};$$

three processes of electroweak top production:

$$q\bar{q}' \to W^{\pm} \to t\bar{b}, \quad \sigma(W^*) = 7.5 \text{ pb},$$
$$gq \to q't\bar{b}, \quad \sigma(Wg) = 180 \text{ pb},$$
$$gb \to tW, \quad \sigma(tW) = 60 \text{ pb};$$

$Wb\bar{b}$ production:

$$q\bar{q}' \to Wb\bar{b}, \sigma(Wb\bar{b}) = 360 \text{ pb};$$

Table 1. Efficiencies (in %) of the separation of signal ($H^\pm$ and $W^\pm$-bosons) and background ($Wg, Wt, \ldots$; see Section 4) events after the application of all cuts {the symbols SH and H correspond to the use of new and old $p_\perp$ cuts [see (14) and (13), respectively]}

	$H^\pm$	$W^\pm$	Wg	Wt	$t\bar{t}$	$Wb\bar{b}$	$W+$jets
SH	0.77	0.5	0.012	0.008	0.003	0.02	5×10^{-5}
H	0.26	0.4	0.007	0.003	0.003	0.01	–

Table 2. Number of events resulting from the application of all cuts for the integrated luminosity of $\int \mathcal{L}dt = 30$ fb^{-1} (the symbols W/B and H/B refer to the signal-to-background ratios calculated, respectively, within the Standard Model and within the Standard Model with allowance for the $H^\pm$-boson contribution)

	$H^\pm$	$W^\pm$	SM	SM + H	W/B	H/B
SH	470	260	960	1430	0.37	0.49
H	260	220	610	870	0.55	0.43

$W+$jet production (generated by PYTHIA): $\sigma(W+\text{jets}) = 59\,000$ pb.

The signal process (1) and all the background reactions (with the exception of $W+$jets production) were simulated by using the TopReX generator. In order to evaluate the last process ($W+$jets), the PYTHIA parameter $k_{\perp\min}$ (the minimal value of the parton transverse momentum) was chosen to be 2 GeV {that is, CKIN(1) = 2 [14]}.

The production of a $t\bar{b}$ pair through process (1) followed by top-quark decay to $bl\nu$ leads to a final state characterized by the presence of one isolated charged lepton (from W-boson decay), a missing energy (neutrino), and two hard B jets from b quarks.

The appropriate cuts that ensure a separation of the signal from the background processes are considered in detail elsewhere [4]. In particular, these cuts include the requirement of two "hard" B jets; that is, the "hard" cut (H)

$$p_\perp(B_1, B_2) \geq p_{T0} \sim 75 \text{ GeV}. \qquad (13)$$

However, this cut leads to a significant modification of the shape of the corresponding $\cos\theta^*$ distributions (9) of t-quark-decay products.

Indeed, Fig. 5, where we present the angular distributions of the b quark (from t-quark decay) that were evaluated at the parton level before and after the application of various cuts on the b-quark transverse momentum, shows that, after the application of the cut in (13), the shape of the angular distribution of the b quark originating from the decay of the right-handed t quark produced via $H^\pm$ exchange changes dramatically and even becomes qualitatively similar to that of the b quark from the decay of the left-handed top quark produced via $W^\pm$ exchange. In view of the actual possibilities of the detector, it will be even more difficult to distinguish between these two distributions.

Therefore, we have considered a different $p_\perp$ cut (a "soft–hard" one) on the final B jets. Namely, we required that the transverse momentum $p_\perp$ of one B_1 jet (from the t quark) not exceed the value of $p_{T1} = 100$ GeV, but that the transverse momentum $p_\perp$ of the other B_2 jet be greater than $p_{T0} = 75$ GeV; that is, the soft–hard (SH) cut amounts to the following requirements:

$$p_\perp(B_1 \text{ from } t) \leq p_{T1} \quad \text{and} \quad p_\perp(B_2) \geq p_{T0}. \qquad (14)$$

It can be seen from the histograms in Figs. 5*d* and 5*h* that this soft–hard cut (14) preserves the shapes of the angular distributions of products originating from the decay of t quarks produced through $H^\pm$ and $W^\pm$ exchanges.

In the ensuing analysis, we apply both versions of $p_\perp$ cuts, that in (13) and that in (14). Thus, the sep-

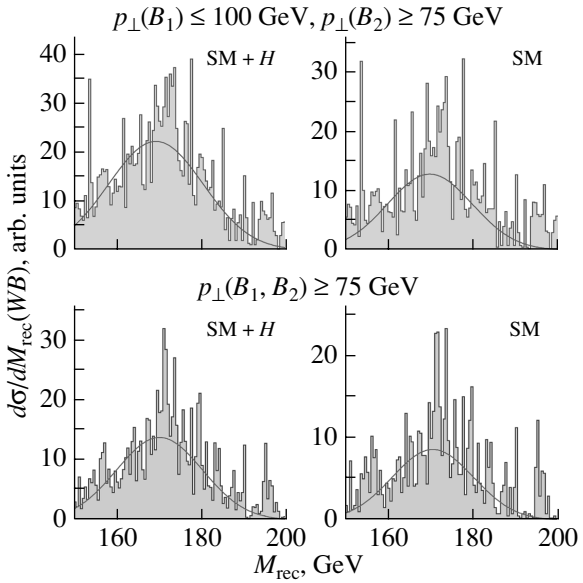

Fig. 6. Distributions $d\sigma/dM_{\text{rec}}(WB)$ with respect to the reconstructed mass of the t quark (the WB system), M_{rec}, upon the application of all cuts. The two upper and lower histograms correspond to the application of the new SH cuts (14) and the old H cuts (13), respectively. The two left histograms (SM + H) represent the contributions from $H^\pm$ and $W^\pm$ and from the background processes, while the two right histograms (SM) show the Standard Model contribution (that is, the $W^\pm$-boson contribution and the contribution of the background processes). The smooth curves represent the results obtained by applying a conventional fitting procedure.

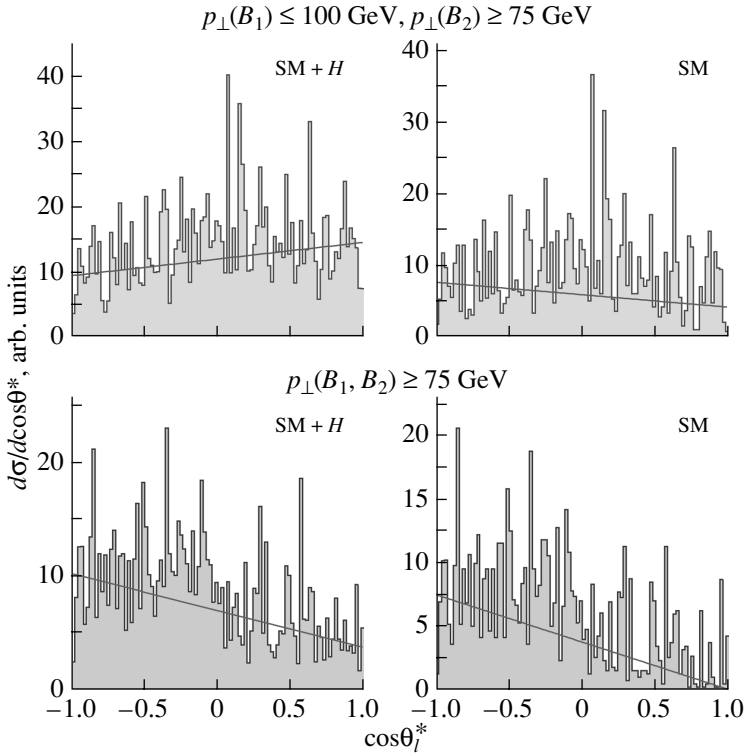

Fig. 7. Distributions $d\sigma/d\cos\theta^*$ for the charged lepton. The histograms were obtained under the same conditions as in Fig. 6. The straight lines represent a fit to the linear dependence in (15).

aration of the signal and background is accomplished by requiring

(i) one and only one isolated lepton (with $p_\perp > 10$ GeV) and at least two hadronic jets (with $p_\perp > 20$ GeV and a pseudorapidity in the region $|\eta| < 4.5$);

(ii) precisely two B-tagged jets (with $p_\perp > 25$ GeV and a pseudorapidity in the region $|\eta| < 2.5$) and no other hadronic jets;

(iii) the total transverse momentum of the reconstructed W boson and two B_1 and B_2 jets within the region $|\mathbf{p}_\perp(W) + \mathbf{p}_\perp(B_1) + \mathbf{p}_\perp(B_2)| \le 10$ GeV;

(iv) the H (hard) cut on $p_\perp$ of B jets [$p_\perp(B_1, B_2) \ge 75$ GeV] or the SH (soft–hard) cut on $p_\perp$ of B jets (one B_1 jet with $p_\perp \le 100$ GeV and the other B_2 jet with $p_\perp \ge 75$ GeV);

(v) the reconstructed mass of the t quark within the range 150–200 GeV, $|M_{\mathrm{rec}}(WB) - m_t| < 25$ GeV.

The resulting efficiencies after the application of all cuts to the signal and background are given in Table 1. One can see that the new SH cut (14) leads to a slightly higher efficiency of signal reconstruction. The resulting number of reconstructed events (for $\int \mathcal{L}dt = 30$ fb^{-1}) and the corresponding signal-to-background ratios are given in Table 2. It can be seen that the application of the old and the new $p_\perp$ cut yields nearly the same signal-to-background ratios. Therefore, either version of $p_\perp$ cuts (SH and H) provides a rather good reconstruction of the top quark in reaction (1).

The distributions with respect to the reconstructed t-quark mass are displayed in Fig. 6. The symbol "SM" corresponds to the calculations within the Standard Model, while the symbol "SM + H" labels the case where this calculation is supplemented with the $H^\pm$-boson contribution. A standard fit gives the following values of the reconstructed t-quark mass (in GeV):

	SM	SM + H
SH	172.4 ± 11.8	171.6 ± 11.4
H	172.8 ± 11.2	172.4 ± 10.8

We now proceed to consider the separation of the $H^\pm$-boson contribution to reaction (1). For this purpose, we explore the difference in the $\cos\theta_l^*$ distributions (where θ_l^* is the lepton emission angle with respect to the direction of the t-quark momentum in the top-quark rest frame) that results from the different polarizations of the t quark produced within the Standard Model (only W exchange) and via $W^\pm$ and

Table 3. Results obtained by fitting the distribution $dN/d\cos\theta_l^*$ in terms of the function $1+\alpha\cdot\cos\theta_l^*$ [the calculations were performed by using the Standard Model (SM) or by supplementing this model with the $H^\pm$-boson contribution (SM + H)]

	α(SM)	α(SM + H)
SH	-0.29 ± 0.06	$+0.21\pm0.05$
H	-0.98 ± 0.05	-0.46 ± 0.06

$H^\pm$ exchanges (see Fig. 5). The distributions with respect to $\cos\theta_l^*$ according to the calculations for the sum of the signal and background events are given in Fig. 7. The two upper two histograms correspond to the new SH cut, while the two lower histograms result from the application of the old H cut. We fit these distributions by using the linear dependence on $\cos\theta_l^*$:

$$\frac{dN}{d\cos\theta_l^*}\propto 1+\alpha\cos\theta_l^*. \qquad (15)$$

The results of the fit are given in Table 3 and in Fig. 7. It is evident that the new SH cut (14) is more sensitive to the $H^\pm$-boson contribution. Indeed, the presence of a charged Higgs boson leads to the reversal of the sign of the slope of the $\cos\theta_l^*$ distribution, while the application of the old H cut only modifies the slope parameter α (see Table 3).

Of course, this result depends on the relative value of the $H^\pm$-boson contribution. Indeed, a decrease in the contribution of the charged Higgs boson is expected for a larger value of $\tan\beta$; as a result, the values of α will be closer to the predictions of the Standard Model. Note that, for large values of $\tan\beta$ (in excess of 10), in which case we have a noticeable contribution of the charged Higgs boson, the product top quark must be left-handed. As a result, the angular distribution must be identical to that in the Standard Model.

5. CONCLUSION

The contribution of charged Higgs bosons to the process of electroweak production of a $t\bar{b}$ pair at LHC has been considered and analyzed in detail. The expressions for matrix elements squared for the corresponding subprocesses have been obtained, and the role of t-quark polarization has been investigated. The cross sections and angular distributions have been calculated at a parton level. The signal and relevant background processes have been simulated by means of PYTHIA in view of the opportunities of the CMS detector at LHC.

It has been shown that the differential distributions (with respect to the transverse momentum $p_\perp$ and the pseudorapidity η) of the t quark and its decay products are nearly identical to those in the production of a $t\bar{b}$ pair within the Standard Model. As a result, it would be difficult to distinguish between the $H^\pm$-boson contribution and $W^\pm$-boson exchange by using a conventional method for top-quark separation from the background. At the same time, the top quark produced through the exchange of a charged Higgs boson has a polarization different from that within the Standard Model. At small values of $\tan\beta$, one should expect the production of right-handed t quarks. The corresponding angular distributions of leptons differ significantly from those predicted by the Standard Model.

In order to separate the $W^\pm$ and $H^\pm$ contributions to reaction (1), we propose the new $p_\perp$ cut (14) for B-tagged hadronic jets. Not only does this soft–hard $p_\perp$ cut ensure the discrimination between the t-quark signal and the background processes, but it also enables one to single out the contribution of the charged Higgs boson to the process in (1).

Of course, the proposed $p_\perp$ cut can help only at small values of $\tan\beta$ (below 0.2). For larger values ($\tan\beta>0.2$), it is necessary to use different kinematical cuts that are sensitive to the contribution of the charged Higgs boson to reaction (1). We plan to investigate this point in the future.

ACKNOWLEDGMENTS

We are grateful to E. Boos, D. Denegri, V. Drollinger, V. Ilyin, A. Kostritsky, N. Krasnikov, M. Mangano, A. Nikitenko, V. Obraztsov, L. Sonnenschein, and N. Stepanov for stimulating discussions.

The work of S.R. Slabospitsky was supported in part by the Russian Foundation for Basic Research (project no. 99-02-16558).

REFERENCES

1. J. F. Gunion, H. E. Haber, G. L. Kane, and S. Dawson, *The Higgs Hunters' Guide* (Addison-Wesley, Reading, 1990).
2. ALEPH Collab. (R. Barate *et al.*), CERN-EP-2000-086; hep-ex/0008005; DELPHI Collab. (P. Abreu *et al.*), Phys. Lett. B **460**, 484 (1999); L3 Collab. (M. Acciarri *et al.*), Phys. Lett. B **466**, 71 (1999); hep-ex/9909044; OPAL Collab. (K. Ackerstaff *et al.*), Phys. Lett. B **426**, 180 (1998); hep-ex/9802004.
3. CDF Collab. (T. Affolder *et al.*), Phys. Rev. D **62**, 012004 (2000); hep-ex/9912013; D0 Collab. (B. Abbott *et al.*), Phys. Rev. Lett. **82**, 4975 (1999); hep-ex/9902028.
4. M. Beneke *et al.*, hep-ph/0003033.

5. A. Djouadi *et al.*, hep-ph/0002258.
6. R. Kinnunen, J. Tuominiemi, and D. Denegri, Technical Note, CMS TN/94-233 (1994); D. Denegri *et al.*, hep-ph/0112045.
7. A. C. Bawa, C. S. Kim, and A. D. Martin, Z. Phys. C **47**, 75 (1990); V. Barger, R. J. N. Phillips, and D. P. Roy, Phys. Lett. B **324**, 236 (1994); S. Moretti and K. Odagiri, Phys. Rev. D **55**, 5627 (1997); J. F. Gunion, Phys. Lett. B **322**, 125 (1994); F. Borzumati, J.-L. Kneur, and N. Polonsky, Phys. Rev. D **60**, 115011 (1999); D. J. Miller, S. Moretti, D. P. Roy, and W. J. Stirling, Phys. Rev. D **61**, 055011 (2000); hep-ph/9906230; A. Belyaev, D. Garcia, J. Guasch, and J. Sola, hep-ph/0203031.
8. S. Cortese and R. Petronzio, Phys. Lett. B **253**, 494 (1991); T. Stelzer and S. Willenbrock, Phys. Lett. B **357**, 125 (1995); hep-ph/9505433.
9. A. P. Heinson, A. S. Belyaev, and E. E. Boos, Phys. Rev. D **56**, 3114 (1997); hep-ph/9612424; A. S. Belyaev, E. E. Boos, and L. V. Dudko, Phys. Rev. D **59**, 075001 (1999); hep-ph/9806332.
10. G. V. Jikia and S. R. Slabospitsky, Phys. Lett. B **295**, 136 (1992).
11. CTEQ Collab. (H. L. Lai *et al.*), Eur. Phys. J. C **12**, 375 (2000); hep-ph/9903282.
12. Particle Data Group (D. E. Groom *et al.*), Eur. Phys. J. C **15**, 1 (2000).
13. S. R. Slabospitsky and L. Sonnenschein, Comput. Phys. Commun. **148**, 87 (2002); hep-ph/0201292.
14. T. Sjöstrand, P. Eden, C. Friberg, *et al.*, Comput. Phys. Commun. **135**, 238 (2001); hep-ph/0010017.
15. CMS Technical Proposal, CERN/LHC/94-43 LHCC/P1 (1994).
16. S. Abdullin, A. Khanov, and N. Stepanov, Technical Note, CMS TN/94-180 (1999).

Translated by S. Slabospitsky

Physics of Atomic Nuclei, Vol. 67, No. 2, 2004, pp. 359–375. From Yadernaya Fizika, Vol. 67, No. 2, 2004, pp. 377–393.

ELEMENTARY PARTICLES AND FIELDS
Theory

Radiative Corrections to QCD Amplitudes in Quasi-Multi-Regge Kinematics*

V. S. Fadin, M. G. Kozlov**, and A. V. Reznichenko****

Budker Institute of Nuclear Physics, Siberian Division, Russian Academy of Sciences, Novosibirsk, 630090 Russia
Novosibirsk State University, Novosibirsk, 630090 Russia

Received March 25, 2003

Abstract—Radiative corrections to QCD amplitudes in the quasi-multi-Regge kinematics are interesting, in particular, since the Reggeized form of these amplitudes is used in the derivation of the NLO BFKL. This form is a hypothesis which must be at least carefully checked, if not proved. We calculate the radiative corrections in the one-loop approximation using the s-channel unitarity. Compatibility of the Reggeized form of the amplitudes with the s-channel unitarity requires fulfillment of the set of nonlinear equations for the Reggeon vertices. We show that these equations are satisfied. © *2004 MAIK "Nauka/Interperiodica"*.

1. INTRODUCTION

In the limit of large c.m. energy $\sqrt{s}$ and fixed momentum transfer $\sqrt{-t}$ (Regge limit), the most appropriate approach to the description of scattering amplitudes is given by the theory of complex angular momenta (Gribov–Regge theory). One of the remarkable properties of QCD is the Reggeization of its elementary particles. Contrary to QED, where the electron does Reggeize in perturbation theory [1], but the photon remains elementary [2], in QCD the gluon does Reggeize [3–5], as well as the quark [6–8].

The phenomenon of Reggeization is very important for high-energy QCD. In particular, the BFKL approach [5] to the description of high-energy QCD processes is based on gluon Reggeization. It was assumed in this approach that the amplitudes with color octets and negative signatures in channels with fixed (not increasing with s) transferred momenta have the Reggeized form. In the leading logarithmic approximation (LLA), when only the leading terms $(\alpha_s \ln s)^n$ are resummed [5], the assumption was made about the amplitudes in the multi-Regge kinematics (MRK). Recall that the MRK means large invariant masses of any pair of final-state particles and fixed transverse momenta; we include here the Regge kinematics (RK) in the MRK as a particular case. The Reggeized form of these amplitudes in the LLA was proved [9], so that, in this approximation, the BFKL approach is completely justified.

Now, the BFKL approach is developed in the next-to-leading approximation (NLA), where the terms $\alpha_s(\alpha_s \ln s)^n$ are also resummed. The kernel of the BFKL equation for the forward scattering ($t = 0$ and color singlet in the t channel) in the next-to-leading order (NLO) has been found [10, 11]. The calculation of the NLO kernel for the nonforward scattering [12] is not far from completion (see [13, 14]). The impact factors of gluons [15] and quarks [16] are calculated in the NLO and the impact factors of the physical (color singlet) particles are under investigation [17–21].

The NLO results are obtained assuming the Reggeized form both for the amplitudes in the quasi-multi-Regge kinematics (QMRK), where a pair of produced particles has fixed invariant mass, and for the MRK amplitudes in the NLA. It is clear that these assumptions must be at least carefully checked, if not proved. It can be done by revision of the "bootstrap" relations [12], appearing from the requirement of compatibility of the Reggeized form of the amplitudes with the s-channel unitarity. For the elastic amplitudes, these relations impose the bootstrap conditions on the color-octet impact factors and the BFKL kernel in the NLO [12]. The conditions for the impact factors of gluons [15] and quarks [16], as well as for the quark part of the kernel [13], were shown to be satisfied at arbitrary spacetime dimension D. For the gluon part of the kernel, fulfillment of the bootstrap condition was proved at $D \to 4$ [22], in particular, because this part was available at that time only in such a limit. Now it can be done at arbitrary D, since the kernel at arbitrary D has been calculated [23].

Evidently, the bootstrap relations must be satisfied for all amplitudes that were assumed to have the

*This article was submitted by the authors in English.

**e-mail: fadin@inp.nsk.su
***e-mail: m.g.kozlov@inp.nsk.su
****e-mail: a.v.reznichenko@inp.nsk.su

Reggeized form, so that there is an infinite set of such relations. Since the amplitudes are expressed in terms of the gluon trajectory and a finite number of Reggeon vertices, it is extremely nontrivial to satisfy all these relations. Nevertheless, it occurs that all of them can be fulfilled if the vertices and trajectory submit to several bootstrap conditions [24]. On the other hand, the fulfillment of all bootstrap relations secures the Reggeized form of the radiative corrections order by order in perturbation theory. In this way, the proof of the Reggeization was constructed in the LLA [9]. An analogous proof can be constructed in the NLA as well [24].

The bootstrap relations for the multiparticle production amplitudes give [24], in particular, stronger restrictions on the octet impact factors and kernel than the relations for the elastic amplitudes. These restrictions are known as the strong bootstrap conditions suggested, without derivation, in [25, 26], which lead to remarkable properties of the color-octet impact factors and the Reggeon vertices [27] that their ratio is a process-independent function. In the NLO, this quite nontrivial property was verified by comparison of such ratio for quarks and gluons [27]. Moreover, the process-independent function mentioned above must be the eigenfunction of the octet kernel. In the part concerning the quark contribution to the kernel, it is proved rather easily [13, 26, 28]. Doing this for the gluon contribution requires much more effort, but recently it was also done [29].

In this paper, we investigate the bootstrap relations for the production amplitudes in the QMRK. We calculate the one-loop radiative corrections to these amplitudes using the s-channel unitarity, derive the bootstrap conditions for the production vertices, and demonstrate that they are fulfilled.

The next section contains all necessary definitions and denotations. Then, in Section 3, we consider the amplitudes with a couple of particles in the fragmentation region of one of the colliding particles. We calculate the one-loop radiative corrections for these amplitudes and derive the bootstrap conditions for the Reggeon vertices in the QMRK in Section 3.1. In Sections 3.2, 3.3, and 3.4 we demonstrate that these conditions are satisfied for quark–antiquark, gluon–gluon, and quark–gluon production, respectively. Next, we consider production of a couple of particles with fixed invariant mass in the central region of rapidities. Section 4.1 contains the calculation of the one-loop radiative corrections and derivation of the bootstrap conditions. Fulfillment of these conditions is proved in Sections 4.2 and 4.3 for quark–antiquark and gluon–gluon production, respectively. Significance of the obtained results is discussed in Section 5.

2. DEFINITIONS AND NOTATION

Considering collisions of high-energy particles A and B with momenta p_A and p_B and masses m_A and m_B, we introduce light-cone 4-vectors p_1 and p_2 so that

$$p_A = p_1 + \left(m_A^2/s\right) p_2, \quad p_B = p_2 + \left(m_B^2/s\right) p_1, \tag{2.1}$$
$$s = 2p_1p_2 \simeq (p_A + p_B)^2,$$

where s is supposed to tend to infinity, and we use the Sudakov decomposition of momenta

$$p = \beta p_1 + \alpha p_2 + p_\perp, \quad s\alpha\beta = p^2 - p_\perp^2 = p^2 + \mathbf{p}^2, \tag{2.2}$$

where the vector denotes components of momenta transverse to the p_A–p_B plane. They are supposed to be limited (not growing with s).

According to the hypothesis of the gluon Reggeization, the amplitude of the process $A + B \to A' + B'$ with a color octet in the t channel and negative signature (which means antisymmetry under the substitution $s \leftrightarrow u \simeq -s$) has the form

$$\mathcal{A}_{AB}^{A'B'} = \Gamma_{A'A}^c \left[\left(\frac{-s}{-t}\right)^{j(t)} - \left(\frac{+s}{-t}\right)^{j(t)}\right] \Gamma_{B'B}^c, \tag{2.3}$$

where

$$t = q^2 \simeq q_\perp^2 = -\mathbf{q}^2, \quad q = p_A - p_{A'} = p_{B'} - p_B; \tag{2.4}$$
$$j(t) = 1 + \omega(t);$$

$j(t)$ is the gluon Regge trajectory; $\Gamma_{P'P}^c$ are the vertices of the Reggeon interactions with scattered particles; and c is a color index. The form (2.3) correctly represents the analytical structure of the scattering amplitude, which is quite simple in the elastic case. In the BFKL approach, it is assumed that this form is valid in the NLA as well as in the LLA. Recall that, in each order of perturbation theory, amplitudes with negative signature do dominate, owing to the cancellation of the leading logarithmic terms in amplitudes with positive signatures, which become pure imaginary in the LLA due to this cancellation. Note that the amplitude of the process $A + B \to A' + B'$ can contain contributions of various color states and signatures in the t channel, so that, strictly speaking, we should indicate somehow on the left-hand side of (2.3) that only the contribution of a color octet with negative signature is retained. But since in this paper we are interested only in such contributions, we have omitted this indication to simplify the notation. We do the same below considering the inelastic amplitudes, so that a color octet and negative signature is always

assumed, without explicit indication, in the channels with gluon quantum numbers.

In the leading order (LO), the vertices of the Reggeon interactions with quarks and gluons have very simple form in the helicity basis:

$$\Gamma^c_{P'P} = gT^c_{P'P}\delta_{\lambda_{P'}\lambda_P}, \tag{2.5}$$

where g is the QCD coupling constant, $T^c_{P'P}$ are the matrix elements of the color group generators in corresponding representations, and λ are helicities of the partons. But we will need a basis-independent form of the vertices. For quarks with momenta p and p' having predominant components along p_1, such a form can be represented as

$$\Gamma^c_{Q'Q} = g\bar{u}(p')t^c\frac{\not{p}_2}{2pp_2}u(p), \tag{2.6}$$

where t^c are the color group generators in the fundamental representation; for antiquarks we have, correspondingly,

$$\Gamma^c_{\bar{Q}'\bar{Q}} = -g\bar{v}(p)t^c\frac{\not{p}_2}{2pp_2}v(p'). \tag{2.7}$$

For gluons with predominant components of momenta along p_1, we will use physical polarization vectors $e(p)p = e(p')p' = 0$ in the light-cone gauge $e(p)p_2 = e(p')p_2 = 0$, so that

$$e(p) = e(p)_\perp - \frac{(e(p)_\perp p_\perp)}{p_2 p}p_2, \tag{2.8}$$
$$e(p') = e(p')_\perp - \frac{(e(p')_\perp p'_\perp)}{p_2 p'}p_2,$$

and

$$\Gamma^c_{G'G} = -g(e^*(p')_\perp e(p)_\perp)T^c_{G'G}, \tag{2.9}$$

with the color generators in the adjoint representation. For momenta with predominant components along p_2, we have to replace in these formulas $p_2 \to p_1$ [evidently, this replacement in (2.8) means change of the gauge]. The gluon trajectory in the LO is given by

$$\omega^{(1)}(t) = \frac{g^2 N_c t}{2(2\pi)^{D-1}}\int\frac{d^{D-2}q_1}{\mathbf{q}_1^2(\mathbf{q}-\mathbf{q}_1)^2}$$
$$= -g^2\frac{N_c\Gamma(1-\epsilon)}{(4\pi)^{D/2}}\frac{\Gamma^2(\epsilon)}{\Gamma(2\epsilon)}(\mathbf{q}^2)^\epsilon. \tag{2.10}$$

Here and in the following, N_c is the number of colors, $D = 4 + 2\epsilon$ is the spacetime dimension taken different from 4 to regularize infrared divergencies, and $\Gamma(x)$ is the Euler function.

The necessary assumption in the derivation of the BFKL equation is the Reggeized form of the production amplitudes in the MRK, which means large invariant masses of any pair of final particles and fixed

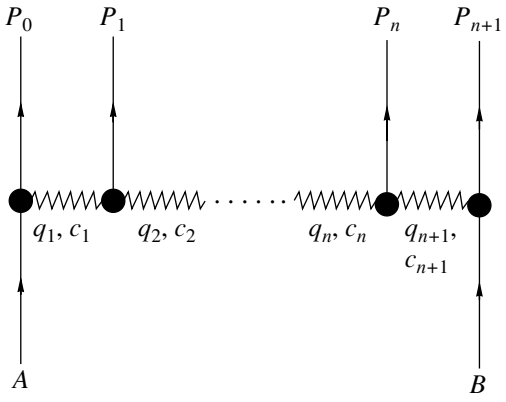

Fig. 1. Schematic representation of the process $A + B \to P_0 + P_1 + \ldots + P_{n+1}$ in the MRK. The zigzag lines represent Reggeized gluon exchange; the black circles denote the Reggeon vertices; q_i are the Reggeon momenta, flowing from left to right; c_i are the color indices.

momentum transfers. Denoting momenta of final particles in the process $A + B \to P_0 + P_1 + \ldots + P_{n+1}$ as k_i, $i = 0{-}(n+1)$ (see Fig. 1),

$$k_i = \beta_i p_1 + \alpha_i p_2 + k_{i\perp}, \tag{2.11}$$
$$s\alpha_i\beta_i = k_i^2 - k_{i\perp}^2 = k_i^2 + \mathbf{k}_i^2,$$

we can set in the MRK

$$\alpha_0 \ll \alpha_1 \ll \cdots \ll \alpha_n \ll \alpha_{n+1}, \tag{2.12}$$
$$\beta_{n+1} \ll \beta_n \ll \cdots \ll \beta_1 \ll \beta_0.$$

Due to Eqs. (2.11) and (2.12), the squared invariant masses

$$s_i = (k_{i-1} + k_i)^2 \approx s\beta_{i-1}\alpha_i = \frac{\beta_{i-1}}{\beta_i}(k_i^2 + \mathbf{k}_i^2) \tag{2.13}$$

are large compared with the squared transverse momenta of produced particles, which are of the order of the squared momentum transfers:

$$s_i \gg \mathbf{k}_i^2 \sim |t_i| = |q_i^2|, \tag{2.14}$$

where

$$q_i = p_A - \sum_{j=0}^{i-1}k_j$$
$$= -\left(p_B - \sum_{j=i}^{n+1}k_j\right) \approx \beta_i p_1 - \alpha_{i-1}p_2 - \sum_{j=0}^{i-1}k_{j\perp},$$
$$t_i = q_i^2 \approx q_{i\perp}^2 = -\mathbf{q}_i^2, \tag{2.15}$$

and product of all s_i is proportional to s:

$$\prod_{i=1}^{n+1}s_i = s\prod_{i=1}^{n}(k_i{}^2 + \mathbf{k}_i^2). \tag{2.16}$$

The production amplitudes have a complicated analytical structure (see, for instance, [30, 31]). Fortunately, only the real parts of these amplitudes are used in the derivation of the BFKL equation in the NLA as well as in the LLA. We restrict ourselves also to consideration of the real parts, although it is not explicitly indicated below. They can be written as (see [12] and references therein)

$$\mathcal{A}_{AB}^{\tilde{A}\tilde{B}+n} = 4(p_A p_B)\Gamma^{c_1}_{\tilde{A}A} \times \left[\prod_{i=1}^{n}\frac{1}{t_i}\gamma^{P_i}_{c_i c_{i+1}}(q_i,q_{i+1})\left(\frac{s_i}{\sqrt{\mathbf{k}_{i-1}^2\mathbf{k}_i^2}}\right)^{\omega(t_i)}\right] \times \frac{1}{t_{n+1}}\left(\frac{s_{n+1}}{\sqrt{\mathbf{k}_n^2\mathbf{k}_{n+1}^2}}\right)^{\omega(t_{n+1})}\Gamma^{c_{n+1}}_{\tilde{B}B}, \quad (2.17)$$

where $\gamma^{P_i}_{c_i c_{i+1}}(q_i,q_{i+1})$ are the so-called Reggeon–Reggeon–particle vertices, i.e., the effective vertices for production of particles P_i with momenta $k_i = q_i - q_{i+1}$ in the collision of the Reggeons with momenta q_i and $-q_{i+1}$ and color indices c_i and c_{i+1}. In the MRK, only gluons can be produced with the vertex

$$\gamma^{G}_{c_1 c_2}(q_1,q_2) = gT^a_{c_1 c_2}e^*_\mu(k)C^\mu(q_2,q_1), \quad (2.18)$$

where a, $k = q_1 - q_2$ and $e(k)$ are, respectively, color index, momentum, and polarization vector of the gluon,

$$C^\mu(q_2,q_1) = -q_1^\mu - q_2^\mu + p_1^\mu\left(\frac{q_1^2}{kp_1} + 2\frac{kp_2}{p_1p_2}\right) - p_2^\mu\left(\frac{q_2^2}{kp_2} + 2\frac{kp_1}{p_1p_2}\right) = -q_{1\perp}^\mu - q_{2\perp}^\mu - \frac{p_1^\mu}{2(kp_1)}(k_\perp^2 - 2q_{1\perp}^2) + \frac{p_2^\mu}{2(kp_2)}(k_\perp^2 - 2q_{2\perp}^2). \quad (2.19)$$

In the light-cone gauge $e(k)p_2 = 0$, we have

$$e^*_\mu(k)C^\mu(q_2,q_1) = -2e^*_\perp(k)\left(q_{1\perp} - k_\perp\frac{q_{1\perp}^2}{k_\perp^2}\right). \quad (2.20)$$

In the NLA, the multi-Regge form is assumed in the BFKL approach for the production amplitudes not only in the MRK, when all produced particles are strongly ordered in rapidity space, but also in the QMRK, when a couple of two particles is produced with rapidities of the same order. The QMRK can be obtained upon replacing one of the particles P_i in the MRK by this couple. Therefore, the QMRK amplitudes have the same form (2.17) as in the MRK with one of the vertices $\gamma^{P_i}_{c_i c_{i+1}}$ or $\Gamma^c_{\tilde{P}P}$ substituted by a vertex for production of the couple.

If the particles P_1 and P_2 are produced in the fragmentation region of the particle A, we have

$$\mathcal{A}_{AB}^{\{P_1P_2\}B'} = 4(p_A p_B)\Gamma^c_{\{P_1P_2\}A}\frac{s^{\omega(t)}}{t}\Gamma^c_{B'B}, \quad (2.21)$$

where now $q = p_A - k$, $k = k_1 + k_2$, and k_1 and k_2 are momenta of the particles P_1 and P_2, respectively; for their Sudakov parameters, we have $\beta_1 \sim \beta_2 \sim 1, \beta_1 + \beta_2 = 1, \alpha_1 \sim \alpha_2 \sim O(1/s)$. The produced particles can be gg or $q\bar{q}$ pairs if the particle A is the gluon and qg when the particle A is the quark.

If rapidities of components of the produced couple (it can be either gg or $q\bar{q}$ pairs) are far away from rapidities of colliding particles, then it is created by two Reggeized gluons, and its production is described by the vertices $\gamma^{Q\bar{Q}}_{c_1c_2}(q_1,q_2)$ or $\gamma^{G_1G_2}_{c_1c_2}(q_1,q_2)$, where q_1, c_1 and $-q_2, c_2$ are momenta and color indices of the Reggeized gluons. The amplitude $\mathcal{A}_{AB}^{A'\{P_1P_2\}B'}$ describing production of the couple P_1 and P_2 with the Sudakov parameters $\alpha_1 \sim \alpha_2 \ll 1$ and $\beta_1 \sim \beta_2 \ll 1$ has the form

$$\mathcal{A}_{AB}^{A'\{P_1P_2\}B'} = 4(p_A p_B)\Gamma^{c_1}_{A'A}\frac{s_1^{\omega(t_1)}}{t_1} \times \gamma^{P_1P_2}_{c_1c_2}(q_1,q_2)\frac{s_2^{\omega(t_2)}}{t_2}\Gamma^{c_2}_{B'B}, \quad (2.22)$$

where

$$q_1 = p_A - p_{A'}, \quad q_2 = -p_B + p_{B'}, \quad t_i = q_i^2 \simeq q_{i\perp}^2, \quad s_1 = (p_{A'} + k)^2, \quad s_2 = (p_{B'} + k)^2, \quad k = k_1 + k_2, k^2 \ll s_{1,2} \ll s. \quad (2.23)$$

Note that, because the QMRK in the unitarity relations leads to loss of the large logarithms, scales of energies in (2.21) and (2.22) are unimportant in the NLA; moreover, the trajectory and the vertices are needed there only in the LO. The trajectory in this order is given by (2.10); the vertices are presented below. Recall that the vertices were extracted from corresponding amplitudes in the Born approximation, so that, at the tree level, Eqs. (2.21) and (2.22) are verified. What has to be checked is their energy dependence, i.e., the Regge factors $s_i^{\omega(t_i)}$.

3. PRODUCTION IN THE FRAGMENTATION REGION

3.1. One-Loop Radiative Corrections and Bootstrap Conditions

To be definite, we consider below production in the fragmentation region of the particle A. In this

section, we use the notation $s_1 = (p_{B'} + p_{P_1})^2$ and $s_2 = (p_{B'} + p_{P_2})^2$. Note that here $s_1 \sim s_2 \sim s$, contrary to the case of production in the central region of rapidities. In the radiative corrections to the amplitude $\mathcal{A}_{AB}^{\{P_1P_2\}B'}$, we have to retain only large logarithmic terms, not making a difference between $\ln s$, $\ln s_1$, and $\ln s_2$. Therefore, the corrections can be calculated using the s-channel unitarity in the same way as was done for the elastic scattering amplitudes in the LLA [5]. The large logarithms are defined by the discontinuities of the amplitude $\mathcal{A}_{AB}^{\{P_1P_2\}B'}$ in the channels s, s_1, and s_2, and we find them using the unitarity relations in these channels.

Let us start with the s-channel discontinuity. In the one-loop approximation, the intermediate states in the unitarity relation can be only two-particle states, so that we have (see Fig. 2*a*)

$$\Im_s \mathcal{A}_{AB}^{\{P_1P_2\}B'} = \frac{1}{2}\sum_{\{\tilde{A}\tilde{B}\}}\int \mathcal{A}_{AB}^{\tilde{A}\tilde{B}}\mathcal{A}_{\tilde{A}\tilde{B}}^{\{P_1P_2\}B'} d\Phi_{\tilde{A}\tilde{B}}, \tag{3.1}$$

where the sum $\sum_{\{\tilde{A}\tilde{B}\}}$ is over all discrete quantum numbers of the particles $\tilde{A}$ and $\tilde{B}$, and $d\Phi_{\tilde{A}\tilde{B}}$ is their phase-space element. Here and in the following, we use the Hermitian property of the Born amplitudes

$$\left(\mathcal{A}_i^f\right)^* = \mathcal{A}_f^i. \tag{3.2}$$

In the region that gives a leading (growing as s) contribution to the imaginary part,

$$d\Phi_{\tilde{A}\tilde{B}} = (2\pi)^D \delta^{(D)}(p_A + p_B - p_{\tilde{A}} - p_{\tilde{B}}) \tag{3.3}$$
$$\times \frac{d^{D-1}p_{\tilde{A}}}{2\epsilon_{\tilde{A}}(2\pi)^{D-1}} \frac{d^{D-1}p_{\tilde{B}}}{2\epsilon_{\tilde{B}}(2\pi)^{D-1}} = \frac{d^{D-2}r_\perp}{2s(2\pi)^{D-2}}.$$

Here and below, $r_\perp$ is the transverse part of the momentum transfer $p_{\tilde{B}} - p_B$. Note that, for production in the fragmentation region, the Sudakov parameters α and β for the momentum transfer $p_{\tilde{B}} - p_B$ are $\sim 1/s$, so that $p_{\tilde{B}} - p_B \simeq r_\perp$. For production in the central region, it is not always correct.

The imaginary parts in the $s_{1,2}$ channels are calculated quite analogously. Take the s_1 channel. Denoting intermediate particles in the unitarity relation in this channel as $\tilde{P}$ and $\tilde{B}$, we obtain (see Fig. 2*b*)

$$\Im_{(p_{B'}+p_{P_1})^2} \mathcal{A}_{AB}^{\{P_1P_2\}B'} \tag{3.4}$$
$$= \frac{1}{2}\sum_{\{\tilde{P}\tilde{B}\}}\int \mathcal{A}_{AB}^{\{\tilde{P}P_2\}\tilde{B}} \mathcal{A}_{\tilde{P}\tilde{B}}^{P_1B'} d\Phi_{\tilde{P}\tilde{B}},$$

with

$$d\Phi_{\tilde{P}\tilde{B}} = (2\pi)^D \delta^{(D)}(p_{P_1} \tag{3.5}$$

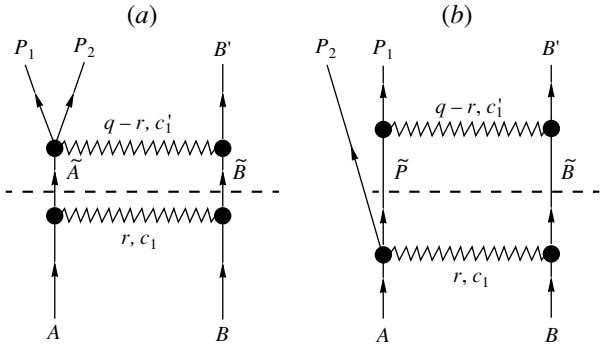

Fig. 2. Schematic representation of the discontinuities of the amplitude $\mathcal{A}_{AB}^{\{P_1P_2\}B'}$ in the (*a*) s channel and (*b*) s_1 channel.

$$+ p_{B'} - p_{\tilde{P}} - p_{\tilde{B}}) \frac{d^{D-1}p_{\tilde{P}}}{2\epsilon_{\tilde{P}}(2\pi)^{D-1}}$$
$$\times \frac{d^{D-1}p_{\tilde{B}}}{2\epsilon_{\tilde{B}}(2\pi)^{D-1}} = \frac{d^{D-2}r_\perp}{2(p_{B'} + p_{P_1})^2(2\pi)^{D-2}}.$$

The s_2-channel imaginary part is obtained from (3.4), (3.5) by the substitution $P_1 \leftrightarrow P_2$.

Since we do not make any difference between $\ln s$, $\ln s_1$, and $\ln s_2$, we need only the sum of the imaginary parts in the s, s_1, and s_2 channels. Using (2.3) and (2.21) in the Born approximation for the amplitudes in (3.1), (3.4), we obtain for the sum

$$\Im \mathcal{A}_{AB}^{\{P_1P_2\}B'} = \frac{s}{(2\pi)^{D-2}} \int \frac{d^{D-2}r_\perp}{r_\perp^2 (q-r)_\perp^2} \tag{3.6}$$
$$\times \sum_{\{i\}} \Gamma_{\{i\}A}^{c_1} \Gamma_{\{P_1P_2\}\{i\}}^{c_1'} \sum_{\{\tilde{B}\}} \Gamma_{\tilde{B}B}^{c_1} \Gamma_{B'\tilde{B}}^{c_1'},$$

where the sum over $\{i\}$ is performed over all possible intermediate states and their quantum numbers. If $\{i\}$ contains two particles, one of them must be P_1 or P_2; in this case, the corresponding subscript in $\Gamma_{\{P_1P_2\}\{i\}}^{c_1'}$ can be omitted.

Recall that we assume everywhere projection on a color octet and negative signature in the t channel. Performing this projection explicitly by the projection operator $\hat{\mathcal{P}}_{8_a}$,

$$\langle c_1 c_1' | \hat{\mathcal{P}}_{8_a} | c_2 c_2' \rangle = \frac{f_{c_1c_1'c} f_{c_2c_2'c}}{N_c}, \tag{3.7}$$

where f_{abc} are the structure constants of the color group, and using the bootstrap property of the LO vertices

$$f_{c_1c_1'c} \sum_{\{\tilde{B}\}} \Gamma_{\tilde{B}B}^{c_1} \Gamma_{B'\tilde{B}}^{c_1'} = -ig\frac{N_c}{2}\Gamma_{B'B}^{c}, \tag{3.8}$$

which is easily derived from (2.5), we get

$$\Im\mathcal{A}_{AB}^{\{P_1P_2\}B'} = \frac{s}{t}\Bigg(- \pi\frac{gt}{(2\pi)^{D-1}} \times \int \frac{d^{D-2}r_\perp}{r_\perp^2(q-r)_\perp^2} if_{c_1c_1'c} \times \sum_{\{i\}} \Gamma^{c_1}_{\{i\}A}(r_\perp)\Gamma^{c_1'}_{\{P_1P_2\}\{i\}}(q_\perp - r_\perp)\Bigg)\Gamma^c_{B'B}. \tag{3.9}$$

Here, we indicate explicitly the dependence of the Reggeon vertices on momentum transfer. Recall that the sum over $\{i\}$ is performed over all possible intermediate states and their quantum numbers. All vertices here are taken in the LO, so that, if an intermediate state contains two particles, one of them must be the same as in the final state; the other changes its transverse momentum and color state, but its helicity is conserved. The real part of the one-loop contribution to the amplitude can be restored from the imaginary part [cf. (2.3)] by the substitution

$$-\pi \to 2\ln s. \tag{3.10}$$

Therefore, comparing (3.9) with the first-order term in the expansion of (2.21) with account of (2.10), we see that the one-loop correction calculated above is compatible with the Reggeized form (2.21) only if

$$\int \frac{d^{D-2}r_\perp}{r_\perp^2(q-r)_\perp^2}\frac{if^{cc_1c_1'}}{N_c} \times \sum_{\{i\}} \Gamma^{c_1}_{\{i\}A}(r_\perp)\Gamma^{c_1'}_{\{P_1P_2\}\{i\}}(q_\perp - r_\perp) = \frac{g}{2}\Gamma^c_{\{P_1P_2\}A}(q_\perp)\int \frac{d^{D-2}r_\perp}{r_\perp^2(q-r)_\perp^2}. \tag{3.11}$$

Equation (3.11) gives the bootstrap conditions for the Reggeon vertices of two-particle production in the fragmentation region. In the next subsections, we show that they are satisfied.

3.2. Quark–Antiquark Production

To produce a $q\bar{q}$ pair, the particle A must be a gluon. Let $p_A = p_1$; a be the color index of the initial gluon; and k_1 and k_2 be the quark and antiquark momenta, respectively,

$$k_{1,2} = \beta_{1,2}p_1 + \frac{m^2+\mathbf{k}_{1,2}^2}{s\beta_{1,2}}p_2 + k_{1,2\perp}, \qquad k_{1\perp} + k_{2\perp} + q_\perp = 0, \tag{3.12}$$

where m is the quark mass. The intermediate states $\{i\}$ in (3.11) can be

(i) one-gluon state with momentum $p_{\bar{A}} = p_1 - r$;

(ii) $q\bar{q}$ state with quark and antiquark momenta $k_1' = k_1 + q - r$ and k_2, respectively;

(iii) $q\bar{q}$ state with quark and antiquark momenta, respectively, k_1 and $k_2' = k_2 + q - r$.

Apart from the "elastic" vertices (2.9), (2.6), and (2.7), the bootstrap condition contains only the Reggeon vertex for $q\bar{q}$ production, which can be found in [15]. In the general case, when the pair is produced by the gluon G with momentum $k = \beta p_1 + \mathbf{k}^2/(\beta s)p_2 + k_\perp$, the vertex can be represented as

$$\Gamma^c_{\{Q\bar{Q}\}G} = (t^at^c)_{i_1i_2}\left(\mathcal{A}((k_1 - x_1k)_\perp) - \mathcal{A}((x_2k_1 - x_1k_2)_\perp)\right) - (t^ct^a)_{i_1i_2} \times \left(\mathcal{A}((-k_2 + x_2k)_\perp) - \mathcal{A}((x_2k_1 - x_1k_2)_\perp)\right), \tag{3.13}$$

where $x_{1,2} = \beta_{1,2}/\beta, x_1 + x_2 = 1$, i_1 and i_2 are quark and antiquark color indices, and a is the color index of the gluon G. The amplitudes $\mathcal{A}(p_\perp)$ in the light-cone gauge (2.8) are rather simple:

$$\mathcal{A}(p_\perp) = \frac{g^2}{p_\perp^2 - m^2}\bar{u}(k_1)\frac{\not{p}_B}{\beta s} \times \left(x_1\not{e}_\perp\not{p}_\perp - x_2\not{p}_\perp\not{e}_\perp - \not{e}_\perp m\right)v(k_2). \tag{3.14}$$

Here, e is the gluon polarization vector, and $u(k_1)$ and $v(k_2)$ are the spin wave functions of the quark and antiquark, respectively.

With the vertices (2.9), (2.6), (2.7), and (3.13), the contribution of either of the three intermediate states to the integrand on the left-hand side of (3.11) is readily calculated and we obtain, correspondingly,

$$\text{(i)}\quad \frac{igf^{cc_1c_1'}}{N_c}T^{c_1}_{a'a}\Big[(t^{a'}t^{c_1'})_{i_1i_2}(\mathcal{A}((k_1 + x_1r)_\perp) - \mathcal{A}((x_2k_1 - x_1k_2)_\perp)) - (t^{c_1'}t^{a'})_{i_1i_2} \times \left(\mathcal{A}((-k_2 - x_2r)_\perp) - \mathcal{A}((x_2k_1 - x_1k_2)_\perp)\right)\Big], \tag{3.15}$$

$$\text{(ii)}\quad \frac{igf^{cc_1c_1'}}{N_c}\Big[(t^{c_1'}t^at^{c_1})_{i_1i_2}(\mathcal{A}((-k_2 - r)_\perp) - \mathcal{A}((-k_2 - x_2r)_\perp)) - (t^{c_1'}t^{c_1}t^a)_{i_1i_2} \times \left(\mathcal{A}((-k_2)_\perp) - \mathcal{A}((-k_2 - x_2r)_\perp)\right)\Big], \tag{3.16}$$

$$\text{(iii)}\quad -\frac{igf^{cc_1c_1'}}{N_c}\Big[(t^at^{c_1}t^{c_1'})_{i_1i_2}(\mathcal{A}((k_1)_\perp) - \mathcal{A}((k_1 + x_1r)_\perp)) - (t^{c_1}t^at^{c_1'})_{i_1i_2} \times \left(\mathcal{A}((k_1 + r)_\perp) - \mathcal{A}((k_1 + x_1r)_\perp)\right)\Big]. \tag{3.17}$$

It is not difficult to see from these expressions that the terms with $\mathcal{A}((k_1+x_1r)_\perp)$ are canceled before integration, due to the commutation relations between t^i, as well as the terms with $\mathcal{A}((-k_2-x_2r)_\perp)$. As for the terms with $\mathcal{A}((k_1+r)_\perp)$ and $\mathcal{A}((-k_2-r)_\perp)$, they cancel each other as a result of integration, due to invariance of the integration measure $d^{D-2}r_\perp/\left(r_\perp^2(q-r)_\perp^2\right)$ with respect to the substitution $(k_1+r)_\perp \leftrightarrow (-k_2-r)_\perp$, with account of $k_{1\perp}+k_{2\perp}+q_\perp=0$. A simple color algebra shows that the remaining terms gather into $(g/2)\Gamma^c_{\{Q\bar{Q}\}A}$, where A is a gluon with momentum $p_A=p_1$ (see (3.13)), which makes it evident that the bootstrap condition (3.11) is satisfied.

3.3. Two-Gluon Production

The case of two-gluon production can be considered quite similarly. Again, the particle A must be a gluon. Using the same notation as before, with the difference that k_1 and k_2 now are the momenta of the produced gluons (so that m is replaced by 0), i_1 and i_2 are their color indices. Denoting their polarization vectors in the light-cone gauge (2.8) e_1 and e_2, we can represent the vertex $\Gamma^c_{\{G_1G_2\}G}$ of two-gluon production [15] in the same form as (3.13):

$$\Gamma^c_{\{G_1G_2\}G}=(T^aT^c)_{i_1i_2}(\mathcal{A}((k_1-x_1k)_\perp) - \mathcal{A}((x_2k_1-x_1k_2)_\perp))-(T^cT^a)_{i_1i_2} \times(\mathcal{A}((-k_2+x_2k)_\perp)-\mathcal{A}((x_2k_1-x_1k_2)_\perp)), \tag{3.18}$$

where the amplitudes $\mathcal{A}(p_\perp)$ now have the form

$$\mathcal{A}(p_\perp)=\frac{2g^2}{p_\perp^2}\Big[x_1x_2(e^*_{1\perp}e^*_{2\perp})(e_\perp p_\perp) - x_1(e^*_{1\perp}e_\perp)(e^*_{2\perp}p_\perp)-x_2(e^*_{2\perp}e_\perp)(e^*_{1\perp}p_\perp)\Big]. \tag{3.19}$$

The intermediate states are now

(i) one-gluon state with gluon momentum $p_{\tilde{A}}=p_1-r$;

(ii) two-gluon state with gluon momenta $k_1'=k_1+q-r$ and k_2;

(iii) two-gluon state with gluon momenta k_1 and $k_2'=k_2+q-r$.

It is easy to see that the contributions of these states to the integrand on the left-hand side of (3.11) are given by the same formulas (3.15)–(3.17) as for the case of quark–antiquark production, with the only difference that the color group generators are taken not in the fundamental but in the adjoint representation. Since in the proof of fulfillment of the bootstrap conditions only the commutation relations of the generators were used, the proof can be applied to the case of two-gluon production as well as to $q\bar{q}$ production.

3.4. Quark–Gluon Production

In the case of quark–gluon production (when the particle A is a quark), the bootstrap condition can be considered in the same way. Now let k be the momentum of the incoming quark and k_1 and k_2 be the momenta of the final quark and gluon, respectively. Note that $k^2=k_1^2=m^2$, so that

$$k=\beta p_1+\frac{\mathbf{k}^2+m^2}{\beta s}p_2+k_\perp, \tag{3.20}$$
$$k_1=\beta_1p_1+\frac{\mathbf{k}_1^2+m^2}{\beta_1 s}p_2+k_{1\perp},$$
$$k_2=\beta_2p_1+\frac{\mathbf{k}_2^2}{\beta_2 s}p_2+k_{2\perp}.$$

Then, from [16], one can obtain

$$\Gamma^c_{\{QG\}Q}=(t^at^c)_{i_1i_2}(\mathcal{A}((x_2k_1-x_1k_2)_\perp) - \mathcal{A}((k_1-x_1k)_\perp))-(t^ct^a)_{i_1i_2} \times(\mathcal{A}((-k_2+x_2k)_\perp)-\mathcal{A}((k_1-x_1k)_\perp)), \tag{3.21}$$

where i_1 and i_2 are now the color indices of the outgoing and incoming quarks, a is the color index of the produced gluon G, and the amplitudes $\mathcal{A}$ now have the form

$$\mathcal{A}(p_\perp)=-\frac{g^2}{p_\perp^2-x_2^2m^2}\bar{u}(k_1)\frac{\not{p}_B}{\beta s} \times\left(x_1\not{e}^*_\perp\not{p}_\perp+\not{p}_\perp\not{e}^*_\perp+\not{e}^*_\perp x_2^2m\right)u(p). \tag{3.22}$$

Possible intermediate states are now the following:

(i) One-quark state with quark momentum $p_{\tilde{A}}=p_A-r$. Its contribution to the integrand on the left-hand side of the bootstrap equation is

$$\frac{igf^{cc_1c_1'}}{N_c}\Big[(t^at^{c_1'}t^{c_1})_{i_1i_2}(\mathcal{A}((x_2k_1-x_1k_2)_\perp) - \mathcal{A}((k_1+x_1r)_\perp))-(t^{c_1'}t^at^{c_1})_{i_1i_2} \times(\mathcal{A}((-k_2-x_2r)_\perp)-\mathcal{A}((k_1+x_1r)_\perp))\Big]; \tag{3.23}$$

(ii) Quark–gluon state with quark and gluon momenta $k_1'=k_1+q-r$ and k_2, respectively. It gives

$$\frac{igf^{cc_1c_1'}}{N_c}\Big[\left(t^{c_1'}t^at^{c_1}\right)_{i_1i_2}(\mathcal{A}((-k_2-x_2r)_\perp) - \mathcal{A}((-k_2-r)_\perp))-\left(t^{c_1'}t^{c_1}t^a\right)_{i_1i_2} \times(\mathcal{A}((-k_2)_\perp)-\mathcal{A}((-k_2-r)_\perp))\Big]; \tag{3.24}$$

(iii) Quark–gluon state with quark and gluon momenta k_1 and $k_2' = k_2 + q - r$. It contributes

$$\frac{igf^{cc_1c_1'}}{N_c}T^{c_1'}_{aa'}\Big[\left(t^{a'}t^{c_1}\right)_{i_1i_2}(\mathcal{A}((k_1+x_1r)_\perp) - \mathcal{A}((k_1)_\perp)) - \left(t^{c_1}t^{a'}\right)_{i_1i_2} \times (\mathcal{A}((k_1+r)_\perp) - \mathcal{A}((k_1)_\perp))\Big]. \quad (3.25)$$

As well as in the case of $q\bar{q}$ production, it is not difficult to see that the terms with $\mathcal{A}((k_1+x_1r)_\perp)$ and $\mathcal{A}((-k_2-x_2r)_\perp)$ are canceled before integration, due to color algebra; the terms with $\mathcal{A}((k_1+r)_\perp)$ and $\mathcal{A}((-k_2-r)_\perp)$ cancel each other as a result of integration, and the remaining terms give $(g/2)\Gamma^c_{\{GQ\}Q}$, where Q is a quark with momentum $p_A = p_1 + (m^2/s)p_2$ [see (3.21)].

This completes the proof that the bootstrap conditions (3.11) are satisfied.

We have considered here the case of qg production. QCD invariance under charge conjugation ensures that the bootstrap condition is fulfilled also for $\bar{q}g$ production.

4. PRODUCTION IN THE CENTRAL REGION

4.1. One-Loop Radiative Corrections and Bootstrap Conditions

Seeing that only large logarithmic terms in the radiative corrections to the amplitude $\mathcal{A}_{AB}^{A'\{P_1P_2\}B'}$ must be retained, the corrections again can be calculated using the s-channel unitarity, as was done for gluon production in the MRK in the LLA [5]. The logarithmic terms in the real part of the amplitude are obtained from the imaginary parts, connected with the discontinuities of the amplitude in channels with great (tending to infinity when $s\to\infty$) invariants, by the substitution (3.10), with the corresponding invariant instead of s. Production of two particles with fixed invariant mass instead of one leads only to technical complications connected with existence of a larger number of such invariants, analogously to the case of two particles in the fragmentation region compared with elastic scattering.

Let the momenta of the produced particles P_1 and P_2 be k_1 and k_2 with $k_1+k_2 = k = q_1 - q_2$; here, $q_1 = p_A - p_{A'}$ and $q_2 = p_{B'} - p_B$ are momentum transfers; note that we can neglect the component of q_1 (q_2) along p_2 (p_1), so that

$$q_1 = \beta p_1 + q_{1\perp}, \quad q_2 = -\alpha p_2 + q_{2\perp}, \quad s\alpha\beta = \mathbf{k}^2. \quad (4.1)$$

In the case of production of one particle with momentum k in the MRK, the large logarithms were defined by the discontinuities in the channels $s_1 = (p_{A'}+k)^2$, $s_2 = (p_{B'}+k)^2$, s, and $(p_{A'}+p_{B'})^2$. Now we have more invariants that are great, but they can be divided into three groups of invariants of the same order ($\sim s_1$, $\sim s_2$, and $\sim s$). Evidently, we have to calculate discontinuities in channels of all these invariants. Since we do not distinguish logarithms of invariants of the same order, the real parts of the amplitude related to discontinuities in channels of invariants $\sim s_a$ (s_a can be s_1, s_2, or s) are obtained from the imaginary parts by the substitution (3.10) with $s\to s_a$. Note that, with our accuracy, $\ln s = \ln s_1 + \ln s_2$; therefore, only two large logarithms in the real part can be considered as independent. We choose as independent $\ln s_1$ and $\ln s_2$. To calculate the contribution with $\ln s_1$ ($\ln s_2$) in the real part, we have to find the sum of the imaginary parts in the channels with invariants of order s_1 (s_2) and of order of s and then make the substitution (3.10) with s_1 (s_2) instead of s.

Therefore, to find the terms with $\ln s_2$ in the real part, we need to calculate the imaginary parts in the channels $s_2 = (p_{B'}+k)^2$, $s_{21} = (p_{B'}+k_1)^2$, $s_{22} = (p_{B'}+k_2)^2$, $s = (p_A+p_B)^2$, $s' = (p_{A'}+p_{B'})^2$, $s_1' = (p_{A'}+k_1+p_{B'})^2$, and $s_2' = (p_{A'}+k_2+p_{B'})^2$, schematically shown in Figs. 3*a*–3*g*. Let us represent the sum of the imaginary parts as

$$\Im\mathcal{A}_{AB}^{A'\{P_1P_2\}B'} = s\Gamma^{c_1}_{A'A}\frac{1}{t_1}\Big(-\pi\frac{gt_2}{(2\pi)^{D-1}} \times \int\frac{d^{D-2}r_\perp}{r_\perp^2(q_2-r)_\perp^2}\mathcal{F}^{P_1P_2}_{c_1c_2}(q_1,q_2,r_\perp)\Big)\frac{1}{t_2}\Gamma^{c_2}_{B'B}. \quad (4.2)$$

Below, a possibility of such a representation (which should be clear to an advanced reader) is shown and the contributions to $\mathcal{F}^{P_1P_2}_{c_1c_2}(q_1,q_2,r_\perp)$ from the imaginary parts in each of the channels are found. Let us start with the s_2 channel (see Fig. 3*a*):

$$\Im_{(3a)}\mathcal{A}_{AB}^{A'\{P_1P_2\}B'} = \frac{1}{2}\sum_{\{\tilde{P}\tilde{B}\}}\int\mathcal{A}_{AB}^{A'\tilde{P}\tilde{B}}\mathcal{A}_{\tilde{P}\tilde{B}}^{\{P_1P_2\}B'}d\Phi_{\tilde{P}\tilde{B}}, \quad (4.3)$$

where $d\Phi_{\tilde{P}\tilde{B}}$ is given by (3.5) with the replacement $p_{P_1}\to k$. As always, $r_\perp = (p_{\tilde{B}} - p_B)_\perp$. The particle $\tilde{P}$ has to be produced in the MRK, so that it must be a gluon. Denoting its momentum by k', we have

$$k' = \beta p_1 - \frac{(q_1-r)_\perp^2}{\beta s}p_2 + (q_1-r)_\perp. \quad (4.4)$$

The possibility of the representation (4.2) for the imaginary part (4.3) becomes evident if one takes

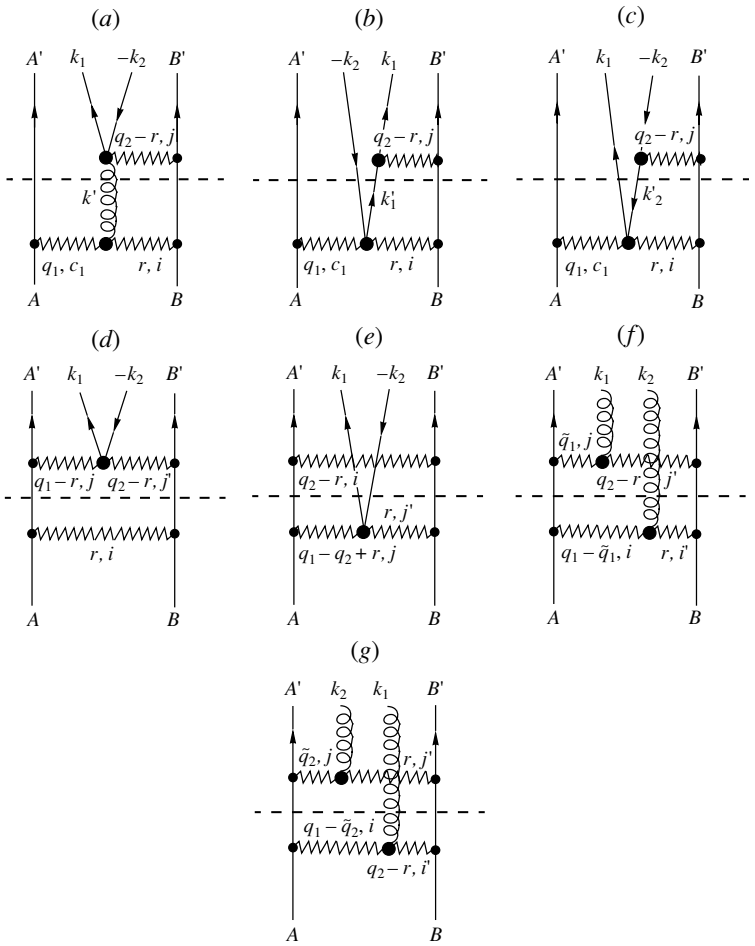

Fig. 3. Schematic representation of the discontinuities of the amplitude $\mathcal{A}_{AB}^{A'\{P_1P_2\}B'}$ in the (a) s_2 channel, (b) s_{21} channel, (c) s_{22} channel, (d) s channel, (e) s' channel, (f) s'_1 channel, and (g) s'_2 channel.

the representations (2.17) and (2.21) in the Born approximation for the amplitudes in (4.3), extracts the antisymmetric color octet in the t_2 channel [$t_2 = (p_B - p_{B'})^2$] by the projection operator (3.7), and uses the bootstrap property of the LO vertices (3.8). For the contribution $\mathcal{F}^a_{c_1c_2}$ to $\mathcal{F}^{P_1P_2}_{c_1c_2}(q_1, q_2, r_\perp)$, one obtains

$$\mathcal{F}^a_{c_1c_2} = if_{ijc_2}\sum_{\{G\}}\gamma^G_{c_1i}(q_1, q_1 - k')\Gamma^j_{\{P_1P_2\}G}. \quad (4.5)$$

Imaginary parts in the channels $(p_{B'} + k_1)^2$ and $(p_{B'} + k_2)^2$ (see Figs. 3*b* and 3*c*) are found quite analogously. For the first of them, we have

$$\Im_{(3b)}\mathcal{A}_{AB}^{A'\{P_1P_2\}B'} = \frac{1}{2}\sum_{\{\tilde{P}\tilde{B}\}}\int \mathcal{A}_{AB}^{A'\{\tilde{P}P_2\}\tilde{B}}\mathcal{A}_{\tilde{P}\tilde{B}}^{P_1B'}d\Phi_{\tilde{P}\tilde{B}}, \quad (4.6)$$

where $d\Phi_{\tilde{P}\tilde{B}}$ is given now just by (3.5). Evidently, the particle $\tilde{P}$ now is of the same kind as P_1. Denoting its momentum by k'_1, we have

$$k'_1 = \beta_1 p_1 + \frac{m_1^2 - (q_1 - k_2 - r)^2_\perp}{\beta_1 s}p_2 + (q_1 - k_2 - r)_\perp, \quad (4.7)$$

where m_1 is its mass. The amplitudes $\mathcal{A}_{AB}^{A'\{\tilde{P}P_2\}\tilde{B}}$ and $\mathcal{A}_{\tilde{P}\tilde{B}}^{P_1B'}$ are given by (2.22) and (2.3), respectively, taken in the Born approximation. After extraction of the antisymmetric color octet in the t_2 channel and use of (3.8), we come to the representation (4.2) with the contribution $\mathcal{F}^b_{c_1c_2}$ to $\mathcal{F}^{P_1P_2}_{c_1c_2}(q_1, q_2, r_\perp)$ equal to

$$\mathcal{F}^b_{c_1c_2} = if_{ijc_2}\sum_{\{\tilde{P}\}}\gamma^{\tilde{P}P_2}_{c_1i}(q_1, q_1 - k'_1 - k_2)\Gamma^j_{P_1\tilde{P}}. \quad (4.8)$$

Evidently,

$$\mathcal{F}^c_{c_1c_2} = \mathcal{F}^b_{c_1c_2}(P_1 \leftrightarrow P_2). \quad (4.9)$$

The imaginary parts shown in Figs. 3*d*–3*g* are calculated in a similar way. For Fig. 3*d*, one has

$$\Im_{(3d)}\mathcal{A}_{AB}^{A'\{P_1P_2\}B'} = \frac{1}{2}\sum_{\{\tilde{A}\tilde{B}\}}\int \mathcal{A}_{AB}^{\tilde{A}\tilde{B}}\mathcal{A}_{\tilde{A}\tilde{B}}^{A'\{P_1P_2\}B'}\,d\Phi_{\tilde{A}\tilde{B}}, \qquad (4.10)$$

where $d\Phi_{\tilde{A}\tilde{B}}$ is given by (3.3); $r_\perp = (p_{\tilde{B}} - p_B)_\perp \simeq p_{\tilde{B}} - p_B$. The amplitudes $\mathcal{A}_{AB}^{\tilde{A}\tilde{B}}$ and $\mathcal{A}_{\tilde{P}\tilde{B}}^{A'\{\tilde{P}P_2\}B'}$ are given by the Born terms of (2.3) and (2.22), respectively. The difference of a further calculation from the preceding ones is that it is necessary to apply the projection operator (3.7) and to use the bootstrap property (3.8) in both the t_1 and the t_2 channel. After this, it becomes clear that again the imaginary parts have the form (4.2) with the contribution to $\mathcal{F}_{c_1c_2}^{P_1P_2}(q_1, q_2, r_\perp)$ equaling

$$\mathcal{F}_{c_1c_2}^{d} = \frac{g}{2}f_{ijc_1}f_{ij'c_2}\frac{q_{1\perp}^2}{(q_1-r)_\perp^2} \times \gamma_{jj'}^{P_1P_2}(q_1 - r_\perp, q_2 - r_\perp). \qquad (4.11)$$

The imaginary part answering Fig. 3*e* is

$$\Im_{(3e)}\mathcal{A}_{AB}^{A'\{P_1P_2\}B'} = \frac{1}{2}\sum_{\{\tilde{A}\tilde{B}\}}\int \mathcal{A}_{AB}^{\tilde{A}\{P_1P_2\}\tilde{B}}\mathcal{A}_{\tilde{A}\tilde{B}}^{A'B'}\,d\Phi_{\tilde{A}\tilde{B}}, \qquad (4.12)$$

where $d\Phi_{\tilde{A}\tilde{B}}$ is given now by (3.3) with the replacement $(p_A + p_B \to p_{A'} + p_{B'})$. It is easy to see that the contribution of this imaginary part to $\mathcal{F}_{c_1c_2}^{P_1P_2}(q_1, q_2, r_\perp)$ is obtained from $\mathcal{F}_{c_1c_2}^{d}$ by the substitution $r \leftrightarrow q_2 - r$. Since the integration measure in (4.2) is invariant under this substitution, we can set

$$\mathcal{F}_{c_1c_2}^{e} = \mathcal{F}_{c_1c_2}^{d}. \qquad (4.13)$$

Finally, Figs. 3*f* and 3*g* appear only in the case when the particles P_1 and P_2 are gluons. The imaginary part answering Fig. 3*f* is

$$\Im_{(3f)}\mathcal{A}_{AB}^{A'\{P_1P_2\}B'} = \frac{1}{2}\sum_{\{\tilde{A}\tilde{B}\}}\int \mathcal{A}_{AB}^{\tilde{A}P_2\tilde{B}}\mathcal{A}_{\tilde{A}\tilde{B}}^{A'P_1B'}\,d\Phi_{\tilde{A}\tilde{B}}. \qquad (4.14)$$

The amplitudes entering (4.14) are given by (2.17) with $n = 1$ in the Born approximation. Again applying the projection operator (3.7) and using the bootstrap property (3.8) in the t_1 and t_2 channels, we obtain

$$\mathcal{F}_{c_1c_2}^{f} = \frac{g}{2}f_{i'j'c_2}f_{ijc_1}\frac{q_{1\perp}^2}{\tilde{q}_{1\perp}^2(q_1-\tilde{q}_1)_\perp^2}\gamma_{ii'}^{P_2} \times (q_1 - \tilde{q}_1, q_1 - \tilde{q}_1 - k_2)\gamma_{jj'}^{P_1}(\tilde{q}_1, \tilde{q}_1 - k_1), \qquad (4.15)$$

where $\tilde{q}_1 = \beta_1 p_1 + (k_1 + q_2 - r)_\perp$. Evidently,

$$\mathcal{F}_{c_1c_2}^{g} = \mathcal{F}_{c_1c_2}^{f}(P_1 \leftrightarrow P_2). \qquad (4.16)$$

Note that $\mathcal{F}_{c_1c_2}^{f}$ is invariant under simultaneous substitution $P_1 \leftrightarrow P_2$ (which means, in particular, $k_1 \leftrightarrow k_2$) and $r_\perp \leftrightarrow (q_2 - r)_\perp$. The last substitution can be considered as a redefinition of $r_\perp$. Since the integration measure in (4.2) is invariant under this redefinition, we can take

$$\mathcal{F}_{c_1c_2}^{g} = \mathcal{F}_{c_1c_2}^{f}. \qquad (4.17)$$

Therefore, we have

$$\mathcal{F}_{c_1c_2}^{P_1P_2}(q_1, q_2, r) = \mathcal{F}_{c_1c_2}^{a} + \mathcal{F}_{c_1c_2}^{b} + \mathcal{F}_{c_1c_2}^{c} + 2\mathcal{F}_{c_1c_2}^{d} + 2\mathcal{F}_{c_1c_2}^{f}, \qquad (4.18)$$

where the terms on the right-hand side are given, respectively, by Eqs. (4.5), (4.8), (4.9), (4.11), and (4.15).

As was discussed earlier, the terms with $\ln s_2$ in the real part of the amplitude $\mathcal{A}_{AB}^{A'\{P_1P_2\}B'}$ are obtained from (4.2) by the substitution (3.10) with s_2 instead of s. Comparing the obtained result with (2.22) with account of (2.10), we see that the one-loop correction calculated above is compatible with the Reggeized form (2.22) only if

$$\int \frac{d^{D-2}r_\perp}{r_\perp^2(q_2-r)_\perp^2}\mathcal{F}_{c_1c_2}^{P_1P_2}(q_1, q_2, r_\perp) = \frac{gN_c}{2}\gamma_{c_1c_2}^{\{P_1P_2\}}(q_1, q_2)\int \frac{d^{D-2}r_\perp}{r_\perp^2(q_2-r)_\perp^2}. \qquad (4.19)$$

Equation (4.19) gives the bootstrap conditions for the vertices of pair production in Reggeon–Reggeon collisions. They are verified in the next subsections.

4.2. Quark–Antiquark Production

For simplicity, we discuss below the case of the massless quarks, although the massive case can be considered quite analogously.

Notation. Recall that k_1 and k_2 are the quark and antiquark momenta, respectively;

$$k_i = \beta_i p_1 + \alpha_i p_2 + k_{i\perp}, i = 1, 2, \qquad (4.20)$$
$$s\alpha_i\beta_i = -k_{i\perp}^2 = \mathbf{k}_i^2;$$

$$\beta_i = x_i\beta, \quad \beta = \beta_1 + \beta_2; \quad k = k_1 + k_2 = q_1 - q_2;$$

and we can set

$$q_1 = \beta p_1 + q_{1\perp}, \quad q_2 = -\alpha p_2 + q_{2\perp}, \qquad (4.21)$$
$$\beta = \beta_1 + \beta_2, \quad \alpha = \alpha_1 + \alpha_2.$$

We also use

$$k' = \beta p_1 - \frac{(q_1 - r)_\perp^2}{\beta s}p_2 + (q_1 - r)_\perp, \qquad (4.22)$$

$$k_1' = \beta_1 p_1 - \frac{(q_1 - k_2 - r)_\perp^2}{\beta_1 s} p_2 + (q_1 - k_2 - r)_\perp,$$

$$k_2' = \beta_2 p_1 - \frac{(q_1 - k_1 - r)_\perp^2}{\beta_2 s} p_2 + (q_1 - k_1 - r)_\perp.$$

The function $\mathcal{F}^{P_1P_2}_{c_1c_2}(q_1, q_2, r_\perp)$ in (4.19) is expressed in terms of the Reggeon vertices defined in (2.6), (2.7), (2.18), and (3.13) and the effective vertex of quark–antiquark production in Reggeon–Reggeon collisions. The last vertex was found in [32] and has the form

$$\gamma^{Q\bar{Q}}_{c_1c_2}(q_1, q_2) = \frac{1}{2} g^2 \bar{u}(k_1) \times \left[t^{c_1} t^{c_2} a(q_1; k_1, k_2) - t^{c_2} t^{c_1} \overline{a(q_1; k_2, k_1)} \right] v(k_2), \tag{4.23}$$

where $a(q_1; k_1, k_2)$ and $\overline{a(q_1; k_2, k_1)}$ can be written [33] in the following way:

$$a(q_1; k_1, k_2) = \frac{4 \not{p}_1 \not{Q}_1 \not{p}_2}{s \tilde{t}_1} - \frac{1}{k^2} \not{\Gamma}, \qquad \overline{a(q_1; k_2, k_1)} = \frac{4 \not{p}_2 \not{Q}_2 \not{p}_1}{s \tilde{t}_2} - \frac{1}{k^2} \not{\Gamma}, \tag{4.24}$$

with

$$\tilde{t}_1 = (q_1 - k_1)^2, \quad \tilde{t}_2 = (q_1 - k_2)^2, \quad Q_1 = q_{1\perp} - k_{1\perp}, \quad Q_2 = q_{1\perp} - k_{2\perp}, \tag{4.25}$$

$$\Gamma = 2 \left[(q_1 + q_2)_\perp - \beta p_A \left(1 - 2 \frac{\vec{q}_1^{\,2}}{s\alpha\beta} \right) + \alpha p_B \left(1 - 2 \frac{\vec{q}_2^{\,2}}{s\alpha\beta} \right) \right].$$

Further, for denominators in the Reggeon vertices, we use the notation $D(p, q)$ and $d(p, q)$:

$$D(p, q) = x_1 p_\perp^2 + x_2 q_\perp^2, \;\; d(p, q) = (x_1 p_\perp - x_2 q_\perp)^2; \qquad D(p, q) = d(p, q) + x_1 x_2 (p_\perp + q_\perp)^2. \tag{4.26}$$

Seeing that, for arbitrary $p_\perp$,

$$\bar{u}(k_1) \not{p}_\perp v(k_2) = \bar{u}(k_1) \frac{\not{p}_2}{s\beta} \left(\frac{\not{k}_{1\perp} \not{p}_\perp}{x_1} + \frac{\not{p}_\perp \not{k}_{2\perp}}{x_2} \right) v(k_2), \tag{4.27}$$

we can represent $a(q_1; k_1, k_2)$ and $\overline{a(q_1; k_2, k_1)}$ as

$$a(q_1; k_1, k_2) = \frac{4}{s\beta} \not{p}_2 b(q_1; k_1, k_2), \qquad \overline{a(q_1; k_2, k_1)} = \frac{4}{s\beta} \not{p}_2 \overline{b(q_1; k_2, k_1)}, \tag{4.28}$$

where

$$b(q_1; k_1, k_2) = \frac{\not{k}_{1\perp} (\not{k}_{1\perp} - \not{q}_{1\perp})}{D(k_1 - q_1, k_1)} - \frac{x_1 x_2}{d(k_2, k_1)} \times \left(\frac{q_{1\perp}^2 \not{k}_{1\perp} \not{k}_{2\perp}}{D(k_2, k_1)} - \frac{\not{k}_{1\perp} \not{q}_{1\perp}}{x_1} - \frac{\not{q}_{1\perp} \not{k}_{2\perp}}{x_2} - q_{1\perp}^2 + 2(q_{1\perp}(k_1 + k_2)_\perp) \right) - 1,$$

$$\overline{b(q_1; k_2, k_1)} = \frac{(\not{k}_{2\perp} - \not{q}_{1\perp}) \not{k}_{2\perp}}{D(k_2, k_2 - q_1)} - \frac{x_1 x_2}{d(k_2, k_1)} \times \left(\frac{q_{1\perp}^2 \not{k}_{1\perp} \not{k}_{2\perp}}{D(k_2, k_1)} - \frac{\not{k}_{1\perp} \not{q}_{1\perp}}{x_1} - \frac{\not{q}_{1\perp} \not{k}_{2\perp}}{x_2} - q_{1\perp}^2 + 2(q_{1\perp}(k_1 + k_2)_\perp) \right) - 1. \tag{4.29}$$

This form of $a(q_1; k_1, k_2)$ and $\overline{a(q_1; k_2, k_1)}$ permits one to perform quite readily the summation over spin projections λ of intermediate quarks and antiquarks in the contributions $\mathcal{F}^b_{c_1c_2}$ and $\mathcal{F}^c_{c_1c_2}$ to $\mathcal{F}^{P_1P_2}_{c_1c_2}(q_1, q_2, r_\perp)$; for example,

$$\sum_\lambda \bar{u}(k_1) \frac{\not{p}_2}{\beta_1 s} u^\lambda(k_1') \bar{u}^\lambda(k_1') a(q_1; k_1', k_2) v(k_2) = \bar{u}(k_1) a(q_1; k_1', k_2) v(k_2). \tag{4.30}$$

Independent color structures. It is easy to calculate the number of independent color structures for production of a $q\bar{q}$ pair by two Reggeized gluons. Indeed, the pair can be either in a color singlet or in a color octet state. Due to the color symmetry, each of these states can be produced only by the same state of two Reggeized gluons, which are color octets. Since there are one singlet and two octets (symmetric and antisymmetric) in the decomposition of the product of two octets into irreducible representations, the number of independent color structures is three. Their choice is not unique. We take the following one:

$$\mathcal{R}_1^{c_1c_2} = \frac{1}{N_c} f^{c_1ia} f^{c_2ib} (t^a t^b + t^b t^a), \qquad \mathcal{R}_2^{c_1c_2} = i f^{c_1c_2i} t^i, \quad \mathcal{R}_3^{c_1c_2} = t^{c_1} t^{c_2} + t^{c_2} t^{c_1}. \tag{4.31}$$

From the equality

$$t^a t^b = \frac{1}{2N_c} \delta^{ab} + \frac{1}{2} d^{abc} t^c + \frac{1}{2} i f^{abc} t^c, \tag{4.32}$$

it is seen that the first and third structures contain a singlet and a symmetric octet, whereas the second structure contains only an antisymmetric octet.

Representation of $\mathcal{F}^{P_1P_2}_{c_1c_2}(q_1, q_2, r)$. Using this color structure, we can represent each of the contributions $\mathcal{F}^i_{c_1c_2}$ entering $\mathcal{F}^{P_1P_2}_{c_1c_2}(q_1, q_2, r)$ (4.18) in the

form

$$\mathcal{F}^i_{c_1c_2} = \frac{g^3N_c}{s\beta}\bar{u}(k_1)\not{p}_2\sum_{n=1}^{3}\mathcal{R}^{c_1c_2}_n\mathcal{L}^i_n v(k_2). \quad (4.33)$$

It is not difficult to find all $\mathcal{L}^i_n$ from the equations presented above.

From (4.5), using the Reggeon–Reggeon–gluon vertex (2.18) in the gauge (2.20) and the vertex for $q\bar{q}$ production in the fragmentation region (3.13), we obtain

$$\mathcal{L}^a_1 = \frac{x_1\not{q}_{1\perp}(\not{k}_{1\perp} - x_1\not{k}'_\perp) - x_2(\not{k}_{1\perp} - x_1\not{k}'_\perp)\not{q}_{1\perp}}{d(k'_2,k_1)} \quad (4.34)$$
$$+ \frac{x_2(x_2\not{k}'_\perp - \not{k}_{2\perp})\not{q}_{1\perp} - x_1\not{q}_{1\perp}(x_2\not{k}'_\perp - \not{k}_{2\perp})}{d(k_2,k'_1)}$$
$$+ \frac{q^2_{1\perp}\big(x_2(\not{k}_{1\perp} - x_1\not{k}'_\perp)\not{k}'_\perp - x_1\not{k}'_\perp(\not{k}_{1\perp} - x_1\not{k}'_\perp)\big)}{k'^2_\perp d(k'_2,k_1)}$$
$$+ \frac{q^2_{1\perp}\big(x_1\not{k}'_\perp(x_2\not{k}'_\perp - \not{k}_{2\perp}) - x_2(x_2\not{k}'_\perp - \not{k}_{2\perp})\not{k}'_\perp\big)}{k'^2_\perp d(k_2,k'_1)};$$

$$\mathcal{L}^a_2 = \frac{x_2(x_2\not{k}'_\perp - \not{k}_{2\perp})\not{q}_{1\perp} - x_1\not{q}_{1\perp}(x_2\not{k}'_\perp - \not{k}_{2\perp})}{d(k_2,k'_1)} \quad (4.35)$$
$$- \frac{x_1\not{q}_{1\perp}(\not{k}_{1\perp} - x_1\not{k}'_\perp) - x_2(\not{k}_{1\perp} - x_1\not{k}'_\perp)\not{q}_{1\perp}}{d(k'_2,k_1)}$$
$$- \frac{q^2_{1\perp}\big(x_2(\not{k}_{1\perp} - x_1\not{k}'_\perp)\not{k}'_\perp - x_1\not{k}'_\perp(\not{k}_{1\perp} - x_1\not{k}'_\perp)\big)}{k'^2_\perp d(k'_2,k_1)}$$
$$+ \frac{q^2_{1\perp}\big(x_1\not{k}'_\perp(x_2\not{k}'_\perp - \not{k}_{2\perp}) - x_2(x_2\not{k}'_\perp - \not{k}_{2\perp})\not{k}'_\perp\big)}{k'^2_\perp d(k_2,k'_1)}$$
$$+ 2\frac{x_1\not{q}_{1\perp}(x_2\not{k}_{1\perp} - x_1\not{k}_{2\perp}) - x_2(x_2\not{k}_{1\perp} - x_1\not{k}_{2\perp})\not{q}_{1\perp}}{d(k_2,k_1)}$$
$$+ 2\frac{q^2_{1\perp}}{k'^2_\perp d(k_2,k_1)}\big(x_2(x_2\not{k}_{1\perp} - x_1\not{k}_{2\perp})\not{k}'_\perp - x_1\not{k}'_\perp(x_2\not{k}_{1\perp} - x_1\not{k}_{2\perp})\big);$$

$$\mathcal{L}^a_3 = 0. \quad (4.36)$$

In the case of $q\bar{q}$ production, the particle $\tilde{P}$ in the sum (4.8) must be a quark with momentum k'_1. Taking the representations (4.23) and (4.28) for the vertex of quark–antiquark production in Reggeon–Reggeon collisions and (2.6) for the quark–quark–Reggeon vertex and summing over spin projections according to (4.30), we have

$$\mathcal{L}^b_1 = -b(q_1;k'_1,k_2), \quad \mathcal{L}^b_2 = -\frac{1}{2}\overline{b(q_1;k_2,k'_1)},$$
$$\mathcal{L}^b_3 = \frac{1}{2}(b(q_1;k'_1,k_2) - \overline{b(q_1;k_2,k'_1)}). \quad (4.37)$$

Quite analogously, we obtain

$$\mathcal{L}^c_1 = -\overline{b(q_1;k'_2,k_1)}, \quad \mathcal{L}^c_2 = \frac{1}{2}b(q_1;k_1,k'_2), \quad (4.38)$$
$$\mathcal{L}^c_3 = -\frac{1}{2}(b(q_1;k_1,k'_2) - \overline{b(q_1;k'_2,k_1)}).$$

The functions $b(q_1;k_1,k_2)$ and $\overline{b(q_1;k_2,k_1)}$ are defined in (4.29).

The quantities $\mathcal{L}^d_n$ are easily obtained from (4.11) with account of the representations (4.23) and (4.28) and are equal to

$$\mathcal{L}^d_1 = \frac{q^2_{1\perp}}{k^2_\perp}\big(b(q_1-r;k_1,k_2) - \overline{b(q_1-r;k_2,k_1)}\big), \quad (4.39)$$

$$\mathcal{L}^d_2 = -\frac{q^2_{1\perp}}{k^2_\perp}\big(b(q_1-r;k_1,k_2) + \overline{b(q_1-r;k_2,k_1)}\big), \quad (4.40)$$

$$\mathcal{L}^d_3 = 0. \quad (4.41)$$

Since in the case of $q\bar{q}$ production the diagrams in Figs. 3*f* and 3*g* cannot contribute, Eqs. (4.33)–(4.41)

together with (4.18) determine the left-hand side of the bootstrap Eq. (4.19). Using (4.23), (4.28), and (4.29), we can represent the right-hand side in the form

$$g\frac{N_c}{2}\gamma^{Q\bar{Q}}_{c_1c_2}(q_1,q_2)=\frac{g^3N_c}{s\beta}\bar{u}(k_1)\not{p}_2\sum_{n=1}^{3}\mathcal{R}_n^{c_1c_2}\mathcal{L}_n v(k_2), \tag{4.42}$$

where

$$\mathcal{L}_1=0, \tag{4.43}$$

$$\mathcal{L}_2=-\frac{1}{2}\big(b(q_1;k_1,k_2)+\overline{b(q_1;k_2,k_1)}\big), \tag{4.44}$$

$$\mathcal{L}_3=\frac{1}{2}\big(b(q_1-r;k_1,k_2)-\overline{b(q_1-r;k_2,k_1)}\big). \tag{4.45}$$

Verification of the bootstrap equation. We have to compare the coefficients in the decomposition into the color structures $\mathcal{R}_n^{c_1c_2}$ in the left and right parts of the bootstrap Eq. (4.19). Let us start with $\mathcal{R}_1^{c_1c_2}$. Consider the sum of $\mathcal{L}_1^i$. Note that, due to the symmetry of the integration measure in (4.19) under the substitution $r_\perp\to(q_{2\perp}-r_\perp)$, we can make this substitution in separate terms in $\mathcal{L}_1^i$. Doing it in the terms with the denominator $D(k_2',k_2'-q_1)$ permits one to convert them into terms with the denominator $D(k_1'-q_1,k_1')$. After that, using the decompositions

$$\frac{x_1x_2}{d(k_2,k_1')D(k_2,k_1')}=\frac{1}{k_\perp'^2}\left(\frac{1}{d(k_2,k_1')}-\frac{1}{D(k_2,k_1')}\right), \tag{4.46}$$

$$\frac{x_1x_2}{d(k_2',k_1)D(k_2',k_1)}=\frac{1}{k_\perp'^2}\left(\frac{1}{d(k_2',k_1)}-\frac{1}{D(k_2',k_1)}\right), \tag{4.47}$$

it is easy to see that the terms with the denominators

$$D(k_2',k_1),D(k_2,k_1'),D(k_1',k_1'-q_1) \tag{4.48}$$

are canceled and we obtain for the sum of $\mathcal{L}_1^i$

$$\frac{x_1x_2q_{1\perp}^2}{d(k_2',k_1)}-\frac{x_1x_2q_{1\perp}^2}{d(k_2,k_1')}+\frac{q_{1\perp}^2\big(d(k_2',k_1)-x_1x_2k_\perp'^2\big)}{k_\perp'^2d(k_2',k_1)} \tag{4.49}$$

$$+\frac{q_{1\perp}^2\big(x_1x_2k_\perp'^2-d(k_2,k_1')\big)}{k_\perp'^2d(k_2,k_1')}=0,$$

as it must be, since the structure $\mathcal{R}_1^{c_1c_2}$ is absent on the right-hand side of the bootstrap equation.

We turn to the color structure $\mathcal{R}_2^{c_1c_2}$. Using (4.46), (4.47), we obtain for the sum of $\mathcal{L}_2^i$

$$-\frac{x_1x_2q_{1\perp}^2}{d(k_2',k_1)}-\frac{x_1x_2q_{1\perp}^2}{d(k_2,k_1')}+\frac{2}{d(k_2,k_1)} \tag{4.50}$$

$$\times\big[2x_1x_2\big(q_{1\perp}(k_{1\perp}+k_{2\perp})\big)-x_1\not{q}_{1\perp}\not{k}_{2\perp}$$

$$-x_2\not{k}_{1\perp}\not{q}_{1\perp}\big]+\frac{q_{1\perp}^2}{k_\perp'^2d(k_2',k_1)}\big(x_1x_2k_\perp'^2-d(k_2',k_1)\big)$$

$$+\frac{q_{1\perp}^2}{k_\perp'^2d(k_2,k_1')}\big(x_1x_2k_\perp'^2-d(k_2,k_1')\big)$$

$$-\frac{q_{1\perp}^2}{k_\perp'^2d(k_2,k_1)}(2x_1x_2k_\perp'^2)$$

$$+2\frac{q_{1\perp}^2}{k_\perp'^2}+\frac{2x_1x_2q_{1\perp}^2\not{k}_{1\perp}\not{k}_{2\perp}}{d(k_2,k_1)D(k_2,k_1)}$$

$$-\frac{(\not{k}_{2\perp}-\not{q}_{1\perp})\not{k}_{2\perp}}{D(k_2,k_2-q_1)}-\frac{\not{k}_{1\perp}(\not{k}_{1\perp}-\not{q}_{1\perp})}{D(k_1-q_1,k_1)}+2.$$

One can readily see that the terms depending on $r_\perp$ cancel each other with the result:

$$-\frac{1}{D(k_1-q_1,k_1)}\big(\not{k}_{1\perp}(\not{k}_{1\perp}-\not{q}_{1\perp})\big) \tag{4.51}$$

$$-\frac{1}{D(k_2,k_2-q_1)}\big((\not{k}_{2\perp}-\not{q}_{1\perp})\not{k}_{2\perp}\big)$$

$$-2\frac{1}{d(k_2,k_1)}\big[x_2\not{k}_{1\perp}\not{q}_{1\perp}$$

$$+x_1\not{q}_{1\perp}\not{k}_{2\perp}+x_1x_2q_{1\perp}^2$$

$$-2x_1x_2\big(q_{1\perp}(k_{1\perp}+k_{2\perp})\big)\big]$$

$$+\frac{x_1x_2}{d(k_2,k_1)D(k_2,k_1)}(2\not{k}_{1\perp}\not{k}_{2\perp}q_{1\perp}^2)+2.$$

It is just $\mathcal{L}_2$, so that, for the color structure $\mathcal{R}_2^{c_1c_2}$, the bootstrap equation is satisfied.

Finally, we consider the color structure $\mathcal{R}_3^{c_1c_2}$. For the sum of $\mathcal{L}_3^i$, we have

$$\frac{\not{k}_{1\perp}'(\not{k}_{1\perp}'-\not{q}_{1\perp})}{D(k_1'-q_1,k_1')}-\frac{(\not{k}_{2\perp}-\not{q}_{1\perp})\not{k}_{2\perp}}{D(k_2,k_2-q_1)} \tag{4.52}$$

$$+\frac{\not{k}_{1\perp}(\not{k}_{1\perp}-\not{q}_{1\perp})}{D(k_1-q_1,k_1)}-\frac{(\not{k}_{2\perp}'-\not{q}_{1\perp})\not{k}_{2\perp}'}{D(k_2',k_2'-q_1)}$$

$$=\frac{\not{k}_{1\perp}(\not{k}_{1\perp}-\not{q}_{1\perp})}{D(k_1-q_1,k_1)}-\frac{(\not{k}_{2\perp}-\not{q}_{1\perp})\not{k}_{2\perp}}{D(k_2,k_2-q_1)},$$

which is exactly $\mathcal{L}_3$.

Thus, the bootstrap equation for $q\bar{q}$ production is satisfied.

4.3. Two-Gluon Production

Notation. In the case of two-gluon production, Eqs. (4.20)–(4.22) are applied as before; but now k_1 and k_2 are the gluon momenta. The effective vertex of two-gluon production in Reggeon–Reggeon collisions in a gauge-invariant form was obtained in [34].

In the light-cone gauge (2.8) for both gluons, the vertex takes the form

$$\gamma_{ij}^{G_1G_2}(q_1,q_2) = 4g^2(e^*_{1\perp})_\alpha(e^*_{2\perp})_\beta \times \Big[\left(T^{i_1}T^{i_2}\right)_{ij} b^{\alpha\beta}(q_1;k_1,k_2) + \left(T^{i_2}T^{i_1}\right)_{ij} b^{\beta\alpha}(q_1;k_2,k_1)\Big], \tag{4.53}$$

where $e_{1,2}$ are the polarization vectors of the produced gluons; $i_{1,2}$ are their color indices; i,j are the color indices of the Reggeons with momenta q_1 and q_2, respectively; and

$$\begin{aligned} b^{\alpha\beta}(q_1;k_1,k_2) &= \frac{1}{2}g_\perp^{\alpha\beta} \\ &\times \left[\frac{x_1x_2}{d(k_2,k_1)}\left(2q_{1\perp}(x_1k_2-x_2k_1)_\perp + q_{1\perp}^2 \times\left(x_2-\frac{x_1k_{2\perp}^2}{D(k_2,k_1)}\right)\right)\right. \\ &\left. - x_2\left(1-\frac{k_{1\perp}^2}{D(q_1-k_1,k_1)}\right)\right] \\ &- \frac{x_2k_{1\perp}^\alpha q_{1\perp}^\beta - x_1q_{1\perp}^\alpha(q_1-k_1)_\perp^\beta}{D(q_1-k_1,k_1)} \\ &- \frac{x_1q_{1\perp}^2k_{1\perp}^\alpha(q_1-k_1)_\perp^\beta}{k_{1\perp}^2D(q_1-k_1,k_1)} \\ &- \frac{x_1q_{1\perp}^\alpha(x_1k_2-x_2k_1)_\perp^\beta + x_2q_{1\perp}^\beta(x_1k_2-x_2k_1)_\perp^\alpha}{d(k_2,k_1)} \\ &+ \frac{x_1q_{1\perp}^2k_{1\perp}^\alpha k_{2\perp}^\beta}{k_{1\perp}^2D(k_2,k_1)} + \frac{x_1x_2q_{1\perp}^2}{d(k_2,k_1)D(k_2,k_1)} \\ &\times\left[(x_1k_2-x_2k_1)_\perp^\alpha k_{2\perp}^\beta + k_{1\perp}^\alpha(x_1k_2-x_2k_1)_\perp^\beta\right]. \end{aligned} \tag{4.54}$$

Here, we use the notation (4.26). Note that one can come to (4.54) starting from the vertex in the gauge $e(k_1)p_1 = 0, e(k_2)p_2 = 0$ [35]. Our $b^{\alpha\beta}(q_1;k_1,k_2)$ can be obtained from $c^{\alpha\beta}(k_1,k_2)$ defined in [35] as the gauge transformation

$$b^{\alpha\beta}(q_1;k_1,k_2) = \left(g_\perp^{\alpha\gamma} - 2\frac{k_{1\perp}^\alpha k_{1\perp}^\gamma}{k_{1\perp}^2}\right)c_\gamma^\beta(k_1,k_2). \tag{4.55}$$

Independent color structures. Contrary to the case of $q\bar{q}$ production, where $\mathcal{F}_{ij}^{P_1P_2}(q_1,q_2,r)$ (4.18) has the most general form in color space, here not all admitted color structures are present. The number of all independent structures is readily calculated. Indeed, the decomposition of the product of two octets ($8\otimes 8 = 1\oplus 8_s\oplus 8_a\oplus 10\oplus 10^*\oplus 27$) contains five different irreducible representations, one of which enters two times. Such a decomposition is valid for two Reggeons as well as for two gluons. Therefore, the total number of admitted independent color structures is eight. It occurs that only three of them enter $\mathcal{F}_{ij}^{G_1G_2}$. Actually, it is predictable and is related to specific color structures of the effective vertices for one-gluon (2.18) and two-gluon production (3.18), (4.53). These vertices are expressed in terms of the color group generators in the adjoint representation. From properties of these generators, it follows that only three independent tensors with four indices can be built from them. Of course, their choice is not unique. We take the following:

$$\begin{aligned} \mathcal{R}_{(1)ij}^{i_1i_2} &= \frac{2}{N_c}\mathrm{Tr}(T^iT^jT^{i_2}T^{i_1}), \\ \mathcal{R}_{(2)ij}^{i_1i_2} &= T_{il}^{i_1}T_{lj}^{i_2}, \mathcal{R}_{(3)ij}^{i_1i_2} = T_{il}^{i_2}T_{lj}^{i_1}. \end{aligned} \tag{4.56}$$

It seems that our choice is the most appropriate; i.e., the coefficients with which these tensors enter $\mathcal{F}_{ij}^{G_1G_2}$ are the least cumbersome.

Let us represent each of the contributions $\mathcal{F}_{ij}^m$ entering $\mathcal{F}_{ij}^{G_1G_2}(q_1,q_2,r)$ (4.18) in the form

$$\mathcal{F}_{ij}^m = 2g^3N_c\sum_{n=1}^3\mathcal{R}_{(n)ij}^{i_1i_2}(e^*_{1\perp})_\alpha(e^*_{2\perp})_\beta\mathcal{L}_{mn}^{\alpha\beta}. \tag{4.57}$$

Writing in the same form the right part of (4.19),

$$\begin{aligned} &g\frac{N_c}{2}\gamma_{ij}^{G_1G_2}(q_1,q_2) \\ &= 2g^3N_c(e^*_{1\perp})_\alpha(e^*_{2\perp})_\beta\sum_{n=1}^3\mathcal{R}_{(n)ij}^{i_1i_2}\mathcal{L}_n^{\alpha\beta}, \end{aligned} \tag{4.58}$$

we have from (4.53)

$$\begin{aligned} \mathcal{L}_1^{\alpha\beta} &= 0, \mathcal{L}_2^{\alpha\beta} = b^{\alpha\beta}(q_1;k_1,k_2), \\ \mathcal{L}_3^{\alpha\beta} &= b^{\beta\alpha}(q_1;k_2,k_1). \end{aligned} \tag{4.59}$$

The coefficients $\mathcal{L}_{mn}^{\alpha\beta}$ in (4.57) are found by straightforward calculation using the vertices (2.9), (2.18), (3.18), and (4.53). With account of (4.18), the bootstrap condition (4.19) requires

$$\begin{aligned} &\int\frac{d^{D-2}r_\perp}{r_\perp^2(q_2-r)_\perp^2} \\ &\times\left(\mathcal{L}_{an}^{\alpha\beta}+\mathcal{L}_{bn}^{\alpha\beta}+\mathcal{L}_{cn}^{\alpha\beta}+2\mathcal{L}_{dn}^{\alpha\beta}+2\mathcal{L}_{fn}^{\alpha\beta}\right) \\ &= \mathcal{L}_n^{\alpha\beta}\int\frac{d^{D-2}r_\perp}{r_\perp^2(q_2-r)_\perp^2} \end{aligned} \tag{4.60}$$

for each n.

Verification of the bootstrap equation. For $n = 1$, we obtain

$$\mathcal{L}_{a1}^{\alpha\beta} = g_\perp^{\alpha\beta}x_1x_2$$

$$\times\left[\frac{(k_1-x_1k')_\perp Q_\perp}{d(k_2',k_1)}+\frac{(k_2-x_2k')_\perp Q_\perp}{d(k_2,k_1')}\right] \quad (4.61)$$
$$-\frac{x_1Q_\perp^\alpha(k_1-x_1k')_\perp^\beta+x_2(k_1-x_1k')_\perp^\alpha Q_\perp^\beta}{(k_1-x_1k')_\perp^2}$$
$$-\frac{x_1Q_\perp^\alpha(k_2-x_2k')_\perp^\beta+x_2(k_2-x_2k')_\perp^\alpha Q_\perp^\beta}{(k_2-x_2k')_\perp^2},$$

$$\mathcal{L}_{b1}^{\alpha\beta}=-b^{\alpha\beta}(q_1;k_1',k_2), \quad (4.62)$$

$$\mathcal{L}_{c1}^{\alpha\beta}=-b^{\beta\alpha}(q_1;k_2',k_1), \quad (4.63)$$

$$\mathcal{L}_{d1}^{\alpha\beta}=\frac{q_{1\perp}^2}{2k_\perp'^2} \quad (4.64)$$
$$\times\left[b^{\alpha\beta}(q_1-r;k_1,k_2)+b^{\beta\alpha}(q_1-r;k_2,k_1)\right],$$

$$\mathcal{L}_{f1}^{\alpha\beta}=-\frac{q_{1\perp}^2}{2(q_1-k_1')_\perp^2k_{1\perp}'^2}\left(k_1'-k_1\frac{k_{1\perp}'^2}{k_{1\perp}^2}\right)_\perp^\alpha \quad (4.65)$$
$$\times\left(q_1-k_1'-k_2\frac{(q_1-k_1')_\perp^2}{k_{2\perp}^2}\right)_\perp^\beta.$$

Here and below, $Q_\perp=(q_1-k'q_{1\perp}^2/k_\perp'^2)_\perp$. According to (4.60), the integrated sum of $\mathcal{L}_{m1}^{\alpha\beta}$ must be zero. One can track the cancellation of separate contributions using the decompositions (4.46), (4.47) and the change of variables $r_\perp\leftrightarrow(q_2-r)_\perp$, at which $D(q_1-k_1',k_1)\leftrightarrow D(k_2',q_1-k_2')$ and, consequently,

$$\frac{-x_1q_{1\perp}^\alpha(q_1-k_1')_\perp^\beta+x_2k_{1\perp}'^\alpha q_{1\perp}^\beta}{D(q_1-k_1',k_1')} \quad (4.66)$$
$$\leftrightarrow\frac{-x_1k_{2\perp}'^\beta q_{1\perp}^\alpha+x_2q_{1\perp}^\beta(q_1-k_2')_\perp^\alpha}{D(k_2',q_1-k_2')}.$$

After that, the cancellation of the terms with $g_\perp^{\alpha\beta}$ follows from trivial relations:

$$2x_1k_\perp'(k_1-x_1k')_\perp-k_{1\perp}^2=-(d(k_2',k_1)+x_1^2k_\perp'^2), \quad (4.67)$$

$$2x_2k_\perp'(k_2-x_2k')_\perp-k_{2\perp}^2=-(d(k_2,k_1')+x_2^2k_\perp'^2). \quad (4.68)$$

To see that the sum of all other terms is zero, the equality

$$\int\frac{d^{D-2}r_\perp}{r_\perp^2(q_2-r)_\perp^2}\left[x_2\left(1-\frac{k_{1\perp}'^2}{D(q_1-k_1',k_1')}\right)\right. \quad (4.69)$$
$$\left.+x_1\left(1-\frac{k_2'^2}{D(k_2',q_1-k_2')}\right)\right]=0,$$

which follows from the change of variables $r_\perp\leftrightarrow(q_2-r)_\perp$ and $x_1+x_2=1$, is helpful.

Let us turn to the case $n=2$ in (4.60). For separate terms in the integrand, we obtain

$$\mathcal{L}_{a2}^{\alpha\beta}=-x_1x_2g_\perp^{\alpha\beta} \quad (4.70)$$
$$\times\left[\frac{Q_\perp(k_2-x_2k')_\perp}{d(k_2,k_1')}+\frac{Q_\perp(x_2k_1-x_1k_2)_\perp}{d(k_2,k_1)}\right]$$
$$+\frac{x_1Q_\perp^\alpha(x_2k_1-x_1k_2)_\perp^\beta+x_2(x_2k_1-x_1k_2)_\perp^\alpha Q_\perp^\beta}{d(k_2,k_1)}$$
$$+\frac{x_1Q_\perp^\alpha(k_2-x_2k')_\perp^\beta+x_2(k_2-x_2k')_\perp^\alpha Q_\perp^\beta}{d(k_2,k_1')},$$

$$\mathcal{L}_{b2}^{\alpha\beta}=b^{\alpha\beta}(q_1;k_1',k_2), \quad (4.71)$$

$$\mathcal{L}_{c2}^{\alpha\beta}=b^{\beta\alpha}(q_1;k_2',k_1)+b^{\alpha\beta}(q_1;k_1,k_2'), \quad (4.72)$$

$$\mathcal{L}_{d2}^{\alpha\beta}=-\frac{q_{1\perp}^2}{2k_\perp'^2}b^{\beta\alpha}(q_1-r;k_2,k_1), \quad (4.73)$$

$$\mathcal{L}_{f2}^{\alpha\beta}=\frac{q_{1\perp}^2}{2(q_1-k_1')_\perp^2k_{1\perp}'^2}\left(k_1'-k_1\frac{k_{1\perp}'^2}{k_{1\perp}^2}\right)_\perp^\alpha \quad (4.74)$$
$$\times\left(q_1-k_1'-k_2\frac{(q_1-k_1')_\perp^2}{k_{2\perp}^2}\right)_\perp^\beta.$$

Although separate contributions in (4.60) are rather complicated, their sum can be greatly simplified using the equalities

$$\int\frac{d^{D-2}r_\perp}{r_\perp^2(q_2-r)_\perp^2}\left[\frac{x_1k_{1\perp}'^\alpha(q_1-k_1')_\perp^\beta}{k_{1\perp}'^2D(q_1-k_1',k_1')}\right. \quad (4.75)$$
$$\left.+\frac{x_2k_{2\perp}'^\beta(q_1-k_2')_\perp^\alpha}{k_{2\perp}'^2D(k_2',q_1-k_2')}-\frac{k_{1\perp}'^\alpha(q_1-k_1')_\perp^\beta}{k_{1\perp}'^2(q_1-k_1')_\perp^2}\right]=0,$$

$$\int\frac{d^{D-2}r_\perp}{r_\perp^2(q_2-r)_\perp^2} \quad (4.76)$$
$$\times\left[\frac{x_1k_{1\perp}^\alpha k_{2\perp}'^\beta}{k_{1\perp}^2D(k_2',k_1)}+\frac{x_2k_{1\perp}^\alpha k_{2\perp}'^\beta}{k_{2\perp}'^2D(k_2',k_1)}\right.$$
$$\left.-\frac{k_{1\perp}^\alpha(q_1-k_1')_\perp^\beta}{k_{1\perp}^2(q_1-k_1')_\perp^2}\right]=0,$$

which readily follow from the change of variables $r_\perp\leftrightarrow(q_2-r)_\perp$, relations (4.67), (4.68), and the no less trivial equality

$$x_2k_\perp'^\beta k_{1\perp}'^\alpha-x_1k_{2\perp}^\beta k_\perp'^\alpha \quad (4.77)$$
$$=k_{1\perp}'^\alpha(x_2k_1'-x_1k_2)_\perp^\beta+k_{2\perp}^\beta(x_2k_1'-x_1k_2)_\perp^\alpha.$$

After that, fulfillment of (4.60) for $n=2$ becomes plain.

Finally, consider (4.60) at $n = 3$. For the coefficients $\mathcal{L}^{\alpha\beta}_{m3}$, we obtain

$$\mathcal{L}^{\alpha\beta}_{a3} = x_1 x_2 g^{\alpha\beta}_{\perp}\left[\frac{Q_\perp(k_2 - x_2k')_\perp}{d(k_2,k_1')} + \frac{Q_\perp(x_2k_1 - x_1k_2)_\perp}{d(k_2,k_1)}\right] \tag{4.78}$$
$$- \frac{x_1Q^\alpha_\perp(k_2 - x_2k')^\beta_\perp + x_2Q^\beta_\perp(k_2 - x_2k')^\alpha_\perp}{d(k_2,k_1')}$$
$$- \frac{x_1Q^\alpha_\perp(x_2k_1 - x_1k_2)^\beta_\perp + x_2Q^\beta_\perp(x_2k_1 - x_1k_2)^\alpha_\perp}{d(k_2,k_1)},$$

$$\mathcal{L}^{\alpha\beta}_{b3} = b^{\beta\alpha}(q_1;k_2,k_1'), \tag{4.79}$$

$$\mathcal{L}^{\alpha\beta}_{c3} = 0, \tag{4.80}$$

$$\mathcal{L}^{\alpha\beta}_{d3} = \frac{q^2_{1\perp}}{2k'^2_\perp}b^{\beta\alpha}(q_1 - r;k_2,k_1), \tag{4.81}$$

$$\mathcal{L}^{\alpha\beta}_{f3} = 0. \tag{4.82}$$

Verification of (4.60) is rather simple here; the trivial equality

$$2x_1k'_\perp(k_2 - x_2k')_\perp + k'^2_{1\perp} = d(k_2,k_1') + x_1^2k'^2_\perp \tag{4.83}$$

is helpful to perform it.

5. SUMMARY AND DISCUSSION

In this paper, we have calculated in the one-loop approximation the leading logarithmic corrections to the QCD amplitudes in the QMRK. We have considered two essentially different kinematics. In one of them, two particles with limited invariant mass are produced in the fragmentation region of one of the colliding particles. In the other, there are two gaps between rapidities of the produced particles and rapidities of colliding ones (production in the central region). The radiative corrections were calculated using the s-channel unitarity. In both cases, we have found that the radiative corrections are just the same as those prescribed by the Reggeized form of the amplitudes. It is worthwhile to note that this form of corrections appears as a result of miraculous cancellations between various contributions. The s-channel unitarity method used by us for the calculation is very economical. Using this method, we have to consider only a few contributions, whereas the number of Feynman diagrams is estimated to be in the hundreds. Nevertheless, even in this approach, the cancellations are quite impressive.

Since in the s-channel unitarity method the radiative corrections are expressed in terms of the Reggeon vertices, the cancellation appears as a result of fulfillment of Eqs. (3.11) and (4.19). Therefore, these equations are the bootstrap conditions necessary for compatibility of the Reggeized form of the amplitudes with the s-channel unitarity.

The gluon Reggeization is one of the remarkable properties of QCD, which is very important at high energies. It is proved in the LLA, but still remains a hypothesis in the NLA. This hypothesis can be checked and, hopefully, proved [24] using the bootstrap requirement, i.e., the demand of compatibility of the Reggeized form of the amplitudes with the s-channel unitarity. The requirement leads to an infinite set of bootstrap relations for the scattering amplitudes. Fulfillment of these relations guarantees the Reggeized form of the radiative corrections order by order in perturbation theory. It occurs that all these relations can be satisfied if the Reggeon vertices and the gluon Regge trajectory submit to several bootstrap conditions. The proof of the gluon Reggeization in the LLA [9] is just a demonstration that fulfillment of the bootstrap conditions in the LO is sufficient to satisfy all bootstrap relations. Hopefully, the same can be done in the NLA [24]. There are no doubts that the Reggeized form of the QMRK amplitudes can be proved in such a way. Since these amplitudes contain the gluon Regge trajectory and the Reggeon–Reggeon–gluon vertex in the LO, the only new (compared with the LLA) thing that is required to perform the proof is fulfillment of the bootstrap conditions (3.11) and (4.19). We will return to this question elsewhere.

ACKNOWLEDGMENTS

One of us (V.S.F.) thanks the Alexander von Humboldt Foundation for the research award and the Universität Hamburg and DESY for their warm hospitality while part of this work was being done.

This work was supported in part by INTAS (grant no. INTAS 00-0036) and the Russian Foundation for Basic Research (project no. 01-02-16042).

REFERENCES

1. M. Gell-Mann, M. L. Goldberger, *et al.*, Phys. Rev. **133**, B145 (1964).
2. S. Mandelstam, Phys. Rev. **137**, B949 (1965).
3. M. T. Grisaru, H. J. Schnitzer, and H.-S. Tsao, Phys. Rev. Lett. **30**, 811 (1973); Phys. Rev. D **8**, 4498 (1973).
4. L. N. Lipatov, Yad. Fiz. **23**, 642 (1976) [Sov. J. Nucl. Phys. **23**, 338 (1976)].

5. V. S. Fadin, E. A. Kuraev, and L. N. Lipatov, Phys. Lett. B **60B**, 50 (1975); E. A. Kuraev, L. N. Lipatov, and V. S. Fadin, Zh. Éksp. Teor. Fiz. **71**, 840 (1976) [Sov. Phys. JETP **44**, 443 (1976)]; **72**, 377 (1977) [**45**, 199 (1977)]; Ya. Ya. Balitskii and L. N. Lipatov, Sov. J. Nucl. Phys. **28**, 822 (1978).
6. V. S. Fadin and V. E. Sherman, Pis'ma Zh. Éksp. Teor. Fiz. **23**, 599 (1976) [JETP Lett. **23**, 548 (1976)]; Zh. Éksp. Teor. Fiz. **72**, 1640 (1977) [Sov. Phys. JETP **45**, 861 (1977)]; V. S. Fadin and R. Fiore, Phys. Rev. D **64**, 114012 (2001); hep-ph/0107010.
7. A. V. Bogdan, V. Del Duca, V. S. Fadin, and E. W. Glover, J. High Energy Phys. **0203**, 032 (2002); hep-ph/0201240.
8. M. I. Kotsky, L. N. Lipatov, A. Principe, and M. I. Vyazovsky, hep-ph/0207169.
9. Ya. Ya. Balitskii, L. N. Lipatov, and V. S. Fadin, in *Proc. of the 14th Leningrad Winter School on Physics of Elementary Particles, Leningrad, 1979*, p. 109.
10. V. S. Fadin and L. N. Lipatov, Phys. Lett. B **429**, 127 (1998).
11. M. Ciafaloni and G. Camici, Phys. Lett. B **430**, 349 (1998).
12. V. S. Fadin and R. Fiore, Phys. Lett. B **440**, 359 (1998).
13. V. S. Fadin, R. Fiore, and A. Papa, Phys. Rev. D **60**, 074025 (1999).
14. V. S. Fadin and D. A. Gorbachev, Pis'ma Zh. Éksp. Teor. Fiz. **71**, 322 (2000) [JETP Lett. **71**, 222 (2000)]; Phys. At. Nucl. **63**, 2157 (2000).
15. V. S. Fadin, R. Fiore, M. I. Kotsky, and A. Papa, Phys. Rev. D **61**, 094005 (2000).
16. V. S. Fadin, R. Fiore, M. I. Kotsky, and A. Papa, Phys. Rev. D **61**, 094006 (2000).
17. V. S. Fadin and A. D. Martin, Phys. Rev. D **60**, 114008 (1999).
18. V. Fadin, D. Ivanov, and M. Kotsky, in *New Trends in High-Energy Physics, Kiev, 2000*, Ed. by L. L. Jenkovszky, p. 190; hep-ph/0007119.
19. J. Bartels, S. Gieseke, and C. F. Qiao, Phys. Rev. D **63**, 056014 (2001); hep-ph/0009102.
20. V. Fadin, D. Ivanov, and M. Kotsky, hep-ph/0106099.
21. J. Bartels, S. Gieseke, and A. Kyrieleis, Phys. Rev. D **65**, 014006 (2002); hep-ph/0107152.
22. V. S. Fadin, R. Fiore, and M. I. Kotsky, Phys. Lett. B **494**, 100 (2000); hep-ph/0007312.
23. V. S. Fadin, R. Fiore, and A. Papa, Phys. Rev. D **63**, 034001 (2001); hep-ph/0008006.
24. V. S. Fadin, *Talk Given at the NATO Advanced Research Workshop Diffraction 2002, Alushta, Crimea, Ukraine*.
25. M. Braun, hep-ph/9901447.
26. M. Braun and G. P. Vacca, Phys. Lett. B **477**, 156 (2000).
27. V. S. Fadin, R. Fiore, M. I. Kotsky, and A. Papa, Phys. Lett. B **495**, 329 (2000); hep-ph/0008057.
28. M. Braun and G. P. Vacca, Phys. Lett. B **454**, 319 (1999).
29. V. S. Fadin and A. Papa, Nucl. Phys. B **640**, 309 (2002); hep-ph/0206079.
30. V. S. Fadin and L. N. Lipatov, Nucl. Phys. B **406**, 259 (1993).
31. J. Bartels, Nucl. Phys. B **175**, 365 (1980).
32. V. S. Fadin and L. N. Lipatov, Nucl. Phys. B **477**, 767 (1996).
33. V. S. Fadin, R. Fiore, A. Flachi, and M. I. Kotsky, Phys. Lett. B **422**, 287 (1998); hep-ph/9711427; V. S. Fadin, M. I. Kotsky, R. Fiore, and A. Flachi, Phys. At. Nucl. **62**, 999 (1999).
34. L. N. Lipatov and V. S. Fadin, Pis'ma Zh. Éksp. Teor. Fiz. **49**, 311 (1989) [JETP Lett. **49**, 352 (1989)]; Yad. Fiz. **50**, 1141 (1989) [Sov. J. Nucl. Phys. **50**, 712 (1989)].
35. V. S. Fadin, M. A. Kotsky, and L. N. Lipatov, Phys. Lett. B **415**, 97 (1997); Yad. Fiz. **61**, 716 (1998) [Phys. At. Nucl. **61**, 641 (1998)].

Physics of Atomic Nuclei, Vol. 67, No. 2, 2004, pp. 376–390. Translated from Yadernaya Fizika, Vol. 67, No. 2, 2004, pp. 394–408.

ELEMENTARY PARTICLES AND FIELDS
Theory

Instantons in the Nonperturbative QCD Vacuum

N. O. Agasian* **and S. M. Fedorov****

Institute of Theoretical and Experimental Physics,
Bol'shaya Cheremushkinskaya ul. 25, Moscow, 117259 Russia

Received November 12, 2002

Abstract—The effect of nonperturbative fields on instantons in QCD is investigated. The nonperturbative vacuum is described in terms of nonlocal gauge-invariant vacuum expectation values of gluon fields. An effective action for instantons is obtained in the bilocal approximation, and it is shown that a stochastic background gluon field leads to an infrared stabilization of instantons. The dependence of a characteristic instanton size on the magnitude of the gluon condensate and on the correlation length in the nonperturbative vacuum is found. The size distribution of instantons that is obtained here is compared with the results of lattice calculations. © *2004 MAIK "Nauka/Interperiodica".*

1. INTRODUCTION

Instantons are the first explicit example of nonperturbative fluctuations of a gluon field in QCD. Instantons were introduced in 1975 by Polyakov and his coauthors [1]. An important step was made in the classic study of 't Hooft [2], where he calculated the semiclassical amplitude of tunneling. In the pioneering studies of Callan, Dashen, and Gross [3, 4], an instanton gas was considered as a model of a vacuum. These topologically nontrivial field configurations provide a possible explanation of some problems in QCD. Instantons make it possible to explain the anomalous breakdown of $U(1)_A$ symmetry and the mass of the η' meson [5, 6]. The mechanism of a spontaneous breakdown of chiral invariance can be explained by the presence of instanton and anti-instanton configurations in the QCD vacuum [7]. A significant role of instantons in scalar and pseudoscalar channels was emphasized in [8]. In QCD, there are a number of other phenomena where the inclusion of instantons is of crucial importance (see [9] and references therein).

At the same time, there are some problems in instanton physics. First, there is an infrared divergence of integrals with respect to the instanton size ρ at large ρ, this preventing the calculation of the instanton contribution to some physical quantities, such as the vacuum gluon condensate. Second, the area law for the Wilson loop cannot be explained within the instanton-gas model—that is, confinement, which is responsible for the formation of the hadron spectrum, does not occur in the semiclassical instanton–anti-instanton vacuum. Moreover, it was shown in [10] that Casimir scaling, which was observed in lattice calculations of the potential of quark–antiquark interaction for heavy quarks in various representations of the $SU(3)$ color group [11], is violated in an instanton gas (see also the discussion of this issue in [12]).

A large number of theoretical studies have been devoted to solving the problem of stabilizing instantons with respect to their size ρ.[1)] To some extent, all of them involve attempts at stabilizing an instanton ensemble by including effects of interaction between pseudoparticles [13]. The phenomenological instanton-liquid model formulated by Shuryak [14, 15] became the most popular. Relying on the hypothesis that instantons dominate the vacuum expectation values of local gluodynamic operators and taking into account the dipole–dipole interaction between an instanton and an anti-instanton, he was able to determine basic features of the instanton medium, such as the mean distance between pseudoparticles, $\bar{R} \sim 1$ fm, and their mean size, $\bar{\rho} \sim 1/3$ fm. Thereby, there arose a relatively small parameter, $\bar{\rho}/\bar{R} \simeq 1/3$, and this made it possible to formulate the pattern of a grained vacuum that consists of instantons and anti-instantons that are rather well separated in space and which are therefore only slightly deformed (that is, the pattern of a dilute medium of pseudoparticles). However, the effect of pair interaction between pseudoparticles, $\exp\{S_{\text{int}}\} \gg 1$, proved to be of importance for the structure of the instanton ensemble, and Shuryak concluded on this basis that the instanton ensemble

*e-mail: agasian@heron.itep.ru
**e-mail: fedorov@heron.itep.ru

[1)] It should be emphasized that, as far back as the pioneering studies on instanton physics by Callan, Dashen, and Gross [3, 4], it was proposed solving some of the aforementioned problems through the phenomenon of instanton breakup into meron–antimeron pairs.

in QCD is an interacting liquid rather than a dilute gas [14].

Quantitatively similar results for the parameters of an instanton liquid were obtained by Diakonov and Petrov [16]. Assuming that the vacuum state in gluodynamics has the form of a superposition of instantons and anti-instantons, those authors found that stabilization with respect to scales occurs owing to the classical repulsion between pseudoparticles that was found in their study. However, a further development of the theory [17] revealed that an instanton ensemble cannot be stabilized by a purely classical interaction. Thus, the dynamical mechanism through which large-size instantons are suppressed in an ensemble of topologically nontrivial fields has yet to be clarified conclusively.

It is more natural to assume that, in addition to semiclassical instantons, the vacuum also features other nonperturbative fields, which, in principle, make it possible to resolve the aforementioned problems. The interaction of a small-size instanton, $\rho < 0.2$ fm, with long-wave gluon fluctuations, which are described in terms of the local vacuum condensate $\langle (gG^a_{\mu\nu})^2 \rangle$, was considered in [18]. It was shown that the effect of such fields leads to a still faster growth of the instanton density with increasing instanton scale ρ. On the other hand, investigation of instantons in a stochastic QCD vacuum parametrized in terms of the nonlocal gauge-invariant expectation values of the gluon-field strength, $\langle \mathrm{tr} G_{\mu\nu}(x)\Phi(x,y)G_{\sigma\lambda}(y)\Phi(y,x)\rangle$, where $\Phi(x,y)$ is the parallel transporter, was began in [19, 20]. It was shown there that, in a nonperturbative vacuum, standard perturbation theory changes in such a way that a nonlocal interaction of a large-size instanton ($\rho > 1$ fm) with a nonperturbative gluon field does not lead to its infrared inflation [20]. Further, it was shown in [21] that a nonlocal interaction of instantons with nonperturbative vacuum fields stabilizes instantons at scales of about the correlation length in the vacuum condensate.

In the present study, we consistently develop a gauge-invariant method for calculating an effective action for an instanton in the nonperturbative vacuum and show that the instanton exists as a stable topologically nontrivial field configuration of characteristic size ρ_c. The value of ρ_c is a function of the properties of the bilocal correlation function $\langle \mathrm{tr} G(x)\Phi(x,y)G(y)\Phi(y,x)\rangle$ for a nonperturbative field; that is, it depends parametrically on two quantities—namely, the magnitude of the gluon condensate, $\langle G^2 \rangle$, and the correlation length in the condensate, T_g, the latter being the the measure of the nonuniformity of the condensate. Here, we do not consider the problem of the distribution of instantons in four-dimensional Euclidean space—that is, the problem of the instanton density N/V. Within the present approach, this would require studying an interacting instanton–anti-instanton ensemble against the background of nonperturbative fluctuations described in terms of gauge-invariant vacuum expectation values of the gluon field.

The ensuing exposition is organized as follows. In Section 2, we describe a general formalism of the effective action for an instanton in a nonperturbative background field. In Section 3, we explore the one-loop renormalization of the instanton action in the presence of nonperturbative fields. It is shown that the perturbative part of the effective action for an instanton is frozen in a nonperturbative background field, reaching a constant value at instanton sizes of $\rho \gtrsim 1\ \mathrm{GeV}^{-1}$. Section 4 is devoted to exploring a direct interaction of instantons with nonperturbative fields, which are parametrized in terms of gauge-invariant nonlocal vacuum expectation values of the gluon-field strength (correlation functions). Using a cluster expansion, we find, by a gauge-invariant method, the effective action for an instanton in the bilocal approximation. Numerical calculations are presented in Section 5, along with the discussion of the results. A derivation of the one-loop renormalization of the effective instanton action in a nonperturbative vacuum in coordinate space and some mathematical details of the calculations are given in the Appendices.

2. GENERAL FORMALISM

Nonperturbative fluctuations exert a double effect on instantons. First, perturbation theory changes in a nonperturbative background field, this leading to changes in the standard one-loop renormalization of the instanton action. Second, there appears a direct nonlocal interaction between instantons and nonperturbative background fields.

The standard Euclidean action in gluodynamics has the form

$$S[A] = \frac{1}{2g_0^2}\int d^4x \mathrm{tr} F^2_{\mu\nu}[A] \qquad (1)$$
$$= \frac{1}{4}\int d^4x F^a_{\mu\nu}[A]F^a_{\mu\nu}[A],$$

where $F_{\mu\nu}[A] = \partial_\mu A_\nu - \partial_\nu A_\mu - i[A_\mu, A_\nu]$ is the gluon-field strength and where we have used the Hermitian matrix form for gauge fields—that is, $A_\mu(x) = g_0 A^a_\mu(x)t^a/2$, $\mathrm{tr} t^a t^b = \delta^{ab}/2$ (t^a are generators of the gauge group). We represent A_μ in the form

$$A_\mu = A^{\mathrm{inst}}_\mu + B_\mu + a_\mu, \qquad (2)$$

where $A_\mu^{\rm inst}$ is an instanton-like field configuration of unit topological charge, $Q_T[A^{\rm inst}] = 1$; a_μ is a quantum field (an expansion in terms of a_μ reduces to perturbation theory, this leading to the phenomenon of asymptotic freedom in gluodynamics); and B_μ is a nonperturbative background field (of zero topological charge), which can be parametrized in terms of nonlocal vacuum expectation values of the gluon-field strength.[2)]

The general form of the effective instanton action in a nonperturbative vacuum is

$$Z = e^{-S_{\rm eff}[A^{\rm inst}]} = \int [Da_\mu] \left\langle e^{-S[A^{\rm inst}+B+a]} \right\rangle, \quad (3)$$

where $\langle \ldots \rangle$ stands for an expectation value with respect to the background field B_μ,

$$\left\langle \hat{O}(B) \right\rangle = \int d\mu(B) \hat{O}(B), \quad (4)$$

with $d\mu(B)$ being the measure of integration with respect to nonperturbative fields, the explicit form of this measure being immaterial for the ensuing analysis.

Expanding $S[A]$ to second-order terms in a_μ inclusive, we obtain

$$Z = \langle Z_1(B) Z_2(B) \rangle, \quad (5)$$

where

$$Z_1(B) = e^{-S[A^{\rm inst}]} \int [Da_\mu] \det(\nabla_\mu^2) \quad (6)$$

$$\times \exp\left[\frac{1}{g_0^2} {\rm tr} \int d^4x \left\{ -(\nabla_\mu a_\nu)^2 + 2iF_{\mu\nu}[a_\mu, a_\nu] \right\} \right],$$

$$Z_2(B) = \exp\{-S[A^{\rm inst} + B] + S[A^{\rm inst}]\}. \quad (7)$$

Here, we have used the notation $\bar{A} \equiv A^{\rm inst} + B$ and $F_{\mu\nu} \equiv F_{\mu\nu}[\bar{A}]$, and $\nabla_\mu a_\nu = \partial_\mu a_\nu - i[\bar{A}_\mu, a_\nu]$ is a covariant derivative. Integration with respect to a and B in Eq. (5) corresponds to averaging over fields that are responsible for physics at different scales. Integration with respect to a_μ takes into account perturbative gluons and describes phenomena at short distances. Averaging over B_μ (formally, interaction with the gluon condensate) takes into account phenomena at scales of about the confinement radius. Therefore, it is physically clear that the above averaging factorizes, and we obtain

$$Z \to \langle Z_1(B) \rangle \langle Z_2(B) \rangle. \quad (8)$$

It should be emphasized that, in the limit of an infinite number of colors, $N_c \to \infty$, the factorization in (8) becomes exact: $Z(N_c \to \infty) \equiv \langle Z_1(B) \rangle \langle Z_2(B) \rangle$. This enables us to write the effective instanton action in a nonperturbative vacuum as the sum of two terms, a perturbative and a nonperturbative one; that is,

$$S_{\rm eff}[A^{\rm inst}] = S_{\rm eff}^{\rm P}[A^{\rm inst}] + S_{\rm eff}^{\rm NP}[A^{\rm inst}], \quad (9)$$

$$S_{\rm eff}^{\rm P}[A^{\rm inst}] = -\ln\langle Z_1(B) \rangle, \quad (10)$$

$$S_{\rm eff}^{\rm NP}[A^{\rm inst}] = -\ln\langle Z_2(B) \rangle \quad (11)$$

$$= -\ln\left\langle \exp\{-S[A^{\rm inst} + B] + S[A^{\rm inst}]\} \right\rangle.$$

3. ONE-LOOP RENORMALIZATION OF THE INSTANTON IN A NONPERTURBATIVE VACUUM

The general expression for the single-instanton field configuration has the well-known form

$$A_\mu^{\rm inst} = 2t^b R^{b\beta} \overline{\eta}_{\mu\nu}^\beta \frac{(x - x_0)_\nu}{(x - x_0)^2} f\left(\frac{(x - x_0)^2}{\rho^2} \right), \quad (12)$$

where

$$R^{b\beta} = 2{\rm tr}\left(\Omega t^\beta \Omega^\dagger t^b\right), \quad \Omega \in SU(N_c), \quad (13)$$

$$b = 1, 2, \ldots, N_c^2 - 1, \quad \beta = 1, 2, 3;$$

$\overline{\eta}_{\mu\nu}^\beta$ are the 't Hooft symbols; and x_0 is the center of an instanton. The matrix $R^{b\beta}$ realizes the embedding of an $SU(2)$ instanton into the $SU(N_c)$ group, this matrix satisfying the relations

$$f^{abc} R^{b\beta} R^{c\gamma} = \varepsilon^{\beta\gamma\delta} R^{a\delta}, \quad R^{b\beta} R^{b\gamma} = \delta^{\beta\gamma}, \quad (14)$$

$$f^{abc} R^{a\alpha} R^{b\beta} R^{c\gamma} = \varepsilon^{\alpha\beta\gamma}.$$

In the singular gauge, the profile function $f(z)$ satisfies the boundary conditions $f(0) = 1$ and $f(\infty) = 0$, and the respective classical solution has the form

$$f(z^2) = \frac{1}{1 + z^2}. \quad (15)$$

The probability of finding an instanton is determined by the classical action functional $S_{\rm cl}[A]$ on the manifold specified by the solution given by Eqs. (12) and (15); that is,

$$w \sim \exp\{-S_{\rm cl}[A_\mu^{\rm inst}]\} = \exp\{-8\pi^2/g_0^2\}. \quad (16)$$

The preexponential factor was calculated in [2]. The result for the single-instanton contribution to the QCD generating functional is $Z_{\rm I} = \int dn(\rho, x_0, R)$, where dn is the differential density of instantons,

$$dn(\rho, x_0, R) = [dR] d^4x_0 \frac{d\rho}{\rho^5} d_0(\rho), \quad (17)$$

$$d_0(\rho) = \frac{4.6 \exp\{-1.68 N_c\}}{\pi^2 (N_c - 1)! (N_c - 2)!} \left(\frac{8\pi^2}{g^2(\rho)} \right)^{2N_c} \quad (18)$$

[2)] Within the method of operator-product expansion and in QCD sum rules, a nonperturbative field is characterized by a set of local gluon condensates, $\langle G^2 \rangle$, $\langle G^3 \rangle$, ...

$$\times \exp\left\{-\frac{8\pi^2}{g^2(\rho)}\right\},$$

with $[dR]$ being the Haar measure of the $SU(N_c)$ group. In the two-loop approximation of gluodynamics, the coupling constant $g^2(\rho)$ has the form

$$\frac{8\pi^2}{g^2(\rho)} = b\ln\left(\frac{1}{\rho\Lambda}\right) + \frac{b_1}{b}\ln\ln\left(\frac{1}{\rho\Lambda}\right) + O\left(\frac{1}{\ln(1/\rho\Lambda)}\right), \quad (19)$$

$$b = \frac{11}{3}N_c, \qquad b_1 = \frac{17}{3}N_c,$$

where $\Lambda \equiv \Lambda_{\rm PV}$ corresponds to the Pauli–Villars regularization scheme, $\Lambda \sim 200$ MeV.

Callan, Dashen, and Gross were the first to show that, in a constant gauge field, an instanton behaves as a four-dimensional color dipole [4]. Shifman, Vainshtein, and Zakharov [18] generalized this result to the case where a small-size instanton ($\rho < 0.2$ fm) interacts with nonperturbative long-wave fluctuations described in terms of the local vacuum condensate $\langle G^2\rangle$. As a result, $d_0(\rho)$ is replaced by $d_{\rm eff}(\rho)$, where

$$d_{\rm eff}(\rho) \propto (\Lambda\rho)^b\left(1 + \frac{4\pi^4\langle G^2\rangle}{(N_c^2-1)g^4}\rho^4 + \cdots\right). \quad (20)$$

Thus, we arrive at the well-known problem of the inflation of the instanton size ρ.

Let us now consider the question of how the perturbative renormalization of the effective action for an instanton changes in a nonperturbative vacuum [20]. For this, we will make use of the background-field method that was developed in [22, 23] and which, for our purposes, was most conveniently formulated by Polyakov [23] in considering the phenomenon of asymptotic freedom in non-Abelian gauge theories.

In the absence of the term proportional to $F_{\mu\nu}[a_\mu, a_\nu]$, expression (6) for Z_1 involves four independent components of the field a_μ, and integration with respect to them yields $\left[\det^{-1/2}(\nabla_\mu^2)\right]^4$. Taking into account the ghost determinant in (6), we obtain $\left[\det^{-1/2}(\nabla_\mu^2)\right]^2$. It follows that, in accord with what might have been expected, there are in all two physical polarizations for the field a_μ rather than four. The last term in (6), that which is proportional to $F_{\mu\nu}[a_\mu, a_\nu]$, describes the interaction of an external field with the spin of the gluon a_μ.

Hence, there occur two effects. First, there is the motion of charged particles in an external electromagnetic field $F_{\mu\nu}$; in just the same way as orbital Landau diamagnetism, it leads to the emergence of screening. Second, there is a direct interaction of $F_{\mu\nu}$ with the spin of the field a_μ; in the second order in the external field, it yields an antiscreening term, as in the case of the Pauli paramagnetic effect. With a logarithmic accuracy, these two phenomena can be separated. In the absence of the term proportional to $F_{\mu\nu}[a_\mu, a_\nu]$ in (6), the expression for $S^{\rm P} = -\ln Z_1$ fully corresponds to the effective action in massless scalar electrodynamics with allowance for an isotopic factor. In the second order in the background field, the diamagnetic contribution to $S^{\rm P}$ can therefore be represented in the form

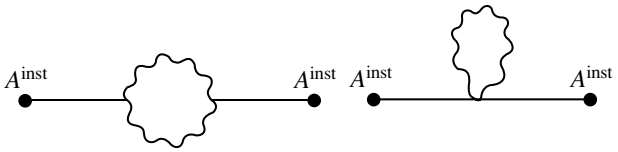

Fig. 1. Diagrams for $\Pi_{\rm dia}$.

$$S^{\rm P}_{\rm dia} = \int \frac{d^4q}{(2\pi)^4}\Pi^{ab}_{\mu\nu{\rm dia}}(q)\bar{A}^a_\mu(q)\bar{A}^b_\nu(-q), \quad (21)$$

where $\Pi_{\rm dia}$ is given by the diagrams in Fig. 1.

Let us first consider the simpler case of $\bar{A} = A^{\rm inst}$—that is, the case where the nonperturbative field B_μ is set to zero, $B_\mu = 0$—and show how the renormalization of the classical instanton action is reproduced within standard perturbation theory. We then have

$$\Pi^{ab}_{\mu\nu{\rm dia}}(q) = 2f^{acd}f^{bcd}\Pi^{({\rm sc})}_{\mu\nu}(q) = 2N_c\delta^{ab}\Pi^{({\rm sc})}_{\mu\nu}(q). \quad (22)$$

The factor of 2 in (22) stems from two physical polarizations of the field a_μ. The expression for the polarization operator in massless scalar electrodynamics has the form

$$\Pi^{({\rm sc})}_{\mu\nu}(q) = -\frac{1}{4}\int\frac{d^4p}{(2\pi)^4}\frac{(2p+q)_\mu(2p+q)_\nu}{p^2(p+q)^2} + \frac{1}{2}\delta_{\mu\nu}\int\frac{d^4p}{(2\pi)^4}\frac{1}{p^2} = \Pi_1(q^2)(q^2\delta_{\mu\nu} - q_\mu q_\nu). \quad (23)$$

The result for Π_1 in the leading-logarithm approximation is well known to be

$$\Pi_1(q^2) = \frac{1}{192\pi^2}\ln\frac{\Lambda_0^2}{q^2}, \quad (24)$$

where Λ_0 is an ultraviolet cutoff. Thus, we have

$$\Pi^{ab}_{\mu\nu{\rm dia}}(q) = 2N_c\delta^{ab}(q^2\delta_{\mu\nu} - q_\mu q_\nu)\Pi_1(q^2). \quad (25)$$

Considering that the linear part of $F_{\mu\nu}$ satisfies the relation

$$F^a_{\mu\nu}(q)F^b_{\mu\nu}(-q) = 2(q^2\delta_{\mu\nu} - q_\mu q_\nu)\bar{A}^a_\mu(q)\bar{A}^b_\nu(-q) \quad (26)$$

and substituting (25) and (26) into (21), we obtain

$$S^{\rm P}_{\rm dia} = \frac{1}{4}\int \frac{d^4q}{(2\pi)^4}\Pi_{\rm dia}(q^2)F^a_{\mu\nu}(q)F^a_{\mu\nu}(-q), \quad (27)$$

$$\Pi_{\rm dia}(q^2) = 4N_c\Pi_1(q^2) = \frac{N_c}{48\pi^2}\ln\frac{\Lambda_0^2}{q^2}.$$

We note that, in (27), the field strength involves only the linear part proportional to $\partial_\mu A_\nu$. From gauge and renormalization invariance, it is clear, however, that cubic and quartic terms (that is, those that are proportional to A^3 and A^4, respectively) will appear in the expression for $S^{\rm P}_{\rm dia}$ in such a way that they complement $F^2_{\mu\nu}$ to the standard non-Abelian form.

Following Polyakov [23], we represent the paramagnetic term in the form

$$S^{\rm P}_{\rm para} = -\frac{1}{2g_0^4}\int \frac{d^4q}{(2\pi)^4}F^a_{\mu\nu}(q)F^b_{\lambda\rho}(-q) \quad (28)$$
$$\times f^{acd}f^{bef}\langle a^c_\mu a^d_\nu(+q)a^e_\lambda a^f_\rho(-q)\rangle$$
$$\simeq -\frac{N_c}{4g_0^4}\int \frac{d^4q}{(2\pi)^4}F^a_{\mu\nu}(q)F^a_{\mu\nu}(-q)$$
$$\times\int \frac{d^4q}{(2\pi)^4}\frac{2g_0^4}{p(p+q)^2} = \frac{1}{4}\int\frac{d^4q}{(2\pi)^4}\Pi_{\rm para}(q^2)$$
$$\times F^a_{\mu\nu}(q)F^a_{\mu\nu}(-q),$$

where

$$\Pi_{\rm para}(q^2) = -\frac{N_c}{4\pi^2}\ln\frac{\Lambda_0^2}{q^2}. \quad (29)$$

Bringing all of the above results together, we arrive at the one-loop renormalization of the instanton action in the form

$$S^{\rm P} = \frac{1}{4}\int\frac{d^4q}{(2\pi)^4}\left(\frac{1}{g_0^2}+\Pi(q^2)\right)F^a_{\mu\nu}(q)F^a_{\mu\nu}(-q), \quad (30)$$

where

$$\Pi(q^2) = \Pi_{\rm dia}(q^2)+\Pi_{\rm para}(q^2) \quad (31)$$
$$= \frac{N_c}{\pi^2}\left(\frac{1}{48}-\frac{1}{4}\right)\ln\frac{\Lambda_0^2}{q^2} = -\frac{11}{3}N_c\frac{1}{16\pi^2}\ln\frac{\Lambda_0^2}{q^2}.$$

As might have been expected, an effective charge $g^2(q)$ defined at the external-field momentum q arises in $S^{\rm P}$:

$$\frac{1}{g^2(q)} = \frac{1}{g_0^2}-\frac{11}{3}N_c\frac{1}{16\pi^2}\ln\frac{\Lambda_0^2}{q^2}. \quad (32)$$

Using standard renormalization-group considerations, we perform a normalization to the momentum:

$$\Lambda = \Lambda_0\exp\left\{-\frac{8\pi^2}{bg^2(\Lambda_0)}\right\}. \quad (33)$$

We then have

$$\frac{1}{g^2(q)} = \frac{b}{16\pi^2}\ln\frac{q^2}{\Lambda^2}. \quad (34)$$

We further consider $S^{\rm P}$, treating the background field as an instanton. Since $F^2_{\mu\nu}$ is a gauge-invariant quantity, we employ the regular gauge

$$F^a_{\mu\nu}(x) = -4\eta^a_{\mu\nu}\frac{\rho^2}{(x^2+\rho^2)^2}. \quad (35)$$

Considering that the Fourier transform in four-dimensional Euclidean space is

$$f(q) = \int d^4x e^{iqx}f(x) = \frac{4\pi^2}{q}\int\limits_0^\infty r^2drf(r)J_1(qr), \quad (36)$$
$$r = |x|,$$

we obtain

$$F^a_{\mu\nu}(q) = \int d^4x e^{iqx}F^a_{\mu\nu}(x) \quad (37)$$
$$= -16\pi^2\eta^a_{\mu\nu}\frac{\rho^2}{q}\int\limits_0^\infty\frac{r^2dr}{(r^2+\rho^2)^2}J_1(qr)$$
$$= -8\pi^2\eta^a_{\mu\nu}\rho^2K_0(\rho q),$$

where $K_0(x)$ is a modified Bessel function of the first kind. It can easily be proven that, on the manifold specified by the solution in (37), the classical action functional takes the standard instanton value; that is,

$$S_{\rm cl}[A^{\rm inst}] = \frac{1}{4g_0^2}\int\frac{d^4q}{(2\pi)^4}F^a_{\mu\nu}(q)F^a_{\mu\nu}(-q) \quad (38)$$

$$= \frac{8\pi^2}{g_0^2}3\rho^4\int\limits_0^\infty q^3dqK_0^2(\rho q) = \frac{8\pi^2}{g_0^2}$$
$$\times\left(\int\limits_0^\infty q^3dqK_0^2(\rho q) = \frac{1}{3\rho^4}\right).$$

Substituting (37) into (30), we obtain

$$S^{\rm P}[A^{\rm inst}] = 8\pi^2\cdot 3\rho^4\int\limits_0^\infty q^3dqK_0^2(\rho q)\frac{1}{g^2(q)}. \quad (39)$$

Let us introduce the dimensionless variable $x = \rho q$ and rewrite (39) in the form

$$S^{\rm P}[A^{\rm inst}] = 8\pi^2\cdot 3\int\limits_0^\infty x^3dxK_0^2(x)\frac{1}{g^2(x/\rho)}, \quad (40)$$

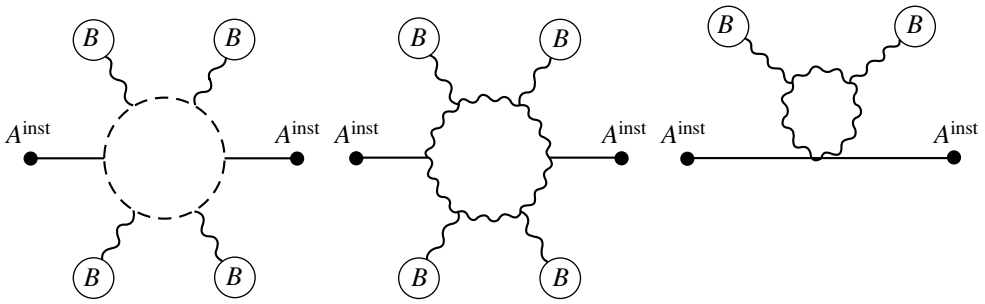

Fig. 2. Diagrams for the polarization operator in a nonperturbative background field, $\Pi_{\rm NP}$.

where

$$\frac{1}{g^2(x/\rho)} = \frac{b}{16\pi^2}\ln\frac{x^2}{\Lambda^2\rho^2} \tag{41}$$
$$= \frac{b}{16\pi^2}\ln\frac{1}{\Lambda^2\rho^2} + \frac{b}{16\pi^2}\ln x^2.$$

Thus, we eventually arrive at

$$S^{\rm P}(\rho) = \frac{8\pi^2}{g^2(\rho)} + \text{const} = b\ln\frac{1}{\Lambda\rho} + \text{const}. \tag{42}$$

We have reproduced the standard expression for $S^{\rm P}(\rho)$. In the instanton density $d(\rho)$, the constant from Eq. (42) appears as a preexponential factor and is immaterial in our approach. We will now show how the relations obtained above change upon taking into account nonperturbative vacuum fluctuations.

In [24], it was shown that, in a nonperturbative vacuum, the polarization operator decreases exponentially in the infrared region in proportion to $|x-y|^{-4}\exp\{-m_*|x-y|\}$, where $m_* \simeq 0.75m_{0^{++}} \sim 1$ GeV, with 0^{++} being the lightest glueball with vacuum quantum numbers (see Appendix 1), instead of showing a standard power-law behavior of the form $|x-y|^{-4}$. We will employ this phenomenon in considering instantons in a nonperturbative vacuum. As can be seen from (10), averaging over the field B is performed—that is, the polarization operator in (30) is represented by the diagrams in Fig. 2.

In expression (30) for the effective action, we must therefore replace the perturbative expression for the polarization operator by $\Pi_{\rm NP}(q^2)$,

$$\Pi_{\rm NP}(q^2) \simeq \frac{11}{3}N_c\frac{1}{16\pi^2}\ln\frac{q^2+m_*^2}{\Lambda_0^2}, \tag{43}$$

which is the polarization operator in a nonperturbative background field as calculated in [24].

The effective action (30) can then be represented as

$$S^{\rm P}_{\rm eff}[A^{\rm inst}] = \frac{1}{4}\int\frac{d^4q}{(2\pi)^4}F^a_{\mu\nu}(q)F^a_{\mu\nu}(-q)\frac{1}{g^2_{\rm NP}(q^2)}, \tag{44}$$

where

$$\frac{1}{g^2_{\rm NP}(q^2)} = \frac{b}{16\pi^2}\ln\frac{q^2+m_*^2}{\Lambda^2}. \tag{45}$$

Substituting the Fourier transform (37) of the instanton field into (44) and introducing the variable $x=\rho q$, we obtain

$$S^{\rm P}_{\rm eff}[A^{\rm inst}] = 24\pi^2\int_0^\infty x^3dxK_0^2(x)\frac{1}{g^2_{\rm NP}(x)}, \tag{46}$$
$$\frac{1}{g^2_{\rm NP}(x)} = \frac{b}{16\pi^2}\ln\frac{x^2+m_*^2\rho^2}{\Lambda^2\rho^2}.$$

Since ln is a slowly varying function and since the characteristic region of integration in (46) lies around the point $x\sim 1$ ($K_0(x\gg 1)\simeq\sqrt{\pi/2x}e^{-x}$), the factor $1/g^2_{\rm NP}(x)$ can be taken, with a logarithmic accuracy, outside the integral sign at the characteristic point $x=1$. In this way, we obtain [19, 20]

$$S^{\rm P}_{\rm eff}(\rho) = \frac{8\pi^2}{g^2_{\rm NP}(1)} = \frac{b}{2}\ln\frac{1/\rho^2+m_*^2}{\Lambda^2}. \tag{47}$$

From (47), it follows that the perturbative result (42) is recovered for small-size instantons ($\rho \ll 1/m_*$) and that the quantity $S^{\rm P}_{\rm eff}$ tends to a constant for $\rho \gg 1/m_*$.

A derivation of formula (47) in coordinate space is given in Appendix 1.

Table 1. Lattice data from [28] for the correlation length

	T_g, fm
$SU(2)$ "quenched"	0.16 ± 0.02
$SU(3)$ "quenched"	0.22 ± 0.02
$SU(3)$ "full"	0.34

4. INSTANTON INTERACTION WITH NONPERTURBATIVE VACUUM FIELDS

We will now consider the effect of nonperturbative fields on instantons; that is, we will calculate $\langle Z_2\rangle$. In this study, we will use the method of vacuum correlation functions that was proposed by Dosch and Simonov [25]. The QCD vacuum is described in terms of gauge-invariant vacuum expectation values of gluon fields (correlation functions),

$$\Delta_{\mu_1\nu_1\ldots\mu_n\nu_n} = \langle \mathrm{tr} G_{\mu_1\nu_1}(x_1)\Phi(x_1,x_2) \times G_{\mu_2\nu_2}(x_2)\ldots G_{\mu_n\nu_n}(x_n)\Phi(x_n,x_1)\rangle,$$

where $G_{\mu\nu}$ is the tensor of the gluon-field strength and $\Phi(x,y) = P\exp\left(i\int_y^x B_\mu dz_\mu\right)$ is the parallel transporter, which is necessary for preserving gauge invariance. In order to explain the effects being considered, it is sufficient, in many cases, to retain only a bilocal correlation function. Moreover, there exist some pieces of evidence that corrections arising upon taking into account higher correlation functions are quite modest, amounting to a few percent in a number of cases [10, 26].

The most general form of the bilocal correlation function, whose tensor structure follows from antisymmetry with respect to Lorentz indices, is

$$\langle g^2 G^a_{\mu\nu}(x,x_0)G^b_{\rho\sigma}(y,x_0)\rangle = \langle G^2\rangle\frac{\delta^{ab}}{N_c^2-1} \times \left\{\frac{D(z)}{12}(\delta_{\mu\rho}\delta_{\nu\sigma}-\delta_{\mu\sigma}\delta_{\nu\rho}) + \frac{\bar D(z)}{6} \times (n_\mu n_\rho\delta_{\nu\sigma} + n_\nu n_\sigma\delta_{\mu\rho} - n_\mu n_\sigma\delta_{\nu\rho} - n_\nu n_\rho\delta_{\mu\sigma})\right\}, \quad (48)$$

where

$$G_{\mu\nu}(x,x_0) = \Phi(x_0,x)G_{\mu\nu}(x)\Phi(x,x_0); \quad (49)$$

$n_\mu = z_\mu/|z| = (x-y)_\mu/|x-y|$ is a unit vector; $\langle G^2\rangle \equiv \langle g^2 G^a_{\mu\nu}G^a_{\mu\nu}\rangle$; and, as follows from the normalization condition, $D(0)+\bar D(0) = 1$. The equations that relate the functions $D(z)$ and $\bar D(z)$ to the standard functions $D(z)$ and $D_1(z)$, which are used in [25–28], are given in Appendix 2.

The functions $D(z)$ and $\bar D(z)$ contain both a perturbative and a nonperturbative contribution. In the following, we do not take into account the perturbative part, since it has already been included in $S^{\mathrm{P}}_{\mathrm{eff}}$. Data on the nonperturbative components of the functions in question come predominantly from numerical lattice calculations. The gluon condensate $\langle G^2\rangle$ is also determined from lattice data, but there is also an independent estimate of this quantity from an analysis of the charmonium spectrum on the basis of QCD sum rules: $\langle G^2\rangle \simeq 0.5$ GeV^4 [29]. According to data from lattice calculations, the functions $D(z)$ and $\bar D(z)$ decrease exponentially: $D(z) = A_0\exp(-z/T_g)$ and $\bar D(z) = A_1 z\exp(-z/T_g)/T_g$, where T_g is the correlation length, whose value was determined in the lattice calculations performed in [27, 30] and was estimated analytically in [31] at $T_g \sim 0.2$ fm. In addition, it follows from lattice calculations that $A_1 \ll A_0$ ($A_1 \sim A_0/10$). The results of the lattice calculations from the article of Di Giacomo [28] are given in Table 1, where the $SU(3)$ "full" row corresponds to chromodynamics featuring four quarks, while the $SU(2)$ and $SU(3)$ "quenched" rows refer to, respectively, pure $SU(2)$ and pure $SU(3)$ gluodynamics. The bilocal correlation function was also determined on a lattice without invoking the procedure of cooling [30], and a value of about 0.1 to 0.2 fm was found for the correlation length in the approximation where no account is taken of dynamical quarks.

The value of $\langle G^2\rangle = 1.02\pm0.1$ GeV^4, which was obtained by Narison [32] on the basis of sum rules, is in good agreement with the gluon-condensate value of $\langle G^2\rangle = 0.87$ GeV^4 from the lattice calculations performed in [27] for $SU(3)$ QCD.

In order to calculate the quantity $S^{\mathrm{NP}}_{\mathrm{eff}}$ given by (11), we make use of a cluster expansion, which is well known in statistical physics [33]; that is,

$$\langle\exp(x)\rangle = \exp\left(\sum_n \frac{\langle\langle x^n\rangle\rangle}{n!}\right), \quad (50)$$

where $\langle x\rangle = \langle\langle x\rangle\rangle$, $\langle x^2\rangle = \langle\langle x^2\rangle\rangle + \langle x\rangle^2$, $\langle x^3\rangle = \langle\langle x^3\rangle\rangle + 3\langle x\rangle\langle\langle x^2\rangle\rangle + \langle x\rangle^3$, ...

The coefficients in the cluster expansion can easily be determined upon representing it in the form

$$\langle 1\rangle = \langle\langle 1\rangle\rangle, \quad \langle 1\,2\rangle = \langle\langle 1\,2\rangle\rangle + \langle 1\rangle\langle 2\rangle, \quad (51)$$
$$\langle 1\,2\,3\rangle = \langle\langle 1\,2\,3\rangle\rangle + \langle 1\rangle\langle\langle 2\,3\rangle\rangle + \langle 2\rangle\langle\langle 1\,3\rangle\rangle + \langle 3\rangle\langle\langle 1\,2\rangle\rangle + \langle 1\rangle\langle 2\rangle\langle 3\rangle, \ldots.$$

Further, we will slightly modify expression (11) for $S^{\mathrm{NP}}_{\mathrm{eff}}$ by supplementing the expression in the relevant exponent with $S[B]$; that is,

$$S^{\mathrm{NP}}_{\mathrm{eff}}[A^{\mathrm{inst}}] = -\ln\left\langle\exp\{-S[A^{\mathrm{inst}}+B] + S[A^{\mathrm{inst}}] + S[B]\}\right\rangle. \quad (52)$$

In the bilocal approximation, this modification will change only the normalization of the generating func-

tional,[3)] but this is immaterial for the ensuing analysis.

The nonperturbative part of the effective instanton action has the form

$$S_{\rm eff}^{\rm NP} = \langle S[A^{\rm inst}+B] - S[B] - S[A^{\rm inst}]\rangle \quad (53)$$
$$-\frac{1}{2}\Big(\Big\langle (S[A^{\rm inst}+B] - S[B] - S[A^{\rm inst}])^2\Big\rangle$$
$$-\Big\langle S[A^{\rm inst}+B] - S[B] - S[A^{\rm inst}]\Big\rangle^2\Big) + \ldots.$$

We retain only the term $\frac{1}{2}\langle\langle\big(S[A^{\rm inst}+B] - S[B] - S[A^{\rm inst}]\big)^2\rangle\rangle$, discarding higher order terms. The next terms of the cluster expansion decrease in proportion to $1/g^{2n}$. In [21], it is shown that, at the scale of the characteristic instanton size, the coupling constant is $g^2(\rho_c)\sim 4$; therefore, $1/g^2$ is a small parameter. There is yet another small parameter, $1/N_c$.

Using the Fock–Schwinger gauge $x_\mu A_\mu = x_\mu B_\mu = 0$ (which automatically holds for the instanton field $A_\mu^{\rm inst}$ by virtue of the properties of the 't Hooft symbols) and considering that

$$S[A^{\rm inst}+B] - S[B] - S[A^{\rm inst}] \quad (54)$$
$$= \frac{1}{2g^2}\int d^4x {\rm tr}\Big\{-([A_\mu^{\rm inst}, B_\nu] - [A_\nu^{\rm inst}, B_\mu])^2$$
$$+ 2F_{\mu\nu}[A^{\rm inst}]G_{\mu\nu}[B]$$
$$- 4i(F_{\mu\nu}[A^{\rm inst}] + G_{\mu\nu}[B])[A_\mu^{\rm inst}, B_\nu]\Big\},$$

we obtain

$$S_{\rm eff}^{\rm NP} = S_{\rm dia} + \frac{1}{2}S_{\rm dia}^2 + S_{\rm para} + S_1 + S_2, \quad (55)$$

where, in the bilocal approximation, we have

$$S_{\rm dia} = -\frac{1}{2g^2}\int d^4x \quad (56)$$
$$\times\Big\langle {\rm tr}\Big[\big([A_\mu^{\rm inst}, B_\nu] - [A_\nu^{\rm inst}, B_\mu]\big)^2\Big]\Big\rangle,$$

$$S_{\rm para} = -\frac{1}{2g^4}\int d^4x d^4y \quad (57)$$
$$\times\Big\langle {\rm tr}\big(F_{\mu\nu}^{\rm inst}(x)G_{\mu\nu}(x)\big){\rm tr}\big(F_{\rho\sigma}^{\rm inst}(y)G_{\rho\sigma}(y)\big)\Big\rangle,$$

$$S_1 = \frac{2}{g^4}\int d^4x d^4y \quad (58)$$
$$\times\Big\langle {\rm tr}\big(F_{\mu\nu}^{\rm inst}[A_\mu^{\rm inst}, B_\nu]\big)_x {\rm tr}\big(F_{\rho\sigma}^{\rm inst}[A_\rho^{\rm inst}, B_\sigma]\big)_y\Big\rangle,$$

$$S_2 = \frac{2i}{g^4}\int d^4x d^4y \quad (59)$$
$$\times\Big\langle {\rm tr}\big(F_{\mu\nu}^{\rm inst}G_{\mu\nu}\big)_x {\rm tr}\big(F_{\rho\sigma}^{\rm inst}[A_\rho^{\rm inst}, B_\sigma]\big)_y\Big\rangle.$$

We use the notation $S_{\rm dia}$ (diamagnetic) and $S_{\rm para}$ (paramagnetic) for the contributions in (56) and (57) to instanton interaction with the background field. The physical motivation behind this notation is discussed in detail elsewhere [20].

Here, it is also considered that

$$\langle {\rm tr}(G_{\mu\nu}(A_\mu^{\rm inst}B_\nu - B_\nu A_\mu^{\rm inst}))\rangle \quad (60)$$
$$= i\frac{g^3}{2}f^{abc}\langle G_{\mu\nu}^a B_\nu^c\rangle A_\mu^{{\rm inst}\,b} \propto f^{abc}\delta^{ac} = 0.$$

In the Fock–Schwinger gauge, we have

$$B_\mu(x) = x_\nu\int_0^1 \alpha d\alpha G_{\nu\mu}(\alpha x). \quad (61)$$

In the following, we therefore replace the vacuum expectation values in (56)–(59) by correlation functions. In general, the instanton field has the form

$$A_\mu^{\rm inst}(x) = \Phi(x, x_0)A_\mu^{\rm sing}(x - x_0)\Phi(x_0, x), \quad (62)$$

where $\Phi(x, y)$ is the parallel transporter and $A_\mu^{\rm sing}(x - x_0)$ is an instanton in the gauge fixed by Eqs. (12) and (15) (singular gauge). For the field-strength tensor, we then have

$$F_{\mu\nu}^{\rm inst} = \partial_\mu A_\nu^{\rm inst} - \partial_\nu A_\mu^{\rm inst} - i[A_\mu^{\rm inst}, A_\nu^{\rm inst}] \quad (63)$$
$$= \Phi(x, x_0)F_{\mu\nu}^{\rm sing}(x - x_0)\Phi(x_0, x) + \ldots.$$

Here, the ellipsis stands for terms that involve the background field B and which lead to higher order correlation functions [20]—recall that we retain only a bilocal correlation function.

Together with the background field, the parallel transporter forms gauge-invariant combinations, which, upon averaging, are replaced by bilocal correlation functions. By way of example, we indicate that, for $S_{\rm para}$, we have

$$S_{\rm para} = -\frac{1}{2g^4}\int d^4x d^4y\big\langle {\rm tr}\,(F_{\mu\nu}(x)G_{\mu\nu}(x)) \quad (64)$$
$$\times {\rm tr}\,(F_{\rho\sigma}(y)G_{\rho\sigma}(y))\,\big\rangle = -\frac{1}{2g^4}\int d^4x d^4y$$
$$\times\big\langle {\rm tr}\,\big(\Phi(x, x_0)F_{\mu\nu}^{\rm sing}(x - x_0)\Phi(x_0, x)G_{\mu\nu}(x)\big)$$
$$\times {\rm tr}\,\big(\Phi(y, x_0)F_{\rho\sigma}^{\rm sing}(y - x_0)\Phi(x_0, y)G_{\rho\sigma}(y)\big)\big\rangle$$
$$= -\frac{1}{2g^4}\int d^4x d^4y\big\langle {\rm tr}\,\big(F_{\mu\nu}^{\rm sing}(x - x_0)G_{\mu\nu}(x, x_0)\big)$$
$$\times {\rm tr}\,\big(F_{\rho\sigma}^{\rm sing}(y - x_0)G_{\rho\sigma}(y, y_0)\big)\,\big\rangle = -\frac{1}{8g^2}$$

[3)] In order to demonstrate this, we indicate that, if one employs expression (11) as a starting point, then, in the bilocal approximation, additional terms of the form $\langle G^2\rangle\int d^4x$ will appear in (55); since these terms are independent of $A^{\rm inst}$, they only lead to a change in the normalization of Z_2.

$$\times \int d^4x d^4y \left(F^{\rm sing}_{\mu\nu}(x-x_0)\right)^a \left(F^{\rm sing}_{\rho\sigma}(y-x_0)\right)^b$$
$$\times \left\langle g^2 G^a_{\mu\nu}(x,x_0) G^b_{\rho\sigma}(y,x_0)\right\rangle.$$

Similar calculations for the various contributions to $S^{\rm NP}_{\rm eff}$ in (55) that are expressed in terms of the gauge-invariant bilocal correlation function lead to the following expressions (in order to avoid encumbering the notation used, we will henceforth everywhere suppress the superscript "sing" on the instanton field in the singular gauge; that is, $A^{\rm sing}_\mu \equiv A_\mu$):

$$S_{\rm dia} = \frac{1}{2}\int d^4x \int\limits_0^1 \alpha d\alpha \int\limits_0^1 \beta d\beta f^{abc} f^{dec} \qquad (65)$$
$$\times \left(A^a_\mu A^d_\mu x_\lambda x_\rho \langle g^2 G^b_{\lambda\nu}(\alpha x, x_0) G^e_{\rho\nu}(\beta x, x_0)\rangle\right.$$
$$\left. - A^a_\mu A^d_\nu x_\lambda x_\rho \langle g^2 G^b_{\lambda\nu}(\alpha x, x_0) G^e_{\rho\mu}(\beta x, x_0)\rangle\right),$$
$$S_{\rm para} = -\frac{1}{8g^2}\int d^4x d^4y F^a_{\mu\nu}(x) F^b_{\rho\sigma}(y) \qquad (66)$$
$$\times \langle g^2 G^a_{\mu\nu}(x,x_0) G^b_{\rho\sigma}(y,x_0)\rangle,$$
$$S_1 = -\frac{1}{2}\int d^4x d^4y F^a_{\mu\nu}(x) A^b_\mu(x) F^d_{\rho\sigma}(y) \qquad (67)$$
$$\times A^e_\rho(y) f^{abc} f^{def} \int\limits_0^1 \alpha d\alpha \int\limits_0^1 \beta d\beta x_\xi y_\eta$$
$$\times \langle g^2 G^c_{\xi\nu}(\alpha x, x_0) G^f_{\eta\sigma}(\beta y, x_0)\rangle,$$
$$S_2 = -\frac{1}{2g}\int d^4x d^4y \int\limits_0^1 \alpha d\alpha F^a_{\mu\nu}(x) F^b_{\rho\sigma}(y) \qquad (68)$$
$$\times f^{bcd} A^c_\rho(y) y_\xi \langle g^2 G^a_{\mu\nu}(x,x_0) G^d_{\xi\sigma}(\alpha y, x_0)\rangle.$$

Using expression (48) for the gauge-invariant condensate $\langle g^2 G^a_{\mu\nu}(x,x_0) G^b_{\rho\sigma}(y,x_0)\rangle$, we obtain

$$S_{\rm dia} = \frac{\langle G^2\rangle}{12}\frac{N_c}{N_c^2-1} \qquad (69)$$
$$\times \int d^4x \int\limits_0^1 \alpha d\alpha \int\limits_0^1 \beta d\beta x^2 (A^a_\mu(x))^2$$
$$\times [D((\alpha-\beta)x) + 2\bar{D}((\alpha-\beta)x)],$$
$$S_{\rm para} = -\frac{\langle G^2\rangle}{48g^2}\frac{1}{N_c^2-1}\int d^4x d^4y \qquad (70)$$
$$\times \left[F^a_{\mu\nu}(x) D(x-y) F^a_{\mu\nu}(y)\right.$$
$$\left. + 4\frac{(x-y)_\mu (x-y)_\rho}{(x-y)^2} F^a_{\mu\nu}(x) \bar{D}(x-y) F^a_{\rho\nu}(y)\right],$$
$$S_1 = -\frac{\langle G^2\rangle}{24}\frac{1}{N_c^2-1} \qquad (71)$$
$$\times \int d^4x d^4y \int\limits_0^1 \alpha d\alpha \int\limits_0^1 \beta d\beta (xy\delta_{\nu\sigma} - x_\sigma y_\nu) f^{abe}$$
$$\times f^{cde} F^a_{\mu\nu}(x) A^b_\mu(x) F^c_{\rho\sigma}(y) A^d_\rho(y)$$
$$\times D(\alpha x - \beta y) + O(\bar{D}),$$
$$S_2 = \frac{\langle G^2\rangle}{12g}\frac{1}{N_c^2-1}\int d^4x d^4y f^{abc} F^a_{\rho\sigma}(y) \qquad (72)$$
$$\times A^b_\rho(y) F^c_{\sigma\nu}(x) y_\nu \int\limits_0^1 \alpha d\alpha D(x-\alpha y) + O(\bar{D}).$$

Here, it is considered that

$$x_\mu \tilde{B}_\mu(x) \equiv x_\mu \left(\Phi(x_0,x) B_\mu(x) \Phi(x_0,x)\right) \qquad (73)$$
$$= \Phi(x_0,x)\left(x_\mu B_\mu(x)\right)\Phi(x_0,x) = 0,$$

whence it follows that

$$\tilde{B}_\mu(x) = x_\nu \int \alpha d\alpha \tilde{G}_{\mu\nu}(\alpha x) \qquad (74)$$
$$= x_\nu \int \alpha d\alpha G_{\mu\nu}(\alpha x, x_0) + \ldots,$$

where, similarly to (63), we have

$$\tilde{G}_{\mu\nu}(x) = \partial_\nu \tilde{B}_\mu - \partial_\mu \tilde{B}_\nu - i[\tilde{B}_\mu, \tilde{B}_\nu] \qquad (75)$$
$$= \Phi(x_0,x) G_{\mu\nu}(x) \Phi(x,x_0) + \ldots$$
$$= G_{\mu\nu}(x,x_0) + \ldots.$$

Thus, we have obtained, in the bilocal approximation, the effective action for an instanton in a nonperturbative vacuum.[4)] From a numerical analysis, it can be seen that the characteristic size of an instanton in QCD is $\rho_c \sim 0.25$–0.3 fm. The field at the center of an instanton of this size is strong, $F^2_{\mu\nu}(x = x_0, \rho_c) = 192/\rho_c^4 \gg \langle G^2\rangle$; therefore, the classical instanton solution is not severely deformed in the region $|x| < \rho$, which makes a dominant contribution to the integrals in (69)–(72).

The asymptotic behavior of the instanton solution far off the center, $|x| \gg \rho$, was comprehensively studied in [16, 34, 35]. Our calculations reveal that the asymptotic behavior of the classical instanton solution has virtually no effect on ρ_c at reasonable values of the condensate $\langle G^2\rangle$ and of the correlation length T_g.

Further, it is necessary to determine the function $D(z)$. We take the Gaussian form $D(z) = \exp(-\mu^2 z^2)$, $\mu \equiv 1/T_g$. The function $D(z)$ decreases monotonically, the characteristic correlation length being T_g. Numerical calculations reveal that the exact

[4)] The tensor structure of an instanton was used to derive expressions (69)–(72).

form of $D(z)$ and the inclusion of $\bar{D}(z)$ have but a slight effect on the characteristic instanton size ρ_c in a nonperturbative vacuum (see Appendix 3).

We make use of the standard profile function $f = \rho^2/(\rho^2 + x^2)$. Of course, the true profile of an instanton (that is, that which minimizes the action functional) differs from this one, but an investigation of the dependence of S_{eff} on ρ will make it possible to establish the character of the behavior of instantons (inflation versus stabilization) and to estimate the characteristic size of instantons in a nonperturbative vacuum.

Upon integration with respect to spatial angles, we arrive at

$$S_{\text{dia}} = \frac{2\pi^2}{g^2}\frac{\langle G^2\rangle}{\mu^4}\frac{N_c}{N_c^2-1}\zeta^4\int\limits_0^\infty dx\frac{x^3}{(x^2+\zeta^2)^2}\varphi(x), \tag{76}$$

$$S_{\text{para}} = \frac{-16\pi^4}{g^4}\frac{\langle G^2\rangle}{\mu^4}\frac{1}{N_c^2-1}\zeta^4 \times\int\limits_0^\infty dxdy\frac{x^2y^2e^{-(x^2+y^2)}I_3(2xy)}{(x^2+\zeta^2)^2(y^2+\zeta^2)^2}, \tag{77}$$

$$S_1 = \frac{-64\pi^4}{g^4}\frac{\langle G^2\rangle}{\mu^4}\frac{1}{N_c^2-1}\zeta^8 \times\int\limits_0^\infty dxdy\frac{x^2y^2}{(x^2+\zeta^2)^3(y^2+\zeta^2)^3} \times\int\limits_0^1 d\alpha\int\limits_0^1 d\beta e^{-(\alpha^2x^2+\beta^2y^2)} \times(I_1(2\alpha\beta xy)+I_3(2\alpha\beta xy)), \tag{78}$$

$$S_2 = \frac{-64\pi^4}{g^4}\frac{\langle G^2\rangle}{\mu^4}\frac{1}{N_c^2-1}\zeta^6 \times\int\limits_0^\infty dxdy\frac{x^2y^2e^{-x^2}}{(x^2+\zeta^2)^2(y^2+\zeta^2)^3} \times\int\limits_0^1 d\alpha e^{-\alpha^2y^2}I_3(2\alpha xy), \tag{79}$$

where $I_n(x) = e^{-i\pi n/2}J_n(ix)$ is a Bessel function of an imaginary argument (Infeld function); $\zeta \equiv \mu\rho$; and

$$\varphi(x) = \int\limits_0^1 \alpha d\alpha\int\limits_0^1 \beta d\beta e^{-(\alpha-\beta)^2x^2} \tag{80}$$

$$= e^{-x^2}\left(\frac{1}{3x^2}-\frac{1}{6x^4}\right)+\frac{1}{6x^4}-\frac{1}{2x^2}+\frac{2}{3x}\Phi(x),$$

with $\Phi(x) = \int\limits_0^x e^{-\xi^2}d\xi$ being the error function.

We have investigated the asymptotic behavior of the effective instanton action and its dependence on the dimensionless parameter $\zeta \equiv \mu\rho$. For small-size instantons, $\rho \ll 1/\mu$ ($\zeta \to 0$), we have

$$S_{\text{dia}} \to -\frac{\pi^2}{2g^2}\frac{N_c}{N_c^2-1}\langle G^2\rangle\rho^4\ln(\mu\rho), \tag{81}$$

$$S_{\text{para}} + S_1 + S_2 \to -\frac{2\pi^4}{g^4}\frac{\langle G^2\rangle}{N_c^2-1}\rho^4 + O\left(\langle G^2\rangle\rho^4(\mu\rho)\right). \tag{82}$$

In the opposite case of large instanton sizes, $\rho \gg 1/\mu$ ($\zeta \to \infty$), the corresponding results are

$$S_{\text{dia}} \to \frac{\pi^{7/2}}{6g^2}\frac{N_c}{N_c^2-1}\langle G^2\rangle\frac{\rho^3}{\mu}, \tag{83}$$

$$S_{\text{para}} + S_1 + S_2 \to \text{const}. \tag{84}$$

The differential instanton density is given by $dn/d^4zd\rho \propto \exp(-S_{\text{eff}})$. Thus, the growth of S_{dia} with increasing instanton size ρ means that the diamagnetic interaction of instantons with nonperturbative fields leads to an infrared stabilization with respect to the size ρ.

5. DISCUSSION AND CONCLUSION

In the present study, we have explored the behavior of an instanton in a nonperturbative vacuum parametrized in terms of gauge-invariant vacuum expectation values of the gluon-field strengths. We have derived the effective instanton action in the bilocal approximation and shown that the diamagnetic term S_{dia} leads to an infrared stabilization of instantons.

Our numerical results for S_{eff} are given in Fig. 3. The three curves correspond to $S_{\text{eff}}^{\text{P}}(\rho)$, $S_{\text{eff}}^{\text{NP}}(\rho)$, and $S_{\text{eff}}(\rho) = S_{\text{eff}}^{\text{P}}(\rho) + S_{\text{eff}}^{\text{NP}}(\rho)$ in the case of $SU(3)$ gluodynamics at $\langle G^2\rangle = 1.0$ GeV^4 and $T_g = 0.3$ fm.

In Table 2, the values of ρ_c are presented for various values of $\langle G^2\rangle$ and T_g in the case of $SU(3)$ gluodynamics. The values of ρ_c for $N_f = 2$ QCD are listed in Table 3.

The differential instanton density $dn/d^4zd\rho \propto \exp(-S_{\text{eff}})$ and the corresponding lattice data from [36] are shown in Fig. 4. All of the graphs are normalized to the generally accepted instanton density of 1 fm^{-4}. An instanton size of $\bar{\rho} \sim 1/3$ fm was first obtained by Polikarpov and Veselov [37] from numerical lattice calculations. It is worth noting that, over the past years, lattice calculations yielded different results (see [38]). For the instanton size, different groups quote results that agree within a

Table 2. Values of ρ_c (in fm) for various values of T_g and $\langle G^2\rangle$ ($N_c = 3$, $N_f = 0$)

T_g, fm	$\langle G^2\rangle$, GeV^4			
	0.5	1.0	1.5	2.0
0.10	0.305	0.256	0.230	0.213
0.15	0.282	0.236	0.213	0.197
0.20	0.268	0.226	0.204	0.189
0.25	0.256	0.219	0.198	0.184
0.30	0.254	0.215	0.194	0.181
0.35	0.250	0.212	0.191	0.178

Table 3. Values of ρ_c (in fm) for various values of T_g and $\langle G^2\rangle$ ($N_c = 3$, $N_f = 2$)

T_g, fm	$\langle G^2\rangle$, GeV^4			
	0.5	1.0	1.5	2.0
0.10	0.308	0.258	0.232	0.215
0.15	0.284	0.238	0.215	0.199
0.20	0.270	0.227	0.205	0.191
0.25	0.262	0.221	0.199	0.185
0.30	0.256	0.216	0.195	0.182
0.35	0.252	0.213	0.192	0.179

factor of 2—for example, $\bar\rho = 0.3$–0.6 fm for $SU(3)$ gluodynamics. In what is concerned with the density N/V, there is absolutely no agreement. The general trend is the following: lattice calculations yield higher instanton densities and larger instanton sizes than what is implied by phenomenology.

Thus, our result for ρ_c agrees with the phenomenological value $\bar\rho$ and with lattice data. Moreover, we can adduce some physical arguments that explain the existing discrepancies with some lattice data leading to instanton sizes larger than their phenomenological counterparts. Lattice calculations involve the cooling procedure, within which one discards some lattice configurations of the gluon field. This procedure may change the value of the gluon condensate $\langle G^2\rangle$. As a result, the size distribution of instantons is calculated at the gluon-condensate value $\langle G^2\rangle_{\rm cool}$, which differs from the physical value $\langle G^2\rangle$. It should be noted that the uncooled size distribution of instantons was studied by Ringwald and Schrempp [39], who introduced a scaling variable ("cooling radius"), which may help to single out information about the uncooled distribution.

Figure 5 shows ρ_c as a function of $\langle G^2\rangle$ for various values of T_g. It can be seen that an increase in $\langle G^2\rangle$ leads to a decrease in the instanton size, this effect being due to the nonlocal diamagnetic interaction of instantons with nonperturbative fields. Figure 6 displays ρ_c as a function of T_g for various values of $\langle G^2\rangle$. The smaller the value of T_g, the larger the instanton size. Physically, it is clear that less correlated nonperturbative fields ($T_g \to 0$) have a less pronounced effect on the instanton configuration occupying a four-dimensional Euclidean volume of characteristic size $\rho\,(\rho \gg T_g)$. On the other hand, perturbative quantum fluctuations tend to inflate the instanton; therefore, ρ_c increases with decreasing T_g.

In the present study, we have not gone beyond the bilocal approximation. As was indicated above, this approximation is sufficient not only for a qualitative but also for a quantitative description of some phenomena in nonperturbative QCD [26]. In the problem being considered, there are two small parameters. These are $1/g^2(\rho_c) \sim 0.15$–0.25 and $1/N_c$, and their powers increase in higher terms of the cluster expansion. Moreover, one can estimate leading terms in the cluster expansion. From our numerical calculations, it follows that the terms $S_{\rm dia}$, $\frac{1}{2}S^2_{\rm dia}$, $\frac{1}{3}S^3_{\rm dia}$, etc., are dominant in the region $\rho \gtrsim \rho_c$. Summing them, we obtain $S_{\rm dia} + \frac{1}{2}S^2_{\rm dia} + \frac{1}{3}S^3_{\rm dia} + \ldots = -\ln(1 - S_{\rm dia})$. Thus, not only does the inclusion of higher order terms of the cluster expansion preserve stabilization, but this even leads to a reduction of ρ_c. We can therefore conclude that the proposed model describes the physics of the stabilization of an individual instanton in a nonperturbative vacuum not only qualitatively but also quantitatively, to a fairly high precision.

ACKNOWLEDGMENTS

We are indebted to Yu.A. Simonov for stimulating discussions and enlightening comments. We are also grateful to E.-M. Ilgenfritz, A.B. Kaidalov, V.A. Novikov, and A.V. Yung for discussions on the results obtained in this study.

This work was supported by the Russian Foundation for Basic Research (project no. 00-02-17836) and INTAS (grant no. 110).

APPENDIX 1

Derivation of S^P_{eff} in Coordinate Space

Let us consider the derivation of Eq. (47) in coordinate space [19].

We start from expression (6) for the generating functional and, performing normalization to the case of $A^{\rm inst} = 0$, arrive at the effective instanton action in a nonperturbative background field in the form

$$S_{\rm eff}[A^{\rm inst}] = S^{\rm P}_{\rm eff}[A^{\rm inst}] + S^{\rm NP}_{\rm eff}[A^{\rm inst}], \qquad \text{(A.1)}$$

$$S^{\rm P}_{\rm eff} = S_{\rm cl} - \ln\left\langle \frac{\det\nabla^2}{\det\nabla_0^2}\left(\frac{\det D^2}{\det D_0^2}\right)^{1/2}\right\rangle, \qquad \text{(A.2)}$$

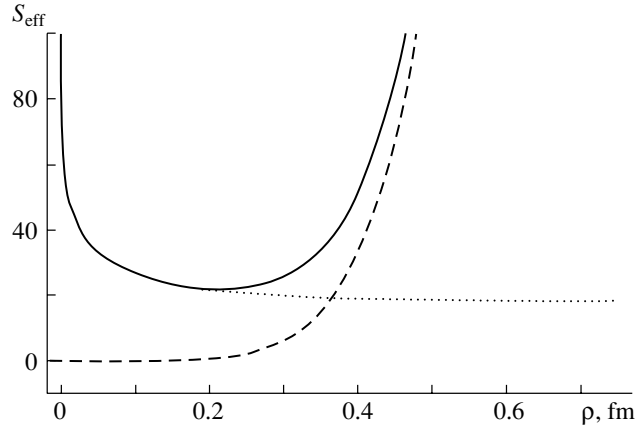

Fig. 3. Effective-action components (dotted curve) $S_{\text{eff}}^{\text{P}}$ and (dashed curve) $S_{\text{eff}}^{\text{NP}}$ and (solid curve) total effective action $S_{\text{eff}} = S_{\text{eff}}^{\text{P}} + S_{\text{eff}}^{\text{NP}}$ versus ρ for $N_c = 3$, $N_f = 0$, $T_g = 0.3$ fm, and $\langle G^2 \rangle = 1.0\ \text{GeV}^4$.

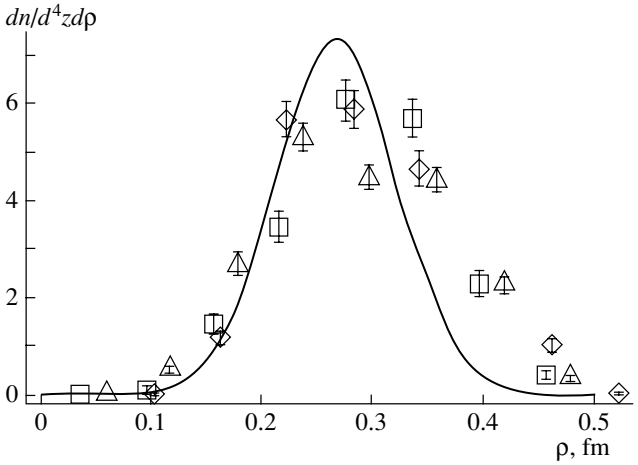

Fig. 4. Instanton density $dn/d^4zd\rho$ and respective lattice data from [36] for $N_c = 3$, $N_f = 0$, $T_g = 0.2$ fm, and $\langle G^2 \rangle = 0.5\ \text{GeV}^4$.

$$S_{\text{eff}}^{\text{NP}} = -\ln\left\langle \exp\{-S[A^{\text{inst}} + B] + S[A^{\text{inst}}] + S[B]\}\right\rangle, \tag{A.3}$$

where

$$S_{\text{cl}} = 8\pi^2/g_0^2, \tag{A.4}$$
$$\nabla^2 = (\nabla_\mu[A^{\text{inst}} + B])^2,$$
$$(D^2)_{\mu\nu} = -\nabla^2\delta_{\mu\nu} + 2iF_{\mu\nu}[A^{\text{inst}} + B],$$

and the subscript "0" labels quantities where it is necessary to set $A^{\text{inst}} = 0$.

Retaining terms in (A.2) that are quadratic in the instanton field and using expression (62), we find for the contribution of ghosts, for example, that (one can obtain the contribution of gluons in a similar way, and the final result will involve two physical polarizations of a gluon)

$$S_{\text{eff}}^{\text{P}} = \int d^4x d^4y \text{tr} A_\mu^{\text{sing}}(x)\partial_\mu\partial_\nu\tilde{\Pi}(x,y)A_\nu^{\text{sing}}(y), \tag{A.5}$$

where the gauge-invariant two-point function $\tilde{\Pi}$ is given by

$$\tilde{\Pi}(x,y) = \langle\Phi_{\text{adj}}(0,x)\nabla_0^{-2}(x,y)\Phi_{\text{adj}}(y,0)\nabla_0^{-2}(y,x)\rangle. \tag{A.6}$$

Here, $\nabla_0^{-2}(x,y) = \langle x|1/\nabla_0^2|y\rangle$ is the ghost propagator. In (A.6), one can easily recognize the two-gluon correlation function subjected to the additional condition that the adjoint parallel transporter Φ_{adj} passes through the instanton position $x_0 = 0$. The mass spectrum of $\tilde{\Pi}$ is bounded from below by the two-gluon correlation function not subjected to this condition, Π_0, the lowest state of the latter being the 0^{++} glueball of mass about 1.5 GeV. In the large-N_c approximation, $\Pi_0(Q)$ has only poles [24],

$$\Pi_0(q^2) = \sum_{n=1}^{\infty}\frac{C_n}{q^2 + M_n^2}, \tag{A.7}$$
$$M_n^2 = 4\pi\sigma_{\text{adj}}n + \text{const},$$

as in the $\bar{q}q$ case (σ_{adj} is the string tension in the adjoint representation). Highly excited states in (A.7) lead to

$$\Pi_0(q^2) \sim \psi\left(\frac{q^2 + m_0^2}{m_0^2}\right) + \text{const}, \tag{A.8}$$
$$\psi(x) = \frac{\Gamma'(x)}{\Gamma(x)}, \quad m_0^2 = 4\pi\sigma_{\text{adj}} \simeq M_{0^{++}}^2.$$

Replacing $\tilde{\Pi}$ by Π_0 in (A.5) and making a Fourier transformation, we arrive at

$$S_{\text{eff}}^{\text{P}} = \frac{1}{4}\int\frac{d^4q}{(2\pi)^4}\left(\frac{1}{g_0^2} + \Pi_0(q^2)\right)\tilde{F}_{\mu\nu}^a(q)\tilde{F}_{\mu\nu}^a(-q), \tag{A.9}$$

where we have used the notation $\tilde{F}_{\mu\nu}$ for the instanton field (63).

Over the entire Euclidean space, $\Pi_0(q^2)$ can be approximated as [19, 20, 24]

$$\Pi_0(q^2) \simeq \frac{11N_c}{48\pi^2}\ln\frac{q^2 + m_*^2}{\Lambda^2}, \tag{A.10}$$

where m_* is related to m_0 by the equation

$$m_*^2 = m_0^2 e^{-C} \approx 0.56m_0^2, \tag{A.11}$$
$$C = -\Psi(1) = 0.577\ldots.$$

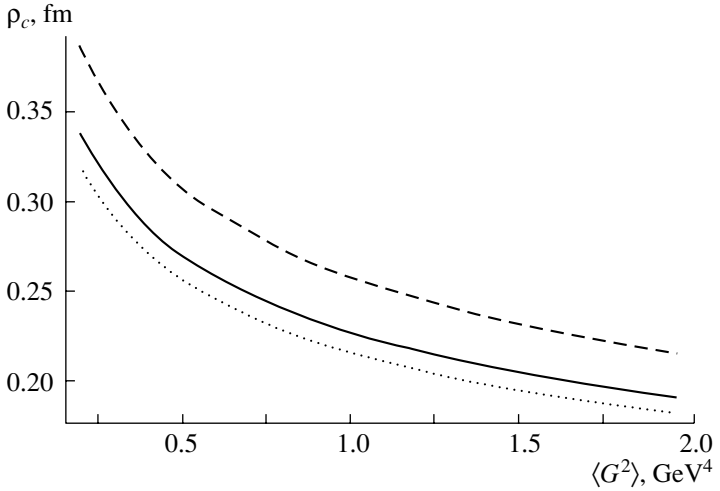

Fig. 5. Instanton size as a function of the gluon condensate ($N_c = 3$, $N_f = 0$) for $T_g =$ (dashed curve) 0.1, (solid curve) 0.2, and (dotted curve) 0.3 fm.

Substituting into (A.9) $\tilde{F}^a_{\mu\nu}(q) = -8\pi^2\eta^a_{\mu\nu}\rho^2 K_0(\rho q)$, where $K_0(z)$ is a modified Bessel function of the first kind, we obtain

$$S^{\rm P}_{\rm eff}(\rho) = 24\pi^2 \int\limits_0^\infty x^3 dx K_0^2(x)\frac{1}{g^2(x)} \simeq \frac{8\pi^2}{g^2(1)}, \tag{A.12}$$

where we have defined the effective charge as

$$\frac{1}{g^2(x)} = \frac{b}{16\pi^2}\ln\frac{x^2+m_*^2\rho^2}{\Lambda^2\rho^2}, \tag{A.13}$$
$$b = \frac{11}{3}N_c,$$

which obviously coincides with (47).

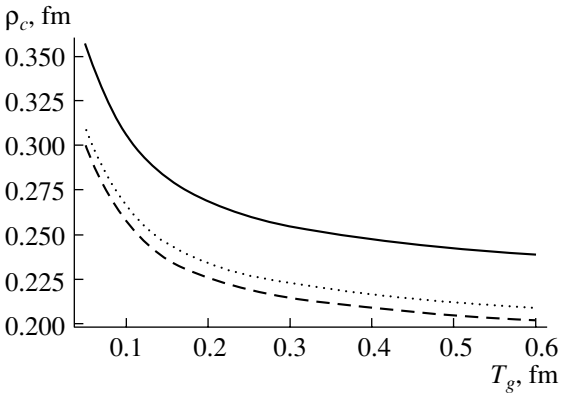

Fig. 6. Instanton size as a function of the correlation length ($N_c = 3$, $N_f = 0$) for $\langle G^2\rangle =$ (solid curve) 0.5, (dotted curve) 0.87, and (dashed curve), 1.0 GeV^4.

APPENDIX 2

Bilocal Correlation Function

For the bilocal correlation function, use is usually made of a parametrization that differs somewhat from that in (48) [25–28]; that is,

$$\langle {\rm tr} G_{\mu\nu}(x)\Phi(x,y)G_{\rho\sigma}(y)\Phi(y,x)\rangle \tag{A.14}$$
$$\sim (\delta_{\mu\rho}\delta_{\nu\sigma} - \delta_{\mu\sigma}\delta_{\nu\rho})\left[\tilde{D}(z) + \tilde{D}_1(z)\right]$$
$$+ (z_\mu z_\rho\delta_{\nu\sigma} + z_\nu z_\sigma\delta_{\mu\rho} - z_\mu z_\sigma\delta_{\nu\rho} - z_\nu z_\rho\delta_{\mu\sigma})\frac{\partial\tilde{D}_1}{\partial z^2}.$$

Obviously, one can establish the relationship between our definition and that in (A.14):

$$\tilde{D}(z) + \tilde{D}_1(z) \to D(z), \tag{A.15}$$
$$\frac{1}{2}z^2\frac{\partial\tilde{D}_1}{\partial z^2} \to \bar{D}(z).$$

The correlation function (A.14) was determined in the lattice calculations performed in [27]. The functions $\tilde{D}(z)$ and $\tilde{D}_1(z)$ were approximated as follows:

$$\tilde{D}(z) = A_0\exp(-|z|/T_g) + \frac{a_0}{z^4}\exp(-|z|/\lambda), \tag{A.16}$$
$$\tilde{D}_1(z) = A_1\exp(-|z|/T_g) + \frac{a_1}{z^4}\exp(-|z|/\lambda).$$

The second terms on the right-hand sides of the equalities in (A.16) correspond to a perturbative contribution. The numerical values of T_g that were obtained in [27, 28] are listed in Table 1. Moreover, it was found in those studies that the ratio A_1/A_0 is small, $A_1/A_0 \simeq 0.1$. Returning to our notation (D and $\bar{D}$), we find for the nonperturbative component that

$$D(z) = (A_0 + A_1)e^{-z/T_g}, \tag{A.17}$$

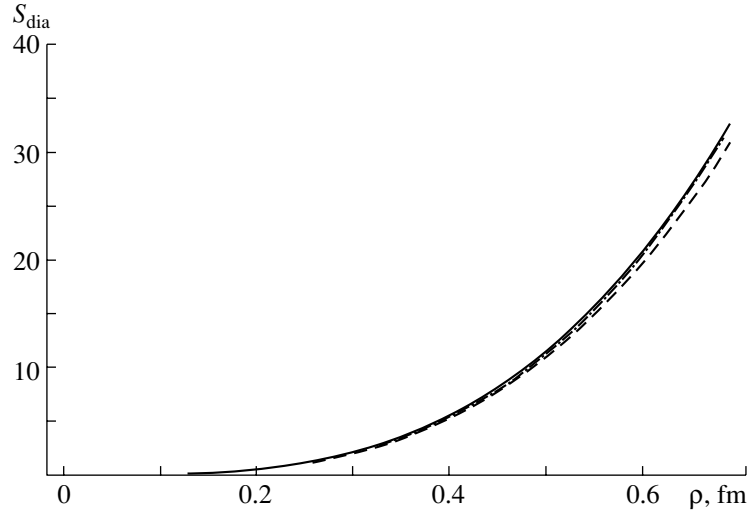

Fig. 7. Diamagnetic contribution S_{dia} (dashed curve) with and (solid curve) without allowance for $\bar{D}(z)$. The dash-dotted curve represents S_{dia} at $D(z) = \exp\{-|z|/T_g\}$ and $\bar{D}(z) = 0$.

$$\bar{D}(z) = -\frac{1}{4}\frac{z}{T_g}A_1 e^{-z/T_g}.$$

It is obvious that, in the region $z \sim T_g$, which makes a dominant contribution to all of the quantities calculated in Section 4, $\bar{D}(z) \ll D(z)$ by virtue of the fact that $A_1 \ll A_0$.

In our calculations, we use the Gaussian parametrization

$$\tilde{D}(z) = A_0 e^{-z^2/T_g^2}, \qquad \text{(A.18)}$$
$$\tilde{D}_1(z) = A_1 e^{-z^2/T_g^2}.$$

In accordance with this, we have

$$D(z) = (A_0 + A_1)e^{-z^2/T_g^2}, \qquad \text{(A.19)}$$
$$\overline{D}(z) = -\frac{1}{2}\frac{z^2}{T_g^2}A_1 e^{-z^2/T_g^2},$$

and $\bar{D}(z) \ll D(z)$ in the region $z \sim T_g$ as before.

APPENDIX 3

Dependence of S_{dia} on the Functions D and $\bar{D}$

Let us address the question of what numerical changes in the effective action are induced by taking into account the function $\bar{D}(z)$ in the bilocal correlation function (48). It was shown above that, as ρ increases, the nonlocal diamagnetic interaction leads to the stabilization of an instanton. Accordingly, we consider corrections to S_{dia} that arise upon taking into account $\bar{D}$ in the case where an exponential parametrization is chosen for the bilocal correlation function. Starting from expressions (69)–(72) and taking into account expression (A.19), we obtain [instead of (76)]

$$S_{\text{dia}} = \frac{2\pi^2}{g^2}\frac{\langle G^2\rangle}{\mu^4}\frac{N_c}{N_c^2-1}\zeta^4\int_0^\infty dx\frac{x^3}{(x^2+\zeta^2)^2}\varphi(x), \qquad \text{(A.20)}$$

$$\varphi(x) = \int_0^1 \alpha d\alpha \int_0^1 \beta d\beta\Big[(A_0+A_1)e^{-(\alpha-\beta)^2x^2} - A_1(\alpha-\beta)^2x^2e^{-(\alpha-\beta)^2x^2}\Big],$$
$$A_0 \simeq 0.9, \quad A_1 \simeq 0.1.$$

Figure 7 shows S_{dia} as a function of ρ according to the calculations by formulas (76), (80), and (A.20). It can be seen that the resulting distinction is insignificant; therefore, our approximation, where we have disregarded $\bar{D}(z)$ against $D(z)$, is quite legitimate. The same figure also shows the quantity S_{dia} calculated under the assumption that $D(z) = e^{-|z|/T_g}$ and $\bar{D}(z) = 0$. It is obvious that the specific form of the function $D(z)$ does not have a significant effect on the final result. It is only necessary that this function be monotonically decreasing and have a characteristic value of the correlation length T_g.

REFERENCES

1. A. M. Polyakov, Phys. Lett. B **59B**, 79 (1975); A. A. Belavin, A. M. Polyakov, A. S. Shvarts, and Y. S. Tyupkin, Phys. Lett. B **59B**, 85 (1975).
2. G. 't Hooft, Phys. Rev. D **14**, 3432 (1976).
3. C. G. Callan, R. F. Dashen, and D. J. Gross, Phys. Lett. B **63B**, 334 (1976).

4. C. G. Callan, R. F. Dashen, and D. J. Gross, Phys. Rev. D **17**, 2717 (1978); **19**, 1826 (1979).
5. G. 't Hooft, Phys. Rev. Lett. **37**, 8 (1976).
6. E. Witten, Nucl. Phys. B **149**, 285 (1979); G. Veneziano, Nucl. Phys. B **159**, 213 (1979).
7. D. Diakonov and V. Y. Petrov, Nucl. Phys. B **272**, 457 (1986).
8. B. V. Geshkenbein and B. L. Ioffe, Nucl. Phys. B **166**, 340 (1980).
9. T. Schafer and E. V. Shuryak, Rev. Mod. Phys. **70**, 323 (1998).
10. Yu. A. Simonov, Pis'ma Zh. Éksp. Teor. Fiz. **71**(4), 9 (2000) [JETP Lett. **71**, 127 (2000)]; V. I. Shevchenko and Yu. A. Simonov, Phys. Rev. Lett. **85**, 1811 (2000).
11. G. S. Bali, Nucl. Phys. B (Proc. Suppl.) **83**, 422 (2000); Phys. Rep. **343**, 1 (2001).
12. M. Fukushima, E.-M. Ilgenfritz, and H. Toki, Phys. Rev. D **64**, 034503 (2001).
13. E.-M. Ilgenfritz and M. Muller-Preussker, Nucl. Phys. B **184**, 443 (1981).
14. E. V. Shuryak, Nucl. Phys. B **203**, 93 (1982).
15. E. V. Shuryak, Phys. Rep. **115**, 151 (1984).
16. D. Diakonov and V. Y. Petrov, Nucl. Phys. B **245**, 259 (1984).
17. I. I. Balitsky and A. V. Yung, Phys. Lett. B **168B**, 113 (1986); A. V. Yung, Nucl. Phys. B **297**, 47 (1988).
18. M. A. Shifman, A. I. Vainshtein, and V. I. Zakharov, Nucl. Phys. B **163**, 46 (1980).
19. N. O. Agasian and Yu. A. Simonov, Mod. Phys. Lett. A **10**, 1755 (1995).
20. N. O. Agasian, Yad. Fiz. **59**, 317 (1996) [Phys. At. Nucl. **59**, 297 (1996)].
21. N. O. Agasian and S. M. Fedorov, J. High Energy Phys. **0112**, 019 (2001); hep-ph/0111305.
22. L. F. Abbot, Nucl. Phys. B **184**, 189 (1981).
23. A. M. Polyakov, *Gauge Fields and Strings* (Harwood, Chur, 1987).
24. Yu. A. Simonov, Yad. Fiz. **58**, 113 (1995) [Phys. At. Nucl. **58**, 107 (1995)]; Yu. A. Simonov and J. A. Tjon, Ann. Phys. (N.Y.) **300**, 54 (2002).
25. H. G. Dosch, Phys. Lett. B **190**, 177 (1987); H. G. Dosch and Yu. A. Simonov, Phys. Lett. B **205**, 339 (1988); Yu. A. Simonov, Nucl. Phys. B **307**, 512 (1988).
26. A. Di Giacomo, H. G. Dosch, V. I. Shevchenko, and Yu. A. Simonov, hep-ph/0007223.
27. M. Campostrini, A. Di Giacomo, and G. Mussardo, Z. Phys. C **25**, 173 (1984); A. Di Giacomo and H. Panagopoulos, Phys. Lett. B **285**, 133 (1992); A. Di Giacomo, E. Meggiolaro, and H. Panagopoulos, hep-lat/9603017; M. D'Elia, A. Di Giacomo, and E. Meggiolaro, Phys. Lett. B **408**, 315 (1997).
28. A. Di Giacomo, hep-lat/0012013.
29. M. A. Shifman, A. I. Vainshtein, and V. I. Zakharov, Nucl. Phys. B **147**, 385, 448 (1979).
30. G. S. Bali, N. Brambilla, and A. Vairo, Phys. Lett. B **421**, 265 (1998).
31. Yu. A. Simonov, Few-Body Syst. **25**, 45 (1998); Yu. A. Simonov, Yad. Fiz. **61**, 941 (1998) [Phys. At. Nucl. **61**, 855 (1998)].
32. S. Narison, Phys. Lett. B **387**, 162 (1996).
33. K. Huang, *Statistical Mechanics* (Wiley, New York, 1963; Mir, Moscow, 1966); A. Isihara, *Statistical Physics* (Academic, New York, 1971; Mir, Moscow, 1973).
34. A. B. Migdal, N. O. Agasyan, and S. B. Khokhlachev, Pis'ma Zh. Éksp. Teor. Fiz. **41**, 405 (1985) [JETP Lett. **41**, 497 (1985)]; N. O. Agasyan and S. B. Khokhlachev, Yad. Fiz. **55**, 1116 (1992) [Sov. J. Nucl. Phys. **55**, 628 (1992)]; Yad. Fiz. **55**, 1126 (1992) [Sov. J. Nucl. Phys. **55**, 633 (1992)]; N. O. Agasian, hep-ph/9803252; hep-ph/9904227.
35. A. E. Dorokhov, S. V. Esaibegian, A. E. Maximov, and S. V. Mikhailov, Eur. Phys. J. C **13**, 331 (2000).
36. A. Hasenfratz and C. Nieter, Phys. Lett. B **439**, 366 (1998).
37. M. I. Polikarpov and A. I. Veselov, Nucl. Phys. B **297**, 34 (1988).
38. J. W. Negele, Nucl. Phys. B (Proc. Suppl.) **73**, 92 (1999); M. Teper, Nucl. Phys. B (Proc. Suppl.) **83**, 146 (2000); M. Garcia Perez, Nucl. Phys. B (Proc. Suppl.) **94**, 27 (2001).
39. A. Ringwald and F. Schrempp, Phys. Lett. B **459**, 249 (1999).

Translated by A. Isaakyan

Physics of Atomic Nuclei, Vol. 67, No. 2, 2004, pp. 391–395. From Yadernaya Fizika, Vol. 67, No. 2, 2004, pp. 409–413.

ELEMENTARY PARTICLES AND FIELDS
Theory

Low-Temperature Relations in QCD*

N. O. Agasian**

Institute of Theoretical and Experimental Physics,
Bol'shaya Cheremushkinskaya ul. 25, Moscow, 117259 Russia

Received January 17, 2003

Abstract—The low-temperature relations for the trace of the energy–momentum tensor in QCD with two and three quarks are obtained. It is shown that the temperature derivatives of the anomalous and normal (quark massive term) contributions to the trace of the energy–momentum tensor in QCD are equal to each other in the low-temperature region. Leading corrections connected with $\pi\pi$ interaction and thermal excitations of K and η mesons are calculated. © *2004 MAIK "Nauka/Interperiodica".*

1. INTRODUCTION

The investigation of the vacuum state behavior under the influence of various external factors is known to be one of the central problems of quantum field theory. In the realm of strong interactions (QCD), the main factors are the temperature and the baryon density. At low temperatures, $T < T_c$ (T_c is temperature of the "hadron–quark-gluon" phase transition), the dynamics of QCD is essentially nonperturbative and is characterized by confinement and spontaneous breaking of chiral symmetry. In the hadronic phase, the partition function of the system is dominated by the contribution of the lightest particles in the physical spectrum. It is well known that, due to the smallness of pion mass as compared to the typical scale of strong interactions, the pion plays a special role among other strongly interacting particles. Therefore, for many problems of QCD at zero temperature, the chiral limit, $M_\pi \to 0$, is an appropriate one. On the other hand, a new mass scale emerges in the physics of QCD phase transitions, namely, the critical transition temperature T_c. Numerically, the critical transition temperature turns out to be close to the pion mass, $T_c \approx M_\pi$.[1)] However, hadron states heavier than pion have masses several times larger than T_c, and therefore their contribution to the thermodynamic quantities is damped by the Boltzmann factor $\sim\exp\{-M_{\rm hadr}/T\}$. Thus, the thermodynamics of the low-temperature hadron phase, $T \lesssim M_\pi$, is described basically in terms of the thermal excitations of relativistic massive pions.

The low-energy theorems, playing an important role in the understanding of the vacuum state properties in quantum field theory, were discovered at almost the same time as quantum field methods applied in particle physics (see, for example, Low theorems [2]). In QCD, they were obtained in the beginning of the 1980s [3]. The QCD low-energy theorems, being derived from very general symmetry considerations and not depending on the details of the confinement mechanism, sometimes give information that is not easy to obtain in another way. Also, they can be used as "physically sensible" restrictions in the construction of effective theories. Recently, they were generalized to finite temperature [4] and a magnetic field case [5]. These theorems were used for investigation of QCD-vacuum phase structure in a magnetic field at finite temperature [6].

A relation between the trace anomaly and thermodynamic pressure in the chiral limit of QCD was first written in [7]. Rigorous derivation of this relation in the framework of the renormalization-group (RG) method in pure-glue QCD was performed in [8] and in QCD with nonzero quark masses in [9].

In the present paper, we derive the low-temperature relations for the trace of the energy–momentum tensor in QCD with two and three light quarks. These relations are based on the general dimensional and renormalization-group properties of the QCD partition function and dominating role of the pion thermal excitations in the hadronic phase. The physical consequences of these relations are discussed, as well as the possibilities of using them in lattice studies of QCD at finite temperature.

2. RENORMALIZATION-GROUP RELATIONS AT FINITE TEMPERATURE

For nonzero quark mass ($m_q \neq 0$), the scale invariance is already broken at the classical level.

*This article was submitted by the author in English.

**e-mail: agasian@heron.itep.ru

1)The deconfining phase transition temperature is the one obtained in lattice calculations $T_c(N_f = 2) \simeq 173$ MeV and $T_c(N_f = 3) \simeq 154$ MeV [1].

Therefore, the pion thermal excitations would change, even in the ideal gas approximation, the value of the gluon condensate with increasing temperature.[2)]

The QCD Euclidean partition function with two quark flavors has the following form ($\beta = 1/T$):

$$Z = \int [DA] \prod_{q=u,d} [D\bar{q}][Dq] \qquad (1)$$
$$\times \exp\left\{ -\int_0^\beta dx_4 \int_V d^3x \mathcal{L} \right\}.$$

Here, the QCD Lagrangian is

$$\mathcal{L} = \frac{1}{4g_0^2}(G^a_{\mu\nu})^2 + \sum_{q=u,d} \bar{q} \qquad (2)$$
$$\times \left[\gamma_\mu \left(\partial_\mu - i\frac{\lambda^a}{2} A^a_\mu \right) + m_{0q} \right] q,$$

where the gauge-fixing and ghost terms have been omitted. The free energy density is given by the relation $\beta V F(T, m_{0u}, m_{0d}) = -\ln Z$. Equation (1) yields the following expression for the gluon condensate:

$$\langle G^2 \rangle (T, m_{0u}, m_{0d}) = 4\frac{\partial F}{\partial (1/g_0^2)}. \qquad (3)$$

The system described by the partition function (1) is characterized by the set of dimensionful parameters $M, T, m_{0q}(M)$ and dimensionless charge $g_0^2(M)$, where M is the ultraviolet cutoff. On the other hand, one can consider the renormalized free energy F_R and, by using the dimensional and RG properties of F_R, recast (3) into a form containing derivatives with respect to the physical parameter T and renormalized masses m_q.

The phenomenon of dimensional transmutation results in the appearance of a nonperturbative dimensionful parameter

$$\Lambda = M \exp\left\{ \int_{\alpha_s(M)}^{\infty} \frac{d\alpha_s}{\beta(\alpha_s)} \right\}, \qquad (4)$$

where $\alpha_s = g_0^2/4\pi$, and $\beta(\alpha_s) = d\alpha_s(M)/d\ln M$ is the Gell-Mann–Low function. Furthermore, as is well known, the quark mass has anomalous dimension γ_m and depends on the scale M. The RG equation for $m_0(M)$, the running mass, is $d\ln m_0/d\ln M = -\gamma_m$, and we use the $\overline{MS}$ scheme, for which β and γ_m are independent of the quark mass [10]. Upon integration, the RG invariant mass is given by

$$m_q = m_{0q}(M) \exp\left\{ \int^{\alpha_s(M)} \frac{\gamma_{m_q}(\alpha_s)}{\beta(\alpha_s)} d\alpha_s \right\}, \qquad (5)$$

where the indefinite integral is evaluated at $\alpha_s(M)$. Next, we note that, since free energy is an RG invariant quantity, its anomalous dimension is zero. Thus, F_R has only a normal (canonical) dimension equal to 4. Making use of the renorm-invariance of Λ, one can write in the most general form

$$F_R = \Lambda^4 f\left(\frac{T}{\Lambda}, \frac{m_u}{\Lambda}, \frac{m_d}{\Lambda} \right), \qquad (6)$$

where f is some function. From (4), (5), and (6), one gets

$$\frac{\partial F_R}{\partial (1/g_0^2)} = \frac{\partial F_R}{\partial \Lambda} \frac{\partial \Lambda}{\partial (1/g_0^2)} + \sum_q \frac{\partial F_R}{\partial m_q} \frac{\partial m_q}{\partial (1/g_0^2)}, \qquad (7)$$

$$\frac{\partial m_q}{\partial (1/g_0^2)} = -4\pi\alpha_s^2 m_q \frac{\gamma_{m_q}(\alpha_s)}{\beta(\alpha_s)}. \qquad (8)$$

With account of (3), the trace of the energy–momentum tensor in QCD is given by [9]

$$\langle \theta^g_{\mu\mu} \rangle = \frac{\beta(\alpha_s)}{16\pi\alpha_s^2} \langle G^2 \rangle \qquad (9)$$
$$= -\left(4 - T\frac{\partial}{\partial T} - \sum_q (1+\gamma_{m_q}) m_q \frac{\partial}{\partial m_q} \right) P_R,$$

where P_R is the renormalized pressure. It is convenient to choose such a large scale that one can take the lowest order expressions, $\beta(\alpha_s) \to -b\alpha_s^2/2\pi$, where $b = (11N_c - 2N_f)/3$ and $1 + \gamma_m \to 1$. Thus, we have the following equations for condensates:

$$\langle G^2 \rangle (T) = \frac{32\pi^2}{b} \qquad (10)$$
$$\times \left(4 - T\frac{\partial}{\partial T} - \sum_q m_q \frac{\partial}{\partial m_q} \right) P_R \equiv \hat{D} P_R,$$

$$\langle \bar{q}q \rangle (T) = -\frac{\partial P_R}{\partial m_q}. \qquad (11)$$

3. LOW-TEMPERATURE RELATIONS FOR $\langle \theta_{\mu\mu} \rangle$

In the hadronic phase, the effective pressure from which one can extract the condensates $\langle G^2 \rangle (T)$ and

[2)] At zero quark mass, the gas of massless noninteracting pions is obviously scale-invariant and therefore does not contribute to the trace of the energy–momentum tensor nor, correspondingly, to the gluon condensate $\langle G^2 \rangle \equiv \langle (gG^a_{\mu\nu})^2 \rangle$.

$\langle\bar{q}q\rangle(T)$ using the general relations (10) and (11) has the form

$$P_{\rm eff}(T) = -\varepsilon_{\rm vac} + P_h(T), \tag{12}$$

where $\varepsilon_{\rm vac} = \frac{1}{4}\langle\theta_{\mu\mu}\rangle$ is the nonperturbative vacuum energy density at $T = 0$ and

$$\langle\theta_{\mu\mu}\rangle = -\frac{b}{32\pi^2}\langle G^2\rangle + \sum_{q=u,d} m_q\langle\bar{q}q\rangle \tag{13}$$

is the trace of the energy–momentum tensor. In Eq. (12), $P_h(T)$ is the thermal hadron pressure. The quark and gluon condensates are given by the equations

$$\langle\bar{q}q\rangle(T) = -\frac{\partial P_{\rm eff}}{\partial m_q}, \tag{14}$$

$$\langle G^2\rangle(T) = \hat{D}P_{\rm eff}, \tag{15}$$

where the operator $\hat{D}$ is defined by the relation (10)

$$\hat{D} = \frac{32\pi^2}{b}\left(4 - T\frac{\partial}{\partial T} - \sum_q m_q\frac{\partial}{\partial m_q}\right). \tag{16}$$

Consider the case $T = 0$. One can use the low-energy theorem for the derivative of the gluon condensate with respect to the quark mass [3]:

$$\frac{\partial}{\partial m_q}\langle G^2\rangle = \int d^4x\langle G^2(0)\bar{q}q(x)\rangle \tag{17}$$
$$= -\frac{96\pi^2}{b}\langle\bar{q}q\rangle + O(m_q),$$

where $O(m_q)$ stands for the terms linear in light-quark masses. Then, one arrives at the following relation:

$$\frac{\partial\varepsilon_{\rm vac}}{\partial m_q} = -\frac{b}{128\pi^2}\frac{\partial}{\partial m_q}\langle G^2\rangle \tag{18}$$
$$+\frac{1}{4}\langle\bar{q}q\rangle = \frac{3}{4}\langle\bar{q}q\rangle + \frac{1}{4}\langle\bar{q}q\rangle = \langle\bar{q}q\rangle.$$

Note that three-fourths of the quark condensate stems from the gluon part of the nonperturbative vacuum energy density. Along the same lines, one arrives at the expression for the gluon condensate

$$-\hat{D}\varepsilon_{\rm vac} = \langle G^2\rangle. \tag{19}$$

Let us consider the case $N_f = 2$. In order to get the dependence of the quark and gluon condensates on T, use is made of the Gell-Mann–Oakes–Renner (GMOR) relation ($\Sigma = |\langle\bar{u}u\rangle| = |\langle\bar{d}d\rangle|$)

$$F_\pi^2 M_\pi^2 = -\frac{1}{2}(m_u + m_d)\langle\bar{u}u + \bar{d}d\rangle = (m_u + m_d)\Sigma. \tag{20}$$

Then, we can find the following relations:

$$\frac{\partial}{\partial m_q} = \frac{\Sigma}{F_\pi^2}\frac{\partial}{\partial M_\pi^2}, \tag{21}$$

$$\sum_{q=u,d} m_q\frac{\partial}{\partial m_q} = (m_u + m_d)\frac{\Sigma}{F_\pi^2}\frac{\partial}{\partial M_\pi^2} = M_\pi^2\frac{\partial}{\partial M_\pi^2}, \tag{22}$$

$$\hat{D} = \frac{32\pi^2}{b}\left(4 - T\frac{\partial}{\partial T} - M_\pi^2\frac{\partial}{\partial M_\pi^2}\right). \tag{23}$$

At low temperature, the main contribution to the pressure comes from thermal excitations of massive pions. The general expression for the pressure reads

$$P_\pi = T^4\varphi(M_\pi/T), \tag{24}$$

where φ is a function of the ratio M_π/T. Then, the following relation is valid:

$$\left(4 - T\frac{\partial}{\partial T} - M_\pi^2\frac{\partial}{\partial M_\pi^2}\right)P_\pi = M_\pi^2\frac{\partial P_\pi}{\partial M_\pi^2}. \tag{25}$$

With account of (14), (15), (18), (22), and (25), one gets

$$\Delta\langle\bar{q}q\rangle = -\frac{\partial P_\pi}{\partial m_q}, \quad \Delta\langle G^2\rangle = \frac{32\pi^2}{b}M_\pi^2\frac{\partial P_\pi}{\partial M_\pi^2}, \tag{26}$$

where $\Delta\langle\bar{q}q\rangle = \langle\bar{q}q\rangle_T - \langle\bar{q}q\rangle$ and $\Delta\langle G^2\rangle = \langle G^2\rangle_T - \langle G^2\rangle$. In view of (22), one can recast (26) in the form

$$\Delta\langle G^2\rangle = -\frac{32\pi^2}{b}\sum_{q=u,d} m_q\Delta\langle\bar{q}q\rangle. \tag{27}$$

Differentiating (27) with respect to T, one obtains

$$\frac{\partial\langle G^2\rangle}{\partial T} = -\frac{32\pi^2}{b}\sum_{q=u,d} m_q\frac{\partial\langle\bar{q}q\rangle}{\partial T}. \tag{28}$$

This can be rewritten as [11]

$$\frac{\partial\langle\theta^g_{\mu\mu}\rangle}{\partial T} = \frac{\partial\langle\theta^q_{\mu\mu}\rangle}{\partial T}, \tag{29}$$

where $\langle\theta^g_{\mu\mu}\rangle = (\beta(\alpha_s)/16\pi\alpha_s^2)\langle G^2\rangle$ and $\langle\theta^q_{\mu\mu}\rangle = \sum m_q\langle\bar{q}q\rangle$ are, respectively, the gluon and quark contributions to the trace of the energy–momentum tensor. Note that, in deriving this result, use was made of the low-energy GMOR relation, and therefore the thermodynamic relation (28), (29) is valid in the light-quark theory. Thus, in the low-temperature region where the excitations of massive hadrons and interactions of pions can be neglected, Eq. (29) becomes a rigorous QCD theorem.

4. LEADING CORRECTIONS TO THE LOW-TEMPERATURE RELATIONS, $N_f = 3$

As was mentioned above, the pion plays an exceptional role in thermodynamics of QCD due to the fact that its mass is numerically close to the phase transition temperature, while the masses of heavier hadrons are several times larger than T_c. It was shown in [12] that, at low temperatures, the contribution to $\langle\bar{q}q\rangle$ generated by the massive states is very small, less than 5% if T is below 100 MeV. At $T = 150$ MeV, this contribution is of the order of 10%. The influence of thermal excitations of massive hadrons on the properties of the gluon and quark condensates in the framework of the conformal–nonlinear σ model was studied in detail in [13].

Let us consider leading corrections to relations (27)–(29) within the framework described above. Clearly, leading corrections are connected with the $\pi\pi$ interaction, since its contribution to the pressure is $\propto e^{-2M_\pi/T}$. Also, account of the s quark leads to the contributions to the pressure $\propto e^{-M_K/T}, e^{-M_\eta/T}$, which are related to the thermal excitations of K and η mesons. Then, pressure in the hadronic phase can be recast in the following form:

$$P_h(T) = P_g(T) + P_{\pi\pi}(T), \tag{30}$$

$$P_g(T) = \sum_{i=\pi,K,\eta} P_i(T), \tag{31}$$

where $P_i(T) = g_i T^4 \varphi(M_i/T)$ is gas pressure of $i = \pi, K, \eta$ meson and g_i is the number of degrees of freedom of the ith state, $g_\pi = 3$, $g_K = 4$, $g_\eta = 1$. Pressure related to $\pi\pi$ interaction in two-loop ChPT in general form is

$$P_{\pi\pi} = T^4 \frac{M_\pi^2}{F_\pi^2} f\left(\frac{M_\pi}{T}\right); \tag{32}$$

here, f is a function of ratio M_π/T, and factor M_π^2/F_π^2 is connected with the $\pi\pi$-interaction vertex. Making use of Gell-Mann–Okubo relations, one gets (analogous to (25))

$$\hat{D}P_g(T) = \frac{32\pi^2}{b} \times \left(4 - T\frac{\partial}{\partial T} - \sum_{q=u,d,s} m_q \frac{\partial}{\partial m_q}\right) P_g(T) = \frac{32\pi^2}{b} \sum_{i=\pi,K,\eta} M_i^2 \frac{\partial P_i}{\partial M_i^2}. \tag{33}$$

For the temperature shift of quark condensates, one has

$$\frac{\Delta\Sigma(T)}{\Sigma} = \frac{\partial P_g}{\partial m_u} = \frac{1}{F_\pi^2}\left(\frac{\partial P_\pi}{\partial M_\pi^2} + \frac{\partial P_K}{\partial M_K^2} + \frac{1}{3}\frac{\partial P_\eta}{\partial M_\eta^2}\right), \tag{34}$$

$$\frac{\Delta\Sigma_s(T)}{\Sigma_s} = \frac{\partial P_g}{\partial m_s} = \frac{1}{F_\pi^2}\left(\frac{\partial P_K}{\partial M_K^2} + \frac{4}{3}\frac{\partial P_\eta}{\partial M_\eta^2}\right). \tag{35}$$

Note that the light π meson does not carry strangeness and thus does not participate in $\langle\bar{s}s\rangle$-condensate "evaporation." The leading contribution to $\Delta\langle\bar{s}s\rangle(T)$ comes from thermal excitations of the lightest strange K meson with a mass several times larger than M_π. Therefore, it is obvious that $\langle\bar{s}s\rangle(T)$ decreases more slowly than $\langle\bar{u}u\rangle = \langle\bar{d}d\rangle$ with the increase in T. In the gas approximation, one finds[3)]

$$\frac{\Delta\Sigma_s(T)/\Sigma_s}{\Delta\Sigma(T)/\Sigma} = \frac{4}{3}\left(\frac{M_K}{M_\pi}\right)^{1/2}\left(\frac{F_\pi}{F_K}\right)^2 e^{(M_\pi - M_K)/T}, \tag{36}$$

and this ratio is of the order of ~ 0.13 at $T \sim 140$ MeV. Analogous to the derivation of Eq. (27) [with account of Eqs. (32)–(35)], one gets

$$-\frac{b}{32\pi^2}\Delta\langle G^2\rangle = \sum_{q=u,d,s} m_q \Delta\langle\bar{q}q\rangle + 2P_{\pi\pi} + \frac{1}{2}M_\pi^2\frac{\partial P_K}{\partial M_K^2}. \tag{37}$$

Let us introduce the functions

$$\theta^{\pm}(T) = \langle\theta^g_{\mu\mu} \pm \theta^q_{\mu\mu}\rangle(T) - \langle\theta^g_{\mu\mu} \pm \theta^q_{\mu\mu}\rangle(0). \tag{38}$$

$\theta^+(T)$ is the thermal part of the trace of the energy–momentum tensor and $\theta^+(T) = \Delta\langle\theta^{\rm tot}_{\mu\mu}\rangle(T) = \varepsilon - 3P$, where $\varepsilon = TdP/dT - P$ is energy density. Then, the function

$$\delta_\theta(T) = \frac{\theta^-(T)}{\theta^+(T)} = \left(2P_{\pi\pi} + \frac{1}{2}M_\pi^2\frac{\partial P_K}{\partial M_K^2}\right)\Big/(\varepsilon - 3P) \tag{39}$$

can be considered as a measure of the deviation from low-temperature relation (27). Let us estimate this correction numerically. One has for $P_{\pi\pi}$ [14]

$$P_{\pi\pi} = -\frac{1}{6}\left(\frac{M_\pi^2}{F_\pi^2}\right)[g_1(M_\pi/T)]^2, \tag{40}$$

[3)] The contribution of the K meson to $\Delta\Sigma_s(T)$ can be obtained from the low-temperature expression for the condensate $\Delta\Sigma(T)$ (see [11]), with the obvious substitution of $M_\pi \to M_K$, $F_\pi \to F_K$ and multiplication by the factor 4/3.

$$g_1(M_\pi/T) = \int \frac{d^3p}{(2\pi)^3}\frac{1}{\omega_\pi\left(e^{\omega_\pi/T}-1\right)}, \qquad (41)$$
$$\omega_\pi = \sqrt{\mathbf{p}^2 + M_\pi^2}.$$

For i-meson gas,

$$P_i = -g_i T \int \frac{d^3p}{(2\pi)^3} \ln\left(1 - e^{-\sqrt{\mathbf{p}^2+M_i^2}/T}\right). \quad (42)$$

Choosing $M_\pi = 140$ MeV, $M_K = 493$ MeV, $F_\pi = 93$ MeV, one can see from numerical calculations that

$$\delta_\theta(T < 150\ \text{MeV}) < 0.04. \qquad (43)$$

Consequently, leading corrections to the low-temperature relation (27) amount to several percent up to the critical temperature.

5. DISCUSSION AND CONCLUSIONS

Thus, the function $\delta_\theta(T)$ at low temperatures is, with good accuracy, close to zero. In the vicinity and at the phase transition point, i.e., in the region of nonperturbative vacuum reconstruction, this function changes drastically. To see it, we first consider pure gluodynamics. It was shown in [15] using the effective dilaton Lagrangian that gluon condensate decreases very weakly with the increase in temperature, up to phase transition point. This result is physically transparent and is the consequence of Boltzmann suppression of thermal glueball excitations in the confining phase.

Further, the dynamical picture of deconfinement based on the reconstruction of the nonperturbative gluonic vacuum was suggested in [16]. Namely, confining and deconfining phases differ first of all in the vacuum fields, i.e., in the value of the gluon condensate and in the gluonic field correlators. The color-magnetic (CM) correlators and their contribution to the condensate are kept intact across the temperature phase transition, while the confining color-electric (CE) part abruptly disappears above T_c. Furthermore, there exist numerical lattice measurements of field correlators near the critical transition temperature T_c, performed by the Pisa group [17], where both CE and CM correlators are found with good accuracy. These data clearly demonstrate the strong suppression of the CE component above T_c and persistence of the CM component. Thus, the function $\partial\delta_\theta(T)/\partial T$ can be represented as a δ function smeared around the critical point T_c with the width $\sim\Delta T$ which defines the fluctuation region of phase transition.

A similar but more complicated and interesting situation takes place in the theory with quarks. The function $\delta_\theta(T)$ contains the quark term, proportional to the chiral phase transition order parameter $\langle\bar{q}q\rangle(T)$. So it is interesting to check relation (29) and to study the behavior of the function $\delta_\theta(T)$ in the lattice QCD at finite temperature. It would allow one both to test the nonperturbative QCD vacuum at the low temperatures in the confining phase and to extract additional information on the thermal phase transitions in QCD.

ACKNOWLEDGMENTS

I am grateful to A.B. Kaidalov, V.A. Novikov, V.A. Rubakov, Yu.A. Simonov, and A.I. Vainshtein for discussions and comments.

The financial support of the Russian Foundation for Basic Research (project no. 00-02-17836) and INTAS (grant no. 110) is gratefully acknowledged.

REFERENCES

1. F. Karsch, E. Laermann, and A. Peikert, Nucl. Phys. B **605**, 579 (2001); F. Karsch, Nucl. Phys. A **698**, 199 (2002).
2. F. E. Low, Phys. Rev. **110**, 974 (1958).
3. V. A. Novikov, M. A. Shifman, A. I. Vainshtein, and V. I. Zakharov, Nucl. Phys. B **191**, 301 (1981); Fiz. Élem. Chastits At. Yadra **13** (3), 542 (1982) [Sov. J. Part. Nucl. **13**, 224 (1982)]; A. A. Migdal and M. A. Shifman, Phys. Lett. B **114B**, 445 (1982); M. A. Shifman, Phys. Rep. **209**, 341 (1991).
4. P. J. Ellis, J. I. Kapusta, and H.-B. Tang, Phys. Lett. B **443**, 63 (1998).
5. N. O. Agasian and I. A. Shushpanov, Pis'ma Zh. Éksp. Teor. Fiz. **70**, 711 (1999) [JETP Lett. **70**, 717 (1999)]; Phys. Lett. B **472**, 143 (2000).
6. N. O. Agasian, Phys. Lett. B **488**, 39 (2000); Yad. Fiz. **64**, 608 (2001) [Phys. At. Nucl. **64**, 554 (2001)]; N. O. Agasian and I. A. Shushpanov, J. High Energy Phys. **10**, 006 (2001).
7. H. Leutwyler, *Lecture given at Workshop on Effective Field Theories* (Dobogoko, Hungary, 1991); Preprint No. UTP-91-43 (Bern Univ., 1991).
8. I. T. Drummond, R. R. Horgan, P. V. Landshoff, and A. Rebhan, Phys. Lett. B **460**, 197 (1999).
9. N. O. Agasian, Pis'ma Zh. Éksp. Teor. Fiz. **74**, 387 (2001) [JETP Lett. **74**, 353 (2001)].
10. I. A. Shushpanov, P. J. Ellis, and J. I. Kapusta, Phys. Rev. C **59**, 2931 (1999).
11. N. O. Agasian, Phys. Lett. B **519**, 71 (2001).
12. P. Gerber and H. Leutwyler, Nucl. Phys. B **321**, 387 (1989).
13. N. O. Agasian, D. Ebert, and E.-M. Ilgenfritz, Nucl. Phys. A **637**, 135 (1998).
14. J. Gasser and H. Leutwyler, Phys. Lett. B **184**, 83 (1987); **188**, 477 (1987).
15. N. O. Agasian, Pis'ma Zh. Éksp. Teor. Fiz. **57**, 200 (1993) [JETP Lett. **57**, 208 (1993)].
16. Yu. A. Simonov, Pis'ma Zh. Éksp. Teor. Fiz. **55**, 605 (1992) [JETP Lett. **55**, 627 (1992)]; Yad. Fiz. **58**, 357 (1995) [Phys. At. Nucl. **58**, 309 (1995)].
17. A. Di Giacomo, E. Meggiolaro, and H. Panagopoulos, Nucl. Phys. B **483**, 371 (1997); M. D'Elia, A. Di Giacomo, and E. Meggiolaro, hep-lat/0205018.

Physics of Atomic Nuclei, Vol. 67, No. 2, 2004, pp. 396–405. Translated from Yadernaya Fizika, Vol. 67, No. 2, 2004, pp. 414–424.

ELEMENTARY PARTICLES AND FIELDS
Theory

Model for Describing the Production of Centauro Events and Strangelets in Heavy-Ion Collisions

S. A. Sadovsky[1)*], Yu. V. Kharlov[1)], A. L. S. Angelis[†2)], E. Gładysz-Dziaduś[3)], V. L. Korotkikh[4)], G. Mavromanolakis[2)], and A. D. Panagiotou[2)]

Received September 18, 2002; in final form, March 21, 2003

Abstract—A phenomenological model for describing the production of Centauro events in relativistic heavy-ion collisions is discussed. The model provides quantitative predictions for kinematical variables, for the baryon number, and for the masses of a Centauro fireball and of its decay products. A Centauro fireball decays predominantly into nucleons, strange hyperons, and possibly strangelets. Centauro events in Pb + Pb collisions at the LHC energy are simulated for the CASTOR detector. The signatures of these events are discussed in detail. © *2004 MAIK "Nauka/Interperiodica"*.

INTRODUCTION

In this study, we present a Monte Carlo model for describing the production of Centauro events [1, 2] in relativistic heavy-ion collisions. The model is based on the phenomenological model formulated previously in [3–6]. At first, a Monte Carlo model was applied to simulating the production of Centauro events and to exploring the possibility of detecting them in collisions of lead nuclei at an energy of $\sqrt{s} = 5.5$ TeV per nucleon by using the CASTOR detector, which was developed for the ALICE experiment [7] at the Large Hadron Collider (LHC at CERN). Later on, it became clear, however, that the infrastructure of the CMS experiment [8] is more appropriate for conducting investigations of this type, and it was decided to perform relevant experiments within CMS.

Originally, the model for describing Centauro events was based on experimental facts that were derived from an analysis of cosmic rays. Experimentally observed features—such as the multiplicities, transverse momenta, and energy spectra of secondaries, along with their pseudorapidity distributions—made it possible to determine the evolution of a Centauro fireball, and this was used as a basis for calculating its thermodynamic parameters and lifetime. An extrapolation of this model to higher energies enabled one to estimate some observables of Centauro events at the LHC energy with allowance for collider kinematics [9].

Within the approach developed here, we make an attempt at more precisely predicting the features of Centauro events and, under some assumptions concerning fundamental features of the Centauro fireball that lead to more detailed predictions of observables of respective events, at giving a quantitative description of the original phenomenological model of the production of these events in nucleus–nucleus collisions. The model is formulated in terms of the impact parameter of a nucleus–nucleus collision, two thermodynamic parameters (the baryochemical potential and temperature) associated with the Centauro fireball, and the nuclear stopping power. In order to construct a fully quantitative model, we formalized all assumptions of the original model and introduced some additional ones. The generator of events that was developed within this model and which was dubbed CNGEN (CeNtauro GENerator)[5)] is able to calculate the parameters of the Centauro fireball and to simulate the complete configuration of an event. The model reproduces all kinematical features of Centaro events that were observed in cosmic-ray experiments.

This article is organized as follows. In Section 1, we give a thermodynamic and a kinematical description of the formation and evolution of Centauro-like events in relativistic nucleus–nucleus collisions and

[†]Deceased.
[1)]Institute for High Energy Physics, Protvino, Moscow oblast, 142284 Russia.
[2)]Nuclear and Particle Physics Division, Physics Department, University of Athens, GR-15771 Athens, Greece.
[3)]Laboratory of High Energy Physics, Institute of Nuclear Physics, ul. Kawiory 26a, PL-30-055 Kraków, Poland.
[4)]Institute of Nuclear Physics, Moscow State University, Vorob'evy gory, Moscow, 119899 Russia.
[*]e-mail: sadovsky@mx.ihep.su

[5)]The code of the CNGEN event generator can be obtained upon a request sent to the electronic address of one of the present authors (kharlov@mx.ihep.su).

1063-7788/04/6702-0396$26.00

calculate some features of the events being considered, such as the respective masses and the energy and multiplicity distributions. In Section 2, we discuss results concerning the detection of such events by the CASTOR detector. Also, Centauro events are compared there with ordinary events simulated with the aid of the HIJING event generator [10]. In addition, the signatures of Centauro events are discussed.

1. PHYSICAL FOUNDATIONS OF THE MODEL FOR DESCRIBING CENTAURO EVENTS

Evolution of a Centauro fireball. A phenomenological description of Centauro events was first proposed in [3–5]. In accordance with the model used there, Centauro events are formed in the projectile-fragmentation region of nucleus–nucleus collisions during the passage of the projectile through the target. Concurrently, the kinetic energy of the projectile is converted into thermal energy, with the result that there arises moderately hot quark matter possessing a high baryochemical potential and initially consisting of the quarks of the nuclei that are involved in the interaction process [4, 5]. This quark matter is referred to as an primary Centauro fireball. At the first stage of its evolution, the fireball consists only of u and d quarks and gluons. Because of the Pauli exclusion principle, a high baryochemical potential prevents gluon fragmentation into $u\bar{u}$ and $d\bar{d}$ quark–antiquark pairs [4]. Therefore, gluons fragment into $s\bar{s}$ pairs, and this leads to the occurrence of partial chemical equilibrium. In the equilibration process, $\bar{s}$ antiquarks are bound by u and d quarks, whereby K^+ and K^0 mesons are formed. The emission of these mesons from the initial fireball leads to a decrease in its temperature and entropy. Upon the emission of K mesons, the fireball transforms into strange quark matter (SQM), which has a relatively long lifetime ($\tau \sim 10^{-9}$ s) [11]. In the case where Centauro events arise in cosmic rays, an SQM fireball can penetrate, owing to this, the atmosphere to mountain-top altitudes. The mechanism of strangeness separation [12] may lead to the accumulation of strange quarks in one or a few small regions within an SQM fireball. After that, the SQM fireball decays explosively into baryons, including strange hyperons and light ($A > 6$) SQM objects (strangelets).

Baryon number of a Centauro fireball. Let us consider collisions of nuclei whose atomic weights are A_1 and A_2 and whose charges are Z_1 and Z_2, respectively. The impact parameter is constrained by the natural condition

$$0 < b < R_1 + R_2,$$

where $R_i = 1.15A_i^{1/3}$ fm ($i = 1, 2$) are the radii of colliding nuclei. A Centauro fireball is formed in the region of nuclear overlap. We assume that all projectile nucleons from the overlap region participate in the interaction process and determine the baryon number of the fireball. Thus, the fireball baryon number N_b can be assessed on the basis of simple geometric considerations. Assuming a uniform distribution of nucleons over a nucleus, one can express N_b in terms of the ratio of the volumes of the projectile region involved in the interaction process (V_{ovrlp}) and of the entire nucleus as a discrete unit (V_1). Specifically, we have

$$N_b = 0.9A_1\frac{V_{\text{ovrlp}}}{V_1}, \qquad (1)$$

where the factor 0.9 has been introduced in order to eliminate the contribution to N_b from the boundary of the overlap region.

It is natural to assume that beam and target nuclei are distributed uniformly over the transverse plane, this being equivalent to a uniform distribution of the impact parameter squared b^2. This assumption determines the form of all distributions considered below. All of the Centauro events recorded in cosmic rays were characterized by a high multiplicity of hadrons ($N_h > 70$); in view of this, the production of a Centauro fireball is subjected here to the constraint $N_b > 50$.

In our quantitative model, we further make the simple assumption that each nucleus–nucleus collision leads to the production of a Centauro fireball that possesses the same thermodynamic properties. This assumption is reasonable if the impact parameter changes quite moderately. A Centauro fireball must be more frequently produced in central than in peripheral collisions because the former have a higher baryon content. For this reason, the distributions displayed in the present article were calculated for Pb + Pb collisions occurring at impact-parameter values in the range $0 < b < 5$ fm.

The distribution of the baryon number of a Centauro fireball produced in Pb + Pb collisions at $\sqrt{s} = 5.5\ A$ TeV is shown in Fig. 1. It is given in arbitrary units, and this concerns all other distributions presented in this article.

Mass of a Centauro fireball. A Centauro fireball is a deconfined-quark-matter lump characterized by a temperature T and a nucleon baryochemical potential μ_b. As is predicted by the phenomenological model used in [4, 5], a fireball has a high baryochemical potential, and this suppresses the production of $\bar{u}$ and $\bar{d}$ antiquarks. The initial stage of fireball evolution is unstable, but, within a time interval of $\Delta t \sim 10^{-23}$ s [5], gluons fragment into $s\bar{s}$ pairs, whereupon

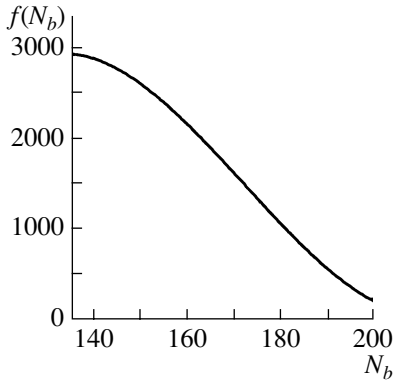

Fig. 1. Distribution of the baryon number of Centauro fireballs produced in Pb + Pb collisions whose impact-parameter values lie in the range $0 < b < 5$ fm.

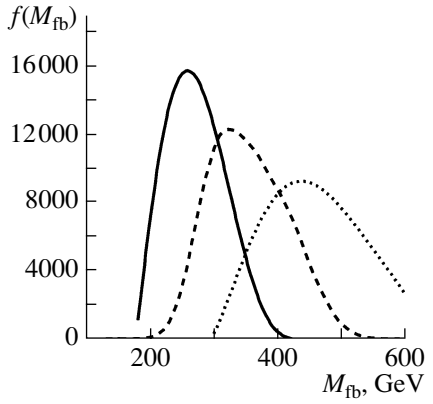

Fig. 2. Mass distribution of a Centauro fireball produced in Pb + Pb collisions at $\sqrt{s} = 5.5\ A$ TeV and $\mu_b = 1.8$ GeV for various values of the fireball temperature: $T =$ (solid curve) 130, (dashed curve) 190, and (dotted curve) 250 MeV.

chemical equilibration is established. In the first order of perturbative QCD, the energy density of product quark–gluon plasma consisting of u, d, and s quarks and gluons and having a temperature T close to the critical temperature T_c is given by [13, 14]

$$\varepsilon = \varepsilon_g + \varepsilon_q + \varepsilon_s,$$

where $q = u, d$. For the contributions of gluons, ε_g, and of quarks, ε_q and ε_s, we have

$$\varepsilon_g = \frac{8\pi^2}{15}T^4\left(1 - \frac{15}{4\pi}\alpha_s\right),$$

$$\varepsilon_q = \frac{7\pi^2}{10}T^4\left(1 - \frac{50}{21\pi}\alpha_s\right) + \left(3\mu_q^2T^2 + \frac{3}{2\pi^2}\mu_q^4\right) \times \left(1 - \frac{2}{\pi}\alpha_s\right),$$

$$\varepsilon_s = \gamma_s\left[\left(\frac{18T^4}{\pi^2}\right)\left(\frac{m_s}{T}\right)^2 K_2\left(\frac{m_s}{T}\right) + 6\left(\frac{m_sT}{\pi}\right)^2\left(\frac{m_s}{T}\right)K_1\left(\frac{m_s}{T}\right)\right],$$

where K_i are modified Bessel functions of the ith order. The strong-interaction coupling constant α_s must be taken at the scale $Q \approx 2\pi T$. At the critical temperature of $T_c = 170$ MeV, it is $\alpha_s = 0.3$ [13]. The parameter γ_s is the strangeness-equilibration factor ($\gamma_s \approx 0.4$). For all degrees of freedom, the total energy density has the form

$$\varepsilon = \frac{37\pi^2}{30}T^4\left(1 - \frac{110}{37\pi}\alpha_s\right) + \left(3\mu_q^2T^2 + \frac{3}{2\pi^2}\mu_q^4\right)\left(1 - \frac{2}{\pi}\alpha_s\right) + \varepsilon_s, \qquad (2)$$

where the quark chemical potential μ_q can be expressed in terms of the baryochemical potential μ_b as $\mu_q = \mu_b/3$.

Other thermodynamic quantities of interest include the pressure P and the quark density $n_q = N_q/V_{\rm fb}$. These are related to the energy density (2) by the equations

$$P = \frac{1}{3}\varepsilon, \qquad n_q = \left(\frac{\partial P}{\partial \mu_q}\right)_T, \qquad (3)$$

$$n_q = 2\left(\mu_qT^2 + \frac{\mu_q^3}{\pi^2}\right)\left(1 - \frac{2}{\pi}\alpha_s\right).$$

Since the number of quarks in the initial fireball, N_q, is determined by the geometry of a given collision as $N_q = 3N_b$, the volume of the fireball $V_{\rm fb}$ in the first order in α_s can be obtained from Eqs. (1) and (3). The result is

$$V_{\rm fb} = \frac{3N_b}{2\left(\mu_qT^2 + \mu_q^3/\pi^2\right)}\left(1 + \frac{2}{\pi}\alpha_s\right). \qquad (4)$$

Given the fireball volume, we can now easily determine its mass from the energy density (2):

$$M_{\rm fb} = \varepsilon V_{\rm fb}. \qquad (5)$$

The mass distribution of a Centauro fireball in Pb + Pb collisions at $\sqrt{s} = 5.5\ A$ TeV, the baryochemical-potential value of $\mu_b = 1.8$ GeV, and various values of its temperature ($T = 130$, 190, and 250 MeV) is displayed in Fig. 2.

Kinematics of a Centauro fireball. Centauro events were observed in experiments with cosmic rays in the projectile-fragmentation region [1, 2]. We assume that the longitudinal-momentum distribution of the product fireball obeys the same scaling law as that which is valid for the production of secondary particles and which, at low energies and high values of x_F, is described by the empirical formula

$$dN/dx_F \sim (1 - x_F)^n, \quad n \approx 3.$$

Each constituent quark belonging to the projectile nucleus and participating in fireball formation traverses the target nucleus. In the fragmentation region, the transverse-momentum distribution of a quark is given by

$$dN_q/dp_T^2 \sim \exp\left(-\frac{p_T^2}{p_0^2}\right),$$

where the slope parameter is $p_0 = 0.3$ GeV/c. The vector sum of the transverse momenta of all quarks involved in the interaction process specifies the transverse momentum of the relevant Centauro fireball.

The fireball-rapidity range can be obtained on the basis of the following assumptions. The maximum rapidity of a fireball is attained when it carries the entire projectile-fragment energy, $E_{\max} = E_{\text{beam}} N_b/A_{\text{beam}}$:

$$y_{\max} = \ln \frac{2E_{\max}}{M_{\text{fb}}}.$$

By way of example, we indicate that, for collisions of lead nuclei at an energy of $\sqrt{s} = 5.5$ TeV per nucleon, we have $N_b = 0.9\,A_{\text{beam}} = 186$, the fireball mass M_{fb} at $T = 190$ MeV and $\mu_b = 1.8$ GeV being 466 GeV. In this case, the maximum rapidity is

$$y_{\max} = 7.69.$$

However, the effect of nuclear stopping is expected to be significant in high-energy heavy-ion collisions, this effect determining the degree to which the energy of the relative motion of colliding nuclei may be transferred to thermodynamic degrees of freedom. The nuclear stopping power can be expressed in terms of the shift Δy_{ns} of the rapidity of particles produced in a nucleus–nucleus collision with respect to the maximum rapidity in an NN collision. The actual rapidity of a Centauro fireball is then given by

$$y_{\text{fb}} = y_{\max} - \Delta y_{\text{fb}}. \tag{6}$$

The quantity Δy_{fb} is related to Δy_{ns} and is a crucial input parameter of the model, the possibility of observing Centauro events being dependent on this parameter. For Δy_{ns}, the mean value predicted by the HIJING [10] and VENUS [15] event generators is 2.3, but values in the range between 2.0 and 3.5 are also probable [5].

Energy conservation in Centauro events. Once the kinematics of a fireball has been completely defined, it is possible to calculate the momentum of the recoil system, which consists of secondary particles from the target nucleus. Denoting by p_{Cn} the 4-momentum of the Centauro fireball and by p_{rec} the 4-momentum of the recoil system, we can write the momentum conservation law as

$$p_{\text{proj}} + p_{\text{targ}} = p_{\text{Cn}} + p_{\text{rec}}.$$

Table 1. Recoil-system mass M_{rec} and rapidity y_{rec} in Pb + Pb collisions for various values of the Centauro fireball rapidity shift Δy_{fb}

Δy_{fb}	$M_{\text{rec}}/\sqrt{s_{aa}}$	y_{rec}
2.0	0.93	−0.07
2.5	0.96	−0.04
3.0	0.97	−0.03
3.5	0.98	−0.02

We also denote by $\sqrt{s_{aa}}$ the collision energy of overlapping fragments in the c.m. frame. If $\sqrt{s_{NN}}$ is the nuclear-collision energy per nucleon, we obviously have $\sqrt{s_{aa}} = N_b\sqrt{s_{NN}}$, where N_b is given by Eq. (1). Disregarding the fireball mass against $\sqrt{s_{aa}}$, we find that the invariant mass of the recoil system, M_{rec}, assumes the form

$$M_{\text{rec}} = \sqrt{s_{aa}}(1-\delta)^{1/2},$$

where $\delta \approx 2M_{\text{fb}} \cosh y_{\text{fb}}/\sqrt{s_{aa}}$. For the recoil-system rapidity y_{rec}, we have

$$\sinh y_{\text{rec}} \approx \frac{\delta/2}{(1-\delta)^{1/2}}.$$

In the case where the nuclear-stopping power is such that Δy_{ns} is about a few units, $\Delta y_{\text{ns}} = 2$–3, the recoil system of particles carries virtually the entire nuclear-collision energy $\sqrt{s_{aa}}$. In this approximation, it can easily be seen that the parameter δ is very small; therefore, the invariant mass of the recoil system is close to $\sqrt{s_{aa}}$, while y_{rec} is small.

For the purposes of illustration, the recoil-system mass and rapidity in central collisions of lead nuclei at an energy of $\sqrt{s} = 5.5$ TeV per nucleon, $\sqrt{s_{aa}} = 1140$ TeV, are given in Table 1 for the Centauro fireball mass of $M_{\text{fb}} = 530$ GeV at various values of Δy_{fb}. From the data in Table 1, it follows that the recoil system is formed in the central-rapidity region; therefore, secondary particles can be recorded in central detectors of relevant experiments. The composition of the recoil system remains unknown.

Fireball in the strange-quark model. It was indicated above that, in the initial Centauro fireball, gluons fragment into $s\bar{s}$ pairs, whereby there occurs chemical equilibration. The density of strange quarks is given by [16]

$$n_s = 1.37 \times 10^{-3}\ \text{GeV}^3 \left(\frac{T}{200\ \text{MeV}}\right) K_2\left(\frac{m_s}{T}\right), \tag{7}$$

where $K_2(x)$ is a modified Bessel function of the second order. Upon the multiplication of Eq. (7) by

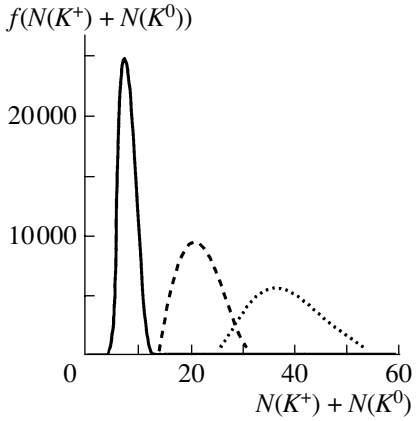

Fig. 3. Distribution of the number of K^+ and K^0 mesons emitted from the Centauro fireball formed in Pb + Pb collisions at an energy of $\sqrt{s} = 5.5$ TeV per nucleon for $\mu_b = 1.8$ GeV at various values of temperature: $T =$ (solid curve) 130, (dashed curve) 190, and (dotted curve) 250 MeV.

the fireball volume V_{fb} (4), one obtains the number of $s\bar{s}$ pairs in the fireball and, hence, the number of emitted K mesons:

$$N_{\bar{s}} = N(K^+) + N(K^0) = n_s V_{\text{fb}}. \qquad (8)$$

For the fireball thermodynamic parameters of $\mu_b =$ 1.8 GeV and $T = 130$, 190, and 250 MeV, Fig. 3 shows the distribution of the number of K mesons emitted from a Centauro fireball produced in Pb + Pb collisions at an energy of $\sqrt{s} = 5.5$ TeV per nucleon. Prior to kaon emission from the fireball, the total number of quarks is $N'_q = 3N_b + 2N_{\bar{s}}$. It follows that, at this stage of fireball evolution, the mean energy per constituent quark is

$$\epsilon'_q = M_{\text{fb}}/N'_q. \qquad (9)$$

After the emission of $2N_{\bar{s}}$ quarks in the form of kaons, the mass of the remaining SQM fireball is determined by the mean energy density (9) and the number of quarks in the fireball (N_q):

$$M'_{\text{fb}} = N_q \epsilon'_q = M_{\text{fb}} \left(1 - \frac{2N_{\bar{s}}}{N_q}\right).$$

Within our model, the emission of antistrangeness is described as the isotropic decay of the initial Centauro fireball into $N_{\bar{s}}$ kaons and an SQM fireball of mass M'_{fb}.

Decay of an SQM fireball. Upon kaon emission, the initial Centauro fireball transforms into slightly strange quark matter with a long lifetime ($\tau \sim 10^{-9}$ s [5]). At the final stage of its evolution, the SQM fireball decays into baryons and strangelets. The latter are light SQM drops of $A > 6$ that are characterized by a high ratio of the strangeness to the baryon number ($S/A \approx 1$) and a low value of the charge-to-mass ratio ($Z/A \approx 0$). For the sake of simplicity, we assume that only one strangelet is formed in an SQM fireball via a random selection of u, d, and s quarks among all quarks of the fireball. If the strangeness of an SQM fireball was not entirely converted into a strangelet, the remaining s quarks form strange hyperons. Baryons are formed via a random selection of three quarks among the quarks of the fireball. Priority is given to the formation of nucleons, those quarks that could not form a nucleon forming strange hyperons. The decay of an SQM fireball is isotropic. In order to describe further decays of kaons and strange hyperons, use is made of the JETSET event generator [17].

General features of Centauro events. The features of Centauro events in Pb + Pb collisions at an energy of $\sqrt{s} = 5.5$ TeV per nucleon are listed in Table 2. For given values of the impact parameter b, temperature T, and the baryochemical potential μ_b, we have calculated the baryon number N_b, the energy density ε, the quark-number density n_q, the fireball volume V_{fb}, the initial-fireball mass M_{fb}, the SQM fireball mass M'_{fb}, the strange-quark-number density n_s, and the number $N(K^{+,0})$ of emitted kaons. For some values of the input model parameters, Centauro events are characterized, especially in central collisions ($b = 0$) and at high temperatures, by a high invariant mass and a large number of kaons. Nucleus–nucleus collisions at large values of the impact parameter may also lead to the production of Centauro events, but the strangeness will be lower in such events.

Secondary particles from Centauro events that were observed in cosmic-ray experiments feature no, or virtually no, photon component. Since our model relies on the assumption that the initial Centauro fireball consists only of u and d quarks and gluons, in which case the production of $\bar{u}$ and $\bar{d}$ antiquarks is suppressed, baryons are dominant among secondary particles from Centauro events.

Kaons emitted from the initial fireball may decay into pions, which provide an additional source of photons. However, the electromagnetic component of such events is suppressed to an extremely high degree. For $\mu_b = 1.8$ GeV and $T = 190$ MeV, Fig. 4 shows the ratio of the multiplicity of hadrons to the total multiplicity (hadrons plus photons) in Centauro events originating from Pb + Pb collisions at an energy of $\sqrt{s} = 5.5$ TeV per nucleon. This ratio is close to unity, its mean value being $\langle N_h/N_{\text{tot}} \rangle = 0.93$; the deviation of this value from unity is due to the photon component. Figure 5 displays the ratio of the total energy of hadrons to the total energy of all components in the same events. This ratio is also close to unity, its mean value being $\langle \sum E_h / \sum E_{\text{tot}} \rangle = 0.99$. It should

Table 2. Features of Centauro events for various values of the impact parameter, temperature, and the baryochemical potential

μ_b, GeV	T, MeV	N_b	ε, GeV/fm^3	n_q, fm^{-3}	V_{fb}, fm^3	M_{fb}, GeV	M'_{fb}, GeV	n_s, fm^{-3}	$N(K^{+,0})$
				$b = 0$					
1.8	130	186	4.3	6.7	83	357	344	0.13	11
	190	186	7.7	9.2	61	466	423	0.48	28
	250	186	13.6	12.5	45	607	515	1.14	50
1.5	130	186	2.7	4.4	125	334	316	0.13	16
	190	186	5.3	6.5	86	460	402	0.48	40
	250	186	10.4	9.2	60	626	503	1.14	68
				$b = 5$ fm					
1.8	130	114	4.3	6.7	51	219	212	0.13	6
	190	114	7.7	9.2	37	286	260	0.48	17
	250	114	13.6	12.5	27	372	315	1.14	31
				$b = 8$ fm					
1.8	130	53	4.3	6.7	24	102	98	0.13	3
	190	53	7.7	9.2	17	133	120	0.48	8
	250	53	13.6	12.5	13	173	147	1.14	14

be emphasized that the above ratios also depend on the thermodynamic parameters of a Centauro fireball. For example, the production of kaons will be more copious at higher temperatures; therefore, there will be more product photons, with the result that the deviations of these ratios from unity will be more pronounced .

Secondary particles that originate from the decay of a Centauro fireball have a higher mean transverse momentum than those from ordinary hadron interactions. The mean transverse momentum $\langle p_T \rangle$ measured in cosmic rays [1, 2] is 1.75 GeV/c. The transverse-momentum distributions of hadrons in Centauro events induced by Pb + Pb collisions at an energy of $\sqrt{s} = 5.5$ TeV per nucleon are given in Fig. 6 for three sets of values of the baryochemical potential μ_b and temperature T: $\mu_b = 1.8$ GeV and $T = 190$ MeV, $\mu_b = 1.8$ GeV and $T = 250$ MeV, and $\mu_b = 3.0$ GeV and $T = 250$ MeV. In these events, the mean values of p_T are 1.34, 1.47, and 1.75 GeV/c, respectively. According to the predictions of the HIJING model, the mean transverse momentum in ordinary hadron events is $\langle p_T \rangle = 0.44$ GeV/c, which is three to four times lower than in Centauro events.

The rapidity distribution of products originating from the decay of a Centauro fireball explicitly depends on the nuclear stopping power. The rapidity distributions of secondary particles (hadrons) are shown in Fig. 7 for three values of the fireball rapidity shift ($\Delta y_{\text{fb}} = 2.0$, 2.5, and 3.0). Obviously, all secondary particles from the decay of a Centauro fireball are distributed in a very forward kinematical region, as was observed in cosmic-ray experiments. According to the data in Table 1, however, a full event that involves the production of a Centauro fireball contains

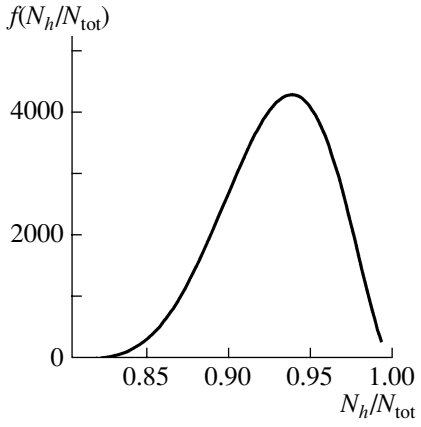

Fig. 4. Distribution of the ratio of the hadron multiplicity to the total multiplicity (hadrons plus photons) in Centauro events for $\mu_b = 1.8$ GeV and $T = 190$ MeV in Pb + Pb collisions at an energy of $\sqrt{s} = 5.5$ TeV per nucleon.

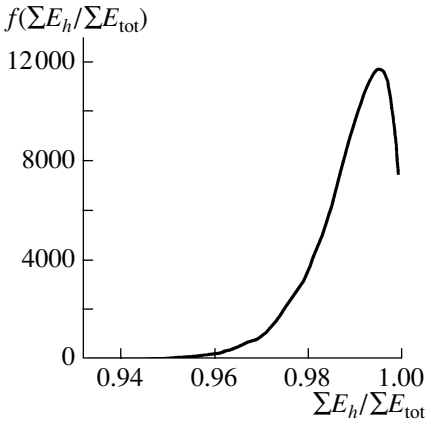

Fig. 5. Distribution of the ratio of the total energy of hadrons to the total energy of all components in Centauro events at $\mu_b = 1.8$ GeV and $T = 190$ MeV in Pb + Pb collisions at an energy of $\sqrt{s} = 5.5$ TeV per nucleon.

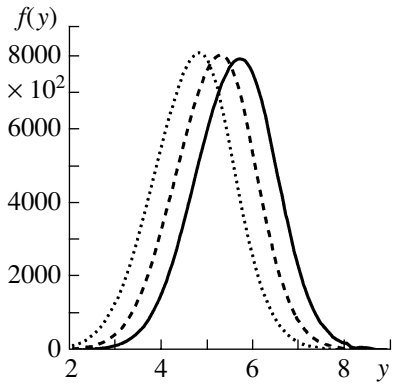

Fig. 7. Rapidity distribution of hadrons in Centauro events induced by Pb + Pb collisions at an energy of $\sqrt{s} = 5.5$ TeV per nucleon for three values of the fireball rapidity shift: $\Delta y_{\rm fb}$ = (solid curve) 2.0, (dashed curve) 2.5, and (dotted curve) 3.0.

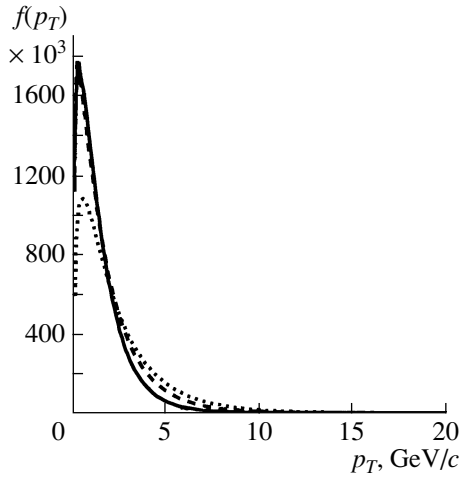

Fig. 6. Transverse-momentum distribution of hadrons in Centauro events induced by Pb + Pb collisions at an energy of $\sqrt{s} = 5.5$ TeV per nucleon at various values of the baryochemical potential and temperature: (solid curve) $\mu_b = 1.8$ GeV and $T = 190$ MeV, (dashed curve) $\mu_b = 1.8$ GeV and $T = 250$ MeV, and (dotted curve) $\mu_b = 3.0$ GeV and $T = 250$ MeV.

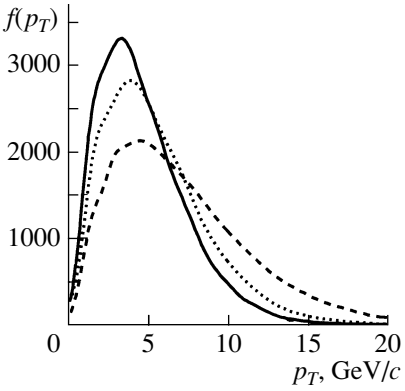

Fig. 8. Transverse-momentum distribution of strangelets originating from the decay of a Centauro fireball in Pb + Pb collisions at an energy of $\sqrt{s} = 5.5$ TeV per nucleon for three sets of values of the baryochemical potential and temperature: (solid curve) $\mu_b = 1.8$ GeV and $T = 190$ MeV, (dashed curve) $\mu_b = 1.8$ GeV and $T = 250$ MeV, and (dotted curve) $\mu_b = 3.0$ GeV and $T = 250$ MeV.

recoil-system particles as well, which are distributed in the central region ($y \approx 0$).

The kinematics of strangelets, which can also be produced in Centauro events, is similar to the kinematics of hadrons. Because of their higher mass, strangelets have a higher transverse momentum. The transverse-momentum distribution of strangelets formed in the decays of a Centauro fireball in Pb + Pb collisions at an energy of $\sqrt{s} = 5.5$ TeV per nucleon is displayed in Fig. 8 for three sets of values of the thermodynamic parameters: $\mu_b = 1.8$ GeV and $T = 190$ MeV, $\mu_b = 1.8$ GeV and $T = 250$ MeV, and $\mu_b = 3.0$ GeV and $T = 250$ MeV. The rapidity distribution of strangelets is given in Fig. 9 for three values of the fireball rapidity shift: $\Delta y_{\rm fb} = 2.0$, 2.5, and 3.0.

2. DETECTION OF CENTAURO EVENTS BY THE CASTOR DETECTOR

In this section, we present the results obtained by calculating the geometric efficiency of the detection of Centauro events by the CASTOR detector at LHC [18–20]. This detector is intended for studying, in Pb + Pb collisions at an energy of $\sqrt{s} = 5.5$ TeV per nucleon, the forward kinematical region, which is rich in baryons. The detector will be installed at a distance of about 16.4 m from the point of interaction

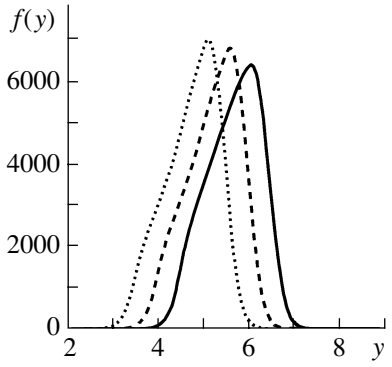

Fig. 9. Rapidity distribution of strangelets produced in the decay of a Centauro fireball in Pb + Pb collisions at an energy of $\sqrt{s} = 5.5$ TeV per nucleon for three values of the fireball rapidity shift: $\Delta y_{\text{fb}} =$ (solid curve) 2.0, (dashed curve) 2.5, and (dotted curve) 3.0.

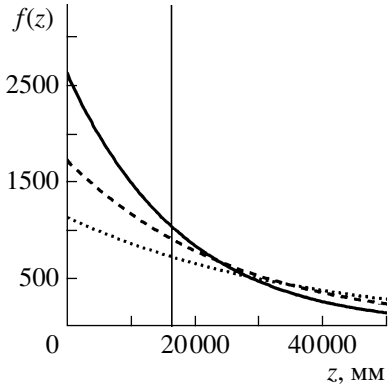

Fig. 10. Decay-length distribution of an SQM fireball at $T = 250$ MeV and $\mu_b = 1.8$ GeV for three values of the fireball rapidity shift: $\Delta y_{\text{fb}} =$ (solid curve) 3.0, (dashed curve) 2.5, and (dotted curve) 2.0. The vertical line at $z = 16.4$ m indicates the detector position.

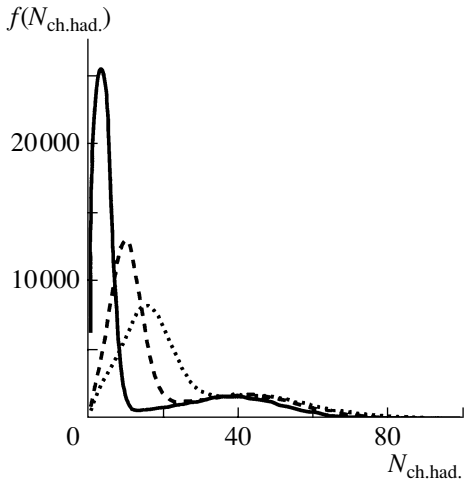

Fig. 11. Multiplicity distribution of charged hadrons in the detector for Centauro events from Pb + Pb collisions at an energy of $\sqrt{s} = 5.5$ TeV per nucleon for the fixed values of $\Delta y_{\text{fb}} = 2.5$ and $\mu_b = 1.8$ GeV at three values of temperature: $T =$ (solid curve) 130, (dashed curve) 190, and (dotted curve) 250 MeV.

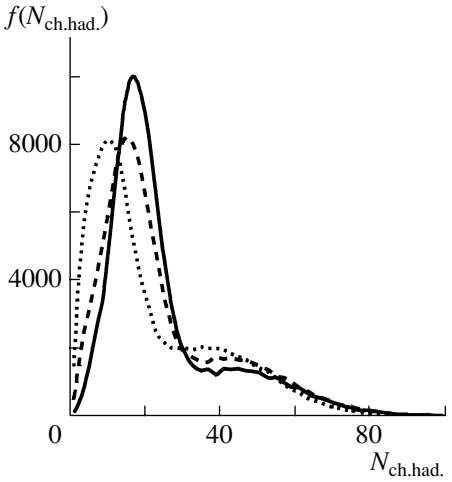

Fig. 12. Multiplicity distribution of charged hadrons in the detector for Centauro events from Pb + Pb collisions at an energy of $\sqrt{s} = 5.5$ TeV per nucleon for the fixed values of $\mu_b = 1.8$ GeV and $T = 250$ MeV at three values of the fireball rapidity shift: $\Delta y_{\text{fb}} =$ (solid curve) 2.0, (dashed curve) 2.5, and (dotted curve) 3.0.

of the beams used. It will be azimuthally symmetric with respect to the beam pipe and will be placed as close to it as is possible. The inner and the outer radius of the detector are, respectively, $R_{\text{in}} = 2.8$ cm and $R_{\text{out}} = 15$ cm, which will make it possible to cover the pseudorapidity range $5.6 < \eta < 7.0$.

Because of its long lifetime in the rest frame, $\tau \sim 10^{-9}$ s, and high rapidity, an SQM fireball may decay far off the point of interaction of the beams involved. The fireball decay length depends on the fireball mass and on the rapidity shift Δy_{fb} (6), which also determines the rapidity of an SQM fireball. For three values of the rapidity shift, $\Delta y_{\text{fb}} = 3.0$, 2.5, and 2.0, Fig. 10 shows the distribution of the fireball decay length at $T = 250$ MeV and $\mu_b = 1.8$ GeV. The detector position is indicated by the vertical solid line. As can be seen, a considerable number of SQM fireballs decay behind the detector; that is, their decay products will escape detection. Only K mesons emitted by the primary fireball at the initial stage of its evolution can be recorded in this case.

The detection of secondary particles from Centauro events also greatly depends on model parameters—namely, on thermodynamic quantities (μ_b and T) that determine the fireball mass, as well as on the fireball rapidity shift Δy_{fb}. We compare the potentials of the CASTOR detector for recording a Centauro fireball formed at various values of T and fixed values

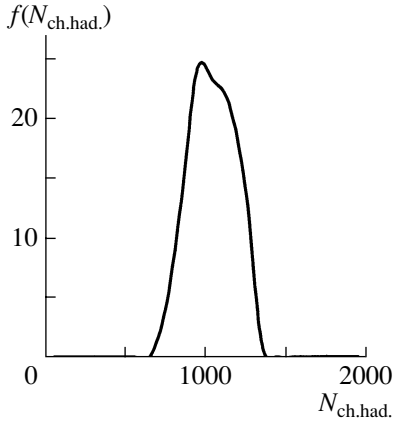

Fig. 13. Multiplicity distribution of charged hadrons in the detector for ordinary Pb + Pb nuclear collisions at an energy of $\sqrt{s} = 5.5$ TeV per nucleon in accordance with the predictions of the HIJING model.

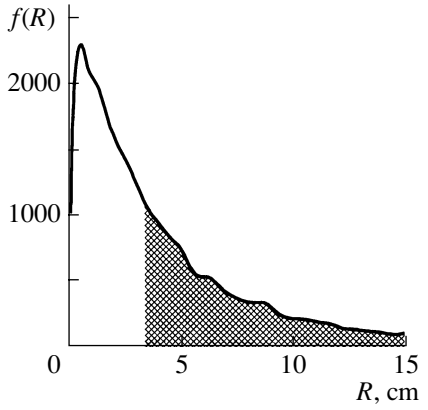

Fig. 14. Distribution of the radius at which strangelets formed in the decay of a Centauro fireball from Pb + Pb collisions at an energy of $\sqrt{s} = 5.5$ TeV per nucleon hit the detector plane for the model-parameter values of $\mu_b = 1.8$ GeV and $T = 250$ MeV at the fireball rapidity shift of $\Delta y_{\text{fb}} = 2.5$. The shaded region represents the acceptance of the CASTOR detector.

of μ_b and Δy_{fb}, as well as at various values of Δy_{fb} at fixed values of the thermodynamic parameters. At the fixed values of $\Delta y_{\text{fb}} = 2.5$ and $\mu_b = 1.8$ GeV, the multiplicity distribution of charged hadrons in the detector is displayed in Fig. 11 for three values of the fireball temperature: $T = 130$, 190, and 250 MeV. The dependence of the charged-hadron multiplicity on the rapidity shift at the fixed values of $\mu_b = 1.8$ GeV and $T = 250$ MeV is illustrated in Fig. 12, the curves there corresponding to $\Delta y_{\text{fb}} = 2.0$, 2.5, and 3.0. The shape of these distributions is distorted by the fireball decay length in accordance with Fig. 10. Sharp peaks at low multiplicities correspond to events where an SQM fireball decays behind the detector and where only K mesons contribute to the recorded multiplicity.

For each set of parameter values, the number of recorded charged hadrons must be compared with the total multiplicity of charged hadrons produced in Centauro events. For various values of the model parameters, the geometric efficiency of detection is presented in Table 3. In the fourth column of this table, the mean geometric efficiency of detection of charged hadrons, $e_{\text{ch.had.}}$, is given for various values of μ_b, T, and Δy_{fb}. The multiplicity of charged hadrons from Centauro events in the detector is rather low—not more than 120, its mean value being within the range 30–60. As follows from Fig. 4, the multiplicity of photons is much lower. The multiplicity of charged particles in Centauro events differs significantly from that which is expected in ordinary nucleus–nucleus collisions, where it is equal to a few thousand. The multiplicity of charged hadrons in the CASTOR detector for Pb + Pb nuclear collisions at an energy of $\sqrt{s} = 5.5$ TeV per nucleon and impact-parameter values in the range $0 < b < 5$ fm is shown in Fig. 13 in accordance with the predictions of the HIJING model. As can be seen from this figure, the multiplicity in ordinary events is, on average, 20 times as high as that in Centauro events.

Table 3. Geometric efficiency e of charged-hadron and strangelet detection versus μ_b, T, and Δy_{fb}

μ_b, GeV	T, MeV	Δy_{fb}	$e_{\text{ch.had.}}$	$e_{\text{str.}}$
1.8	130	2.5	0.38	0.67
1.8	190	2.5	0.42	0.57
1.8	250	2.5	0.46	0.46
1.8	250	2.0	0.42	0.61
1.8	250	3.0	0.35	0.36
3.0	250	2.5	0.39	0.45

Because of their higher mass, strangelets have a longitudinal momentum higher than that of ordinary hadrons. Therefore, stangelets travel in a direction closer to the beam axis. The distribution of the radius at which strangelets produced in the decay of a Centauro fireball in Pb + Pb collisions at an energy of $\sqrt{s} = 5.5$ TeV per nucleon hit the detector plane is displayed in Fig. 14 for the model-parameter values of $\mu_b = 1.8$ GeV and $T = 250$ MeV at the fireball rapidity shift of $\Delta y_{\text{fb}} = 2.5$. The shaded region corresponds to the acceptance of the CASTOR detector. For various values of the model parameters, the geometric efficiency of strangelet detection, e_{str}, is presented in the last column of Table 3. The results for various configurations of the detector can be found in [6, 21].

CONCLUSIONS

Model results concerning the production of Centauro events in heavy-ion collisions at the LHC energy have been presented. The phenomenological model of Centauro events that was initially introduced in [4, 5] provides a consistent explanation of such events. On the basis of this model, we have constructed a quantitative model and the CNGEN event generator, which proved to be quite a useful tool for assessing the geometric efficiency of the detection of Centauro events and strangelets associated with them in experiments planned at LHC. The possibility of observing Centauro events depends greatly on the thermodynamic parameters of the model and on the nuclear stopping power.

Centauro events have the following distinctive features in the CASTOR detector, which is intended for seeking such events in experiments at LHC:

(i) low multiplicity of recorded charged particles, $\langle N_{\text{ch.had.}}\rangle = 50$, in relation to the value of $\langle N_{\text{ch.had.}}\rangle = 1000$ in ordinary hadronic events;

(ii) a strong dominance of the hadron multiplicity, the mean ratio of the hadron multiplicity to the total multiplicity of final-state particles being $\langle N_h/N_{\text{tot}}\rangle > 0.9$ in Centauro events versus $\langle N_h/N_{\text{tot}}\rangle = 0.6$ in ordinary hadronic events;

(iii) a considerable dominance of the total energy of the hadron component in the total energy deposited in the detector in relation to the energy deposition in ordinary events, the mean ratio of these energies being $\langle \sum E_h/\sum E_{\text{tot}}\rangle = 0.99$ in the former case versus $\langle \sum E_h/\sum E_{\text{tot}}\rangle = 0.80$ in the latter case;

(iv) a high mean transverse momentum of final-state particles, $\langle p_T\rangle > 1$ GeV/c versus $\langle p_T\rangle = 0.44$ GeV/c in ordinary hadron collisions.

The model also predicts the possibility of strangelet formation in the decay of a Centauro fireball. If strangelets do indeed exist and if they behave in accordance with the model prediction, the geometric efficiency of their detection by the CASTOR detector is 40 to 60% for $A > 6$ strangelets.

ACKNOWLEDGMENTS

We are grateful to Zbigniew Włodarczyk for enlightening comments.

This work was supported in part by the Polish State Committee for Scientific Research (grant no. 2P03B 011 18) and by the SPUB-M/CERN/P-03/DZ 327/2000 grant.

REFERENCES

1. C. M. G. Lattes, Y. Fugimoto, and S. Hasegawa, Phys. Rep. **65**, 151 (1980).
2. Chacaltaya and Pamir Collab., *Contributions to 23rd ICRC, Calgary, 1993*; ICRR-Report-295-93-7 (1993).
3. A. D. Panagiotou *et al.*, Z. Phys. A **333**, 355 (1989).
4. A. D. Panagiotou *et al.*, Phys. Rev. D **45**, 3134 (1992).
5. M. N. Asprouli, A. D. Panagiotou, and E. Gładysz-Dziaduś, Astropart. Phys. **2**, 167 (1994).
6. E. Gładysz-Dziaduś, Report No. 1879/PH, Inst. Nucl. Phys. (Kraków, 2001); hep-ph/0111163; Part. Nucl. **34**, 564 (2003).
7. ALICE Technical Proposal, CERN/LHCC/95-71.
8. CMS Technical Proposal, CERN/LHCC/94-38.
9. E. Gładysz-Dziaduś and A. D. Panagiotou, in *Proc. of the Int. Symp. on Strangeness and Quark Matter, Krete, 1994,* Ed. by G. Vassiliadis *et al.* (World Sci., Singapore, 1995), p. 265; Internal note ALICE/PHY/95-18.
10. M. Gyulassy and X.-N. Wang, Comput. Phys. Commun. **83**, 307 (1994); Preprint LBL-34346; nucl-th/9502021.
11. O. P. Theodoratou and A. D. Panagiotou, Astropart. Phys. **13**, 173 (2000).
12. C. Greiner, D. H. Rischke, H. Stöcker, and P. Koch, Phys. Rev. D **38**, 2797 (1988).
13. B. Müller, Preprint DUKE-TH-92-36; hep-th/9211010.
14. J. W. Harris and B. Müller, Preprint DUKE-TH-96-105; hep-ph/9602235.
15. K. Werner, Phys. Rep. **232**, 87 (1993).
16. T. S. Biro and J. Zimanyi, Nucl. Phys. A **395**, 241 (1983).
17. T. Sjöstrand, Comput. Phys. Commun. **82**, 74 (1994).
18. A. L. S. Angelis and A. D. Panagiotou, J. Phys. G **23**, 2069 (1997).
19. A. L. S. Angelis *et al.*, hep-ex/9901038; in *Proc. of the XXVIII Int. Symp. on Multiparticle Dynamics, Delphi, Greece, 1998,* Ed. by N. G. Antoniou *et al.* (World Sci., Singapore, 1999), p. 134.
20. A. L. S. Angelis *et al.*, Int. Note ALICE/CAS 1997-07.
21. E. Gładysz-Dziaduś *et al.*, in *Proc. of the 3rd Int. Conf. on Physics and Astrophysics of Quark–Gluon Plasma, Jaipur, 1997,* Ed. by B. C. Sinha *et al.* (Narosa, New Delhi, 1998), p. 554.

Translated by A. Isaakyan

Physics of Atomic Nuclei, Vol. 67, No. 2, 2004, pp. 406–413. Translated from Yadernaya Fizika, Vol. 67, No. 2, 2004, pp. 425–432.

ELEMENTARY PARTICLES AND FIELDS
Theory

Direction of the Expansion of the Volume of Pion Generation in MgMg Collisions at 4.3 GeV/c per Nucleon

M. Kh. Anikina*, Yu. A. Belikov, A. I. Golokhvastov, J. Lukstins, and S. A. Sedykh

Joint Institute for Nuclear Research, Dubna, Moscow oblast, 141980 Russia

Received August 26, 2002

Abstract—The relative velocities of elements of the volume of pion generation in central MgMg interactions at 4.3 GeV/c per nucleon in various directions and spacetime sizes of these elements are investigated by the method employing the interference correlations of negatively charged pions. The results are in agreement with the version where generation-volume elements fly apart predominantly in the longitudinal direction. © *2004 MAIK "Nauka/Interperiodica".*

1. INTRODUCTION

Identical pions emitted from their generation volume (in our case, from the region of a collision of two Mg nuclei) are related by interference correlations, which are significant for pions having close momenta: $p_1 - p_2 \sim \hbar/R$, where R is the size of the generation volume [1] (in the following, we usually use the system of units where $c = \hbar = 1$).

The correlation function $C(p_1 - p_2)$—that is, the ratio of the actual two-particle spectrum of pions to the background spectrum where interference is "switched off" in one way or another—carries information about the spacetime sizes of the generation volume [2–4], about the velocity of the generation volume in a given reference frame [5–7], and about the sizes and velocities of various elements of this volume [8–11]. The correlation function in question can be represented as

$$C(q) = 1 + \left| \int \rho(r) \exp(iqr) d^4 r \right|^2, \qquad (1)$$

where $\rho(r)$ is the spacetime shape of the generation volume (or of an element of this volume)—that is, the distribution of the pion-emission points $r = (t, \mathbf{r})$ (more precisely, of the centers of initial wave packets [12, 13])—and $q = (q_0, \mathbf{q}) = p_1 - p_2$ is the difference of the 4-momenta of two pions [$p = (E, \mathbf{p})$].

The notion of an "element" appears in the case of a nonuniform generation volume whose parts (elements) move in different directions and emit pions into different regions of the momentum spectrum. This gives no way to measure the generation volume for the total ensemble of pions [14], but it is possible to determine the features of various elements of this generation volume for subensembles of pions from bounded regions of the momentum spectrum [8, 10].

It should be emphasized that, upon shrinking the momentum spectrum of pions chosen for an analysis, the spacetime size of an element must not inevitably decrease. For such elements, we can use, for example, two Δ isobars having close velocities and originating from independent production processes that occur in different parts of the nuclear-collision region.

Assuming that the spacetime shape of the generation-volume element in its rest frame is close to a Gaussian distribution,

$$\rho(r) = \frac{1}{(2\pi)^2 R_L R_H R_V T} \qquad (2)$$
$$\times \exp\left(-\frac{r_L^2}{2R_L^2} - \frac{r_H^2}{2R_H^2} - \frac{r_V^2}{2R_V^2} - \frac{t^2}{2T^2} \right),$$

where R_i are the root-mean-square deviations of the pion-emission points and T is the root-mean-square deviation of the pion-emission instants, we find from (1) that

$$C(q) = 1 \qquad (3)$$
$$+ \exp\left(-q_L^2 R_L^2 - q_H^2 R_H^2 - q_V^2 R_V^2 - q_0^2 T^2 \right).$$

(Hereafter, the subscript "L" denotes the longitudinal direction, while the subscripts "H" and "V" denote the directions transverse to the beam that are, respectively, horizontal and vertical.)

By approximating the experimental correlation function by this or some other expression, one can determine the fitted sizes R_i and T of a generation-volume element. The root-mean-square sizes are weakly dependent on the choice of approximation.

*e-mail: anikina@sunhe.jinr.ru

In order to describe an experimental peak better, the approximation given by (3) is usually supplemented with an additional free parameter—a preexponential factor λ. We will not use this factor because, in our case, it appears to be close to unity, so that its presence has virtually no effect on the results (see also [13]). This is likely to be due to a small size of the magnesium nucleus, whose shape is close to a Gaussian one, and to the absence of long-lived resonances because of low energy.

This study is aimed at determining the sizes of elements of the volume of π^--meson generation in central MgMg collisions at 4.3 GeV/c per nucleon and the velocities of these elements in different directions. The description of experimental data and of the procedures used to form the background spectrum and to fit the correlation function can be found in [13], along with the derivation of formula (1), which plays a crucial role in the method of interference correlations.

2. UNIFORM SUBENSEMBLE

Upon fitting the total ensemble of π^- mesons in the MgMg c.m. frame, the parameter T^2, which stands for the variance of the distribution of pion-emission instants, appears to be negative [8, 10]—that is, the experimental correlation function grows with increasing q_0^2 at constant $\mathbf{q}^2$ [10]. The parameter T^2 becomes positive only if one analyzes subensembles of pions falling within bounded regions of the momentum spectrum, $|\mathbf{p}| < p_{\mathrm{cut}} \sim 250$ MeV/c in the c.m. frame of the subensemble [10, 13].

The point is that formula (1) is valid only if pions are emitted independently of one another and if the pion ensemble is uniform (pure)—that is, it is described by a unified initial momentum wave function that is independent of the pion-emission point [4, 13, 14].

The total ensemble of pions emitted by a generation volume that expands at relativistic velocities [8, 10] cannot be uniform since, in this ensemble, the amplitude of the probability with which a pion of given momentum is emitted depends on the emission point [14]. In order to select a uniform subensemble of pions, it is necessary to include only those pions in it that fall within a rather narrow region of the momentum spectrum [13].

A subensemble of pions is likely to be quite uniform if pions are emitted in the same quantum state—that is, in one elementary cell of phase space: $2\pi\hbar$ per degree of freedom [15]. In order to arrive at a momentum–coordinate correlation within an elementary cell, one would have to break it down into smaller cells, but this is impossible. Therefore, the second condition is satisfied if the product of the effective size of a generation-volume element and the effective width of the pion momentum spectrum does not exceed $2\pi\hbar$.

In our case, the root-mean-square radii R_i of elements are approximately equal to 3.5 fm [13]. If $2R_i$ is taken to be the total effective size of an element, the effective width of the momentum spectrum must be less than $2\pi\hbar/2R_i \sim 180$ MeV/c. If pions whose momenta are less in magnitude than some p_{cut} [13] are selected to form a subensemble and if the corresponding sphere in momentum space is filled uniformly, the doubled root-mean-square projection of the momentum onto each direction is then found to be $0.9p_{\mathrm{cut}}$. In order to select a pure subensemble of pions, it is therefore sufficient in our case that the quantity p_{cut} not exceed ~ 200 MeV/c. This estimate will be used below, the more so as it is in good agreement with the experimental boundary for obtaining a positive value of the parameter T^2.

In order to measure an object of greater size, it is necessary to use a subensemble of pions having a softer spectrum. By way of example, we indicate that, for central PbPb or AuAu collisions, the value of p_{cut} must be approximately two times smaller (~ 100 MeV/c), while, for pp collisions, it must be greater by a factor of about four.

Returning to the first condition of validity of formula (1), it should be noted that, if two pions are emitted in the same cell of phase space, their initial wave packets overlap, which could contradict the condition that pions are independent [4]. However, experimentalists do not have a different model-independent formula at their disposal. A factor that inspires optimism here is that, if the interval between the points at which two pions are emitted is spacelike, then these events must be independent, not affecting each other. If the time size of an element is identical to its spatial dimensions (this is close to what occurs in our case [13]), such an interval may be expected for more than 75% of pion pairs (four-dimensional sphere from which one eliminates light cones).

3. MOVING ELEMENT

By virtue of the symmetry of MgMg interactions, the reference frame comoving with the central subensemble of pions ($|\mathbf{p}| < p_{\mathrm{cut}}$ in the MgMg c.m. frame) coincides with the reference frame comoving with the generation-volume element that emitted them, and this makes it possible to perform an interference analysis of this subensemble in the MgMg c.m. frame by using the approximation in Eq. (3) [13]. A factorization of the spatial components and the time component in the parametrization given in (2) assumes that the element in question is at rest. In

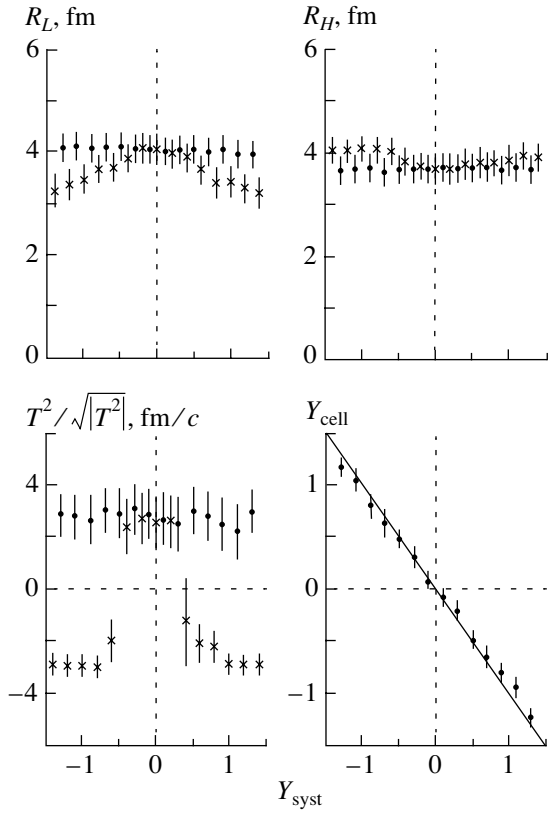

Fig. 1. Sizes and rapidities of the same central generation-volume element that were obtained from a fit to the central subensemble of pions ($|\mathbf{p}| < 200$ MeV in the MgMg c.m. frame) in various reference frames moving along the reaction axis at the rapidities Y_{syst} with respect to the MgMg c.m. frame. The points represent the approximations given by (×) (3) and (•) (4). The solid straight line corresponds to $Y_{\text{cell}} = -Y_{\text{syst}}$.

contrast to what occurs in the moving-element case, where the delay of the emission instant leads to a shift of the emission point, the spatial point of the emission of a pion is not correlated here with the instant of its emission.

An attempt at describing the shape of a moving element in terms of the "immobile" approximation in (3) is given in Fig. 1 (crosses), where the correlation function for the same central subensemble of negatively charged pions ($|\mathbf{p}| < 200$ MeV in the MgMg c.m. frame) is fitted in various reference frames moving at velocities β (rapidities $Y_{\text{syst}} = \ln[(1+\beta)/(1-\beta)]/2$) with respect to the MgMg c.m. frame along the reaction axis. In order to obtain each point, the momenta of pions both from the actual and from the background subensemble were rescaled to the corresponding reference frame prior to fitting.

It can be seen that, as soon as the rapidity of this element with respect to the laboratory frame reaches the value of $|Y_{\text{syst}}| \sim 0.5$, the parameter T^2 becomes negative. With increasing $|Y_{\text{syst}}|$, the size R_L also decreases.

The reason that is responsible for the emergence for the opposite sign of T^2 and which is associated with the procedure used can be seen from Fig. 2, which shows, in the $q_L q_0$ plane, the two-dimensional projections of four correlation functions obtained for the same central subensemble of negatively charged pions in four different reference frames moving along the reaction axis at a rapidity Y_{syst} (see also [16]). The correlation functions in question were additionally bounded along the remaining axes: $|q_H|, |q_V| < 50$ MeV. With increasing Y_{syst}, the correlation peak is extended along the diagonal $q_L = -q_0$ and is contracted along the diagonal $q_L = q_0$.

The maximum of this two-dimensional peak along some straight line parallel to the q_0 axis no longer occurs at $q_0 = 0$ (see vertical dashed straight lines in Fig. 2). Its height along this straight line increases with increasing $|q_0|$ at constant q_L (and q_H and q_V as well), this corresponding to the inverse sign in front of q_0^2 in the approximation given by (3).

The inverse sign is obtained precisely in front of q_0^2 rather than in front of q_L^2, since the straight line that is parallel to the q_L axis and which is at first glance analogous to the preceding one (more specifically, this is a three-dimensional plane intersecting the four-dimensional volume) traverses the kinematically forbidden region $|q_0| > |\mathbf{q}|$, where there are no experimental points (recall that $q_0 = (\mathbf{u} \cdot \mathbf{q})$, where $\mathbf{u}$ is the velocity of the pair: $\mathbf{u} = (\mathbf{p}_1 + \mathbf{p}_2)/(E_1 + E_2)$ [4]). In Fig. 2, we can see the presence of these forbidden cones in the four-dimensional q space. Without them, the isolines at $Y_{\text{syst}} = 0$ would be round (at $R_L = T$—see the next paragraph). In the case of more stringent constraints, $|q_H|, |q_V| \sim 0$, the peaks in Fig. 2 would be completely deprived of their upper and lower sections (bounded by the dash-dotted lines).

For the illustration given in Fig. 2, we did not in fact use the actual two-particle spectrum of pions, since the statistics at our disposal were insufficient in the present case; instead, we took the background spectrum of pion pairs from different events [13], these statistics being ten times as great as those in the actual spectrum. Each such pair was assigned a weight equal to $C(q)$ (3) at $R_i = T = 3.5$ fm, whereupon the quantities q_L and q_0 for each pair both from this and from the usual background spectrum were rescaled to the Y_{syst} frame and were arranged in the two-dimensional q_L–q_0 histograms. It is the ratios of these histograms that are given in Fig. 2. The actual two-dimensional correlation functions for the same pion

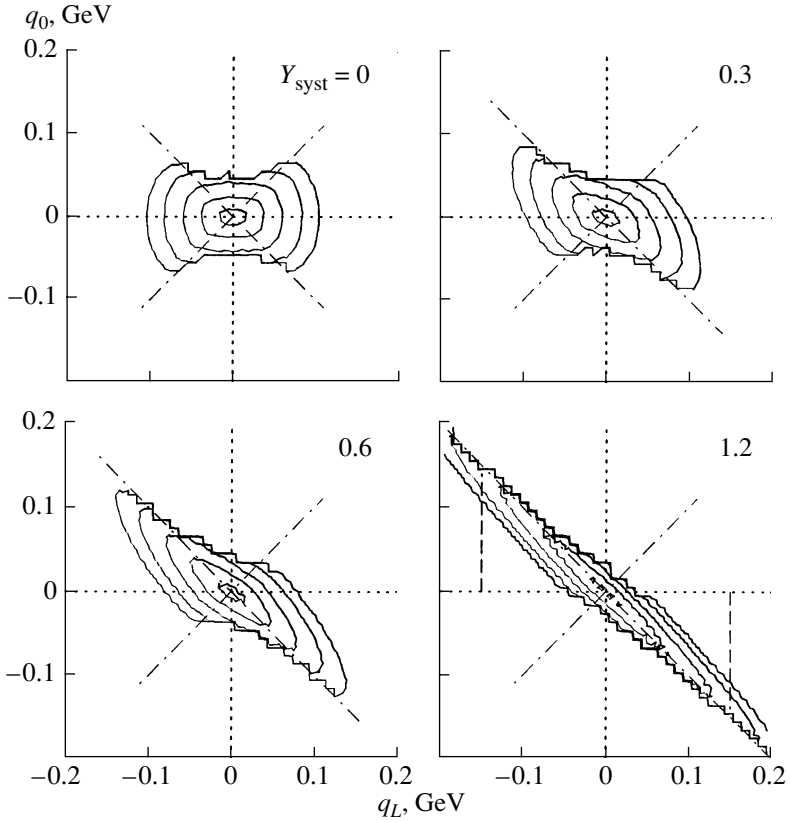

Fig. 2. Two-dimensional projections of the correlation functions for the same central subensemble of pions ($|\mathbf{p}| < 200$ MeV in the MgMg c.m. frame) as obtained in various reference frames moving along the reaction axis at the rapidities Y_{syst} in the MgMg c.m. frame. The correlation functions were additionally bounded along the remaining axes: $|q_H|, |q_V| < 50$ MeV. The dimensions of the element are $R_i = T = 3.5$ fm. The isolines correspond to 3, 10, 30, 60, and 90% of the peak height.

subensemble that were obtained in various reference frames are given in [9].

A negative value of T^2 for the entire ensemble of negatively charged pions in the MgMg c.m. frame [8, 10, 13] is obtained in a similar way. The correlation functions for generation-volume elements that move rapidly in different directions [8, 10] expand along both diagonals, becoming X-shaped (see [9]), while the correlation function at the center of this X shape for the element that is at rest in this frame has a moderately small dimension in q_i. As in the preceding case, the height of the correlation peak grows with increasing q_0^2 at constant $\mathbf{q}^2$. At a rather small momentum size p_{cut} of the subensemble (see Section 2), the size of the diagonal branches of the peak is about the peak width, with the result that the sign of T^2 is normal (the same as that of R_i^2) [13].

At high p_{cut}, other sizes of a nonuniform generation volume must also be distorted. The effective width of the correlation peak along the spatial directions increases owing to the diagonal parts of the X shape, and this must lead to a decrease in the resulting sizes (in inverse proportion to the peak width) even if the subensemble is on average at rest. This may probably explain the decrease in the sizes with increasing p_{cut} in [17, 18], as well as the decrease in R_{side} (and partly in R_{out}) in [19, 20]. Within the procedure used here, a similar reason also leads to the decrease in R_L in Fig. 1—the axisymmetric approximation in (3) does not discriminate between a diagonal peak and an X-shaped one (see also Section 5).

4. CORRECT DESCRIPTION OF THE MOTION

Suppose that an element of the pion-generation volume moves with respect to the frame of observation at a velocity β along some axis—for example, the r_x axis. Making the respective Lorentz transformation of the element shape in (2), $r_x \to \gamma(r_x - \beta t)$ and $t \to \gamma(t - \beta r_x)$, and substituting the result into (1), we then obtain

$$C(q) = 1 + \exp\left\{-\gamma^2(q_x - \beta q_0)^2 R_x^2 - q_y^2 R_y^2 - q_z^2 R_z^2 - \gamma^2(q_0 - \beta q_x)^2 T^2\right\}, \quad (4)$$

where four projections of q are given in the frame of observation, while the radiation time and the sizes

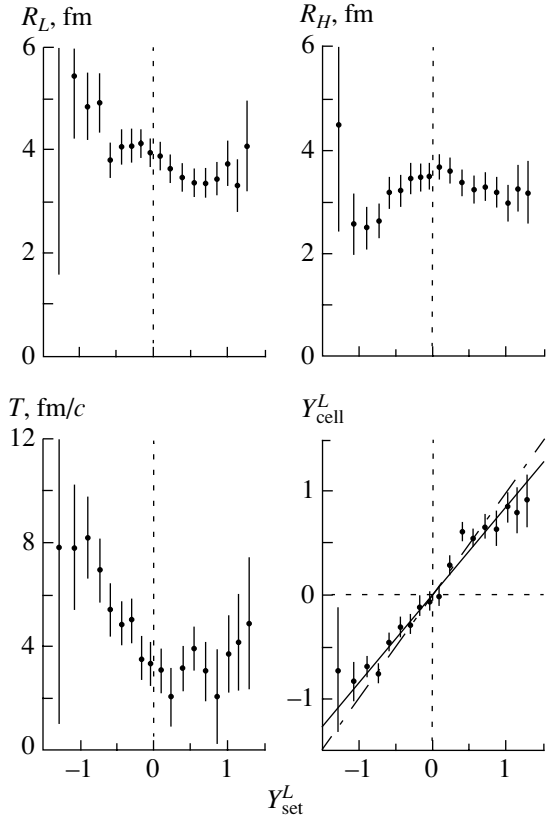

Fig. 3. Sizes and rapidities of various generation-volume elements from a fit of various subensembles of pions having momenta in the region $|\mathbf{p}| < 200$ MeV in reference frames that move along the reaction axis at preset rapidities with respect to the MgMg c.m. frame. The mean rapidity of the subensemble, $Y^L_{\rm set}$, is plotted along the abscissa. The solid straight line represents a linear fit: $Y^L_{\rm cell} = 0.85Y^L_{\rm set}$. The dash-dotted straight line corresponds to $Y^L_{\rm cell} = Y^L_{\rm set}$.

of the element are given in its reference frame. The correlation between the spatial coordinate r_x and the radiation instant t leads to a correlation between q_x and q_0. Of course, the same result could be obtained by making the respective Lorentz transformation of the correlation function in (3): $q_x \to \gamma(q_x - \beta q_0)$ and $q_0 \to \gamma(q_0 - \beta q_x)$; needless to say, the result would be coincident with that which is presented in Fig. 2.

If the absolute value of the velocity β is unknown, it can be deduced, together with the remaining adjustable parameters, from a fit of expression (4) to experimental data [5–11]. The closed symbols in Fig. 1 were obtained by using this, correct, approximation. The spatial dimensions of the element being considered and the pion-emission time are now independent of the frame of observation; concurrently, the element velocities (rapidities $Y_{\rm cell}$) obtained from our fit coincide with the preset ones, $Y_{\rm syst}$, everywhere, with the exception of possibly extreme points, where the width of the correlation function along the diagonal, $q_L = q_0$, becomes commensurate with the histogram-bin size (10 MeV [13]). This problem is solved by constructing a repeated fit in the reference frame where the measured rapidity is $Y_{\rm cell} = 0$.

In the approximation given by Eq. (4), the variables q_0 and q_x appear in the first power; therefore, the experimental histogram with respect to these variables must include both signs, in contrast to the expression in (3), where the histogram involved only the absolute values of all variables. In order to reduce the number of bins, the histogram was constructed from -200 to 200 MeV only for q_0. With respect to q_x, the histogram covered the region 0–200 MeV; that is, it included only the absolute values of q_x, but, if the value of q_x appeared to be negative, the sign of q_0 was reversed (central symmetry—see Fig. 2). Along the q_y and q_z axes, the histogram covered the interval 0–200 MeV.

5. VELOCITIES OF VARIOUS ELEMENTS

The sizes (with the exception of R_V) and the rapidities $Y^L_{\rm cell}$ of various generation-volume elements are given in Fig. 3 according to a fit where expression (4) ($x = L$) was used to describe various subensembles of negatively charged pions moving in the longitudinal direction. Each subensemble included pions of momentum in the region $|\mathbf{p}| <$ 200 MeV in the reference frame moving at a given rapidity (from -1.7 to 1.7 with a step of 0.2) with respect to the MgMg c.m. frame. The mean rapidity $Y^L_{\rm set}$ of pions in each subensemble (for noncentral subensembles, it does not coincide with a preset rapidity of the subensemble center) is plotted along the abscissa.

Errors in this figure and those that follow are purely statistical, but the values at neighboring points are correlated, since they were obtained by using strongly overlapping subensembles—for the sake of clarity, the step was chosen to be rather small. The asymmetry of sizes with respect to the zero of $Y_{\rm set}$ characterizes the magnitude of systematic errors.

Figure 4 shows similar data for subensembles moving in the direction transverse with respect to the beam axis [$x = H$ in (4)]. Here, some of the subensembles did not pass through the fit. The data displayed in Figs. 3 and 4 comply with the results reported in [8, 10]—the generation volume expands both in the longitudinal [8] and in the transverse [10] direction. A linear fit to the data yields the slope parameters of 0.85 ± 0.04 and 0.66 ± 0.07 (the errors are probably underestimated since the points are correlated). These slope parameters could be dependent on $p_{\rm cut}$—for example, all of the rapidities would

be close to zero if the boundary enclosed the entire ensemble of pions.

It should be emphasized that, for the results of an interference analysis to be correct, it must performed in a full four-dimensional form—that is, without integration over some directions. For example, the time coordinate q_0 is often not included in the approximation used. If the correlation functions in Fig. 2 are integrated with respect to q_0—that is, if the respective projections onto the q_L axes are considered—then the peak at $Y_{\rm syst} = 1.2$ will be broader than the peak at $Y_{\rm syst}$=0; hence, the size R_L will be smaller (in inverse proportion to the peak width). This explains a decrease in R_L with increasing velocity of the subensemble with respect to the reference frame of observation in the longitudinal direction in [21] (and in Fig. 1) and a decrease in $R_{\rm out}$ (see [19, 20] and references therein) in the case where the subensemble moves in the transverse direction.

We note that this "decrease" in the dimensions stems precisely from an illegitimate integration with respect to q_0 rather than from a Lorentz contraction by the factor γ [7]. The formula describing this decrease is more complicated [there appears the integral of expression (4) with respect to q_0]—it depends on the choice of approximation and on the parameter T.

Pions from different ends of this moving extended object (generation-volume element) are emitted on average simultaneously in the reference frame comoving with the object rather than with the observer; therefore, a direct measurement of the length by using these pions would lead to a relativistic elongation rather than contraction [4]. In the case of such a nonstandard observation, the shape a moving element would be similar to that in Fig. 2 (but without the elimination of the cones) if the variables q_L and q_0 on the axes are replaced by r_L and t; the length of the element projected onto the r_L axis would then grow (instead of decreasing) with increasing velocity.

But in performing an analysis in the rest frame of an element, such an integration over some direction is usually incorrect (even if $p_{\rm cut}$ is rather low—see the end of Section 3). The point is that, in an interference analysis, this integration is usually performed for the actual and for the background spectrum individually, but the spectra do not factorize with respect to directions even if their ratio (correlation function) factorizes. The ratio of integrals is not equal to the integral of the ratio.

6. DIRECTION OF DIVERGENCE OF ELEMENTS

In the preceding section, we determined the velocity of an element with respect to the MgMg c.m. frame in the same direction in which we selected the subensemble to be studied. In view of the symmetry of the reaction being considered and the symmetry of the directions that were explored, 0° and 90° with respect to the beam axis, this direction of the velocity was the only possible one. But there is no symmetry of the latter type in any other direction; for example, the velocity of an element that corresponds to a subensemble moving at an angle of 45° with respect to the beam axis in the MgMg reference frame may have a direction at the same angle of 45° [precisely from the generation-volume center (central divergence)], a direction closer to the beam axis (longitudinal divergence), or a direction transverse with respect to the beam axis. Here, the answer may be of importance for obtaining deeper insight into the physics of generation-volume expansion.

We investigated this issue in two steps. First, we measured the sizes and the velocity of an element along the direction of the motion of a subensemble. For this purpose, the momenta of all pions were

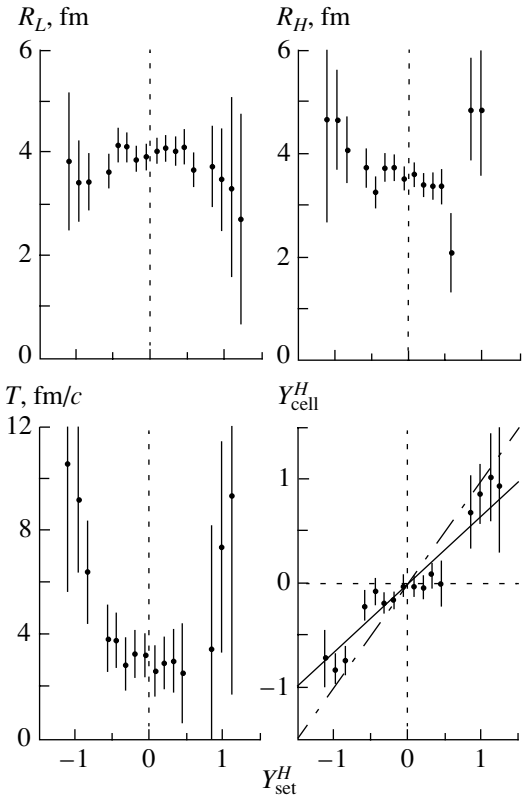

Fig. 4. Sizes and rapidities of various generation-volume elements from a fit to various subensembles of pions having momenta in the region $|\mathbf{p}| < 200$ MeV in reference frames moving across the reaction axis in the horizontal direction at given rapidities with respect to the MgMg c.m. frame. The mean rapidity of the subensemble, $Y^H_{\rm set}$, is plotted along the abscissa. The solid straight line represents a fit: $Y^H_{\rm cell} = 0.66 Y^H_{\rm set}$. The dash-dotted straight line corresponds to $Y^H_{\rm cell} = Y^H_{\rm set}$.

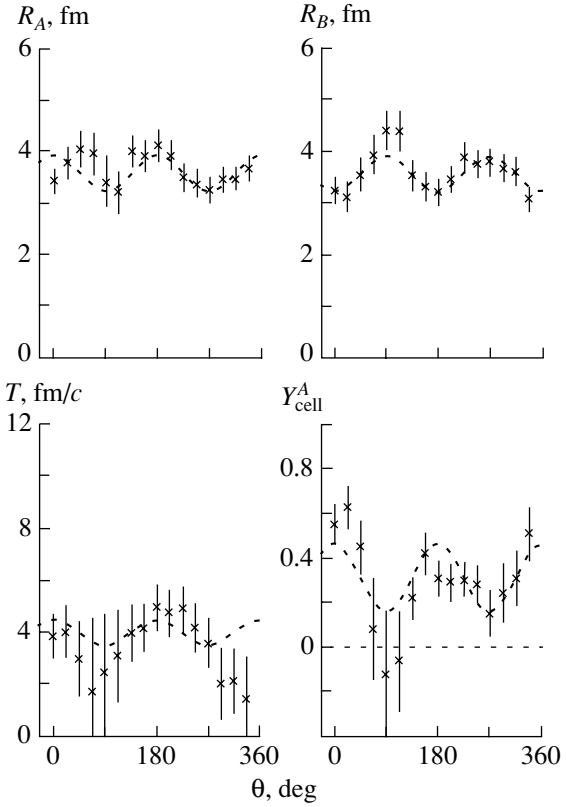

Fig. 5. Sizes and rapidities of various generation-volume elements from a fit to various subensembles of pions having momenta in the region $|\mathbf{p}| < 200$ MeV in reference frames moving at an angle θ with respect to the beam axis (direction A) in the horizontal plane at a rapidity of 0.7 with respect to the MgMg c.m. frame. The rapidities in the direction A (Y^A_{cell}) are given with respect to the MgMg c.m. frame.

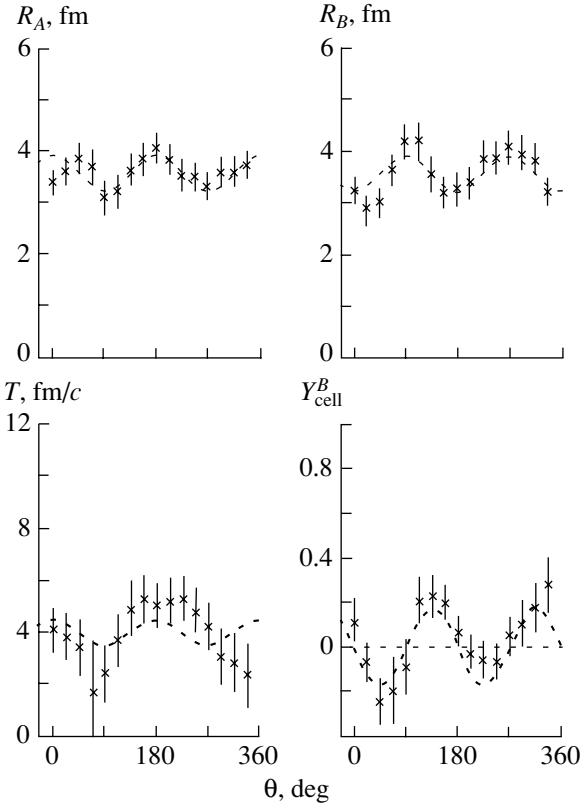

Fig. 6. Sizes and rapidities of the same generation-volume elements as in Fig. 5. Given in this figure are the rapidities Y^B_{cell} in the direction B orthogonal to A in the horizontal plane with respect to the element rest frame in the direction A, where $Y^A_{\text{cell}} = 0$.

rescaled to a reference frame rotated through an angle θ with respect to the beam axis in the horizontal plane in the MgMg c.m. frame: $p_A = p_L \cos\theta + p_H \sin\theta$, $p_B = p_H \cos\theta - p_L \sin\theta$, and $p_C = p_V$; in addition, a subensemble of pions was selected in such a way that their momenta in the reference frame moving at a given rapidity with respect to the MgMg c.m. frame in the direction A lay in the region $|\mathbf{p}| < 200$ MeV. In Fig. 5, we present, versus the angle θ, the results that we obtained for the sizes of elements (all of the sizes with the exception of R_C) and their rapidities Y^A_{cell} in this direction, using the approximation in (4) (at $x = A$, $y = B$, $z = C$). This figure corresponds to the case where the rapidity of the subensemble center is fixed at 0.7.

After that, we transformed the momenta of pions from each such subensemble to the rest frame obtained for a given element in the direction A (where $Y^A_{\text{cell}} = 0$) and constructed a fit with expression (4) for the velocity directed along the B axis that is taken to be orthogonal to the A axis ($x = B$, $y = A$, $z = C$). The results obtained in these reference frames for all of the sizes of the elements (with the exception of R_C) and for their rapidities in the direction B, Y^B_{cell}, are given in Fig. 6.

The reason behind the oscillations of the sizes R_A and R_B in Figs. 5 and 6 is that, as the angle θ is varied, the directions A and B alternately coincide with the directions L and H, with the size R_L being larger than R_H (see Figs. 3, 4). The curves in Figs. 5 and 6 represent the approximations $R_A = a\cos^2\theta + b\sin^2\theta$ and $R_B = a\sin^2\theta + b\cos^2\theta$, where $a = 3.91 \pm 0.07$ fm and $b = 3.24 \pm 0.06$ fm. The time parameter in Figs. 5 and 6 was approximated by the expression $T = c\cos^2\theta + d\sin^2\theta$, where $c = 4.5 \pm 0.3$ fm and $d = 3.5 \pm 0.4$ fm. The rapidity of the element along the direction A in Fig. 5 was approximated by the function $Y^A_{\text{cell}} = e\cos^2\theta + f\sin^2\theta$, where $e = 0.46 \pm 0.04$ and $f = 0.16 \pm 0.06$—that is, the rapidity of the element in the transverse direction is smaller than that in the longitudinal direction at the same rapidity of the subensemble center. All approximations were

chosen by using arguments that take into account symmetry with respect to 0°, 90°, 180°, and 270°. All errors in the parameters of the approximations could be underestimated because neighboring points are correlated (see Section 5).

In order to find the true direction of the motion of an element, it is of course necessary to go over again to a new reference frame, to measure the velocity in the orthogonal direction, etc. However, a qualitative result is already clear. It is in better agreement with the version where generation-volume elements fly apart predominantly in the longitudinal direction.

In the case where the elements fly apart in the central direction, the points Y^B_{cell} at all angles θ would have to lie in the vicinity of zero—that is, there would be no velocity transverse to the direction of the motion of the subensemble. In Fig. 6, this velocity is directed, however, into the forward hemisphere at angles close to 45° and 315° and into the backward hemisphere at angles close to 135° and 225°. The points are rather well approximated by the sine function $Y^B_{\text{cell}} = -g \sin 2\theta$ at the amplitude value of $g = 0.17 \pm 0.03$. Figures 5 and 6 correspond to the case where the rapidity of the subensemble center is fixed at 0.7. At different rapidities of subensembles, data behave similarly.

REFERENCES

1. G. Goldhaber *et al.*, Phys. Rev. **120**, 300 (1960).
2. G. I. Kopylov and M. I. Podgoretskiĭ, Yad. Fiz. **18**, 656 (1973) [Sov. J. Nucl. Phys. **18**, 336 (1973)].
3. G. I. Kopylov, Phys. Lett. B **50B**, 472 (1974).
4. M. I. Podgoretskiĭ, Fiz. Élem. Chastis At. Yadra **20**, 628 (1989) [Sov. J. Part. Nucl. **20**, 266 (1989)].
5. R. Lednitski and V. L. Lyuboshits, Yad. Fiz. **35**, 1316 (1982) [Sov. J. Nucl. Phys. **35**, 770 (1982)].
6. M. I. Podgoretskiĭ, Yad. Fiz. **37**, 455 (1983) [Sov. J. Nucl. Phys. **37**, 272 (1983)].
7. W. A. Zajc, Nucl. Phys. A **525**, 315c (1991).
8. M. Kh. Anikina *et al.*, Preprint No. E1-95-311 (Joint Inst. Nucl. Res., Dubna, 1995).
9. D. Miśkowiec *et al.*, Nucl. Phys. A **610**, 227c (1996).
10. M. Kh. Anikina *et al.*, Phys. Lett. B **397**, 30 (1997).
11. H. Appelshäuser *et al.*, Eur. Phys. J. C **2**, 661 (1998).
12. G. I. Kopylov and M. I. Podgoretskiĭ, Yad. Fiz. **19**, 434 (1974) [Sov. J. Nucl. Phys. **19**, 215 (1974)].
13. M. Kh. Anikina, A. I. Golokhvastov, and J. Lukstins, Yad. Fiz. **65**, 600 (2002) [Phys. At. Nucl. **65**, 573 (2002)].
14. M. G. Bowler, Z. Phys. C **29**, 617 (1985).
15. P. A. M. Dirac, *The Principles of Quantum Mechanics* (Clarendon, Oxford, 1958; Nauka, Moscow, 1960, 1979).
16. B. Tomášik *et al.*, Acta Phys. Slov. **47**, 81 (1997).
17. D. Beavis *et al.*, Phys. Rev. C **34**, 757 (1986).
18. W. B. Christie *et al.*, Phys. Rev. C **47**, 779 (1993).
19. C. Adler *et al.*, Phys. Rev. Lett. **87**, 082301 (2001).
20. K. Adcox *et al.*, Phys. Rev. Lett. **88**, 192302 (2002).
21. T. Alber *et al.*, Z. Phys. C **66**, 77 (1995).

Translated by A. Isaakyan

Physics of Atomic Nuclei, Vol. 67, No. 2, 2004, pp. 414–423. Translated from Yadernaya Fizika, Vol. 67, No. 2, 2004, pp. 433–442.

ELEMENTARY PARTICLES AND FIELDS
Theory

Solving a Relativistic Quasipotential Equation for a Superposition of a Nonlocal Separable and a Local Quasipotential

Yu. D. Chernichenko

Gomel State Technical University, pr. Oktyabrya 48, Gomel, 246746 Belarus

Received October 3, 2002; in final form, February 12, 2003

Abstract—Within the relativistic quasipotential approach to quantum field theory, a method is developed for solving a finite-difference quasipotential equation for the case where a total quasipotential describing the interaction of two relativistic spinless particles of unequal masses is a superposition of a nonlocal separable and a local quasipotential. The cases are investigated where the local component of the total interaction—it is assumed to be known—either admits or does not admit the existence of bound states. This makes it possible to obtain an exact expression for the increment of the phase shift, to determine the conditions of the existence of bound states, and to give a generalization of the Levinson theorem.

1. INTRODUCTION

The main advantage of nonlocal separable interactions is that the partial-wave t matrix for such interactions has a very simple form, and this makes it possible to continue it directly off the energy shell. It is this property that is of paramount importance in nuclear physics and in a many-body problem—in particular, in solving Faddeev equations in the three-body problem. In addition, the application of nonlocal separable interactions in solving the nonrelativistic two-body Schrödinger equation makes it possible to obtain closed expressions for a wide class of such potentials. This approach also proved to be efficient in solving the nonrelativistic inverse-scattering problem [1–4]. However, it cannot be used in dealing with essentially relativistic systems [5, 6]. By way of example, one can indicate that, for systems consisting of light quarks, the contribution of relativistic corrections to the interaction Hamiltonian appears to be commensurate with the main nonrelativistic term. A relativistic approach is also required in studying the radiative decays of mesons and nucleon resonances, where the energy of an emitted photon may be commensurate with or greater than the mass of constituent quarks.

The quasipotential approach [7] has still remained one of the efficient methods for a relativistic treatment of two-body systems [8–11]. In the present study, the problem of solving the finite-difference quasipotential equation for a superposition of a nonlocal separable and a local quasipotential describing the interaction of two relativistic spinless particles of unequal masses ($m_1 \neq m_2$) is considered within the relativistic quasipotential approach to quantum field theory [12]. The need for such a representation of interaction in two-particle systems is dictated, in particular, by the assumptions of the meson theory of nuclear forces. In accordance with this theory, the interaction between two nucleons is local at long distances, but it becomes nonlocal and singular at short distances. In this problem, we can assume that the local part $w(\rho)$ of the total interaction is known and is in accord with experimental data at low energies. Since there is no precise theoretical information about nuclear forces at short distances, we can assume, for the sake of simplicity, that, at such distances, the nonlocal component of the total interaction is separable. Restricting our consideration to the case of spherically symmetric forces and one separable term, we therefore take the total interaction in the form

$$V(\boldsymbol{\rho},\boldsymbol{\rho}';E_{q'}) \equiv V(\boldsymbol{\rho},\boldsymbol{\rho}') = w(\rho)\delta(\boldsymbol{\rho}'-\boldsymbol{\rho}) + \sum_{l=0}^{\infty}(2l+1)\varepsilon_l v_l(\rho)v_l(\rho')P_l\left(\frac{\boldsymbol{\rho}\cdot\boldsymbol{\rho}'}{\rho\rho'}\right), \quad (1)$$

where $P_l(z)$ is a Legendre function of the first kind; $\boldsymbol{\rho} = \rho\mathbf{n}$; $\boldsymbol{\rho}' = \rho'\mathbf{n}'$; $|\mathbf{n}|, |\mathbf{n}'| = 1$; and $\varepsilon_l = \pm 1$.[1)] In the case where the interaction has the form (1), the relativistic analog of the differential Schrödinger equation for the wave function $\Psi_{q'}(\boldsymbol{\rho})$ in the configuration representation for particles of unequal masses is then

[1)] We note that the value of $\varepsilon_l = -1$ corresponds to an attractive interaction, while the value of $\varepsilon_l = 1$ corresponds to a repulsive interaction.

given by[2)]

$$\frac{m'^2}{\mu}\left[\cosh\left(i\lambda'\frac{\partial}{\partial\rho}\right)+\frac{i\lambda'}{\rho}\sinh\left(i\lambda'\frac{\partial}{\partial\rho}\right)\right. \quad (2)$$
$$\left.-\frac{\lambda'^2}{2\rho^2}\Delta_{\theta,\varphi}\exp\left(i\lambda'\frac{\partial}{\partial\rho}\right)-\cosh\chi'\right]\Psi_{q'}(\boldsymbol{\rho})$$
$$+\int d\boldsymbol{\rho}'V(\boldsymbol{\rho},\boldsymbol{\rho}')\Psi_{q'}(\boldsymbol{\rho}')=0,$$

where $\Delta_{\theta,\varphi}$ is the angular part of the Laplace operator, $\lambda'=1/m'$ is the Compton wavelength associated with the effective relativistic particle of mass $m'=\sqrt{m_1m_2}$, and $\mu=m'^2/(m_1+m_2)$.[3)]

Following [14], we expand the wave function $\Psi_{q'}(\boldsymbol{\rho})$ in partial waves; that is,

$$\Psi_{q'}(\boldsymbol{\rho})=\sum_{l=0}^{\infty}(2l+1)i^l\frac{\psi_l(\rho,\chi')}{\rho}P_l\left(\frac{\mathbf{q}'\cdot\boldsymbol{\rho}}{q'\rho}\right), \quad (3)$$
$$q'=|\mathbf{q}'|.$$

Equation (2) can then be recast into the form

$$\left[\nabla+\left(1+\frac{l(l+1)}{r^{(2)}}\right)\nabla^*-2\cosh\chi'+W(r)\right] \quad (4)$$
$$\times\,\psi_l(r,\chi')+\varepsilon_lV_l(r)\int_0^{\infty}dr'V_l(r')\psi_l(r',\chi')=0,$$

where we have introduced the following notation:

$$\nabla=\exp\left(-i\frac{d}{dr}\right),\quad \nabla^*=\exp\left(i\frac{d}{dr}\right),$$
$$V_l(r)=\sqrt{8\pi\lambda'\mu/m'^2}\rho v_l(\rho),$$
$$W(r)=2\mu w(\rho)/m'^2,\quad r^{(2)}=r(r+i),$$
$$\rho=\lambda'r,\quad \rho'=\lambda'r'.$$

Thus, the possibility of representing the total energy of two relativistic spinless particles of unequal masses in the c.m. frame as a quantity that is proportional to the energy of a single effective relativistic particle of mass m' enables one to reduce, within this approach, the relativistic problem of two bodies having unequal masses to a one-body problem [13]. This study, which generalizes the results reported in [14], is devoted to solving Eq. (4) with the boundary condition

$$\psi_l(0,\chi')=0, \quad (5)$$

deriving an expression for the increment of the phase shift, investigating the conditions under which bound states can exist, and generalizing the Levinson theorem for a superposition of a nonlocal separable and a local quasipotential. In doing this, we will assume that the local component $W(r)$ of the total interaction is known and can either admit the existence of n_l bound states at the energies

$$0\le E_j=E_{q'j}/m'=\cosh\chi_j<1, \quad (6)$$
$$\chi_j=i\kappa_j, 0<\kappa_j\le\frac{\pi}{2},\quad j=1,2,\ldots,n_l,$$

or not admit the existence of bound states.

2. PROPERTIES OF THE REGULAR SOLUTION AND SPECTRAL DENSITY FOR A LOCAL QUASIPOTENTIAL

For a unique solution to Eq. (4) with the boundary condition in (5) to exist, it is necessary that the separable quasipotential $V_l(r)$ and the local quasipotential $W(r)$ satisfy the conditions

$$rV_l(r)\in L_1(0,\infty),\quad rW(r)\in L_1(0,\infty). \quad (7)$$

The last requirement in (7) means that the regular solution $\varphi_l(r,\chi')$ and the Jost solution $f_l(r,\chi')$ to the equation

$$\left[\nabla+\left(1+\frac{l(l+1)}{r^{(2)}}\right)\nabla^*-2\cosh\chi'+W(r)\right] \quad (8)$$
$$\times\begin{Bmatrix}\varphi_l(r,\chi')\\ f_l(r,\chi')\end{Bmatrix}=0$$

with the boundary condition

$$\varphi_l(0,\chi')=0 \quad (9)$$

have the following necessary properties.

By using the behavior of the free solutions $s_l(r,\chi')$ and $e_l^{(1)}(r,\chi')$ to Eq. (8) for the case where the interaction is switched off, $W(r)\equiv0$,[4)] a relativistic regular solution $\varphi_l(r,\chi')$ that satisfies the boundary

[2)] Hereafter, we use the system of units where $\hbar=c=1$.

[3)] We recall that, within the present version of the relativistic quasipotential approach to quantum field theory for the case of the interaction of two relativistic spinless particles of unequal masses [13], Eq. (2) describes, in the c.m. frame, the scattering of an effective relativistic particle having a mass m' and a relative 3-momentum $\mathbf{q}'$, the total particle energy $\sqrt{S_{q'}}$ in the c.m. frame being proportional to the energy $E_{q'}=\sqrt{m'^2+\mathbf{q}'^2}=m'\cosh\chi'$ of the effective relativistic particle of mass m',

$$\sqrt{S_{q'}}=(m'/\mu)E_{q'}=(m'^2/\mu)\cosh\chi',$$

where χ' is the rapidity of the effective particle.

[4)] We recall that, in the adopted notation, the behavior of the free solutions $s_l(r,\chi')$ and $e_l^{(1)}(r,\chi')$ is as follows [15]:

$$s_l(r,\chi')\approx e^{i\pi(l+1)}(-r)^{(l+1)}Q_l(\coth\chi')/\Gamma(l+1), r\to0,$$
$$e_l^{(1)}(r,\chi')\approx e^{i(r\chi'-\pi l/2)}, r\chi'\to\infty.$$

condition in (9) and the Jost solution $f_l(r,\chi')$ to Eq. (8) can be chosen in such a way that[5)]

$$\lim_{r\to 0}\frac{e^{-i\pi(l+1)}\Gamma(l+1)}{(-r)^{(l+1)}}\varphi_l(r,\chi')=1, \qquad (10)$$

$$\lim_{r\chi'\to\infty} e^{-i(r\chi'-\pi l/2)}f_l(r,\chi')=1, \qquad (11)$$

where $\Gamma(z)$ is a gamma function; $Q_l(z)$ is a Legendre function of the second kind; and $(-r)^{(\lambda)}$ is a generalized power-law function,

$$(-r)^{(\lambda)}=i^\lambda\Gamma(ir+\lambda)/\Gamma(ir). \qquad (12)$$

One can easily verify that, for complex-valued χ' and real-valued r and l, the regular solution and the Jost solution possess the symmetry properties

$$\varphi_l(r,-\chi')=\varphi_l(r,\chi'), \qquad (13)$$

$$[\varphi_l(r,\chi')]^*=\nu_l(r)\varphi_l(r,\chi'^*), \qquad (14)$$

$$[f_l(r,\chi')]^*=e^{i\pi l}\nu_l(r)f_l(r,-\chi'^*), \qquad (15)$$

where

$$\nu_l(r)=e^{i\pi(l+1)}(r)^{(l+1)}/(-r)^{(l+1)}. \qquad (16)$$

It can be shown that, for $\sinh\chi'\neq 0$, two Jost solutions $f_l(r,\pm\chi')$ are linearly independent because their Wronskian

$$W_\Delta[f_l(r,\chi'),f_l(r,-\chi')] \qquad (17)$$
$$=\begin{vmatrix} f_l(r,\chi') & f_l(r,-\chi') \\ \Delta f_l(r,\chi') & \Delta f_l(r,-\chi')\end{vmatrix}=2ie^{i\pi(l+1)}\frac{\sinh\chi'}{\nu_l(r)}$$

is nonzero.[6)] Therefore, the regular solution $\varphi_l(r,\chi')$ can be represented in the form of a linear combination of two Jost solutions with constant (independent of r) coefficients; that is,

$$\varphi_l(r,\chi')=(1/2iQ_l(\coth\chi')) \qquad (18)$$
$$\times[F_l^W(-\chi')f_l(r,\chi')+e^{i\pi(l+1)}F_l^W(\chi')f_l(r,-\chi')].$$

The function $F_l^W(\chi')$, which can be represented in the form

$$F_l^W(\chi')=(Q_l(\coth\chi')/\sinh\chi') \qquad (19)$$
$$\times\nu_l(r)W_\Delta[f_l(r,\chi'),\varphi_l(r,\chi')]$$

by using the value of the Wronskian in (17), is the Jost function for the local quasipotential $W(r)$ and is related to the corresponding phase shift $\delta_l^W(\chi')$ by the equation

$$F_l^W(\chi')=|F_l^W(\chi')|\exp[-i\delta_l^W(\chi')]. \qquad (20)$$

On the basis of relations (14), (15), (18), and (20), it can be proven that the function in (19) and the respective phase shift possess the following symmetry properties:

$$[F_l^W(\chi')]^*=F_l^W(-\chi'^*), \qquad (21)$$

$$[\delta_l^W(\chi')]^*=\delta_l^W(\chi'^*), \qquad (22)$$

$$\delta_l^W(-\chi')=-\delta_l^W(\chi'). \qquad (23)$$

In addition, it can be found, from the representation in (19) and from expression (10), which describes the behavior of the regular solution $\varphi_l(r,\chi')$ in the vicinity of the point $r=0$, that the Jost solution and the Jost function satisfy the limiting relation

$$F_l^W(\chi')=\lim_{r\to 0}\frac{e^{-i\pi l}(2l+1)Q_l(\coth\chi')}{\Gamma(l+1)\sinh\chi'(-r)^{(-l)}}f_l(r,\chi'). \qquad (24)$$

By using the asymptotic expression in (11) and the representation in (18), we further obtain

$$\varphi_l(r,\chi')=\frac{|F_l^W(\chi')|}{Q_l(\coth\chi')} \qquad (25)$$
$$\times\sin\left[r\chi'-\frac{\pi l}{2}+\delta_l^W(\chi')\right],\quad r\chi'\to\infty.$$

Let us now prove an orthogonality property of two regular solutions to Eq. (8) at two rapidity values χ and χ'^*. For this purpose, we multiply Eq. (8) for the functions $\varphi_l(r,\chi'^*)$ and $\varphi_l(r,\chi)$ by the functions $\varphi_l(r,\chi)$ and $\varphi_l(r,\chi'^*)$, respectively, and take the difference of the equations obtained in this way. By employing the conjugacy property (14) for a regular solution, we then obtain[7)]

$$2(\cosh\chi-\cosh\chi'^*)\varphi_l(r,\chi)\varphi_l^*(r,\chi')$$
$$=\Delta^*\{\nu_l(r)W_\Delta[\varphi_l(r,\chi),\varphi_l(r,\chi'^*)]\}.$$

From this relation, we obtain

$$\int_0^\infty dr\varphi_l(r,\chi)\varphi_l^*(r,\chi')=\sum_{n=1}^\infty\frac{i^{n-1}}{n!2(\cosh\chi-\cosh\chi'^*)}$$
$$\times\frac{d^{n-1}}{dr^{n-1}}\{\nu_l(r)W_\Delta[\varphi_l(r,\chi),\varphi_l(r,\chi'^*)]\}\Big|_0^\infty. \qquad (26)$$

[5)]The choice of the boundary condition for the Jost solution in the form (11) means that, below, we everywhere have $\mathrm{Im}\chi'\geq 0$.

[6)]Here, $\Delta=(\nabla-1)/(-i)$ is the operator of finite-difference differentiation. We recall that, in conventional units, it has the form [16, 17]

$$\Delta=(\nabla-1)/(-i\lambda')=[\exp(-i\lambda' d/d\rho)-1]/(-i\lambda'),$$
$$\lambda'=\hbar/m'c.$$

[7)]Here, $\Delta^*=(\nabla^*-1)/i=[\exp(id/dr)-1]/i$ is the operator conjugate to finite-difference differentiation in the adopted notation.

After carrying out some calculations in (26) with the aid of relations (10), (11), (24), and (25) and considering that the local quasipotential $W(r)$ has n_l bound states at the energies presented in (6), we finally arrive at the orthogonality condition[8)]

$$\int_0^\infty dr\varphi_l(r,\chi)\varphi_l^*(r,\chi') \tag{27}$$

$$= \begin{cases} \dfrac{\delta(E-E')}{d\rho_l(E)/dE}, E=\cosh\chi\geq 1, E'=\cosh\chi'\geq 1; \\ C_{lj}^{-1}\delta_{jj'}, \quad 0\leq E_j=\cosh\chi_j<1, \\ 0\leq E_{j'}=\cosh\chi_{j'}<1; \\ \chi=\chi_j=i\kappa_j, \quad \chi'=\chi_{j'}=i\kappa_{j'}, 0<\kappa_j, \\ \kappa_{j'}\leq\pi/2, \quad j,j'=1,2,\ldots,n_l; \\ 0, \quad E=\cosh\chi\geq 1, \quad 0\leq E_{j'}=\cosh\chi_{j'}<1, \\ \chi'=\chi_{j'}=i\kappa_{j'}, \quad 0<\kappa_{j'}\leq\pi/2. \end{cases}$$

Here,

$$C_{lj}^{-1}=\int_0^\infty dr\varphi_l(r,\chi_j)\varphi_l^*(r,\chi_j)$$

$$=-F_l^W(-\chi_j)\dot{F}_l^W(\chi_j)/[4iQ_l^2(\coth\chi_j)], \tag{28}$$

$$\dot{F}_l^W(\chi_j)=dF_l^W(\chi_j)/d\chi_j, \quad j=1,2,\ldots,n_l,$$

are normalization constants, while the spectral density is in this case given by

$$\frac{d\rho_l(E)}{dE}=\begin{cases} \dfrac{2}{\pi}\sinh^{-1}\chi Q_l^2(\coth\chi)|F_l^W(\chi)|^{-2}, \\ E=\cosh\chi\geq 1; \\ \sum\limits_{j=1}^{n_l}C_{lj}\delta(E-E_j), \quad 0\leq E=\cos\kappa<1, \\ 0\leq E_j=\cosh\chi_j<1, \quad \chi_j=i\kappa_j, \\ 0<\kappa, \quad \kappa_j\leq\pi/2. \end{cases} \tag{29}$$

On the other hand, we have the completeness property[9)]

$$\int_0^\infty d\rho_l(E)\varphi_l(r,\chi)\varphi_l^*(r',\chi) \tag{30}$$

$$=\sum_{j=1}^{n_l}C_{lj}\varphi_l(r,\chi_j)\varphi_l^*(r',\chi_j)$$

$$+\int_0^\infty d\chi\tau_l(\chi)\varphi_l(r,\chi)\varphi_l^*(r',\chi)=\delta(r'-r),$$

where $\tau_l(\chi)=\dfrac{2}{\pi}Q_l^2(\coth\chi)|F_l^W(\chi)|^{-2}$.

3. WAVE FUNCTION AND PHASE SHIFT FOR A SUPERPOSITION OF A NONLOCAL SEPARABLE AND A LOCAL QUASIPOTENTIAL

The orthogonality property (27) and the completeness property (30) enable us to introduce relativistic integral transformations:[10)]

$$\widetilde{\psi}_l(\chi',\chi)=\int_0^\infty dr\psi_l(r,\chi')\varphi_l^*(r,\chi), \tag{31}$$

$$\psi_l(r,\chi')=\int_0^\infty d\rho_l(E)\widetilde{\psi}_l(\chi',\chi)\varphi_l(r,\chi) \tag{32}$$

$$=\sum_{j=1}^{n_l}C_{lj}\widetilde{\psi}_l(\chi',\chi_j)\varphi_l(r,\chi_j)$$

$$+\int_0^\infty d\chi\tau_l(\chi)\widetilde{\psi}_l(\chi',\chi)\varphi_l(r,\chi),$$

$$\widetilde{V}_l(\chi)=\int_0^\infty drV_l(r)\varphi_l^*(r,\chi), \tag{33}$$

[8)] It can easily be shown that, at $\mathrm{Im}\chi_j>0$, any zero χ_j of the Jost function corresponds to a bound state. In order to demonstrate this, we note that, if $F_l^W(\chi_j)=0$, the representation in (18) does indeed lead to the relation

$$\varphi_l(r,\chi_j)=F_l^W(-\chi_j)f_l(r,\chi_j)/2iQ_l(\coth\chi_j).$$

By virtue of the condition in (11), the function $\varphi_l(r,\chi_j)$ then decreases exponentially for $r\to\infty$ and $\mathrm{Im}\chi_j>0$. Thus, we have a bound state at the energy $E_j=\cosh\chi_j$. It should be noted that all zeroes of the Jost function are simple and pure imaginary since $4\sinh(\mathrm{Re}\chi_j)\sin(\mathrm{Im}\chi_j)\int_0^\infty dr|f_l(r,\chi_j)|^2=0$ for $\mathrm{Re}\chi_j=0$ and $\mathrm{Im}\chi_j>0$.

[9)] We note that, in the absence of interaction, the conditions in (27) and (30) reduce to the ordinary orthogonality and completeness conditions for the free solutions $s_l(r,\chi)$ [17]; that is,

$$(2/\pi)\int_0^\infty drs_l(r,\chi)s_l^*(r,\chi')=\delta(\chi'-\chi),$$

$$(2/\pi)\int_0^\infty d\chi s_l(r,\chi)s_l^*(r',\chi)=\delta(r'-r).$$

[10)] We note that, in the absence of a local interaction ($W(r)\equiv 0$), the integral transformations (31)–(34) reduce to the relativistic integral Hankel transformations introduced in [14].

$$V_l(r) = \int_0^\infty d\rho_l(E)\widetilde{V}_l(\chi)\varphi_l(r,\chi) \tag{34}$$

$$= \sum_{j=1}^{n_l} C_{lj}\widetilde{V}_l(\chi_j)\varphi_l(r,\chi_j) + \int_0^\infty d\chi\tau_l(\chi)\widetilde{V}_l(\chi)\varphi_l(r,\chi).$$

By applying the transformations (32) and (34) to Eq. (4), we obtain

$$(\cosh\chi' - \cosh\chi_j)\widetilde{\psi}_l(\chi',\chi_j) = \frac{1}{2}\varepsilon_l N_l(\chi')\widetilde{V}_l(\chi_j), \tag{35}$$

$$(\cosh\chi' - \cosh\chi)\widetilde{\psi}_l(\chi',\chi) = \frac{1}{2}\varepsilon_l N_l(\chi')\widetilde{V}_l(\chi), \tag{36}$$

$$N_l(\chi') = \int_0^\infty d\rho_l(E)\widetilde{\psi}_l(\chi',\chi)\widetilde{U}_l(\chi), \tag{37}$$

where we have set

$$V_l(r) = \nu_l(r)U_l(r). \tag{38}$$

For the function $U_l(r)$, we also have the integral transformations

$$\widetilde{U}_l(\chi) = \int_0^\infty drU_l(r)\varphi_l^*(r,\chi), \tag{39}$$

$$U_l(r) = \int_0^\infty d\rho_l(E)\widetilde{U}_l(\chi)\varphi_l(r,\chi). \tag{40}$$

We note that the conditions in (7) ensure fulfillment of the properties in (10) and (25). It follows that the function $\widetilde{V}_l(\chi)$ is everywhere continuous and that the function $Q_l(\coth\chi)\widetilde{V}_l(\chi)|F_l^W(\chi)|^{-1}$ is differentiable for all $\chi \geq 0$. Moreover, we find from (33) that

$$Q_l(\coth\chi)\widetilde{V}_l(\chi)|F_l^W(\chi)|^{-1} = O(1), \quad |\chi| \to \infty, \tag{41}$$

$$\widetilde{V}_l(\chi) = O(1), \quad \chi \to 0, \tag{42}$$

provided that the conditions in (7) hold. It is obvious that, by virtue of (38) and (39), the estimates in (41) and (42) are also valid for the function $\widetilde{U}_l(\chi)$. In addition, it can be shown that, for real-valued l, the use of the properties in (13) and (14) and of the definition in (38) makes it possible to recast the transformation in (40) into the form

$$V_l(r) = \int_0^\infty d\rho_l(E)\widetilde{U}_l(\chi)\varphi_l^*(r,\chi)$$

$$= \int_0^\infty d\rho_l(E)\widetilde{V}_l(\chi)\varphi_l(r,\chi).$$

With allowance for the real-valuedness of the separable term $V_l(r)$, it follows from this relation that

$$\widetilde{U}_l(\chi) = \widetilde{V}_l^*(\chi). \tag{43}$$

For scattering states, the solutions to Eqs. (35) and (36) can be written as[11)]

$$\widetilde{\psi}_l(\chi',\chi) = \frac{1}{2}\varepsilon_l N_l(\chi')\frac{\widetilde{V}_l(\chi_j)}{\cosh\chi' - \cosh\chi_j}, \tag{44}$$

$$\widetilde{\psi}_l(\chi',\chi) = \frac{\delta(\cosh\chi' - \cosh\chi)}{d\rho_l(\cosh\chi')/d(\cosh\chi')} + \frac{1}{2}\varepsilon_l N_l(\chi')\mathrm{P}\frac{\widetilde{V}_l(\chi)}{\cosh\chi' - \cosh\chi}, \tag{45}$$

$$E' = \cosh\chi' \geq 1.$$

Substituting the solutions in (44) and (45) into (32) and (37) and taking into account the property in (43), we obtain

$$\psi_l(r,\chi') = \varphi_l(r,\chi') + \frac{1}{2}\varepsilon_l N_l(\chi')\sum_{j=1}^{n_l} C_{lj}\frac{\widetilde{V}_l(\chi_j)\varphi_l(r,\chi_j)}{\cosh\chi' - \cosh\chi_j} + \frac{1}{2}\varepsilon_l N_l(\chi')\mathrm{P}\int_0^\infty d\chi\frac{\tau_l(\chi)\widetilde{V}_l(\chi)\varphi_l(r,\chi)}{\cosh\chi' - \cosh\chi}, \tag{46}$$

$$N_l(\chi') = \varepsilon_l\widetilde{V}_l^*(\chi')/\Phi_l(\cosh\chi'), \tag{47}$$

where

$$\Phi_l(\cosh\chi') = \varepsilon_l - \frac{1}{2}\sum_{j=1}^{n_l} C_{lj}\frac{|\widetilde{V}_l(\chi_j)|^2}{\cosh\chi' - \cosh\chi} - \frac{1}{2}\varepsilon_l\mathrm{P}\int_0^\infty d\chi\frac{A_l(\chi)}{\cosh\chi' - \cosh\chi_j}, \tag{48}$$

$$A_l(\chi) = \varepsilon_l\tau_l(\chi)|\widetilde{V}_l(\chi)|^2. \tag{49}$$

The principal values of the integrals in (46) and (48) exist since the function $\widetilde{V}_l(\chi)$ is differentiable and since, by virtue of the conditions in (41) and (42), these integrals converge at both limits. Thus, we

[11)] In expression (45), P symbolizes the principal-value prescription and the coefficient of the delta function is chosen in accordance with the normalization of the wave function—in the absence of a separable interaction ($\varepsilon_l = 0$), the representation in (32) must lead to the regular solution $\varphi_l(r,\chi')$ with the local quasipotential $W(r)$.

conclude that, in the case where the local quasipotential $W(r)$ has n_l bound states, relations (46)–(49) give the only solution to Eq. (4) with the boundary condition (5), provided that the condition in (7) holds. But if the local quasipotential $W(r)$ does not admit the existence of bound states, it is necessary to set $C_{lj} \equiv 0$ in relations (46) and (48).

Let us now use the representation in (18) and recast the solution in (46) into the form

$$\psi_l(r,\chi') = \varphi_l(r,\chi') + \frac{1}{2}\varepsilon_l N_l(\chi') \sum_{j=1}^{n_l} C_{lj} \frac{\widetilde{V}_l(\chi_j)\varphi_l(r,\chi_j)}{\cosh\chi' - \cosh\chi_j} + \varepsilon_l N_l(\chi') \mathrm{P}\frac{1}{2\pi i} \int\limits_{-\infty}^{\infty} d\chi \frac{Q_l(\coth\chi)\widetilde{V}_l(\chi) f_l(r,\chi)}{F_l^W(\chi)(\cosh\chi' - \cosh\chi)}. \quad (50)$$

The principal value of the integral in the solution given by (50) can easily be calculated for $r \to \infty$ if we use the asymptotic expression (11) and the relation

$$\frac{1}{\alpha - i\eta} = i\pi\delta(\alpha) + \mathrm{P}\left(\frac{1}{\alpha}\right), \quad \eta \to +0,$$

and then apply the residue theorem in performing integration along the boundary of the region $0 \le \mathrm{Im}\chi \le \pi/2$. The result is

$$\mathrm{P}\frac{1}{2\pi i} \int\limits_{-\infty}^{\infty} d\chi \frac{Q_l(\coth\chi)\widetilde{V}_l(\chi) f_l(r,\chi)}{F_l^W(\chi)(\cosh\chi' - \cosh\chi)} = -\frac{Q_l(\coth\chi')\widetilde{V}_l(\chi')}{|F_l^W(\chi')|\sinh\chi'} \cos\left[r\chi' - \frac{\pi l}{2} + \delta_l^W(\chi')\right] - \sum_{j=1}^{n_l} \frac{Q_l(\coth\chi_j)\widetilde{V}_l(\chi_j)\exp[i(r\chi_j - \pi l/2)]}{\dot{F}_l^W(\chi_j)(\cosh\chi_j - \cosh\chi')} + O(e^{-\pi r/4}), \quad \eta \to +0.$$

Taking into account the last result, relation (25), and the behavior of the function $\varphi_l(r,\chi_j)$ at large r (see footnote 8), we find the asymptotic behavior of the wave function (50) in the form

$$\psi_l(r,\chi') = \frac{|F_l^W(\chi')|}{Q_l(\coth\chi')} \sin\left[r\chi' - \frac{\pi l}{2} + \delta_l^W(\chi')\right] - \frac{\varepsilon_l N_l(\chi') Q_l(\coth\chi')\widetilde{V}_l(\chi')}{|F_l^W(\chi')|\sinh\chi'} \times \cos\left[r\chi' - \frac{\pi l}{2} + \delta_l^W(\chi')\right] + O(e^{-\pi r/4}), \quad r\chi' \to \infty. \quad (51)$$

Choosing the asymptotic expression for the wave function $\psi_l(r,\chi')$ in the form[12)]

$$\psi_l(r,\chi') = \frac{|F_l^W(\chi')|}{Q_l(\coth\chi')} \sin\left[r\chi' - \frac{\pi l}{2} + \delta_l^W(\chi')\right] + \frac{|F_l^W(\chi')|}{Q_l(\coth\chi')} \tan\delta_l^V(\chi') \cos\left[r\chi' - \frac{\pi l}{2} + \delta_l^W(\chi')\right], \quad r\chi' \to \infty,$$

and comparing this representation with the asymptotic expression in (51), we finally obtain the following expression for the phase-shift increment:

$$\tan\delta_l^V(\chi') = -\frac{\pi}{2}\sinh^{-1}\chi' \frac{\varepsilon_l A_l(\chi')}{\Phi_l(\cosh\chi')}. \quad (52)$$

4. BOUND STATES AND GENERALIZED LEVINSON THEOREM

Suppose that there exists at least one bound state at energy $E' = \cosh\chi' \ge 0$. The solutions to Eqs. (35) and (36) are then given by

$$\widetilde{\psi}_l(\chi',\chi_j) = \frac{1}{2}\varepsilon_l N_l(\chi') \frac{\widetilde{V}_l(\chi_j)}{\cosh\chi' - \cosh\chi_j}, \quad (53)$$

$$\widetilde{\psi}_l(\chi',\chi) = \frac{1}{2}\varepsilon_l N_l(\chi') \mathrm{P}\frac{\widetilde{V}_l(\chi)}{\cosh\chi' - \cosh\chi}. \quad (54)$$

Here, we assume that all of the functions $\widetilde{V}_l(\chi_j)$ and $\widetilde{V}_l(\chi)$ differ from zero. The cases where one or a few of these functions vanish, $\widetilde{V}_l(\chi_j) = 0$ or $\widetilde{V}_l(\chi) = 0$, will be considered below. The substitution of the solutions in (53) and (54) into the equality in (37) leads to an equation for eigenvalues,

$$\Phi_l(E') = \varepsilon_l - \frac{1}{2}\sum_{j=1}^{n_l} C_{lj} \frac{|\widetilde{V}_l(\chi_j)|^2}{E' - E_j} - \frac{1}{2}\varepsilon_l \mathrm{P}\int\limits_0^{\infty} d\chi \frac{A_l(\chi)}{E' - \cosh\chi} = 0. \quad (55)$$

It has solutions $E' \ge 0$ at $\varepsilon_l = \pm 1$, true bound states associated with the total interaction corresponding to the energies

$$0 \le E' = E_{tj'} = \cosh\chi_{tj'} < 1, \quad \chi_{tj'} = i\kappa_{tj'}, \quad (56)$$

[12)] Here, we represent the total phase shift $\delta_l(\chi')$ in the form

$$\delta_l(\chi') = \delta_l^W(\chi') + \delta_l^V(\chi'),$$

where $\delta_l^V(\chi')$ is the phase-shift increment induced by the separable component of the total interaction. We note that, in this case, $\delta_l^V(\chi')$ also depends on the local quasipotential $W(r)$; therefore, this quantity must be distinguished from the phase shift induced by the separable interaction alone—that is, the phase shift in the absence of a local quasipotential [14].

$$0 < \kappa_{tj'} \le \pi/2, \quad j' = 1, 2, \ldots, \sigma_l.$$

At the same time, spurious bound states associated with the separable component of the total interaction correspond to the following energy values [1]:[13)]

$$E' = E_{fk} = \cosh\chi_{fk} \ge 1, \tag{57}$$

$$k = \begin{cases} 1, 2, \ldots, \nu_l, & \varepsilon_l = -1, \\ 0, 1, \ldots, \nu_l - 1, & \varepsilon_l = +1. \end{cases}$$

Let us consider bound states whose energies are given by (56). It is obvious that the boundary condition (5) is satisfied for such states and that their wave function asymptotically tends to zero for $r \to \infty$. This can be proven by substituting the solutions in (53) and (54) into expression (32), transforming the integral with the aid of relations (18) and (11), and thereupon performing integration along the boundary of the region $0 \le \mathrm{Im}\chi \le \pi/2$ by means of the residue theorem. Indeed, the result of these manipulations is given by

$$\psi_l(r, \chi_{tj'}) = O(\exp[-r\min(\pi/4, \kappa_{tj'})]), \quad r \to \infty.$$

Since the energy values in (56) are determined as roots of Eq. (55) at $\varepsilon_l = \pm 1$ and $\Phi_l(1) \ne 0$, we investigate two cases in order to find their number σ_l.

(i) First, we consider the case of $\varepsilon_l = +1$. It is then obvious that $\Phi_l(E') > 1$ for $E' \le 0$, this corresponding to the choice of the upper half ($E_{q'} \ge 0$) of the mass hyperboloid $E_{q'}^2 - \mathbf{q}'^2 = m'^2$. If $\Phi_l(1) > 0$, Eq. (55) has $\sigma_l = n_l$ roots $E_{tj'}$, and this corresponds to a weak nonlocality. In the opposite case—that is, if $\Phi_l(1) < 0$—Eq. (55) has $\sigma_l = n_l - 1$ roots $E_{tj'}$, and this correspond to a strong nonlocality. It is also obvious that the values of $E_{tj'}$ are greater than the corresponding values of E_j. Therefore, the separable interaction is repulsive and can remove one bound state, depending on its strength, the value of $\Phi_l(1)$ being responsible for the magnitude of nonlocality.

(ii) We now consider the case of $\varepsilon_l = -1$. Equation (55) then admits solutions (56) if $\Phi_l(0) \le 0$. In the case of $\Phi_l(1) < 0$, the separable component of the total interaction possesses a weak nonlocality of an attractive type; this does not change the number of bound states of the total interaction ($\sigma_l = n_l$), only leading to a decrease in their energies $E_{tj'}$ with respect to the corresponding energy values E_j. But if $\Phi_l(1) > 0$, the separable component of the total interaction has a strong nonlocality of an attractive type; not only does this circumstance lead to a decrease in the bound-state energies $E_{tj'}$, but, because of a considerable strength of the interaction, may also be the reason for the emergence of an extra bound state ($\sigma_l = n_l + 1$) of energy in the range $E_{t(n_l+1)} > E_j > E_{tj'}$ ($j', j = 1, 2, \ldots, n_l$). It follows that, in this case, the effective particle of mass m' can be considered as a quasilocal one, the value $\Phi_l(1)$ also being responsible for the strength of nonlocality.

Let us now consider the case where one of the functions $\{\widetilde{V}_l(\chi_j)\}$ is equal to zero—for example, $\widetilde{V}_l(\chi_k)$. The function $\Phi_l(E')$ is then continuous at $E' = E_k$; therefore, one of the values in the set $\{E_{tj'}\}$ will be absent. The eigenvalue that is absent—for example, E_{tk}—is then replaced by E_k, while the eigenfunction $\psi_l(r, \chi_{tk})$ coincides with the wave function $\varphi_l(r, \chi_k)$. This means that $V_l(r)$ is orthogonal to $\varphi_l(r, \chi_k)$ and that a superposition of the nonlocal separable interaction $\varepsilon_l V_l(r) V_l(r')$ and the local quasipotential $W(r)$ does not change the wave function $\varphi_l(r, \chi_k)$ and the corresponding energy value $E_k = \cosh\chi_k$. For the same reason, one of the values in the set $\{E_{tj'}\}$—for example, $E_{t(k+1)}$—will be equal to E_k. Therefore, we have degeneracy at the energy E_k, and the wave function $\psi_l(r, \chi_{t(k+1)})$ can be chosen to be orthogonal to the function $\varphi_l(r, \chi_k)$, setting $\widetilde{\psi}_l(\chi_{t(k+1)}, \chi_k) \equiv 0$.

The case where a few functions $\widetilde{V}_l(\chi_j)$ are equal to zero can be considered in a similar way. We note that, for each E_j, the degree of degeneracy cannot be higher than two in any case. But in view of the fact that $d\Phi_l(E')/dE' > 0$ for $0 \le E' \le 1$ and $E' \ne E_j$, at least one of the functions in the set $\{\widetilde{V}_l(\chi_j)\}$ is not zero.[14)]

[13)] In just the same way as in the case of separable potentials in the nonrelativistic case, spurious bound states are discrete levels lying in the continuous spectrum.

[14)] This is not so only at $n_l = 1$ and $\varepsilon_l = -1$. In this case, Eq. (55) takes the form

$$\Phi_l(E') = -1 + \frac{1}{2}\mathrm{P}\int_0^\infty d\chi \frac{|A_l(\chi)|}{\cosh\chi - E'} = 0;$$

that is, it is analogous to that in the case where the local quasipotential does not admit the existence of bound states. We note that this equation has only one root $E' = E_t$ under the condition

$$\frac{2}{\pi}\int_0^\infty d\chi |\widetilde{V}_l(\chi)/F_l^W(\chi)|^2 > 1.$$

This requirement is associated with the fact that, for any $l, \chi \ge 0$, the function $g_l(\chi)$ is bounded; that is,

$$g_l(\chi) = \frac{1}{2}\frac{Q_l^2(\coth\chi)}{\cosh\chi - E_t} \le \max g_l(\chi)$$

$$\approx \frac{\pi(\tanh\chi_{\max})^{2l}}{4^{l+1}\cosh\chi_{\max}}\left[1 - \frac{l+1}{2l+3}\tanh^2\chi_{\max}\right] < 1.$$

Finally, we assume that $\widetilde{V}_l(\chi) \equiv 0$; by virtue of the orthogonality condition (27) and the representation in (33), we then have

$$V_l(r) = \sum_{j=1}^{n_l} a_j \varphi_l(r, \chi_j).$$

Equation (55) then takes the form

$$\Phi_l(E') = \varepsilon_l - \frac{1}{2}\sum_{j=1}^{n_l} C_{lj} \frac{|\widetilde{V}_l(\chi_j)|^2}{E' - E_j} = 0. \qquad (58)$$

In this case, however, Eq. (58) cannot have more than n_l roots $E_{tj'}$ since $\Phi_l(0) > \varepsilon_l$ and $\Phi_l(1) < \varepsilon_l$. From Eq. (4), it can then be seen that the bound-state wave functions $\psi_l(r, \chi_{tj'})$ are linear combinations of the functions $\varphi_l(r, \chi_j)$ and that the scattering-state wave function $\psi_l(r, \chi)$ coincides with the wave function $\varphi_l(r, \chi)$. There are changes only in the energies of bound states; also, it follows from expression (52) that $\delta_l^V(\chi) \equiv 0$.

We note that Eq. (58) can also have one (and only one) root $E' = E_f \geq 1$, and only in the case where $\varepsilon_l = +1$ and $\Phi_l(1) < 0$ does this occur because we have

$$\frac{d\Phi_l(E')}{dE'} = \frac{1}{2}\sum_{j=1}^{n_l} C_{lj} \frac{|\widetilde{V}_l(\chi_j)|^2}{(E' - E_j)^2} > 0$$

at $E' \geq 1$ and $\Phi_l(E') \approx 1$ in the limit $E' \to +\infty$. It will be shown below that this value of the energy E_f corresponds to a spurious bound state.

For the general case, we will now consider spurious bound states at energies (57), whose values E_{fk} are determined as the roots of Eq. (55). If such solutions to Eq. (55) exist, the required solutions to Eqs. (35) and (36) are given by (53) and (54), as before. Therefore, the wave function takes the form (51), where the first term is omitted; that is,

$$\psi_l(r, \chi_{fk}) = -\frac{\varepsilon_l N_l(\chi_{fk}) Q_l(\coth\chi_{fk}) \widetilde{V}_l(\chi_{fk})}{|F_l^W(\chi_{fk})| \sinh\chi_{fk}} \times \cos\left[r\chi_{fk} - \frac{\pi l}{2} + \delta_l^W(\chi_{fk})\right] + O(e^{-\pi r/4}), \quad r \to \infty.$$

From this formula, it follows that the wave function $\psi_l(r, \chi_{fk})$ asymptotically tends to zero, if

$$\widetilde{V}_l(\chi_{fk}) = 0. \qquad (59)$$

Thus, simultaneous fulfillment of the conditions in (55) and (59) is a necessary and sufficient condition for the existence of spurious bound states at energies (57) since the boundary condition (5) is also satisfied. In turn, fulfillment of the conditions in (55) and (59) means that, at the energy values in (57), the phase-shift increment $\delta_l^V(\chi')$ decreases with increasing χ', passing through the values πk (k is an integer). This is because both the numerator and the denominator on the right-hand side of the equality in (52) vanish at these energy values by virtue of the conditions in (55) and (59). But it follows from the definitions in (48) and (49) and the conditions in (7) that the functions $\Phi_l(\cosh\chi')$ and $A_l(\chi')$ exist and are differentiable. In addition, the function $A_l(\chi')$ has a zero of at least the second order at the points $\chi' = \chi_{fk}$, while the function $\Phi_l(\cosh\chi')$ has, at these points, only a simple zero since

$$\left.\frac{d\Phi_l(\cosh\chi')}{d\chi'}\right|_{\chi'=\chi_{fk}} = \frac{\sinh\chi_{fk}}{2} \times \left[\sum_{j=1}^{n_l} C_{lj} \frac{|\widetilde{V}_l(\chi_j)|^2}{(\cosh\chi_{fk} - \cosh\chi_j)^2} + \mathrm{P}\int_0^\infty d\chi \frac{|A_l(\chi)|}{(\cosh\chi_{fk} - \cosh\chi)^2}\right] > 0.$$

This means that, at $\chi' = \chi_{fk}$, the quantity $\tan\delta_l^V(\chi')$ vanishes and changes sign; that is,

$$\delta_l^V(\chi_{fk}) = \pi k, \quad k = \begin{cases} 1, 2, \ldots, \nu_l, & \varepsilon_l = -1, \\ 0, 1, \ldots, \nu_l - 1, & \varepsilon_l = +1, \end{cases} \qquad (60)$$

$$\left.\frac{d\delta_l^V(\chi')}{d\chi'}\right|_{\chi'=\chi_{fk}} < 0.$$

If the denominator on the right-hand side of (52) does not vanish at $\chi' = \chi_{fk}$, the increment of the phase shift will only touch the straight lines $\delta_l^V = \pi k$ (k is an integer) from above or from below, but it will not intersect them—that is the phase-shift increment has extrema at these points,.

Thus, we can state that, if the phase-shift increment $\delta_l^V(\chi')$ intersects the straight lines $\delta_l^V = \pi k$ ($k = \{0, 1, \ldots, \nu_l - 1, \varepsilon_l = +1; 1, 2, \ldots, \nu_l, \varepsilon_l = -1\}$) from above as the quantity χ' increases—that is, the conditions in (55) and (59) are satisfied—spurious bound states associated with the separable component of the total interaction correspond to the energies in (57). Studying the behavior of $\delta_l^V(\chi')$ as a function of χ', one can therefore obtain the values of the energy E_{fk} at which spurious bound states exist, the value of ε_l being determined by the sign of the phase-shift increment $\delta_l^V(\chi')$ at high energies ($\chi' \to +\infty$). By using the estimate in (41) and expression (52), we finally find that $\tan\delta_l^V(\infty) = 0$.

In the case where the local quasipotential $W(r)$ does not admit bound states, spurious bound states whose energies are given by (57) can be considered in a similar way. In this case, the energies E_{fk} of such spurious bound states are also determined by the roots of Eq. (55), where it is now necessary to set $C_{lj} \equiv 0$. It is obvious that, for spurious bound states, we also arrive at the previous results in this case as well. This means that, in general, we can choose the function $\delta_l^V(\chi')$ in such a way as to ensure fulfillment of the condition

$$\delta_l^V(\infty) = 0. \tag{61}$$

In order to generalize the Levinson theorem, we note that the Jost function for the total interaction,

$$F_l(\chi') = |F_l(\chi')| \exp[-i\delta_l(\chi')],$$

is analytic in the band $0 \le \mathrm{Im}\chi' \le \pi/2$, has σ_l ($\sigma_l = n_l - 1$, n_l, or $n_l + 1$) simple zeros (56) there [so that $F_l(\chi_{tj'}) = 0$], and does not have poles there. Applying the logarithmic-residue theorem to the Jost function $F_l(\chi')$ for the boundary Γ^+ of the region $0 \le \mathrm{Im}\chi' \le \pi/2$ and taking into account the contribution to the variation from ν_l spurious bound states [property (60)] and the fact that the phase shift is odd, we then obtain

$$\begin{aligned} 2\pi\sigma_l &= -i \lim_{R\to+\infty,\eta\to+0} \int_{\Gamma^+} d\ln F_l(\chi') \\ &= -\lim_{R\to+\infty,\eta\to+0} \mathrm{var}\delta_l(\chi')|_{\Gamma^+} \\ &= -2\pi\nu_l + 2[\delta_l(0) - \delta_l(\infty)], \end{aligned}$$

where $\mathrm{var}\delta_l(\chi')|_{\Gamma^+}$ is the variation of the phase shift upon the circumvention of the point χ' around the closed contour Γ^+, which is the boundary of the band $0 \le \mathrm{Im}\chi' \le \pi/2$. From here and from the condition in (61), we obtain the generalized Levinson theorem for the superposition of a nonlocal separable interaction and a local quasipotential that admits the existence of n_l bound states. The result is[15)]

$$\delta_l^V(0) = \pi(\sigma_l - n_l + \nu_l). \tag{62}$$

It should be noted that we always have $\delta_l^V(0) \ge 0$ apart from the only case where $\delta_l^V(0) = -\pi$ ($\varepsilon_l = -1$), which occurs at $n_l \ne 0$, $\sigma_l = n_l - 1$, and $\nu_l = 0$. This case differs significantly both from the purely separable case ($W(r) \equiv 0$) and from the case where the local quasipotential $W(r)$ does not admit the existence of bound states: in either case, we always have $\delta_l^V(0) = \pi(\sigma_l + \nu_l) \ge 0$, $\sigma_l = 0, 1$.

[15)] As always, we have set $\delta_l(\infty) = 0$ and taken into account the usual Levinson theorem for a local quasipotential that admits n_l bound states; that is,

$$\delta_l^W(0) - \delta_l^W(\infty) = \delta_l^W(0) = \pi n_l.$$

5. CONCLUSION

Within the relativistic quasipotential approach to quantum field theory, a method has been constructed for solving the finite-difference quasipotential equation involving a total quasipotential that describes the interaction of two relativistic spinless particles of unequal masses. The total interaction that is a superposition of a nonlocal separable and a local quasipotential was assumed to be spherically symmetric, and its local component was assumed to be known and to be such that it admits the existence of n_l bound states. The developed method is directly associated with the possibility of representing the total c.m. energy of two relativistic spinless particles of unequal masses as a quantity that is proportional to the energy of an effective relativistic particle of mass m'. It has been shown that the regular solution for a local quasipotential satisfies the orthogonality and completeness conditions at all energy values both in the case where this quasipotential admits the existence of bound states and in the case where it does not admit their existence. This has permitted finding an expression for the increment of the phase shift and investigating its properties, determining the conditions under which true and spurious bound states may exist, performing a comparison with the nonrelativistic case, and generalizing the Levinson theorem.

ACKNOWLEDGMENTS

I am grateful to Yu.S. Vernov, V.V. Andreev, V.N. Kapshai, I.L. Solovtsov, and Ya. Shnir for interest in this study and enlightening discussions on the results presented here.

REFERENCES

1. K. Chadan, Nuovo Cimento **10**, 892 (1958).
2. M. Bolsterli and J. MacKenzie, Phys. (N.Y.) **2**, 141 (1965).
3. F. Tabakin, Phys. Rev. **177**, 1443 (1969).
4. R. L. Mills and J. F. Reading, J. Math. Phys. (N.Y.) **10**, 321 (1969).
5. R. Barbieri, R. Kogerler, Z. Kunszt, and R. Gatto, Nucl. Phys. B **105**, 125 (1976).
6. R. McClary and N. Byers, Phys. Rev. D **28**, 1692 (1983).
7. A. A. Logunov and A. N. Tavkhelidze, Nuovo Cimento **29**, 380 (1963).
8. A. P. Martynenko and R. N. Faustov, Teor. Mat. Fiz. **64**, 179 (1985); Yad. Fiz. **61**, 534 (1998) [Phys. At. Nucl. **61**, 471 (1998)]; Yad. Fiz. **63**, 915 (2000) [Phys. At. Nucl. **63**, 845 (2000)]; Yad. Fiz. **64**, 1358 (2001) [Phys. At. Nucl. **64**, 1282 (2001)].
9. N. A. Boikova, Yu. N. Tyukhtyaev, and R. N. Faustov, Yad. Fiz. **64**, 986 (2001) [Phys. At. Nucl. **64**, 917 (2001)].

10. V. N. Kapshai and T. A. Alferova, J. Phys. A (London) **32**, 5329 (1999).
11. N. B. Skachkov and I. L. Solovtsov, Yad. Fiz. **30**, 1079 (1979) [Sov. J. Nucl. Phys. **30**, 562 (1979)]; Teor. Mat. Fiz. **41**, 205 (1979); Yad. Fiz. **31**, 1332 (1980) [Sov. J. Nucl. Phys. **31**, 686 (1980)]; Teor. Mat. Fiz. **43**, 330 (1980).
12. V. G. Kadyshevsky, Nucl. Phys. B **6**, 125 (1968).
13. V. G. Kadyshevskiĭ, M. D. Mateev, and R. M. Mir-Kasimov, Yad. Fiz. **11**, 692 (1970) [Sov. J. Nucl. Phys. **11**, 388 (1970)].
14. Yu. D. Chernichenko, Yad. Fiz. **63**, 2068 (2000) [Phys. At. Nucl. **63**, 1976 (2000)].
15. I. V. Amirkhanov, G. V. Grusha, and R. M. Mir-Kasimov, Fiz. Élem. Chastits At. Yadra **12**, 651 (1981) [Sov. J. Part. Nucl. **12**, 262 (1981)].
16. V. G. Kadyshevskiĭ, R. M. Mir-Kasimov, and N. B. Skachkov, Yad. Fiz. **9**, 212 (1969) [Sov. J. Nucl. Phys. **9**, 125 (1969)].
17. V. G. Kadyshevskiĭ, R. M. Mir-Kasimov, and N. B. Skachkov, Fiz. Élem. Chastits At. Yadra **2**, 635 (1972) [Sov. J. Part. Nucl. **2** (3), 69 (1972)].

Translated by A. Isaakyan

Physics of Atomic Nuclei, Vol. 67, No. 2, 2004, pp. 424–426. From Yadernaya Fizika, Vol. 67, No. 2, 2004, pp. 443–445.

ELEMENTARY PARTICLES AND FIELDS
Theory

On the Determination of Quark Masses from the Dalitz Plot for the Decay $\eta \to \pi^+\pi^-\pi^0$*

B. V. Martemyanov** **and V. S. Sopov**

Institute of Theoretical and Experimental Physics,
Bol'shaya Cheremushkinskaya ul. 25, Moscow, 117259 Russia

Received January 17, 2003

Abstract—An experimental Dalitz plot distribution for the decay $\eta \to \pi^+\pi^-\pi^0$ is fitted by the theoretical one obtained in chiral perturbation theory with unitarity corrections taken into account. The fit shows that the difference of light-quark masses is larger than is expected from electromagnetic mass differences of neutral and charged kaons. © *2004 MAIK "Nauka/Interperiodica".*

1. INTRODUCTION

Since the decay $\eta \to 3\pi$ cannot conserve both C parity and isospin simultaneously, it can go due to either weak or electromagnetic or the isospin-violating part of strong interactions. Weak interactions are too weak to explain the observed decay probability. Electromagnetic interactions are strongly suppressed in this decay by chiral symmetry, so the decay is due almost exclusively to the isospin-breaking part of the QCD Hamiltonian [1].

In chiral perturbation theory (ChPT), the decay width Γ depends on the quark mass ratios and theoretically calculable factor $\bar{\Gamma}$:

$$\Gamma = \left(\frac{Q_{\rm DT}}{Q}\right)^4 \bar{\Gamma}, \qquad (1)$$

where

$$Q^{-2} = \frac{m_d^2 - m_u^2}{m_s^2 - \hat{m}^2}, \quad \hat{m} = \frac{m_d + m_u}{2}, \qquad (2)$$

m_u, m_d, and m_s are up, down, and strange-quark masses,

$$Q_{\rm DT}^{-2} = \frac{\left(\left(m_{K^0}^2 - m_{K^+}^2\right) - \left(m_{\pi^0}^2 - m_{\pi^+}^2\right)\right) m_{\pi^0}^2}{\left(m_K^2 - m_{\pi^0}^2\right) m_K^2} = (24.1)^2, \qquad (3)$$

with $m_K^2 = (m_{K^+}^2 + m_{K^0}^2 - m_{\pi^+}^2 + m_{\pi^0}^2)/2$.

Note that $Q = Q_{\rm DT}$ and $\Gamma = \bar{\Gamma}$ if electromagnetic mass differences of kaons and pions are equal to each other, which is the case in the lowest order of ChPT [2] (Dashen theorem—DT).

Both experimentally known decay width Γ and theoretically calculable factor $\bar{\Gamma}$ have uncertainties. The experimental uncertainties of Γ are [3]

$$\Gamma = 281 \pm 28 \text{ eV}. \qquad (4)$$

The uncertainties of $\bar{\Gamma}$ are not so definite. In the lowest order of ChPT [4],

$$\bar{\Gamma} = 66 \text{ eV}. \qquad (5)$$

The first corrections (one loop-corrections) move $\bar{\Gamma}$ to the value [2]

$$\bar{\Gamma} = 167 \pm 50 \text{ eV}. \qquad (6)$$

Higher order corrections (taken into account by the dispersion method [5, 6]) give a larger result with some uncertainties. In [5], they were estimated to be

$$\bar{\Gamma} = 209 \pm 20 \text{ eV}. \qquad (7)$$

The difference between Γ and $\bar{\Gamma}$ means that Q is different from $Q_{\rm DT}$ and the ratio of quark masses m_u/m_d can be measured by the deviation of Γ from $\bar{\Gamma}$. Surely, the higher the accuracy of Γ and $\bar{\Gamma}$, the clearer will be the difference between $Q_{\rm DT}$ and Q. The accuracy of Γ is purely of experimental origin. The accuracy of $\bar{\Gamma}$ is partly of theoretical origin (order of ChPT used, the inclusion of final-state interaction in the decay width), but partly of experimental origin—some unknown quantities in the theoretical scheme could be better adjusted if the Dalitz plot distribution were known better.

In [5, 6], the factor $\bar{\Gamma}$ was calculated by taking into account the results of one-loop order of ChPT and the unitarity corrections that allow the effects of the rescatterings of two pions to be summed in all orders of ChPT. The subtraction polynomial was taken from

*This article was submitted by the authors in English.

** e-mail: martemja@heron.itep.ru

the decomposition of the one-loop-order amplitude. This polynomial, therefore, had uncertainties connected to higher orders of ChPT corrections to the amplitude. In what follows, we will fix the uncertainties of the polynomial by fitting the experimental data on a Dalitz plot distribution. As a result, we obtain an improved value of $\bar{\Gamma}$ and, hence, improved values of light-quark masses.

2. SIMULATION OF $\eta \to \pi^+\pi^-\pi^0$ DALITZ-PLOT DISTRIBUTION AND ITS FIT BY χ^2 METHOD

In order to simulate an experimental Dalitz plot distribution, we have taken it in a form

$$1 + ay + by^2 + cx^2, \tag{8}$$

where

$$y = \frac{3T_0}{T} - 1, \quad x = \frac{\sqrt{3}}{T}(T_+ - T_-), \tag{9}$$
$$T = T_+ + T_- + T_0,$$

and T_+, T_-, and T_0 are the kinetic energies of pions in the rest frame of $\eta \to \pi^+\pi^-\pi^0$ decay. The parameters a, b, and c were taken from one of the best known experimental results [7]:

$$a = -1.17 \pm 0.02, \quad b = 0.21 \pm 0.03, \tag{10}$$
$$c = 0.06 \pm 0.04.$$

The Dalitz plot was divided into $100 = 10 \times 10$ bins ($x \times y$) that have an equal number of events for the distribution considered. Then the number of events n in each bin was simulated by a Gaussian distribution with the variance equal to n. Fitting this distribution of events over the bins by the same form $1 + ay + by^2 + cx^2$ of Dalitz plot distribution, we get the parameters a, b, and c equal to the experimental values within experimental errors for approximately $N = 100n \approx 1\,000\,000$ events.

As a next step, we have taken an approximate solution to unitary equations for the amplitude of $\eta \to \pi^+\pi^-\pi^0$ decay from Eq. (5.28) of [5]. It contains the subtraction polynomial

$$P(s) = \alpha + \beta s_a + \gamma s_a^2 + \delta(s_b - s_c)^2, \tag{11}$$

where s_a, s_b, and s_c are invariant masses squared of $\pi^+\pi^-$, $\pi^+\pi^0$, and $\pi^-\pi^0$ pairs, respectively. For the values of parameters α, β, γ, and δ within the regions

$$\alpha = -1.28 \pm 0.14, \quad \beta = 21.81 \pm 1.52\ \mathrm{GeV}^{-2}, \tag{12}$$
$$\gamma = 4.09 \pm 3.18\ \mathrm{GeV}^{-4}, \quad \delta = 4.19 \pm 1.08\ \mathrm{GeV}^{-4}$$

(the case of zero subtraction points [5]), the "Minuit" fit of the experimental Dalitz plot distribution has terminated on the values

$$\alpha_0 = -1.17, \beta_0 = 21.74\ \mathrm{GeV}^{-2}, \tag{13}$$
$$\gamma_0 = 7.02\ \mathrm{GeV}^{-4}, \delta_0 = 5.23\ \mathrm{GeV}^{-4}$$

with $\chi^2/N_{\mathrm{d.o.f.}} = 134/(100-4)$.

Equally possible (with the same value of $\chi^2/N_{\mathrm{d.o.f.}}$) is the fit

$$\alpha = \alpha_0 C, \quad \beta = \beta_0 C[\,\mathrm{GeV}^{-2}], \tag{14}$$
$$\gamma = \gamma_0 C[\,\mathrm{GeV}^{-4}], \quad \delta = \delta_0 [C\ \mathrm{GeV}^{-4}]$$

because the normalization factor of the amplitude is not defined by the Dalitz plot distribution. Varying constant C in such a way as to stay within the above-mentioned limits on parameters α, β, γ, and δ, we obtain $C = 1^{+0.008}_{-0.03}$. The indefiniteness of constant C can be translated to the indefiniteness of the width $\bar{\Gamma}$:

$$\bar{\Gamma} = 213^{+3}_{-12}\ \mathrm{eV}. \tag{15}$$

The obtained result is very close to the result (7) of [5]. This coincidence might be the occasional one and future experimental data on Dalitz plot distribution will give a slightly different value of the width $\bar{\Gamma}$.

3. CONCLUSION

We have fitted the amplitude of the decay $\eta \to \pi^+\pi^-\pi^0$ calculated within ChPT in next-to-leading order and with unitarity corrections (final-state interaction of pions) to the experimental data [7] on Dalitz plot distribution taken into account [5]. The obtained results for the width $\bar{\Gamma}$ [see Eq. (1)] mean that $Q \neq Q_{\mathrm{DT}}$ and the difference of u- and d-quark masses is slightly larger than what follows from the Dashen theorem for electromagnetic mass differences of kaons and of pions, in which case $Q = Q_{\mathrm{DT}}$. The Dashen theorem says that $m_u/m_d = 0.57$, while the result (7) of [5] on quantity $\bar{\Gamma}$ for $\eta \to \pi^+\pi^-\pi^0$ decay gives $m_u/m_d = 0.52$.

ACKNOWLEDGMENTS

This work was partially supported by the Russian Foundation for Basic Research, project no. 02-02-16957.

REFERENCES

1. D. G. Sutherland, Phys. Lett. **23**, 384 (1966); J. S. Bell and D. G. Sutherland, Nucl. Phys. B **4**, 315 (1968); R. Baur, J. Kambor, and D. Wyler, Nucl. Phys. B **460**, 127 (1996).
2. J. Gasser and H. Leutwyler, Nucl. Phys. B **250**, 539 (1985).

3. K. Hagiwara *et al.*, Phys. Rev. D **66**, 010001 (2002).
4. H. Osborn and D. J. Wallace, Nucl. Phys. B **20**, 23 (1970); J. A. Cronin, Phys. Rev. **161**, 1483 (1967).
5. J. Kambor, C. Wiesendanger, and D. Wyler, Nucl. Phys. B **465**, 215 (1996).
6. A. V. Anisovich and H. Leutwyler, Phys. Lett. B **375**, 335 (1996).
7. M. Gormley *et al.*, Phys. Rev. D **2**, 501 (1970).

Physics of Atomic Nuclei, Vol. 67, No. 2, 2004, pp. 427–429. Translated from Yadernaya Fizika, Vol. 67, No. 2, 2004, pp. 446–448.

LETTERS TO THE EDITOR

Third S_{11} Resonance in the Reaction $\gamma p \to \eta p$

V. A. Tryasuchev

Tomsk Polytechnic University, Tomsk, 634004 Russia

Received April 8, 2003

An isobar model of the reaction

$$\gamma p \to \eta p \qquad (1)$$

at photon energies in the region $K_0 \leq 2.5$ GeV was proposed in [1]. This model takes into account 11 nucleon resonances, including resonances of high L, and the contribution of the vector mesons ρ and ω. In constructing the model, particular attention was given to obtain a good description of relevant experimental data over the photon-energy region $K_0 \leq 1.1$ GeV, including those on the differential cross sections [2, 3], the beam asymmetry Σ [4], and the target asymmetry T [5]. In order to extend the applicability range of the model to high energies, use was made of experimental data obtained 30 years ago because the results of the cross-section measurements in the range $K_0 = 0.75$–1.95 GeV at the Jefferson Laboratory were published later [6]. The calculated energy dependence of the total cross section for the process in (1) is compared retrospectively with those experimental data in Fig. 1. From this figure, it can be seen that, over the photon-energy range 1.1–1.7 GeV, the experimental values are systematically in excess of the theoretical results calculated on the basis of the model proposed in [1] (dashed curve). In order to remove this discrepancy, the model was refined by including in it, in addition to the known $S_{11}(1535)$ and $S_{11}(1650)$ resonances, a third S_{11} resonance, its parameters being set to

$$W_r = 1825\ \text{MeV}, \quad \Gamma_r = 160\ \text{MeV}, \qquad (2)$$
$$\gamma^E = 0.275\ \text{MeV},$$

where γ^E is the geometric mean of the electromagnetic (Γ_γ) and strong ($\Gamma_{\eta p}$) widths of the resonance (a detailed description of the model can be found in [7]). Although the parameters of the new S_{11} resonance were estimated by means of an eyeball fit, the values in (2) are characterized by rather small uncertainties (within 10%), and this circumstance was among the motivations for writing the present article. Assuming that the ratio $\Gamma_{\eta p}/\Gamma_r$ varies within the range 0.5–0.01, we find that the invariant helicity amplitude for the photoexcitation of the new resonance varies within the range $A^p_{1/2} = 0.021$–0.151 $(\text{GeV})^{-1/2}$, which lies much lower than the values of $A^p_{1/2}$ for the above two s-wave resonances; that is, the contribution of the $S_{11}(1825)$ resonance to the process in (1) is smaller than the contribution of the two known resonances. Our conclusions are valid for the total width (2), which is very close to the total widths of the $S_{11}(1535)$ and $S_{11}(1650)$ resonances. The effect of the $S_{11}(1840)$ resonance on the predictions of the existing model of photoproduction [1] is shown in Fig. 2. It can be seen from Figs. 2*a* and 2*d* that this effect is hardly visible at the boundaries of the interval $K_0 = 1.025$–1.9 GeV, whence it follows that the above modification to the model proposed in [1] would not disturb a good description of low-energy experimental data.

The cross section for the process in (1) is model-dependent at small and large η-meson emission angles [1, 8–10]; therefore, experimental data for both small ($\theta < 45^\circ$) and large ($\theta > 135^\circ$) η-meson emission angles are required for discriminating between the existing models. Our isobar model differs from other models of this type [8–10] in that it explicitly involves high-spin resonances [such as $F_{15}(1990)$, $G_{17}(12\,190)$, $G_{19}(2250)$, and $H_{19}(2220)$], which give rise to a substantial anisotropy in the cross section for the process in (1) at $K_0 > 1.5$ GeV (Fig. 2). In view of this, the estimates of the total cross sections derived in [6] from the differential cross sections $d\sigma/d\Omega(\theta)$ measured over the range $45^\circ < \theta < 135^\circ$ cannot be adopted without reservations, since these estimates depend on the method for extrapolating the differential cross sections to the range of angles θ inaccessible to measurements (see [6]).

The inclusion of a third s-wave resonance in our investigation of the reaction in (1) is not of heuristic character because it was long ago predicted by quark models of baryons and was observed in some other processes [6, 9–12]. Our values of its parameters in (2) are in astonishingly good agreement with the parameters of the third S_{11} resonance that were determined from data on the decay process $J/\psi \to p\bar{p}\eta$ [9] ($W_r = 1800 \pm 40$ MeV, $\Gamma_r = 165^{+165}_{-85}$ MeV). However, they are inconsistent with the values resulting from the investigation of the process in (1) on the

1063-7788/04/6702-0427$26.00

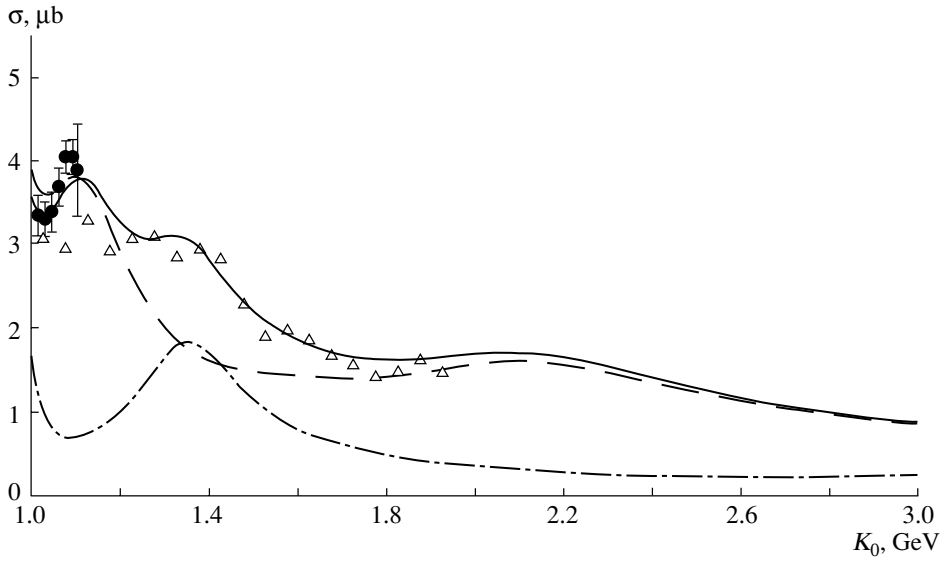

Fig. 1. Integrated cross section for the process $\gamma p \to \eta p$ as a function of the photon energy K_0 in the laboratory frame: (dashed curve) predictions of the model proposed in [1]; (solid curve) the predictions of the analogous model modified by including a third S_{11} resonance whose parameters are set to the values in (2); (dash-dotted curve) results of the calculation that takes into account the background from the model proposed in [1] and the contributions of the s-wave resonances, including a third S_{11} resonance whose parameters are set to the values in (2); and (closed circles and open triangles) experimental data from [3] and [6], respectively.

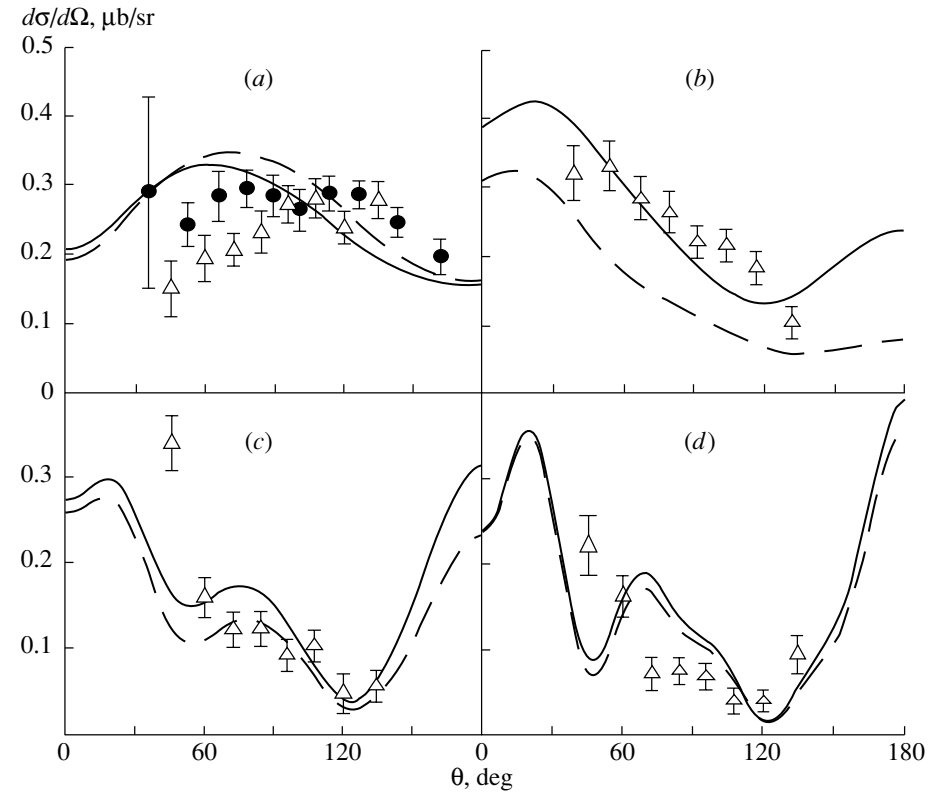

Fig. 2. Differential cross sections $d\sigma/d\Omega$ for the process $\gamma p \to \eta p$ versus the η-meson emission angle θ in the c.m. frame for various values of the incident-photon energy K_0: (*a*) 1025, (*b*) 1325, (*c*) 1625, and (*d*) 1925 MeV. Shown in the figure are the results of the calculations based on (dashed curve) the model proposed in [1] and (solid curve) the analogous model modified by including a third S_{11} resonance whose parameters are set to the values in (2). The displayed experimental data were borrowed from (●) [3] and (△) [6].

basis of the constituent quark model assuming the breakdown of $SU(6) \otimes O(3)$ symmetry [10] ($W_r = 1776$ MeV, $\Gamma_r = 268$ MeV). In discussing new S_{11} resonances, mention should be made of the study performed by Chen *et al.* [11], who present the results of a global analysis of data on pion photoproduction on protons and pion–proton scattering over a wide range of energies and obtained indications of the existence of a third and a fourth S_{11} resonance at $M_r = W_r = 1846 \pm 47$ MeV and $M_r = W_r = 2113 \pm 70$ MeV, respectively. As to their total widths, they were estimated to be above 300 MeV (their specific values remained uncertain). It should also be noted that the process in (1) was successfully described in [12] without introducing an additional s-wave resonance, but such a resonance was required for describing data on the reaction $\gamma p \to \eta' p$. Finally, the position of the third S_{11} resonance according to the predictions of the hypercentral constituent quark model is $W_r = 1861$ MeV [13].

Thus, the S_{11} resonance that is necessary for adequately describing experimental data from [6], but which was disregarded in [1], has the parameter values given in (2), which are consistent with the results of recent theoretical and experimental studies.

REFERENCES

1. V. A. Tryasuchev, Russ. Phys. J. **46**, 403 (2003).
2. B. Krusche, J. Ahrens, G. Anton, *et al.*, Phys. Rev. Lett. **74**, 3736 (1995).
3. F. Renard, M. Anghinolfi, O. Bartaliniet, *et al.*, Phys. Lett. B **528,** 215 (2002).
4. J. Ajaka, M. Anghinolfi, V. Bellini, *et al.*, Phys. Rev. Lett. **81,** 1797 (1998).
5. A. Bock *et al.*, Phys. Rev. Lett. **81**, 534 (1998).
6. M. Dugger, B. G. Ritchie, J. Ball, *et al.*, Phys. Rev. Lett. **89,** 222002 (2002).
7. V. A. Tryasuchev, Yad. Fiz. **65**, 1717 (2002) [Phys. At. Nucl. **65**, 1673 (2002)].
8. W.-T. Chiang, S. N. Yang, L. Tiator, and D. Drechsel, Nucl. Phys. A **700,** 429 (2002).
9. BES Collab. (J. Z. Bai *et al.*), Phys. Lett. B **510**, 75 (2001).
10. B. Saghai and Z. Li, nucl-th/0202007.
11. G.-Y. Chen, S. S. Kamalov, S. Y. Yang, *et al.*, nucl-th/0210013.
12. W.-T. Chiang, S. N. Yang, L. Tiator, *et al.*, nucl-th/0212106.
13. M. M. Giannini, E. Santopinto, and A. Vassalo, nucl-th/0111073.

Translated by R. Rogalyov